MAX-PLANCK-INSTITUT FÜR RADIOASTRONOMIE
BONN

The Influence of Stellar Objects onto the Interstellar Medium: Isotopic Compositions and Maser Lines

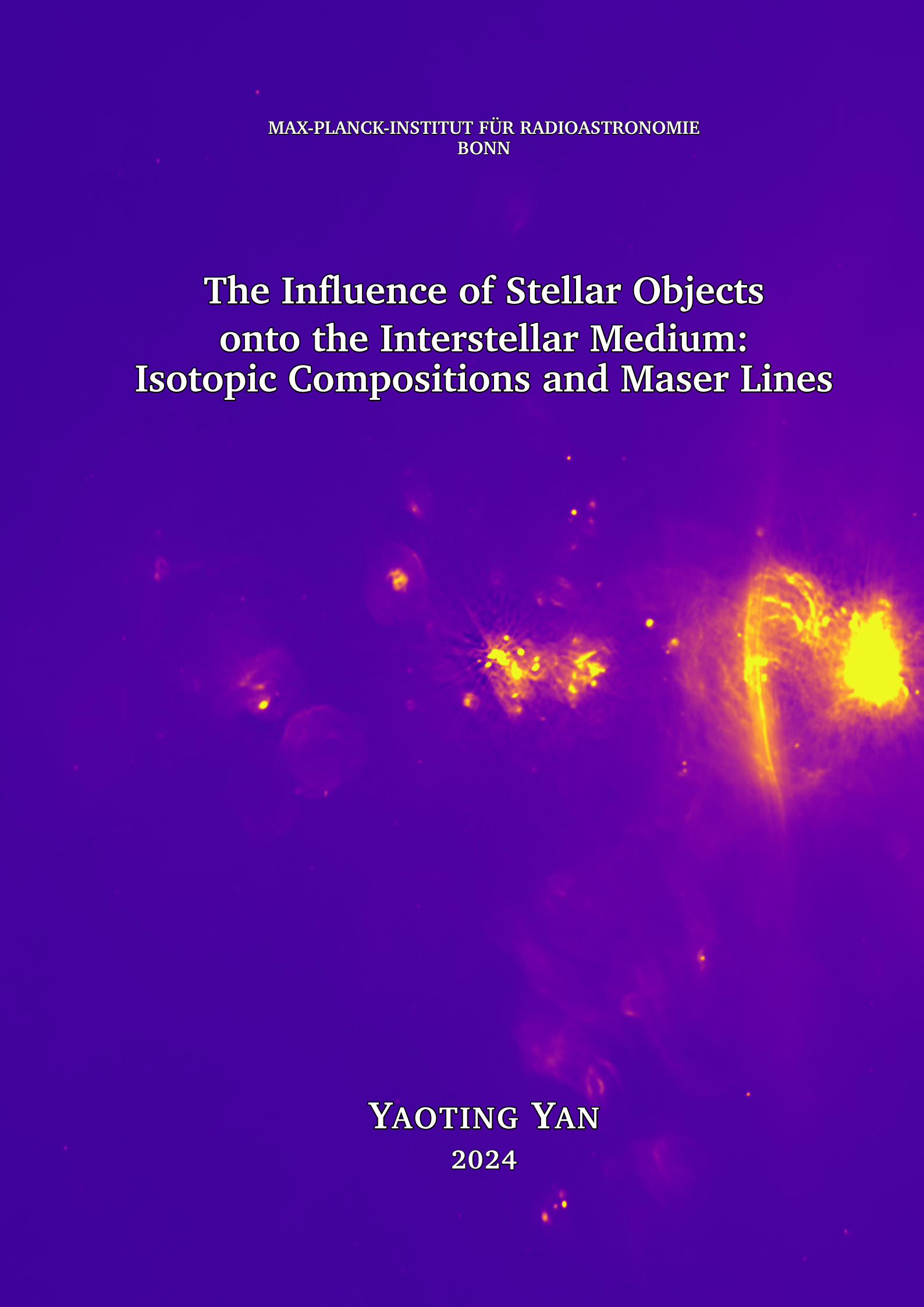

YAOTING YAN

2024

Cover illustration: Radio continuum image of the Galactic center region at a frequency around 6 GHz from the GLObal view on STAR formation in the Milky Way survey (GLOSTAR). One target of this thesis, Sagittarius B2, is located at the center of this figure. Image reproduced with permission from the GLOSTAR team (http://glostar.mpifr-bonn.mpg.de).

MAX-PLANCK-INSTITUT FÜR RADIOASTRONOMIE
BONN

The Influence of Stellar Objects onto the Interstellar Medium: Isotopic Compositions and Maser Lines

Dissertation

zur

Erlangung des Doktorgrades (*Dr. rer. nat.*)

der

Mathematisch-Naturwissenschaftlichen Fakultät

der

Rheinischen Friedrich–Wilhelms–Universität Bonn

vorgelegt von
Yaoting YAN
aus
Shanxi, China

Bonn 2024

Angefertigt mit Genehmigung der Mathematisch-Naturwissenschaftlichen Fakultät
der Rheinischen Friedrich–Wilhelms–Universität Bonn

1. Gutachter/Betreuerin / Referee/Supervisor: Prof. Dr. Karl M. Menten
2. Gutachter / Referee: Prof. Dr. Pavel Kroupa

Tag der Promotion / *Conferral Date*: 22.10.2024
Erscheinungsjahr / *Year of Publication*: 2024

To my grandparents

"The world turns round and round now around 400 years have flown since Galileo's telescope first focused the unknown."

&

"We'll stand on the Shoulders of Giants. And every step follows the one before and opens up a new frontier to explore."

Shoulders of Giants
An AstroCappella song for the International Year of Astronomy 2009

RHEINISCHE FRIEDRICH–WILHELMS–UNIVERSITÄT BONN

Abstract

by Yaoting Yan

for the degree of

Doctor rerum naturalium

This thesis investigates the influence of stellar objects onto the interstellar medium (ISM), following two lines of research, determining isotope ratios over much of the Milky Way and observing interstellar ammonia masers.

Isotope abundance ratios provide a powerful tool to probe stellar nucleosynthesis, to evaluate the composition of stellar ejecta and to constrain the chemical evolution of the Milky Way. With the IRAM 30-meter telescope, we performed observations of the $J = 2{-}1$ and $3{-}2$ rotational transitions of various rare isotopologic variants of carbon monosulfide (CS), namely $C^{33}S$, $C^{34}S$, $C^{36}S$, ^{13}CS, $^{13}C^{33}S$, and $^{13}C^{34}S$, toward a large sample of 110 high-mass star-forming regions (HMSFRs). We measured the $^{12}C/^{13}C$, $^{32}S/^{34}S$, $^{32}S/^{33}S$, $^{32}S/^{36}S$, $^{34}S/^{33}S$, $^{34}S/^{36}S$, and $^{33}S/^{36}S$ abundance ratios based on isotopologues of CS, thus avoiding significant saturation effects. With accurate distances obtained from trigonometric parallaxes, we confirm the previously identified $^{12}C/^{13}C$ and $^{32}S/^{34}S$ gradients as a function of Galactocentric distance. There is no $^{34}S/^{33}S$ gradient, but ratios are well below the values commonly reported in earlier publications. This is a consequence of accounting for the full hyperfine structure splitting of the $C^{33}S$ lines. The average $^{34}S/^{33}S$ value, after corrections for opacity, is 4.35 ± 0.44, which is lower than the value of 5.61 in the solar system. For the first time, we report positive gradients of $^{32}S/^{33}S$, $^{34}S/^{36}S$, $^{33}S/^{36}S$ and $^{32}S/^{36}S$ in our Galaxy. The Galactic $^{12}C/^{13}C$ gradients derived based on measurements of CN, $C^{18}O$, and H_2CO are in agreement with our results from $C^{34}S$ and indicate that chemical fractionation has little effect on $^{12}C/^{13}C$ ratios. It should be noted, however, that $^{12}C/^{13}C$ ratios near the Galactic center are higher than expected by linearly extrapolating data from the Galactic disk. The measured $^{34}S/^{33}S$ ratios as a function of Galactocentric radius indicate that ^{33}S has a nucleosynthesis origin similar to that ^{34}S. Interstellar $^{34}S/^{33}S$ values near the solar neighborhood suggest that the solar system ratio is, as perhaps also the $^{18}O/^{17}O$ ratio, peculiar. Our measurements support that ^{36}S is a purely secondary nucleus; however, we note that data for lines containing this isotope are still sparse, particularly in the inner Galaxy. The predicted $^{12}C/^{13}C$ ratios from the latest Galactic chemical evolution (GCE) models are in good agreement with our results, while our $^{32}S/^{34}S$ and $^{32}S/^{36}S$ ratios show larger differences at larger Galactocentric distances. $^{32}S/^{33}S$ ratios show an offset across the entire inner 12 kpc of the Milky Way. All of this can serve as a guideline for further refinements of GCE models.

Molecular maser lines are signposts of star formation, probing the excitation and kinematics of very compact regions in the close environment of young stellar objects and

providing useful targets for trigonometric parallax measurements. With the Effelsberg 100-m telescope, we discovered widespread non-metastable NH_3 maser emission toward 17 high mass star forming regions (HMSFRs) in the Milky Way. This doubles the number of known non-metastable ammonia masers in our Galaxy. These maser lines arise from energy levels between 342 K up and 1449 K above the ground state and probe the hot dense immediate neighborhoods of newly formed stars. With our higher angular resolution interferometric measurements from the Karl G. Jansky Very Large Array (JVLA), we determined detailed locations for maser spots emitted in multiple non-stable transitions toward a variety of regions. We greatly increase the number of detections in the Galaxy in all the lines targeted. The detected maser spots are not resolved by our JVLA observations. Lower limits to the brightness temperature are >400 K and reach values up to several 10^5 K, manifesting the lines' maser nature. In view of the masers' velocity differences with respect to adjacent hot molecular cores and/or ultra-compact (UC) HII regions, it is argued that all the measured ammonia maser lines may be associated with shocks caused either by outflows or by the expansion of UCHII regions. Furthermore, we recently detected linear and circular polarization of NH_3 masers in Sgr B2.

List of publications

Relevant First-Author Publications

The following list indicates the relevant first-author publications that are discussed and presented in this thesis. This dissertation research project resulted in four peer-reviewed and published research publications. In addition, one more manuscript is in preparation for submission to the Astrophysics & Astronomy journal.

1. **Yan, Y. T.**; Henkel, C.; Kobayashi, C.; Menten, K. M.; Gong, Y.; Zhang, J. S.; Yu, H. Z.; Yang, K.; Xie, J. J.; Wang, Y. X.; (2023), *Direct measurements of carbon and sulfur isotope ratios in the Milky Way*, Astronomy & Astrophysics, 670, A98. DOI:10.1051/0004-6361/202244584

   Author's Contribution: Y. T. Y. provided useful comments and helped improve the observational proposals, projects of 045-19 (PI, C. H.) and 022-20 (PI, H. Z. Y.), for the IRAM 30-meter telescope. Y. T. Y. performed the observations under project 022-20 in 2020 August remotely at Köln. Y. T. Y. handled the scientific analysis and wrote the manuscript under supervision. Y. T. Y. used the molecular parameters from the Cologne Database for Molecular Spectroscopy and Python scripts provided by Y. G. to check the Local Thermodynamic Equilibrium (LTE) deviations. C. K. provided the results and parameters of the Galactic chemical evolution model. All of the Co-authors gave useful comments and improved the manuscript.

2. **Yan, Y. T.**; Henkel, C.; Menten, K. M.; Gong, Y.; Ott, J.; Wilson, T. L.; Wootten, A.; Brunthaler, A.; Zhang, J. S.; Chen, J. L.; Yang, K.; (2022), *Discovery of ammonia (9,6) masers in two high-mass star-forming regions*, Astronomy & Astrophysics, 659, A5. DOI:10.1051/0004-6361/202142891

   Author's Contribution: Y. T. Y. performed remote observations with the Effelsberg 100-meter telescope at Bonn in 2020 January as well as at Köln in 2021. Y. T. Y. wrote and proposed a proposal to the Karl G. Jansky Very Large Array (JVLA) and got accepted as a priority of B in semester 21A C-configuration (project ID: 21A-157). Y. T. Y. performed data reduction with the GILDAS/CLASS package and the Common Astronomy Software Applications package (CASA) for single dish and interferometry data, respectively. Y. T. Y. wrote the manuscript under supervision. All of the Co-authors gave useful comments and suggestions to the proposal and manuscript.

3. **Yan, Y. T.**; Henkel, C.; Menten, K. M.; Gong, Y.; Nguyen, H.; Ott, J.; Ginsburg A., Wilson, T. L.; Brunthaler, A.; Belloche, A.; Zhang, J. S.; Budaiev, N.; Jeff, D.; (2022), *Discovery of non-metastable ammonia masers in Sagittarius B2*, Astronomy & Astrophysics, 666, L15. DOI:10.1051/0004-6361/202245024

Author's Contribution: Y. T. Y. performed remote observations with the Effelsberg 100-meter telescope at Bonn on 2020 January 3 as well as at Köln in 2021 and 2022. Y. T. Y. wrote and proposed a proposal to the Karl G. Jansky Very Large Array (JVLA) and got accepted as a priority of A in semester 22A A-configuration (project ID: 22A-106). Y. T. Y. performed data reduction with the GILDAS/CLASS package and the Common Astronomy Software Applications package (CASA) for single dish and interferometry data, respectively. Moreover, Y. T. Y. identified maser spots in two different ways, a normal method by eyes and an automated program of source extraction code (SEC) within CASA. Y. T. Y. wrote the manuscript under supervision. H. N. provided the SEC and guided Y. T. Y. how to use it. All of the Co-authors gave useful comments and suggestions to the proposal and manuscript.

4. **Yan, Y. T.**; Henkel, C.; Menten, K. M.; Wilson, T. L.; Wootten, A.; Gong, Y.; Wyrowski, F.; Yang, W.; Brunthaler, A.; Kraus, A.; Winkel, B.; (2024), *Discovery of widespread non-metastable ammonia masers in the Milky Way*, Astronomy & Astrophysics, 686, A205. DOI:10.1051/0004-6361/202348931

   Author's Contribution: Y. T. Y. wrote the Effelsberg proposal (project ID: 34-22) under supervision. Y. T. Y. performed the observations remotely at Köln from 2023 February to May as well as on July 3. Y. T. Y. calibrated and reduced the data. Y. T. Y. wrote the manuscript under supervision. All of the Co-authors gave useful comments and suggestions to the proposal and manuscript. In addition, Y. G. did the remote observation at Bonn on November 27, 2022. A. K. and B. W. provided help with the observations and data reduction.

5. **Yan, Y. T.**; Surcis, G.; Henkel, C.; Lankhaar, B.; Gong, Y.; Nguyen, H.; Wilson, T. L.; Menten, K. M.; *Polarization measurements of ammonia masers in Sagittarius B2*, in preparation

   Author's Contribution: Y. T. Y. performed the polarization calibration to the JVLA data (project ID: 22A-106) and did the primary calculation for polarized masers. Y. T. Y. wrote the manuscript under supervision. G. S. checked the linear and circular polarization detections as well as re-calculated the polarization parameters and plotted the related spectra. B. L. will perform the calculation of the radiative transfer model for the ammonia lines.

Relevant Co-Authored Publications

The author of this dissertation has contributed as a co-author to these papers throughout the duration of this thesis project.

1. Zhu, Feng-Yao; Wang, Junzhi; **Yan, Yaoting**; Zhu, Qing-Feng; Li, Juan; (2023), *Origins of the shocks in high-mass starless clump candidates*, Monthly Notices of the Royal Astronomical Society, 523, 2770Z. 10.1093/mnras/stad1604

   Author's Contribution: Y. T. Y. performed the remote observations with the IRAM 30-meter telescope at Bonn in 2020 April. Y. T. Y. provided useful comments which have improved the manuscript.

2. Zhao, J. Y.; Zhang, J. S.; Wang, Y. X.; Qiu, J. J.; **Yan, Y. T.**; Yu, H. Z.; Chen, J. L.; Zou, Y. P.; (2023), *A Multitransition Methanol Survey toward a Large Sample of High-mass Star-forming Regions*, The Astrophysical Journal Supplement, 266, 29. 10.3847/1538-4365/acc323

   Author's Contribution: Y. T. Y. performed the remote observations with the IRAM 30 meter telescope at Köln in 2020 August and September as well as in 2021 April. Y. T. Y. provided useful comments which have improved the manuscript.

3. Zhu, Feng-Yao; Wang, Junzhi; **Yan, Yaoting**; Zhu, Qing-Feng; Li, Juan; (2023), *Spatial distributions and kinematics of shocked and ionized gas in M17*, Monthly Notices of the Royal Astronomical Society, 522, 503Z. 10.1093/mnras/stad996

   Author's Contribution: Y. T. Y. performed the remote observations with the IRAM 30-meter telescope at Köln from 2020 December to 2021 January. Y. T. Y. provided useful comments which have improved the manuscript.

4. Wang, Y. X.; Zhang, J. S.; Yu, H. Z.; Wang, Y.; **Yan, Y. T.**; Chen, J. L.; Zhao, J. Y.; Zou, Y. P.; (2023), *A Possible Chemical Clock in High-mass Star-forming Regions: $N(HC_3N)/N(N_2H^+)$?*, The Astrophysical Journal Supplement, 264, 48. 10.3847/1538-4365/acafe6

   Author's Contribution: Y. T. Y. performed the remote observations with the IRAM 30-meter telescope at Köln in 2020 August. Y. T. Y. provided useful comments which have improved the manuscript.

5. Qiu, Jian-Jie; Zhang, Yong; Nakashima, Jun-ichi; Zhang, Jiang-Shui; Koning, Nico; Tang, Xin-Di; **Yan, Yao-Ting**; Feng, Huan-Xue; (2023), *Molecules in the peculiar age-defying source IRAS 19312+1950*, Astronomy & Astrophysics, 669, A121. 10.1051/0004-6361/202244559

Author's Contribution: Y. T. Y. provided useful comments and suggestions which have improved the manuscript.

6. Wang, Y. X.; Zhang, J. S.; **Yan, Y. T.**; Qiu, J. J.; Chen, J. L.; Zhao, J. Y.; Zou, Y. P.; Wu, X. C.; He, X. L.; Gong, Y. B.; Cai, J. H.; (2022), *Cyanopolyyne line survey towards high-mass star-forming regions with TMRT*, Astronomy & Astrophysics, 663, A177. DOI:10.1051/0004-6361/202142450

   Author's Contribution: Y. T. Y. provided useful comments which have improved the manuscript.

7. Chen, J. L.; Zhang, J. S.; Henkel, C.; **Yan, Y. T.**; Yu, H. Z.; Qiu, J. J.; Tang, X. D.; Wang, J.; Liu, W.; Wang, Y. X.; Zheng, Y. H.; Zhao, J.; (2021), *Interstellar Nitrogen Isotope Ratios: New NH_3 Data from the Galactic Center out to the Perseus Arm*, The Astrophysical Journal Supplement, 257, 39. DOI:10.3847/1538-4365/ac205a

   Author's Contribution: C. H. derived Y. T. Y. to the Effelsberg 100-meter telescope in 2019 December. Y. T. Y. performed the observations on-site at Effelsberg in 2019 December and remotely at Bonn in 2020 January. Y. T. Y. performed the calibration to the Effelsberg raw data with help from Benjamin Winkel at MPIfR. Furthermore, Y. T. Y. provided help on the calculations of the RADEX non-LTE model. Y. T. Y. gave comments and suggestions which improved the manuscript.

8. Martín, S.; Mangum, J. G.; Harada, N.; Costagliola, F.; Sakamoto, K.; Muller, S.; Aladro, R.; Tanaka, K.; Yoshimura, Y.; Nakanishi, K.; Herrero-Illana, R.; Mühle, S.; Aalto, S.; Behrens, E.; Colzi, L.; Emig, K. L.; Fuller, G. A.; García-Burillo, S.; Greve, T. R.; Henkel, C.; Holdship, J.; Humire, P.; Hunt, L.; Izumi, T.; Kohno, K.; König, S.; Meier, D. S.; Nakajima, T.; Nishimura, Y.; Padovani, M.; Rivilla, V. M.; Takano, S.; van der Werf, P. P.; Viti, S.; **Yan, Y. T.**; (2021), *ALCHEMI: an ALMA Comprehensive High-resolution Extragalactic Molecular Inventory. Survey presentation and first results from the ACA array*, Astronomy & Astrophysics, 656, A46. DOI:10.1051/0004-6361/202141567

   Author's Contribution: Y. T. Y. provided useful comments which have improved the manuscript.

9. Xie, Jin-Jin; Wu, Jing-Wen; Fuller, Gary A.; Peretto, Nicolas; Ren, Zhi-Yuan; Chen, Long-Fei; **Yan, Yao-Ting**; Li, Guo-Dong; Duan, Yan; Xia, Ji-Feng; Wang, Yong-Xiong; Li, Di.; (2021), *Studying infall in infrared dark clouds with multiple HCO^+ transitions*, Research in Astronomy and Astrophysics, 21, 208. DOI:10.1088/1674-4527/21/8/208

   Author's Contribution: Y. T. Y. provided useful comments which have improved the manuscript. In addition, Y. T. Y. helped to produce some spectra.

10. Yu, H. Z.; Zhang, J. S.; Henkel, C.; **Yan, Y. T.**; Liu, W.; Tang, X. D.; Langer, N.; Luan, T. C.; Chen, J. L.; Wang, Y. X.; Deng, G. G.; Zou, Y. P.; (2020), *Galactic Interstellar Sulfur Isotopes: A Radial* $^{32}S/^{34}S$ *Gradient?*, The Astrophysical Journal, 899, 145. DOI:10.3847/1538-4357/aba8f1

    Author's Contribution: Y. T. Y. provided useful comments which have improved the manuscript.

11. Zhang, J. S.; Liu, W.; **Yan, Y. T.**; Yu, H. Z.; Liu, J. T.; Zheng, Y. H.; Romano, D.; Zhang, Z. -Y.; Wang, J. Z.; Chen, J. L.; Wang, Y. X.; Zhang, W. J.; Lu, H. H.; Chen, L. S.; Zou, Y. P.; Yang, H. Q.; Wen, T.; Lu, F. S.; (2020), *A Systematic Observational Study on Galactic Interstellar Ratio* $^{18}O/^{17}O$*. I.* $C^{18}O$ *and* $C^{17}O$ *J = 1-0 Data Analysis*, The Astrophysical Journal Supplement, 249, 6. DOI:10.3847/1538-4365/ab9112

    Author's Contribution: Y. T. Y. provided useful comments which have improved the manuscript.

Contents

Chapter 1

Introduction

Overview

Curiosity has been driving humans to explore the universe, its past, present, and potential future. When we look up into the sky with our naked eyes at night at places that are far away from the activities of humans, we can see thousands of stars. We may question what exists between these stars, is it empty because it is black? The question is no. On the opposite, it is filled up with interstellar matter, gas, and dust. It is the interstellar medium (ISM). Stars, born inside the ISM from interstellar gas and dust, spend their whole lives in the ISM, enriching its chemical composition by providing feedback when they die. Energies and baryons are then transferred into different phases of the interstellar medium as shown in Fig. 1.1. Gas and dust in the ISM play a key role in this life cycle. The interaction between stars and ISM is complicated and not fully understood. The aim of this thesis is to study the influence of stellar objects on the ISM in the Milky Way from two different perspectives and to further help us to better understand star formation.

The first line of research we pursued is isotopic composition. The most interesting and important element is carbon, which is the basic element of life on Earth. ^{12}C is mainly formed in massive stars on short timescales by Helium burning, and is thus called a predominantly primary isotope (e.g., Timmes et al. 1995). In contrast, ^{13}C is produced via CNO processing with seeds of ^{12}C from earlier stellar generations in low- and intermediate-mass stars or novae (e.g., Henkel et al. 1994; Meyer 1994; Wilson & Rood 1994). It is a secondary isotope. The primary to secondary isotope ratios can help us to trace stellar nucleosynthesis, to evaluate the composition of stellar ejecta, and to constrain the chemical evolution of the Milky Way. In this thesis, the molecule of interest is carbon monosulfide (CS). It is a simple diatomic molecule exhibiting strong line emission and possessing eight stable isotopologues, which allows us not only to determine the carbon isotope ratios but also the so far poorly studied sulfur isotope ratios.

Stars can also excite maser emission through their radiation or by triggering specific collisional processes. Maser is an acronym for "microwave amplification by stimulated emission of radiation". The first detection of an interstellar ammonia maser was made in the $(J, K) = (3,3)$ metastable line toward the massive star-forming region W33 (Wilson et al. 1982). The search for ammonia masers in the ISM is more difficult than that for other molecular maser species, e.g., H_2O and CH_3OH. Ammonia masers turn out to be less frequent. The second goal of this thesis is thus to study these comparatively rare ammonia masers in the Milky Way and to try to find connections

Table 1.1: Table of some relevant ISM phases, adapted from Draine (2011), Snell (2015), and Girichidis et al. (2020).

Component	Temperature (K)	Density (cm^{-3})	Fractional ionization
Stellar outflows	50–10^3	1–10^6	···
Molecular gas	10–20	$> 10^2$	$< 10^{-6}$
Cold neutral medium (CNM)	50–100	20–50	$\sim 10^{-4}$
Warm neutral medium (WNM)	6×10^3–10^4	0.2–0.5	~ 0.1
Warm ionized medium (WIM)	$\sim 8\times10^3$	0.2–0.5	1.0
HII regions	10^4	1–10^4	1.0
Hot ionized medium (HIM)	$\sim 10^6$	$\sim 10^{-2}$	1.0

between ammonia masers and stellar activity.

1.1 The interstellar medium

The ISM hosts about 10% of the baryons in our Galaxy (Draine 2011). It is mainly composed of interstellar gas, mostly hydrogen and helium, and small solid dust particles and has a gas-to-dust mass ratio of ~ 100. The ISM is pervaded by cosmic ray particles produced by energetic stellar processes, irradiated by electromagnetic radiation, and influenced by an interstellar magnetic field and by gravitation. All the components mentioned above together lead to an ISM being active and complex. The temperatures and number densities of the ISM range from 10 to 10^7 Kelvins and from 10^{-2} to 10^9 cm^{-3}, respectively. Therefore, the ISM can be divided into several main phases. These include the hot ionized medium (HIM), the HII regions, the warm ionized medium (WIM), the warm neutral medium (WNM), the cold neutral medium (CNM), the molecular gas, and stellar outflows.

The HIM is the component with the highest temperatures in the ISM that could exceed one million Kelvin, which is similar to the temperatures of the solar corona and is so also called coronal gas. Gas in this phase is collisionally ionized due to supernova explosions. Its density is extremely low, at only about 10^{-2} cm^{-3}. The HII regions have temperatures of about 10^4 K and are clouds of hot plasma mainly consisting of electrons and protons, formed from the photoionization of hydrogen caused by the ultraviolet radiation from nearby massive stars. The density of HII regions can range from 1 to 10^6 cm^{-3}. When the densities go down to about 0.2–0.5 cm^{-3} and temperatures are about 10^3 K, another phase appears, called the warm ionized medium (WIM). It is widespread and contains at least 90% of the ionized hydrogen within the interstellar medium (Haffner et al. 2009). The neutral gas in the ISM can be divided into two different phases: the warm neutral medium (WNM) and the cold neutral medium (CNM). Molecular gas commonly has a lower temperature and a higher density in the CNM than in the WNM. In regions of dense molecular gas, star formation could precede. Stellar outflows are the feedback from both high- and low-mass stars into the ISM. All of these phases of the ISM are summarized in Table 1.1.

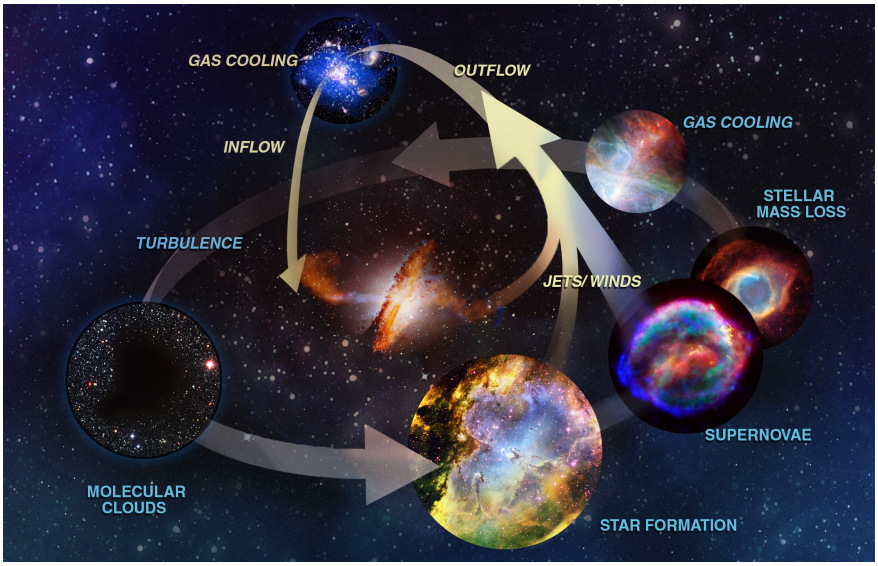

Figure 1.1: The life cycle of baryons [Credits: NASA/JPL; Habitable Exoplanet Observatory (HabEx) Final Report 2019].

Stars are born in the ISM, and almost all of them spend their whole lives in the ISM enriching the chemical components of the ISM and providing feedback to the ISM during specific (mostly late) phases of their life. The energies and baryons are transferred into different phases in this cycle as shown in Fig. 1.1. The interaction between stars and the ISM is complicated and still not completely understood.

1.2 The origin of elements

In the very early phase right after the Big Bang, only helium and a small amount of lithium were created from hydrogen nuclei in significant quantities. In astrophysics, elements heavier than He are called 'metals'. Carbon and heavier elements were produced much later in the interior of stars. The pioneering work on nucleosynthesis in massive stars was conducted by Hoyle (1946, 1954), Burbidge et al. (1957), and Cameron (1957). We now know that a dense molecular cloud may collapse under its own gravity and begin to heat up until the temperature is high enough to start nuclear hydrogen fusion. Then a new star is born. H burning converts ^{1}H into ^{4}He via the proton-proton (pp) chain and the carbon-nitrogen-oxygen (CNO) cycles in stars with masses smaller and larger than 1.2 solar mass, respectively. A He core is then created in the star's center, continues to grow by H burning, and heating up. He burning starts to generate heavier elements like carbon, oxygen, and some neon. The low and intermediate-mass stars ($M < 8M_{\odot}$) evolve through the asymptotic giant branch (AGB) and planetary nebula stage, resulting in white dwarfs after He burning has ended. Massive stars continue to burn with heavier elements as fuel, i.e., carbon burning, neon burning, oxygen burning, and silicon burning, resulting in an iron core in the center. An onion-like structure with different shells composed of different elements, shown in Figure 1.2, is

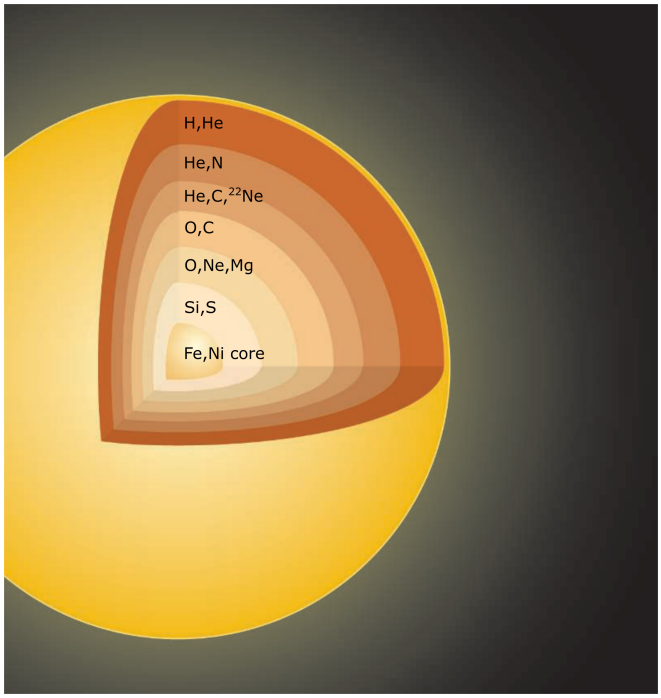

Figure 1.2: An onion-like structure with different element shells in a massive star, taken from Clayton (2007).

formed inside a massive star before it becomes a core-collapse supernova. Such events as well as other physical processes could produce much heavier nuclei than ^{56}Fe. These include type II supernovae (SNe II), hypernovae (HNe), electron-capture supernovae (ECSNe), and magneto-rotational supernovae (MRSNe). The evolution of the origin of elements from different nucleosynthesis processes at different cosmic times in the periodic table is shown in Figure 1.3.

Metals synthesized in one stellar generation are called primary elements. The secondary element formation requires pre-existing nuclei from the primary processes in stars. Therefore the primary to secondary element ratios can provide us with the history of stellar nucleosynthesis and help us to study the influence of stars onto the ISM.

1.3 Isotopic compositions

Isotope abundance ratios provide a powerful tool for tracing stellar nucleosynthesis, evaluating the composition of stellar ejecta, and constraining the chemical evolution of the Milky Way (Wilson & Rood 1994). In particular, the ^{12}C/^{13}C ratio is one of the most useful tracers of the relative degree of primary to secondary processing. ^{12}C is a predominantly primary nucleus formed by He burning in massive stars on short timescales (e.g., Timmes et al. 1995). ^{13}C is produced on a longer timescale via CNO processing of ^{12}C seeds from earlier stellar generations during the red giant phase in

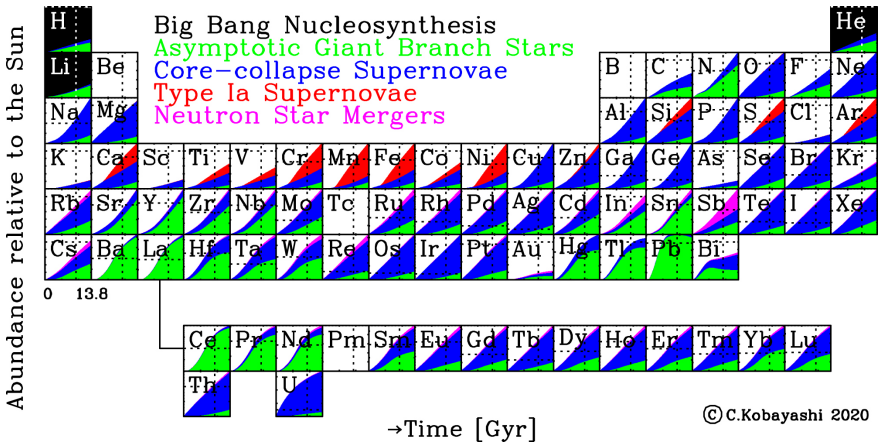

Figure 1.3: The evolution of the origin of elements at different cosmic times in the periodic table, taken from Kobayashi et al. (2020). Different processes related to different objects are shown in different colors. Big Bang nucleosynthesis is presented in black, and stellar nucleosynthesis in AGB stars is shown in green. The contribution of core-collapse supernovae is shown in blue. The enhancement of elements from type Ia supernovae (SNe Ia) and neutron-star mergers (NSMs) are presented in red and magenta, respectively.

low- and intermediate-mass stars or novae (e.g., Henkel et al. 1994; Meyer 1994; Wilson & Rood 1994). $^{12}C/^{13}C$ ratios are expected to be low in the central molecular zone (CMZ) around the Galactic center and high in the Galactic outskirts, because the Galaxy formed from inside out (e.g., Chiappini et al. 2001; Pilkington et al. 2012).

Observations indeed indicate a gradient of $^{12}C/^{13}C$ ratios across the Galaxy. Wilson et al. (1976) and Whiteoak & Gardner (1979) measured the $J_{Ka,Kc} = 1_{1,0} - 1_{1,1}$ lines of $H_2^{12}CO$ and $H_2^{13}CO$ near 5 GHz toward 11 and 24 Galactic continuum sources, respectively. While ignoring the effects of photon trapping, the results suggested that the $^{12}C/^{13}C$ ratios may vary with galactocentric distance (R_{GC}). With the additional measurement of the $J_{Ka,Kc} = 2_{1,1} - 2_{1,2}$ line of H_2CO at 14.5 GHz, Henkel et al. (1980, 1982, 1983, 1985) also reported a gradient after correcting for effects of optical depth and photon trapping. Langer & Penzias (1990) used the optically thin lines of $C^{18}O$ and $^{13}C^{18}O$ to trace the carbon isotope ratios. They also found a systematic $^{12}C/^{13}C$ gradient across the Galaxy, ranging from about 20–25 near the Galactic center, to 30–50 in the inner Galactic disk, to ∼70 in the local interstellar medium (ISM). Wouterloot & Brand (1996), complementing these investigations by also including the far outer Galaxy, encountered ratios in excess of 100 and demonstrated that the gradient found in the inner Galaxy continues farther out. Milam et al. (2005) obtained $^{12}C/^{13}C = 6.01R_{GC} + 12.28$ based on the CN measurements of Savage et al. (2002). Here and elsewhere, R_{GC} denotes the galactocentric distance in units of kiloparsecs (kpc). By combining previously obtained H_2CO and $C^{18}O$ results with these CN data, Milam et al. (2005) obtained $^{12}C/^{13}C = 6.21R_{GC} + 18.71$.

More recently, Halfen et al. (2017) reported observations of a variety of molecules

(e.g., H_2CS, CH_3CCH, NH_2CHO, CH_2CHCN, and CH_3CH_2CN) and their ^{13}C-substituted species toward Sgr B2(N). These authors obtained an average $^{12}C/^{13}C$ value of 24 ± 7 in the Galactic center region, which is close to results using $^{12}CH/^{13}CH$ (15.8 ± 2.4, Sgr B2(M)) by Jacob et al. (2020) and the particularly solid $^{12}C^{34}S/^{13}C^{34}S$ ratio ($22.1^{+3.3}_{-2.4}$, +50 km s^{-1} Cloud) from Humire et al. (2020) who used a variety of CS isotopologues and rotational transitions. Yan et al. (2019) proposed a linear fit of $^{12}C/^{13}C = (5.08 \pm 1.10)R_{GC} + (11.86 \pm 6.60)$ based on a large survey of H_2CO. The latter includes data from the center to the outskirts of the Milky Way well beyond the Perseus Arm. However, data from the CMZ are underrepresented and the assumption of a linear gradient encompassing both the disk and the central molecular zone is not quite fulfilled (see also Appendix A). Also the number of sources beyond the Perseus arm was small, meaning that there is still space for improvement.

While the carbon isotope ratio has drawn much attention in the past, it is not the only isotope ratio that can be studied at radio wavelengths and that has a significant impact on our understanding of the chemical evolution of the Galaxy. The isotope ratios of sulfur are providing complementary information on stellar nucleosynthesis that is not traced by the carbon isotope ratio. Sulfur is quite special in that it provides a total of four stable isotopes, ^{32}S, ^{34}S, ^{33}S, and ^{36}S. In the Solar System, their abundance ratios are 95.02 : 4.21 : 0.75 : 0.021, respectively (Anders & Grevesse 1989). ^{32}S and ^{34}S are synthesized during stages of hydrostatic oxygen-burning preceding a type II supernova event or during stages of explosive oxygen-burning in a supernova of type Ia. ^{33}S is synthesized in explosive oxygen- and neon-burning, which is also related to massive stars. The s-process nucleosynthesis reduces the amount of ^{33}S and transfers it to ^{30}Si (Clayton 2007). ^{36}S may be an s-process nucleus. The comprehensive calculations of Woosley & Weaver (1995) indicate that ^{32}S and ^{33}S are primary (in the sense that the stellar yields do not strongly depend on the initial metallicity of the stellar model), while ^{34}S is not a clean primary isotope; its yield decreases with decreasing metallicity. According to Thielemann & Arnett (1985) and Langer (1989), ^{36}S is produced as a purely secondary isotope in massive stars, with a possible (also secondary) contribution from asymptotic giant branch (AGB) stars. Only a small fraction of ^{36}S is destroyed during supernova explosions (Woosley, priv. comm.). Comparing "primary" and "secondary" nuclei, we might therefore expect the presence of weak $^{32}S/^{34}S$ and $^{34}S/^{33}S$ gradients and a stronger $^{32}S/^{36}S$ gradient as a function of galactocentric radius.

There is a strong and widespread molecular species that allows us to measure carbon and sulfur isotope ratios simultaneously, namely carbon monosulfide (CS). CS is unique in that it is a simple diatomic molecule exhibiting strong line emission and possessing eight stable isotopologues, which allows us to determine the above-mentioned carbon and sulfur isotope ratios. Six isotopologues have been detected so far in the ISM (e.g., Chin et al. 1996; Mauersberger et al. 1996; Humire et al. 2020; Yu et al. 2020).

Making use of the CS species, Chin et al. (1996) and Mauersberger et al. (1996) obtained average abundance ratios of 24.4 ± 5.0, 6.3 ± 1.0, and 115 ± 17 for $^{32}S/^{34}S$, $^{34}S/^{33}S$, and $^{34}S/^{36}S$ for the ISM, respectively. The latter is approximately half the solar value, but similar to the value found in IRC+10216 (Mauersberger et al. 2004). Recently, Humire et al. (2020) published $^{32}S/^{34}S$ ratios of $16.3^{+2.1}_{-1.7}$ and 17.9 ± 5.0 for

the +50 km s^{-1} cloud and Sgr B2(N) near the Galactic center, respectively. These are only slightly lower than the value of 22 in the Solar System. There is an obvious and confirmed $^{32}S/^{34}S$ gradient (Chin et al. 1996; Yu et al. 2020) from the inner Galaxy out to a galactocentric distance of 12.0 kpc. Nevertheless, there is a lack of data at small and large galactocentric distances.

We have thus performed a more systematic study on CS and its isotopologues toward 110 high-mass star-forming regions (HMSFRs). $^{12}C/^{13}C$ and $^{32}S/^{34}S$ ratios can be directly derived from integrated $^{12}C^{34}S/^{13}C^{34}S$ (hereafter $C^{34}S/^{13}C^{34}S$) and $^{13}C^{32}S/^{13}C^{34}S$ (hereafter $^{13}CS/^{13}C^{34}S$) intensities, respectively. Also, $^{34}S/^{33}S$ and $^{34}S/^{36}S$ values could be obtained with measurements of $C^{34}S$, $^{12}C^{33}S$ (hereafter $C^{33}S$), and $^{12}C^{36}S$ (hereafter $C^{36}S$). Furthermore, $^{32}S/^{33}S$ and $^{32}S/^{36}S$ ratios can then be derived with the resulting $^{34}S/^{33}S$ and $^{34}S/^{36}S$ values combined with the $^{32}S/^{34}S$ ratios. The analysis and results are presented in Sections 3 and Appendix A.

1.4 Ammonia masers

1.4.1 Physics of the ammonia molecule

The ammonia (NH_3) molecule has a pyramidal shape with a base plane of three hydrogen atoms and a nitrogen atom at the top. It is a symmetric top molecule with inversion (Fig. 1.4) and well studied in laboratory microwave spectroscopy (Townes & Schawlow 1955, 1975; Kukolich 1967). Several properties make NH_3 unique and very useful especially in astrophysics. The rotational states of NH_3 are represented by two principal quantum numbers (J, K). J is the total angular momentum quantum number and K is the projection of J onto the NH_3 symmetry axis. For each K-ladder, the lowest states, for which $(J = K)$, are called metastable states because they can only decay very slow (10^9 s) through $\Delta\ k{=}\pm3$ ($K = |k|$) transitions (Oka et al. 1971). The upper states ($J > K$) can decay relatively rapidly (10–100 s) through far-infrared $\Delta\ J{=}\pm1$, $\Delta\ k{=}\pm0$ transitions and are called non-metastable. Thus the metastable states can easily be populated via $\Delta\ k{=}\pm3$ collisional processes, while non-metastable states will be difficult to be populated in normal astrophysical environments.

There are two distinct NH_3 species that exist because of the orientations of the hydrogen atom spins. These are ortho-NH_3 ($K = 0$ *or* $3n$, n an integer, all H spins parallel) and para-NH_3 ($K \neq 3n$, at least one H spin not parallel). Transitions between ortho- and para-NH_3 are forbidden because normal collisional and radiative transitions do not change the spin orientations (Ho & Townes 1983).

Besides the rotational motions, the NH_3 molecule also has vibrational motions. The inversion splitting of each rotational level arises from the hindered vibrational motion of the nitrogen through the plane of the three hydrogen atoms, as illustrated in Fig. 1.4 (e.g., Townes & Schawlow 1955; Morris et al. 1973). The inversion doublets for rotational states with $K{=}0$ are not allowed due to the Pauli exclusion principle (Laughton et al. 1976). The inversion transitions ($\Delta\ J{=}\pm0$, $\Delta\ K{=}\pm0$) of the vibrational ground states of NH_3 are in the microwave range. Figure 1.5 shows the energy-level diagram of the vibrational ground state of ammonia up to an energy level as high as around

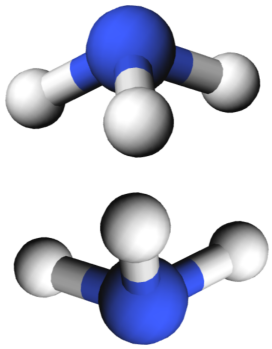

Figure 1.4: The inversion of the ammonia molecule. The three-dimensional rendering of ammonia is taken from PubChem (https://pubchem.ncbi.nlm.nih.gov/), an open chemistry database.

1600 K. Each inversion transition's lower level is presented at its real energy value while the distance to the upper level is exaggerated. As mentioned before, metastable states can easily be populated via $\Delta\ k{=}\pm3$ collisional processes. Thus thermally excited transitions in the $\lambda\sim$1cm wavelength inversion transitions of ammonia are regarded as a reliable thermometer of molecular clouds (e.g., Walmsley & Ungerechts 1983; Danby et al. 1988). In the ISM the ammonia molecule was discovered five decades ago (Cheung et al. 1968). Furthermore, the hyperfine structure interactions between the electric quadrupole moment of the ^{14}N nucleus and the electric field of the electrons can split the inversion doublets. The hyperfine structure can be used to directly evaluate the opacities of NH_3 emission and is very useful for determining NH_3 column densities in the ISM.

1.4.2 The maser principle

Stimulated emission was established as a theoretical concept in Albert Einstein's 1917 paper, "*On the quantum theory of radiation*" (Einstein 1917). When an atom is in the excited state, there are two ways to give off its energy in the form of emission of radiation. The first one is spontaneous emission of radiation, in this case, an atom emits its energy without any external causation. Another one is stimulated emission of radiation when an excited atom emits its energy due to interaction with an external radiation field. Two quanta, the external one and the one emitted by the atom itself, will be involved in this phenomenon. Their frequencies and directivities coincide and thus these two quanta are indistinguishable. This induced emission led scientists started to think stimulated emission might in principle give amplification(Tolman 1924). The probability of an induced emission is often small in normal situations. In thermal equilibrium, the spontaneous emission dominates, and, with respect to the statistical weights, more atoms/molecules are at a lower energy level and not in the excited states. To make such a significantly induced emission happen, one needs the population of the excited state, which is larger than the one in the ground state. This is population

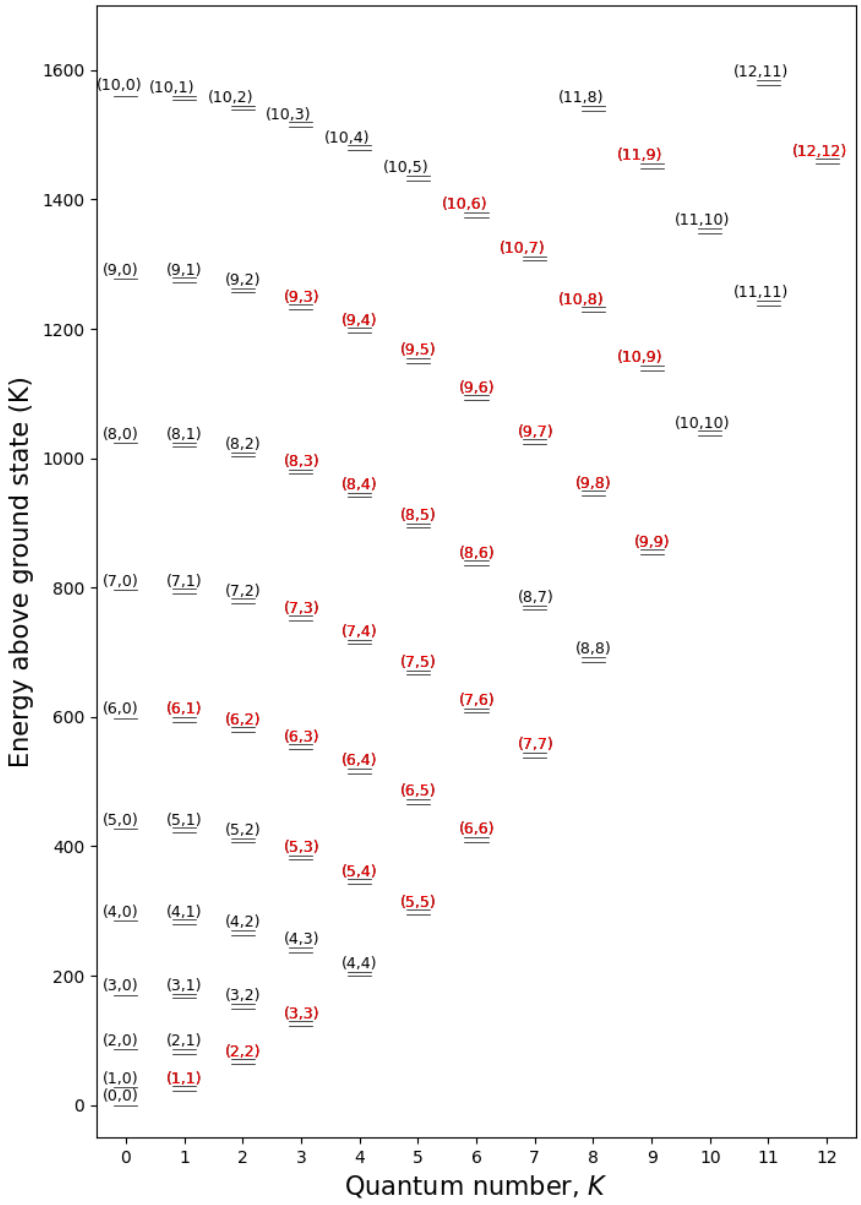

Figure 1.5: Energy-level diagram for the vibrational ground state of ammonia, NH_3. The energy above the ground state of a given transition of NH_3 is taken from the Jet Propulsion Laboratory (JPL) molecular line catalog (https://spec.jpl.nasa.gov/). Each inversion transition's lower level stays at its real energy value while the distance to the upper level is exaggerated. 34 transitions were found as masers in the interstellar medium, marked in red.

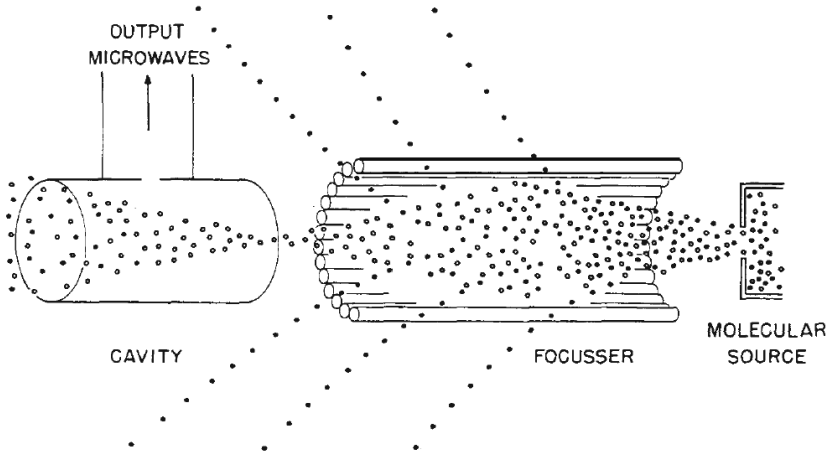

Figure 1.6: The ammonia maser produced in the laboratory by Charles H. Townes and his group members, taken from Charles H. Townes's Nobel Lecture (https://www.nobelprize.org/prizes/physics/1964/townes/lecture/).

inversion.

The first maser known by humans was realized in the $(J, K) = (3, 3)$ inversion transition of the NH_3 molecule by Charles H. Townes and his group members in the laboratory (Gordon et al. 1954). They invented the acronym maser, for ***M****icrowave* ***A****mplification by* ***S****timulated* ***E****mission of* ***R****adiation*. Figure 1.6 shows that they used inhomogeneous electric fields to remove molecules in the ground state and focus the excited molecules into the cavity on the left. Relative to statistical equilibrium, an overpopulation of the transitions upper energy level is attained, the so-called population inversion. Given this contribution and many other works Charles H. Townes and his group members have done with masers and lasers, he was awarded the Nobel Prize in Physics in 1964 together with Nicolay G. Basov and Aleksandr M. Prokhorov.

A particularly simple way to make masers is by using a three-level maser system, as shown in Fig. 1.7. In this system, the atoms or molecules have three different energy levels, the ground level E_1, intermediary/excited level E_2, and the highest energy level E_3. The system will absorb radiation, the pumping radiation, to bring the atoms/molecules from the ground state, E_1, to the highest energy level E_3. The lifetime of atoms/molecules in E_3 may be short leading to a rapid decay to E_2. This will lead to an 'overpopulation' of the level E_2 relative to E_1, leading to a 'population inversion'. The decay of atoms/molecules from E_2 to E_1 is much slower and can be 'stimulated' by a photon with a frequency corresponding to the difference in energy of levels 2 and 1. In this process, another photon with the same phase and frequency as the incident photon is produced coherently, which leads to amplification.

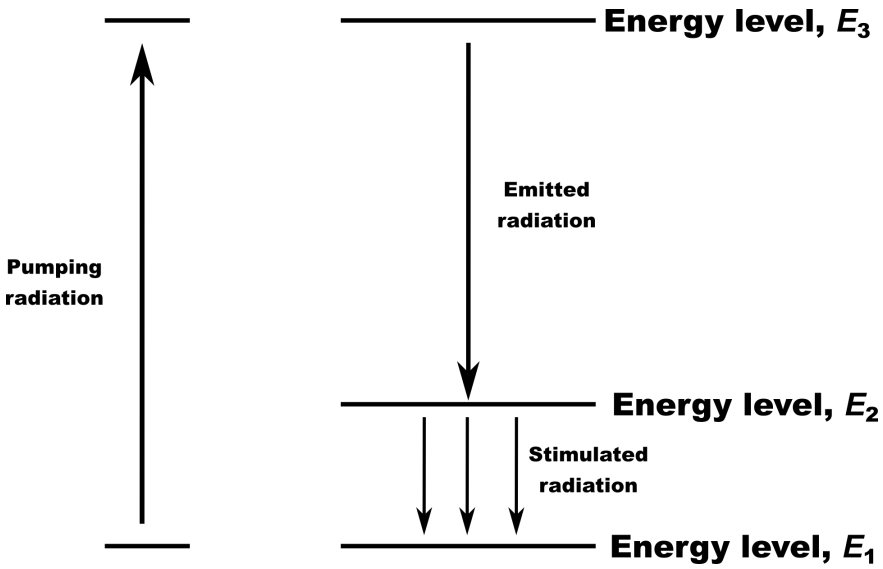

Figure 1.7: A three-level maser system.

1.4.3 The discovery of NH_3 masers in the Milky Way

Masers cannot only be produced in the laboratory but they also occur naturally in the ISM. Molecular maser lines are signposts of star formation. While H_2O masers can be associated with low and high masss young stellar objects, other widespread maser lines, from OH and CH_3OH, are only found in high mass star forming regions (Menten 1991). They probe the excitation and kinematics of very compact regions in the close environment of young stellar objects and provide useful targets for trigonometric parallax measurements (e.g., Menten et al. 2007; Reid et al. 2009b, 2014, 2019). In spite of the rare ammonia masers in the ISM, they could provide us with a better understanding of the influence of young stars on the ISM.

The ammonia molecule was discovered in the ISM more than five decades ago (Cheung et al. 1968). Since then, it has been a most valuable tool to investigate the physical properties of molecular clouds (e.g., Ho & Townes 1983). As mentioned in Sect. 1.4.1, thermally excited transitions in the $\lambda \sim$1cm wavelength inversion transitions of ammonia are regarded as a reliable thermometer of molecular clouds (e.g., Walmsley & Ungerechts 1983; Danby et al. 1988).

Ammonia masers have attracted attention since the first detection of maser action in the $(J, K) = (3,3)$ metastable ($J = K$) line toward the massive star-forming region W33 (Wilson et al. 1982). Subsequent observations have led to the detection of new metastable ammonia masers, including $^{15}NH_3$ (3,3) (Mauersberger et al. 1986), $^{15}NH_3$ (4,4) (Schilke et al. 1991), NH_3 (1,1) (Gaume et al. 1996), NH_3 (2,2) (Mills et al. 2018), NH_3 (5,5) (Cesaroni et al. 1992), NH_3 (6,6) (Beuther et al. 2007), NH_3 (7,7), NH_3 (9,9), and NH_3 (12,12) (Henkel et al. 2013). These have led to the discovery of metastable maser lines in 22 different regions (Mauersberger et al. 1986, 1987; Wilson & Henkel 1988; Wilson et al. 1990; Pratap et al. 1991; Cesaroni et al. 1992; Wilson

& Schilke 1993; Mangum & Wootten 1994; Kraemer & Jackson 1995; Zhang & Ho 1995; Zhang et al. 1999; Walsh et al. 2007; Hunter et al. 2008; Galván-Madrid et al. 2009; Brogan et al. 2011; Urquhart et al. 2011; Walsh et al. 2011; Wang et al. 2012; Henkel et al. 2013; Hoffman & Joyce 2014; McEwen et al. 2016; Mills et al. 2018; Hogge et al. 2019; Mei et al. 2020; Towner et al. 2021). Compared with the metastable ammonia masers, detected non-metastable ($J > K$) ammonia maser transitions are more numerous. The first highly excited non-metastable ammonia maser was detected by Madden et al. (1986) in the (J, K) = (9,6) and (6,3) lines. Thereafter, many other NH_3 non-metastable inversion transition lines have been identified as masers, including the (5,3), (5,4), (6,1), (6,2), (6,4), (6,5), (7,3), (7,4), (7,5) (7,6), (8,3), (8,4), (8,5), (8,6), (9,3), (9,4), (9,5), (9,7), (9,8), (10,6), (10,7), (10,8), (10,9), and (11,9) transitions (e.g., Mauersberger et al. 1987, 1988; Walsh et al. 2007; Hoffman 2012; Henkel et al. 2013; Mei et al. 2020).

So far, a total of 34 NH_3 inversion transitions ($\Delta K = 0$ and $\Delta J = 0$) have been identified as masers. They are marked in red in the energy-level diagram in Figure 1.5 and listed in Table 1.2. Among these, and despite arising from energy levels as high as 1090 K above the ground state, the NH_3 (9,6) maser stands out as being the strongest and most variable one in W51-IRS2 (e.g., Henkel et al. 2013). Maser emission in this line has only been detected in five HMSFRs, W51, NGC7538, W49, DR21 (OH) (Madden et al. 1986), and Sgr B2(N) (Mei et al. 2020). The NH_3 (3,3) masers are thought to be collisionally excited (e.g., Flower et al. 1990; Mangum & Wootten 1994); in contrast, the pumping mechanism of the NH_3 (9,6) masers is less well constrained (Madden et al. 1986). Brown & Cragg (1991) have studied ortho-ammonia and found that infrared radiation could possibly pump the (6,3) inversion line, but they did not extend their model to the (9,6) transition due to the fact that collision rate coefficients are only known for inversion levels up to $J = 6$ (e.g., Danby et al. 1988).

Table 1.2: Catalog of ammonia transitions having been identified as masers in the ISM.

Number	Transition (J, K)	ν (MHz)	$E_{\rm low}/k$ (K)	$E_{\rm up}/k$ (K)	Discovery source & Reference
1	(1,1)	23694.49550	22.12769	23.26484	DR21, a
2	(2,2)	23722.63330	63.30956	64.44806	Sgr B2(M), b
3	(3,3)	23870.12920	122.39346	123.53904	W33, c
4	(5,5)	24532.98870	294.19337	295.37076	G9.26+0.19, d
5	(5,4)	22653.02200	342.22451	343.31167	W51-IRS2, e
6	(5,3)	21285.27500	379.43682	380.45835	W51-IRS2, f
7	(6,6)	25056.02500	406.85658	408.05908	NGC6334, g
8	(6,5)	22732.42900	465.55043	466.64141	W3(OH), h
9	(6,4)	20994.61700	513.33957	514.34714	Sgr B2(N), i
10	(6,3)	19757.53800	550.36513	551.31333	NGC7538, j
11	(6,2)	18884.69500	576.73689	577.64321	W51-IRS2, f

continued.

Number	Transition (J,K)	ν (MHz)	$E_{\rm low}/k$ (K)	$E_{\rm up}/k$ (K)	Discovery source & Reference
12	(6,1)	18391.56200	592.52954	593.41219	Sgr B2(N), i
13	(7,7)	25715.18200	537.31664	538.55077	W51-IRS2, f
14	(7,6)	22924.94000	606.67824	607.77846	W51-IRS2, f
15	(7,5)	20804.83000	665.02736	666.02583	W51-IRS2, e
16	(7,4)	19218.46500	712.53838	713.46072	W51-IRS2, f
17	(7,3)	18017.33700	749.35187	750.21656	Sgr B2(N), i
18	(8,6)	20719.22100	834.46640	835.46076	NGC6334, k
19	(8,5)	18808.50700	892.42835	893.33101	W51-IRS2, f
20	(8,4)	17378.11000	939.62715	940.46116	Sgr B2(N), i
21	(8,3)	16455.09900	976.19662	976.98634	Sgr B2(N), i
22	(9,9)	27477.94300	851.45423	852.77295	W51-IRS2, f
23	(9,8)	23657.47100	942.18255	943.31792	W51-IRS2, e
24	(9,7)	20735.45200	1021.61682	1022.61196	W51-IRS2, f
25	(9,6)	18499.39000	1089.99977	1090.88760	W51, NGC7538, W49, DR21(OH), j
26	(9,5)	16798.13400	1147.53483	1148.34101	Sgr B2(N), i
27	(9,4)	15523.90000	1194.38934	1195.13437	Sgr B2(N), i
28	(9,3)	14376.81700	1230.70171	1231.39168	Sgr B2(N), i
29	(10,9)	24205.28700	1136.46581	1137.62748	W51-IRS2, f
30	(10,8)	20852.52700	1226.43274	1227.43349	W51-IRS2, e
31	(10,7)	18285.43400	1305.21064	1306.08820	W51-IRS2, f
32	(10,6)	16319.32400	1373.03592	1373.81912	NGC7538, l
33	(11,9)	21070.73900	1448.86263	1449.87386	NGC6334, k
34	(12,12)	31424.94300	1454.90272	1456.41088	W51-IRS2, f
35	$^{15}NH_3$ (3,3)	22789.42170	124.64182	125.73554	NGC7538, m
36	$^{15}NH_3$ (4,3)	21637.89450	238.70035	239.73880	NGC7538, n
37	$^{15}NH_3$ (4,4)	23046.01580	202.51921	203.62523	NGC7538, n

Notes. The parameters of ammonia lines are taken from the Jet Propulsion Laboratory (JPL) molecular line catalog (Pickett et al. 1998, https://spec.jpl.nasa.gov/) and the Cologne Database for Molecular Spectroscopy (CDMS, Müller et al. 2005; Endres et al. 2016). For the last column, see a Gaume et al. (1996), b Mills et al. (2018), c Wilson et al. (1982), d Cesaroni et al. (1992), e Mauersberger et al. (1987), f Henkel et al. (2013), g Beuther et al. (2007), h Mauersberger et al. (1988), i Mei et al. (2020), j Madden et al. (1986), k Walsh et al. (2007), l Hoffman (2012), m Mauersberger et al. (1986), n Schilke et al. (1991).

NH_3 (9,6) masers are found to be strongly variable, similar to H_2O masers (Madden et al. 1986; Pratap et al. 1991; Henkel et al. 2013). In W51-IRS2, Henkel et al. (2013) found that the (9,6) line showed significant variations in line shape within a time interval of only two days. Mapping of the (9,6) maser toward W51 with very long

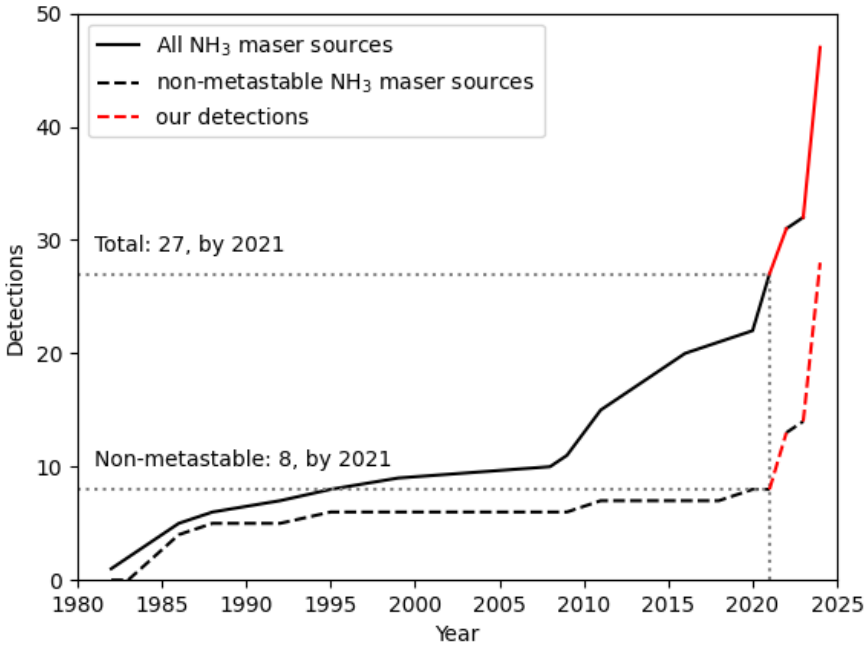

Figure 1.8: The total of 47 detections of ammonia masers in the Milky Way. The red lines indicate our 17 detections of non-metastable NH_3 maser sources and one detection of a metastable NH_3 maser source in this thesis.

baseline interferometry (VLBI) suggests that the masers are closer to the H_2O masers than to the OH masers or to ultracompact (UC) H II regions (Pratap et al. 1991). While Henkel et al. (2013) and Goddi et al. (2015) showed that the SiO and NH_3 masers in W51-IRS2 are very close to each other, their positions, differing by 0.″065 (∼0.015 pc), do not fully coincide.

Figure 1.8 shows a total of 47 detections of ammonia masers in the Milky Way to date, including our 17 detections of non-metastable NH_3 source and one detection of metastable NH_3 maser source in this thesis. The targets containing ammonia masers are listed in Table 1.3. Except for the NH_3 (3,3) masers proposed to be associated with four supernova remnants (McEwen et al. 2016), almost all the other ammonia masers are detected in high-mass star-forming regions (HMSFRs). However, while many HMSFRs host water (H_2O), hydroxyl (OH), or methanol (CH_3OH) masers, ammonia masers are quite rare in these sources, and the role that the environment of a young high-mass star plays in their excitation remains unclear. Therefore, dedicated searches for ammonia masers in HMSFRs are indispensable in regard to their overall incidence and association with different environments, which can provide additional constraints on the physical parameters of the gas and the pumping mechanisms of ammonia masers.

Table 1.3: A catalog of sources hosting ammonia masers.

Number	source	metastable ($J = K$)	non-metastable ($J > K$)	source type	Discovery Reference
1	W33	Y	N	SFR	a
2	DR 21	Y	Y	SFR	b, c, d, e
3	NGC7538	N	Y	SFR	c, f, g
4	W51	Y	Y	SFR	c, h, i, j
5	W49	N	Y	SFR	c
6	W3(OH)	N	Y	SFR	k
7	G9.26+0.19	Y	N	SFR	l
8	NGC6334	Y	Y	SFR	m, n, o
9	IRAS20126+4104	Y	N	SFR	p
10	G05.89-0.39	Y	N	SFR	q
11	G19.61-0.23	N	Y	SFR	r
12	G23.33-0.30	Y	N	SNR	r, s
13	G030.7206-00.0826	Y	N	SFR	t
14	G20.08-0.14N	Y	N	SFR	u
15	G35.03+0.35	Y	N	SFR	v
16	G28.34+0.06	Y	N	SFR	w
17	W44	Y	N	SNR	x
18	G5.7-0.0	Y	N	SNR	x
19	W51C	Y	N	SNR	x
20	IC443	Y	N	SNR	x

continued.

Number	source	metastable ($J = K$)	non-metastable ($J > K$)	source type	Discovery Reference
21	Sgr B2(M)	Y	Y	SFR	y, z, this thesis
22	Sgr B2(N)	N	Y	SFR	z, z1, this thesis
23	G10.34-0.14	Y	N	SFR	z2
24	G14.33-0.64	Y	N	SFR	z2
25	G18.89-0.47	Y	N	SFR	z2
26	G19.36-0.03	Y	N	SFR	z2
27	G28.83-0.25	Y	N	SFR	z2
28	CepA	N	Y	SFR	z3, this thesis
29	G34.26+0.15	N	Y	SFR	z3, this thesis
30	Sgr B2(NS)	N	Y	SFR	z, this thesis
31	Sgr B2(S)	N	Y	SFR	z, this thesis
32	G358.931-0.030	N	Y	SFR	z4
33	G010.47+0.03	N	Y	SFR	z5, this thesis
34	G012.21-0.10	N	Y	SFR	z5, this thesis
35	G019.61-0.23	N	Y	SFR	z5, this thesis
36	G024.79+0.08	N	Y	SFR	z5, this thesis
37	G029.95-0.02	Y	Y	SFR	z5, this thesis
38	G030.21-0.19	N	Y	SFR	z5, this thesis
39	G030.60+0.18	N	Y	SFR	z5, this thesis
40	G030.70-0.07	N	Y	SFR	z5, this thesis
41	G030.79+0.20	N	Y	SFR	z5, this thesis
42	G031.41+0.30	N	Y	SFR	z5, this thesis
43	G032.74-0.08	N	Y	SFR	z5, this thesis
44	G035.19-0.74	N	Y	SFR	z5, this thesis
45	G043.79-0.13	N	Y	SFR	z5, this thesis
46	G048.98-0.30	Y	N	SFR	z5, this thesis
47	G111.53+0.76	N	Y	SFR	z5, this thesis
count		24	28		

Notes. SFR: star-forming region, SNR: supernova remnant. Y indicates a detection and N marks a non-detection. a Wilson et al. (1982), b Guilloteau et al. (1983), c Madden et al. (1986), d Mangum & Wootten (1994), e Gaume et al. (1996), f Hoffman (2012), g Hoffman & Joyce (2014), h Zhang & Ho (1995), i Mauersberger et al. (1987), j Henkel et al. (2013), k Mauersberger et al. (1988), l Cesaroni et al. (1992), m Kraemer & Jackson (1995), n Beuther et al. (2007), o Walsh et al. (2007), p Zhang et al. (1999), q Hunter et al. (2008), r Walsh et al. (2011), s Hogge et al. (2019), t Urquhart et al. (2011), u Galván-Madrid et al. (2009), v Brogan et al. (2011), w Wang et al. (2012), x McEwen et al. (2016), y Mills et al. (2018), z Yan et al. (2022a), z1 Mei et al. (2020), z2 Towner et al. (2021), z3, Yan et al. (2022b), z4 McCarthy et al. (2023), z5 Yan et al. (2024)

Chapter 2

Observations

Overview

Radio waves, like visible light, are electromagnetic radiation. But radio waves are invisible to our naked eyes. Using radio telescopes equipped with special receivers, we can obtain information that cannot be seen in the visible light from extraterrestrial objects, opening up a very different view onto the universe (see Figure 2.1). In this chapter, we describe the basics of radio astronomy, the radio telescopes used in this thesis, and our observations based on these radio facilities. For further readings refer to *Tools of Radio Astronomy* (Rohlfs & Wilson 2004; Wilson et al. 2013), *Essential Radio Astronomy* (Condon & Ransom 2016), and *Interferometry and Synthesis in Radio Astronomy* (Thompson et al. 2017).

2.1 The radio window

Since Karl Jansky detected radio signals from extraterrestrial sources with his antennas (Figure 2.2) in 1931 (Jansky 1932, 1933a,b), a new window has opened for humans to catch the universe's landscape, which is the realm of radio astronomy. The total range of frequency for ground-based radio astronomy is roughly from ν ~10 MHz to ν ~1.5 THz, corresponding to the wavelengths from λ ~30 m to λ ~0.2 mm (Wilson et al. 2013). Figure 2.3 shows the atmospheric windows from ground sites at different wavelengths. The atmosphere is transparent to radio waves, which provides a unique opportunity to obtain another view of the universe that is quite different from that seen at optical wavelengths. It is obvious that the midplane of the Milky Way in the optical band is dark because the dust in the interstellar medium blocks the light. Radio waves are longer than the size of dust grains and can reach Earth even through the Galactic midplane (Figure 2.1).

The transparency of the atmosphere is not continuous at radio frequencies because of the absorption of molecules. The main effects come from two molecules, water (H_2O) and oxygen (O_2). These two molecular species show strongly pressure broadened lines in the troposphere and cause attenuation over a wide range around their resonance frequencies. Especially the oxygen lines make it impossible for astronomers to observe the frequency ranges of 52 GHz$<\nu<$68 GHz and of 116 GHz$<\nu<$120 GHz from the ground and the water vapor line at ν ~22.235 GHz (λ ~1.35 cm) causes relatively mild absorption with a width of about 4 GHz (Condon & Ransom 2016). At higher frequencies (in the (sub)millimeter part of the radio band), several strong H_2O lines, e.g., at ν ~183, 325, 380 GHz, are far more efficient in blocking astronomical radiation

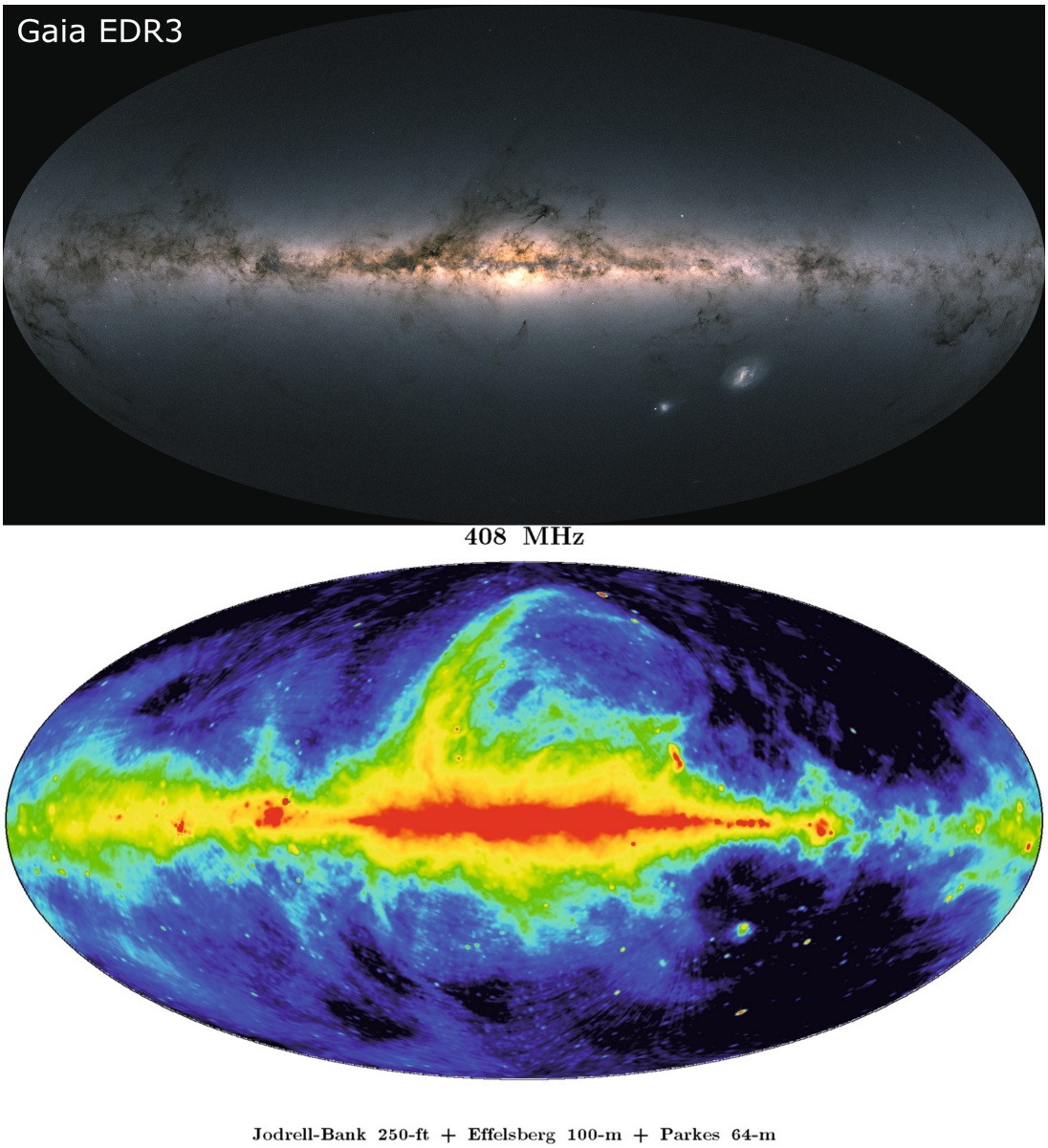

Figure 2.1: The sky maps at optical and radio wavelengths. **Top:** All sky distribution of stars observed by the European Space Agency's Gaia satellite (Gaia Collaboration et al. 2022), taken from Gaia's Early Data Release 3 [Credits: ESA/Gaia/DPAC; CC BY-SA 3.0 IGO. Acknowledgment: A. Moitinho]. Brighter regions present contain more bright stars, as you can see in the middle of the image where the Galactic center region is located. The darker regions across the Galactic plane indicate the extinction of starlight due to interstellar dust. **Bottom:** a full sky map of the radio continuum radiation at 408 MHz, taken from Wielebinski (2009). The measurements were carried out by using the 100-meter Effelsberg, the 64-meter Parkes and the Jodrell Bank MkI & MkIA telescopes (Haslam et al. 1981, 1982).

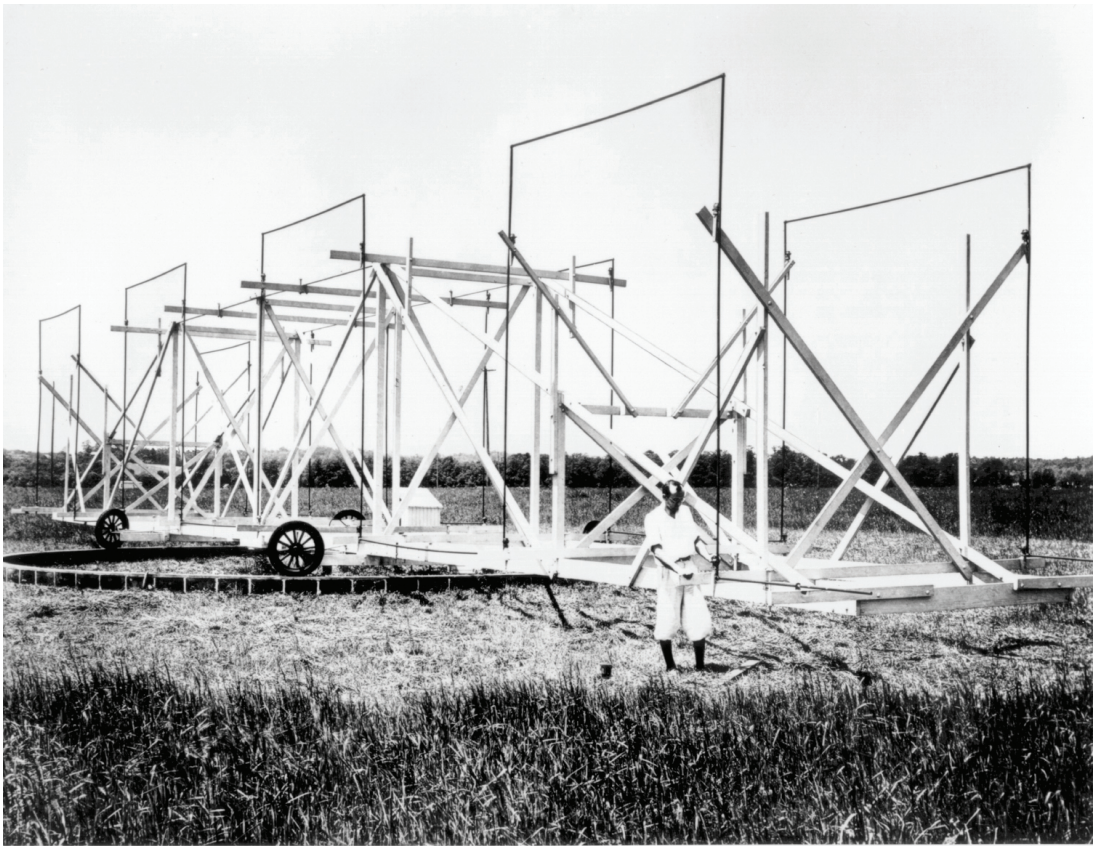

Figure 2.2: Karl Jansky and his antenna. Credit: NRAO/AUI/NSF

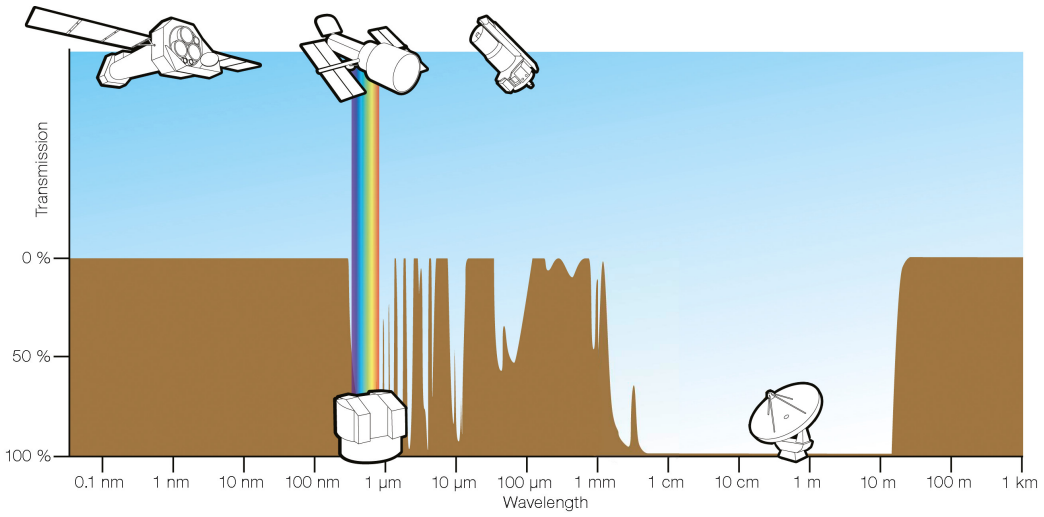

Figure 2.3: Transparency of the Earth's atmosphere from the X-ray regime (left) to long radio wavelengths. Only a few atmospheric windows are accessible from ground-based sites and the atmosphere is nearly transparent at radio and optical frequencies. Credit: ESA/Hubble, F. Granato

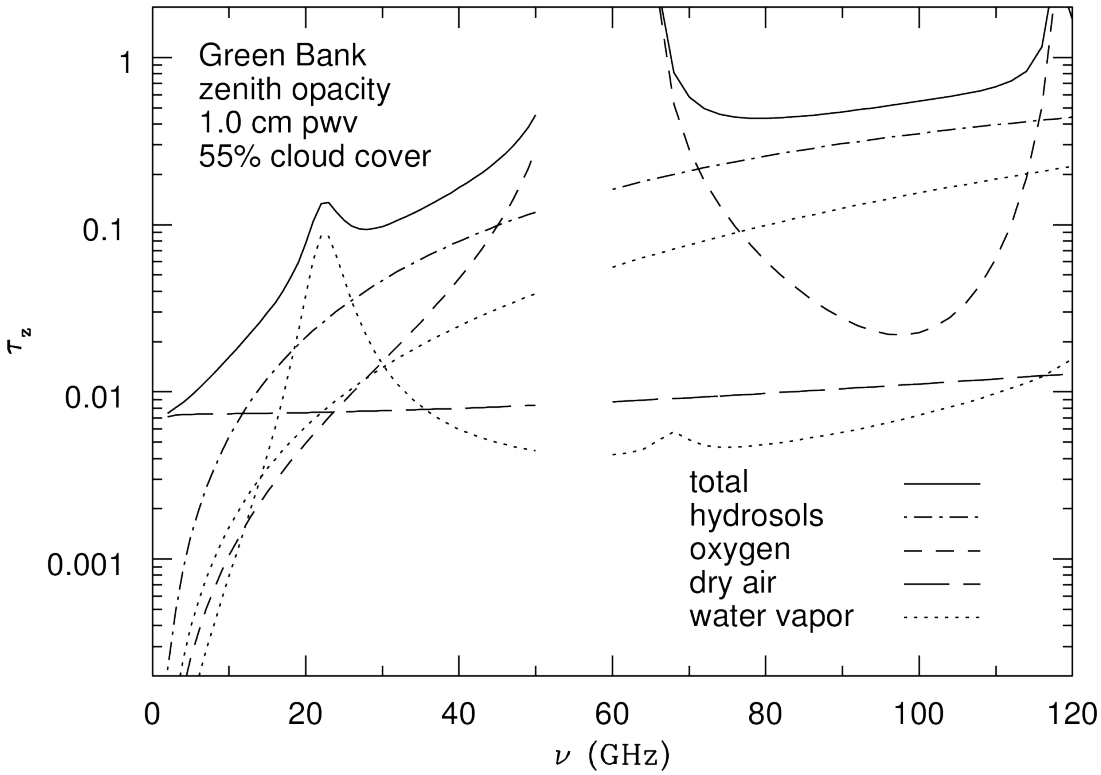

Figure 2.4: The atmospheric zenith opacity at Green Bank, taken from (Condon & Ransom 2016).

than the 22.2 GHz line (Liebe 1981). There is also a continuum component opacity of water vapor that exists due to the far line wings of its infrared wavelength transitions (e.g., Rosenkranz 1998; Thompson et al. 2017). These two components of atmospheric water vapor are sensitive to the column density of precipitable water vapor (pwv) at the site of a telescope along the vertical line of sight through the atmosphere (Condon & Ransom 2016). In addition, hydrosols in the clouds and dry air also increase the total opacity. Fig. 2.4 shows the atmospheric zenith opacity τ_z at Green Bank in summer, the atmospheric transmission is given by exp(-τ). Furthermore, free electrons in the ionosphere make the terrestrial atmosphere opaque at low frequencies, below 4.5 MHz during the night or below 11 MHz during the day time because of different electron densities, which vary based on solar activity (Wilson et al. 2013). On the other hand, man-made electronic devices, such as mobile phones, microwave ovens, and satellites, can create radio frequency interference (RFI) that is harmful to radio astronomy [1]. Radio astronomers have put some efforts to reduce the RFI as much as possible (e.g., Fridman & Baan 2001), while the recent unexpected strong RFI from the Starlink satellite constellation of SpaceX will also need to be considered and resolved seriously [2] (Di Vruno et al. 2023).

[1] https://public.nrao.edu/telescopes/radio-frequency-interference/
[2] https://www.mpg.de/20610867/radi-satellite-constellations

The following sections, Sections 2.2, 2.3, 2.4, and 2.5, are based on the descriptions of flux density, black body radiation, radiative transfer, and interferometry in *Tools of Radio Astronomy* (Rohlfs & Wilson 2004; Wilson et al. 2013), *Essential Radio Astronomy* (Condon & Ransom 2016) and *Interferometry and Synthesis in Radio Astronomy* (Thompson et al. 2017). The symbols used for each equation are consistent throughout the whole thesis.

2.2 The definition of flux density

Considering an antenna has an infinitesimal surface $\mathrm{d}\sigma$ (Fig. 2.5), the received infinitesimal power $\mathrm{d}P$ (in watts) in an infinitesimal bandwidth $\mathrm{d}\nu$ (in Hz), in an infinitesimal solid angle $\mathrm{d}\Omega$ (in sr^{-1})is given by

$$\mathrm{d}P = I_\nu \, cos\theta \, \mathrm{d}\Omega \, \mathrm{d}\sigma \, \mathrm{d}\nu, \tag{2.1}$$

while θ is the angle between the direction of radiation and the normal to the surface of the detector. The brightness, I_ν, also called specific intensity or intensity is then quantitatively defined as

$$I_\nu = \frac{\mathrm{d}P}{cos\theta \, \mathrm{d}\Omega \, \mathrm{d}\sigma \, \mathrm{d}\nu}. \tag{2.2}$$

It is in units of W m^{-2} Hz^{-1} sr^{-1}. The total flux density of the source is then obtained by integration over the solid angle Ω subtended by the source

$$S_\nu = \int_\Omega I_\nu(\theta, \varphi) cos\theta \mathrm{d}\Omega, \tag{2.3}$$

in units of W m^{-2} Hz^{-1}. Since radio sources are usually very faint, radio astronomers use a specific radio astronomical flux density unit, Jansky (Jy).

$$1 \text{ Jy} = 10^{-26} \text{ W m}^{-2} \text{ Hz}^{-1} = 10^{-23} \text{ erg s}^{-1} \text{ cm}^{-2} \text{ Hz}^{-1}. \tag{2.4}$$

2.3 Black body radiation

The spectral distribution of the radiation per unit frequency interval of an ideal blackbody radiator is given by Planck's law

$$B_\nu(T) = \frac{2h\nu^3}{c^2} \frac{1}{e^{h\nu/kT} - 1}, \tag{2.5}$$

where h is Planck's constant with $h = 6.626 \times 10^{-27}$ erg sec, k is Boltzmann's constant with $k_\mathrm{B} = 1.381 \times 10^{-16}$ erg K^{-1}. c is the speed of light, and T is the blackbody's absolute temperature in units of K.

In most cases in radio astronomy, $h\nu \ll kT$ i.e. $h\nu/kT \ll 1$. Then the Taylor-series approximation for the exponential $e^{h\nu/kT}$ in equation 2.5 is

$$e^{h\nu/kT} \approx 1 + \frac{h\nu}{kT} + \cdots, \tag{2.6}$$

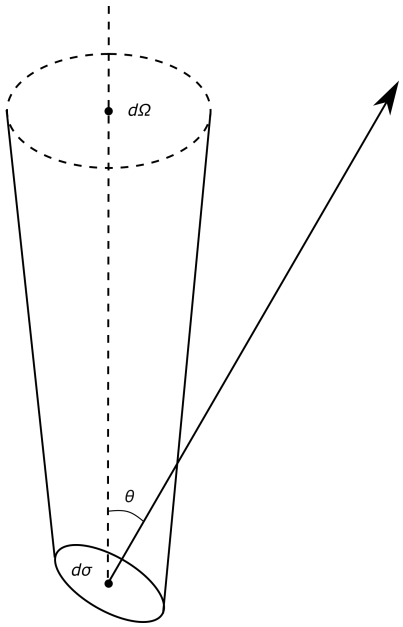

Figure 2.5: The definition of brightness (figure adapted from Wilson et al. 2013).

and results in the Rayleigh-Jeans approximation

$$B_\nu(\nu, T) \approx \frac{2h\nu^3}{c^2}\frac{kT}{h\nu} = \frac{2kT\nu^2}{c^2}. \tag{2.7}$$

Thus the brightness of a blackbody radiator is proportional to ν^2. In radio astronomy, brightness temperature T_B is defined as approaching the Rayleigh-Jeans law by the equation

$$I_\nu = \frac{2kT_B\nu^2}{c^2}. \tag{2.8}$$

Then the brightness temperature becomes

$$T_B = \frac{I_\nu c^2}{2k\nu^2}. \tag{2.9}$$

2.4 Radiative transfer

The specific intensity, I_ν, along a ray consists of absorption and emission. The distance along the ray between the source and the detector is s. The linear absorption coefficient is defined as $\kappa \equiv \frac{\mathrm{d}P}{\mathrm{d}s}$, $\mathrm{d}P$ is the infinitesimal probability of a photon being absorbed, and $\mathrm{d}s$ is infinitesimal distance. The emission coefficient is defined as $j_\nu \equiv \frac{I_\nu}{\mathrm{d}s}$. Combined together, absorption and emission, enter the equation of radiative transfer

$$\frac{\mathrm{d}I_\nu}{\mathrm{d}s} = -\kappa I_\nu + j_\nu. \tag{2.10}$$

If there is only absorption along the ray (Fig. 2.6), i.e. the emission part is $j_\nu = 0$, we can get

$$\frac{\mathrm{d}I_\nu}{\mathrm{d}s} = -\kappa I_\nu + j_\nu = -\kappa I_\nu, \tag{2.11}$$

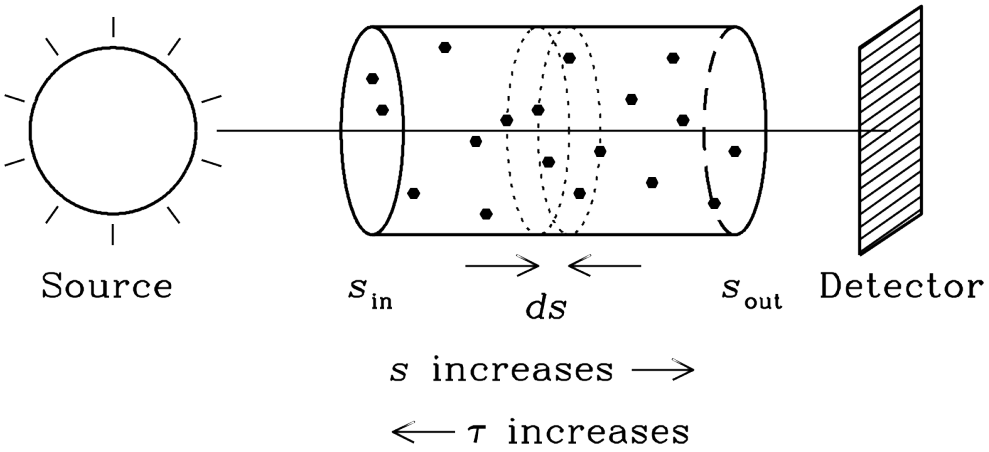

Figure 2.6: The detector receives radiation from a source, and between detector and source is material with thickness ds that can cause absorption (figure taken from Condon & Ransom 2016).

$$\frac{\mathrm{d}I_\nu}{I_\nu} = -\kappa \mathrm{d}s. \tag{2.12}$$

By integrating these two sides of the above equation, we obtain

$$\int_{S_{in}}^{S_{out}} \frac{\mathrm{d}I_\nu}{I_\nu} = -\int_{S_{in}}^{S_{out}} \kappa \mathrm{d}s = \ln I_\nu \Big|_{S_{in}}^{S_{out}}, \tag{2.13}$$

$$-\int_{S_{in}}^{S_{out}} \kappa \mathrm{d}s = \ln[I_\nu(S_{out})] - \ln[I_\nu(S_{in})] = \ln \frac{I_\nu(S_{out})}{I_\nu(S_{in})}, \tag{2.14}$$

$$\exp[-\int_{S_{in}}^{S_{out}} \kappa \mathrm{d}s] = \frac{I_\nu(S_{out})}{I_\nu(S_{in})}. \tag{2.15}$$

The optical depth, τ, is defined as

$$\tau = \int_{S_{in}}^{S_{out}} \kappa \mathrm{d}s, \tag{2.16}$$

or

$$\mathrm{d}\tau = -\kappa \mathrm{d}s. \tag{2.17}$$

Combining equations 2.15 and 2.16, we can obtain

$$\frac{I_\nu(S_{out})}{I_\nu(S_{in})} = \exp(-\tau). \tag{2.18}$$

When $\tau \gg 1$ and $\tau \ll 1$, the medium is optically thick and optically thin, respectively.

To describe the radiative transfer in the physical view we need to introduce the Einstein Coefficients. Considering the simplest way in a two-level system, the excited level E_2 and a lower state E_1 (Fig. 2.7). Three Einstein Coefficients connect these two levels. They are A_{21}, the coefficient for spontaneous emission, B_{12}, the coefficient for

absorption and B_{21}, the coefficient for stimulated emission. In a stationary state, the intensity of emitted radiation, that is spontaneous emission and stimulated emission, should equal the intensity of absorbed radiation. Thus we have

$$N_2 A_{21} + N_2 B_{21} \bar{U} = N_1 B_{12} \bar{U}, \tag{2.19}$$

where N_1 and N_2 are the densities of these two energy levels. $\bar{U}$ is the average energy density of the radiation field and is described as

$$\bar{U} = 4\pi \bar{I}/c. \tag{2.20}$$

The frequency of this transition depends on the energy difference between these two energy levels, that is

$$h\nu_0 = E_2 - E_1. \tag{2.21}$$

A normalized line profile function, $\varphi(\nu)$, describes the absorption line

$$\int_0^\infty \varphi(\nu) \mathrm{d}\nu = 1. \tag{2.22}$$

Then the average intensity $\bar{I}$ in equation 2.20 can be defined as

$$\bar{I} = \int_0^\infty I_\nu \varphi(\nu) \mathrm{d}\nu \tag{2.23}$$

when the intensity of the radiation field is I_ν. Considering the system in full thermodynamic equilibrium (TE) and according to the Boltzmann distribution, the populations at different energy levels can be characterized as

$$\frac{N_2}{N_1} = \frac{g_2}{g_1} e^{-h\nu_0/kT}, \tag{2.24}$$

where g_1 and g_2 are the statistical weights of the different states. From equations 2.19 and 2.24 we can get

$$\begin{aligned} \bar{U} &= \frac{N_2 A_{21}}{N_1 B_{12} - N_2 B_{21}} \\ &= \frac{A_{21}}{\frac{N_1}{N_2} B_{12} - B_{21}} \\ &= \frac{A_{21}}{\frac{g_1}{g_2} B_{12} e^{h\nu_0/kT} - B_{21}} \\ &= \frac{A_{21}}{(\frac{g_1}{g_2} \frac{B_{12}}{B_{21}} e^{h\nu_0/kT} - 1) B_{21}} \end{aligned} \tag{2.25}$$

while in TE and according to Plank's law in Section 2.3 we get

$$\begin{aligned} \bar{U} &= \frac{4\pi}{c} B_\nu(T) \\ &= \frac{8\pi h\nu_0^3}{c^3} \frac{1}{e^{h\nu_0/kT} - 1}. \end{aligned} \tag{2.26}$$

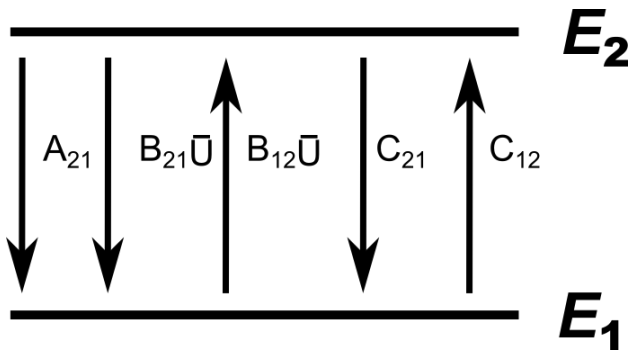

Figure 2.7: Transitions between the two energy levels E_1 and E_2. They are connected by the Einstein Coefficients and collisions.

These two equations, 2.25 and 2.26, should be identical and this can be the case when

$$g_1 B_{12} = g_2 B_{21}, \tag{2.27}$$

and

$$A_{21} = \frac{8\pi h\nu^3}{c^3} B_{21}. \tag{2.28}$$

Now, considering the radiation of this system passes through a material with thickness ds to reach the detector as shown in Fig. 2.6. The intensity, I_ν, received by the detector consists of three parts described by the three Einstein coefficients mentioned above. They are d$E_e(\nu)$, d$E_a(\nu)$, and d$E_s(\nu)$ refer to the total energy for the spontaneous emission, absorption, and stimulated emission, respectively. Then we can get

$$\mathrm{d}E_e(\nu) + \mathrm{d}E_s(\nu) - \mathrm{d}E_a(\nu) = \mathrm{d}I_\nu \mathrm{d}\Omega \mathrm{d}\delta \mathrm{d}\nu \mathrm{d}t. \tag{2.29}$$

The total energy for the spontaneous emission is

$$\mathrm{d}E_e(\nu) = h\nu_0 N_2 A_{21} \varphi_e(\nu) \mathrm{d}V \frac{\mathrm{d}\Omega}{4\pi} \mathrm{d}\nu \mathrm{d}t, \tag{2.30}$$

for the absorption

$$\mathrm{d}E_a(\nu) = h\nu_0 N_1 B_{12} \frac{4\pi}{c} I_\nu \varphi_a(\nu) \mathrm{d}V \frac{\mathrm{d}\Omega}{4\pi} \mathrm{d}\nu \mathrm{d}t, \tag{2.31}$$

and for the stimulated emission

$$\mathrm{d}E_s(\nu) = h\nu_0 N_2 B_{21} \frac{4\pi}{c} I_\nu \varphi_e(\nu) \mathrm{d}V \frac{\mathrm{d}\Omega}{4\pi} \mathrm{d}\nu \mathrm{d}t. \tag{2.32}$$

$\varphi_e(\nu)$ and $\varphi_a(\nu)$ are the line profiles for radiation of emission and absorption, respectively. They can regarded as the same in astrophysics, that is

$$\varphi_e(\nu) = \varphi_a(\nu) = \varphi(\nu). \tag{2.33}$$

$\mathrm{d}V$ is the volume unit and $\mathrm{d}V = \mathrm{d}\delta\mathrm{d}s$. Then combining equations 2.30, 2.31, 2.32, and 2.33, we can get

$$\mathrm{d}E_e(\nu)+\mathrm{d}E_s(\nu)-\mathrm{d}E_a(\nu) = \frac{h\nu_0}{4\pi}(N_2A_{21}+N_2B_{21}\frac{4\pi}{c}I_\nu-N_1B_{12}\frac{4\pi}{c}I_\nu)\varphi(\nu)\mathrm{d}\Omega\mathrm{d}\delta\mathrm{d}s\mathrm{d}\nu\mathrm{d}t. \tag{2.34}$$

From equations 2.29 and 2.34, we find the following equations of radiative transfer with Einstein coefficients

$$\begin{aligned}\frac{\mathrm{d}I_\nu}{\mathrm{d}s} &= \frac{h\nu_0}{4\pi}(N_2A_{21} + N_2B_{21}\frac{4\pi}{c}I_\nu - N_1B_{12}\frac{4\pi}{c}I_\nu)\varphi(\nu)\\ &= \frac{h\nu_0}{4\pi}N_2A_{21}\varphi(\nu) + \frac{h\nu_0}{c}(N_2B_{21} - N_1B_{12})I_\nu\varphi(\nu)\\ &= \frac{h\nu_0}{4\pi}N_2A_{21}\varphi(\nu) - \frac{h\nu_0}{c}(N_1B_{12} - N_2B_{21})I_\nu\varphi(\nu).\end{aligned} \tag{2.35}$$

Compared to equation 2.10, we can get the solutions for the emission (j_ν) and absorption coefficients (κ) with the Einstein coefficients. They are

$$j_\nu = \frac{h\nu_0}{4\pi}N_2A_{21}\varphi(\nu), \tag{2.36}$$

and

$$\begin{aligned}\kappa &= \frac{h\nu_0}{c}(N_1B_{12} - N_2B_{21})\varphi(\nu)\\ &= \frac{h\nu_0}{c}N_1B_{12}(1 - \frac{g_1N_2}{g_2N_1})\varphi(\nu).\end{aligned} \tag{2.37}$$

The expression for the absorption, $(1 - \frac{g_1N_2}{g_2N_1})$, contains the correction for stimulated emission. Dividing equation 2.36 by equation 2.37, we get

$$\begin{aligned}\frac{j_\nu}{\kappa} &= \frac{2h\nu_0^3}{c^2}\frac{N_2B_{21}}{N_1B_{12}}(1 - \frac{g_1N_2}{g_2N_1})^{-1}\\ &= \frac{2h\nu_0^3}{c^2}\frac{g_1N_2}{g_2N_1}(1 - \frac{g_1N_2}{g_2N_1})^{-1}\\ &= \frac{2h\nu_0^3}{c^2}(\frac{g_2N_1}{g_1N_2} - 1)^{-1}.\end{aligned} \tag{2.38}$$

In local thermodynamic equilibrium (LTE) we have according to Kirchhoff's law,

$$\begin{aligned}\frac{j_\nu}{\kappa} &= B_\nu(T)\\ &= \frac{2h\nu^3}{c^2}\frac{1}{e^{h\nu/kT} - 1}.\end{aligned} \tag{2.39}$$

Combined with the populations at different energy levels in equation 2.24, then we can

get

$$\begin{aligned}\kappa &= \frac{c^2}{2h\nu_0^3}(e^{h\nu/kT}-1)j_\nu \\ &= \frac{c^2}{2h\nu_0^3}(e^{h\nu/kT}-1)\frac{h\nu_0}{4\pi}\frac{g_2}{g_1}N_1 e^{-h\nu/kT}A_{21}\varphi(\nu) \\ &= \frac{c^2}{8\pi\nu_0^2}\frac{g_2}{g_1}N_1 A_{21}(1-e^{-h\nu/kT})\varphi(\nu).\end{aligned} \tag{2.40}$$

With respect to the absorption, the correction for stimulated emission is $(1-e^{-h\nu/kT})$. In the radio frequency range $h\nu/kT \ll 1$, thus

$$1-e^{-h\nu/kT} \approx \frac{h\nu}{kT}+\cdots, \tag{2.41}$$

and equation 2.40 becomes

$$\kappa = \frac{c^2}{8\pi\nu_0^2}\frac{g_2}{g_1}N_1 A_{21}(h\nu/kT)\varphi(\nu). \tag{2.42}$$

This means stimulated emission is important and cancels most of the absorption at the radio frequency range.

In the interstellar medium, collisions are also important. To account for the part of collisions, we introduce the collisional rate coefficients, C_{ij}, in units in $\mathrm{cm^3 s^{-1}}$. They are expressed by

$$C_{ij} = N_i C_{ij} = N_i \int_0^\infty \sigma_{ij}(v) v f(v) dv, \tag{2.43}$$

where σ_{ij} is the collision cross section and $f(v)$ is the velocity distribution function for the colliding particles. We have

$$f(v) = (\frac{2}{\pi})^{1/2} v^2 (\frac{m_r}{kT_K})^{3/2} e^{-m_r v^2/(2kT_K)}, \tag{2.44}$$

where $m_r = \frac{m_a m_b}{m_a+m_b}$ is the reduced mass of the colliding particles and T_K is the kinetic temperature. The collision rates depend on temperature and are proportional to the number density of particles. C_{12} and C_{21} are the collisional rate coefficients for the transitions from level 1 to level 2 and level 2 to level 1, respectively. In the stationary state, equation 2.19 becomes

$$N_2(A_{21}+B_{21}\bar{U}+C_{21}) = N_1(B_{12}\bar{U}+C_{12}). \tag{2.45}$$

The excitation temperature, T_{ex}, is defined based on equation 2.24

$$\frac{N_2}{N_1} = \frac{g_2}{g_1}e^{-h\nu_0/kT_{ex}}. \tag{2.46}$$

If collisions dominate at kinetic temperature, T_K, the principle of detailed balance leads to

$$\begin{aligned}\frac{C_{12}}{C_{21}} &= \frac{N_2}{N_1} \\ &= \frac{g_2}{g_1}e^{-h\nu_0/kT_K}.\end{aligned} \tag{2.47}$$

From equation 2.26, we connected the average energy density $\bar{U}$ with brightness temperature

$$\bar{U} = \frac{8\pi h\nu_0^3}{c^3}\frac{1}{e^{h\nu_0/kT_B}-1}. \tag{2.48}$$

Substituting equations 2.47 and 2.48 together with 2.27 and 2.28 into equation 2.45, we get

$$\frac{N_1 g_2}{N_2 g_1} = e^{h\nu/kT_B}\frac{A_{21}+C_{21}(1-e^{-h\nu/kT_B})}{A_{21}+C_{21}e^{-h\nu/kT_K}(e^{h\nu/kT_B}-1)}. \tag{2.49}$$

Then we can get

$$\frac{N_2 g_1}{N_1 g_2} = e^{-h\nu/kT_B}\frac{A_{21}+C_{21}e^{-h\nu/kT_K}(e^{h\nu/kT_B}-1)}{A_{21}+C_{21}(1-e^{-h\nu/kT_B})}. \tag{2.50}$$

From equation 2.46 we obtain

$$\frac{N_2 g_1}{N_1 g_2} = e^{-h\nu_0/kT_{ex}}. \tag{2.51}$$

These two equations, 2.50 and 2.51, should be identical, thus we have

$$e^{-h\nu_0/kT_{ex}} = e^{-h\nu/kT_B}\frac{A_{21}+C_{21}e^{-h\nu/kT_K}(e^{h\nu/kT_B}-1)}{A_{21}+C_{21}(1-e^{-h\nu/kT_B})}. \tag{2.52}$$

With $h\nu/k \ll T_{ex}$, T_B, and T_K and let us define

$$T_0 = h\nu/k. \tag{2.53}$$

Then from equation 2.52 and with a Taylor-series approximation we can get the relations among T_{ex}, T_B, and T_K. That is

$$\begin{aligned} T_{ex} &= T_K\frac{A_{21}T_B + C_{21}T_0}{A_{21}T_K + C_{21}T_0} \\ &= T_K\frac{T_B + T_0(C_{21}/A_{21})}{T_K + T_0(C_{21}/A_{21})}. \end{aligned} \tag{2.54}$$

If radiation dominates the rate equation, that is $A_{21} \gg C_{21}$, from equation 2.54 we can get $T_{ex} \to T_B$. On the other hand, if collisions dominate, that is $A_{21} \ll C_{21}$, we get the approximation $T_{ex} \to T_K$. In conditions with high density, the collision rate C_{ij} increases with increasing density N based on equation 2.43. This will cause the excitation temperature T_{ex} to be equal to the kinetic temperature T_K. The result will be the opposite in a low density situation, that is $T_{ex} = T_B$. The critical density is defined as when $A_{21} \approx C_{21} \approx N^*\langle\sigma v\rangle$.

2.4.1 Maser emission processes

As introduced in Section 1.4.2, maser emission occurs in case of population inversion. That is

$$N_2 > \frac{g_2}{g_1}N_1 \tag{2.55}$$

in the two-level system. Based on the definition of excitation temperature, T_{ex}, in equation 2.46, the state of population inversion will result in a negative T_{ex}. Considering a three-level system as shown in Fig. 1.7, the radiative transfer equation 2.35 connects the lowest two levels with a transition at a certain frequency ν_0. Assuming $g_1 = g_2$, then we have $B_{12} = B_{21}$. Let $A_{21} = A$ and $B_{12} = B_{21} = B$, we have

$$\begin{aligned}\frac{\mathrm{d}I_\nu}{\mathrm{d}s} &= \frac{h\nu_0}{4\pi}N_2A\varphi(\nu) - \frac{h\nu_0}{c}(N_1B - N_2B)I_\nu\varphi(\nu) \\ &= \frac{h\nu_0}{4\pi}\varphi(\nu)[N_2A + \frac{4\pi}{c}(N_2 - N_1)BI_\nu].\end{aligned} \tag{2.56}$$

The stimulated emission, M, over the beam solid angle of the radiation (Ω_m) is then written as

$$M = \frac{4\pi}{c}B\bar{I} = \frac{4\pi}{c}BI\frac{\Omega_m}{4\pi}. \tag{2.57}$$

In this system, we need the pumping radiation. P_{13} and P_{23} are the pumping rates from levels 1 and 2 to the third level, respectively. Collisions can also contribute to the populations at levels 1 and 2. From equation 2.45 if the system is stationary, we have

$$N_2(A + M_{21} + C_{21} + P_{23}) = N_1(M_{12} + C_{12} + P_{13}). \tag{2.58}$$

A is negligible compared to C and M for microwave masers, Let $C_{12} \approx C_{21} \approx C$ and $M_{12} \approx M_{21} \approx M$, we can get

$$N_2(M + C + P_{23}) = N_1(M + C + P_{13}). \tag{2.59}$$

The populations at levels 1 and 2 follow the relation

$$\frac{N_2}{N_1} = \frac{M + C + P_{13}}{M + C + P_{23}}. \tag{2.60}$$

When pumping radiation dominates the population inversion, that is $M = C = 0$, then we have

$$\Delta n_0 = N_2 - N_1 = n\frac{P_{13} - P_{23}}{P_{13} + P_{23}}, n = N_1 + N_2. \tag{2.61}$$

When $C \neq 0$ and $C \neq M$, let $P = P_{13} + P_{23}$, we have

$$\Delta n = \frac{\Delta n_0}{1 + \frac{2(C+M)}{P}}. \tag{2.62}$$

Substituting equations 2.62 and 2.57 into equation 2.56, we can get

$$\begin{aligned}\frac{\mathrm{d}I_\nu}{\mathrm{d}s} &= \frac{h\nu_0}{4\pi}N_2A\varphi(\nu) + \frac{h\nu_0}{c}B\varphi(\nu)\frac{\Delta n_0 I_\nu}{1 + \frac{2C+2M}{P}} \\ &= \frac{h\nu_0}{4\pi}N_2A\varphi(\nu) + \frac{h\nu_0}{c}B\varphi(\nu)\frac{\Delta n_0 I_\nu}{(1 + 2C/P)(1 + \frac{I_\nu 2B\Omega_M}{cP+2cC})}.\end{aligned} \tag{2.63}$$

Let

$$\alpha = \frac{h\nu_0}{c}B\frac{\Delta n_0}{1 + 2C/P}\varphi(\nu), \tag{2.64}$$

$$I_s = \frac{cP + 2cC}{2B\Omega_M} = \frac{cP}{2B\Omega_m}(1 + 2C/P), \tag{2.65}$$

and

$$\varepsilon = \frac{h\nu_0}{4\pi} N_2 A \varphi(\nu). \tag{2.66}$$

We then have the simple formula

$$\frac{\mathrm{d}I_\nu}{\mathrm{d}s} = \frac{\alpha I_\nu}{1 + I_\nu/I_s} + \varepsilon. \tag{2.67}$$

The part expressed by ε is regarded as a constant in most astrophysical situations and can often be neglected. When $I_\nu \ll I_s$ we can find the solution for the unsaturated maser at $\nu = \nu_0$

$$I_{\nu 0} = I_0 e^{\alpha_0 l} + \frac{\varepsilon}{\alpha_0}(e^{\alpha_0 l} - 1), \tag{2.68}$$

where α_0 is the value for the line center and l is the length along the line of sight within the maser region. For $I_\nu \gg I_s$ we can get the solution for a saturated maser,

$$I_{\nu 0} = I_0 + (\alpha_0 I_s + \varepsilon) l. \tag{2.69}$$

The intensity of masers increases exponentially with l in the unsaturated state while it increases linearly under saturated conditions.

2.5 Interferometry

The angular resolution of a radio telescope depends on its diameter (D) and the observed frequency (ν), that is $\theta \approx 1.2\lambda/D$ (Condon & Ransom 2016), where $\lambda = c/\nu$. This means if one wants to have a better angular resolution, then one should use a shorter wavelength or go to a larger telescope. The largest fully steerable single-dish telescopes have a diameter of about 100 m. The Effelsberg 100-m telescope was the first of this kind (see details in Sect. 2.6.2). Its highest angular resolution is about $10''$ at the highest frequency (or at the shortest wavelength ~3 mm), which is not good enough to obtain accurate positions and adequate angular resolution for many compact sources, e.g. one of the topics of this thesis, astronomical masers, which have a typical size in the sub-arcsecond range.

The simplest radio interferometer contains two radio antennas, often called elements, whose measured signals are correlated. Figure 2.8 shows a two element multiplying interferometer. Its baseline is b, the distance between these two dishes, and the baseline vector is $\vec{b}$. Both antennas point toward the same distant source in the direction specified by the unit vector $\hat{s}$. The signals from the distant source have different distances to reach these two antennas, in time the lag is $\tau_\mathrm{g} = \frac{\vec{b}\cdot\hat{s}}{c} = \frac{b\cos\theta}{c}$, caused by the geometric delay $b\cos\theta$, experienced by the antenna on the left hand side of Fig. 2.8. Naturally, the longer the baseline $\vec{b}$, the smaller changes in the direction $\hat{s}$ are required to modify the incoming wave pattern, thus increasing the angular resolution. At time t, the output voltages of these two antennas are

$$V_1 = V\cos[\omega(t - \tau_\mathrm{g})] \quad \text{and} \quad V_2 = V\cos(\omega t), \tag{2.70}$$

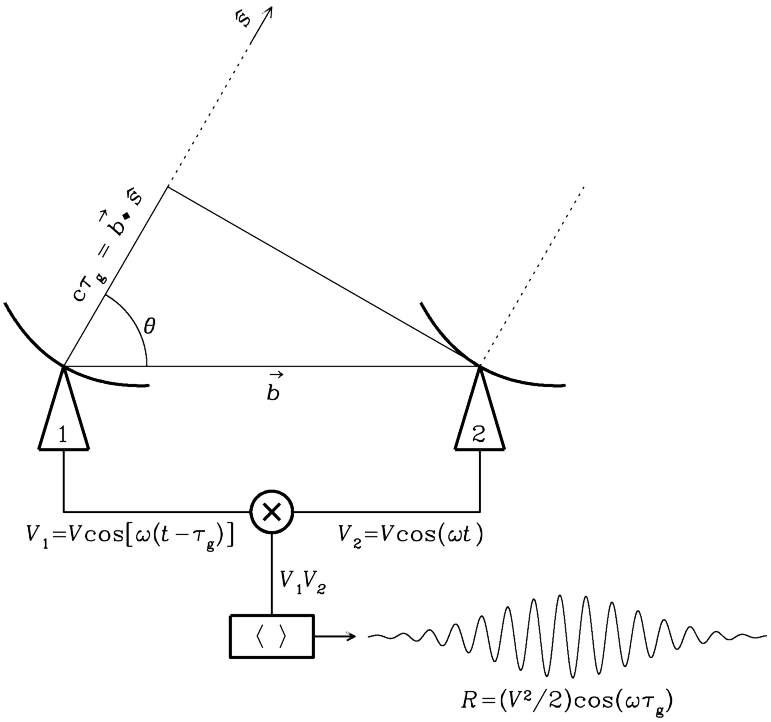

Figure 2.8: The two element multiplying interferometer, taken from Condon & Ransom (2016).

where ω is the angular frequency, $\omega \equiv 2\pi\nu$, and ν is the center frequency in the radio frequency range that these two antennas are targeting. The response (output voltage), R, of a correlator that multiplies these two voltages is

$$\begin{aligned} R = \langle V_1 V_2 \rangle = V_1 V_2 &= V^2 \cos[\omega(t-\tau_{\rm g})]\cos(\omega t) \\ &= \left(\frac{V^2}{2}\right)[\cos(2\omega t - \omega\tau_{\rm g}) + \cos(\omega\tau_{\rm g})]. \end{aligned} \tag{2.71}$$

The high-frequency part $\cos(2\omega t - \omega\tau_{\rm g})$ will be removed by the correlator after a long time to only keep the more slowly varying part. Then the correlator response is

$$R = \left(\frac{V^2}{2}\right)\cos(\omega\tau_{\rm g}). \tag{2.72}$$

While the source direction is changing due to Earth's rotation, $\tau_{\rm g}$ is changing, which causes sinusoids, called fringes, adding to the correlator output voltage (as shown in Fig. 2.8). The fringe phase is $\phi = \omega\tau_{\rm g} = \frac{\omega}{c} b\cos\theta$ (Condon & Ransom 2016).

To measure a source with sky brightness distribution, $I_\nu(\hat{s})$, at frequency ν, we need to obtain both even and odd parts of a source brightness distribution, i.e., $I = I_{\rm E} + I_{\rm O}$ of the sinusoids. Such a two element multiplying interferometer in Fig. 2.8 with a "cosine" correlator can only detect the even part $I_{\rm E}$. Thus we also need a "sine" correlator that can detect the odd part $I_{\rm O}$. The output of these two correlators are

$$R_{\rm c} = \int I(\hat{s})\cos(2\pi\vec{b}\cdot\hat{s}/\lambda)d\Omega \tag{2.73}$$

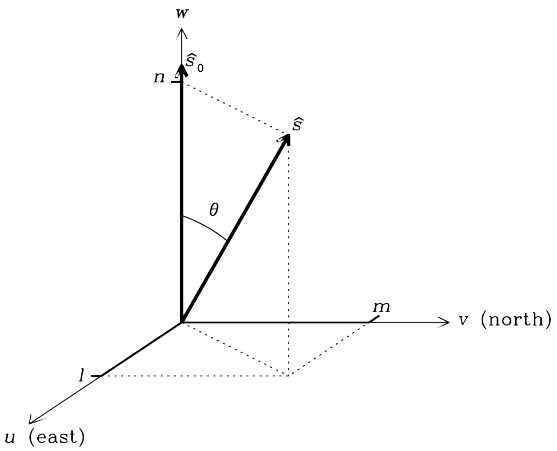

Figure 2.9: The (u, v, w) coordinate system for interferometers in three dimensions, taken from Condon & Ransom (2016).

and

$$R_{\rm s} = \int I(\hat{s}) \sin(2\pi \vec{b} \cdot \hat{s}/\lambda) d\Omega. \tag{2.74}$$

To combine the even and odd parts, i.e., the cosine and sine correlator outputs, we need a complex correlator that can mathematically merge these two parts by using Euler's formula

$$e^{i\phi} = \cos\phi + i \sin\phi. \tag{2.75}$$

$\mathcal{V}$ is the complex visibility and is defined by $\mathcal{V} \equiv R_{\rm c} - iR_{\rm s}$. A is the visibility amplitude, $A = (R_{\rm c}^2 + R_{\rm s}^2)^{1/2}$. Then we can get $\mathcal{V} = Ae^{-i\phi}$, ϕ is the visibility phase and $\phi = \tan^{-1}(R_{\rm s}/R_{\rm c})$. The output from a complex correlator is

$$\mathcal{V} = \int I(\hat{s}) \exp(-i2\pi \vec{b} \cdot \hat{s}/\lambda)\, d\Omega. \tag{2.76}$$

For interferometers in three dimensions, we have the (u, v, w) coordinate system, as shown in Fig. 2.9. The projections of $\hat{s}$ onto the $u-$, $v-$, and $w-$axes are l, m, and n, respectively. Since $d\Omega = \frac{dl\, dm}{(1-l^2-m^2)^{1/2}}$, the output V in the three dimensions is

$$\mathcal{V}(u, v, w) = \int\int \frac{I_\nu(l, m)}{(1 - l^2 - m^2)^{1/2}} \exp[-i2\pi(ul + vm + wn)] dl\, dm. \tag{2.77}$$

Aperture-synthesis interferometers consist of multiple dishes and can span up to hundred thousands of kilometers (e.g. the radioastron space antenna in combination with Earth-bound facilities). For example, the Karl G. Jansky Very Large Array (JVLA, see details in Sect. 2.6.3), used in this thesis to measure the accurate positions of ammonia masers, has 28 (27 active currently) antennas with a diameter of 25 meters. Its A-configuration is the most extended one and has a size of 22.62 miles (or about 36.40 kilometers) across[3]. It has the high angular resolution of a large telescope with

[3]https://public.nrao.edu/telescopes/vla/

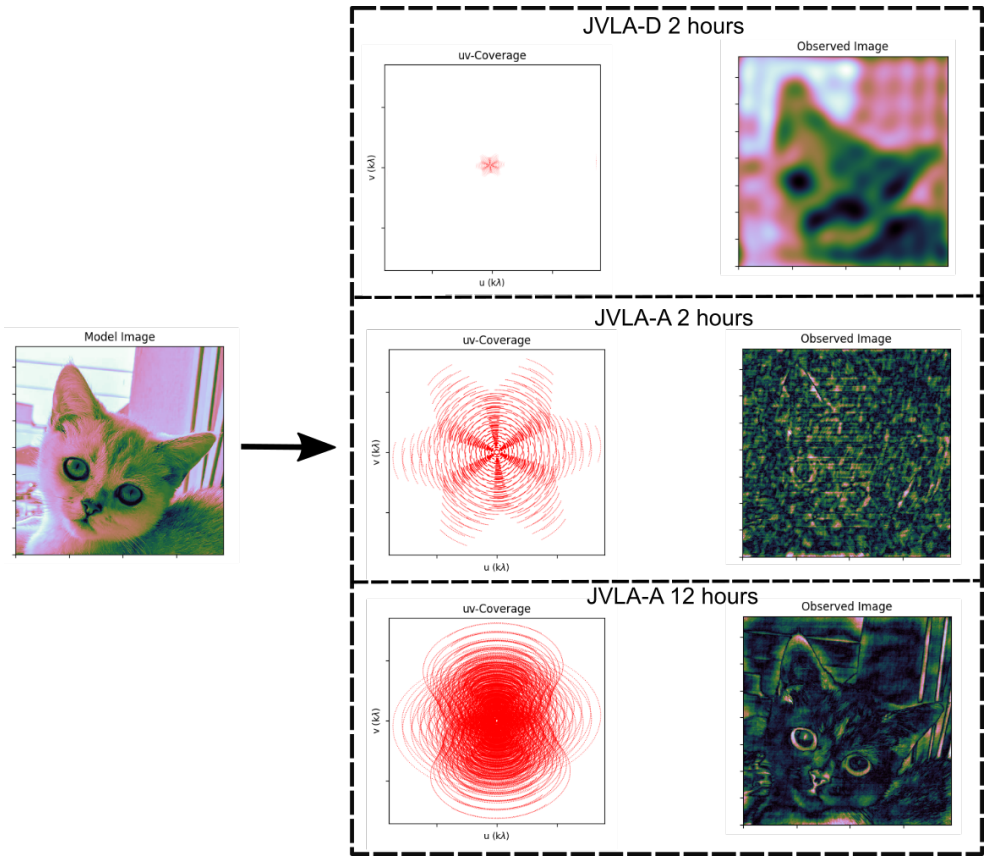

Figure 2.10: Examples of simulated observation with JVLA A- and D-configurations. The model image of a cat is shown on the left. The uv-coverages and observed images with JVLA D- and A-configurations after 2 hours as well as A-configuration after 12 hours are shown in the black boxes. The observations were simulated with friendlyVRI (Copyright: Cormac R. Purcell and Roy Truelove).

a diameter of 36.40 km and the wide field of view of a 25-m telescope, the latter is the so-called primary beam. The most compact array of JVLA is the D-configuration. The minimal baseline is 0.04 km and the maximal baseline is around 1.02 km. When observing an extended source, the missing spacings, i.e. the minimal baseline can cause missing flux density in interferometer data (Condon & Ransom 2016). Supplementary measurements by a single dish with a diameter larger than the minimal baseline can solve this problem (Condon & Ransom 2016). For example, the Effelsberg 100-m telescope can fill in the missing baselines of JVLA D-configuration observations.

Figure 2.10 shows simulated observations of a cat with JVLA A- and D-configurations. The JVLA A-configuration provides higher angular resolution and can show finer details than the JVLA D-array, as shown in the figure. After a longer integration time, more uv-coverage can show a more precise distribution of the source.

2.6 The facilities used in this thesis

In this thesis, we used three different facilities. These are the 30-meter IRAM radio telescope located in Spain, the 100-meter radio telescope at Effelsberg located in Germany, and the Karl G. Jansky Very Large Array in the United States. Details are presented in the following sections.

2.6.1 The 30-meter IRAM radio telescope

The 30-meter IRAM radio telescope[4], shown in Fig. 2.11, located in the Spanish Sierra Nevada. Its altitude is 2850 meters and it is one of the most powerful single-dish telescopes for millimeter wave astronomy in the world. The frequency coverage is 80 to 370 GHz, that is 3 to 0.8 millimeters in wavelength.

Currently, the IRAM 30-m hosts three different frontends, including two heterodyne receivers, the spectral line Eight MIxer Receiver (EMIR) and the HEterodyne Receiver Array (HERA), as well as the new wide field-of-view camera NIKA-2. EMIR has four bands, E090, E150, E230, and E330 with frequency ranges of 72.68–117 GHz, 125–184 GHz, 202–274 GHz, and 277–375 GHz, respectively. The atmospheric transmission under typical weather conditions at 2 mm (blue) and 4 mm (red) of precipitable water vapor (pwv) for these four bands at the IRAM 30-m is shown in Fig. 2.12.

In this thesis we used the EMIR receiver in two bands, E090 and E150, to cover a bandwidth of ∼16 GHz (from 90.8 to 98.2 GHz and 138.4 to 146.0 GHz) simultaneously in dual polarisation. Our observations were performed in 2019 June, July, and October under project 045-19 (PI, Christian Henkel) as well as in 2020 August within project 022-20 (PI, Hongzhi Yu). Our lines of interest are the $J = 2{-}1$ transitions of CS, $C^{33}S$, $C^{34}S$, $C^{36}S$, ^{13}CS, $^{13}C^{33}S$, and $^{13}C^{34}S$ as well as the $J = 3{-}2$ transitions of $C^{33}S$, $C^{34}S$, $C^{36}S$, and ^{13}CS. We used the wide-mode FTS backend with a resolution of 195 kHz, corresponding to ∼0.6 km s^{-1} and ∼0.4 km s^{-1} at 96 GHz and 145 GHz, respectively.

The observations were performed in total-power position-switching mode and the off position was set at 30′ in azimuth. Pointing was checked every 2 hours using nearby quasars. Focus calibrations were done at the beginning of the observations and during sunset and sunrise toward strong quasars. The main beam brightness temperature, $T_{\rm MB}$, was derived from the antenna temperatures $T_{\rm A}^*$ via the relation $T_{\rm MB} = T_{\rm A}^* \times F_{\rm eff}/B_{\rm eff}$ ($F_{\rm eff}$: forward hemisphere efficiency; $B_{\rm eff}$: main beam efficiency) with corresponding telescope efficiencies[5]: $F_{\rm eff}/B_{\rm eff}$ are 0.95/0.81 and 0.93/0.73 in the 90.8-98.2 GHz and 138.4-146.0 GHz frequency ranges, respectively. The system temperatures were 100-160 K and 170-300 K on a $T_{\rm A}^*$ scale for the E090 and E150 band observations. The half power beam width (HPBW) for each transition was calculated as HPBW(″)=2460/ν(GHz). Rest frequencies, excitations of the upper levels above the ground state, Einstein coefficients for spontaneous emission, and respective beam sizes are listed in Table 3.1. The results are presented in Section 3 and Appendix A.

[4]IRAM is supported by INSU/CNRS (France), MPG (Germany) and IGN (Spain).
[5]https://publicwiki.iram.es/Iram30mEfficiencies

Figure 2.11: The 30-meter IRAM radio telescope. Credit: IRAM, K.Zacher.

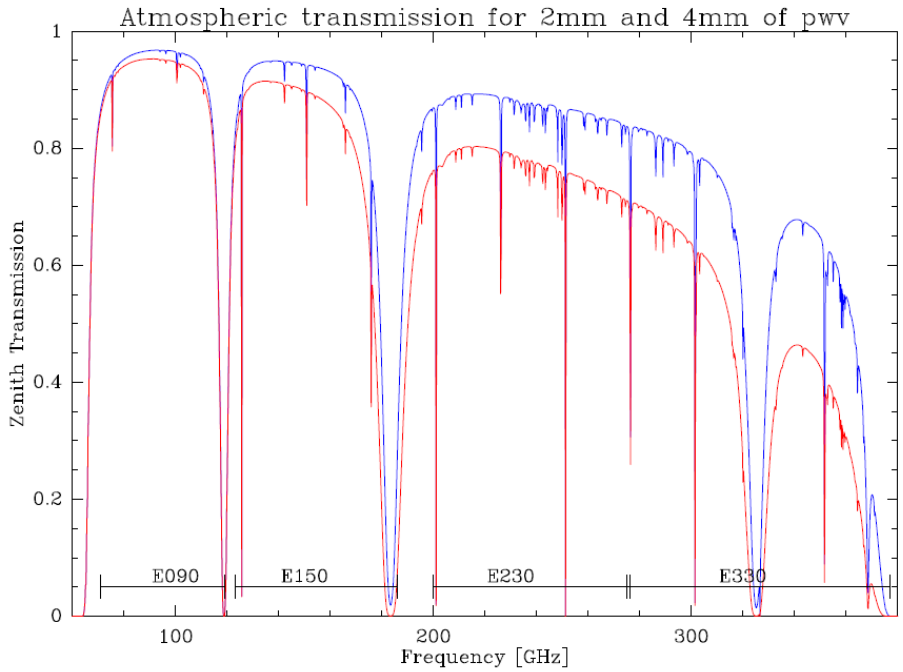

Figure 2.12: The atmospheric transmission at the IRAM 30-m under typical weather conditions at 2 mm (blue) and 4 mm (red) of pwv. Credit: IRAM.

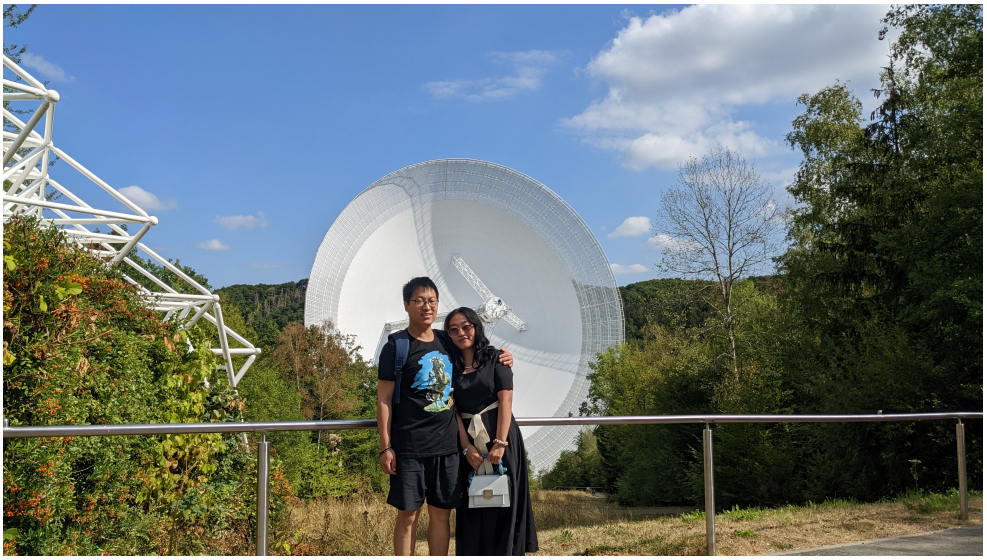

Figure 2.13: The 100-meter Effelsberg radio telescope, my fiancée, Siqi Guo (郭思祺) and me. The photo was taken during the institute's party in 2022 by Dr. Yan Gong.

2.6.2 The 100-meter Effelsberg telescope

The 100-meter Effelsberg radio telescope[6] was constructed since 1967 and has been fully operated since 1972 by the Max-Planck-Institut für Radioastronomie (MPIfR) in Bonn. It is still one of the largest single-dish and most powerful radio telescopes on Earth, even after more than five decades of full operations (Fig. 2.13). Its frequency coverage is 300 MHz to 90 GHz, that is 90 centimeters to 3.5 millimeters in wavelength. The Effelsberg 100-m telescope has multiple receivers at the prime focus and the secondary focus. They are continuing technical upgrades all the time. In this thesis, we used the new K-band receiver, which is the S14mm double beam secondary focus receiver.

The receiver can simultaneously cover the entire K-band frequency range, i.e., 18.0–26.0 GHz. Its band is divided into four 2.5 GHz-wide subbands with frequency ranges of 18.0–20.5 GHz, 19.9–22.4 GHz, 21.6–24.1 GHz, and 23.5–26.0 GHz. Each subband has 65536 channels, providing a channel width of 38.1 kHz, corresponding to $\sim$0.62 km s^{-1} at 18.5 GHz, $\sim$0.57 km s^{-1} at 20.0 GHz, $\sim$0.52 km s^{-1} at 22.0 GHz, $\sim$0.47 km s^{-1} at 24.0 GHz, and $\sim$0.44 km s^{-1} at 26.0 GHz.

Our observations with the Effelsberg 100-m telescope span three and a half years, from 2020 January to 2023 July, consisting of on-site and remote observations (Fig. 2.14). The observations were performed in position switching mode with the off position $10'$ in azimuth away from the source. The half power beam width (HPBW) was $49 \times 18.5/\nu(\mathrm{GHz})$ arcseconds, that is $49''$ at 18.5 GHz, the frequency of the NH_3 (9,6) line. A high spectral resolution backend with 65536 channels and a bandwidth of 300 MHz was employed to measure the NH_3 (9,6) maser sources, providing a channel width of 0.07 km s^{-1} at 18.5 GHz.

[6] https://www.mpifr-bonn.mpg.de/en/effelsberg

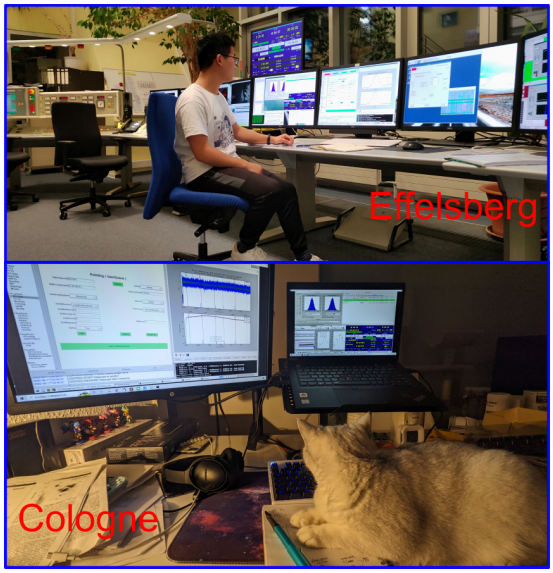

Figure 2.14: On-site observations (top) and remote observations (bottom, together with our cute "girl" Naicha) at Cologne with the Effelsberg 100-meter telescope.

Pointing and focus calibrations were done at the beginning of the observations, during sunset and sunrise, as well as every hour towards NGC 7027. The calibrator was measured between elevations of 30 and 60 degrees. Pointing was checked using nearby quasars prior to on-source integrations. The elevations on our targets were in a range of 10 to 55 degrees. The system temperatures were 60–220 K on a main-beam brightness temperature, $T_{\rm MB}$, scale. The flux density was calibrated to the data, which were split into small chunks with bandwidths of 300 MHz, based on continuum cross scans of NGC 7027 (Winkel et al. 2012). Its flux density was adopted from Ott et al. (1994). The $T_{\rm MB}/S$ ratios are 1.95 K/Jy, 1.73 K/Jy, and 1.68 K/Jy at 18.5 GHz, 22.2 GHz, and 24.0 GHz, respectively. Calibration uncertainties were estimated to be $\pm$10%.

Figure 2.15 shows the telescope and weather conditions during our K-band line survey (project ID: 34-22) in November 2022, and in February, April, May, as well as in July 2023. The pictures were taken from the webcam at Effelsberg station at different epoch measurements.

2.6.3 The Karl G. Jansky Very Large Array

The Karl G. Jansky Very Large Array[7] (Fig. 2.16) was constructed starting in 1972 and was formally inaugurated in 1980 by the National Radio Astronomy Observatory (NRAO). It has 28 (27 active currently) antennas with a diameter of 25 meters. The unique "Y" shape of the JVLA allows it to modify configurations by using a specially-designed rail truck. The JVLA has four configurations, they are the A, B, C, and D-configurations. The A-configuration is the most extended one and has a size of 22.62

[7]https://public.nrao.edu/telescopes/vla/

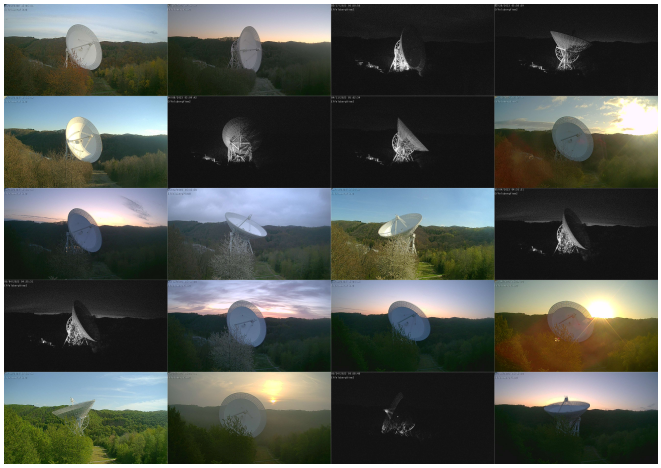

Figure 2.15: Effelsberg station at different epochs during our K-band line survey (project ID: 34-22) from November 2022 to July 2023.

miles across. The D-configuration is the most compact one and has a size of 0.64 miles across. In this thesis, we used the C-configuration to observe the NH_3 (9,6) masers in Cepheus A (Cep A) and G34.26+0.15 (see details in Section 4 and Appendix B) as well as the A-configuration to measure the widespread non-metastable ammonia masers in Sagittarius B2 (Sgr B2, see details in Section 5 and Appendix C).

The frequency coverage of the JVLA is from 1.0 GHz to 50 GHz. Our observations of the NH_3 (9,6) line toward Cep A and G34.26+0.15 were obtained on 2021 July 13 in the C configuration (project ID: 21A-157, PI: Yaoting Yan). We employed 27 antennas for the observations. The primary beam of the JVLA antennas is $150''$ (FWHM) at 18.5 GHz. A mixture of mixed three-bit and eight-bit samplers were used to perform the observations. For the NH_3 (9,6) line observations, we used one subband with the eight-bit sampler covering a bandwidth of 16 MHz with full polarization, eight recirculations, and four baseline board pairs (BIBPs) to provide a velocity range of 260 km s^{-1} with a channel spacing of 0.13 km s^{-1}. Two additional subbands of bandwidth 16 MHz were used to cover the NH_3 (8,5) and (10,7) lines. A three-bit sampler with 32 subbands, each with a bandwidth of 128 MHz to cover a total range of 4 GHz between 20–24 GHz, was used to measure the continuum emission. 3C 286 with a flux density of 2.89 Jy at 18.5 GHz (Perley & Butler 2013) was used as a calibrator for pointing, flux density, bandpass, and polarization. J2230+6946 and J1851+0035 served as gain calibrators for Cep A and G34.26+0.15, respectively. The on-source times were 4^m30^s and 4^m50^s toward Cep A and G34.26+0.15, respectively.

Toward Sgr B2, we observed six NH_3 lines, the (5,1), (6,3), (7,4), (8,5), (9,6), and (10,7) transitions (Table 5.1), with the JVLA in the A-configuration (project ID: 22A-106, PI: Yaoting Yan). Eight-bit samplers were used to perform the observations. For the NH_3 (9,6) and (10,7) line observations, we used two subbands with the eight-bit samplers covering a bandwidth of 16 MHz with full polarization, eight recirculations, and four baseline board pairs (BLBPs) to provide a velocity range of 260 km s^{-1} with

Figure 2.16: The Karl G. Jansky Very Large Array. Credit: Bettymaya Foott, NRAO/AUI/NSF.

a channel spacing of 0.13 km s^{-1}. Four additional subbands of bandwidth 16 MHz were used to cover the NH_3 (5,1), (6,3), (7,4), and (8,5) lines. The remaining ten subbands of the eight-bit sampler with a bandwidth of 128 MHz were used to measure the continuum emission between 18 and 20 GHz. The primary beam of the JVLA antennas is 150″ (FWHM) at 18.5 GHz, covering all prominent star-forming regions in Sgr B2 simultaneously. 3C 286 was used as a calibrator for pointing, flux density, bandpass, and polarization (Perley & Butler 2013). J1745-2900 served as our gain calibrator during the observations. The on-source time was 30 minutes toward Sgr B2.

Chapter 3

Carbon and sulfur isotope ratios in the Milky Way

This chapter is a summary of the refereed article published in Astronomy and Astrophysics (see Appendix A) titled **"Direct measurements of carbon and sulfur isotope ratios in the Milky Way"** by:

Y. T. Yan, C. Henkel, C. Kobayashi, K. M. Menten,
Y. Gong, J. S. Zhang, H. Z. Yu, K. Yang,
J. J. Xie, and Y. X. Wang
2023, A&A, 670, A98.
DOI:10.1051/0004-6361/202244584

3.1 Context

As discussed in Chapter 1.3, observations indeed indicate gradients of $^{12}C/^{13}C$ and $^{32}S/^{34}S$ ratios across the Galaxy. Previous measurements on $^{12}C/^{13}C$ ratios are mostly based on molecules with significant optical depth, for example, CN and H_2CO, which could negatively affect the results. The published $^{32}S/^{34}S$ gradients are based on the double isotope method, which needs formerly determined $^{12}C/^{13}C$ ratios, and enhances the uncertainties. Moreover, data from the central molecular zone (CMZ) are lacking. There were not many sources being part of the innermost Galactic disk, and also the number of sources beyond the Perseus arm was small, indicating that there is still significant space for improvement.

3.2 Aims

We aim to measure the $^{12}C/^{13}C$, $^{32}S/^{34}S$, $^{32}S/^{33}S$, $^{32}S/^{36}S$, $^{34}S/^{33}S$, $^{34}S/^{36}S$, and $^{33}S/^{36}S$ isotope ratios across the Milky Way. With the isotope ratios and accurate distances, we intend to confirm the gradients of $^{12}C/^{13}C$ and $^{32}S/^{34}S$ that were reported in previous publications. Also, we aim to check the so far obtained uniform values of $^{34}S/^{33}S$ and to establish $^{32}S/^{33}S$, $^{32}S/^{36}S$, $^{34}S/^{36}S$, and $^{33}S/^{36}S$ gradients in our Galaxy.

3.3 Our sample

In total, 110 high-mass star-forming regions (HMSFRs) in the Galaxy are part of our survey. Among these 110 objects, 98 sources have accurate distances with trigonometric parallax data (Reid et al. 2009a, 2014, 2019) from the Bar and Spiral Structure Legacy (BeSSeL) Survey[1]. For 12 of our targets without trigonometric parallax data, we estimated their kinematic distances from the Revised Kinematic Distance calculator[2] (Reid et al. 2014).

3.4 Lines of interest

Carbon monosulfide (CS) is a strong and widespread molecular species that allows us to measure carbon and sulfur isotope ratios simultaneously. With the IRAM 30 meter telescope[3], we performed observations of the J = 2–1 transitions of CS, $C^{33}S$, $C^{34}S$, $C^{36}S$, ^{13}CS, $^{13}C^{33}S$, and $^{13}C^{34}S$ as well as the J = 3–2 transitions of $C^{33}S$, $C^{34}S$, $C^{36}S$, and ^{13}CS toward 110 HMSFRs in 2019 June, July, and October as well as in 2020 August. Rest frequencies, excitation of the upper levels above the ground state, Einstein coefficients for spontaneous emission, and respective beam sizes are listed in Table 3.1.

Table 3.1: Observed spectral line parameters[a].

Isotopolog	Transition	ν_0[b] (MHz)	E_{up}[c] (K)	$A_{u,l}$[d] (s^{-1})	HPBW[e] ($''$)
CS	2-1	97980.953	7.1	1.68×10^{-5}	25.1
$C^{33}S$	2-1	97172.064	7.0	1.64×10^{-5}	25.3
$C^{34}S$	2-1	96412.95	6.9	1.60×10^{-5}	25.5
$C^{36}S$	2-1	95016.722	6.8	1.53×10^{-5}	25.9
^{13}CS	2-1	92494.308	6.7	1.41×10^{-5}	26.6
$^{13}C^{33}S$	2-1	91685.241	6.6	1.38×10^{-5}	26.8
$^{13}C^{34}S$	2-1	90926.026	6.5	1.34×10^{-5}	27.1
$C^{33}S$	3-2	145755.732	14.0	5.92×10^{-5}	16.9
$C^{34}S$	3-2	144617.101	13.9	5.78×10^{-5}	17.0
$C^{36}S$	3-2	142522.785	13.7	5.54×10^{-5}	17.3
^{13}CS	3-2	138739.335	13.3	5.11×10^{-5}	17.7

Notes. [(a)] From the Cologne Database for Molecular Spectroscopy (CDMS, Müller et al. 2005; Endres et al. 2016). [(b)] Rest frequency. [(c)] Upper energy level. [(d)] Einstein coefficient for spontaneous emission from upper level u to lower level l. [(e)] Half power beam width.

[1] http://bessel.vlbi-astrometry.org
[2] http://bessel.vlbi-astrometry.org/revised_kd_2014
[3] IRAM is supported by INSU/CNRS (France), MPG (Germany) and IGN (Spain).

3.5 Data reduction

We used the GILDAS/CLASS[4] package to analyze the spectral line data. The spectra of the $J = 2$–1 transitions of CS, $C^{33}S$, $C^{34}S$, $C^{36}S$, ^{13}CS, $^{13}C^{33}S$, and $^{13}C^{34}S$ as well as the $J = 3$–2 transitions of $C^{33}S$, $C^{34}S$, $C^{36}S$, and ^{13}CS toward one of our targets, DR21, are shown in Fig. 3.1, after subtracting first-order polynomial baselines and applying Hanning smoothing.

Among our sample of 110 targets, we detected the $J = 2$–1 line of CS toward 106 sources, which yields a detection rate of 96%. The $J = 2$–1 transitions of $C^{34}S$, ^{13}CS, $C^{33}S$, and $^{13}C^{34}S$ were successfully detected in 90, 82, 46, and 17 of our sources with signal-to-noise (S/N) ratios of greater than 3, respectively. The $J = 3$–2 lines of $C^{34}S$, ^{13}CS, and $C^{33}S$ were detected in 87, 71, and 42 objects with S/Ns of $\geq$3.0. Relevant for the evaluation of isotope ratios is the fact that for 17 sources with 19 velocity components, the S/Ns of the $J = 2$–1 transition of $^{13}C^{34}S$ are greater than 3, which allows us to determine the $^{12}C/^{13}C$ and $^{32}S/^{34}S$ ratios directly with the $J = 2$–1 lines of $C^{34}S$, ^{13}CS, and $^{13}C^{34}S$. Toward 82 targets with 90 radial velocity components, the $J = 2$–1 transitions of $C^{34}S$ and ^{13}CS were both detected with S/Ns of $\geq$3.0. The $J = 3$–2 lines of $C^{34}S$ and ^{13}CS were both found in 71 objects with 73 radial velocity components and S/Ns of $\geq$3.0. Furthermore, the $J = 2$–1 and $J = 3$–2 transitions of $C^{34}S$ and $C^{33}S$ were detected with S/Ns of $\geq$3.0 toward 46 and 42 sources, respectively.

The $C^{36}S$ $J = 2$–1 line was successfully detected with S/Ns of $\geq$3.0 toward three targets, namely W3OH, the +50 km s^{-1} cloud near the Galactic center, and DR21. As $C^{36}S$ and $^{13}C^{33}S$ are the least abundant among the CS isotopologs, tentative detection with S/Ns of $\sim$2.0 are also presented here but not included in further analyses. In another five objects, the $C^{36}S$ $J = 2$–1 line was tentatively detected. For the $C^{36}S$ $J = 3$–2 transitions, we report one detection with an S/N larger than 3.0 toward Orion-KL and five tentative detections. The $J = 2$–1 lines of $^{13}C^{33}S$ were tentatively detected toward three sources, namely Orion-KL, W51-IRS2, and DR21.

3.6 Results

In this section, we present the carbon and sulfur isotope ratios derived from different detected CS isotopologs. In order to avoid problems with line saturation that might affect our results, we first estimate the optical depths of the various lines.

3.6.1 Optical depth

The main isotopolog, CS, is usually optically thick in massive star-forming regions (e.g. Linke & Goldsmith 1980). Therefore, the $^{12}C/^{13}C$ and $^{32}S/^{34}S$ ratios cannot be determined from the line intensity ratios of $I(CS)/I(^{13}CS)$ and $I(CS)/I(C^{34}S)$. We estimate the maximum optical depth of the CS, ^{13}CS, and $C^{34}S$ $J = 2$–1 lines and apply the corrections for optical depth to $C^{34}S$ and ^{13}CS in the following analyses.

[4] https://www.iram.fr/IRAMFR/GILDAS/

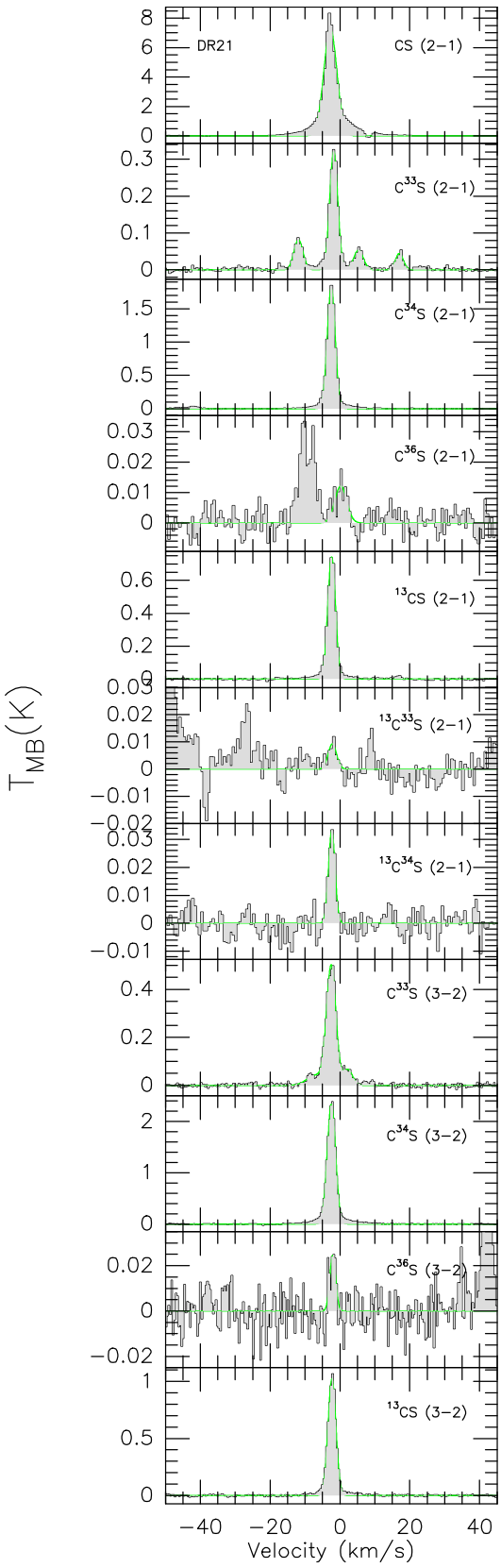

Figure 3.1: Line profiles of the $J = 2$–1 transitions of CS, $C^{33}S$, $C^{34}S$, $C^{36}S$, ^{13}CS, $^{13}C^{33}S$, and $^{13}C^{34}S$ as well as the $J = 3$–2 transitions of $C^{33}S$, $C^{34}S$, $C^{36}S$, and ^{13}CS toward one typical target (DR21) of our large sample of 110 sources, after subtracting first-order polynomial baselines. The main beam brightness temperature scales are presented on the left hand side of the profiles. Adapted from Fig. 1 in Yan et al. (2023).

3.6.2 $^{12}C/^{13}C$ ratios

The $^{12}C/^{13}C$ ratios are directly derived from the integrated intensity ratios of $C^{34}S$ and $^{13}C^{34}S$ with small corrections of optical depth. We obtain from our measurements the following $^{12}C/^{13}C$ gradient in the Milky Way:

$$^{12}C/^{13}C = (4.77 \pm 0.81) R_{GC} + (20.76 \pm 4.61). \quad (3.1)$$

The correlation coefficient is 0.82. Our results are shown in Fig. 3.2.

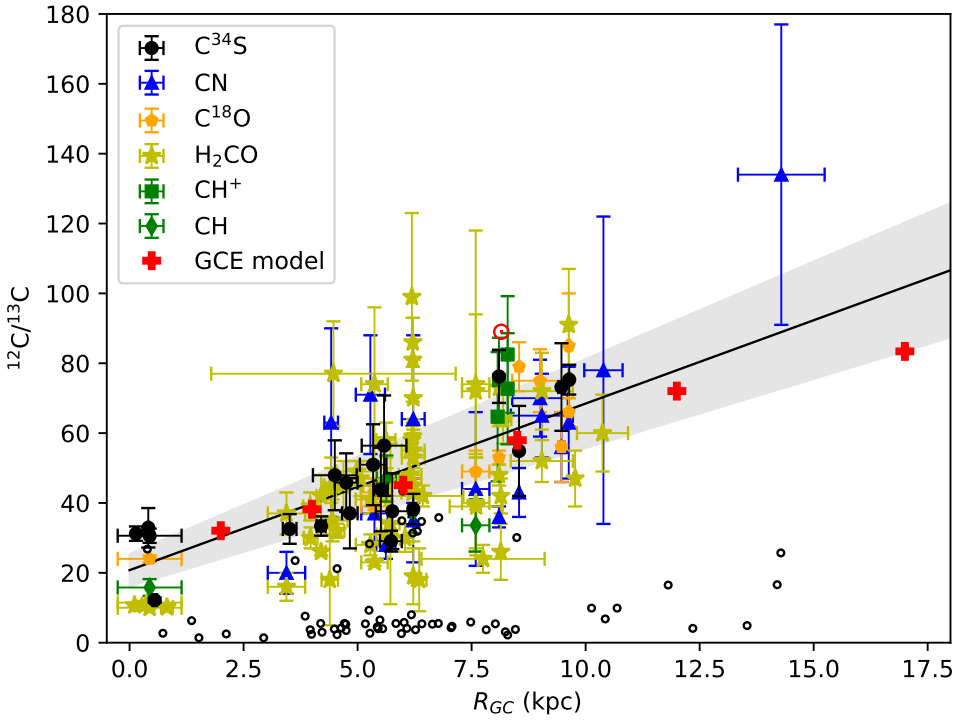

Figure 3.2: $^{12}C/^{13}C$ isotope ratios from $C^{34}S/^{13}C^{34}S$, $CN/^{13}CN$, $C^{18}O/^{13}C^{18}O$, $H_2CO/H_2^{13}CO$, $CH^+/^{13}CH^+$, and $CH/^{13}CH$ are plotted as functions of the distance from the Galactic center, adapted from Fig. 3 in Yan et al. (2023) and references therein. The red symbol $\odot$ indicates the $^{12}C/^{13}C$ isotope ratio of the Sun. The filled black circles are the results obtained from $C^{34}S$ with (small) corrections of opacity in the current work, and the resulting first-order polynomial fit is plotted as a solid line, with the gray-shaded area showing the 1σ interval of the fit. The open black circles are the 3σ lower limits obtained from nondetections of $^{13}C^{34}S$ in this thesis. The red crosses visualize the results from the GCE model of Kobayashi et al. (2011, 2020).

3.6.3 $^{32}S/^{34}S$ ratios

For the first time, we established a $^{32}S/^{34}S$ gradient directly from measurements of ^{13}CS and $^{13}C^{34}S$ from the $J = 2$–1 lines after correcting for optical depth effects:

$$^{32}S/^{34}S = (0.73 \pm 0.36)R_{GC} + (16.50 \pm 2.07). \quad (3.2)$$

We also derive the $^{32}S/^{34}S$ values from measurements of $C^{34}S$ and ^{13}CS and the carbon isotope ratio gradient obtained from our $^{13}C^{34}S$ measurements in Chatper 3.6.2, the so called double isotope method. A gradient with $^{32}S/^{34}S = (0.75 \pm 0.13)R_{GC}+(15.52 \pm 0.78)$ was obtained based on a large dataset of 90 values from our detections of ^{13}CS and $C^{34}S$ $J = 2$–1 lines with corrections of opacity, which is within the errors consistent with the trend obtained directly from ^{13}CS and $^{13}C^{34}S$.

3.6.4 $^{34}S/^{33}S$ ratios

We determine the $^{34}S/^{33}S$ ratios directly from the $C^{34}S/C^{33}S$ intensity ratios with corrections of optical depths and hyperfine splitting effects. We find that there is no systematic dependence of the $^{34}S/^{33}S$ ratios on galactocentric distance (Fig. 3.3). We obtain an average $^{34}S/^{33}S$ value of 4.35 ± 0.44 from our sample in the $J = 2$–1 transition.

3.6.5 $^{32}S/^{33}S$ ratios

We derive the $^{32}S/^{33}S$ values from the $^{34}S/^{33}S$ ratios in Chapter 3.6.4 by combining the $^{32}S/^{34}S$ ratios which we directly obtained from $^{13}CS/^{13}C^{34}S$ and present in Chapter 3.6.3. An approximately constant $^{34}S/^{33}S$ ratio across the Galactic plane leads to a $^{32}S/^{33}S$ gradient in our Galaxy (Fig. 3.3): $^{32}S/^{33}S = (2.64 \pm 0.77)R_{GC} + (70.80 \pm 5.57)$, with a correlation coefficient of 0.46.

3.6.6 $^{34}S/^{36}S$, $^{33}S/^{36}S$, and $^{32}S/^{36}S$ ratios

$^{34}S/^{36}S$ ratios are derived from the line ratios of $C^{34}S$ and $C^{36}S$. We find novel potential indications for a positive $^{34}S/^{36}S$ gradient with galactocentric radius. Combining the ratios of Mauersberger et al. (1996) — after applying new distances with our results, the following fit could be achieved:

$$^{34}S/^{36}S = (10.34 \pm 2.74)R_{GC} + (57.45 \pm 18.59), \quad (3.3)$$

with a correlation coefficient of 0.71. As the $^{34}S/^{33}S$ ratios show a uniform distribution across our Galaxy (see details in Chapter 3.6.4), a $^{33}S/^{36}S$ gradient is also expected. We obtain $(2.38 \pm 0.67)R_{GC}+(13.21 \pm 4.48)$. We also derive the $^{32}S/^{36}S$ ratios by applying our $^{32}S/^{34}S$ gradient to the $^{34}S/^{36}S$ ratios in Mauersberger et al. (1996). A linear fit to the $^{32}S/^{36}S$ ratios yields:

$$^{32}S/^{36}S = (314 \pm 55)R_{GC} + (659 \pm 374), \quad (3.4)$$

with a correlation coefficient of 0.84.

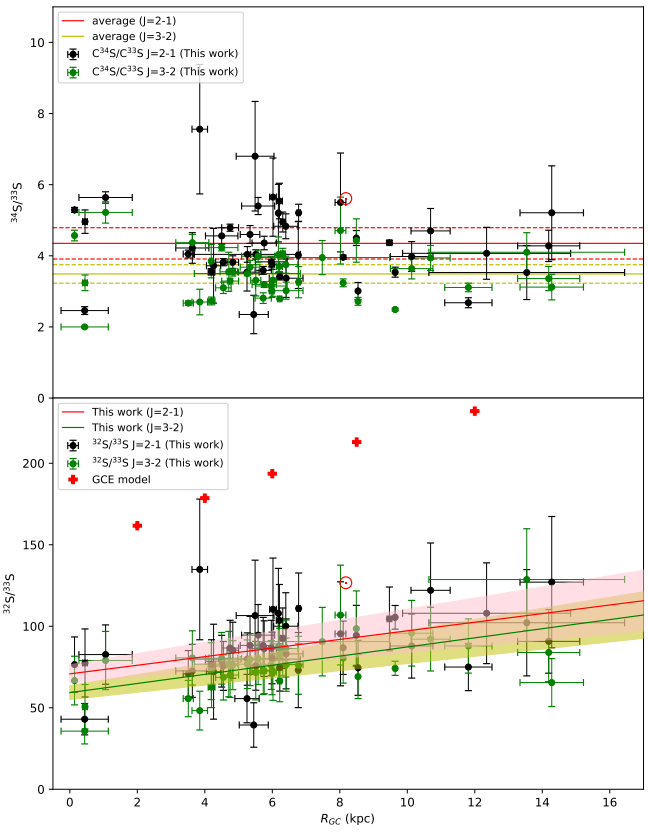

Figure 3.3: $^{34}S/^{33}S$ and $^{32}S/^{33}S$ isotope ratios plotted as functions of the distance from the Galactic center. Adapted from Fig. 7 in Yan et al. (2023). The red crosses are the results from the GCE model of Kobayashi et al. (2011, 2020, see also Chapter 3.6.8).

3.6.7 Interstellar C, N, O, and S isotope ratios

We collect several isotope ratios from archival publications with respect to primary or secondary synthesis in stellar objects, which are $^{12}C/^{13}C$, $^{32}S/^{34}S$, $^{32}S/^{33}S$, and $^{32}S/^{36}S$ ratios. The data is presented here in Table 3.2.

Table 3.2: Interstellar C, N, O, and S isotope ratios. Adapted from Table 7 in Yan et al. (2023).

	Molecule	CMZ	Inner disk	Local ISM	Outer Galaxy	Solar System [*]
$^{12}C/^{13}C$	$C^{34}S^{a}$	27 ± 3	41 ± 9	66 ± 10	74 ± 8	89
	CN^{b}	···	44 ± 12	41 ± 11	66 ± 19	
	$C^{18}O^{c}$	24 ± 1	41 ± 2	60 ± 5	70 ± 10	
	H_2CO^{d}	···	40 ± 7	50 ± 13	64 ± 10	
	average	25 ± 2	42 ± 9	54 ± 10	69 ± 12	
$^{14}N/^{15}N$	CN^{e}	···	269 ± 59	314 ± 104	289 ± 85	270
	HCN^{f}	···	284 ± 63	398 ± 48	388 ± 32	
	HNC^{f}	···	363 ± 100	378 ± 79	395 ± 74	
	N_2H^{+g}	···	900 ± 250	496 ± 65	581 ± 140	
	$NH_3{}^{h}$	40 ± 13	175 ± 46	297 ± 99	96 ± 44	
$^{16}O/^{18}O$	H_2CO^{i}	263 ± 45	327 ± 32	560 ± 25	625 ± 144	490
$^{18}O/^{17}O$	CO^{j}	3.4 ± 0.1	3.6 ± 0.2	3.9 ± 0.4	4.8 ± 0.6	5.5
$^{16}O/^{17}O^{**}$		894 ± 155	1177 ± 132	2184 ± 244	3000 ± 786	2625
$^{32}S/^{34}S^{a}$		19 ± 2	18 ± 4	24 ± 4	28 ± 3	23
$^{34}S/^{33}S^{a}$		4.2 ± 0.2	4.3 ± 0.4	4.2 ± 0.5	4.1 ± 0.3	5.6
$^{32}S/^{33}S^{a}$		70 ± 16	82 ± 19	88 ± 21	105 ± 19	127
$^{34}S/^{36}S^{a}$		41 ± 4	122 ± 18	111 ± 16	161 ± 32	200
$^{32}S/^{36}S^{a}$		884 ± 104	2382 ± 368	2752 ± 458	4150 ± 828	4525

Notes. The inner disk values refer to the mean values at galactocentric distances of 2.0 kpc $\leq R_{GC} \leq$ 6.0 kpc. The local ISM values refer to 7.5 kpc $\leq R_{GC} \leq$ 8.5 kpc. The outer Galaxy values point to 9.0 kpc $\leq R_{GC} \leq$ 11.0 kpc. [(*)] From Anders & Grevesse (1989). [(a)] This work, Yan et al. (2023). [(b)] From Savage et al. (2002) and Milam et al. (2005). [(c)] From Langer & Penzias (1990, 1993), Wouterloot & Brand (1996), and Keene et al. (1998). [(d)] From Henkel et al. (1980, 1982, 1983, 1985) and Yan et al. (2019). [(e)] From Adande & Ziurys (2012), Ritchey et al. (2015), and Fontani et al. (2015). [(f)] From Adande & Ziurys (2012) and Colzi et al. (2018) [(g)] From Ritchey et al. (2015). [(h)] From Chen et al. (2021). [(i)] From Gardner & Whiteoak (1981) and Wilson & Rood (1994). [(j)] From Zhang et al. (2020). [(**)] The $^{16}O/^{17}O$ ratios are derived from $^{16}O/^{18}O$ and $^{18}O/^{17}O$ values.

3.6.8 Galactic chemical environment

$^{12}C/^{13}C$, $^{32}S/^{34}S$, $^{32}S/^{33}S$, and $^{32}S/^{36}S$ ratios at R_{GC} = 2.0, 4.0, 6.0, 8.5, 12.0, and 17.0 kpc are calculated by making use of a Galactic chemical evolution (GCE) model from Kobayashi et al. (2011, 2020). The initial mass function, adopted from Kroupa (2001, 2008), and nucleosynthesis yields are the same for different galactic radii but star formation and inflow timescales (τ_s and τ_i) depend on the Galactic radius (see Kobayashi et al. 2000 for the definition of the timescales). Adopted values are τ_s = 1.0, 2.0, 3.0, 4.6, 6.5, and 8.8 Gyr as well as τ_i = 4.0, 5.0, 5.0, 5.0, 7.0, and 50.0 Gyr for R_{GC} = 2.0, 4.0, 6.0, 8.5, 12.0, and 17.0 kpc, respectively. The predicted $^{12}C/^{13}C$ ratios are in good agreement with our results (Fig. 3.2), while $^{32}S/^{34}S$ and $^{32}S/^{36}S$ ratios

show significant deviations at larger galactocentric distances. $^{32}S/^{33}S$ ratios show an offset along the entire inner 12 kpc of the Milky Way (Fig. 3.3).

3.7 Conclusions

We measured the $^{12}C/^{13}C$, $^{32}S/^{34}S$, $^{32}S/^{33}S$, $^{32}S/^{36}S$, $^{34}S/^{33}S$, $^{34}S/^{36}S$, and $^{33}S/^{36}S$ abundance ratios with rare CS isotopologs, thus avoiding significant saturation effects. With accurate distances obtained from parallax data, we confirm previously identified $^{12}C/^{13}C$ and $^{32}S/^{34}S$ gradients as a function of galactocentric distance. In the central molecular zone, $^{12}C/^{13}C$ ratios are higher than suggested by a linear fit to the disk values as a function of galactocentric radius. While $^{32}S/^{34}S$ ratios near the Galactic center and in the inner disk are similar, this is not the case for $^{12}C/^{13}C$, when comparing central values with those near galactocentric radii of 5 kpc. As was already known, there is no $^{34}S/^{33}S$ gradient but the average ratio of 4.35 ± 0.44 derived from the $J = 2$–1 transition lines of $C^{34}S$ and $C^{33}S$ is well below previously reported values. A comparison between solar and local interstellar $^{32}S/^{34}S$ and $^{34}S/^{33}S$ ratios suggests that the Solar System may have been formed from gas with a particularly high ^{34}S abundance. For the first time, we report positive gradients of $^{32}S/^{33}S$, $^{34}S/^{36}S$, $^{33}S/^{36}S$, and $^{32}S/^{36}S$ in our Galaxy. The predicted $^{12}C/^{13}C$ ratios from the latest Galactic chemical-evolution models (e.g., Kobayashi et al. 2020; Romano et al. 2021; Colzi et al. 2022a) are in good agreement with our results. While $^{32}S/^{34}S$ and $^{32}S/^{36}S$ ratios show larger differences at larger galactocentric distances, $^{32}S/^{33}S$ ratios show an offset across the entire inner 12 kpc of the Milky Way. Taken together, our findings in this thesis provide useful guidelines for further refinements of models of the chemical evolution of the Galaxy.

Chapter 4

Discovery of ammonia (9,6) masers in Cepheus A and G34.26+0.15

This chapter is a summary of the refereed article published in Astronomy and Astrophysics (see Appendix B) titled **"Discovery of ammonia (9,6) masers in two high-mass star-forming regions"** by:

Y. T. Yan, C. Henkel, K. M. Menten, Y. Gong, J. Ott, T. L. Wilson, A. Wootten, A. Brunthaler, J. S. Zhang, J. L. Chen, and Y. Kai
2022, A&A, 659, A5.
DOI:10.1051/0004-6361/202142891

4.1 Context

As discussed in Chapter 1.4, the NH_3 (J, K) = (9,6) maser, arising from energy levels as high as 1090 K above the ground state, stands out as being the strongest and most variable one in W51-IRS2 (e.g., Henkel et al. 2013). Prior to our publication in this Chapter, maser emission in this line has only been detected in five high-mass star-forming regions (HMSFRs), W51, NGC7538, W49, DR21 (OH) (Madden et al. 1986), and Sgr B2(N) (Mei et al. 2020). The pumping mechanism of NH_3 (9,6) masers is not well constrained (Madden et al. 1986) till now. Brown & Cragg (1991) have studied ortho-ammonia and found that it could possibly pump the (6,3) inversion line, but they did not extend their model to the (9,6) transition due to the fact that collision rates are only known for inversion levels up to $J = 6$ (e.g., Danby et al. 1988).

4.2 Aims

In January 2020, we discovered new NH_3 (9,6) masers in two sources, G34.26+0.15 and Cepheus A with the 100-meter Effelsberg telescope[1]. This was an unexpected and surprise detection thanks to the excellent broadband S14mm double beam secondary focus receiver at Effelsberg. The goal of this project is to obtain positions of these new sources with subarcsecond precision and to relate these positions, obtained with the Karl G. Jansky Very Large Array (JVLA), to other relevant tracers of massive star

[1]Based on observations with the 100-meter telescope of the MPIfR (Max-Planck-Institut für Radioastronomie) at Effelsberg.

formation. We want to connect the (9,6) maser phenomenon with properties of other ammonia lines and to pinpoint locations of particular activity, as well as to provide a better understanding of the physics of these massive star forming regions.

4.3 Method

We carried out NH_3 (9,6) observations toward Cepheus A and G34.26+0.15 with the Effelsberg 100-meter telescope in 2020 January and 2021 February, July, and August. Higher angular resolution measurements were obtained on 2021 July 13 with the JVLA of the National Radio Astronomy Observatory[2] (NRAO) in the C configuration (project ID: 21A-157, PI: Yaoting Yan). We not only cover the NH_3 (9,6) line but also cover the NH_3 (8,5) and (10,7) lines as well as the continuum emission.

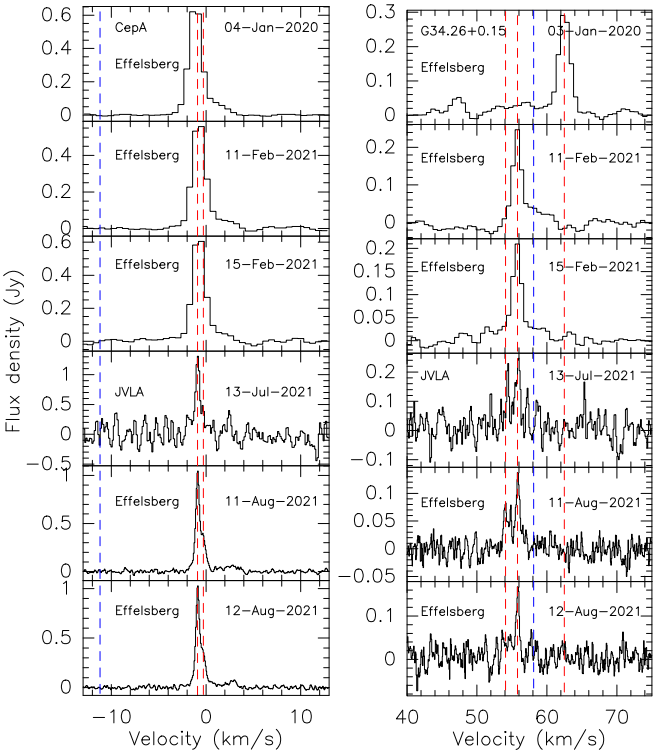

Figure 4.1: Spectra from NH_3 (9,6) transition lines at different epochs. The systemic velocities are indicated by dashed blue lines. The dashed red lines indicate the central velocities of the major ammonia emission components. Adapted from Fig. 1 in Yan et al. (2022b).

4.4 Results

We detected NH_3 (9,6) masers toward Cep A and G34.26+0.15 at all epochs we observed. The spectra are shown in Fig. 4.1. We identify one maser spot in Cep A and three maser spots toward G34.26+0.15 with our higher angular resolution data from the JVLA. We do not detect NH_3 (8,5) and (10,7) emissions by our JVLA observations. However, we detect six published compact continuum sources, HW2, HW3a, HW3b,

[2]The National Radio Astronomy Observatory is a facility of the National Science Foundation operated under cooperative agreement by Associated Universities, Inc.

HW3c, HW3d, and HW9, in Cep A and three main continuum objects, A, B, and C, in G34.26+0.15 with our JVLA data. The 1.36 cm continuum flux is determined toward individual compact source components in these two targets.

4.5 Conclusions

We discover NH_3 (9,6) masers in two HMSFRs, Cep A and G34.26+0.15. The narrow line width of the emission features ($\Delta V_{1/2}$ $\leq$2.0 km s^{-1}) and their high brightness temperatures ($>$ 400 K) indicate the maser nature of the lines. The JVLA-detected emission indicates that the NH_3 (9,6) maser in Cep A originates from a sub-arcsecond-sized region slightly ($0\farcs28 \pm 0\farcs10$) to the west of the peak position of the 1.36 cm continuum object, HW2. In G34.26+0.15, three NH_3 (9,6) maser spots are observed: one is close to the head of the cometary UC H II region C, and the other two are emitted from a compact region to the west of the HC H II region A (Fig. 4.2). We suggest that the (9,6) masers may be connected to outflowing gas. Higher angular resolution JVLA and VLBI observations are planned to provide more accurate positions and constraints on pumping scenarios.

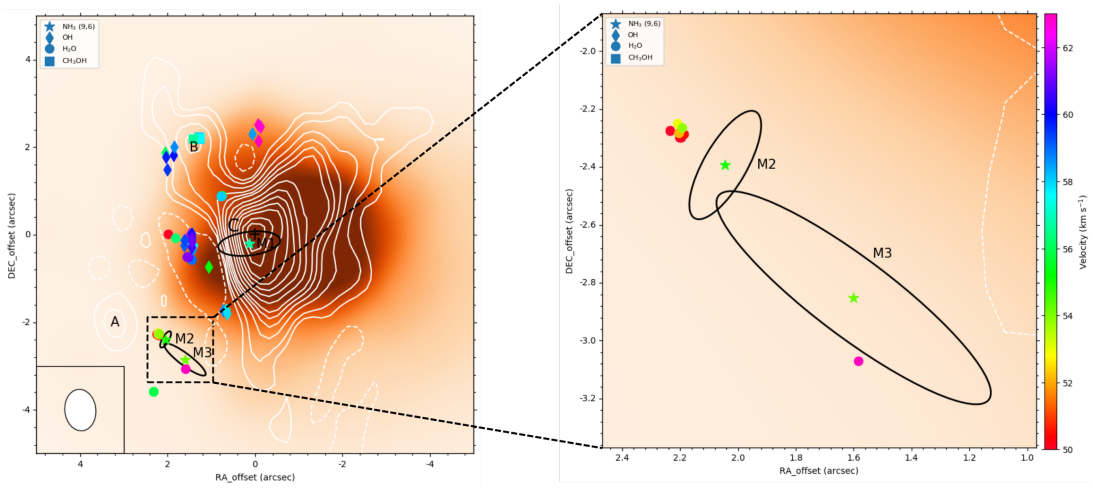

Figure 4.2: 1.36 cm JVLA continuum map of G34.26+0.15 presented as white contours. The background image is the *Spitzer* 4.5 μm emission, taken from the Galactic Legacy Infrared Mid-Plane Survey Extraordinaire (GLIMPSE; Benjamin et al. 2003; Churchwell et al. 2009). The black ellipses show the positions of NH_3 (9,6) emissions with stars at their center (i.e., M1, M2, and M3). OH (Zheng et al. 2000), H_2O (Imai et al. 2011), and CH_3OH (Bartkiewicz et al. 2016) masers are presented as diamonds, circles, and squares, respectively. The color bar indicates the velocity range (V_{LSR}) of maser spots. Adapted from Fig. 4 in (Yan et al. 2022b).

Chapter 5

Discovery of widespread NH_3 maser emission toward Sagittarius B2

This chapter is a summary of the refereed article published in Astronomy and Astrophysics in the section of "Letters to the Editor" (see Appendix C) titled **"Discovery of non-metastable ammonia masers in Sagittarius B2"** by:

Y. T. Yan, C. Henkel, K. M. Menten, Y. Gong, H. Nguyen, J. Ott, A. Ginsburg, T. L. Wilson, A. Brunthaler, A. Belloche, J. S. Zhang, N. Budaiev, and D. Jeff
2022, A&A, 666, L15.
DOI:10.1051/0004-6361/202245024

5.1 Context

Sgr B2 is located at a projected distance of ∼100 pc from Sgr A* (Reid et al. 2009b), the compact radio source associated with the supermassive black hole in the Galactic center at a distance of $8.178 \pm 0.013_{\rm stat.} \pm 0.022_{\rm sys.}$ kpc (GRAVITY Collaboration et al. 2019). This region is normally divided into three high-mass star-forming cores: Sgr B2(N), Sgr B2(M), and Sgr B2(S) (see our Fig. 5.1 for the locations of these). Detected molecular maser species are OH, H_2O, H_2CO, CH_3OH class I, and class II, as well as NH_3 (see Yan et al. 2022a, and references therein).

5.2 Aims

In 2020 January, with the Effelsberg 100-m telescope, we discovered strong NH_3 (9,6) and (10,7) masers toward a single position slightly south of Sgr B2(M). Our purpose is to obtain positions with subarcsecond precision and to relate these positions to those of other relevant tracers of massive star formation (e.g. H_2O, OH, and CH_3OH masers).

5.3 Method

We observed the NH_3 (9,6) and (10,7) lines toward Sgr B2 with the 100-meter Effelsberg telescope[1] at 12 epochs in January 2020, February and August 2021, as well as in March,

[1]Based on observations with the 100-meter telescope of the MPIfR (Max-Planck-Institut für Radioastronomie) at Effelsberg.

May, June, July, and August 2022. We performed interferometric measurements of six NH_3 lines, the (5,1), (6,3), (7,4), (8,5), (9,6), and (10,7) transitions, as well as continuum, toward Sgr B2 on 5 March 2022 with the Karl G. Jansky Very Large Array (JVLA) of the National Radio Astronomy Observatory[2] (NRAO) in the A-configuration (project ID: 22A-106, PI: Yaoting Yan).

We used the GILDAS/CLASS[3] package (Pety 2005) and the Common Astronomy Software Applications package (CASA[4]; McMullin et al. 2007) to reduce the Effelsberg and JVLA data, respectively. We present the parameters of observed lines with the JVLA in Table 5.1.

5.4 Results

We found that (9,6) maser emissions are quite widespread in Sgr B2, not only residing in Sgr B2(M), but also in Sgr B2(N) and Sgr B2(S), while (10,7) masers were detected in a more limited region comprising Sgr B2(M) and Sgr B2(N). A map of NH_3 (9,6) spectra from the Effelsberg telescope is presented in Fig. 5.2.

We detected a total of 22 known compact H II regions (Gaume et al. 1995; De Pree et al. 1998, 2014, 2015) with our JVLA observations. We identified 18 maser spots in the NH_3 (6,3), (7,4), (8,5), (9,6), and (10,7) transitions from the JVLA higher angular resolution measurements. We did not find any emission in the NH_3 (5,1) line from Sgr B2. NH_3 (6,3) masers arise from four different locations, named 63A, 63B, 63C, and 63D. NH_3 (7,4), (8,5), (9,6), and (10,7) masers are detected toward three, two, four, and five spots, respectively.

Among the 18 maser spots detected in Sgr B2, 50% are located in Sgr B2(N). These are seen in the NH_3 (6,3) transition toward 63A and 63B, in the (7,4) transition toward 74A, in the (8,5) line toward 85A, in the (9,6) transition toward 96A and 96B, as well as in the (10,7) line toward 107A, 107B, and 107C. Four of these sources, 85A, 96A, 96B, and 107C, are close to the UCH II region K2 (see Fig. 5.3). We only detected one maser spot, 63C, in the NH_3 (6,3) transition toward Sgr B2(NS). Five maser spots were detected in Sgr B2(M) and three maser spots were found in Sgr B2(S).

5.5 Conclusions

We report the discovery of NH_3 non-metastable (6,3), (7,4), (8,5), (9,6), and (10,7) masers in Sgr B2(M) and Sgr B2(N), an NH_3 (6,3) maser in Sgr B2(NS), as well as NH_3 (7,4), (9,6), and (10,7) masers in Sgr B2(S). High angular resolution data from the JVLA A-configuration reveal 18 maser spots. Nine maser spots arise from Sgr B2(N), one from Sgr B2(NS), five from Sgr B2(M), and three originate in Sgr B2(S). All of these increase the number of (6,3), (7,4), (8,5), (9,6), and (10,7) maser detections in

[2]The National Radio Astronomy Observatory is a facility of the National Science Foundation, operated under a cooperative agreement by Associated Universities, Inc.

[3]https://www.iram.fr/IRAMFR/GILDAS/

[4]https://casa.nrao.edu/

Table 5.1: Summary of the JVLA observations toward Sgr B2. Adapted from Table. 1 in Yan et al. (2022a).

Transition	ν	$E_{\rm low}/k$	Baseband	Synthesized beam	Linear resolution	P.A.		rms
(J, K)	(GHz)	(K)		(arcsec)	(au)	(deg)	(K mJy^{-1})	(mJy beam^{-1})
(5,1)	19.838346	422	A0/C0	0.198 × 0.085	1624 × 697	−9.807	184	3.32
(6,3)	19.757538	551	A0/C0	0.203 × 0.087	1665 × 713	−9.806	177	4.30
(7,4)	19.218465	713	A0/C0	0.209 × 0.089	1714 × 730	−9.661	178	3.85
(8,5)	18.808507	892	B0/D0	0.214 × 0.091	1755 × 746	−9.527	177	3.54
(9,6)	18.499390	1089	B0/D0	0.215 × 0.097	1763 × 795	−7.385	171	3.79
(10,7)	18.285434	1303	B0/D0	0.220 × 0.094	1804 × 771	−9.874	177	2.95

Notes. Columns (1) and (2): observed lines and corresponding rest frequencies, taken from Henkel et al. (2013). Column (3): $E_{\rm low}/k$: energy above the ground state of the lower level of a given inversion doublet; k is the Boltzmann constant; $(E_{\rm up} - E_{\rm low})/k \sim 1.0$–$1.5$K. Column (4): baseline board pairs' setup, see details on the VLA resources page. Column (5): synthesized beam. Column (6): linear resolution at a distance of 8.2 kpc. Column (7): position angle of the synthesized beam. Column (8): conversion factor from mJy to Kelvin for each transition was calculated with $1.222 \times 10^3/(\nu^2\theta_{\rm maj}\theta_{\rm min})$, where ν is the frequency in units of GHz; $\theta_{\rm maj}$ and $\theta_{\rm min}$ are the major and minor axis of the synthesized beam in units of arcseconds[a]. Column (9): rms noise in a channel image.

[a]https://science.nrao.edu/facilities/vla/proposing/TBconv

our Galaxy from three to six, two to four, two to three, seven to nine, and one to four. Compared to the Effelsberg 100-m telescope data, the JVLA data indicate no missing flux. The detected maser spots are not resolved by our JVLA observations. Lower limits to the brightness temperature are >3000 K and reach up to 6×10^5 K, manifesting their maser nature. Long-term Effelsberg monitoring (19 months) indicates that the intensities of the (9,6) masers in Sgr B2(M), as well as the (9,6) and (10,7) masers in Sgr B2(N), show noticeable variations. However, the (10,7) maser in Sgr B2(M) is stable. While the NH_3 masers all arise near hot cores, there are many hot cores that do not exhibit NH_3 maser emission. All of these non-metastable ammonia maser lines show redshifted or blueshifted features that may be related to outflows or UCHII expansion.

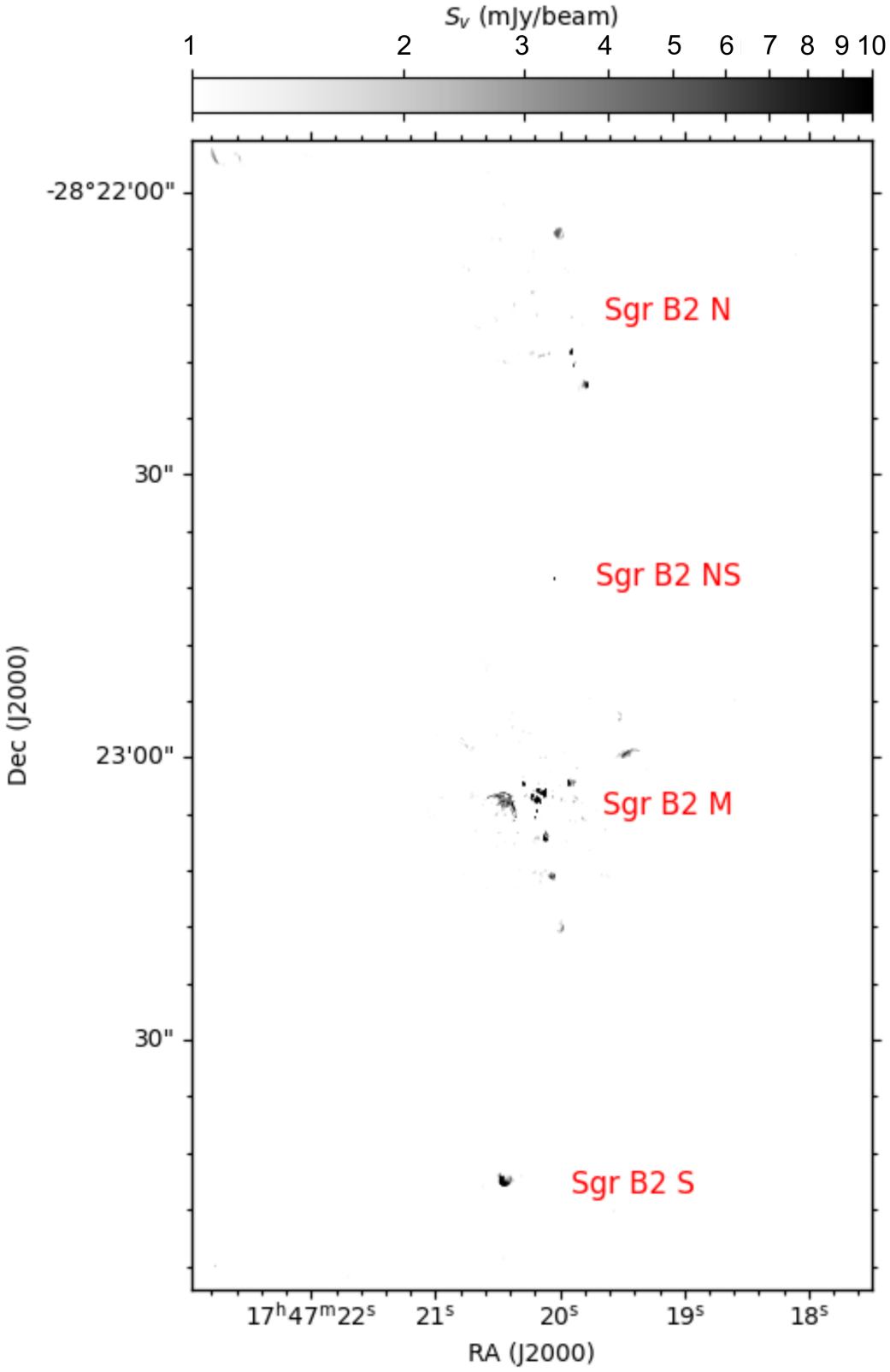

Figure 5.1: JVLA 1.6-cm continuum map of Sgr B2, shown in gray. Adapted from Fig. 1 in Yan et al. (2022a).

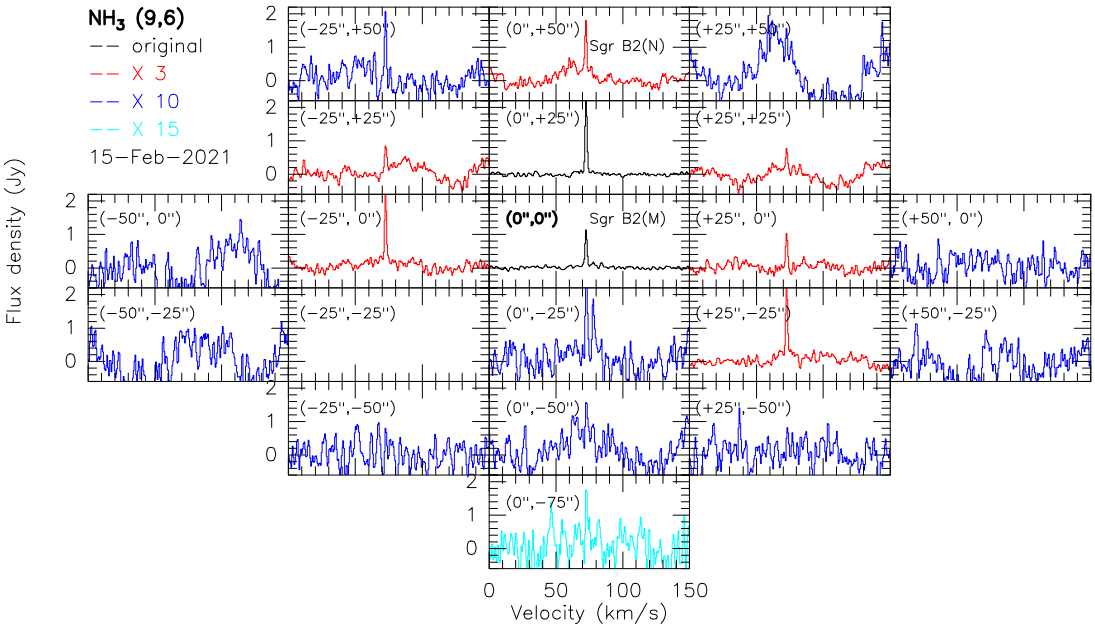

Figure 5.2: NH_3 (9,6) line profiles observed with the Effelsberg 100-m telescope over the region of Sgr B2. The black spectra show the original flux density scales. The red, blue, and cyan spectra are presented after multiplying the flux densities by factors of three, ten, and fifteen, respectively. Adapted from Fig. A.2 in Yan et al. (2022a).

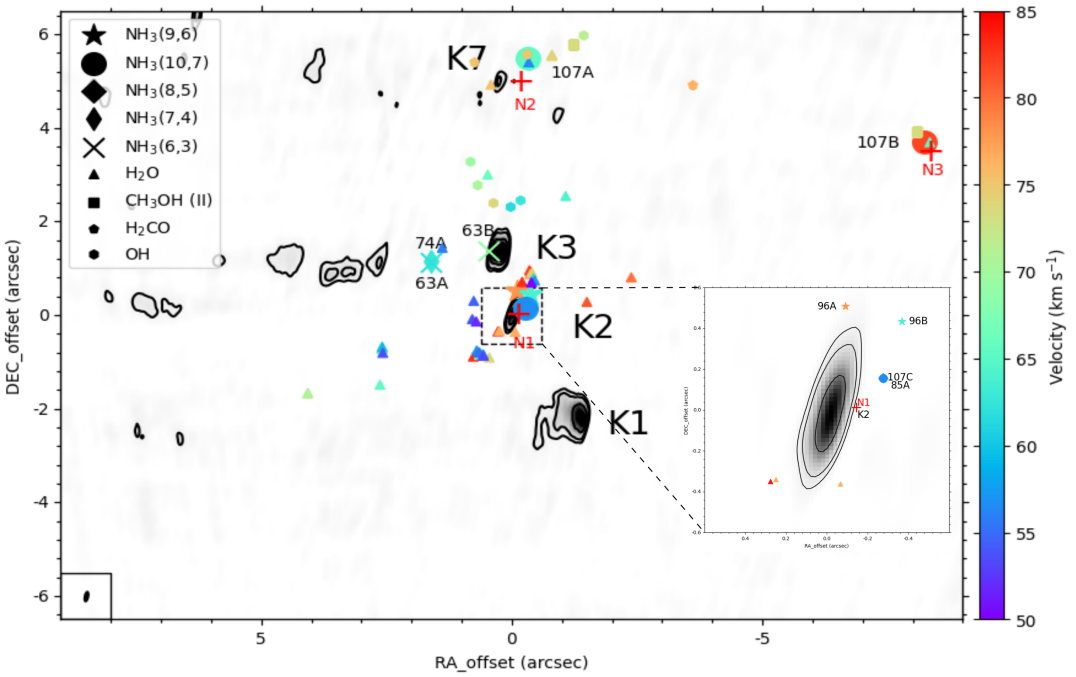

Figure 5.3: JVLA 1.6 cm continuum map of Sgr B2(N), shown by the gray shaded areas. The crosses, thin diamonds, diamonds, stars, and circles show the positions of NH_3 (6,3), (7,4), (8,5), (9,6), and (10,7) emissions. H_2O (McGrath et al. 2004), class II CH_3OH (Caswell 1996; Lu et al. 2019), H_2CO (Mehringer et al. 1994; Hoffman et al. 2007; Lu et al. 2019), and OH (Gaume & Claussen 1990) masers are presented as triangles, squares, pentagons, and hexagons, respectively. The color bar indicates the velocity range (V_{LSR}) of maser spots. Red crosses mark the positions of the hot cores Sgr B2(N1), N2, and N3, taken from the 3 mm imaging line survey "Exploring Molecular Complexity with ALMA" (EMoCA, Bonfand et al. 2017). The systemic velocities of the hot cores N1, N2, and N3 are V_{LSR} = 64 km s^{-1}, V_{LSR} = 74 km s^{-1} and V_{LSR} = 74 km s^{-1}, respectively(Bonfand et al. 2017). Adapted from Fig. 2 in Yan et al. (2022a).

Chapter 6

Discovery of widespread non-metastable ammonia masers in the Milky Way

This chapter is a summary of the refereed article published in Astronomy and Astrophysics (see Appendix D) titled **"Discovery of widespread non-metastable ammonia masers in the Milky Way"** by:

Y. T. Yan, C. Henkel, K. M. Menten, T. L. Wilson, A. Wootten, Y. Gong, F. Wyrowski, W. Yang, A. Brunthaler, A. Kraus, B. Winkel,
2024, A&A, 686, A205.
DOI:10.1051/0004-6361/202348931

6.1 Context

Searching for ammonia maser emission in 119 Galactic high-mass star-forming regions (HMSFRs) with 22 GHz H_2O maser emission, we report the discovery of non-metastable NH_3 inversion line masers toward 14 of these sources. This doubles the number of known non-metastable ammonia masers in our Galaxy, including nine new very high excitation $(J, K) = (9,6)$ maser sources. These maser lines, including NH_3 (5,4), (6,4), (6,5), (7,6), (8,6), (9,6), (9,8), (10,8), and (11,9), arise from energy levels of 342 K, 513 K, 465 K, 606 K, 834 K, 1090 K, 942 K, 1226 K, and 1449 K above the ground state. Additionally, we tentatively report a new metastable NH_3 (3,3) maser in G048.49 and an NH_3 (7,7) maser in G029.95. All of the newly detected NH_3 maser lines have blueshifted or redshifted velocities with respect to the source systemic velocities. Among the non-metastable ammonia maser lines, larger velocity distributions, offset from the source systemic velocities, are found in the ortho-NH_3 ($K = 3n$) than in the para-NH_3 ($K \neq 3n$) transitions.

6.2 Aims

Ammonia masers are rare in the ISM compared to other maser species, i.e., those of OH, H_2O, and CH_3OH. Over the last five decades after the first detection of astronomical masers, numerous successful maser surveys were carried out on different molecules and

led to thousands of detections in the Milky Way. So far, ammonia maser lines have only been detected in 32 sources. We summarise the sources that are known to host ammonia masers in Table 1.3. We aim to search for new ammonia maser sources with the 100-m Effelsberg telescope and to expand our understanding of ammonia masers.

6.3 Method

We selected 119 HMSFRs with high NH_3 column densities ($N_{NH_3} \geq 10^{15.5}$ cm^{-2}) that are known to host water masers from previous K-band surveys. The sample is mainly based on the APEX Telescope Large Area Survey of the Galaxy (ATLASGAL, Schuller et al. 2009) catalogs (Wienen et al. 2012, 2018), and the Red MSX Source survey (RMS, Urquhart et al. 2011). Our sample is listed in Appendix D together with the systemic local standard of rest (LSR) velocities and the source beam averaged NH_3 column densities, which are based on ammonia (1,1), (2,2), and (3,3) thermal emission in previous studies with typical beam sizes of order 32" at Green Bank and 38" at Effelsberg. We performed a K-band line survey with the 100-m Effelsberg telescope of this source sample. The S14mm double beam secondary focus receiver was employed to simultaneously cover the entire K-band frequency range, i.e. 18.0–26.0 GHz (see example in Fig. 6.1). The receiver band was divided into four 2.5 GHz-wide subbands with the frequency ranges of 18.0–20.5 GHz, 19.9–22.4 GHz, 21.6–24.1 GHz, and 23.5–26.0 GHz. Each subband has 65536 channels, providing a channel width of 38.1 kHz, changing from ∼0.62 km s^{-1} at 18.5 GHz to ∼0.44 km s^{-1} at 26.0 GHz.

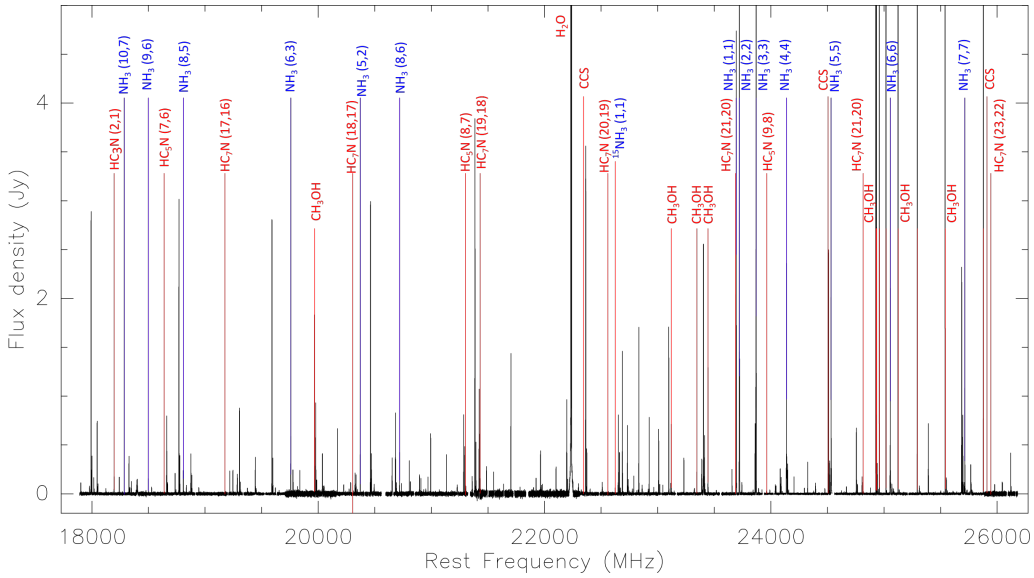

Figure 6.1: Overview spectrum of the K-band line survey toward the high-mass star-forming region Orion KL with the Effelsberg 100-m telescope (Gong et al. 2015), strong lines are marked.

6.4 Results

We detected 15 new ammonia maser sources, resulting in a detection rate of ∼13%. These maser lines, including NH_3 (J, K) = (5,4), (6,4), (6,5), (7,7), (7,6), (8,6), (9,6), (9,8), (10,8), (11,9) and possibly the (3,3) line arise from energy levels of 342 K, 513 K, 465 K, 537 K, 606 K, 834 K, 1090 K, 942 K, 1226 K, 1449 K and 122 K above the ground state.

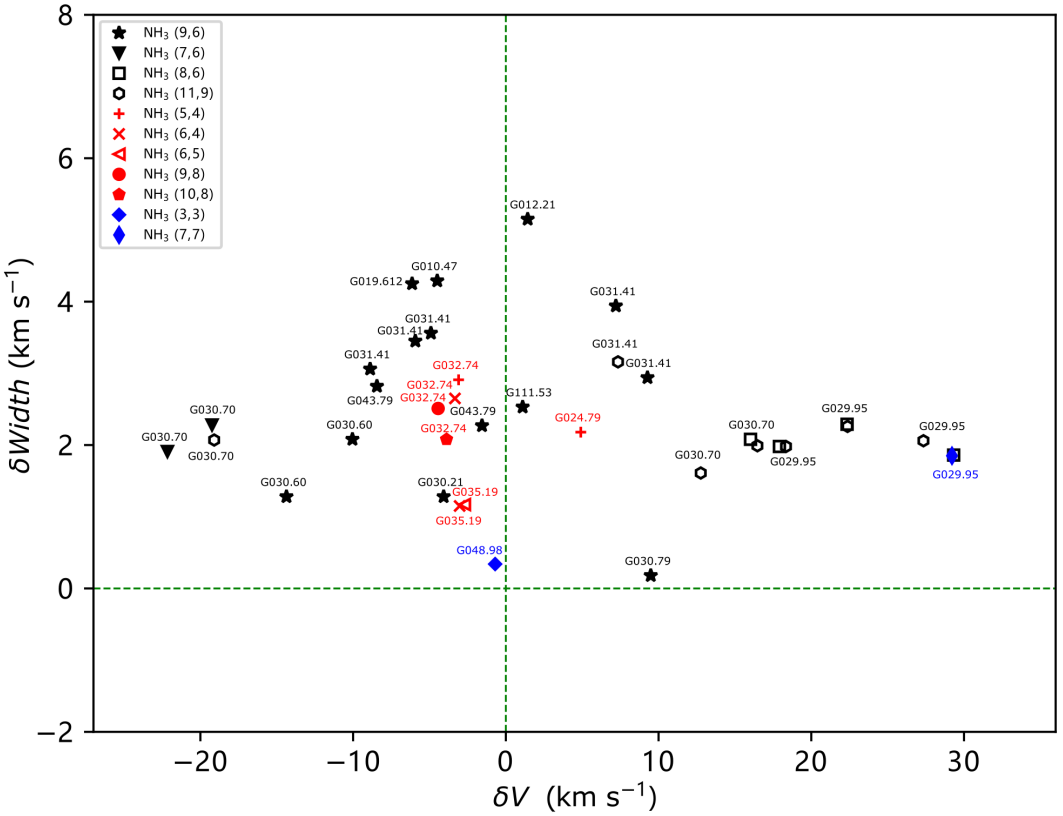

Figure 6.2: Comparison of velocities and line widths of ammonia maser lines to the intrinsic line widths of ammonia (J, K) = (1,1) thermal emission. The number of data points is substantially larger than the number of newly detected sources due to the occasional presence of more than one maser line in a given source and more than one velocity component in a specific maser line. $\delta V = V_{\rm LSR}$(maser)-$V_{\rm LSR}$(NH_3(1,1)), is the deviation from velocities of the NH_3 maser lines to those of the NH_3 (1,1) thermal emission. $\delta Width = \Delta V_{1/2}$($NH_3$(1,1))-$\Delta V_{1/2}$(maser), refers to the difference between the line widths of ammonia maser lines and the intrinsic line widths of an individual NH_3 hyperfine structure component. The green dashed lines indicate positions with zero deviation. The metastable NH_3 transitions are marked in blue. Among the non-metastable NH_3 lines, ortho-NH_3 is presented in black, and para-NH_3 is given in red.

Figure 6.2 shows the comparison of line widths of ammonia maser lines to the intrinsic line widths of hyperfine components of the (J, K) = (1,1) thermal emission

as well as the difference between the systemic velocities of the sources and the maser velocities. We derived the intrinsic line width by using the hyperfine fitting in CLASS for the NH_3 (1,1) line. All of these maser lines have narrower features than the intrinsic NH_3 (1,1) thermal emission. This further confirms their maser nature. Furthermore, their velocities are shifted with respect to the source's systemic LSR velocities, by at least 0.7 km s^{-1}, and reaching up to 30 km s^{-1}. This is similar to recent discoveries of non-metastable NH_3 masers with $\delta V \sim 10$ km s^{-1} in Cep A, $\delta V \sim 4$ km s^{-1} in G34.26+0.15, and δV in a range of 0.3 km s^{-1} to 24 km s^{-1} toward the Sgr B2 complex (Yan et al. 2022b,a). Fourteen of the new ammonia maser sources contain non-metastable ammonia masers, which doubles the number of non-metastable ammonia maser detections in our Galaxy. Among the non-metastable ammonia maser lines, larger velocity distributions are found in the ortho-NH_3 ($K = 3n$) than in the para-NH_3 ($K \neq 3n$) transitions. The velocity range of para-NH_3 masers is limited within $\pm$5 km s^{-1} with respect to the source's systemic velocities, marked as red in Fig. 6.2. This is enlarged to about $\pm$30 km s^{-1} for ortho-NH_3 masers.

Among the 14 non-metastable ammonia maser sources, NH_3 (9,6) masers are the most common and are detected in nine objects. The spectra of NH_3 (9,6) masers are shown in Fig. 6.3. The observations at different epochs indicate that the flux densities of these NH_3 (9,6) masers vary by at least 50% over time scales of several months. The NH_3 (11,9) transition with an energy level of 1449 K above the ground state, the highest value in our maser sample, was detected towards G031.41 (spectra can be found in Appendix D). In addition, NH_3 (11,9) masers were also detected in G029.95-0.02 (hereafter G029.95) and G030.70-0.07 (hereafter G030.70). In G029.95, NH_3 (8,6) and (7,7) masers could be identified. Toward G030.70, we also detected NH_3 (7,6) and (8,6) masers. Three targets, G024.79+0.08 (hereafter G024.79), G032.74-0.08 (hereafter G032.74), and G035.19-0.74 (hereafter G035.19), only host para-NH_3 masers. Toward G024.79, we only detected an NH_3 (5,4) maser. Toward G032.74, four transitions were identified as masers, i.e., the NH_3 (5,4), (6,4), (9,8), and (10,8) lines. Two NH_3 maser lines, the (6,4) and (6,5) transitions, were detected in G035.19.

The frequencies of the NH_3 (1,1), (2,2), and (3,3) transitions are within a range of only 200 MHz. The peak flux density ratios of NH_3 (3,3)/(1,1) and (3,3)/(2,2) towards G048.98-0.30 (hereafter G048.98) are $\sim$0.83 and $\sim$1.14, respectively, based on previous 100-m Green Bank Telescope (GBT) observations in 2010 (Urquhart et al. 2011), while these are $\sim$1.57 and $\sim$2.22 from our measurements. However, the ratios of NH_3 (1,1)/(2,2) remain consistent, which are $\sim$1.38 and $\sim$1.42, within the uncertainties due to noise in these two data sets. This indicates that the NH_3 (3,3) emission in G048.98 has become stronger and likely shows a maser nature.

6.5 Conclusions

We detected at least 14 and likely 15 new ammonia maser sources in the Milky Way, based on our K-band line survey with the 100-meter Effelsberg telescope. Our total sample consists of 119 sources exhibiting 22 GHz H_2O maser emission, thus yielding a

detection rate in excess of 10%. Fourteen of the newly detected masers are encountered in non-metastable inversion transitions and this doubles the number of non-metastable NH_3 masers in our Galaxy. Metastable ammonia masers are also detected in one or two sources, i.e. an NH_3 (7,7) maser in G029.95 and likely an NH_3 (3,3) maser in G048.98. Narrow line widths compared to those of ammonia $(J, K) = (1,1)$ thermal emission, as well as variations in flux density, indicate their maser nature. All of the NH_3 masers in our detections have blueshifted or redshifted velocities with respect to the source systemic LSR velocities.

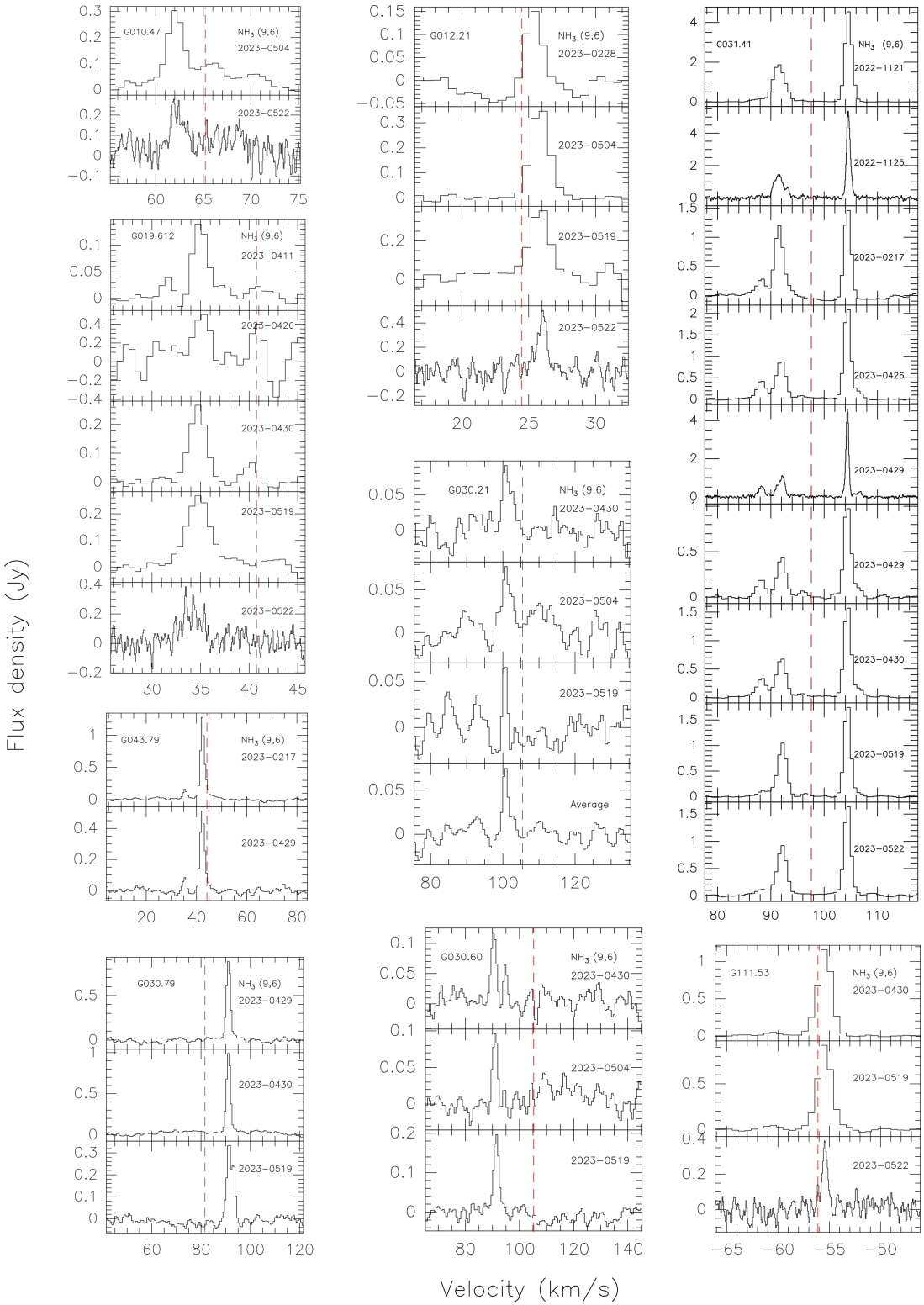

Figure 6.3: NH_3 (9,6) spectra observed at different epochs towards nine sources. The dashed red lines indicate the systemic velocities of the sources. Taken from Fig. 2 in Yan et al. (2024).

Chapter 7

Polarization measurements of ammonia masers in Sagittarius B2

This chapter is in preparation and will be submitted to Astronomy and Astrophysics.

Y. T. Yan, Surcis, G.; Henkel, C.; Lankhaar, B.;
Gong, Y.; Nguyen, H.; Wilson, T. L.;
Menten, K. M.;
in preparation

7.1 Context

In Section 5 and Appendix C, we reported the discovery of widespread non-metastable NH_3 masers toward the Sagittarius B2 molecular cloud and star-forming region complex. Two transitions of NH_3, the (9,6) and (10,7) lines, were measured in full polarization mode. Two maser spots, 96C, and 107B show clear polarization signals. The remaining three (9,6) and four (10,7) maser spots do not show any sign of linear or circular polarization. Polarization would allow us to quantify the presence of a regular magnetic field along the line-of-sight.

7.2 Method

Observations of two NH_3 lines, the (9,6), and (10,7) transitions, toward Sgr B2 were made on 2022 March 05 with the JVLA of the National Radio Astronomy Observatory[1] (NRAO) in the A-configuration (project ID: 22A-106, PI: Yaoting Yan). The full details and the identification of maser spots can be found in Section 5 and Appendix C.

The polarization calibration steps are as follows. First, we derived the polarization properties of the polarization calibrator, 3C286, from online resources of NRAO[2]. The corresponding Stokes values are obtained from Perley & Butler (2013, 2017). Then, the *setjy* task in CASA was used to set the polarization calibration model and the results in the model column were checked manually. The cross-hand delays were solved by using 3C286. J1745-2900 served as our gain calibrator and was used to solve the leakage terms with the task *polcal*. The R-L phase was then calibrated by also using

[1]The National Radio Astronomy Observatory is a facility of the National Science Foundation operated under cooperative agreement by Associated Universities, Inc.

[2]https://science.nrao.edu/facilities/vla/docs/manuals/obsguide/modes/flux-density-scale-polarization-leakage-polarization-angle-tables

the same task *polcal*. Finally, we derived all of the calibration solutions and applied them to our data using the task *applycal*. Then the I, Q, U, and V cubes were imaged using the *tclean* task in CASA with an image size of 4 arcsec × 4 arcsec for each maser spot instead of the whole image in Section 5 and Appendix C. The phase center of each maser spot can be found in Appendix C. All of the images were corrected for primary beam response. Figure 7.1 presents the comparison of the parallel-hand correlations (RR and LL) of calibrator 3C286 after polarization calibration. The exact agreement between these two distributions as well as their peak positions indicates our polarization calibration is perfect.

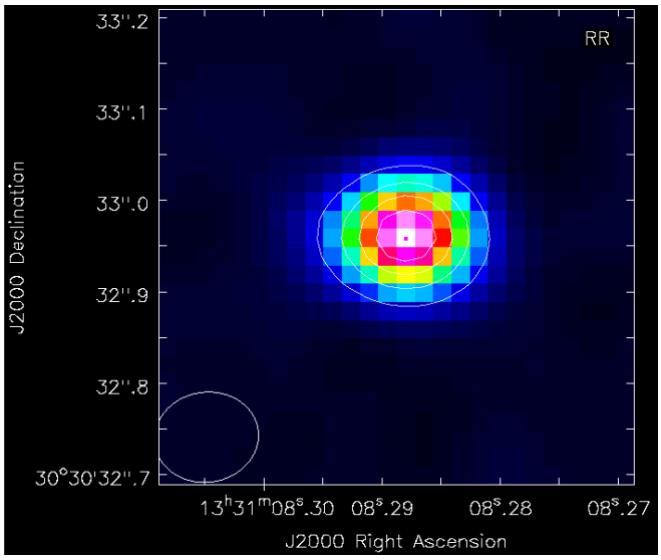

Figure 7.1: Comparison of the parallel-hand correlations (RR and LL) of calibrator 3C 286 after polarization calibration. RR: background image, LL: white contours.

7.3 Results

Two maser spots, 96C, and 107B show clear polarization information. Their Stokes IQUV images in the strongest channel and spectra are shown in Figs. 7.2, 7.3, and 7.4. We did not detect any polarization signals from the other three NH_3 (9,6) maser spots, i.e. 96A, 96B, and 96D, as well as from the other four NH_3 (10,7) maser spots, i.e. 107A, 107C, 107D, and 107E. The non-detection from these seven maser spots indicates the polarization signals from 96C and 107B are real. Figures 7.5 and 7.6 show Stokes IQUV images from 96A and 107A. Only noise can be found in their Stokes Q, U, and V images. Stokes IQUV spectra from 96A and 107A are shown in Fig. 7.7.

We calculated the linear polarization fraction (P_l) and polarization angle (P_a) for maser spots 96C and 107B with the following equations:

$$P_\mathrm{l} = \frac{\mathrm{POLI}}{I}, \tag{7.1}$$

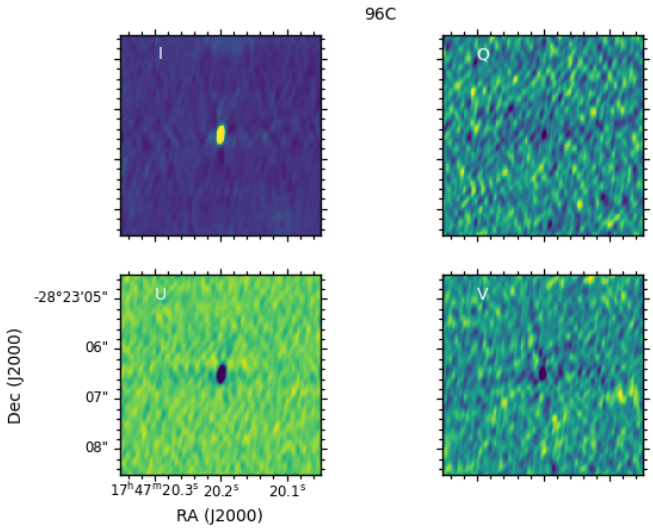

Figure 7.2: Stokes IQUV images of maser spot, 96C.

$$P_{\rm a} = 1/2 \times atan\frac{U}{Q}, \tag{7.2}$$

where POLI is the polarized intensity and POLI=$\sqrt{Q^2+U^2}$. The calculated linear polarization spectra, linear polarization fraction, and polarization angles are shown in Fig. 7.8. The total intensity can affect the observed circular spectra and can be removed following equation (3) in Vlemmings et al. (2002). The real circular polarization spectrum (V^*) of 107B is presented in Fig. 7.9.

The data analysis process is still ongoing. Application of a radiative transfer model is planned to explain the observed polarization of ammonia masers and to obtain information on the magnetic field as well as the pumping scenario of ammonia masers.

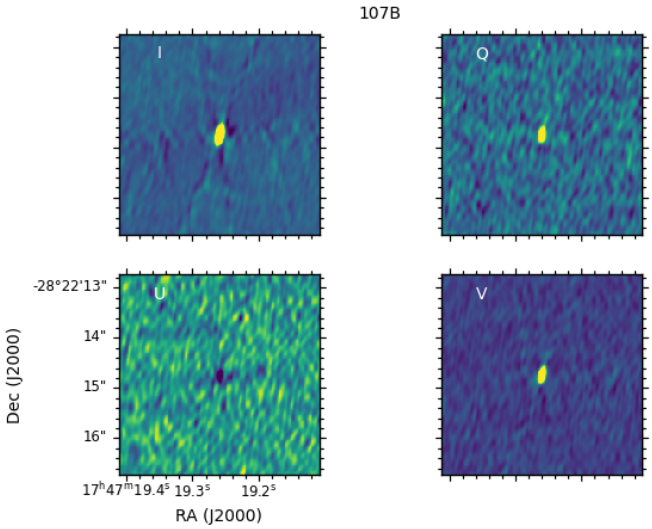

Figure 7.3: Stokes IQUV images of maser spot, 107B.

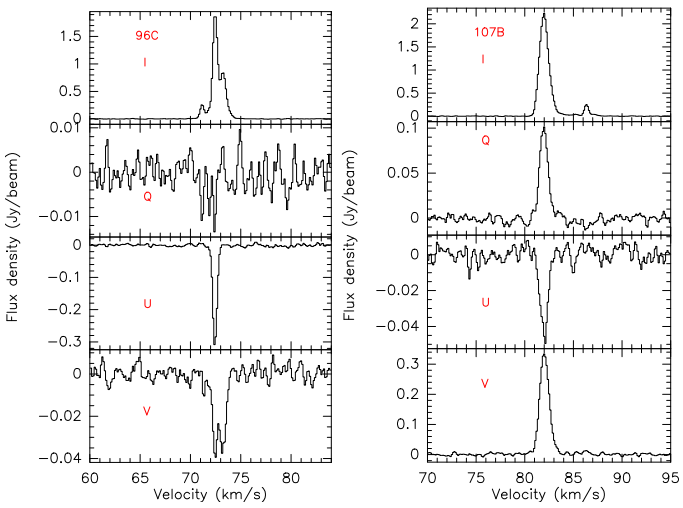

Figure 7.4: Stokes I, Q, U and V spectra of maser spots, 96C and 107B.

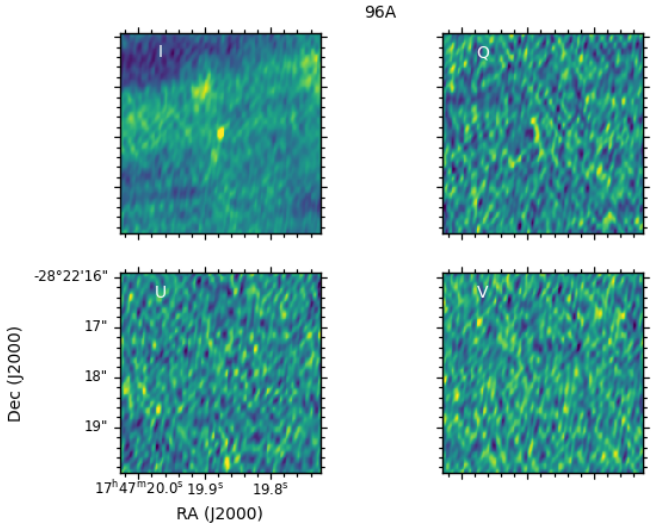

Figure 7.5: Stokes IQUV images of maser spot, 96A.

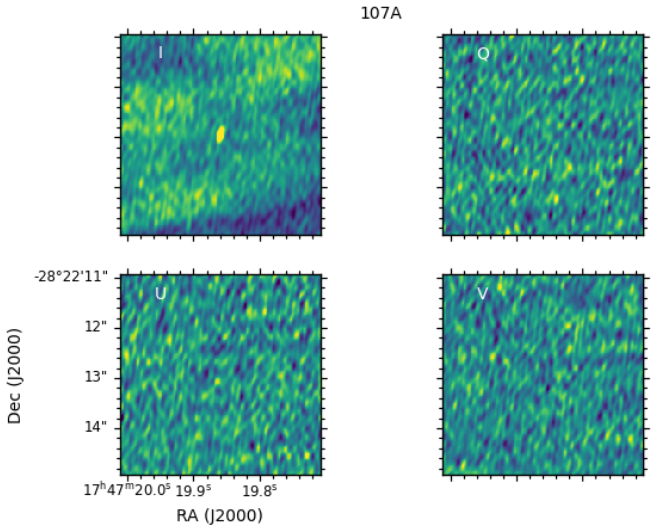

Figure 7.6: Stokes IQUV images of maser spot, 107A.

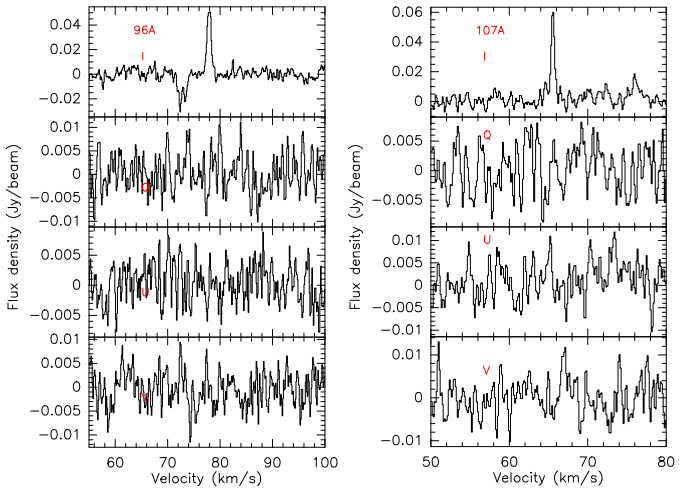

Figure 7.7: Stokes I, Q, U and V spectra of maser spots, 96A and 107A.

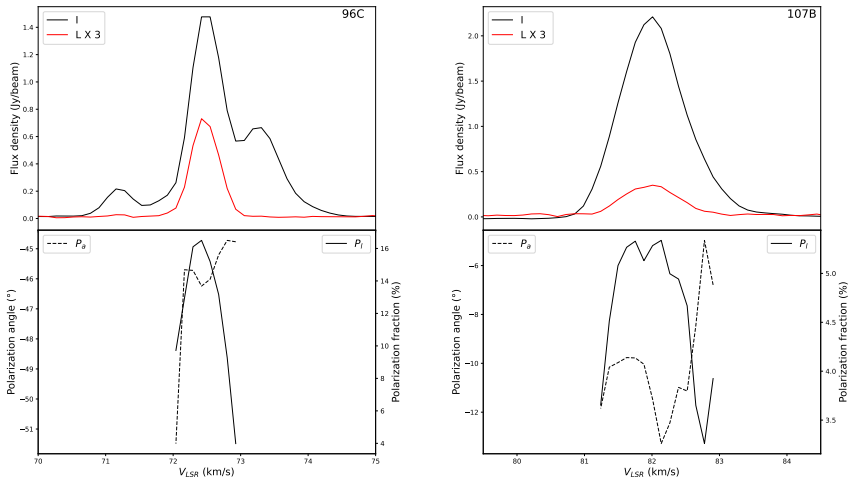

Figure 7.8: **Top:** Total intensity (black) and linear polarization (red) spectra of maser spots, 96C and 107B. **Bottom:** Linear polarization fraction (P_l) and polarization angles (P_a) along the velocities.

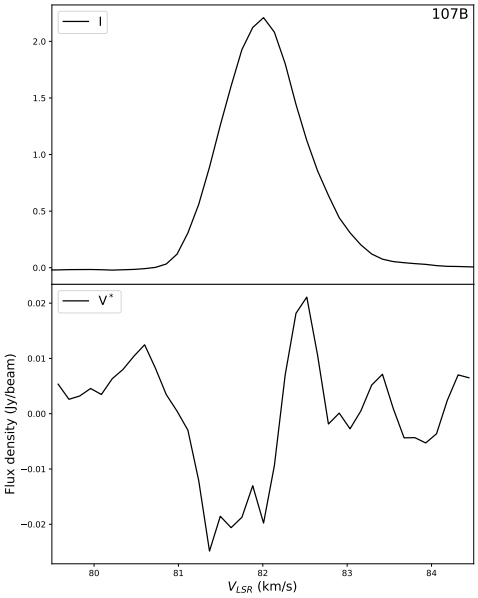

Figure 7.9: Total intensity (top) and the real circular polarization (bottom) spectra of maser spot, 107B.

Chapter 8

Summary and outlook

8.1 Summary

This PhD thesis studies the influence of stellar objects onto the interstellar medium (ISM) by using two different tools, isotope ratios and ammonia masers. Isotope abundance ratios provide a powerful tool to trace stellar nucleosynthesis, to evaluate the composition of stellar ejecta and to constrain the chemical evolution of the Milky Way. Molecular maser lines are signposts of high-mass star formation, probing the excitation and kinematics of very compact regions in the close environment of young stellar objects and providing useful targets for trigonometric parallax measurements.

8.1.1 Isotope abundance ratios

We used the IRAM 30 meter telescope to perform observations of the $J = 2-1$ transitions of CS, $C^{33}S$, $C^{34}S$, $C^{36}S$, ^{13}CS, $^{13}C^{33}S$, and $^{13}C^{34}S$ as well as the $J = 3-2$ transitions of $C^{33}S$, $C^{34}S$, $C^{36}S$, and ^{13}CS toward a large sample of 110 HMSFRs. The CS $J = 2-1$ line was detected toward 106 sources, with a detection rate of 96%. The $J = 2-1$ transitions of $C^{34}S$, ^{13}CS, $C^{33}S$, $^{13}C^{34}S$, and $C^{36}S$ were successfully detected in 90, 82, 46, 17, and 3 of our sources, respectively. The $J = 3-2$ lines of $C^{34}S$, ^{13}CS, $C^{33}S$, and $C^{36}S$ were detected in 87, 71, 42, and 1 object(s). All the detected rare CS isotopologs exhibit optically thin lines and allow us to measure the isotope ratios of $^{12}C/^{13}C$, $^{32}S/^{34}S$, $^{32}S/^{33}S$, $^{32}S/^{36}S$, $^{34}S/^{33}S$, $^{34}S/^{36}S$, and $^{33}S/^{36}S$ with only minor saturation corrections. Our main results are as follows:

- Based on the measurements of $C^{34}S$ and $^{13}C^{34}S$ $J = 2-1$ transitions, we directly measured the $^{12}C/^{13}C$ ratios with corrections of opacity. With accurate distances obtained from parallax data (Reid et al. 2009a, 2014, 2019), we confirm the previously determined $^{12}C/^{13}C$ gradient. A least-squares fit to our data results in $^{12}C/^{13}C = (4.77 \pm 0.81)R_{GC}+(20.76 \pm 4.61)$, with a correlation coefficient of 0.82.

- The Galactic $^{12}C/^{13}C$ gradients derived based on measurements of CN (Savage et al. 2002; Milam et al. 2005), $C^{18}O$ (Langer & Penzias 1990; Wouterloot & Brand 1996; Keene et al. 1998), and H_2CO (Henkel et al. 1980, 1982, 1983, 1985; Yan et al. 2019) are in agreement with our results from $C^{34}S$ and emphasize that chemical fractionation has little effect on $^{12}C/^{13}C$ ratios.

- While previously it had been assumed that a linear fit would provide a good simulation of carbon isotope ratios as a function of galactocentric distance, our

analysis reveals that this does not hold for the Galactic center region. While $^{12}C/^{13}C$ ratios are lowest in this part of the Milky Way, they clearly surpass values expected from a linear fit to the Galactic disk sources. This indicates that there is no strict linear correlation of carbon isotope ratios across the Galaxy.

- We confirm the previously determined $^{32}S/^{34}S$ gradients (Chin et al. 1996; Yu et al. 2020; Humire et al. 2020) with the direct method from ^{13}CS and $^{13}C^{34}S$, as well as the double isotope method also using $^{12}C/^{13}C$ ratios in the $J = 2{-}1$ and $J = 3{-}2$ transitions. Opacity corrections could be applied to the $J = 2{-}1$ transitions, but not to the $J = 3{-}2$ lines that may show, on average, slightly higher opacities. A $^{32}S/^{34}S$ gradient of $(0.75 \pm 0.13)R_{GC}+(15.52 \pm 0.78)$ was obtained based on a large dataset of 90 values from our double isotope method in the $J = 2{-}1$ transition. The 19 sources permitting the direct determination of this ratio with $^{13}CS/^{13}C^{34}S$ yield $^{32}S/^{34}S=(0.73 \pm 0.36)R_{GC}+(16.50 \pm 2.07)$.

- Differences between the behavior of the $^{12}C/^{13}C$ and $^{32}S/^{34}S$ ratios as a function of galactocentric distance are reported and should be used as input for further chemical models: (a) In the inner disk the $^{12}C/^{13}C$ ratios at $R_{GC} \geq 4.0$ kpc are clearly higher than the value in the CMZ, while the $^{32}S/^{34}S$ ratios in the CMZ and inner disk are similar, as already suggested for the first time by Humire et al. (2020). (b) In the local ISM, the $^{12}C/^{13}C$ ratio is well below the Solar System value but $^{32}S/^{34}S$ is still quite close to it. All of this indicates that, unlike ^{13}C, ^{34}S is not a clean secondary isotope.

- There is no notable $^{34}S/^{33}S$ gradient across the Galaxy. Ratios are well below the values commonly reported in earlier publications. This is a consequence of accounting for the full hyperfine structure splitting of the $C^{33}S$ lines. The average value of $^{34}S/^{33}S$ derived from the $J = 2{-}1$ transition lines after corrections for opacity toward our sample is 4.35 ± 0.44.

- While there is no $^{34}S/^{33}S$ gradient with galactocentric radius, interstellar $^{34}S/^{33}S$ values near the solar neighborhood are well below the Solar System ratio, most likely suggesting the Solar System ratio is peculiar, and perhaps also the $^{18}O/^{17}O$ ratio. A comparison of local interstellar and Solar System $^{32}S/^{34}S$ and $^{34}S/^{33}S$ ratios suggests that the Solar System may have been formed from gas and dust with a peculiarly high ^{34}S abundance. The data also indicate that ^{33}S is not a clean primary or secondary product of nucleosynthesis, similarly to ^{34}S.

- For the first time, we report a $^{32}S/^{33}S$ gradient in our Galaxy: $^{32}S/^{33}S = (2.64 \pm 0.77)R_{GC} + (70.80 \pm 5.57)$, with a correlation coefficient of 0.46.

- We find first potential indications for a positive $^{34}S/^{36}S$ gradient with galactocentric radius. Combined $^{34}S/^{36}S$ ratios from Mauersberger et al. (1996) and our new data with corrections of opacity in the $J = 2{-}1$ transition and applying new up-to-date distances yield a linear fit of $^{34}S/^{36}S = (10.34{\pm}2.74)R_{GC}+(57.45{\pm}18.59)$, with a correlation coefficient of 0.71. Considering the uniform $^{34}S/^{33}S$ ratios in

our Galaxy, a $^{33}S/^{36}S$ gradient of $(2.38 \pm 0.67)R_{GC}+(13.21 \pm 4.48)$ is also obtained.

- For the first time, we report a tentative $^{32}S/^{36}S$ gradient with galactocentric radius: $^{32}S/^{36}S = (314 \pm 55)R_{GC} + (659 \pm 374)$, with a correlation coefficient of 0.84. Our measurements are consistent with ^{36}S being a purely secondary nucleus. However, observations of $^{34}S/^{36}S$ and $^{32}S/^{36}S$ isotope ratios are still relatively few, especially in the CMZ and the inner disk within $R_{GC} = 5.0$ kpc.

- The predicted $^{12}C/^{13}C$ ratios from the latest Galactic chemical evolution models (e.g., Kobayashi et al. 2020; Romano et al. 2021; Colzi et al. 2022b) are in good agreement with our results, while $^{32}S/^{34}S$ and $^{32}S/^{36}S$ ratios show significant differences at larger galactocentric distances. $^{32}S/^{33}S$ ratios even show clear offsets along the entire inner 12 kpc of the Milky Way. Taken together, these findings provide useful guidelines for further refinements of models of the chemical evolution of the Galaxy.

8.1.2 Ammonia masers

Ammonia (NH_3) masers are rare in the ISM compared to other maser species, i.e., those of OH, H_2O, and CH_3OH. With the 100-meter Effelsberg telescope, we drastically enlarged the number of non-metastable NH_3 maser sources in our Galaxy. We have detected 17 new non-metastable and at least one but possibly two metastable NH_3 maser sources in the Milky Way. Three of them, Cepheus A, G34.26+0.15, and the Sagittarius B2 complex, were first detected in 2020 January by chance. We then explored a systematic K-band survey to search for new ammonia masers with the 100-meter Effelsberg telescope from 2022 November to 2023 July. Our total sample consists of 119 sources exhibiting 22 GHz H_2O maser emission. We detected at least 14 and likely 15 new ammonia maser sources thus yielding a detection rate in excess of 10%. Fourteen of the newly detected masers are encountered in non-metastable inversion transitions and this doubles the number of non-metastable NH_3 masers in our Galaxy. Metastable ammonia masers are also detected in one or two sources, i.e. an NH_3 (7,7) maser in G029.95 and likely an NH_3 (3,3) maser in G048.98. Narrow line widths compared to those of ammonia $(J, K) = (1,1)$ thermal emission, as well as variations in flux density, indicate their maser nature. All of the NH_3 masers in our detections have blueshifted or redshifted velocities with respect to the systemic LSR velocities of the sources.

The intensity of the (9,6) maser in G34.26+0.15 is decreasing with time, while toward Cep A the maser is stable based on 20 months of monitoring at Effelsberg. Linearly interpolating the integrated intensities obtained at Effelsberg as a function of time, the JVLA measurements show that there is no missing flux density on scales on the order of 1.2 arcsec (4×10^{-3} and 2×10^{-2} pc) to the total single-dish flux. The JVLA-detected emission indicates that the NH_3 (9,6) maser in Cep A originates from a sub-arcsecond-sized region slightly ($0\farcs28 \pm 0\farcs10$) to the west of the peak position of the 1.36 cm continuum object, HW2. In G34.26+0.15, three NH_3 (9,6) maser spots are

observed: one is close to the head of the cometary UC H II region C, and the other two are emitted from a compact region to the west of the HC H II region A. We suggest that the (9,6) masers may be connected to outflowing gas. Higher angular resolution JVLA and VLBI observations are planned to provide more accurate positions and constraints on pumping scenarios.

High angular resolution data from the JVLA A-configuration toward Sgr B2 reveal 18 maser spots. We detected NH_3 non-metastable (6,3), (7,4), (8,5), (9,6), and (10,7) masers in Sgr B2(M) and Sgr B2(N), an NH_3 (6,3) maser in Sgr B2(NS), as well as NH_3 (7,4), (9,6), and (10,7) masers in Sgr B2(S). Nine maser spots arise from Sgr B2(N), one from Sgr B2(NS), five from Sgr B2(M), and three originate in Sgr B2(S). Compared to the Effelsberg 100-m telescope data, the JVLA data indicate no missing flux. The detected maser spots are not resolved by our JVLA observations. Lower limits to the brightness temperature are >3000 K and reach up to 6×10^5 K, manifesting their maser nature. Long-term Effelsberg monitoring (19 months) indicates that the intensities of the (9,6) masers in Sgr B2(M), as well as the (9,6) and (10,7) masers in Sgr B2(N), show noticeable variations. However, the (10,7) maser in Sgr B2(M) is stable. While the NH_3 masers all arise near hot cores, there are many hot cores that do not exhibit NH_3 maser emission. All of these non-metastable ammonia maser lines show redshifted or blueshifted features that may be related to outflows or UCHII expansion.

8.2 Outlook

This PhD thesis has revealed that there is no strict linear correlation of carbon isotope ratios across the Galaxy and sulfur isotope ratios are not well re-produced by Galactic chemical evolution models. Even though $^{12}C/^{13}C$ ratios in the Milky Way have been well performed in several studies, there is still a lack of $^{12}C/^{13}C$ ratio measurements between the CMZ and a galactocentric distance of 3 kpc. Further observations will be needed to focus on these regions in our Galaxy as well as other galaxies, i.e., NGC 253, to test the findings in this thesis and help us to better understand the chemical evolution in galaxies. Observations of $^{34}S/^{36}S$ and $^{32}S/^{36}S$ isotope ratios are still relatively few in our Galaxy, especially in the CMZ and the inner disk within $R_{GC} = 5.0$ kpc. This is another direction for future studies. Furthermore, in order to better understand our Galaxy, we also need to find similar objects, for example, the nearby starburst galaxy, NGC 253. I am leading a project on carbon and sulfur isotope ratios in NGC 253 within the ALCHEMI (an ALMA Comprehensive High-resolution Extragalactic Molecular Inventory, Martín et al. 2021) framework. The results will be compared to the carbon and sulfur isotope ratios in our Galaxy presented in this thesis. We have also expanded our measurements in the Milky Way to silicon and its isotopic molecules. The observations of SiO and its isotopologues have been finished with the IRAM 30-m and the Effelsberg 100-m telescopes. The data will be analyzed in future studies and will provide us with information on different stellar nucleosynthesis processes regarding the production of carbon and sulfur.

This PhD thesis has greatly enlarged the sample of sources that host ammonia masers in the Milky Way and allowed us to look deeper into the mysteries of ammonia masers. The number of this sample is sufficient to systematically study the physical parameters, to compare the difference between different ammonia transitions, and to find the connections with the star formation processes and NH_3 masers. This is planned in future publications within our Effelsberg K-band line survey project, together with studies of water and methanol masers. Since non-metastable NH_3 masers usually have shown various flux densities at different epoch observations, we have monitored these masers with the Effelsberg 100-m telescope for at least one year. The data will be analyzed to check whether these masers are saturated or not. Of course, higher angular resolution observations are planned to provide precise physical positions and sizes of the newly identified ammonia masers in this thesis. This may give us also more constraints on pumping scenarios.

Appendix A

Direct measurements of carbon and sulfur isotope ratios in the Milky Way

A&A 670, A98 (2023)
https://doi.org/10.1051/0004-6361/202244584
© The Authors 2023

Astronomy & Astrophysics

Direct measurements of carbon and sulfur isotope ratios in the Milky Way

Y. T. Yan (闫耀庭)[1,⋆], C. Henkel[1,2,3], C. Kobayashi[4], K. M. Menten[1], Y. Gong (龚龑)[1], J. S. Zhang (张江水)[5], H. Z. Yu (余鸿智)[5,6], K. Yang (杨楷)[7,8], J. J. Xie (谢津津)[9], and Y. X. Wang (汪友鑫)[5]

[1] Max-Planck-Institut für Radioastronomie, Auf dem Hügel 69, 53121 Bonn, Germany
e-mail: yyan@mpifr-bonn.mpg.de; astrotingyan@gmail.com
[2] Astronomy Department, Faculty of Science, King Abdulaziz University, PO Box 80203, Jeddah 21589, Saudi Arabia
[3] Xinjiang Astronomical Observatory, Chinese Academy of Sciences, 830011 Urumqi, PR China
[4] Centre for Astrophysics Research, Department of Physics, Astronomy and Mathematics, University of Hertfordshire, Hatfield AL10 9AB, UK
[5] Center for Astrophysics, Guangzhou University, 510006 Guangzhou, PR China
[6] Ural Federal University, 19 Mira Street, 620002 Ekaterinburg, Russia
[7] School of Astronomy and Space Science, Nanjing University, 163 Xianlin Avenue, Nanjing 210023, PR China
[8] Key Laboratory of Modern Astronomy and Astrophysics (Nanjing University), Ministry of Education, Nanjing 210023, PR China
[9] Shanghai Astronomical Observatory, Shanghai 200030, PR China

Received 22 July 2022 / Accepted 6 December 2022

ABSTRACT

Context. Isotope abundance ratios provide a powerful tool for tracing stellar nucleosynthesis, evaluating the composition of stellar ejecta, and constraining the chemical evolution of the Milky Way.
Aims. We aim to measure the $^{12}C/^{13}C$, $^{32}S/^{34}S$, $^{32}S/^{33}S$, $^{32}S/^{36}S$, $^{34}S/^{33}S$, $^{34}S/^{36}S$, and $^{33}S/^{36}S$ isotope ratios across the Milky Way.
Methods. With the IRAM 30 meter telescope, we performed observations of the $J = 2–1$ transitions of CS, $C^{33}S$, $C^{34}S$, $C^{36}S$, ^{13}CS, $^{13}C^{33}S$, and $^{13}C^{34}S$ as well as the $J = 3–2$ transitions of $C^{33}S$, $C^{34}S$, $C^{36}S$, and ^{13}CS toward a large sample of 110 high-mass star-forming regions.
Results. We measured the $^{12}C/^{13}C$, $^{32}S/^{34}S$, $^{32}S/^{33}S$, $^{32}S/^{36}S$, $^{34}S/^{33}S$, $^{34}S/^{36}S$, and $^{33}S/^{36}S$ abundance ratios with rare isotopologs of CS, thus avoiding significant saturation effects. With accurate distances obtained from parallax data, we confirm previously identified $^{12}C/^{13}C$ and $^{32}S/^{34}S$ gradients as a function of galactocentric distance. In the central molecular zone, $^{12}C/^{13}C$ ratios are higher than suggested by a linear fit to the disk values as a function of galactocentric radius. While $^{32}S/^{34}S$ ratios near the Galactic center and in the inner disk are similar, this is not the case for $^{12}C/^{13}C$, when comparing central values with those near galactocentric radii of 5 kpc. As was already known, there is no $^{34}S/^{33}S$ gradient but the average ratio of 4.35 ± 0.44 derived from the $J = 2–1$ transition lines of $C^{34}S$ and $C^{33}S$ is well below previously reported values. A comparison between solar and local interstellar $^{32}S/^{34}S$ and $^{34}S/^{33}S$ ratios suggests that the Solar System may have been formed from gas with a particularly high ^{34}S abundance. For the first time, we report positive gradients of $^{32}S/^{33}S$, $^{34}S/^{36}S$, $^{33}S/^{36}S$, and $^{32}S/^{36}S$ in our Galaxy. The predicted $^{12}C/^{13}C$ ratios from the latest Galactic chemical-evolution models are in good agreement with our results. While $^{32}S/^{34}S$ and $^{32}S/^{36}S$ ratios show larger differences at larger galactocentric distances, $^{32}S/^{33}S$ ratios show an offset across the entire inner 12 kpc of the Milky Way.

Key words. nuclear reactions, nucleosynthesis, abundances – Galaxy: evolution – Galaxy: formation – ISM: abundances – HII regions – ISM: molecules

1. Introduction

Isotope abundance ratios provide a powerful tool for tracing stellar nucleosynthesis, evaluating the composition of stellar ejecta, and constraining the chemical evolution of the Milky Way (Wilson & Rood 1994). In particular, the $^{12}C/^{13}C$ ratio is one of the most useful tracers of the relative degree of primary to secondary processing. ^{12}C is a predominantly primary nucleus formed by He burning in massive stars on short timescales (e.g., Timmes et al. 1995). ^{13}C is produced on a longer timescale via CNO processing of ^{12}C seeds from earlier stellar generations during the red giant phase in low- and intermediate-mass stars or novae (e.g., Henkel et al. 1994; Meyer 1994; Wilson & Rood 1994). $^{12}C/^{13}C$ ratios are expected to be low in the central molecular zone (CMZ) and high in the Galactic outskirts, because the Galaxy formed from the inside out (e.g., Chiappini et al. 2001; Pilkington et al. 2012).

Observations indeed indicate a gradient of $^{12}C/^{13}C$ ratios across the Galaxy. Wilson et al. (1976) and Whiteoak & Gardner (1979) measured the $J_{Ka,Kc} = 1_{1,0}–1_{1,1}$ lines of $H_2^{12}CO$ and $H_2^{13}CO$ near 5 GHz toward 11 and 24 Galactic continuum sources, respectively. While ignoring effects of photon trapping, the results suggested that the $^{12}C/^{13}C$ ratios may vary with galactocentric distance (R_{GC}). With the additional measurement of the $J_{Ka,Kc} = 2_{1,1}–2_{1,2}$ line of H_2CO at 14.5 GHz,

⋆ Member of the International Max Planck Research School (IMPRS) for Astronomy and Astrophysics at the universities of Bonn and Cologne.

Open Access article, published by EDP Sciences, under the terms of the Creative Commons Attribution License (https://creativecommons.org/licenses/by/4.0), which permits unrestricted use, distribution, and reproduction in any medium, provided the original work is properly cited.
This article is published in open access under the Subscribe to Open model. Open access funding provided by Max Planck Society.

Henkel et al. (1980, 1982, 1983, 1985) also reported a gradient after correcting for effects of optical depth and photon trapping. Langer & Penzias (1990) used the optically thin lines of $C^{18}O$ and $^{13}C^{18}O$ to trace the carbon isotope ratios. They also found a systematic $^{12}C/^{13}C$ gradient across the Galaxy, ranging from about 20–25 near the Galactic center, to 30–50 in the inner Galactic disk, to ∼70 in the local interstellar medium (ISM). Wouterloot & Brand (1996), complementing these investigations by also including the far outer Galaxy, encountered ratios in excess of 100 and demonstrated that the gradient found in the inner Galaxy continues farther out. Milam et al. (2005) obtained $^{12}C/^{13}C = 6.01R_{GC} + 12.28$ based on the CN measurements of Savage et al. (2002). Here and elsewhere, R_{GC} denotes the galactocentric distance in units of kiloparsecs (kpc). By combining previously obtained H_2CO and $C^{18}O$ results with these CN data, Milam et al. (2005) obtained $^{12}C/^{13}C = 6.21R_{GC} + 18.71$.

More recently, Halfen et al. (2017) reported observations of a variety of molecules (e.g., H_2CS, CH_3CCH, NH_2CHO, CH_2CHCN, and CH_3CH_2CN) and their ^{13}C-substituted species toward Sgr B2(N). These authors obtained an average $^{12}C/^{13}C$ value of 24 ± 7 in the Galactic center region, which is close to results using $^{12}CH/^{13}CH$ (15.8 ± 2.4, Sgr B2(M)) by Jacob et al. (2020) and the particularly solid $^{12}C^{34}S/^{13}C^{34}S$ ratio ($22.1^{+3.3}_{-2.4}$, +50 km s^{-1} Cloud) from Humire et al. (2020) who use a variety of CS isotopologs and rotational transitions. Yan et al. (2019) proposed a linear fit of $^{12}C/^{13}C = (5.08 \pm 1.10)R_{GC} + (11.86 \pm 6.60)$ based on a large survey of H_2CO. The latter includes data from the center to the outskirts of the Milky Way well beyond the Perseus Arm. However, data from the CMZ are not similar to those thoroughly traced by Humire et al. (2020), not many sources from the innermost Galactic disk could be included in this survey, and also the number of sources beyond the Perseus arm was small, meaning that there is still space for improvement.

While the carbon isotope ratio has drawn much attention in the past, it is not the only isotope ratio that can be studied at radio wavelengths and that has a significant impact on our understanding of the chemical evolution of the Galaxy. The isotope ratios of sulfur are providing complementary information on stellar nucleosynthesis that is not traced by the carbon isotope ratio. Sulfur is special in that it provides a total of four stable isotopes, ^{32}S, ^{34}S, ^{33}S, and ^{36}S. In the Solar System, abundance ratios are 95.02:4.21:0.75:0.021, respectively (Anders & Grevesse 1989). ^{32}S and ^{34}S are synthesized during stages of hydrostatic oxygen-burning preceding a type II supernova event or during stages of explosive oxygen-burning in a supernova of type Ia; ^{33}S is synthesized in explosive oxygen- and neon-burning, which is also related to massive stars; and ^{36}S may be an s-process nucleus. The comprehensive calculations of Woosley & Weaver (1995) indicate that ^{32}S and ^{33}S are primary (in the sense that the stellar yields do not strongly depend on the initial metallicity of the stellar model), while ^{34}S is not a clean primary isotope; its yield decreases with decreasing metallicity. According to Thielemann & Arnett (1985) and Langer (1989), ^{36}S is produced as a purely secondary isotope in massive stars, with a possible (also secondary) contribution from asymptotic giant branch (AGB) stars. Only a small fraction of ^{36}S is destroyed during supernova explosions (Woosley, priv. comm.). Comparing "primary" and "secondary" nuclei, we might therefore expect the presence of weak $^{32}S/^{34}S$ and $^{34}S/^{33}S$ gradients and a stronger $^{32}S/^{36}S$ gradient as a function of galactocentric radius.

There is a strong and widespread molecular species that allows us to measure carbon and sulfur isotope ratios simultaneously, namely carbon monosulfide (CS). CS is unique in that it is a simple diatomic molecule exhibiting strong line emission and possessing eight stable isotopologs, which allows us to determine the above-mentioned carbon and sulfur isotope ratios. Six isotopologs have been detected so far in the ISM (e.g., Chin et al. 1996; Mauersberger et al. 1996; Humire et al. 2020; Yu et al. 2020).

Making use of the CS species, Chin et al. (1996) and Mauersberger et al. (1996) obtained average abundance ratios of 24.4 ± 5.0, 6.3 ± 1.0, and 115 ± 17 for $^{32}S/^{34}S$, $^{34}S/^{33}S$, and $^{34}S/^{36}S$ for the ISM, respectively. The latter is approximately half the solar value, but similar to the value found in IRC+10216 (Mauersberger et al. 2004). Recently, Humire et al. (2020) published $^{32}S/^{34}S$ ratios of $16.3^{+2.1}_{-1.7}$ and 17.9 ± 5.0 for the +50 km s^{-1} cloud and Sgr B2(N) near the Galactic center, respectively. These are only slightly lower than the value of 22 in the Solar System. There is an obvious and confirmed $^{32}S/^{34}S$ gradient (Chin et al. 1996; Yu et al. 2020) from the inner Galaxy out to a galactocentric distance of 12.0 kpc. Nevertheless, there is a lack of data at small and large galactocentric distances.

We are performing systematic observational studies on isotope ratios in the Milky Way, including $^{12}C/^{13}C$ (Yan et al. 2019), $^{14}N/^{15}N$ (Chen et al. 2021),$^{18}O/^{17}O$ (Zhang et al. 2015, 2020a, 2020b; Li et al. 2016), and $^{32}S/^{34}S$ (Yu et al. 2020). We have thus performed a more systematic study on CS and its isotopologs toward 110 high-mass star-forming regions (HMSFRs). $^{12}C/^{13}C$ and $^{32}S/^{34}S$ ratios can be directly derived from integrated $^{12}C^{34}S/^{13}C^{34}S$ (hereafter $C^{34}S/^{13}C^{34}S$) and $^{13}C^{32}S/^{13}C^{34}S$ (hereafter $^{13}CS/^{13}C^{34}S$, see Sect. 3.2) intensities, respectively. Also, $^{34}S/^{33}S$ and $^{34}S/^{36}S$ values could be obtained with measurements of $C^{34}S$, $^{12}C^{33}S$ (hereafter $C^{33}S$), and $^{12}C^{36}S$ (hereafter $C^{36}S$). Furthermore, $^{32}S/^{33}S$ and $^{32}S/^{36}S$ ratios can then be derived with the resulting $^{34}S/^{33}S$ and $^{34}S/^{36}S$ values combined with the $^{32}S/^{34}S$ ratios (see Sects. 3.4–3.7). In Sect. 2, we describe the source selection and observations for our large sample. Section 3 presents our results on $^{12}C/^{13}C$, $^{32}S/^{34}S$, $^{34}S/^{33}S$, $^{32}S/^{33}S$, $^{34}S/^{36}S$, and $^{32}S/^{36}S$ ratios. Section 4 discusses potential processes that could contaminate and affect the isotope ratios derived in the previous section and provides a detailed comparison with results from earlier studies. Our main results are summarized in Sect. 5.

2. Source selection and observations

2.1. Sample selection and distance

In 2019, we selected 18 HMSFRs from the Galactic center region to the outer Galaxy beyond the Perseus arm. To enlarge this sample, we chose 92 sources from the Bar and Spiral Structure Legacy (BeSSeL) Survey[1] in 2020. These 92 targets were recently released by the BeSSeL project (Reid et al. 2019) and not observed by Yu et al. (2020). In total, 110 objects in the Galaxy are part of our survey. The coordinates of our sample sources are listed in Table A.1. Determining trigonometric parallaxes is a very direct and accurate method to measure the distance of sources from the Sun (Reid et al. 2009, 2014, 2019). Over the past decade, mainly thanks to the BeSSeL project, the trigonometric parallaxes of approximately 200 HMSFRs have been determined across the Milky Way through dedicated

[1] http://bessel.vlbi-astrometry.org

high-resolution observations of molecular maser lines. Therefore, this is a good opportunity to investigate carbon and sulfur isotope ratios with well-determined distances across the Galaxy. The galactocentric distance ($R_{\rm GC}$) can be obtained with the heliocentric distance d from the trigonometric parallax data base of the BeSSeL project using

$$R_{\rm GC} = \sqrt{(R_0 \cos(l) - d)^2 + R_0^2 \sin^2(l)}, \quad (1)$$

(Roman-Duval et al. 2009). $R_0 = 8.178 \pm 0.013_{\rm stat.} \pm 0.022_{\rm sys.}$ kpc (GRAVITY Collaboration 2019) describes the distance from the Sun to the Galactic center, l is the Galactic longitude of the source, and d is the distance either directly derived from the trigonometric parallax data based on the BeSSeL project or a kinematic distance in cases where no such distance is yet available. Because the uncertainty in R_0 is very small, it will be neglected in the following analysis. For 12 of our targets without trigonometric parallax data, we estimated their kinematic distances from the Revised Kinematic Distance calculator[2] (Reid et al. 2014). The resulting distances indicate that 6 of these 12 sources are located in the CMZ, namely SgrC, the +20 km s^{-1} cloud, the +50 km s^{-1} cloud, G0.25, G1.28+0.07, and SgrD. Four targets belong to the inner Galactic disk, namely PointC1, CloudD, Clump2, and PointD1. Two sources, W89-380 and WB89-391, are in the outer regions beyond the Perseus arm. The heliocentric distances (d) and the galactocentric distances ($R_{\rm GC}$) for our sample are listed in Cols. 6 and 7 of Table A.1.

2.2. Observations

We observed the $J = 2$–1 transitions of CS, C^{33}S, C^{34}S, C^{36}S, ^{13}CS, ^{13}C^{33}S, and ^{13}C^{34}S as well as the $J = 3$–2 transitions of C^{33}S, C^{34}S, C^{36}S, and ^{13}CS toward 110 HMSFRs with the IRAM 30 meter telescope[3] in 2019 June, July, and October under project 045-19 (PI, Christian Henkel) as well as in 2020 August within project 022-20 (PI, Hongzhi Yu). The on + off source integration times for our sources range from 4.0 min to 10.8 h. These values are given in Table A.3. The EMIR receiver with two bands, E090 and E150, was used to cover a bandwidth of ∼16 GHz (from 90.8 to 98.2 GHz and 138.4 to 146.0 GHz) simultaneously in dual polarisation. We used the wide-mode FTS backend with a resolution of 195 kHz, corresponding to ∼0.6 km s^{-1} and ∼0.4 km s^{-1} at 96 GHz and 145 GHz, respectively. The observations were performed in total-power position-switching mode and the off position was set at 30′ in azimuth. Pointing was checked every 2 h using nearby quasars. Focus calibrations were done at the beginning of the observations and during sunset and sunrise toward strong quasars. The main beam brightness temperature, $T_{\rm MB}$, was obtained from the antenna temperature $T_{\rm A}^*$ via the relation $T_{\rm MB} = T_{\rm A}^* \times F_{\rm eff}/B_{\rm eff}$ ($F_{\rm eff}$: forward hemisphere efficiency; $B_{\rm eff}$: main beam efficiency) with corresponding telescope efficiencies[4]: $F_{\rm eff}/B_{\rm eff}$ are 0.95/0.81 and 0.93/0.73 in the frequency ranges of 90.8–98.2 GHz and 138.4–146.0 GHz, respectively. The system temperatures were 100–160 K and 170–300 K on a $T_{\rm A}^*$ scale for the E090 and E150 band observations. The half power beam width (HPBW) for each transition was calculated as HPBW(″) = 2460/ν(GHz). Rest frequencies, excitations of the upper levels above the ground state, Einstein coefficients for spontaneous emission, and respective beam sizes are listed in Table 1.

Table 1. Observed spectral line parameters.

Isotopolog	Transition	ν_0 [a] (MHz)	$E_{\rm up}$ [b] (K)	$A_{\rm u,l}$ [c] (s^{-1})	HPBW [d] (″)
CS	2–1	97980.953	7.1	1.68×10^{-5}	25.1
C^{33}S	2–1	97172.064	7.0	1.64×10^{-5}	25.3
C^{34}S	2–1	96412.95	6.9	1.60×10^{-5}	25.5
C^{36}S	2–1	95016.722	6.8	1.53×10^{-5}	25.9
^{13}CS	2–1	92494.308	6.7	1.41×10^{-5}	26.6
^{13}C^{33}S	2–1	91685.241	6.6	1.38×10^{-5}	26.8
^{13}C^{34}S	2–1	90926.026	6.5	1.34×10^{-5}	27.1
C^{33}S	3–2	145755.732	14.0	5.92×10^{-5}	16.9
C^{34}S	3–2	144617.101	13.9	5.78×10^{-5}	17.0
C^{36}S	3–2	142522.785	13.7	5.54×10^{-5}	17.3
^{13}CS	3–2	138739.335	13.3	5.11×10^{-5}	17.7

Notes. From the Cologne Database for Molecular Spectroscopy (CDMS, Müller et al. 2005; Endres et al. 2016). [a]Rest frequency. [b]Upper energy level. [c]Einstein coefficient for spontaneous emission from upper u to lower l level. [d]Half power beam width.

2.3. Data reduction

We used the GILDAS/CLASS[5] package to analyze the spectral line data. The spectra of the $J = 2$–1 transitions of CS, C^{33}S, C^{34}S, C^{36}S, ^{13}CS, ^{13}C^{33}S, and ^{13}C^{34}S as well as the $J = 3$–2 transitions of C^{33}S, C^{34}S, C^{36}S, and ^{13}CS toward one of our targets, DR21, are shown in Fig. 1, after subtracting first-order polynomial baselines and applying Hanning smoothing. The spectra of all 110 targets, also after first-order polynomial-baseline removal and Hanning smoothing, are presented in Fig. B.1.

Among our sample of 110 targets, we detected the $J = 2$–1 line of CS toward 106 sources, which yields a detection rate of 96%. The $J = 2$–1 transitions of C^{34}S, ^{13}CS, C^{33}S, and ^{13}C^{34}S were successfully detected in 90, 82, 46, and 17 of our sources with signal-to-noise ratios (S/N) of greater than 3, respectively. The $J = 3$–2 lines of C^{34}S, ^{13}CS, and C^{33}S were detected in 87, 71, and 42 objects with S/Ns of ≥3.0. Line parameters from Gaussian fitting are listed in Table A.3. Relevant for the evaluation of isotope ratios is the fact that for 17 sources with 19 velocity components, the S/Ns of the $J = 2$–1 transition of ^{13}C^{34}S are greater than 3, which allows us to determine the ^{12}C/^{13}C and ^{32}S/^{34}S ratios directly with the $J = 2$–1 lines of C^{34}S, ^{13}CS, and ^{13}C^{34}S. Toward 82 targets with 90 radial velocity components, the $J = 2$–1 transitions of C^{34}S and ^{13}CS were both detected with S/Ns of ≥3.0. The $J = 3$–2 lines of C^{34}S and ^{13}CS were both found in 71 objects with 73 radial velocity components and S/Ns of ≥3.0. Furthermore, the $J = 2$–1 and $J = 3$–2 transitions of C^{34}S and C^{33}S were detected with S/Ns of ≥3.0 toward 46 and 42 sources, respectively.

The C^{36}S $J = 2$–1 line was successfully detected with S/Ns of ≥3.0 toward three targets, namely W3OH, the +50 km s^{-1} cloud near the Galactic center, and DR21. As C^{36}S and ^{13}C^{33}S are the least abundant among the CS isotopologs, tentative detection with S/Ns of ∼2.0 are also presented here but not included in further analyses. In another five objects, the C^{36}S $J = 2$–1 line was tentatively detected. For the C^{36}S $J = 3$–2 transitions, we report one detection with an S/N larger than 3.0 toward

[2] http://bessel.vlbi-astrometry.org/revised_kd_2014
[3] IRAM is supported by INSU/CNRS (France), MPG (Germany) and IGN (Spain).
[4] https://publicwiki.iram.es/Iram30mEfficiencies
[5] https://www.iram.fr/IRAMFR/GILDAS/

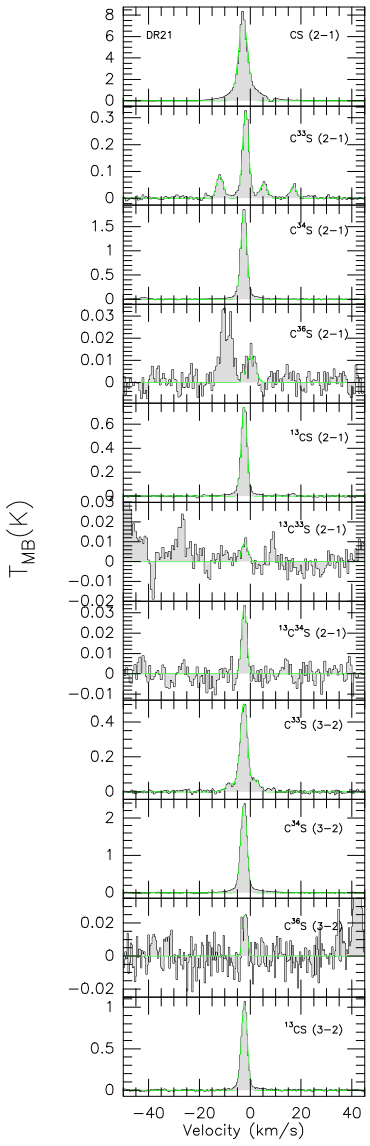

Fig. 1. Line profiles of the $J = 2$–1 transitions of CS, $C^{33}S$, $C^{34}S$, $C^{36}S$, ^{13}CS, $^{13}C^{33}S$, and $^{13}C^{34}S$ as well as the $J = 3$–2 transitions of $C^{33}S$, $C^{34}S$, $C^{36}S$, and ^{13}CS toward one typical target (DR21) of our large sample of 110 sources, after subtracting first-order polynomial baselines. The main beam brightness temperature scales are presented on the left hand side of the profiles. The spectra of all 110 objects in our sample are shown in Fig. B.1.

Orion-KL and five tentative detections. The $J = 2$–1 lines of $^{13}C^{33}S$ were tentatively detected toward three sources, namely Orion-KL, W51-IRS2, and DR21. Integration times and 1σ noise levels of the observed transitions are listed in Cols. 3 and 4 of Table A.3 for each target.

3. Results

In the following, we first estimate the optical depths of the various lines to avoid problems with line saturation that might affect our results. We then present the carbon and sulfur isotope ratios derived from different detected CS isotopologs.

3.1. Optical depth

The main isotopolog, CS, is usually optically thick in massive star-forming regions (e.g. Linke & Goldsmith 1980; Yu et al. 2020). Therefore, the $^{12}C/^{13}C$ and $^{32}S/^{34}S$ ratios cannot be determined from the line intensity ratios of $I(CS)/I(^{13}CS)$ and $I(CS)/I(C^{34}S)$. However, assuming that the $J = 2$–1 transitions of CS, $C^{34}S$, and ^{13}CS share the same beam filling factor and excitation temperature, we can estimate the maximum optical depth of the ^{13}CS $J = 2$–1 line from:

$$\frac{T_{\rm mb}(^{12}{\rm CS})}{T_{\rm mb}(^{13}{\rm CS})} \sim \frac{1-{\rm e}^{-\tau(^{13}{\rm CS}){\rm R_C}}}{1-{\rm e}^{-\tau(^{13}{\rm CS})}},\ R_{\rm C} = \frac{^{12}{\rm C}}{^{13}{\rm C}}, \tag{2}$$

where $T_{\rm mb}$ is the peak main beam brightness temperature derived from the best Gaussian-fitting result and listed in Col. 8 of Table A.3. In this case, the $^{12}C/^{13}C$ ratios can be derived from the integrated line intensities of $C^{34}S$ and $^{13}C^{34}S$ with the assumption of $\tau(C^{34}S) < 1.0$, which then also implies $\tau(^{13}C^{34}S) < 1.0$ (see details in Sect. 3.2). Multiplying $\tau(^{13}CS)$ by $R_C = {}^{12}C/{}^{13}C$, we can get the peak opacity $\tau(CS) = \tau(^{13}CS)R_C$. The maximum optical depth of $C^{34}S$ can be obtained from:

$$\frac{T_{\rm mb}(C^{34}S)}{T_{\rm mb}(^{13}CS)} = \frac{1-{\rm e}^{-\tau(C^{34}S)}}{1-{\rm e}^{-\tau(^{13}CS)}}, \tag{3}$$

where $T_{\rm mb}$ is the peak main beam brightness temperature derived from the best Gaussian-fitting result and listed in Col. 8 of Table A.3. As shown in Table 2, the peak optical depths of the $J = 2$–1 lines of CS, $C^{34}S$, and ^{13}CS for our 17 targets with detections of $^{13}C^{34}S$ range from 1.29 to 8.79, 0.12 to 0.55, and 0.05 to 0.34, respectively. Therefore, $C^{34}S$ and ^{13}CS in these 17 objects are optically thin, even though they belong, on average, to the more opaque ones, being successfully detected in $^{13}C^{34}S$ (see below). Nevertheless, the corrections for optical depth are applied to $C^{34}S$ and ^{13}CS with factors of f_1 and f_2, respectively.

$$f_1 = \frac{\tau(C^{34}S)}{1-{\rm e}^{-\tau(C^{34}S)}} \quad \text{and} \tag{4}$$

$$f_2 = \frac{\tau(^{13}CS)}{1-{\rm e}^{-\tau(^{13}CS)}} \tag{5}$$

are listed in Cols. 7 and 8 of Table 2, respectively.

For those 82 sources with detections of $J = 2$–1 CS, $C^{34}S$, and ^{13}CS, the optical depths were calculated based on the $^{12}C/^{13}C$ gradient that we derived from our $C^{34}S$ and $^{13}C^{34}S$ measurements (for details, see Sect. 3.2). In Table A.2, the peak opacities of the $J = 2$–1 lines of CS, $C^{34}S$, and ^{13}CS for these 82 targets range from 0.34 to 14.48, 0.02 to 0.74, and 0.01 to 0.39, respectively. The CS $J = 2$–1 lines are optically thick with $\tau(CS) > 1.0$ in most sources (89%) of our sample, while they tend to be optically thin in seven objects, namely Point C1 ($\tau(CS) \leq 0.59$), Sgr C ($\tau(CS) \leq 0.54$), Cloud D ($\tau(CS) \leq 0.64$), G1.28+0.07 ($\tau(CS) \leq 0.82$), Sgr D ($\tau(CS) \leq 0.45$), and Point D1 ($\tau(CS) \leq 0.34$). In contrast, the transitions from rare isotopologs, the $C^{34}S$ and ^{13}CS $J = 2$–1 lines in our sample, are all optically thin, as their maximum optical depths are less than 0.8 and 0.4, respectively. In the following, we are therefore motivated to consider all CS isotopologs as optically thin, except CS itself. This allows us to use ratios of integrated intensity of all the rare CS isotopologs – but not CS itself – to derive the carbon

Table 2. Isotope ratios derived with the $J = 2$–1 transitions of $C^{34}S$, ^{13}CS, and $^{13}C^{34}S$.

Source	V_{LSR}	R_{GC}	Optical depth			Corrections for Optical depth		$^{12}C/^{13}C$	$^{32}S/^{34}S$
	(km s^{-1})	(kpc)	CS	$C^{34}S$	^{13}CS	f_1	f_2		
W3OH	–46.96	9.64 ± 0.03	8.289 ± 0.083	0.292 ± 0.003	0.127 ± 0.001	1.2	1.1	75.30 ± 4.27	29.80 ± 1.68
Orion-KL	8.17	8.54 ± 0.00	3.722 ± 0.037	0.180 ± 0.002	0.074 ± 0.001	1.1	1.0	54.89 ± 12.90	21.24 ± 4.67
G359.61−00.24	19.33	5.51 ± 0.15	3.531 ± 0.035	0.204 ± 0.002	0.089 ± 0.001	1.1	1.0	43.85 ± 11.95	17.31 ± 4.79
+50 km s^{-1} cloud	46.79	0.02 ± 0.04	4.278 ± 0.043	0.192 ± 0.002	0.151 ± 0.002	1.1	1.1	31.22 ± 2.06	21.71 ± 1.40
SgrB2	53.18	0.55 ± 0.05	1.290 ± 0.013	0.140 ± 0.001	0.113 ± 0.001	1.1	1.1	12.18 ± 0.73	9.77 ± 0.58
SgrB2	66.54	0.44 ± 0.70	8.119 ± 0.081	0.523 ± 0.005	0.341 ± 0.003	1.3	1.2	30.62 ± 2.04	18.99 ± 1.31
SgrB2	83.38	0.41 ± 0.02	2.417 ± 0.024	0.097 ± 0.001	0.077 ± 0.001	1.0	1.0	32.90 ± 5.65	26.24 ± 4.49
G006.79−00.25	20.87	4.75 ± 0.25	8.789 ± 0.088	0.484 ± 0.005	0.242 ± 0.002	1.3	1.1	45.82 ± 8.39	19.46 ± 3.63
G010.32−00.15	11.99	5.34 ± 0.29	5.039 ± 0.050	0.237 ± 0.002	0.111 ± 0.001	1.1	1.1	50.95 ± 11.58	21.55 ± 5.05
G019.36−00.03	26.40	5.58 ± 0.49	6.789 ± 0.068	0.332 ± 0.003	0.141 ± 0.001	1.2	1.1	56.41 ± 14.37	21.19 ± 5.53
G024.78+00.08	110.72	3.51 ± 0.15	8.038 ± 0.080	0.554 ± 0.006	0.322 ± 0.003	1.3	1.2	32.56 ± 4.25	16.08 ± 2.12
G028.39+00.08	78.01	4.83 ± 0.17	8.705 ± 0.087	0.443 ± 0.004	0.291 ± 0.003	1.2	1.2	37.04 ± 10.05	18.74 ± 5.12
G028.83−00.25	87.19	4.50 ± 0.48	7.283 ± 0.073	0.388 ± 0.004	0.183 ± 0.002	1.2	1.1	47.93 ± 10.00	19.73 ± 4.16
G030.70−00.06	89.94	4.20 ± 0.10	7.088 ± 0.071	0.448 ± 0.004	0.263 ± 0.003	1.2	1.1	33.39 ± 2.77	18.07 ± 1.52
G030.74−00.04	91.82	5.76 ± 0.36	5.924 ± 0.059	0.404 ± 0.004	0.191 ± 0.002	1.2	1.1	37.63 ± 10.87	15.61 ± 4.59
G030.81−00.05	98.89	5.73 ± 0.24	4.691 ± 0.047	0.306 ± 0.003	0.187 ± 0.002	1.2	1.1	29.07 ± 2.99	14.97 ± 1.44
W51-IRS2	61.07	6.22 ± 0.06	1.883 ± 0.019	0.119 ± 0.001	0.052 ± 0.001	1.1	1.0	38.26 ± 4.35	16.70 ± 1.92
DR21	–2.49	8.10 ± 0.00	7.079 ± 0.071	0.270 ± 0.003	0.106 ± 0.001	1.1	1.1	76.22 ± 7.57	27.48 ± 2.84
NGC7538	–57.12	9.47 ± 0.07	3.433 ± 0.034	0.131 ± 0.001	0.050 ± 0.001	1.1	1.0	73.19 ± 12.54	26.72 ± 4.57

Notes. Velocities were obtained from measurements of $C^{34}S$, see Table A.3.

and sulfur isotope ratios we intend to study. Small corrections accounting for the optical depths are applied to the $C^{34}S$ and ^{13}CS $J = 2$–1 lines with factors of f_1 and f_2, respectively, and are listed in Cols. 7 and 8 of Table A.2. The optical depths of the $J = 3$–2 transitions cannot be estimated, as the CS $J = 3$–2 line was not covered by our observations because of bandwidth limitations. However, the $^{32}S/^{34}S$ ratios for a given source obtained through the double isotope method from the $J = 2$–1 and $J = 3$–2 transitions are in good agreement, indicating that the $C^{34}S$ and ^{13}CS $J = 3$–2 lines in our sample are also optically thin (see details in Sect. 3.3).

The RADEX non Local Thermodynamic Equilibrium (LTE) model (van der Tak et al. 2007) was used to calculate the variation of excitation temperature, T_{ex}, with optical depth. Frequencies, energy levels, and Einstein A coefficients for spontaneous emission were taken from the Cologne Database for Molecular Spectroscopy (CDMS; Müller et al. 2005; Endres et al. 2016). Recent collision rates for CS with para- and ortho-H_2 (Denis-Alpizar et al. 2018) were used. Figure 2 shows the excitation temperatures and opacities of $C^{34}S$ $J = 2$–1 for a kinetic temperature of 30 K and a molecular hydrogen density of 10^5 cm^{-3}. Variations of T_{ex} within about 2 K for our sample targets with optical depths of $0.02 \leq \tau(C^{34}S) \leq 0.74$ can barely affect our results.

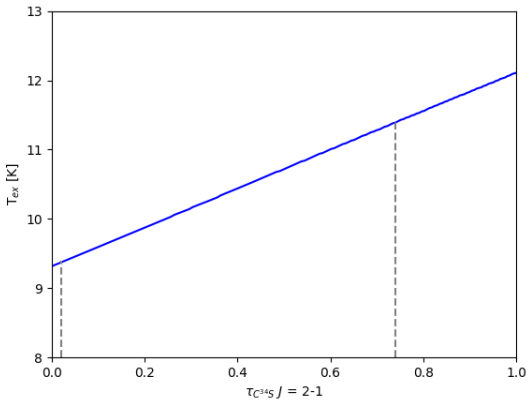

Fig. 2. Excitation temperature, T_{ex}, as a function of optical depth for the $J = 2$–1 transition of $C^{34}S$. The gray dashed lines indicate the range of opacities for our sample sources.

3.2. $^{12}C/^{13}C$ and $^{32}S/^{34}S$ ratios derived directly from $^{13}C^{34}S$

3.2.1. $^{12}C/^{13}C$ ratios

The $^{12}C/^{13}C$ ratios derived from the integrated intensity ratios of $C^{34}S$ and $^{13}C^{34}S$ with corrections of optical depth are listed in Table 2. Figure 3 shows our results as filled black circles. A gradient of $^{12}C/^{13}C$ is obtained with an unweighted least-squares fit:

$$^{12}C/^{13}C = (4.77 \pm 0.81)R_{GC} + (20.76 \pm 4.61). \quad (6)$$

The correlation coefficient is 0.82. Around the CMZ toward the +50 km s^{-1} cloud and SgrB2, four velocity components of $C^{34}S$ and $^{13}C^{34}S$ were detected and then an average $^{12}C/^{13}C$ value of 27 ± 3 is derived. The uncertainties given here and below are standard deviations of the mean. Eleven objects within a range of 3.50 kpc < R_{GC} < 6.50 kpc in the inner Galactic disk lead to an average $^{12}C/^{13}C$ value of 41 ± 9. In the Local arm near the Sun, the $^{13}C^{34}S$ lines were detected toward two sources, Orion-KL and DR21. These provide an average $^{12}C/^{13}C$ value of 66 ± 10, which is lower than the Solar System ratio. The other two targets beyond the solar neighborhood belong to the Perseus arm and show a slightly higher value of 74 ± 8.

For sources with detections of $C^{34}S$ and nondetections of $^{13}C^{34}S$, 3σ lower limits of the $^{12}C/^{13}C$ ratio have been derived

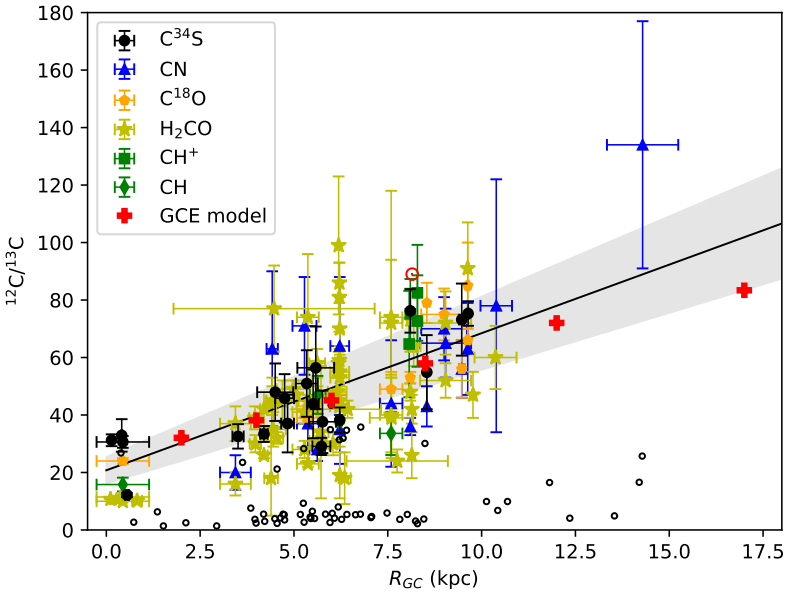

Fig. 3. $^{12}C/^{13}C$ isotope ratios from $C^{34}S/^{13}C^{34}S$, $CN/^{13}CN$, $C^{18}O/^{13}C^{18}O$, $H_2CO/H_2^{13}CO$, $CH^+/^{13}CH^+$, and $CH/^{13}CH$ are plotted as functions of the distance from the Galactic center. The red symbol ⊙ indicates the $^{12}C/^{13}C$ isotope ratio of the Sun. The filled black circles are the results obtained from $C^{34}S$ with corrections of opacity in the current work, and the resulting first-order polynomial fit is plotted as a solid line, with the gray-shaded area showing the 1σ interval of the fit. The open black circles are the 3σ lower limits obtained from nondetections of $^{13}C^{34}S$ in the current work. The blue triangles, orange pentagons, yellow stars, green squares, and green diamonds are values determined from CN (Savage et al. 2002; Milam et al. 2005), $C^{18}O$ (Langer & Penzias 1990; Wouterloot & Brand 1996; Keene et al. 1998), H_2CO (Henkel et al. 1980, 1982, 1983, 1985; Yan et al. 2019), CH^+ (Ritchey et al. 2011), and CH (Jacob et al. 2020), respectively, using the most up-to-date distances. The red crosses visualize the results from the GCE model of Kobayashi et al. (2011, 2020, see also Sect. 4.9).

and are shown as open black circles in Fig. 3. All these lower limits are below the $^{12}C/^{13}C$ gradient we describe above.

3.2.2. $^{32}S/^{34}S$ ratios

The $^{32}S/^{34}S$ ratios directly derived from the integrated intensity ratios of $^{13}CS/^{13}C^{34}S$ from the $J = 2$–1 lines with corrections of optical depth are listed in Table 2 and are plotted as a function of galactocentric distance in Fig. 4. With an unweighted least-squares fit, a gradient with a correlation coefficient of 0.47 can be obtained:

$$^{32}S/^{34}S = (0.73 \pm 0.36)R_{GC} + (16.50 \pm 2.07). \quad (7)$$

An average $^{32}S/^{34}S$ ratio of 19 ± 2 is obtained in the CMZ, which is based on the measurements from two sources, namely the +50 km s^{-1} cloud next to the Galactic center and Sgr B2. In the inner Galactic disk at a range of 3.50 kpc < R_{GC} < 6.50 kpc, $^{13}C^{34}S$ was detected toward 11 objects, leading to an average $^{32}S/^{34}S$ value of 18 ± 4. For sources in the Local and the Perseus arm beyond the Sun, the $^{32}S/^{34}S$ ratios are 24 ± 4 and 28 ± 3, respectively. This reveals a gradient from the inner Galactic disk to the outer Galaxy, but none from the CMZ to the inner disk.

For sources with detections of ^{13}CS and nondetections of $^{13}C^{34}S$, we determined 3σ lower limits to the $^{32}S/^{34}S$ ratio, which are shown as open black circles in Fig. 4. All these lower limits are below the $^{32}S/^{34}S$ gradient we describe above.

3.3. $^{32}S/^{34}S$ ratios obtained through the double isotope method

The $^{32}S/^{34}S$ values can also be derived from measurements of $C^{34}S$ and ^{13}CS using the carbon gradient obtained from our $^{13}C^{34}S$ measurements above by applying the following equation:

$$\frac{^{32}S}{^{34}S} = R_C \frac{I(^{13}CS)}{I(C^{34}S)}, \quad (8)$$

where R_C is the $^{12}C/^{13}C$ ratio derived from Eq. (6). The uncertainty on this latter is also included in our error budget. The $^{32}S/^{34}S$ ratios in the $J = 2$–1 transitions were calculated with corrections of optical depth for 83 targets with 90 radial velocity components, in which the $C^{34}S$ and ^{13}CS $J = 2$–1 lines were both detected, and are listed in Col. 7 of Table A.2. An unweighted least-squares fit to these values yields

$$^{32}S/^{34}S(2{-}1) = (0.75 \pm 0.13)R_{GC} + (15.52 \pm 0.78), \quad (9)$$

with a correlation coefficient of 0.54. The $C^{34}S$ and ^{13}CS $J = 3$–2 lines were both detected in 71 objects with 73 radial velocity components. The $^{32}S/^{34}S$ ratios derived with Eq. (8) from the $J = 3$–2 transition are shown in Col. 8 of Table A.2. An unweighted least-squares fit to the $J = 3$–2 transition yields

$$^{32}S/^{34}S(3{-}2) = (0.99 \pm 0.14)R_{GC} + (16.05 \pm 0.95), \quad (10)$$

which is within the errors, and is consistent with the trend obtained from the $J = 2$–1 transition (Eq. (9)). However, we note that we do not have CS $J = 3$–2 data, and therefore no opacity corrections could be applied to our $C^{34}S$ $J = 3$–2 spectra (see also Sect. 3.4).

3.4. $^{34}S/^{33}S$ ratios

The $^{34}S/^{33}S$ ratios can be determined directly from the intensity ratios of $C^{34}S/C^{33}S$. The $^{34}S/^{33}S$ ratios from the $J = 2$–1 lines were then corrected for optical depths derived in Sect. 3.1. However, both the $J = 2$–1 and $J = 3$–2 transitions of $C^{33}S$ are split by hyperfine structure (HFS) interactions (Bogey et al. 1981), which may affect the deduced values of $^{34}S/^{33}S$.

The $C^{33}S$ $J = 2$–1 line consists of eight hyperfine components distributed over about 9.0 MHz (Müller et al. 2005; Endres et al. 2016), which corresponds to a velocity range of about 28 km s^{-1}. Following the method introduced in Appendix D in Gong et al. (2021), and assuming that the intrinsic width of each HFS line is 1 km s^{-1}, the $J = 2$–1 line profile can be reproduced by four components (see Fig. 5, upper left panel). In this case, the

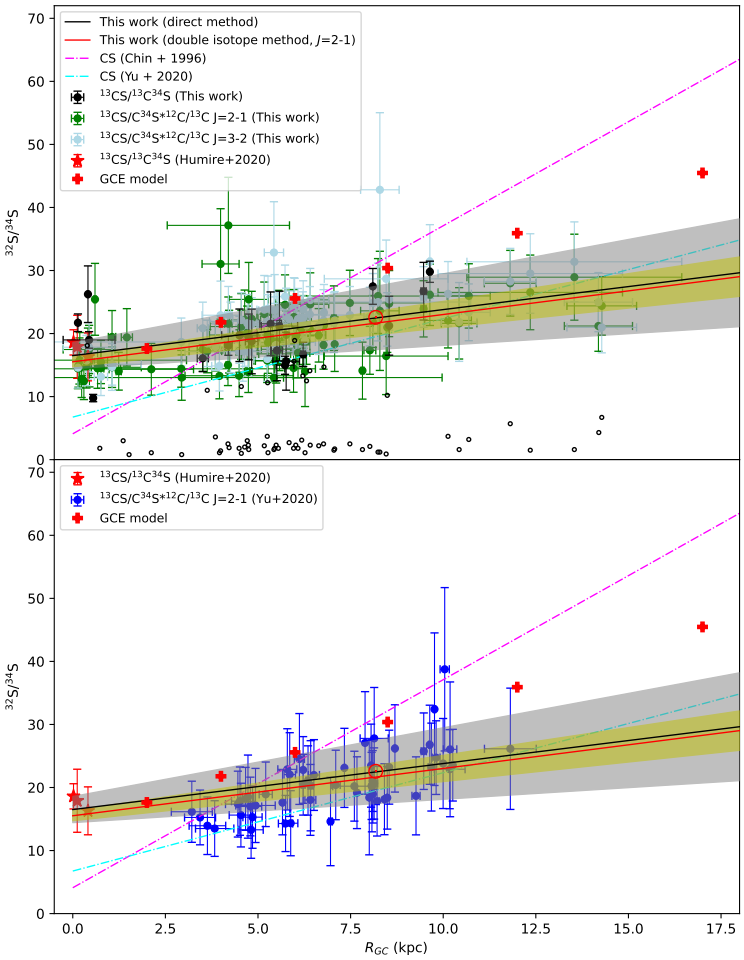

Fig. 4. $^{32}S/^{34}S$ isotope ratios as functions of the distance from the Galactic center. The symbol ⊙ indicates the $^{32}S/^{34}S$ isotope ratio in the Solar System. In the upper panel, the $^{32}S/^{34}S$ ratios directly derived from $^{13}CS/^{13}C^{34}S$ in the $J = 2–1$ transition and obtained from the double isotope method in the $J = 2–1$ transition with corrections for optical depth are plotted as black and green dots, respectively. The $^{32}S/^{34}S$ ratios without corrections of opacity in the $J = 3–2$ transition are plotted as light blue dots. The 3σ lower limits of $^{32}S/^{34}S$ ratios obtained from non-detections of $^{13}C^{34}S$ in the current work are shown as open black circles. The $^{32}S/^{34}S$ ratios in Yu et al. (2020) derived from the double isotope method in the $J = 2–1$ transitions are shown as blue dots in the lower panel. The $^{32}S/^{34}S$ values in the CMZ obtained from $^{13}CS/^{13}C^{34}S$ in Humire et al. (2020) are plotted as red stars in both panels. The resulting first-order polynomial fits to $^{32}S/^{34}S$ ratios with the direct method and the double isotope method from the $J = 2–1$ transition in this work are plotted as black and red solid lines in the two panels, respectively, with the gray and yellow shaded areas showing the 1 σ intervals of the fits. The magenta and cyan dashed-dotted lines show the $^{32}S/^{34}S$ gradients from Chin et al. (1996) and Yu et al. (2020). The red crosses visualize the results from the GCE model of Kobayashi et al. (2011, 2020, see also Sect. 4.9).

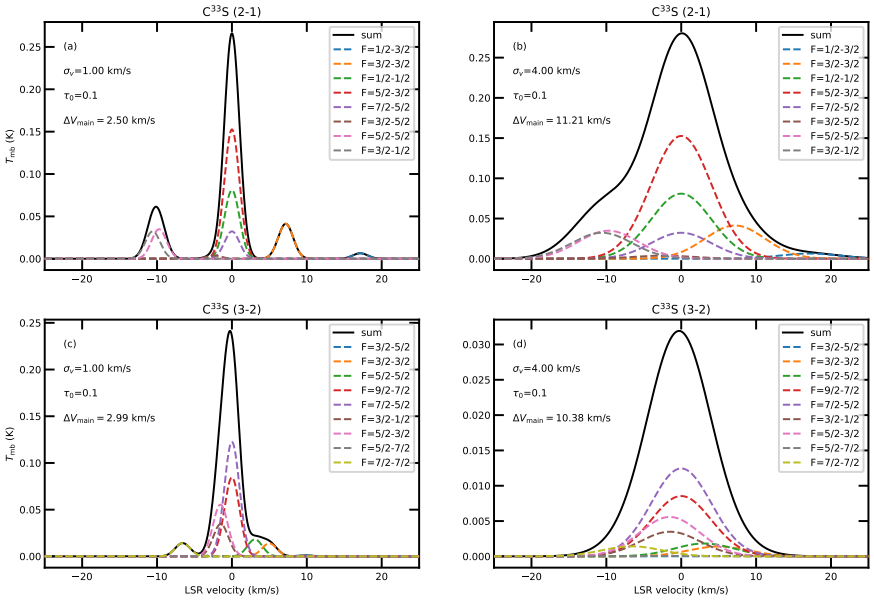

Fig. 5. Synthetic $C^{33}S$ (2–1) and $C^{33}S$ (3–2) spectra for two intrinsic line widths, 1.0 km s^{-1} (*left panels*) and 4.0 km s^{-1} (*right panels*).

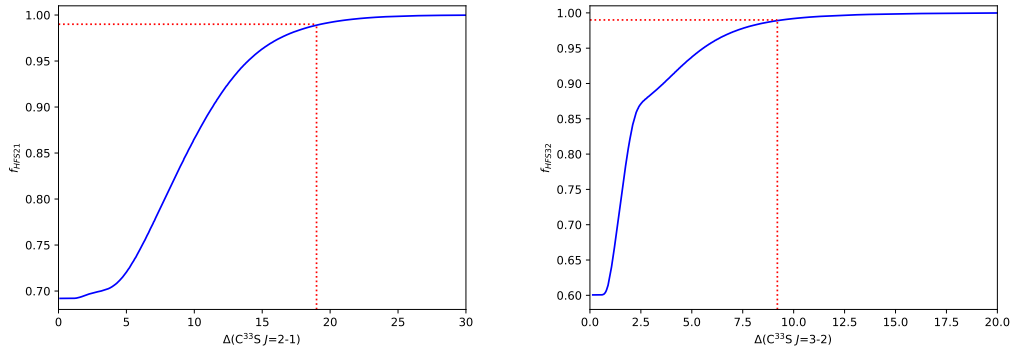

Fig. 6. Blue lines are curves showing the theoretical dependencies of the HFS factors, $f_{21\mathrm{HFS}}$ (*left*) and $f_{32\mathrm{HFS}}$ (*right*), on the line width of the $C^{33}S$ main component for sources in which only the main component was detected. The red dotted vertical and horizontal lines indicate the values of the minimal line widths where the factors are reaching almost 1.0, 19.0 km s^{-1} for the $J = 2$–1 transition ($f_{21\mathrm{HFS}} \sim 0.99$) and 9.2 km s^{-1} for the $J = 3$–2 transition ($f_{32\mathrm{HFS}} \sim 0.99$).

main component (I_{main}) consists of four HFS lines ($F = 7/2$–$5/2$, $F = 5/2$–$3/2$, $F = 1/2$–$1/2$, $F = 3/2$–$5/2$), which account for 70% of the total intensity. Among the 46 sources with detections of the $C^{33}S$ $J = 2$–1 line, all of the four components were detected in 10 targets. Toward 16 objects, only the three components with the lowest velocities were detected, accounting for 98% of the total intensity. For the remaining 20 sources, only the main component was detected. Based on the above assumptions, 30% of the total intensity would be missed. The situation is different when the main component becomes broader. If the line width of the main component is larger than 10 km s^{-1}, 87% of the total intensity is covered by the main spectral feature. When the line width of the main component is larger than 19.0 km s^{-1}, then almost all HFS lines are included. In Fig. 6, we show the dependence of the HFS factor for the $J = 2$–1 line, $f_{21\mathrm{HFS}}$, on the line width of the main component. Depending on the specific condition of each target, we derived $f_{21\mathrm{HFS}}$ for each source. The values are listed in Table 3.

The $C^{33}S$ $J = 3$–2 line consists of nine hyperfine components covering about 8.0 MHz (Müller et al. 2005; Endres et al. 2016), corresponding to a velocity range of about 16 km s^{-1}. Assuming that the intrinsic width of each HFS line is 1 km s^{-1}, the $J = 3$–2 line profile can be characterized by three components (see also Fig. 5). All these three components are detected in only two sources, Orion-KL and DR21. The main component consists of four HFS lines ($F = 5/2$–$3/2$, $F = 3/2$–$1/2$, $F = 7/2$–$5/2$, $F = 9/2$–$7/2$), which account for 86% of the total intensity. When the line width becomes larger than 9.2 km s^{-1}, almost all of the HFS lines overlap. The HFS factors ($f_{32\mathrm{HFS}}$) of the $J = 3$–2 transition obtained individually for each source are listed in Table 3.

We calculated the $^{34}S/^{33}S$ intensity ratios and present them in Table 3. Applying corrections accounting for the effect of hyperfine splitting, the $^{34}S/^{33}S$ ratios are derived and are also listed in Table 3. The $^{34}S/^{33}S$ values obtained from the $J = 2$–1 transitions are always higher than the ones derived from the $J = 3$–2 lines toward the same source, with the exception of G097.53+03.18. This difference could be caused by the lack of corrections of optical depth in the $J = 3$–2 transition. The average values of $^{34}S/^{33}S$ toward our sample are 4.35 ± 0.44 and 3.49 ± 0.26 in the $J = 2$–1 and $J = 3$–2 transitions, respectively. The $^{34}S/^{33}S$ ratios were found to be independent of galactocentric distance (Fig. 7).

After applying the opacity correction of the $J = 2$–1 transition to the $J = 3$–2 line in the same source, $^{34}S/^{33}S$ ratios in the $J = 3$–2 transition are higher than the $^{34}S/^{33}S$ values in the $J = 2$–1 transition in seven targets, suggesting that the $C^{34}S$ $J = 3$–2 lines in these seven sources are less opaque than the $C^{34}S$ $J = 2$–1 lines. The seven targets are the +20 km s^{-1} cloud, G023.43−00.18, G028.39+00.08, G028.83−00.25, G073.65+00.19, G097.53+03.18, and G109.87+02.11. A comparison of the corrected $^{34}S/^{33}S$ ratios in these two transitions is shown in Fig. 8. On the other hand, toward the other 32 objects of the whole sample of 39 sources with detections in these two transitions, the $^{34}S/^{33}S$ ratios in the $J = 3$–2 transition are still lower than the $^{34}S/^{33}S$ values in the $J = 2$–1 transitions. This suggests that the $C^{34}S$ $J = 3$–2 lines may be more opaque than the $C^{34}S$ $J = 2$–1 lines. The ratios of $^{34}S/^{33}S$ values without corrections of opacity in the $J = 3$–2 transition and the corrected $^{34}S/^{33}S$ values from the $J = 2$–1 lines in 31 targets of these 32 sources are within the range of 1.02 to 1.71, which suggest that the optical depths of $C^{34}S$ in the $J = 3$–2 transition in these objects range from 0.05 to 1.20 based on Eq. (4). The maximum optical depth of the $C^{34}S$ $J = 3$–2 line toward the additional source, G024.85+00.08, which has not considered until now, is estimated to be 2.6.

3.5. $^{32}S/^{33}S$ ratios

The $^{32}S/^{33}S$ values can also be derived from the $^{34}S/^{33}S$ ratios in Sect. 3.4 using the $^{32}S/^{34}S$ ratios – which we directly obtained from $^{13}CS/^{13}C^{34}S$ and present in Sect. 3.2.2 – by applying the following equation:

$$\frac{^{32}S}{^{33}S} = \frac{^{34}S}{^{33}S} \times \frac{^{32}S}{^{34}S}. \quad (11)$$

For sources where we did not detect $^{13}C^{34}S$, the $^{32}S/^{34}S$ ratios derived from the double isotope method in Sect. 3.3 are used. Their uncertainty is also included in our error budget. The resulting $^{32}S/^{33}S$ ratios are listed in Table 4. As in the case of the $^{34}S/^{33}S$ ratios, the $^{32}S/^{33}S$ values obtained from the $J = 2$–1 transitions with corrections for optical depth are slightly larger than the ones from the $J = 3$–2 transitions without opacity corrections toward the same source.

In the CMZ, $^{32}S/^{33}S$ $J = 2$–1 ratios toward four targets, namely the +20 km s^{-1} cloud, the +50 km s^{-1} cloud, Sgr B2, and Sgr D, lead to an average value of 70 ± 16. In the inner Galaxy, in a galactocentric distance range of 2.0 kpc ≤ R_{GC} ≤ 6.0 kpc, an average $^{32}S/^{33}S$ ratio of 82 ± 19 was derived from values in

Table 3. Corrected $^{34}S/^{33}S$ isotope ratios.

Source	R_{GC}	$J = 2–1$				$J = 3–2$			
	(kpc)	FWHM (km s^{-1})	$C^{34}S/C^{33}S$	f_{21HFS}	$^{34}S/^{33}S$	FWHM (km s^{-1})	$C^{34}S/C^{33}S$	f_{32HFS}	$^{34}S/^{33}S$
WB89-380	14.19 ± 0.92	3.60	5.70 ± 0.58	0.70	4.28 ± 0.44	3.87	3.70 ± 0.37	0.91	3.36 ± 0.34
WB89-391	14.28 ± 0.94	1.03	6.75 ± 1.71	0.69	5.21 ± 1.32	2.19	3.67 ± 0.42	0.85	3.12 ± 0.36
W3OH	9.64 ± 0.03	4.41	3.04 ± 0.12	1.00	3.54 ± 0.14	6.14	2.59 ± 0.04	0.96	2.49 ± 0.04
Orion-KL	8.54 ± 0.00	4.25	2.77 ± 0.22	1.00	3.01 ± 0.24	8.33	2.74 ± 0.12	0.99	2.72 ± 0.11
+20 km s^{-1} cloud	0.03 ± 0.03	24.78	4.89 ± 0.14	1.00	5.64 ± 0.16	20.12	5.22 ± 0.30	1.00	5.22 ± 0.30
G359.61−00.24	5.51 ± 0.15	3.17	3.63 ± 0.12	1.00	4.04 ± 0.13	10.44	3.33 ± 0.45	0.99	3.31 ± 0.44
+50 km s^{-1} cloud	0.02 ± 0.04	24.29	4.80 ± 0.06	1.00	5.29 ± 0.07	21.28	4.57 ± 0.15	1.00	4.57 ± 0.15
G000.31−00.20	5.25 ± 0.36	3.58	4.65 ± 0.70	0.70	3.54 ± 0.53	...	...	...	...
SgrB2	0.44 ± 0.70	21.14	2.23 ± 0.10	0.99	2.46 ± 0.11	21.22	2.00 ± 0.03	1.00	2.00 ± 0.03
SgrD	0.45 ± 0.07	2.73	7.01 ± 0.47	0.70	4.96 ± 0.33	4.00	3.56 ± 0.24	0.91	3.24 ± 0.22
G006.79−00.25	4.75 ± 0.25	2.73	3.79 ± 0.08	0.98	4.79 ± 0.10	3.32	3.68 ± 0.09	0.89	3.29 ± 0.08
G007.47+00.05	12.35 ± 2.49	3.12	5.41 ± 0.97	0.70	4.07 ± 0.73	...	...	...	...
G010.32−00.15	5.34 ± 0.29	2.66	4.16 ± 0.22	0.98	4.60 ± 0.25	3.74	4.07 ± 0.21	0.90	3.68 ± 0.19
G010.62−00.33	5.49 ± 0.56	2.70	6.37 ± 1.45	0.98	6.80 ± 1.54	...	...	...	...
G011.10−00.11	4.26 ± 0.21	1.45	5.36 ± 1.52	0.69	3.72 ± 1.05	...	...	...	...
G016.86−02.15	5.97 ± 0.47	3.32	3.47 ± 0.12	0.98	3.83 ± 0.14	4.33	3.42 ± 0.14	0.92	3.15 ± 0.13
G017.02−02.40	6.40 ± 0.36	3.74	4.49 ± 0.33	0.98	4.83 ± 0.35	4.03	4.11 ± 0.26	0.91	3.75 ± 0.24
G017.63+00.15	6.77 ± 0.04	2.74	5.41 ± 1.27	0.70	4.02 ± 0.94	...	...	...	...
G018.34+01.76	6.31 ± 0.07	2.30	4.79 ± 0.28	0.98	4.95 ± 0.28	3.00	4.59 ± 0.16	0.88	4.06 ± 0.15
G019.36−00.03	5.58 ± 0.49	3.02	4.58 ± 0.20	0.98	5.40 ± 0.24	5.09	4.25 ± 0.18	0.94	3.99 ± 0.17
G023.43−00.18	3.63 ± 0.49	3.81	3.75 ± 0.38	0.98	4.22 ± 0.43	5.06	4.65 ± 0.24	0.94	4.37 ± 0.23
G024.78+00.08	3.51 ± 0.15	4.29	2.86 ± 0.08	1.00	4.05 ± 0.11	6.36	2.76 ± 0.06	0.96	2.67 ± 0.06
G024.85+00.08	3.85 ± 0.23	1.27	9.43 ± 2.27	0.69	7.56 ± 1.82	3.20	3.03 ± 0.40	0.89	2.70 ± 0.36
G028.30−00.38	4.71 ± 0.26	...	...	...	...	2.68	4.05 ± 0.63	0.88	3.55 ± 0.55
G028.39+00.08	4.83 ± 0.17	3.04	3.33 ± 0.15	0.98	3.82 ± 0.18	4.39	3.84 ± 0.12	0.92	3.54 ± 0.11
G028.83−00.25	4.50 ± 0.48	2.27	3.80 ± 0.19	0.98	4.56 ± 0.23	3.94	4.65 ± 0.10	0.91	4.23 ± 0.09
G030.70−00.06	4.20 ± 0.10	4.85	2.80 ± 0.07	1.00	3.55 ± 0.09	6.29	2.84 ± 0.12	0.96	2.73 ± 0.11
G030.74−00.04	5.76 ± 0.36	3.55	3.61 ± 0.15	0.98	4.36 ± 0.19	4.24	3.48 ± 0.08	0.92	3.19 ± 0.08
G030.78+00.20	4.19 ± 0.05	...	...	...	...	4.17	4.20 ± 0.51	0.92	3.85 ± 0.47
G030.81−00.05	5.73 ± 0.24	6.15	3.05 ± 0.09	1.00	3.59 ± 0.11	7.34	2.88 ± 0.15	0.98	2.81 ± 0.15
G031.24−00.11	7.48 ± 2.00	...	...	...	...	4.15	4.32 ± 0.52	0.92	3.95 ± 0.48
G032.74−00.07	4.55 ± 0.23	4.54	3.44 ± 0.09	0.98	3.82 ± 0.10	8.07	3.15 ± 0.16	0.98	3.10 ± 0.16
G032.79+00.19	5.26 ± 1.57	4.78	3.75 ± 0.21	0.98	4.04 ± 0.22	8.17	3.56 ± 0.06	0.98	3.50 ± 0.06
G034.41+00.23	5.99 ± 0.06	4.56	3.39 ± 0.13	1.00	3.76 ± 0.14	6.28	3.13 ± 0.18	0.96	3.01 ± 0.18
G034.79−01.38	6.21 ± 0.09	2.40	4.21 ± 0.37	0.98	5.54 ± 0.50	3.34	4.14 ± 0.16	0.89	3.70 ± 0.14
G036.11+00.55	5.45 ± 0.43	2.57	2.75 ± 0.63	0.70	2.35 ± 0.54	...	...	...	...
G037.42+01.51	6.78 ± 0.05	3.18	5.02 ± 0.23	0.98	5.21 ± 0.24	4.78	3.50 ± 0.48	0.93	3.26 ± 0.44
G040.28−00.21	6.02 ± 0.10	3.72	6.79 ± 1.33	0.70	5.65 ± 1.10	6.43	3.43 ± 0.47	0.97	3.31 ± 0.45
G045.45+00.06	6.41 ± 0.50	6.08	4.07 ± 0.66	0.75	3.37 ± 0.54	5.28	3.20 ± 0.25	0.94	3.02 ± 0.24
G048.99−00.29	6.18 ± 0.02	3.74	7.02 ± 1.10	0.70	5.20 ± 0.81	4.78	4.32 ± 0.54	0.93	4.03 ± 0.50
W51-IRS2	6.22 ± 0.06	8.55	3.19 ± 0.09	1.00	3.42 ± 0.10	8.72	2.82 ± 0.01	0.99	2.79 ± 0.01
G071.31+00.82	8.02 ± 0.16	2.25	7.18 ± 1.81	0.70	5.50 ± 1.39	2.42	5.43 ± 1.08	0.87	4.71 ± 0.94
G073.65+00.19	13.54 ± 2.90	2.76	4.71 ± 1.02	0.70	3.53 ± 0.76	2.88	4.65 ± 0.62	0.88	4.10 ± 0.55
G075.29+01.32	10.69 ± 0.58	2.86	6.27 ± 0.85	0.70	4.70 ± 0.63	2.83	4.47 ± 0.40	0.88	3.94 ± 0.35
DR21	8.10 ± 0.00	2.71	3.45 ± 0.05	1.00	3.96 ± 0.06	3.15	3.27 ± 0.11	0.99	3.24 ± 0.11
G090.92+01.48	10.13 ± 0.63	3.40	5.31 ± 0.56	0.70	3.98 ± 0.42	3.79	4.02 ± 0.32	0.91	3.64 ± 0.29
G097.53+03.18	11.81 ± 0.70	5.22	2.45 ± 0.13	1.00	2.68 ± 0.14	5.47	3.28 ± 0.12	0.95	3.11 ± 0.12
G109.87+02.11	8.49 ± 0.01	3.19	4.28 ± 0.21	0.98	4.50 ± 0.21	3.90	4.88 ± 0.67	0.91	4.43 ± 0.61
NGC7538	9.47 ± 0.07	3.71	4.17 ± 0.07	0.98	4.37 ± 0.06	...	...	...	...

Notes. Full width at half maximum values were obtained from measurements of $C^{33}S$; see Table A.3. The $^{34}S/^{33}S$ isotope ratios from the $J = 2–1$ transition are corrected for the optical depth effect and the ones in the 3–2 line without corrections for opacity.

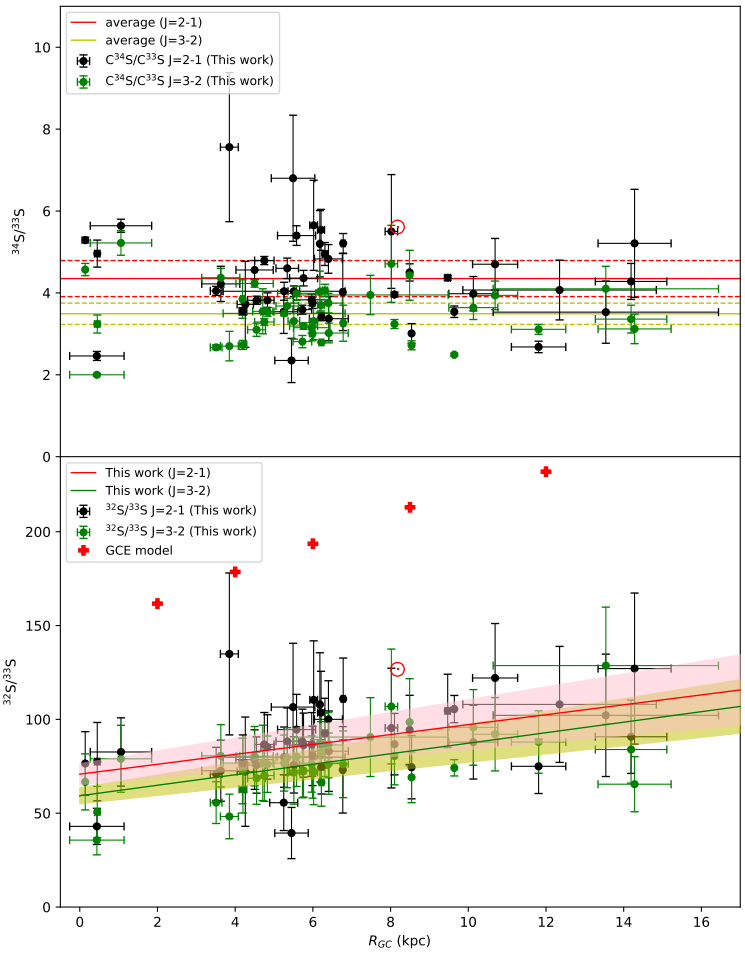

Fig. 7. ^{34}S/^{33}S and ^{32}S/^{33}S isotope ratios (for the latter, see Eqs. (12) and (13)) plotted as functions of the distance from the Galactic center. Top: ^{34}S/^{33}S ratios derived from C^{34}S/C^{33}S in the $J = 2$–1 and $J = 3$–2 transitions plotted as black and green dots, respectively. The red solid and the two dashed lines show the average value and its standard deviation, 4.35 ± 0.44, of ^{34}S/^{33}S with corrections of optical depth toward our sample in the $J = 2$–1 transition. The yellow solid and the two dashed lines show the average value and its standard deviation, 3.49 ± 0.26, of ^{34}S/^{33}S toward our sample in the $J = 3$–2 transition. The red symbol ⊙ indicates the ^{34}S/^{33}S isotope ratio in the Solar System. Bottom: Black and green dots show the ^{32}S/^{33}S ratios in the $J = 2$–1 and $J = 3$–2 transitions, respectively. The red symbol ⊙ indicates the ^{32}S/^{33}S value in the Solar System. The resulting first-order polynomial fits to the ^{32}S/^{33}S ratios in the $J = 2$–1 and $J = 3$–2 transitions in this work are plotted as red and green solid lines, respectively, with the pink and yellow shaded area showing the 1 σ standard deviations. The red crosses are the results from the GCE model of Kobayashi et al. (2011, 2020, see also Sect. 4.9).

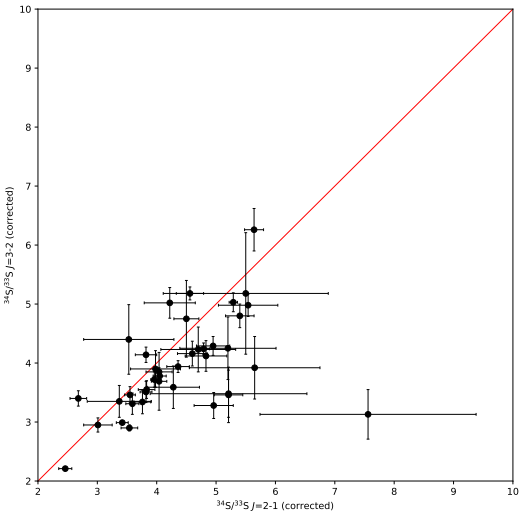

Fig. 8. Comparison of ^{34}S/^{33}S ratios between the $J = 2$–1 and 3–2 data. The $J = 2$–1 ratios are opacity corrected, while the same correction factors were also applied to the $J = 3$–2 data. The red solid line indicates that the ^{34}S/^{33}S ratios are equal in these two transitions.

20 sources. Near the solar neighborhood, in a galactocentric distance range of 7.5 kpc ≤ R_{GC} ≤ 8.5 kpc, ^{32}S/^{33}S ratios were obtained toward four objects, Orion-KL, G071.31+00.82, DR21, and G109.87+02.11, resulting in an average value of 88 ± 21. For the outer Galaxy, beyond the local arm, we were able to deduce an average ^{32}S/^{33}S ratio of 105 ± 19 from ^{32}S/^{33}S values in four sources. All these average values provide us with an indication of the existence of a ^{32}S/^{33}S gradient in the Galaxy. An unweighted least-squares fit to the $J = 2$–1 transition data from 46 sources yields

$$^{32}\mathrm{S}/^{33}\mathrm{S}(2-1) = (2.64 \pm 0.77)R_{\mathrm{GC}} + (70.80 \pm 5.57). \quad (12)$$

In the $J = 3$–2 transition with data from 42 targets, an unweighted least-squares fit can be obtained with

$$^{32}\mathrm{S}/^{33}\mathrm{S}(3-2) = (2.80 \pm 0.59)R_{\mathrm{GC}} + (59.30 \pm 4.22). \quad (13)$$

The ^{32}S/^{33}S gradients derived from these two transitions have similar slopes but obviously different intercepts. The lower intercept in the $J = 3$–2 transition could be due to the fact that we could not correct the values for optical-depth effects. If this difference is caused only by the opacity, then an average optical depth in the C^{34}S $J = 3$–2 transition of about 0.4 can be derived with Eq. (4).

Table 4. $^{32}S/^{33}S$ isotope ratios.

Source	R_{GC}	$^{32}S/^{33}S$	
	(kpc)	$J = 2–1$	$J = 3–2$
WB89-380	14.19 ± 0.92	90.74 ± 19.53	83.93 ± 17.90
WB89-391	14.28 ± 0.94	127.07 ± 40.26	65.46 ± 14.69
W3OH	9.64 ± 0.03	105.49 ± 7.26	74.20 ± 4.35
Orion-KL	8.54 ± 0.00	74.50 ± 16.85	69.12 ± 13.51
+20 km s^{-1} cloud	0.03 ± 0.03	82.63 ± 18.20	78.98 ± 17.86
G359.61−00.24	5.51 ± 0.15	75.75 ± 14.99	71.69 ± 16.86
+50 km s^{-1} cloud	0.02 ± 0.04	76.49 ± 16.96	66.68 ± 14.92
G000.31−00.20	5.25 ± 0.36	55.61 ± 14.84	···
SgrB2	0.44 ± 0.70	42.98 ± 9.62	35.66 ± 7.84
SgrD	0.45 ± 0.07	77.48 ± 20.88	50.61 ± 13.66
G006.79−00.25	4.75 ± 0.25	86.65 ± 17.01	70.08 ± 13.79
G007.47+00.05	12.35 ± 2.49	107.98 ± 30.91	···
G010.32−00.15	5.34 ± 0.29	88.27 ± 17.82	79.56 ± 15.99
G010.62−00.33	4.26 ± 0.21	106.56 ± 33.99	···
G011.10−00.11	5.49 ± 0.56	72.13 ± 29.12	···
G016.86−02.15	5.97 ± 0.47	86.63 ± 17.00	76.23 ± 15.01
G017.02−02.40	6.40 ± 0.36	100.03 ± 20.54	86.36 ± 17.47
G017.63+00.15	6.77 ± 0.04	73.12 ± 23.04	···
G018.34+01.76	6.31 ± 0.07	92.66 ± 18.57	86.44 ± 16.87
G019.36−00.03	5.58 ± 0.49	94.55 ± 18.78	80.16 ± 15.89
G023.43−00.18	3.63 ± 0.49	72.63 ± 16.26	80.58 ± 16.63
G024.78+00.08	3.51 ± 0.15	70.88 ± 14.22	55.64 ± 11.12
G024.85+00.08	3.85 ± 0.23	134.87 ± 43.15	48.25 ± 11.88
G028.30−00.38	4.71 ± 0.26	···	76.82 ± 20.06
G028.39+00.08	4.83 ± 0.17	85.30 ± 17.17	76.11 ± 15.02
G028.83−00.25	4.50 ± 0.48	78.57 ± 15.87	80.37 ± 15.83
G030.70−00.06	4.20 ± 0.10	76.54 ± 15.18	62.68 ± 12.57
G030.74−00.04	5.76 ± 0.36	86.28 ± 17.07	72.73 ± 14.12
G030.78+00.20	4.19 ± 0.05	···	72.50 ± 17.46
G030.81−00.05	5.73 ± 0.24	88.21 ± 17.23	72.72 ± 14.52
G031.24−00.11	7.48 ± 2.00	···	90.57 ± 21.01
G032.74−00.07	4.55 ± 0.23	75.67 ± 14.99	68.63 ± 13.88
G032.79+00.19	5.26 ± 1.57	79.87 ± 16.07	76.72 ± 14.93
G034.41+00.23	5.99 ± 0.06	80.54 ± 15.82	72.63 ± 14.63
G034.79−01.38	6.21 ± 0.09	103.60 ± 22.03	82.58 ± 16.21
G036.11+00.55	5.45 ± 0.43	39.43 ± 13.64	···
G037.42+01.51	6.78 ± 0.05	110.92 ± 21.76	76.06 ± 17.77
G040.28−00.21	6.02 ± 0.10	110.40 ± 31.44	71.86 ± 17.32
G045.45+00.06	6.41 ± 0.50	83.04 ± 21.44	76.44 ± 16.33
G048.99−00.29	6.18 ± 0.02	107.90 ± 27.60	87.21 ± 20.50
W51-IRS2	6.22 ± 0.06	74.69 ± 14.46	66.43 ± 12.72
G071.31+00.82	8.02 ± 0.16	95.37 ± 31.90	106.87 ± 30.60
G073.65+00.19	13.54 ± 2.90	102.16 ± 32.61	128.66 ± 31.17
G075.29+01.32	10.69 ± 0.58	122.06 ± 29.02	92.08 ± 19.53
DR21	8.10 ± 0.00	86.80 ± 16.37	80.51 ± 15.38
G090.92+01.48	10.13 ± 0.63	87.88 ± 19.68	95.73 ± 20.14
G097.53+03.18	11.81 ± 0.70	74.99 ± 14.50	87.92 ± 16.65
G109.87+02.11	8.49 ± 0.01	94.41 ± 18.40	98.52 ± 23.17
NGC7538	9.47 ± 0.07	104.53 ± 19.54	···

Notes. The $^{32}S/^{33}S$ isotope ratios from the $J = 2–1$ transition are corrected for the line saturation effects, while the ones in the 3–2 line are not corrected because of the missing main isotopic species.

3.6. $^{34}S/^{36}S$ ratios

The detection of $C^{36}S$ in the $J = 2–1$ and $J = 3–2$ transitions allows us to also calculate $^{34}S/^{36}S$ ratios. Around the CMZ, the $C^{36}S$ $J = 2–1$ line in the +50 km s^{-1} cloud was detected, resulting in a $^{34}S/^{36}S$ ratio of 41 ± 4. In the local arm toward DR21 and Orion-KL (Menten et al. 2007; Xu et al. 2013), the $C^{36}S$ $J = 2–1$ and $J = 3–2$ transitions were detected, respectively, leading to $^{34}S/^{36}S$ values of 117 ± 24 and 83 ± 7. This yields an average $^{34}S/^{36}S$ ratio of 100 ± 16 in the ISM near the Sun. In the Perseus arm beyond the Solar System (Xu et al. 2006), we detected the $C^{36}S$ $J = 2–1$ line toward W3OH and obtained

Table 5. Isotope ratios of $^{34}S/^{36}S$ and $^{32}S/^{36}S$.

Source	R_{GC}	$^{34}S/^{36}S$		$^{32}S/^{36}S$	
	(kpc)	$J=2$–1	$J=3$–2	$J=2$–1	$J=3$–2
W3OH	9.64 ± 0.03	140 ± 16	174 ± 29 (*)	4181 ± 531	5195 ± 919 (*)
Orion-KL	8.54 ± 0.00	92 ± 53 (*)	83 ± 7	1954 ± 1207 (*)	1765 ± 414
+20 km s^{-1} cloud	0.03 ± 0.03	69 ± 11 (*)	···	1015 ± 278 (*)	···
+50 km s^{-1} cloud	0.02 ± 0.04	41 ± 4	···	884 ± 104	···
G024.78+00.08	3.51 ± 0.15	151 ± 39 (*)	226 ± 66 (*)	2424 ± 699 (*)	3640 ± 1164 (*)
G030.81−00.05	5.73 ± 0.24	55 ± 15 (*)	···	829 ± 233 (*)	···
W51-IRS2	6.22 ± 0.06	109 ± 27 (*)	203 ± 45 (*)	1814 ± 506 (*)	3397 ± 855 (*)
DR21	8.10 ± 0.00	117 ± 24	159 ± 64 (*)	3223 ± 742	4384 ± 1829 (*)
NGC7538	9.47 ± 0.07	···	109 ± 28 (*)	···	2912 ± 897 (*)
Below are the isotope ratios of $^{34}S/^{36}S$ and $^{32}S/^{36}S$ from Mauersberger et al. (1996)					
W3OH	9.64 ± 0.03	···	181 ± 49	···	4118 ± 1124
Orion-KL	8.54 ± 0.00	···	104 ± 7	···	2281 ± 174
IRAS15491 (**)	5.48 ± 0.31	···	108 ± 15	···	2120 ± 307
IRAS15520 (**)	5.67 ± 0.31	128 ± 32	133 ± 11	2531 ± 641	2629 ± 243
IRAS16172 (**)	5.03 ± 0.29	121 ± 18	119 ± 14	2334 ± 361	2296 ± 287
NGC6334A	6.87 ± 0.12	108 ± 15	154 ± 20	2232 ± 322	3183 ± 431
NGC6334B	6.87 ± 0.12	163 ± 46	156 ± 26	3369 ± 960	3225 ± 552
W51(M)	6.22 ± 0.004	105 ± 11	104 ± 15	2119 ± 237	2099 ± 313

Notes. (*)Values with large uncertainties are derived from the tentative detection of $C^{36}S$ lines. (**)For these three sources without parallax data, their kinematic distances were estimated (for details, see Sect. 2.1). The $^{34}S/^{36}S$ and $^{32}S/^{36}S$ isotope ratios in this work from the $J=2$–1 transition are corrected for the optical depth effects, while the ones for the 3–2 line could not be corrected.

a $^{34}S/^{36}S$ value of 140 ± 16. These results reveal the possibility of the existence of a $^{34}S/^{36}S$ gradient from the Galactic center region to the outer Galaxy. Five tentative detections in the $C^{36}S$ $J=2$–1 line and also five tentative detections in the $J=3$–2 line provide additional $^{34}S/^{36}S$ ratios but with large uncertainties. All of the $^{34}S/^{36}S$ values are listed in Table 5 and are plotted as a function of the distance to the Galactic center in Fig. 9.

3.7. $^{32}S/^{36}S$ ratios

As in the case of the $^{32}S/^{33}S$ ratios, the $^{32}S/^{36}S$ values could also be obtained from the resulting $^{34}S/^{36}S$ ratios in Sect. 3.6 and the $^{32}S/^{34}S$ ratios in Sect. 3.2.2 using the following equation:

$$\frac{^{32}S}{^{36}S} = \frac{^{34}S}{^{36}S} \times \frac{^{32}S}{^{34}S}. \quad (14)$$

The uncertainties of both isotope ratios in the product on the right-hand side of the equation are included in our error budget. The resulting $^{32}S/^{36}S$ ratios are listed in Table 5. In the CMZ, a $^{32}S/^{36}S$ ratio of 884 ± 104 is obtained toward the +50 km s^{-1} cloud. $^{32}S/^{36}S$ values of 1765 ± 414 and 3223 ± 742 are derived toward Orion-KL and DR21, leading to an average $^{32}S/^{36}S$ value of 2494 ± 578 in the local regions near the Solar System. In the Perseus arm beyond the solar neighborhood toward W3OH, we obtain the highest $^{32}S/^{36}S$ value, 4181 ± 531. All these results indicate that there could be a positive $^{32}S/^{36}S$ gradient from the Galactic center region to the outer Galaxy. Figure 9 shows the $^{32}S/^{36}S$ ratios plotted as a function of the distance to the Galactic center.

4. Discussion

With the measurements of optically thin lines of the rare CS isotopologs, $C^{34}S$, ^{13}CS, $C^{33}S$, $^{13}C^{34}S$, and $C^{36}S$, we derived $^{12}C/^{13}C$, $^{32}S/^{34}S$, $^{34}S/^{33}S$, $^{32}S/^{33}S$, $^{34}S/^{36}S$, and $^{32}S/^{36}S$ isotope ratios. Combined with accurate galactocentric distances, we established a $^{32}S/^{33}S$ gradient for the first time and confirmed the existing gradients of $^{12}C/^{13}C$ and $^{32}S/^{34}S$, as well as uniform $^{34}S/^{33}S$ ratios across the Milky Way, which are lower than previously reported. Furthermore, we may have detected $^{34}S/^{36}S$ and $^{32}S/^{36}S$ gradients for the first time. In Sect. 4.1, we compare the $^{12}C/^{13}C$ gradient obtained in this work with previous published ones derived from a variety of molecular species. A comparison between the $^{32}S/^{34}S$ gradients we obtained and previously published ones is presented in Sect. 4.2. The condition of LTE for $C^{33}S$ with its HFS line ratios is discussed in Sect. 4.3. We then also compare our results on $^{34}S/^{33}S$ ratios with previously published values and discuss the $^{32}S/^{33}S$ gradient. In Sect. 4.4, we evaluate whether or not $^{34}S/^{36}S$, $^{33}S/^{36}S$, and $^{32}S/^{36}S$ ratios may show gradients with galactocentric distance. Observational bias due to distance effects, beam size effects, and chemical fractionation are discussed. A comparison of several isotopes with respect to primary or secondary synthesis is provided in Sect. 4.8. Results from a Galactic chemical evolution (GCE) model, trying to simulate the observational data, are presented in Sect. 4.9.

4.1. Comparisons of $^{12}C/^{13}C$ ratios determined with different species

$^{12}C/^{13}C$ ratios have been well studied in the CMZ where the value is about 20–25 (e.g., Henkel et al. 1983; Güsten et al. 1985; Langer & Penzias 1990; Milam et al. 2005; Riquelme et al. 2010; Belloche et al. 2013; Halfen et al. 2017; Humire et al. 2020),

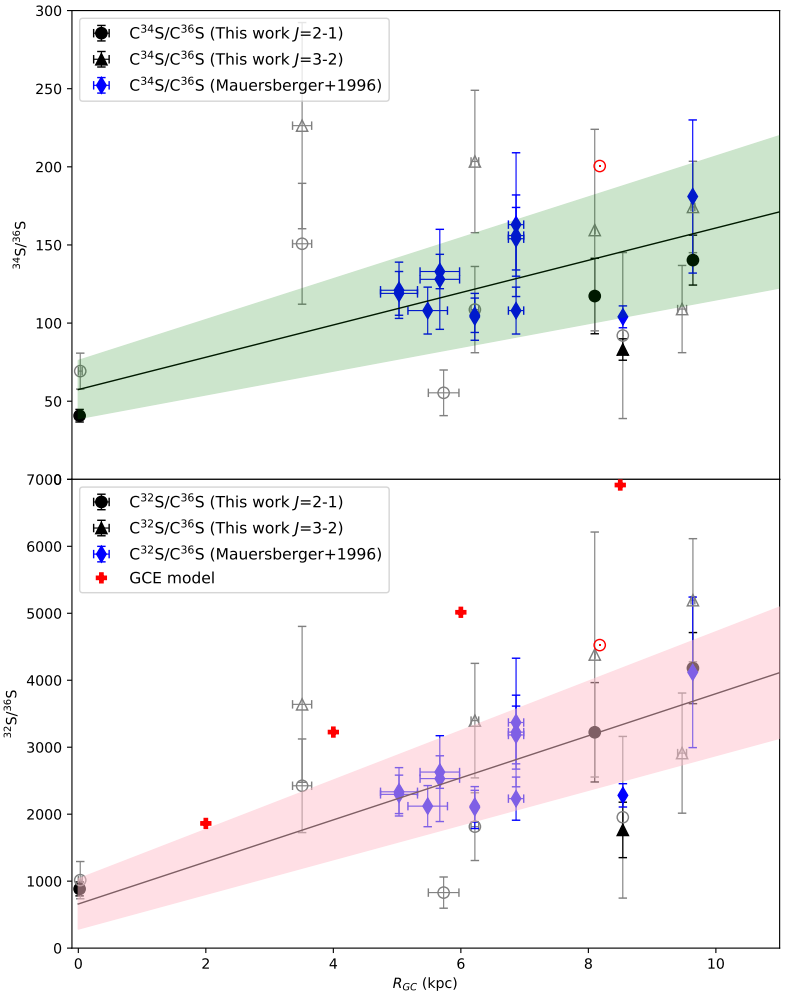

Fig. 9. $J = 2$–1 (opacity corrected) and $J = 3$–2 (no opacity corrections) $^{34}S/^{36}S$ and $^{32}S/^{36}S$ isotope ratios (see Eqs. (18) and (19)) plotted as functions of the distance from the Galactic center. *Top*: Filled black circles and filled black triangle present the $^{34}S/^{36}S$ ratios in the $J = 2$–1 and $J = 3$–2 transitions derived from $C^{34}S/C^{36}S$ in this work with detections of $C^{36}S$, respectively. The open gray circles and open gray triangles present the $^{34}S/^{36}S$ ratios in the $J = 2$–1 and $J = 3$–2 transitions derived from $C^{34}S/C^{36}S$ in this work with tentative detections of $C^{36}S$, respectively. The blue diamonds show the $^{34}S/^{36}S$ ratios in Mauersberger et al. (1996). The red symbol ⊙ indicates the $^{34}S/^{36}S$ isotope ratio in the Solar System. The resulting first-order polynomial fit to the $^{34}S/^{36}S$ ratios in Mauersberger et al. (1996) and this work, excluding the values from tentative detections, is plotted as a black solid line, with the green shaded area showing the 1 σ interval of the fit. *Bottom*: $^{32}S/^{36}S$ ratios obtained from $^{34}S/^{36}S$ ratios combined with the $^{32}S/^{34}S$ ratios derived in this work. The filled black circles and filled black triangle present the values in the $J = 2$–1 and $J = 3$–2 transitions from this work with detections of $C^{36}S$, respectively. The open gray circles and open gray triangles present ratios in the $J = 2$–1 and $J = 3$–2 transitions from this work with tentative detections of $C^{36}S$, respectively. The $^{32}S/^{36}S$ ratios derived with $^{34}S/^{36}S$ values from Mauersberger et al. (1996) are plotted as blue diamonds. The red symbol ⊙ indicates the $^{32}S/^{36}S$ isotope ratio in the Solar System. The $^{32}S/^{36}S$ gradient, excluding tentative detections, is plotted as a black solid line, with the pink shaded area showing the 1 σ interval of the fit. The red crosses visualize results from the GCE model of Kobayashi et al. (2011, 2020, see Sect. 4.9).

similar to the results that we obtained from $C^{34}S$ in the current work. In the inner Galaxy, the $^{12}C/^{13}C$ ratios are higher than the values in the CMZ, which were ∼50 as derived from $H_2^{12}CO/H_2^{13}CO$ in Henkel et al. (1985) and 41 ± 9 from $C^{34}S/^{13}C^{34}S$ in this work. As can be inferred from Fig. 3, $^{12}C/^{13}C$ ratios at 3.0 kpc ≤ R_{GC} ≤ 4.0 kpc might be as low as in the CMZ, but this is so far tentative and uncertain, as we only have one detection (G024.78+00.08) in this region and data from other groups referring to this small galactocentric interval are also relatively few. In the local regions near the Solar System, an average $^{12}C/^{13}C$ ratio of 66 ± 10 was obtained from $C^{34}S/^{13}C^{34}S$ in this work, which is consistent with $^{12}C/^{13}C$ values derived from other molecular species and their ^{13}C isotopes, that are 75 ± 9 from $C^{18}O$ (Keene et al. 1998), 60 ± 19 from CN (Milam et al. 2005), 74 ± 8 from CH^+ (Ritchey et al. 2011), and 53 ± 16 from H_2CO (Yan et al. 2019). All these $^{12}C/^{13}C$ values for the solar neighborhood are well below the value for the Sun (89, Anders & Grevesse 1989; Meibom et al. 2007). This indicates that ^{13}C has been enriched in the local ISM during the last 4.6 billion years following the formation of the Solar System. Beyond the Sun, at a galactocentric distance of about 10 kpc, our results from $C^{34}S/^{13}C^{34}S$ show a slightly higher value of 67 ± 8, which is similar to $^{12}C/^{13}C$ ratios from CN (66 ± 20), $C^{18}O$ (69 ± 10), and H_2CO (64 ± 10). These values are still below the value for the Sun. In the far outer Galaxy at 13.8 kpc toward WB89 437, Wouterloot & Brand (1996) found a 3σ lower limit of 201 ± 15 from $C^{18}O/^{13}C^{18}O$. This suggests that the $^{12}C/^{13}C$ gradient extends well beyond the solar neighborhood to the outer Galaxy. Additional sources with large galactocentric distances have to be measured to further improve the statistical significance of this result.

Previously published $^{12}C/^{13}C$ ratios derived from CN (Savage et al. 2002; Milam et al. 2005), $C^{18}O$ (Langer & Penzias 1990; Wouterloot & Brand 1996; Keene et al. 1998), H_2CO (Henkel et al. 1980, 1982, 1983, 1985; Yan et al. 2019), CH^+ (Ritchey et al. 2011), and CH (Jacob et al. 2020) are shown in Fig. 3, but with respect to the new distance values (see details in Sect. 2.1). In Fig. 10, the $^{12}C/^{13}C$ values from different molecular species are projected onto the Galactic plane. This also visualizes the gradient from the Galactic center to the Galactic outer regions beyond the Solar System. In Table 6, the fitting results for the old and new distances are presented. The comparison shows that the adoption of the new distances has indeed an effect on the fitting results, such as for the $^{12}CN/^{13}CN$ gradient. In

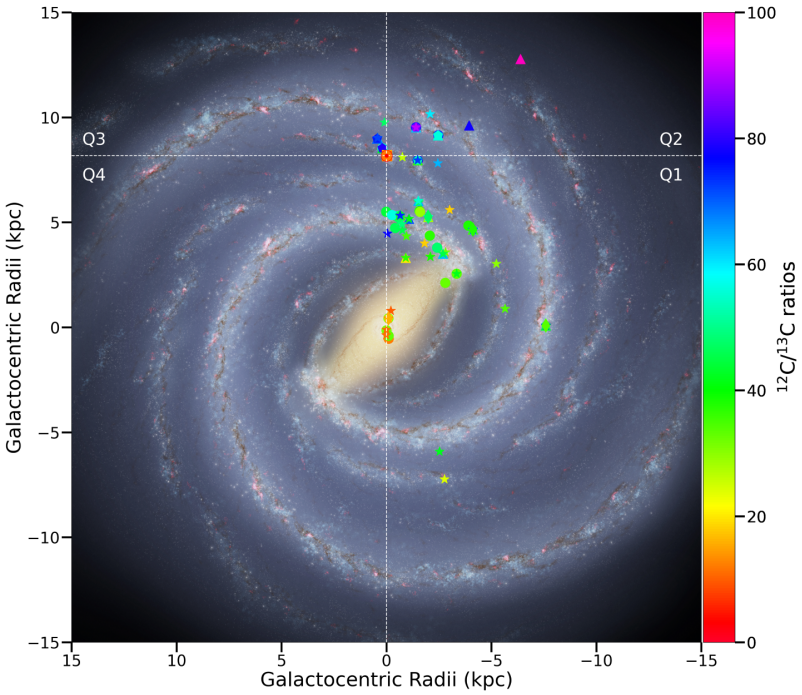

Fig. 10. Distribution of $^{12}C/^{13}C$ ratios from 93 sources in the Milky Way. The background image is the structure of the Milky Way from the artist's impression [Credit: NASA/JPL-Caltech/ESO/R. Hurt]. The $^{12}C/^{13}C$ isotope ratios with corrections for optical depth from $C^{34}S/^{13}C^{34}S$ in this work are plotted as circles. The triangles, pentagons, stars, squares, and diamonds indicate the $^{12}C/^{13}C$ ratios derived from $CN/^{13}CN$ (Savage et al. 2002; Milam et al. 2005), $C^{18}O/^{13}C^{18}O$ (Langer & Penzias 1990; Wouterloot & Brand 1996; Keene et al. 1998), $H_2CO/H_2^{13}CO$ (Henkel et al. 1980, 1982, 1983, 1985; Yan et al. 2019), $CH^+/^{13}CH^+$ (Ritchey et al. 2011), and $CH/^{13}CH$ (Jacob et al. 2020), respectively. The red symbol ⊙ indicates the position of the Sun. The color bar on the right-hand side indicates the range of the $^{12}C/^{13}C$ ratios.

Table 6. Measurements of the $^{12}C/^{13}C$ gradient.

	Previous fitting results		This work	
	Slope	Intercept	Slope	Intercept
$CN^{(a)}$	6.01 ± 1.19	12.28 ± 9.33	6.75 ± 1.44	5.57 ± 11.29
$C^{18}O^{(b)}$	5.41 ± 1.07	19.03 ± 7.90	5.72 ± 1.20	14.56 ± 9.25
$H_2CO^{(c)}$	5.08 ± 1.10	11.86 ± 6.60	5.43 ± 1.04	13.87 ± 6.38
$C^{34}S$ (this work)	···	···	4.77 ± 0.81	20.76 ± 4.61

Notes. Fitting results for the old (*left*) and new (*right*) distances, respectively. $^{(a)}$From Savage et al. (2002) and Milam et al. (2005). $^{(b)}$From Langer & Penzias (1990), Wouterloot & Brand (1996), and Keene et al. (1998). $^{(c)}$From Henkel et al. (1980, 1982, 1983, 1985) and Yan et al. (2019).

Savage et al. (2002) and Milam et al. (2005), the slope and intercept become (6.75 ± 1.44) and (5.77 ± 11.29) from (6.01 ± 1.19) and (12.28 ± 9.33), respectively. The fitting for $H_2^{12}CO/H_2^{13}CO$ from Henkel et al. (1980, 1982, 1983, 1985) and Yan et al. (2019) becomes (5.43 ± 1.04) and (13.87 ± 6.38) from (5.08 ± 1.10) and (11.86 ± 6.60), respectively. The Galactic $^{12}C/^{13}C$ gradients derived based on measurements of CN, $C^{18}O$, and H_2CO are in agreement with our results from $C^{34}S$ and therefore indicate that chemical fractionation has little effect on the $^{12}C/^{13}C$ ratios. It is noteworthy that all these fits show a significant discrepancy with observations from the Galactic center. Indeed, they suggest values of 5–17 at R_{GC} = 0, substantially below observed values of 20–25 (see also Tables 6, 7). While the values in the CMZ are clearly lower than in the inner Galactic disk (with the potential exception at galactocentric distances of 2.0–4.0 kpc), they are larger than suggested by a linear fit encompassing the entire inner 12.0 kpc of the Galaxy.

4.2. The $^{32}S/^{34}S$ gradient across the Milky Way

The existence of a $^{32}S/^{34}S$ gradient was first proposed by Chin et al. (1996) based on observations of ^{13}CS and $C^{34}S$ J = 2–1 lines toward 20 mostly southern HMSFRs with galactocentric distances of between 3.0 and 9.0 kpc. Very recently, Yu et al. (2020) confirmed the existence of this $^{32}S/^{34}S$ gradient and enlarged the sample of measurements of ^{13}CS and $C^{34}S$ J = 2–1 lines to a total of 61 HMSFRs from the inner Galaxy out to a galactocentric distance of 12.0 kpc. In the CMZ, Humire et al. (2020) found $^{32}S/^{34}S$ ratios of $16.3^{+2.1}_{-1.7}$ and 17.9 ± 5.0 for the +50 km s^{-1} cloud and Sgr B2(N), which is consistent with our values derived from $^{13}C^{34}S$ and also with our results using the double isotope method. In the inner disk at 2.0 kpc ≤ R_{GC} ≤ 6.0 kpc, a similar $^{32}S/^{34}S$ value of 18 ± 4 was derived based on our results in Sects. 3.2.2 and 3.3. While $^{12}C/^{13}C$ ratios in the inner disk at R_{GC} ≥ 4.0 kpc are clearly higher than in the CMZ (see details in Sect. 4.1), this is not the case for $^{32}S/^{34}S$. On the contrary, $^{32}S/^{34}S$ ratios in the CMZ and inner disk are similar, as already suggested for the first time by Humire et al. (2020). In the local ISM, our results lead to an average $^{32}S/^{34}S$ ratio of 24 ± 4, which is close to the value in the Solar System (22.57, Anders & Grevesse 1989). That is also differing from the $^{12}C/^{13}C$ ratio and its clearly subsolar value in the local ISM. A more detailed discussion is given in Sect. 4.8.

For the first time, we established a $^{32}S/^{34}S$ gradient directly from measurements of ^{13}CS and $^{13}C^{34}S$ (see Sect. 3.2.2 for details). Similar $^{32}S/^{34}S$ gradients were also found in the $^{32}S/^{34}S$ values derived by the double isotope method with the J = 2–1 and J = 3–2 transitions (for details, see Sect. 3.3). A gradient of $^{32}S/^{34}S = (0.75 \pm 0.13)R_{GC}+(15.52 \pm 0.78)$ was obtained based on a large dataset of 90 values from our detections of ^{13}CS and $C^{34}S$ J = 2–1 lines with corrections of opacity, which is flatter than previous ones presented by Chin et al. (1996) and

Table 7. Interstellar C, N, O, and S isotope ratios.

	Molecule	CMZ	Inner disk	Local ISM	Outer Galaxy	Solar System[(*)]
$^{12}C/^{13}C$	$C^{34}S$ [(a)]	27 ± 3	41 ± 9	66 ± 10	74 ± 8	89
	CN [(b)]	···	44 ± 12	41 ± 11	66 ± 19	
	$C^{18}O$ [(c)]	24 ± 1	41 ± 2	60 ± 5	70 ± 10	
	H_2CO [(d)]	···	40 ± 7	50 ± 13	64 ± 10	
	average	25 ± 2	42 ± 9	54 ± 10	69 ± 12	
$^{14}N/^{15}N$	CN [(e)]	···	269 ± 59	314 ± 104	289 ± 85	270
	HCN [(f)]	···	284 ± 63	398 ± 48	388 ± 32	
	HNC [(f)]	···	363 ± 100	378 ± 79	395 ± 74	
	N_2H^+ [(g)]	···	900 ± 250	496 ± 65	581 ± 140	
	NH_3 [(h)]	40 ± 13	175 ± 46	297 ± 99	96 ± 44	
$^{16}O/^{18}O$	H_2CO [(i)]	263 ± 45	327 ± 32	560 ± 25	625 ± 144	490
$^{18}O/^{17}O$	CO [(j)]	3.4 ± 0.1	3.6 ± 0.2	3.9 ± 0.4	4.8 ± 0.6	5.5
$^{16}O/^{17}O$ [(**)]		894 ± 155	1177 ± 132	2184 ± 244	3000 ± 786	2625
$^{32}S/^{34}S$ [(a)]		19 ± 2	18 ± 4	24 ± 4	28 ± 3	23
$^{34}S/^{33}S$ [(a)]		4.2 ± 0.2	4.3 ± 0.4	4.2 ± 0.5	4.1 ± 0.3	5.6
$^{32}S/^{33}S$ [(a)]		70 ± 16	82 ± 19	88 ± 21	105 ± 19	127
$^{34}S/^{36}S$ [(a)]		41 ± 4	122 ± 18	111 ± 16	161 ± 32	200
$^{32}S/^{36}S$ [(a)]		884 ± 104	2382 ± 368	2752 ± 458	4150 ± 828	4525

Notes. The inner disk values refer to the mean values at galactocentric distances of 2.0 kpc ≤ R_{GC} ≤ 6.0 kpc. The local ISM values refer to 7.5 kpc ≤ R_{GC} ≤ 8.5 kpc. The outer Galaxy values point to 9.0 kpc ≤ R_{GC} ≤ 11.0 kpc. [(*)]From Anders & Grevesse (1989). [(a)]This work. [(b)]From Savage et al. (2002) and Milam et al. (2005). [(c)]From Langer & Penzias (1990, 1993), Wouterloot & Brand (1996), and Keene et al. (1998). [(d)]From Henkel et al. (1980, 1982, 1983, 1985) and Yan et al. (2019). [(e)]From Adande & Ziurys (2012), Ritchey et al. (2015), and Fontani et al. (2015). [(f)]From Adande & Ziurys (2012) and Colzi et al. (2018) [(g)]From Ritchey et al. (2015). [(h)]From Chen et al. (2021). [(i)]From Gardner & Whiteoak (1981) and Wilson & Rood (1994). [(j)]From Zhang et al. (2020a). [(**)]The $^{16}O/^{17}O$ ratios are derived with values of $^{16}O/^{18}O$ and $^{18}O/^{17}O$.

Yu et al. (2020). Following Yu et al. (2020), the gradient does not significantly change when the ratios in the CMZ or in the outer regions are excluded, indicating that the $^{32}S/^{34}S$ gradient is robust (see Fig. 11).

4.3. $C^{33}S$

We detected at least three components of the $C^{33}S$ $J = 2–1$ line toward 26 sources. This will guide us to obtain information with respect to LTE or nonLTE conditions. As mentioned in Sect. 3.4, the main component (I_{main}) consists of four HFS lines ($F = 7/2$-$5/2$, $F = 5/2$-$3/2$, $F = 1/2$–$1/2$, $F = 3/2$-$5/2$). Under LTE conditions in the optically thin case, the ratio between the other identified components (not belonging to the main one) and the main component can be obtained:

$$R_{211} = \frac{I(F = 3/2–1/2 + F = 5/2–5/2)}{I_{main}} = 0.25, \quad (15)$$

$$R_{212} = \frac{I(F = 3/2–3/2)}{I_{main}} = 0.15, \quad (16)$$

$$R_{213} = \frac{I(F = 1/2–3/2)}{I_{main}} = 0.02. \quad (17)$$

A detailed examination of our 26 objects is presented in Table 8. Except for Orion-KL there is no evidence for nonLTE effects. All the remaining sources are found to be compatible with LTE conditions. The spectra of CS, $C^{34}S$, and ^{13}CS toward Orion-KL show broad wings (see Fig. 12), which might lead to a highly complex $C^{33}S$ $J = 2–1$ line shape, which may be what is causing apparent LTE deviations in Orion-KL.

No systematic dependence of the $^{34}S/^{33}S$ ratios on galactocentric distance was found in previous studies. The average $^{34}S/^{33}S$ values were 6.3 ± 1.0 and 5.9 ± 1.5 in Chin et al. (1996) and Yu et al. (2020), respectively. A particularly low $^{34}S/^{33}S$ ratio of 4.3 ± 0.2 was found in the Galactic center region by Humire et al. (2020). These authors speculated about the possible presence of a gradient with low values at the center. However, in view of the correction for HFS in Sect. 3.4, it appears that this is simply an effect of different HFS correction factors, with the one at the Galactic center with its wide spectral lines being 1.0, thus (exceptionally) not requiring a downward correction. Yu et al. (2020) considered the effect of HFS, while they overestimated the ratio of the main component to the total intensity of the $C^{33}S$ $J = 2–1$ line (for details, see their Sect. 4.2). This resulted in higher $^{34}S/^{33}S$ values. However, the $^{34}S/^{33}S$ ratios appear to be independent of galactocentric distance based on our results (see details in Sect. 3.4). The average $^{34}S/^{33}S$ value with corrections of optical depth toward our sample in the $J = 2–1$ transition is 4.35 ± 0.44, which is similar to the value in the Galactic center region derived by Humire et al. (2020) and lower than the value of 5.61 in the Solar System (Anders & Grevesse 1989). This indicates that no systematic variation exists in the $^{34}S/^{33}S$ ratios in our Galaxy, that ^{33}S is (with respect to stellar nucleosynthesis) similar to ^{34}S, and that the Solar System (see Fig. 7) must be peculiar. An approximately constant $^{34}S/^{33}S$ ratio with opacity correction from the $J = 2–1$ transition across the Galactic plane leads to a $^{32}S/^{33}S$ gradient in our Galaxy as we already mentioned in Sect. 3.5: $^{32}S/^{33}S = (2.64 ± 0.77)R_{GC} + (70.80 ± 5.57)$, with a correlation coefficient of 0.46.

Table 8. Line intensity ratios of $C^{33}S$ $J = 2–1$ hyperfine components.

Source	FWHM (km s^{-1})	R_{211}	R_{212}	R_{213}
W3OH	4.41	0.29 ± 0.04	0.15 ± 0.03	0.05 ± 0.03
Orion-KL	4.25	0.60 ± 0.02	0.30 ± 0.01	0.44 ± 0.02
G359.61−00.24	3.17	0.40 ± 0.05	0.62 ± 0.05	0.14 ± 0.04
G006.79−00.25	2.73	0.28 ± 0.02	0.17 ± 0.02	···
G010.32−00.15	2.66	0.27 ± 0.04	0.23 ± 0.06	···
G016.86−02.15	3.32	0.30 ± 0.05	0.18 ± 0.03	···
G017.02−02.40	3.74	0.17 ± 0.03	0.17 ± 0.08	···
G018.34+01.76	2.30	0.24 ± 0.07	0.13 ± 0.06	···
G019.36−00.03	3.02	0.29 ± 0.06	0.14 ± 0.04	···
G023.43−00.18	3.81	0.40 ± 0.14	1.15 ± 0.34	···
G024.78+00.08	4.29	0.34 ± 0.03	0.21 ± 0.03	0.08 ± 0.03
G028.39+00.08	3.04	0.26 ± 0.04	0.24 ± 0.06	···
G028.83−00.25	2.27	0.25 ± 0.04	0.18 ± 0.03	···
G030.70−00.06	4.85	0.33 ± 0.02	0.23 ± 0.03	0.11 ± 0.02
G030.74−00.04	3.55	0.19 ± 0.03	0.25 ± 0.06	···
G030.81−00.05	6.15	0.27 ± 0.03	0.16 ± 0.02	0.14 ± 0.02
G032.74−00.07	4.54	0.36 ± 0.04	0.16 ± 0.03	···
G032.79+00.19	4.78	0.09 ± 0.05	1.72 ± 0.28	···
G034.41+00.23	4.56	0.32 ± 0.04	0.28 ± 0.04	0.12 ± 0.03
G034.79−01.38	2.40	0.44 ± 0.15	0.14 ± 0.06	···
G037.42+01.51	3.18	0.20 ± 0.05	0.10 ± 0.02	···
W51-IRS2	8.55	0.13 ± 0.09	3.63 ± 0.36	0.71 ± 0.13
DR21	2.71	0.28 ± 0.01	0.20 ± 0.01	0.14 ± 0.01
G097.53+03.18	5.22	0.30 ± 0.05	0.13 ± 0.04	0.14 ± 0.04
G109.87+02.11	3.19	0.23 ± 0.06	0.38 ± 0.07	···
NGC7538	3.71	0.22 ± 0.01	0.21 ± 0.01	···

Notes. Full width at half maximum values of the main component were obtained from measurements of $C^{33}S$; see Table A.3. The errors provided here are 1σ.

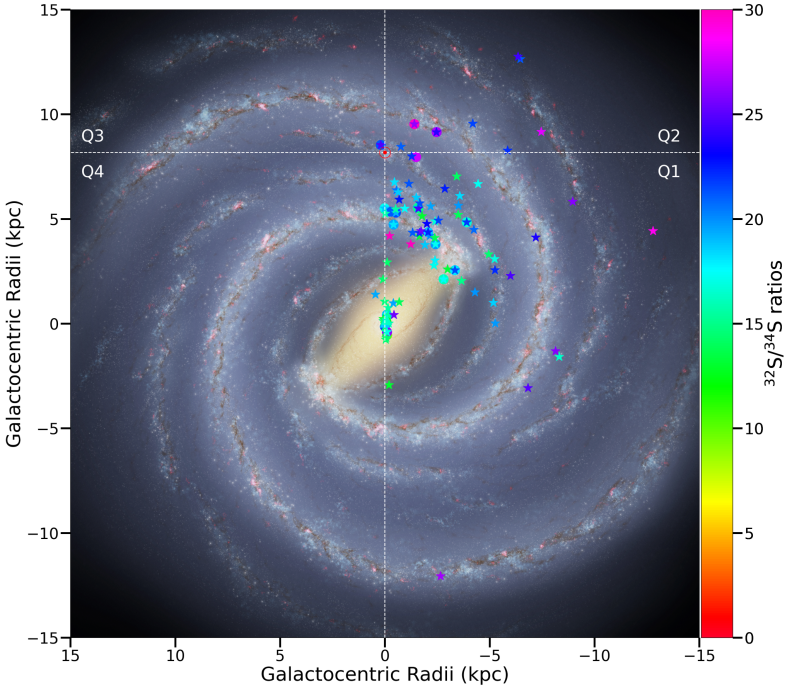

Fig. 11. Distribution of $^{32}S/^{34}S$ ratios from 112 sources in the Milky Way. The background image is the structure of the Milky Way from the artist's impression (Credit: NASA/JPL-Caltech/ESO/R. Hurt). The $^{32}S/^{34}S$ isotope ratios with corrections of opacity derived in this work from $^{13}CS/^{13}C^{34}S$ and the double isotope method in the $J = 2–1$ transition are plotted as circles and stars, respectively. The triangles indicate the results from the CMZ obtained by Humire et al. (2020). The red symbol ⊙ indicates the position of the Sun. The color bar on the right-hand side indicates the range of the $^{32}S/^{34}S$ ratios.

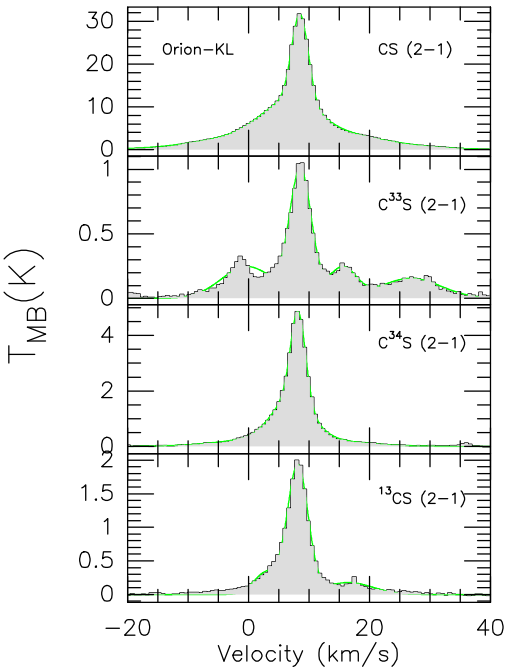

Fig. 12. Line profiles of the $J = 2$–1 transitions of CS, $C^{33}S$, $C^{34}S$, and ^{13}CS toward Orion-KL.

4.4. $C^{36}S$

As mentioned in Sect. 3.6, we find novel potential indications for a positive $^{34}S/^{36}S$ gradient with galactocentric radius. The ^{36}S-bearing molecule $C^{36}S$ was first detected by Mauersberger et al. (1996). These authors observed the $J = 2$–1 and 3–2 transitions toward eight Galactic molecular hot cores at galactocentric distances of between 5.0 kpc and 10.0 kpc. Mauersberger et al. (1996) reported an average $^{34}S/^{36}S$ ratio of 115 ± 17, which is smaller than the value in the Solar System (200.5, Anders & Grevesse 1989). This is consistent with this nucleus being of a purely secondary nature. Combining the ratios of Mauersberger et al. (1996) – after applying new distances (see details in Table 5) – with our results in the $J = 2$–1 transition, the following fit could be achieved:

$$^{34}S/^{36}S = (10.34 \pm 2.74)R_{GC} + (57.45 \pm 18.59), \quad (18)$$

with a correlation coefficient of 0.71. As the $^{34}S/^{33}S$ ratios show a uniform distribution across our Galaxy (see details in Sect. 4.3), a $^{33}S/^{36}S$ gradient is also expected. We obtain $(2.38 \pm 0.67)R_{GC}+(13.21 \pm 4.48)$. After applying our $^{32}S/^{34}S$ gradient to the $^{34}S/^{36}S$ ratios in Mauersberger et al. (1996) with Eq. (9), $^{32}S/^{36}S$ ratios were then derived and listed in Table 5. Combined with our results in the $J = 2$–1 transition, a linear fit to the $^{32}S/^{36}S$ ratios is obtained:

$$^{32}S/^{36}S = (314 \pm 55)R_{GC} + (659 \pm 374), \quad (19)$$

with a correlation coefficient of 0.84. The $^{34}S/^{36}S$ and $^{32}S/^{36}S$ ratios are plotted as functions of galactocentric distances in Fig. 9. Measurements of $^{34}S/^{36}S$, $^{33}S/^{36}S$, and $^{32}S/^{36}S$ are still not numerous. More sources with detected $C^{36}S$ lines would be highly desirable, especially in the CMZ and the inner disk within $R_{GC} = 5.0$ kpc.

4.5. Observational bias due to distance effects

While we have so far analyzed isotope ratios as a function of galactocentric distances, there might be a bias in the sense that the ratios could at least in part also depend on the distance from Earth, a bias caused by different linear resolutions. In Appendix B, the $^{12}C/^{13}C$, $^{32}S/^{34}S$, $^{34}S/^{33}S$, and $^{32}S/^{33}S$, as well as the $^{34}S/^{36}S$ and $^{32}S/^{36}S$ isotope ratios are plotted as functions of the distance from the Sun and shown in Figs. B.2 to B.5, respectively. No apparent gradients can be found, which indicates that any observational bias on account of distance-dependent effects is not significant for $^{12}C/^{13}C$, $^{32}S/^{34}S$, $^{32}S/^{33}S$, $^{34}S/^{36}S$, and $^{32}S/^{36}S$. This agrees with the findings of Yu et al. (2020, see their Sect. 4.5).

4.6. Beam size effects

A good way to check whether the different beam sizes for different lines could affect our results is to compare the isotope ratios derived from different transitions at different frequencies observed with different beam sizes. As shown in Sect. 3.3, $^{32}S/^{34}S$ ratios obtained from the double isotope method in the $J = 2$–1 and 3–2 transitions are in good agreement, suggesting that the effect of beam size is negligible. Furthermore, Humire et al. (2020) found an average $^{32}S/^{34}S$ ratio of 17.9 ± 5.0 in the envelope of Sgr B2(N) with the Atacama Large Millimetre/submillimetre Array (ALMA) with 1.″6 beam size, which is consistent with our results in the CMZ from the IRAM 30 meter telescope with beam sizes of about 27″. Yu et al. (2020) derived similar $^{32}S/^{34}S$ and $^{34}S/^{33}S$ ratios from different telescopes – that is, the IRAM 30 meter and the ARO 12 meter – toward six HMSFRs and concluded that beam-size effects are insignificant (see details in their Sect. 4.1). All this suggests that beam-size effects could not obviously affect our results.

4.7. Chemical fractionation

Isotopic fractionation could possibly affect the isotope ratios derived from the molecules in the interstellar medium. Watson et al. (1976) firstly proposed that gas-phase CO should have a tendency to be enriched in ^{13}CO because of the charge-exchange reaction of CO with $^{13}C^+$. Several theoretical studies also support this mechanism (e.g., Langer et al. 1984; Viti et al. 2020), which was then extended to other carbon bearing species (Loison et al. 2020). Formaldehyde forming in the gas phase is suggested to be depleted in the ^{13}C bearing isotopolog (e.g., Langer et al. 1984). However, if H_2CO originates from dust grain mantles, then the ^{13}C bearing isotopolog might be enhanced relative to species like methanol and CO (Wirström et al. 2012; Yan et al. 2019). Recently, Colzi et al. (2020) performed a new gas-grain chemical model and proposed that molecules formed starting from atomic carbon could also show ^{13}C enhancements through the reaction $^{13}C + C_3 \rightarrow {}^{12}C + {}^{13}CC_2$. As already mentioned in Sect. 4.1, the Galactic $^{12}C/^{13}C$ gradient derived from $C^{34}S$ in this work is in good agreement with previous results based on measurements of CN, $C^{18}O$, and H_2CO. Therefore, chemical fractionation cannot greatly affect the carbon isotope ratios.

To date, little is known about sulfur fractionation. Loison et al. (2019) proposed a low ^{34}S enrichment through the reaction of $^{34}S^+ + CS \rightarrow S^+ + C^{34}S$ in dense clouds. A slight enrichment in ^{13}C was predicted for CS with the $^{13}C^+ + CS \rightarrow C^+ + {}^{13}CS$ reaction (Loison et al. 2020). $^{32}S/^{34}S$ ratios derived directly from ^{13}CS and $^{13}C^{34}S$ and the double isotope method involving $^{12}C/^{13}C$ ratios (Eq. (8)) turn out to agree very well, suggesting

Table 9. Comparison of isotope ratios at different galactocentric distances. Given are percentage enhancements.

	CMZ ↓ Inner disk	CMZ ↓ Outer Galaxy	Inner disk ↓ Outer Galaxy	Local ISM ↓ Solar System
$^{12}C/^{13}C$	68 ± 33	176 ± 54	64 ± 21	65 ± 31
$^{16}O/^{18}O$	24 ± 9	138 ± 61	91 ± 43	–12 ± 5
$^{16}O/^{17}O$	32 ± 8	236 ± 111	155 ± 73	20 ± 13
$^{32}S/^{34}S$	–5 ± 11	47 ± 10	56 ± 18	–4 ± 17
$^{32}S/^{33}S$	17 ± 8	50 ± 16	28 ± 6	44 ± 34
$^{32}S/^{36}S$	169 ± 50	369 ± 125	74 ± 31	64 ± 27

that sulfur fractionation is negligible as previously suggested by Humire et al. (2020) and in this work.

4.8. Interstellar C, N, O, and S isotope ratios

The data collected so far allow us to evaluate the status of several isotopes with respect to primary or secondary synthesis in stellar objects. From the data presented here in Table 7, we choose the $^{12}C/^{13}C$, $^{32}S/^{34}S$, $^{32}S/^{33}S$, and $^{32}S/^{36}S$ ratios because ^{12}C is mostly primary (Timmes et al. 1995) while ^{32}S is definitely a primary nucleus (Woosley & Weaver 1995), against which the other isotopes can be evaluated. A question arises as to whether all these ratios, as well as those from nitrogen and oxygen, can be part of the same scheme.

Comparing the CMZ with the ratios in the inner disk, the CMZ with the outer Galaxy, the inner disk with the ratios in the outer Galaxy, and the local ISM values with those of the Solar System, we obtain increases in values for $^{12}C/^{13}C$, $^{32}S/^{34}S$, $^{32}S/^{33}S$, and $^{32}S/^{36}S$ ratios. All of these values are listed in Table 9. Percentages are clearly highest between ^{32}S and ^{36}S. These indicate that ^{36}S is, as opposed to ^{32}S, definitely secondary. Percentages between ^{12}C and ^{13}C are also high but not as extreme, presumably because ^{12}C is also synthesized in longer lived stars of intermediate mass (e.g., Kobayashi et al. 2020). More difficult to interpret are the $^{32}S/^{33}S$ and $^{32}S/^{34}S$ ratios, where percentages are smaller, indicating that ^{33}S and ^{34}S are, as already mentioned in Sect. 4.3, neither fully primary nor secondary. However, percentages in the case of the $^{32}S/^{33}S$ ratio systematically surpass those of the $^{32}S/^{34}S$ ratio, suggesting a more secondary origin of ^{33}S with respect to ^{34}S, even though $^{34}S/^{33}S$ appears to be constant across the Galaxy. Finally, local interstellar $^{32}S/^{34}S$ and $^{32}S/^{33}S$ ratios behave strikingly differently with respect to solar values. While $^{32}S/^{34}S$ is (almost) solar, $^{32}S/^{33}S$ is far below the solar value. Peculiar Solar System abundance ratios may be the easiest way to explain this puzzling situation. Most likely there is an overabundance of ^{34}S in the gas and dust that formed the Solar System.

Another clearly primary isotope is ^{16}O, which allows us to look for $^{16}O/^{18}O$ and $^{16}O/^{17}O$ ratios (Henkel & Mauersberger 1993; Henkel et al. 1994; Wilson 1999; Wouterloot et al. 2008; Zhang et al. 2020a). The high percentages in the $^{16}O/^{17}O$ ratios show that ^{17}O is more secondary than ^{18}O, which is consistent with models of stellar nucleosynthesis, because ^{17}O is a main product of the CNO cycle while ^{18}O can also be synthesized by helium burning in massive stars.

$^{14}N/^{15}N$ can also be measured; both nuclei can be synthesized in rotating massive stars and AGB stars as primary products (e.g., Meynet & Maeder 2002; Kobayashi et al. 2011, 2020; Limongi & Chieffi 2018). However, most of the ^{14}N is produced through CNO cycling, and is therefore secondary (e.g., Kobayashi et al. 2011; Karakas & Lattanzio 2014). The production of ^{15}N remains to be understood and may be related to novae (e.g., Kobayashi et al. 2020; Romano 2022). None of the stable nitrogen isotopes are purely primary. While ^{14}N appears to be less secondary than ^{15}N (Audouze et al. 1975; Henkel et al. 1994; Wilson 1999; Adande & Ziurys 2012; Ritchey et al. 2015; Colzi et al. 2018; Chen et al. 2021), in this case we do not have a clear calibration against an isotope that can be considered to be mainly primary. Remarkably, Colzi et al. (2022) reported a rising $^{14}N/^{15}N$ gradient that peaks at $R_{GC} = 11$ kpc and then decreases, and suggested that ^{15}N could be mainly produced by novae on long timescales.

4.9. Galactic chemical environment

Kobayashi et al. (2020) established a Galactic chemical evolution (GCE) model based on the GCE model in Kobayashi et al. (2011) with updates with respect to new solar abundances and also accounting for failed supernovae, super-AGB stars, the s-process from AGB stars, and various r-process sites. Based on this GCE model, the predicted $^{12}C/^{13}C$, $^{32}S/^{34}S$, $^{32}S/^{33}S$, and $^{32}S/^{36}S$ ratios at R_{GC} = 2.0, 4.0, 6.0, 8.5, 12.0, and 17.0 kpc are obtained and plotted in Figs. 3, 4, 7, and 9. The initial mass function and nucleosynthesis yields are the same for different galactic radii but star formation and inflow timescales (τ_s and τ_i) depend on the Galactic radius (see Kobayashi et al. 2000 for the definition of the timescales). Adopted values are τ_s = 1.0, 2.0, 3.0, 4.6, 6.5, and 8.8 Gyr as well as τ_i = 4.0, 5.0, 5.0, 5.0, 7.0, and 50.0 Gyr for R_{GC} = 2.0, 4.0, 6.0, 8.5, 12.0, and 17.0 kpc, respectively. The predicted $^{12}C/^{13}C$ ratios are in good agreement with our results, while $^{32}S/^{34}S$ and $^{32}S/^{36}S$ ratios show significant deviations at larger galactocentric distances. $^{32}S/^{33}S$ ratios show an offset along the entire inner 12 kpc of the Milky Way. This indicates that current models of Galactic chemical evolution are still far from perfect. In this context, our data will serve as a useful guideline for further even more refined GCE models.

Very recently, Colzi et al. (2022) predicted $^{12}C/^{13}C$ gradients with four different models addressing nova systems (see details in their Table 2 and Sect. 4), following Romano et al. (2017, 2019, 2021). The gradients from these four models are shown in Fig. 13. The results from model 1 show a large deviation with respect to the observed values. The other three models could reproduce the ratios within the dispersion at galactocentric radii beyond the solar neighborhood, while the inner Galaxy is not as well reproduced.

5. Summary

We used the IRAM 30 meter telescope to perform observations of the J = 2–1 transitions of CS, $C^{33}S$, $C^{34}S$, $C^{36}S$, ^{13}CS, $^{13}C^{33}S$, and $^{13}C^{34}S$ as well as the J = 3–2 transitions of $C^{33}S$, $C^{34}S$, $C^{36}S$, and ^{13}CS toward a large sample of 110 HMSFRs. The CS J = 2–1 line was detected toward 106 sources, with a detection rate of 96%. The J = 2–1 transitions of $C^{34}S$, ^{13}CS, $C^{33}S$, $^{13}C^{34}S$, and $C^{36}S$ were successfully detected in 90, 82, 46, 17, and 3 of our sources, respectively. The J = 3–2 lines of $C^{34}S$, ^{13}CS, $C^{33}S$, and $C^{36}S$ were detected in 87, 71, 42, and 1 object(s). All the detected rare CS isotopologs exhibit optically thin lines and allow us to measure the isotope ratios of $^{12}C/^{13}C$, $^{32}S/^{34}S$, $^{32}S/^{33}S$, $^{32}S/^{36}S$, $^{34}S/^{33}S$, $^{34}S/^{36}S$, and $^{33}S/^{36}S$ with only minor saturation corrections. Our main results are as follows:

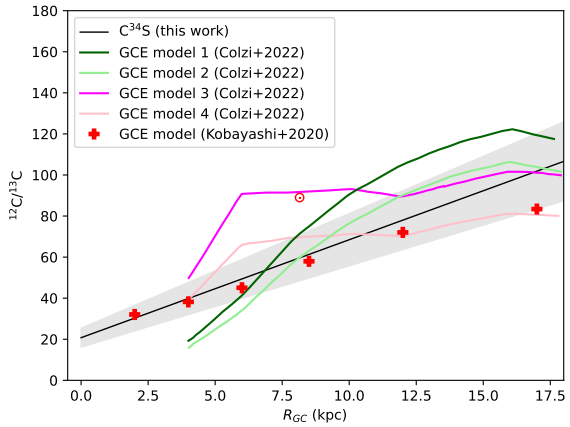

Fig. 13. $^{12}C/^{13}C$ isotope ratios from observations in this work and GCE models. The red symbol ⊙ indicates the $^{12}C/^{13}C$ isotope ratio of the Sun. The $^{12}C/^{13}C$ gradient obtained from $C^{34}S$ in the current work is plotted as a black solid line, with the gray shaded area showing the 1σ interval of the fit. The red crosses visualize the results from the GCE model of Kobayashi et al. (2011, 2020, see also Sect. 4.9). The dark green, light green, magenta, and pink lines refer to the predicted gradients from models in Table 2 from Colzi et al. (2022).

- Based on the measurements of $C^{34}S$ and $^{13}C^{34}S$ $J = 2$–1 transitions, we directly measured the $^{12}C/^{13}C$ ratios with corrections of opacity. With accurate distances obtained from parallax data (Reid et al. 2009, 2014, 2019), we confirm the previously determined $^{12}C/^{13}C$ gradient. A least-squares fit to our data results in $^{12}C/^{13}C = (4.77 \pm 0.81)R_{GC} + (20.76 \pm 4.61)$, with a correlation coefficient of 0.82.
- The Galactic $^{12}C/^{13}C$ gradients derived based on measurements of CN (Savage et al. 2002; Milam et al. 2005), $C^{18}O$ (Langer & Penzias 1990; Wouterloot & Brand 1996; Keene et al. 1998), and H_2CO (Henkel et al. 1980, 1982, 1983, 1985; Yan et al. 2019) are in agreement with our results from $C^{34}S$ and emphasize that chemical fractionation has little effect on $^{12}C/^{13}C$ ratios.
- While previously it had been assumed that a linear fit would provide a good simulation of carbon isotope ratios as a function of galactocentric distance, our analysis reveals that this does not hold for the Galactic center region. While $^{12}C/^{13}C$ ratios are lowest in this part of the Milky Way, they clearly surpass values expected from a linear fit to the Galactic disk sources. This indicates that there is no strict linear correlation of carbon isotope ratios across the Galaxy.
- We confirm the previously determined $^{32}S/^{34}S$ gradients (Chin et al. 1996; Yu et al. 2020; Humire et al. 2020) with the direct method from ^{13}CS and $^{13}C^{34}S$, as well as the double isotope method also using $^{12}C/^{13}C$ ratios in the $J = 2$–1 and $J = 3$–2 transitions. Opacity corrections could be applied to the $J = 2$–1 transitions, but not to the $J = 3$–2 lines that may show, on average, slightly higher opacities. A $^{32}S/^{34}S$ gradient of $(0.75 \pm 0.13)R_{GC}+(15.52 \pm 0.78)$ was obtained based on a large dataset of 90 values from our double isotope method in the $J = 2$–1 transition. The 19 sources permitting the direct determination of this ratio with $^{13}CS/^{13}C^{34}S$ yield $^{32}S/^{34}S=(0.73 \pm 0.36)R_{GC}+(16.50 \pm 2.07)$.
- Differences between the behavior of the $^{12}C/^{13}C$ and $^{32}S/^{34}S$ ratios as a function of galactocentric distance are reported and should be used as input for further chemical models: (a) In the inner disk the $^{12}C/^{13}C$ ratios at $R_{GC} \geq 4.0$ kpc are clearly higher than the value in the CMZ, while the $^{32}S/^{34}S$ ratios in the CMZ and inner disk are similar, as already suggested for the first time by Humire et al. (2020). (b) In the local ISM, the $^{12}C/^{13}C$ ratio is well below the Solar System value but $^{32}S/^{34}S$ is still quite close to it. All of this indicates that, unlike ^{13}C, ^{34}S is not a clean secondary isotope.
- There is no notable $^{34}S/^{33}S$ gradient across the Galaxy. Ratios are well below the values commonly reported in earlier publications. This is a consequence of accounting for the full hyperfine structure splitting of the $C^{33}S$ lines. The average value of $^{34}S/^{33}S$ derived from the $J = 2$–1 transition lines after corrections for opacity toward our sample is 4.35 ± 0.44.
- While there is no $^{34}S/^{33}S$ gradient with galactocentric radius, interstellar $^{34}S/^{33}S$ values near the solar neighborhood are well below the Solar System ratio, most likely suggesting the Solar System ratio is peculiar, and perhaps also the $^{18}O/^{17}O$ ratio. A comparison of local interstellar and Solar System $^{32}S/^{34}S$ and $^{34}S/^{33}S$ ratios suggests that the Solar System may have been formed from gas and dust with a peculiarly high ^{34}S abundance. The data also indicate that ^{33}S is not a clean primary or secondary product of nucleosynthesis, similarly to ^{34}S .
- For the first time, we report a $^{32}S/^{33}S$ gradient in our Galaxy: $^{32}S/^{33}S = (2.64 \pm 0.77)R_{GC} + (70.80 \pm 5.57)$, with a correlation coefficient of 0.46.
- We find first potential indications for a positive $^{34}S/^{36}S$ gradient with galactocentric radius. Combined $^{34}S/^{36}S$ ratios from Mauersberger et al. (1996) and our new data with corrections of opacity in the $J = 2$–1 transition and applying new up-to-date distances yield a linear fit of $^{34}S/^{36}S = (10.34 \pm 2.74)R_{GC} + (57.45 \pm 18.59)$, with a correlation coefficient of 0.71. Considering the uniform $^{34}S/^{33}S$ ratios in our Galaxy, a $^{33}S/^{36}S$ gradient of $(2.38 \pm 0.67)R_{GC}+(13.21 \pm 4.48)$ is also obtained.
- For the first time, we report a tentative $^{32}S/^{36}S$ gradient with galactocentric radius: $^{32}S/^{36}S = (314 \pm 55)R_{GC} + (659 \pm 374)$, with a correlation coefficient of 0.84. Our measurements are consistent with ^{36}S being a purely secondary nucleus. However, observations of $^{34}S/^{36}S$ and $^{32}S/^{36}S$ isotope ratios are still relatively few, especially in the CMZ and the inner disk within $R_{GC} = 5.0$ kpc.
- The predicted $^{12}C/^{13}C$ ratios from the latest Galactic chemical evolution models (e.g., Kobayashi et al. 2020; Romano et al. 2021; Colzi et al. 2022) are in good agreement with our results, while $^{32}S/^{34}S$ and $^{32}S/^{36}S$ ratios show significant differences at larger galactocentric distances. $^{32}S/^{33}S$ ratios even show clear offsets along the entire inner 12 kpc of the Milky Way. Taken together, these findings provide useful guidelines for further refinements of models of the chemical evolution of the Galaxy.

Acknowledgements. We wish to thank the referee for useful comments. Y.T.Y. is a member of the International Max Planck Research School (IMPRS) for Astronomy and Astrophysics at the Universities of Bonn and Cologne. Y.T.Y. would like to thank the China Scholarship Council (CSC) and the Max-Planck-Institut für Radioastronomie (MPIfR) for the financial support. Y.T.Y. also thanks his fiancee, Siqi Guo, for her support during this pandemic period. C.K. acknowledges funding from the UK Science and Technology Facility Council through grant ST/R000905/1 and ST/V000632/1. The work was also partly funded by a Leverhulme Trust Research Project Grant on "Birth of Elements". We thank the IRAM staff for help provided during the observations.

References

Adande, G. R., & Ziurys, L. M. 2012, ApJ, 744, 194
Anders, E., & Grevesse, N. 1989, Geochim. Cosmochim. Acta, 53, 197
Audouze, J., Lequeux, J., & Vigroux, L. 1975, A&A, 43, 71
Belloche, A., Müller, H. S. P., Menten, K. M., Schilke, P., & Comito, C. 2013, A&A, 559, A47
Bogey, M., Demuynck, C., & Destombes, J. L. 1981, Chem. Phys. Lett., 81, 256
Chen, J. L., Zhang, J. S., Henkel, C., et al. 2021, ApJS, 257, 39
Chiappini, C., Matteucci, F., & Romano, D. 2001, ApJ, 554, 1044
Chin, Y. N., Henkel, C., Whiteoak, J. B., Langer, N., & Churchwell, E. B. 1996, A&A, 305, 960
Colzi, L., Fontani, F., Caselli, P., et al. 2018, A&A, 609, A129
Colzi, L., Sipilä, O., Roueff, E., Caselli, P., & Fontani, F. 2020, A&A, 640, A51
Colzi, L., Romano, D., Fontani, F., et al. 2022, A&A, 667, A151
Denis-Alpizar, O., Stoecklin, T., Guilloteau, S., & Dutrey, A. 2018, MNRAS, 478, 1811
Endres, C. P., Schlemmer, S., Schilke, P., Stutzki, J., & Müller, H. S. P. 2016, J. Mol. Spectrosc., 327, 95
Fontani, F., Caselli, P., Palau, A., Bizzocchi, L., & Ceccarelli, C. 2015, ApJ, 808, L46
Gardner, F. F., & Whiteoak, J. B. 1981, MNRAS, 194, 37P
Gong, Y., Belloche, A., Du, F. J., et al. 2021, A&A, 646, A170
GRAVITY Collaboration (Abuter, R., et al.) 2019, A&A, 625, A10
Güsten, R., Henkel, C., & Batrla, W. 1985, A&A, 149, 195
Halfen, D. T., Woolf, N. J., & Ziurys, L. M. 2017, ApJ, 845, 158
Henkel, C., & Mauersberger, R. 1993, A&A, 274, 730
Henkel, C., Walmsley, C. M., & Wilson, T. L. 1980, A&A, 82, 41
Henkel, C., Wilson, T. L., & Bieging, J. 1982, A&A, 109, 344
Henkel, C., Wilson, T. L., Walmsley, C. M., & Pauls, T. 1983, A&A, 127, 388
Henkel, C., Guesten, R., & Gardner, F. F. 1985, A&A, 143, 148
Henkel, C., Wilson, T. L., Langer, N., Chin, Y. N., & Mauersberger, R. 1994, Interstellar CNO Isotope Ratios, eds. T. L. Wilson, & K. J. Johnston, 439, 72
Humire, P. K., Thiel, V., Henkel, C., et al. 2020, A&A, 642, A222
Jacob, A. M., Menten, K. M., Wiesemeyer, H., et al. 2020, A&A, 640, A125
Karakas, A. I., & Lattanzio, J. C. 2014, PASA, 31, e030
Keene, J., Schilke, P., Kooi, J., et al. 1998, ApJ, 494, L107
Kobayashi, C., Tsujimoto, T., & Nomoto, K. 2000, ApJ, 539, 26
Kobayashi, C., Karakas, A. I., & Umeda, H. 2011, MNRAS, 414, 3231
Kobayashi, C., Karakas, A. I., & Lugaro, M. 2020, ApJ, 900, 179
Langer, N. 1989, A&A, 210, 93
Langer, W. D., & Penzias, A. A. 1990, ApJ, 357, 477
Langer, W. D., & Penzias, A. A. 1993, ApJ, 408, 539
Langer, W. D., Graedel, T. E., Frerking, M. A., & Armentrout, P. B. 1984, ApJ, 277, 581
Li, H.-K., Zhang, J.-S., Liu, Z.-W., et al. 2016, Res. Astron. Astrophys., 16, 47
Limongi, M., & Chieffi, A. 2018, ApJS, 237, 13
Linke, R. A., & Goldsmith, P. F. 1980, ApJ, 235, 437
Loison, J.-C., Wakelam, V., Gratier, P., et al. 2019, MNRAS, 485, 5777
Loison, J.-C., Wakelam, V., Gratier, P., & Hickson, K. M. 2020, MNRAS, 498, 4663
Mauersberger, R., Henkel, C., Langer, N., & Chin, Y. N. 1996, A&A, 313, L1
Mauersberger, R., Ott, U., Henkel, C., Cernicharo, J., & Gallino, R. 2004, A&A, 426, 219
Meibom, A., Krot, A. N., Robert, F., et al. 2007, ApJ, 656, L33
Menten, K. M., Reid, M. J., Forbrich, J., & Brunthaler, A. 2007, A&A, 474, 515
Meyer, B. S. 1994, ARA&A, 32, 153
Meynet, G., & Maeder, A. 2002, A&A, 390, 561
Milam, S. N., Savage, C., Brewster, M. A., Ziurys, L. M., & Wyckoff, S. 2005, ApJ, 634, 1126
Müller, H. S. P., Schlöder, F., Stutzki, J., & Winnewisser, G. 2005, J. Mol. Struct., 742, 215
Pilkington, K., Few, C. G., Gibson, B. K., et al. 2012, A&A, 540, A56
Reid, M. J., Menten, K. M., Zheng, X. W., et al. 2009, ApJ, 700, 137
Reid, M. J., Menten, K. M., Brunthaler, A., et al. 2014, ApJ, 783, 130
Reid, M. J., Menten, K. M., Brunthaler, A., et al. 2019, ApJ, 885, 131
Riquelme, D., Amo-Baladrón, M. A., Martín-Pintado, J., et al. 2010, A&A, 523, A51
Ritchey, A. M., Federman, S. R., & Lambert, D. L. 2011, ApJ, 728, 36
Ritchey, A. M., Federman, S. R., & Lambert, D. L. 2015, ApJ, 804, L3
Roman-Duval, J., Jackson, J. M., Heyer, M., et al. 2009, ApJ, 699, 1153
Romano, D. 2022, A&AR, 30, 7
Romano, D., Matteucci, F., Zhang, Z. Y., Papadopoulos, P. P., & Ivison, R. J. 2017, MNRAS, 470, 401
Romano, D., Matteucci, F., Zhang, Z.-Y., Ivison, R. J., & Ventura, P. 2019, MNRAS, 490, 2838
Romano, D., Magrini, L., Randich, S., et al. 2021, A&A, 653, A72
Savage, C., Apponi, A. J., Ziurys, L. M., & Wyckoff, S. 2002, ApJ, 578, 211
Thielemann, F. K., & Arnett, W. D. 1985, ApJ, 295, 604
Timmes, F. X., Woosley, S. E., & Weaver, T. A. 1995, ApJS, 98, 617
van der Tak, F. F. S., Black, J. H., Schöier, F. L., Jansen, D. J., & van Dishoeck, E. F. 2007, A&A, 468, 627
Viti, S., Fontani, F., & Jiménez-Serra, I. 2020, MNRAS, 497, 4333
Watson, W. D., Anicich, V. G., & Huntress, W. T., J. 1976, ApJ, 205, L165
Whiteoak, J. B., & Gardner, F. F. 1979, MNRAS, 188, 445
Wilson, T. L. 1999, Rep. Prog. Phys., 62, 143
Wilson, T. L., & Rood, R. 1994, ARA&A, 32, 191
Wilson, T. L., Bieging, J., Downes, D., & Gardner, F. F. 1976, A&A, 51, 303
Wirström, E. S., Charnley, S. B., Geppert, W. D., & Persson, C. M. 2012, in 43rd Annual Lunar and Planetary Science Conference, Lunar and Planetary Science Conference, 1611
Woosley, S. E., & Weaver, T. A. 1995, ApJS, 101, 181
Wouterloot, J. G. A., & Brand, J. 1996, A&AS, 119, 439
Wouterloot, J. G. A., Henkel, C., Brand, J., & Davis, G. R. 2008, A&A, 487, 237
Xu, Y., Reid, M. J., Zheng, X. W., & Menten, K. M. 2006, Science, 311, 54
Xu, Y., Li, J. J., Reid, M. J., et al. 2013, ApJ, 769, 15
Yan, Y. T., Zhang, J. S., Henkel, C., et al. 2019, ApJ, 877, 154
Yu, H. Z., Zhang, J. S., Henkel, C., et al. 2020, ApJ, 899, 145
Zhang, J. S., Sun, L. L., Riquelme, D., et al. 2015, ApJS, 219, 28
Zhang, J. S., Liu, W., Yan, Y. T., et al. 2020a, ApJS, 249, 6
Zhang, J. S., Yan, Y. T., Liu, W., et al. 2020b, in IAU General Assembly, 278

Appendix A: Additional Tables

Table A.1. Source list.

Sources	R.A.(J2000) (h m s)	Dec.(J2000) ($^\circ$ $'$ $''$)	$V_{\rm LSR}$ (km s^{-1})	Spiral Arm	d (kpc)	$R_{\rm GC}$ (kpc)
WB89-380*	01:07:51.3000	+65:21:25.000	-86.62 ± 0.02	···	7.85 ± 1.04	14.19 ± 0.92
WB89-391*	01:19:25.4000	+65:45:50.000	-85.93 ± 0.01	···	7.83 ± 1.06	14.28 ± 0.94
W3OH	02:27:03.9000	+61:52:24.000	−47 ± 3	Per	1.95 ± 0.04	9.64 ± 0.03
Orion-KL	05:35:14.2000	−05:22:31.000	3 ± 5	Loc	0.41 ± 0.00	8.54 ± 0.00
PointC1*	17:32:33.2000	−31:40:31.400	-64.18 ± 0.98	···	6.80 ± 0.16	1.46 ± 0.15
G359.13+00.03	17:43:25.6109	−29:39:17.551	−1 ± 10	GC	6.06 ± 1.14	2.12 ± 1.14
SgrC*	17:44:47.0000	−29:28:24.800	70.06 ± 0.07	···	8.05 ± 0.04	0.15 ± 0.03
+20 km s^{-1} cloud*	17:45:37.5700	−29:05:22.600	6.80 ± 0.12	···	8.20 ± 0.04	0.03 ± 0.03
G359.61−00.24	17:45:39.0697	−29:23:30.265	21 ± 5	CtN	2.67 ± 0.15	5.51 ± 0.15
SgrA	17:45:40.5400	−29:00:16.280	53 ± 1	GC	8.18 ± 0.04	0.00 ± 0.04
+50 km s^{-1} cloud*	17:45:50.2000	−28:59:41.000	46.78 ± 0.07	···	8.20 ± 0.04	0.02 ± 0.04
G359.93−00.14	17:46:01.9183	−29:03:58.674	−10 ± 10	GC	5.52 ± 0.89	2.65 ± 0.89
G000.37+00.03	17:46:21.4012	−28:35:39.821	37 ± 10	3kF	8.00 ± 3.01	0.19 ± 2.88
G0.25*	17:46:09.1000	−28:42:12.000	39.70 ± 0.19	···	8.55 ± 0.04	0.37 ± 0.04
CloudD*	17:46:24.4000	−28:33:20.000	23.32 ± 0.55	···	8.85 ± 0.17	0.67 ± 0.17
G000.31−00.20	17:47:09.1092	−28:46:16.278	18 ± 3	ScN	2.92 ± 0.36	5.25 ± 0.36
SgrB2	17:47:20.4000	−28:23:02.000	62 ± 5	GC	7.75 ± 0.72	0.44 ± 0.70
G1.28+0.07*	17:48:22.0000	−27:48:19.000	98.64 ± 0.61	···	7.94 ± 0.04	0.30 ± 0.03
SgrD*	17:48:42.2400	−28:01:27.770	63.37 ± 0.86	···	7.76 ± 0.07	0.45 ± 0.07
G001.00−00.23	17:48:55.2845	−28:11:48.240	2 ± 5	···	11.11 ± 7.04	2.94 ± 7.03
G001.14−00.12	17:48:48.5410	−28:01:11.350	−16 ± 3	Nor	5.15 ± 4.28	3.03 ± 4.27
Clump2*	17:51:24.8000	−26:00:04.000	80.82 ± 0.61	···	7.21 ± 0.11	1.06 ± 0.10
G002.70+00.04	17:51:45.9766	−26:35:57.070	93 ± 5	···	9.90 ± 10.29	1.77 ± 10.05
PointD1*	17:59:17.8000	−24:24:37.900	117.60 ± 0.14	···	7.18 ± 0.09	1.24 ± 0.07
G006.79−00.25	18:01:57.7525	−23:12:34.245	22 ± 5	Nor	3.47 ± 0.25	4.75 ± 0.25
G007.47+00.05	18:02:13.1823	−22:27:58.981	−14 ± 10	OSC	20.41 ± 2.50	12.35 ± 2.49
G008.34−01.00	18:08:04.0510	−22:13:26.566	5 ± 5	SgN	1.56 ± 0.10	6.64 ± 0.10
G009.21−00.20	18:06:52.8421	−21:04:27.878	102 ± 5	ScN	3.30 ± 1.05	4.95 ± 1.01
G010.32−00.15	18:09:01.4549	−20:05:07.854	10 ± 5	ScN	2.92 ± 0.30	5.34 ± 0.29
G010.62−00.33	18:10:17.9849	−19:54:04.646	−6 ± 5	3kN	2.76 ± 0.58	5.49 ± 0.56
G011.10−00.11	18:10:28.2470	−19:22:30.216	29 ± 5	ScN	4.07 ± 0.23	4.26 ± 0.21
W33	18:13:54.000	−17:55:48.000	34 ± 5	ScN	2.92 ± 0.31	5.37 ± 0.30
G013.71−00.08	18:15:36.9814	−17:04:32.108	44 ± 5	Nor	3.79 ± 0.20	4.59 ± 0.18
G015.66−00.49	18:20:59.7470	−15:33:09.800	−4 ± 5	3kN	4.55 ± 0.60	3.99 ± 0.50
G016.86−02.15	18:29:24.4085	−15:16:04.141	17 ± 3	SgN	2.35 ± 0.51	5.97 ± 0.47
G017.02−02.40	18:30:36.2931	−15:14:28.384	22 ± 3	SgN	1.88 ± 0.38	6.40 ± 0.36
G017.55−00.12	18:23:17.9084	−13:42:47.146	44 ± 10	SgN	2.01 ± 0.15	6.29 ± 0.14
G017.63+00.15	18:22:26.3821	−13:30:11.951	25 ± 10	SgN	1.49 ± 0.04	6.77 ± 0.04
G018.34+01.76	18:17:58.1254	−12:07:24.893	28 ± 3	SgN	2.00 ± 0.08	6.31 ± 0.07
G019.00−00.02	18:25:44.7778	−12:22:45.886	93 ± 5	Nor	4.05 ± 1.03	4.55 ± 0.84
G019.36−00.03	18:26:25.7796	−12:03:53.267	27 ± 3	ScN	2.84 ± 0.56	5.58 ± 0.49
G019.49+00.11	18:26:09.1691	−11:52:51.354	121 ± 5	···	3.07 ± 0.94	5.38 ± 0.81
G022.35+00.06	18:31:44.1199	−09:22:12.336	80 ± 5	Nor	4.33 ± 2.02	4.49 ± 1.46
G023.20−00.37	18:34:55.1794	−08:49:15.206	82 ± 10	Nor	4.18 ± 0.60	4.64 ± 0.43
G023.25−00.24	18:34:31.2397	−08:42:47.306	63 ± 3	ScN	5.92 ± 1.79	3.60 ± 0.79
G023.38+00.18	18:33:14.3240	−08:23:57.500	75 ± 3	Nor	4.81 ± 0.58	4.22 ± 0.37
G023.43−00.18	18:34:39.1870	−08:31:25.405	97 ± 3	Nor	5.88 ± 1.11	3.63 ± 0.49
G024.63−00.32	18:37:22.7091	−07:31:42.093	43 ± 5	ScN	4.13 ± 0.77	4.75 ± 0.53
G024.78+00.08	18:36:12.5614	−07:12:10.840	111 ± 3	Nor	6.67 ± 0.71	3.51 ± 0.15
G024.85+00.08	18:36:18.3867	−07:08:50.834	111 ± 5	Nor	5.68 ± 0.52	3.85 ± 0.23
G028.14−00.00	18:42:42.5896	−04:15:35.128	100 ± 5	ScF	6.33 ± 0.92	3.96 ± 0.21
G028.30−00.38	18:44:21.9666	−04:17:39.904	87 ± 5	ScN	4.52 ± 0.45	4.71 ± 0.26
G028.39+00.08	18:42:51.9822	−03:59:54.494	75 ± 5	ScN	4.33 ± 0.28	4.83 ± 0.17
G028.83−00.25	18:44:51.0865	−03:45:48.378	87 ± 5	ScN	5.00 ± 1.00	4.50 ± 0.48
G029.98+00.10	18:45:39.9622	−02:34:32.581	109 ± 10	ScF	6.41 ± 0.41	4.14 ± 0.07
G030.19−00.16	18:47:03.0698	−02:30:36.268	108 ± 3	ScN	4.72 ± 0.22	4.74 ± 0.11

Table A.1. continued.

Sources	R.A.(J2000) (h m s)	Dec.(J2000) ($^\circ$ $'$ $''$)	V_{LSR} (km s^{-1})	Spiral Arm	d (kpc)	R_{GC} (kpc)
G030.22−00.18	18:47:08.2979	−02:29:29.330	113 ± 3	ScN	3.52 ± 0.40	5.43 ± 0.26
G030.41−00.23	18:47:40.7589	−02:20:30.907	103 ± 3	ScN	3.95 ± 0.33	5.17 ± 0.20
G030.70−00.06	18:47:36.7983	−02:00:54.341	89 ± 3	ScF	6.54 ± 0.85	4.20 ± 0.10
G030.74−00.04	18:47:39.7248	−01:57:24.974	88 ± 3	ScN	3.07 ± 0.52	5.76 ± 0.36
G030.78+00.20	18:46:48.0864	−01:48:53.946	82 ± 5	ScN	7.14 ± 1.63	4.19 ± 0.05
G030.81−00.05	18:47:46.9751	−01:54:26.416	105 ± 5	ScF	3.12 ± 0.36	5.73 ± 0.24
G030.97−00.14	18:48:22.0433	−01:48:30.750	77 ± 3	ScN	3.40 ± 0.25	5.55 ± 0.17
G031.24−00.11	18:48:45.0808	−01:33:13.200	24 ± 10	Per	13.16 ± 2.42	7.48 ± 2.00
G032.74−00.07	18:51:21.8624	−00:12:06.220	56 ± 5	SgF	7.94 ± 1.01	4.55 ± 0.23
G032.79+00.19	18:50:30.7330	−00:01:59.280	16 ± 10	Per	9.71 ± 2.92	5.26 ± 1.57
G033.39+00.00	18:52:14.6412	+00:24:54.374	43 ± 5	ScF	8.85 ± 2.27	4.93 ± 0.93
G034.41+00.23	18:53:18.0319	+01:25:25.500	60 ± 10	SgN	2.94 ± 0.10	5.99 ± 0.06
G034.79−01.38	18:59:45.9838	+01:01:18.947	45 ± 5	SgN	2.62 ± 0.14	6.21 ± 0.09
G035.79−00.17	18:57:16.8905	+02:27:58.007	61 ± 5	SgF	8.85 ± 1.02	5.27 ± 0.43
G036.11+00.55	18:55:16.7927	+03:05:05.392	75 ± 5	AqS	4.07 ± 0.93	5.45 ± 0.43
G037.42+01.51	18:54:14.3481	+04:41:39.647	41 ± 3	SgN	1.88 ± 0.07	6.78 ± 0.05
G037.47−00.10	19:00:07.1430	+03:59:52.975	58 ± 3	SgF	11.36 ± 3.87	6.97 ± 2.71
G038.03−00.30	19:01:50.4676	+04:24:18.900	30 ± 7	SgF	10.53 ± 2.44	6.49 ± 1.54
G038.11−00.22	19:01:44.1513	+04:30:37.400	76 ± 5	AqS	4.13 ± 0.60	5.55 ± 0.25
G040.28−00.21	19:05:41.2146	+06:26:12.698	74 ± 5	AqS	3.37 ± 0.22	6.02 ± 0.10
G040.42+00.70	19:02:39.6192	+06:59:09.052	−7 ± 5	Per	12.82 ± 2.14	8.46 ± 1.67
G040.62−00.13	19:06:01.6288	+06:46:36.140	31 ± 3	Per	12.50 ± 3.28	8.24 ± 2.50
G041.15−00.20	19:07:14.3676	+07:13:18.025	60 ± 3	SgF	8.00 ± 1.15	5.69 ± 0.37
G041.22−00.19	19:07:21.3772	+07:17:08.115	59 ± 5	SgF	8.85 ± 1.72	6.03 ± 0.77
G042.03+00.19	19:07:28.1834	+08:10:53.433	−36 ± 5	Per	14.08 ± 2.38	9.70 ± 1.97
G043.03−00.45	19:11:38.9819	+08:46:30.665	56 ± 5	SgF	7.69 ± 1.12	5.84 ± 0.33
G045.45+00.06	19:14:21.2658	+11:09:15.872	19 ± 5	SgF	8.40 ± 1.20	6.41 ± 0.50
G045.49+00.12	19:14:11.3553	+11:13:06.370	58 ± 3	SgF	6.94 ± 1.16	5.96 ± 0.24
G045.80−00.35	19:16:31.0795	+11:16:11.985	64 ± 5	SgF	7.30 ± 1.23	6.08 ± 0.32
G048.99−00.29	19:22:26.1348	+14:06:39.133	67 ± 10	SgF	5.62 ± 0.54	6.18 ± 0.02
G049.04−01.07	19:25:22.2504	+13:47:19.525	56 ± 3	SgN	6.10 ± 0.82	6.22 ± 0.10
G049.26+00.31	19:20:44.8571	+14:38:26.864	0 ± 5	Per	8.85 ± 1.25	7.12 ± 0.62
G049.34+00.41	19:20:32.4472	+14:45:45.390	68 ± 5	SgF	4.15 ± 0.53	6.32 ± 0.10
G049.41+00.32	19:20:59.2098	+14:46:49.613	−12 ± 5	Per	7.58 ± 1.78	6.61 ± 0.61
G049.59−00.24	19:23:26.6068	+14:40:16.955	63 ± 5	SgF	4.59 ± 0.19	6.27 ± 0.02
W51-IRS2	19:23:39.8000	+14:31:05.000	38 ± 5	SgN	5.13 ± 1.87	6.22 ± 0.06
G054.10−00.08	19:31:48.7978	+18:42:57.096	40 ± 5	LoS	4.33 ± 0.58	6.64 ± 0.04
G058.77+00.64	19:38:49.1269	+23:08:40.205	33 ± 3	LoS	3.34 ± 0.45	7.05 ± 0.06
G059.47−00.18	19:43:28.3504	+23:20:42.522	26 ± 3	LoS	1.87 ± 0.08	7.41 ± 0.03
G059.83+00.67	19:40:59.2938	+24:04:44.177	34 ± 3	LoS	4.13 ± 0.24	7.07 ± 0.00
G060.57−00.18	19:45:52.4949	+24:17:43.237	4 ± 5	Per	8.26 ± 1.02	8.29 ± 0.52
G070.18+01.74	20:00:54.4874	+33:31:28.224	−23 ± 5	Per	6.41 ± 0.66	8.51 ± 0.28
G071.31+00.82	20:07:31.2593	+33:59:41.491	9 ± 5	Loc	4.69 ± 0.62	8.02 ± 0.16
G071.52−00.38	20:12:57.8943	+33:30:27.083	11 ± 3	Loc	3.61 ± 0.34	7.82 ± 0.04
G073.65+00.19	20:16:21.9320	+35:36:06.094	−76 ± 10	Out	13.33 ± 3.56	13.54 ± 2.90
G074.56+00.84	20:16:13.3617	+36:43:33.920	−1 ± 5	Loc	2.72 ± 0.62	7.90 ± 0.04
G075.29+01.32	20:16:16.0120	+37:35:45.810	−58 ± 5	Out	9.26 ± 0.86	10.69 ± 0.58
DR21	20:39:01.8000	+42:19:40.900	−3 ± 3	Loc	1.50 ± 0.08	8.10 ± 0.00
G090.92+01.48	21:09:12.9685	+50:01:03.664	−70 ± 5	Out	5.85 ± 1.06	10.13 ± 0.63
G097.53+03.18	21:32:12.4343	+55:53:49.689	−73 ± 5	Out	7.52 ± 0.96	11.81 ± 0.70
G108.20+00.58	22:49:31.4775	+59:55:42.006	−49 ± 10	Per	4.41 ± 0.72	10.43 ± 0.48
G108.42+00.89	22:49:58.8760	+60:17:56.650	−51 ± 5	Per	2.50 ± 0.31	9.28 ± 0.17
G109.87+02.11	22:56:18.0559	+62:01:49.562	10 ± 5	Loc	0.81 ± 0.02	8.49 ± 0.01
NGC7538	23:13:45.4000	+61:29:11.400	−57 ± 5	Per	2.65 ± 0.12	9.47 ± 0.07

Notes. Column (1): source name; Columns (2) and (3): Equatorial coordinates; Column (4): Local Standard of Rest velocity; Column (5): the spiral arm, GC, Con, 3kN/F, Nor, ScN/F, SgN/F, Loc, Per, Out, OSC, LoS, and AqS indicate Galactic center region, connecting arm, 3 kpc arm (near/far), Norma arm, Scutum-Centaurus arm (near/far), Sagittarius arm (near/far), Local arm, Perseus arm, Outer arm, Outer-Scutum-Centaurus arm, Local arm spur, and Aquarius spur, respectively. See details in Reid et al. (2019); Column (6): the heliocentric distance, derived with parallaxes from the BeSSeL Survey (Reid et al. 2019); Column (7): galactocentric distance following equation (1). [(*)]For those 12 sources without parallax data and an asterisk in column 1, kinematic distances were estimated (see details in Section 2.1).

Table A.2. $^{32}S/^{34}S$ isotope ratios derived through the double isotope method with the $J = 2$-1 and $J = 3$-2 transitions of $C^{34}S$ and ^{13}CS.

Source	V_{LSR}	R_{GC}	Optical depth $J = 2$-1			Corrections for optical depth		$^{32}S/^{34}S$	
	(km s^{-1})	(kpc)	CS	$C^{34}S$	^{13}CS	f_1	f_2	2-1	3-2
WB89-380	-86.62	14.19 ± 0.92	3.111 ± 0.598	0.135 ± 0.137	0.035 ± 0.000	1.1	1.0	21.20 ± 4.01	24.98 ± 4.69
WB89-391	-85.93	14.28 ± 0.94	5.189 ± 0.996	0.223 ± 0.226	0.058 ± 0.001	1.1	1.0	24.39 ± 4.64	20.98 ± 4.04
W3OH	-46.96	9.64 ± 0.03	8.520 ± 1.671	0.310 ± 0.003	0.128 ± 0.001	1.2	1.1	26.15 ± 4.87	31.42 ± 5.85
Orion-KL	8.24	8.54 ± 0.00	6.035 ± 1.189	0.166 ± 0.002	0.096 ± 0.001	1.1	1.0	24.75 ± 5.24	25.41 ± 4.86
PointC1	-64.18	1.46 ± 0.15	0.588 ± 0.128	0.037 ± 0.000	0.021 ± 0.000	1.0	1.0	19.40 ± 4.55	···
G359.13+00.03	-2.03	2.12 ± 1.14	5.526 ± 1.188	0.420 ± 0.004	0.179 ± 0.002	1.2	1.1	14.34 ± 4.11	···
SgrC	-44.31	0.24 ± 0.07	0.538 ± 0.123	0.048 ± 0.000	0.025 ± 0.000	1.0	1.0	12.81 ± 2.95	···
SgrC	70.06	0.15 ± 0.03	0.406 ± 0.094	0.031 ± 0.000	0.019 ± 0.000	1.0	1.0	14.87 ± 3.38	···
+20 km s^{-1} cloud	6.80	0.03 ± 0.03	4.523 ± 1.030	0.293 ± 0.003	0.200 ± 0.002	1.2	1.1	14.65 ± 3.20	15.13 ± 3.31
G359.61−00.24	19.33	5.51 ± 0.15	4.307 ± 0.874	0.219 ± 0.002	0.092 ± 0.001	1.1	1.0	18.75 ± 3.66	21.66 ± 4.20
+50 km s^{-1} cloud	46.78	0.02 ± 0.04	3.096 ± 0.717	0.203 ± 0.002	0.147 ± 0.001	1.1	1.1	14.46 ± 3.20	14.59 ± 3.23
CloudD	23.32	0.67 ± 0.17	0.641 ± 0.144	0.040 ± 0.000	0.026 ± 0.000	1.0	1.0	14.47 ± 3.16	···
G000.37+00.03	39.98	0.19 ± 2.88	5.508 ± 1.266	0.283 ± 0.003	0.254 ± 0.003	1.1	1.1	15.78 ± 4.38	···
G0.25	10.68	0.76 ± 0.53	1.590 ± 0.352	0.102 ± 0.001	0.061 ± 0.001	1.1	1.0	14.52 ± 3.20	···
G0.25	38.59	0.37 ± 0.04	1.269 ± 0.290	0.091 ± 0.001	0.057 ± 0.001	1.0	1.0	14.79 ± 3.43	15.72 ± 3.98
G000.31−00.20	18.43	5.25 ± 0.36	2.876 ± 0.585	0.158 ± 0.002	0.063 ± 0.001	1.1	1.0	15.71 ± 3.47	15.97 ± 3.54
SgrB2	53.93	0.44 ± 0.70	3.404 ± 0.780	0.207 ± 0.002	0.154 ± 0.002	1.1	1.1	17.47 ± 3.83	17.83 ± 3.91
SgrB2	80.88	0.41 ± 0.02	1.318 ± 0.304	0.083 ± 0.001	0.062 ± 0.001	1.0	1.0	17.09 ± 3.78	16.40 ± 3.65
G1.28+0.07	98.64	0.30 ± 0.03	0.991 ± 0.225	0.048 ± 0.000	0.043 ± 0.000	1.0	1.0	12.45 ± 2.92	···
G1.28+0.07	177.50	0.18 ± 0.00	0.817 ± 0.187	0.049 ± 0.000	0.037 ± 0.000	1.0	1.0	15.65 ± 3.66	···
SgrD	-15.20	2.93 ± 3.62	6.357 ± 1.342	0.422 ± 0.004	0.183 ± 0.002	1.2	1.1	14.41 ± 2.92	18.67 ± 3.79
SgrD	40.31	0.76 ± 0.18	1.060 ± 0.238	0.072 ± 0.001	0.043 ± 0.000	1.0	1.0	15.48 ± 3.42	13.16 ± 2.99
SgrD	63.37	0.45 ± 0.07	0.448 ± 0.102	0.024 ± 0.000	0.020 ± 0.000	1.0	1.0	15.62 ± 4.08	···
G001.00−00.23	0.97	2.94 ± 7.03	9.963 ± 2.102	0.486 ± 0.005	0.286 ± 0.003	1.3	1.2	13.02 ± 3.60	···
Clump2	14.19	4.20 ± 1.65	2.093 ± 0.428	0.085 ± 0.001	0.048 ± 0.000	1.0	1.0	37.16 ± 7.62	···
Clump2	80.82	1.06 ± 0.10	1.500 ± 0.331	0.084 ± 0.001	0.057 ± 0.001	1.0	1.0	19.46 ± 4.19	14.69 ± 3.70
Clump2	141.00	0.60 ± 0.03	1.982 ± 0.445	0.113 ± 0.001	0.082 ± 0.001	1.1	1.0	25.43 ± 5.70	···
PointD1	117.60	1.24 ± 0.07	0.340 ± 0.075	0.026 ± 0.000	0.012 ± 0.000	1.0	1.0	14.02 ± 2.99	···
G006.79−00.25	20.88	4.75 ± 0.25	10.743 ± 2.200	0.529 ± 0.005	0.247 ± 0.002	1.3	1.1	18.09 ± 3.53	21.30 ± 4.16
G007.47+00.05	-14.58	12.35 ± 2.49	4.106 ± 0.794	0.146 ± 0.001	0.052 ± 0.001	1.1	1.0	26.53 ± 5.92	29.52 ± 6.31
G010.32−00.15	12.00	5.34 ± 0.29	5.185 ± 1.054	0.252 ± 0.003	0.112 ± 0.001	1.1	1.1	19.19 ± 3.73	21.62 ± 4.20
G010.62−00.33	-3.68	5.49 ± 0.56	2.809 ± 0.570	0.170 ± 0.002	0.060 ± 0.001	1.1	1.0	15.67 ± 3.52	18.19 ± 4.57
G011.10−00.11	29.91	4.26 ± 0.21	···	···	···	···	···	···	19.39 ± 5.60
G013.71−00.08	46.81	4.59 ± 0.18	···	···	···	···	···	···	17.28 ± 4.84
G015.66−00.49	-5.54	3.99 ± 0.50	2.177 ± 0.451	0.096 ± 0.001	0.055 ± 0.001	1.0	1.0	31.04 ± 8.76	22.91 ± 5.41
G016.86−02.15	17.60	5.97 ± 0.47	5.396 ± 1.089	0.244 ± 0.002	0.110 ± 0.001	1.1	1.1	22.62 ± 4.36	24.20 ± 4.66
G017.02−02.40	19.91	6.40 ± 0.36	4.005 ± 0.805	0.191 ± 0.002	0.078 ± 0.001	1.1	1.0	20.71 ± 3.98	23.03 ± 4.42
G017.63+00.15	22.41	6.77 ± 0.04	3.027 ± 0.606	0.126 ± 0.001	0.057 ± 0.001	1.1	1.0	18.19 ± 3.84	22.05 ± 4.91
G018.34+01.76	33.53	6.31 ± 0.07	2.168 ± 0.436	0.109 ± 0.001	0.043 ± 0.000	1.1	1.0	18.72 ± 3.60	21.29 ± 4.08
G019.00−00.02	59.71	4.55 ± 0.84	2.031 ± 0.417	0.117 ± 0.001	0.048 ± 0.000	1.1	1.0	21.11 ± 5.23	···
G019.36−00.03	26.40	5.58 ± 0.49	7.251 ± 1.470	0.381 ± 0.004	0.153 ± 0.002	1.2	1.1	17.51 ± 3.39	20.09 ± 3.89
G022.35+00.06	84.17	4.49 ± 1.46	3.948 ± 0.811	0.200 ± 0.002	0.094 ± 0.001	1.1	1.0	13.31 ± 3.31	17.13 ± 4.21
G023.20−00.37	77.61	4.64 ± 0.43	6.823 ± 1.399	0.341 ± 0.003	0.159 ± 0.002	1.2	1.1	22.17 ± 4.73	18.57 ± 3.76
G023.38+00.18	75.57	4.22 ± 0.37	3.793 ± 0.783	0.148 ± 0.001	0.093 ± 0.001	1.1	1.0	18.72 ± 4.97	···
G023.43−00.18	102.10	3.63 ± 0.49	5.077 ± 1.057	0.284 ± 0.003	0.133 ± 0.001	1.1	1.1	17.21 ± 3.43	18.44 ± 3.68
G024.63−00.32	42.69	4.75 ± 0.53	4.346 ± 0.890	0.223 ± 0.002	0.100 ± 0.001	1.1	1.1	25.42 ± 5.86	···
G024.78+00.08	110.70	3.51 ± 0.15	14.485 ± 3.024	0.743 ± 0.007	0.386 ± 0.004	1.4	1.2	17.50 ± 3.48	20.84 ± 4.14
G024.85+00.08	109.00	3.85 ± 0.23	5.589 ± 1.160	0.301 ± 0.003	0.143 ± 0.001	1.2	1.1	17.84 ± 3.76	17.87 ± 3.70
G028.14−00.00	98.72	3.96 ± 0.21	3.678 ± 0.762	0.315 ± 0.003	0.093 ± 0.001	1.2	1.0	13.29 ± 3.64	14.86 ± 3.97
G028.30−00.38	85.55	4.71 ± 0.26	4.379 ± 0.897	0.185 ± 0.002	0.101 ± 0.001	1.1	1.1	20.14 ± 4.22	21.64 ± 4.55
G028.39+00.08	78.01	4.83 ± 0.17	8.785 ± 1.797	0.320 ± 0.003	0.201 ± 0.002	1.2	1.1	22.33 ± 4.37	21.50 ± 4.19
G028.83−00.25	87.19	4.50 ± 0.48	7.885 ± 1.620	0.420 ± 0.004	0.187 ± 0.002	1.2	1.1	17.23 ± 3.37	19.00 ± 3.72
G030.19−00.16	103.10	4.74 ± 0.11	3.792 ± 0.777	0.199 ± 0.002	0.087 ± 0.001	1.1	1.0	13.89 ± 3.24	17.04 ± 3.72
G030.22−00.18	103.90	5.43 ± 0.26	2.214 ± 0.449	0.135 ± 0.001	0.047 ± 0.000	1.1	1.0	13.01 ± 3.94	32.85 ± 8.06
G030.41−00.23	105.10	5.17 ± 0.20	2.345 ± 0.478	0.127 ± 0.001	0.052 ± 0.001	1.1	1.0	23.09 ± 5.08	23.79 ± 5.42
G030.70−00.06	89.94	4.20 ± 0.10	11.017 ± 2.274	0.495 ± 0.005	0.270 ± 0.003	1.3	1.1	21.56 ± 4.24	22.96 ± 4.51
G030.74−00.04	91.83	5.76 ± 0.36	9.418 ± 1.905	0.437 ± 0.004	0.195 ± 0.002	1.2	1.1	19.79 ± 3.82	22.80 ± 4.39
G030.78+00.20	81.94	4.19 ± 0.05	6.244 ± 1.289	0.342 ± 0.003	0.153 ± 0.002	1.2	1.1	15.01 ± 3.26	18.83 ± 3.91
G030.81−00.05	98.90	5.73 ± 0.24	9.272 ± 1.876	0.337 ± 0.003	0.193 ± 0.002	1.2	1.1	24.57 ± 4.74	25.88 ± 4.98
G031.24−00.11	21.08	7.48 ± 2.00	3.306 ± 0.658	0.135 ± 0.001	0.059 ± 0.001	1.1	1.0	24.86 ± 5.18	22.93 ± 4.53
G032.74−00.07	37.21	4.55 ± 0.23	5.966 ± 1.225	0.254 ± 0.003	0.140 ± 0.001	1.1	1.1	19.81 ± 3.89	22.14 ± 4.33
G032.79+00.19	14.15	5.26 ± 1.57	3.793 ± 0.772	0.192 ± 0.002	0.083 ± 0.001	1.1	1.0	19.77 ± 3.83	21.92 ± 4.25
G034.41+00.23	57.73	5.99 ± 0.06	4.573 ± 0.923	0.211 ± 0.002	0.093 ± 0.001	1.1	1.0	21.42 ± 4.13	24.13 ± 4.64
G034.79−01.38	45.95	6.21 ± 0.09	13.430 ± 2.704	0.625 ± 0.006	0.267 ± 0.003	1.3	1.1	18.70 ± 3.60	22.32 ± 4.30

Table A.2. continued.

Source	V_{LSR}	R_{GC}	Optical depth $J=2$-1			Corrections for optical depth		$^{32}S/^{34}S$	
	(km s^{-1})	(kpc)	CS	C^{34}S	^{13}CS	f_1	f_2	2-1	3-2
G035.79−00.17	61.48	5.27 ± 0.43	4.295 ± 0.874	0.227 ± 0.002	0.094 ± 0.001	1.1	1.0	18.58 ± 4.89	23.95 ± 5.17
G036.11+00.55	76.15	5.45 ± 0.43	9.082 ± 1.844	0.416 ± 0.004	0.194 ± 0.002	1.2	1.1	16.78 ± 4.34	23.71 ± 5.64
G037.42+01.51	43.87	6.78 ± 0.05	2.584 ± 0.517	0.118 ± 0.001	0.049 ± 0.000	1.1	1.0	21.29 ± 4.06	23.33 ± 4.45
G038.11−00.22	83.12	5.55 ± 0.25	5.925 ± 1.201	0.277 ± 0.003	0.125 ± 0.001	1.1	1.1	21.63 ± 5.23	21.60 ± 5.00
G040.28−00.21	73.65	6.02 ± 0.10	6.889 ± 1.390	0.348 ± 0.003	0.139 ± 0.001	1.2	1.1	19.54 ± 4.06	21.71 ± 4.32
G040.42+00.70	12.50	8.46 ± 1.67	2.892 ± 0.571	0.194 ± 0.196	0.047 ± 0.000	1.1	1.0	16.43 ± 6.11	28.68 ± 6.15
G040.62−00.13	32.84	8.24 ± 2.50	2.458 ± 0.486	0.108 ± 0.001	0.041 ± 0.000	1.1	1.0	25.95 ± 5.94	25.00 ± 6.17
G043.03−00.45	57.54	5.84 ± 0.33	5.524 ± 1.116	0.229 ± 0.002	0.114 ± 0.001	1.1	1.1	22.25 ± 4.63	22.26 ± 4.50
G045.45+00.06	58.08	6.41 ± 0.50	4.570 ± 0.918	0.211 ± 0.002	0.089 ± 0.001	1.1	1.0	24.64 ± 4.99	25.31 ± 5.02
G045.49+00.12	60.59	5.96 ± 0.24	5.985 ± 1.208	0.174 ± 0.002	0.122 ± 0.001	1.1	1.1	14.53 ± 3.84	···
G045.80−00.35	59.12	6.08 ± 0.32	6.549 ± 1.320	0.300 ± 0.003	0.132 ± 0.001	1.2	1.1	16.95 ± 3.98	22.31 ± 4.84
G048.99−00.29	68.01	6.18 ± 0.02	2.061 ± 0.415	0.106 ± 0.001	0.041 ± 0.000	1.1	1.0	20.75 ± 4.21	21.64 ± 4.32
G049.59−00.24	57.06	6.27 ± 0.02	2.366 ± 0.476	0.157 ± 0.158	0.047 ± 0.000	1.1	1.0	13.99 ± 5.57	18.91 ± 5.12
W51-IRS2	61.09	6.22 ± 0.06	2.989 ± 0.602	0.141 ± 0.001	0.059 ± 0.001	1.1	1.0	21.84 ± 4.18	23.81 ± 4.56
G054.10−00.08	38.45	6.64 ± 0.04	4.402 ± 0.883	0.198 ± 0.002	0.084 ± 0.001	1.1	1.0	19.72 ± 4.24	21.14 ± 4.46
G058.77+00.64	32.36	7.05 ± 0.06	2.964 ± 0.592	0.150 ± 0.002	0.055 ± 0.001	1.1	1.0	22.44 ± 5.12	21.72 ± 4.74
G059.83+00.67	34.70	7.07 ± 0.00	3.534 ± 0.706	0.176 ± 0.002	0.065 ± 0.001	1.1	1.0	18.31 ± 4.32	22.08 ± 4.58
G060.57−00.18	4.84	8.29 ± 0.52	4.541 ± 0.898	0.140 ± 0.001	0.075 ± 0.001	1.1	1.0	23.60 ± 9.45	42.80 ± 12.23
G071.31+00.82	9.00	8.02 ± 0.16	4.412 ± 0.874	0.195 ± 0.002	0.075 ± 0.001	1.1	1.0	17.34 ± 3.80	22.69 ± 4.66
G071.52−00.38	10.65	7.82 ± 0.04	2.923 ± 0.580	0.117 ± 0.001	0.050 ± 0.001	1.1	1.0	14.12 ± 4.52	···
G073.65+00.19	-73.62	13.54 ± 2.90	3.881 ± 0.747	0.141 ± 0.001	0.045 ± 0.000	1.1	1.0	28.94 ± 6.82	31.38 ± 6.33
G075.29+01.32	-56.64	10.69 ± 0.58	3.360 ± 0.655	0.143 ± 0.001	0.047 ± 0.000	1.1	1.0	25.97 ± 5.10	23.37 ± 4.50
DR21	-2.50	8.10 ± 0.00	6.458 ± 1.278	0.285 ± 0.003	0.108 ± 0.001	1.1	1.1	21.92 ± 4.12	24.85 ± 4.67
G090.92+01.48	-71.92	10.13 ± 0.63	3.569 ± 0.698	0.139 ± 0.001	0.052 ± 0.001	1.1	1.0	22.08 ± 4.36	26.30 ± 5.12
G097.53+03.18	-71.18	11.81 ± 0.70	4.859 ± 0.942	0.181 ± 0.002	0.063 ± 0.001	1.1	1.0	27.98 ± 5.21	28.27 ± 5.24
G108.20+00.58	-50.70	10.43 ± 0.48	1.816 ± 0.355	0.109 ± 0.110	0.026 ± 0.000	1.1	1.0	21.62 ± 5.66	21.84 ± 6.25
G109.87+02.11	-10.88	8.49 ± 0.01	2.944 ± 0.582	0.141 ± 0.001	0.048 ± 0.000	1.1	1.0	20.98 ± 3.97	22.24 ± 4.24
NGC7538	-57.12	9.47 ± 0.07	3.293 ± 0.646	0.136 ± 0.001	0.050 ± 0.000	1.1	1.0	23.92 ± 4.46	25.81 ± 4.81

Notes. Velocities were obtained from measurements of C^{34}S, see Table A.3. The $^{32}S/^{34}S$ isotope ratios from the $J=2$-1 transition are corrected for the optical depth effect and the ones in the 3-2 line without corrections of opacity.

Table A.3. Line Parameters derived from Gaussian-fitting.

Source	transitions	Time (mins)	rms (mK)	V_{LSR} (km s^{-1})	FWHM (km s^{-1})	$\int T_{MB}dv$ (K km s^{-1})	T_{MB} (K)
WB89-380	CS (2-1)	533	3.48	-86.48 ± 0.00	3.66 ± 0.00	4.87 ± 0.00	1.250
	C^{33}S (2-1)	533	3.16	-85.86 ± 0.12	3.60 ± 0.28	0.10 ± 0.01	0.026
	C^{34}S (2-1)	533	2.91	-86.62 ± 0.02	3.24 ± 0.04	0.57 ± 0.01	0.166
	C^{36}S (2-1)	533	3.38	···	···	···	···
	^{13}CS (2-1)	533	3.57	-86.49 ± 0.08	2.99 ± 0.16	0.14 ± 0.01	0.045
	^{13}C^{33}S (2-1)	533	3.74	···	···	···	···
	^{13}C^{34}S (2-1)	533	3.57	···	···	···	···
	C^{33}S (3-2)	533	7.82	-86.33 ± 0.15	3.87 ± 0.43	0.20 ± 0.02	0.049
	C^{34}S (3-2)	533	5.97	-86.38 ± 0.02	3.17 ± 0.05	0.74 ± 0.01	0.221
	C^{36}S (3-2)	267	8.16	···	···	···	···
	^{13}CS (3-2)	533	5.63	-86.12 ± 0.05	2.56 ± 0.14	0.21 ± 0.01	0.077
WB89-391	CS (2-1)	649	3.63	-85.99 ± 0.00	1.51 ± 0.01	1.69 ± 0.01	1.050
	C^{33}S (2-1)	649	3.90	-85.12 ± 0.05	1.03 ± 0.15	0.04 ± 0.00	0.039
	C^{34}S (2-1)	649	3.88	-85.93 ± 0.01	1.18 ± 0.03	0.27 ± 0.00	0.212
	C^{36}S (2-1)	649	3.04	···	···	···	···
	^{13}CS (2-1)	649	2.96	-85.85 ± 0.03	1.24 ± 0.08	0.08 ± 0.00	0.060
	^{13}C^{33}S (2-1)	649	2.88	···	···	···	···
	^{13}C^{34}S (2-1)	649	3.07	···	···	···	···
	C^{33}S (3-2)	649	5.48	-85.71 ± 0.10	2.19 ± 0.32	0.09 ± 0.01	0.039
	C^{34}S (3-2)	649	4.72	-85.92 ± 0.01	1.22 ± 0.02	0.33 ± 0.01	0.258
	C^{36}S (3-2)	324	5.43	···	···	···	···
	^{13}CS (3-2)	649	4.71	-85.67 ± 0.03	1.12 ± 0.08	0.08 ± 0.00	0.066
W3OH	CS (2-1)	278	14.27	-47.52 ± 0.00	5.96 ± 0.01	54.93 ± 0.04	8.660

Table A.3. continued.

Source	transitions	Time (mins)	rms (mK)	V_{LSR} (km s^{-1})	FWHM (km s^{-1})	$\int T_{MB} dv$ (K km s^{-1})	T_{MB} (K)
	$C^{33}S$ (2-1)	278	4.39	-56.14 ± 0.60	5.43 ± 0.60	0.70 ± 0.07	0.120
	$C^{33}S$ (2-1)	278	4.39	-46.23 ± 0.60	4.41 ± 0.60	2.42 ± 0.07	0.517
	$C^{33}S$ (2-1)	278	4.39	-38.83 ± 0.60	3.90 ± 0.60	0.37 ± 0.07	0.088
	$C^{33}S$ (2-1)	278	4.39	-28.56 ± 0.60	4.70 ± 0.60	0.11 ± 0.07	0.022
	$C^{34}S$ (2-1)	278	12.81	-46.96 ± 0.01	4.43 ± 0.02	10.95 ± 0.03	2.320
	$C^{36}S$ (2-1)	278	4.48	-54.05 ± 0.48	5.82 ± 1.42	0.08 ± 0.01	0.013
	$C^{36}S$ (2-1)	278	4.48	-45.87 ± 0.31	4.51 ± 0.74	0.09 ± 0.01	0.018
	^{13}CS (2-1)	278	4.98	-46.80 ± 0.01	4.21 ± 0.01	4.69 ± 0.01	1.040
	$^{13}C^{33}S$ (2-1)	278	5.31	...	...	...	...
	$^{13}C^{34}S$ (2-1)	278	4.28	-46.57 ± 0.09	3.19 ± 0.20	0.17 ± 0.01	0.049
	$C^{33}S$ (3-2)	278	8.55	-47.09 ± 0.40	6.14 ± 0.40	7.01 ± 0.12	1.070
	$C^{34}S$ (3-2)	278	8.27	-46.93 ± 0.00	5.07 ± 0.01	18.14 ± 0.02	3.360
	$C^{36}S$ (3-2)	139	9.38	-47.21 ± 0.42	4.54 ± 0.89	0.12 ± 0.02	0.025
	$C^{36}S$ (3-2)	139	9.38	-2.40 ± 0.18	3.52 ± 0.47	0.18 ± 0.02	0.047
	^{13}CS (3-2)	278	8.98	-46.79 ± 0.01	4.83 ± 0.01	8.55 ± 0.02	1.660
Orion-KL	CS (2-1)	93	211.00	6.85 ± 0.10	10.30 ± 0.34	71.80 ± 4.05	6.550
	CS (2-1)	93	211.00	8.55 ± 0.01	3.24 ± 0.04	70.49 ± 1.37	20.400
	CS (2-1)	93	211.00	7.77 ± 0.18	26.88 ± 0.61	145.10 ± 4.17	5.070
	$C^{33}S$ (2-1)	93	15.27	-0.19 ± 0.01	10.07 ± 0.31	2.65 ± 0.07	0.247
	$C^{33}S$ (2-1)	93	15.27	8.62 ± 0.02	4.25 ± 0.05	4.42 ± 0.04	0.976
	$C^{33}S$ (2-1)	93	15.27	15.54 ± 0.11	5.30 ± 0.22	1.33 ± 0.05	0.235
	$C^{33}S$ (2-1)	93	15.27	26.87 ± 0.14	11.77 ± 0.62	1.94 ± 0.08	0.155
	$C^{34}S$ (2-1)	93	52.04	7.16 ± 0.12	7.33 ± 0.48	10.92 ± 0.78	1.400
	$C^{34}S$ (2-1)	93	52.04	8.24 ± 0.02	2.86 ± 0.07	9.68 ± 0.48	3.180
	$C^{34}S$ (2-1)	93	52.04	6.46 ± 0.53	20.45 ± 2.35	8.03 ± 0.95	0.369
	$C^{36}S$ (2-1)	93	14.10	9.77 ± 1.05	9.26 ± 6.38	0.34 ± 0.17	0.035
	^{13}CS (2-1)	93	18.79	3.04 ± 0.63	4.93 ± 0.63	1.74 ± 0.24	0.332
	^{13}CS (2-1)	93	18.79	8.16 ± 0.63	4.03 ± 0.63	8.12 ± 0.24	1.890
	^{13}CS (2-1)	93	18.79	16.52 ± 0.63	9.52 ± 0.63	1.81 ± 0.24	0.178
	$^{13}C^{33}S$ (2-1)	93	9.64	7.29 ± 0.69	4.40 ± 1.01	0.08 ± 0.02	0.016
	$^{13}C^{34}S$ (2-1)	93	13.44	2.60 ± 0.05	10.85 ± 1.85	0.36 ± 0.06	0.031
	$^{13}C^{34}S$ (2-1)	93	13.44	8.15 ± 0.07	2.57 ± 0.45	0.21 ± 0.03	0.077
	$C^{33}S$ (3-2)	93	200.00	7.43 ± 0.10	6.75 ± 0.33	20.36 ± 0.74	2.830
	$C^{33}S$ (3-2)	93	200.00	17.83 ± 0.60	8.33 ± 1.62	4.63 ± 0.75	0.522
	$C^{34}S$ (3-2)	93	57.74	3.07 ± 0.00	9.73 ± 0.13	19.85 ± 0.02	1.920
	$C^{34}S$ (3-2)	93	57.74	8.04 ± 0.00	3.73 ± 0.02	32.34 ± 0.16	8.140
	$C^{34}S$ (3-2)	93	57.74	11.96 ± 0.00	13.80 ± 0.29	16.24 ± 0.28	1.110
	$C^{36}S$ (3-2)	46	26.24	8.75 ± 0.27	7.18 ± 0.60	0.90 ± 0.07	0.118
	^{13}CS (3-2)	93	42.87	-16.75 ± 0.12	10.40 ± 0.40	5.93 ± 0.16	0.536
	^{13}CS (3-2)	93	42.87	-4.70 ± 0.15	4.38 ± 0.40	1.44 ± 0.13	0.310
	^{13}CS (3-2)	93	42.87	6.65 ± 0.07	4.33 ± 0.35	4.28 ± 0.41	0.929
	^{13}CS (3-2)	93	42.87	8.33 ± 0.02	2.69 ± 0.04	8.36 ± 0.18	2.920
	^{13}CS (3-2)	93	42.87	7.61 ± 0.10	12.33 ± 0.36	15.03 ± 0.50	1.150
PointC1	CS (2-1)	220	8.22	-73.99 ± 0.45	32.71 ± 0.55	14.65 ± 0.41	0.421
	CS (2-1)	220	8.22	-62.26 ± 0.04	12.45 ± 0.19	7.78 ± 0.29	0.587
	CS (2-1)	220	8.22	-44.07 ± 0.13	15.77 ± 0.67	4.82 ± 0.46	0.287
	CS (2-1)	220	8.22	-29.16 ± 0.50	56.53 ± 3.09	2.66 ± 1.17	0.044
	CS (2-1)	220	8.22	-11.64 ± 0.43	25.80 ± 1.04	6.38 ± 0.69	0.232
	$C^{33}S$ (2-1)	220	9.72	...	...	...	...
	$C^{34}S$ (2-1)	220	11.39	-64.18 ± 0.98	39.08 ± 2.90	1.64 ± 0.09	0.039
	$C^{36}S$ (2-1)	220	9.08	...	...	...	...
	^{13}CS (2-1)	220	6.41	-59.58 ± 1.58	75.58 ± 4.37	1.72 ± 0.07	0.021
	$^{13}C^{33}S$ (2-1)	220	6.89	...	...	...	...
	$^{13}C^{34}S$ (2-1)	220	9.31	...	...	...	...
	$C^{33}S$ (3-2)	220	24.68	...	...	...	...
	$C^{34}S$ (3-2)	220	17.27	...	...	...	...
	$C^{36}S$ (3-2)	110	30.90	...	...	...	...

Table A.3. continued.

Source	transitions	Time (mins)	rms (mK)	V_{LSR} (km s^{-1})	FWHM (km s^{-1})	$\int T_{MB} dv$ (K km s^{-1})	T_{MB} (K)
	^{13}CS (3-2)	220	15.08	-38.94 ± 0.12	0.59 ± 0.36	-0.03 ± 0.01	-0.052
G359.13+00.03	CS (2-1)	4	54.36	-17.85 ± 0.70	35.51 ± 1.60	12.47 ± 0.48	0.330
	CS (2-1)	4	54.36	-1.69 ± 0.05	3.97 ± 0.14	4.57 ± 0.18	1.080
	CS (2-1)	4	54.36	34.69 ± 0.28	2.48 ± 0.58	0.49 ± 0.15	0.185
	CS (2-1)	4	54.36	39.26 ± 0.99	12.71 ± 1.91	1.83 ± 0.28	0.135
	C^{33}S (2-1)	4	53.40	...	...	...	...
	C^{34}S (2-1)	4	53.56	-2.03 ± 0.16	4.24 ± 0.40	1.69 ± 0.13	0.374
	C^{36}S (2-1)	4	52.77	...	...	...	...
	^{13}CS (2-1)	4	53.20	-1.68 ± 0.36	4.62 ± 1.23	0.88 ± 0.16	0.178
	^{13}C^{33}S (2-1)	4	54.66	...	...	...	...
	^{13}C^{34}S (2-1)	4	60.09	...	...	...	...
	C^{33}S (3-2)	4	97.29	...	...	...	...
	C^{34}S (3-2)	4	93.38	-2.11 ± 0.41	5.97 ± 0.93	1.63 ± 0.22	0.256
	C^{36}S (3-2)	4	87.02	...	...	...	...
	^{13}CS (3-2)	4	86.80	-1.79 ± 0.69	5.05 ± 1.40	0.70 ± 0.18	0.131
SgrC	CS (2-1)	93	13.58	-43.23 ± 0.15	19.73 ± 0.37	26.15 ± 0.41	1.245
	CS (2-1)	93	13.58	69.62 ± 0.08	13.33 ± 0.20	27.66 ± 0.34	1.949
	C^{33}S (2-1)	93	14.36	71.61 ± 0.91	11.58 ± 1.81	0.37 ± 0.06	0.0304
	C^{34}S (2-1)	93	13.79	-44.31 ± 0.26	17.73 ± 0.72	2.13 ± 0.07	0.113
	C^{34}S (2-1)	93	13.79	70.06 ± 0.07	10.46 ± 0.39	1.78 ± 0.05	0.160
	C^{36}S (2-1)	93	13.50	...	...	...	...
	^{13}CS (2-1)	93	13.88	-45.39 ± 0.61	20.76 ± 1.63	1.26 ± 0.08	0.057
	^{13}CS (2-1)	93	13.88	70.48 ± 0.29	12.50 ± 0.79	1.24 ± 0.06	0.093
	^{13}C^{33}S (2-1)	93	12.08	...	...	...	...
	^{13}C^{34}S (2-1)	93	71.57	...	...	...	...
	C^{33}S (3-2)	93	33.18	...	...	...	...
	C^{34}S (3-2)	93	23.52	-42.80 ± 1.32	14.15 ± 2.97	0.66 ± 0.12	0.044
	C^{34}S (3-2)	93	23.52	70.45 ± 0.40	7.85 ± 0.94	0.88 ± 0.09	0.106
	C^{36}S (3-2)	46	41.94	...	...	...	...
	^{13}CS (3-2)	93	26.63	71.41 ± 0.77	13.59 ± 1.83	0.85 ± 0.10	0.059
+20 km s^{-1} cloud	CS (2-1)	127	24.41	-7.44 ± 0.00	14.73 ± 0.24	12.62 ± 0.17	0.805
	CS (2-1)	127	24.41	12.40 ± 0.02	49.77 ± 2.10	24.57 ± 0.13	0.464
	CS (2-1)	127	24.41	2.02 ± 0.03	11.10 ± 0.07	33.78 ± 0.59	2.860
	CS (2-1)	127	24.41	12.50 ± 0.12	22.90 ± 0.16	57.64 ± 0.43	2.370
	CS (2-1)	127	24.41	45.81 ± 0.06	11.49 ± 0.39	11.33 ± 0.30	0.927
	C^{33}S (2-1)	127	12.36	6.80 ± 0.27	24.78 ± 0.78	3.19 ± 0.08	0.121
	C^{34}S (2-1)	127	35.93	6.80 ± 0.12	19.78 ± 0.28	15.61 ± 0.19	0.741
	C^{36}S (2-1)	127	10.60	3.11 ± 0.74	10.03 ± 2.20	0.26 ± 0.04	0.025
	^{13}CS (2-1)	127	22.15	7.04 ± 0.10	18.91 ± 0.23	10.57 ± 0.11	0.525
	^{13}C^{33}S (2-1)	127	11.40	...	...	...	...
	^{13}C^{34}S (2-1)	127	10.64	7.46 ± 1.02	19.66 ± 2.43	0.53 ± 0.06	0.025
	C^{33}S (3-2)	127	25.06	6.14 ± 0.55	20.12 ± 1.43	1.93 ± 0.11	0.090
	C^{34}S (3-2)	127	29.38	6.03 ± 0.11	18.92 ± 0.26	10.08 ± 0.12	0.500
	C^{36}S (3-2)	64	32.62	...	...	...	...
	^{13}CS (3-2)	127	25.95	6.20 ± 0.15	18.77 ± 0.35	6.74 ± 0.11	0.338
G359.61−00.24	CS (2-1)	85	193.00	19.68 ± 0.03	6.95 ± 0.11	59.20 ± 0.67	8.000
	C^{33}S (2-1)	85	12.08	10.81 ± 0.60	6.19 ± 0.60	0.36 ± 0.03	0.054
	C^{33}S (2-1)	85	12.08	19.90 ± 0.60	3.17 ± 0.60	0.90 ± 0.03	0.266
	C^{33}S (2-1)	85	12.08	26.45 ± 0.60	9.53 ± 0.60	0.56 ± 0.03	0.056
	C^{33}S (2-1)	85	12.08	38.12 ± 0.60	4.43 ± 0.60	0.13 ± 0.03	0.028
	C^{34}S (2-1)	85	10.26	19.33 ± 0.03	4.15 ± 0.08	7.08 ± 0.10	1.603
	C^{36}S (2-1)	85	11.78	...	...	...	...
	^{13}CS (2-1)	85	11.80	19.47 ± 0.03	3.92 ± 0.10	2.95 ± 0.06	0.708
	^{13}C^{33}S (2-1)	85	9.62	...	...	...	...
	^{13}C^{34}S (2-1)	85	10.75	19.75 ± 0.69	5.76 ± 2.27	0.18 ± 0.05	0.029
	C^{33}S (3-2)	85	21.73	12.36 ± 1.05	4.44 ± 1.40	0.13 ± 0.14	0.028
	C^{33}S (3-2)	85	21.73	19.08 ± 0.09	3.30 ± 0.28	1.01 ± 0.15	0.288

Table A.3. continued.

Source	transitions	Time (mins)	rms (mK)	V_{LSR} (km s^{-1})	FWHM (km s^{-1})	$\int T_{MB}dv$ (K km s^{-1})	T_{MB} (K)
	$C^{33}S$ (3-2)	85	21.73	20.69 ± 0.93	10.44 ± 1.21	1.55 ± 0.30	0.140
	$C^{34}S$ (3-2)	85	43.68	19.43 ± 0.02	4.69 ± 0.07	8.97 ± 0.10	1.800
	$C^{36}S$ (3-2)	85	19.08	...	...	...	...
	^{13}CS (3-2)	85	30.32	19.53 ± 0.03	4.43 ± 0.10	4.13 ± 0.07	0.876
SgrA	CS (2-1)	89	329.42	...	...	...	...
	$C^{33}S$ (2-1)	89	14.66	...	...	...	...
	$C^{34}S$ (2-1)	89	23.74	...	...	...	...
	$C^{36}S$ (2-1)	89	14.97	...	...	...	...
	^{13}CS (2-1)	89	16.34	53.44 ± 0.87	16.50 ± 2.30	0.79 ± 0.11	0.045
	$^{13}C^{33}S$ (2-1)	89	13.09	...	...	...	...
	$^{13}C^{34}S$ (2-1)	89	25.80	...	...	...	...
	$C^{33}S$ (3-2)	89	22.66	...	...	...	...
	$C^{34}S$ (3-2)	89	31.59	...	...	...	...
	$C^{36}S$ (3-2)	89	23.98	...	...	...	...
	^{13}CS (3-2)	89	19.32	...	...	...	...
+50 km s^{-1} cloud	CS (2-1)	70	142.00	48.03 ± 0.07	33.37 ± 0.14	234.30 ± 0.92	6.600
	$C^{33}S$ (2-1)	70	14.22	47.30 ± 0.15	24.29 ± 0.35	6.64 ± 0.08	0.257
	$C^{34}S$ (2-1)	70	32.94	46.78 ± 0.07	23.46 ± 0.16	31.86 ± 0.19	1.280
	$C^{36}S$ (2-1)	70	9.40	45.11 ± 1.29	27.32 ± 3.07	0.86 ± 0.08	0.029
	$C^{36}S$ (2-1)	70	9.40	103.30 ± 1.71	31.52 ± 4.20	0.80 ± 0.09	0.024
	^{13}CS (2-1)	70	17.63	47.36 ± 0.05	22.32 ± 0.11	22.54 ± 0.10	0.949
	$^{13}C^{33}S$ (2-1)	70	13.09	...	...	...	...
	$^{13}C^{34}S$ (2-1)	70	20.17	47.40 ± 0.84	17.96 ± 1.95	1.10 ± 0.10	0.058
	$C^{33}S$ (3-2)	70	33.99	46.00 ± 0.33	21.28 ± 0.79	4.79 ± 0.15	0.212
	$C^{34}S$ (3-2)	70	28.13	45.98 ± 0.06	22.13 ± 0.14	21.89 ± 0.12	0.929
	$C^{36}S$ (3-2)	35	38.80	...	...	...	...
	^{13}CS (3-2)	70	25.86	46.42 ± 0.08	21.45 ± 0.19	15.21 ± 0.12	0.666
G359.93−00.14	CS (2-1)	4	89.65	-22.98 ± 0.60	10.53 ± 0.60	-13.39 ± 0.19	-1.190
	CS (2-1)	4	89.65	-9.21 ± 0.60	6.14 ± 0.60	1.89 ± 0.19	0.289
	CS (2-1)	4	89.65	14.54 ± 0.60	22.28 ± 0.60	-10.33 ± 0.19	-0.435
	CS (2-1)	4	89.65	26.60 ± 0.60	10.11 ± 0.60	-3.46 ± 0.19	-0.322
	CS (2-1)	4	89.65	55.53 ± 0.60	5.87 ± 0.60	2.14 ± 0.19	0.343
	$C^{33}S$ (2-1)	4	50.50	...	...	...	...
	$C^{34}S$ (2-1)	4	52.33	-23.43 ± 0.79	11.80 ± 2.00	-1.56 ± 0.22	-0.125
	$C^{36}S$ (2-1)	4	49.02	...	...	...	...
	^{13}CS (2-1)	4	62.40	-23.82 ± 0.90	9.05 ± 2.71	-1.13 ± 0.25	-0.117
	$^{13}C^{33}S$ (2-1)	4	49.20	...	...	...	...
	$^{13}C^{34}S$ (2-1)	4	55.82	...	...	...	...
	$C^{33}S$ (3-2)	4	94.85	...	...	...	...
	$C^{34}S$ (3-2)	4	87.77	...	...	...	...
	$C^{36}S$ (3-2)	4	86.19	...	...	...	...
	^{13}CS (3-2)	4	80.79	...	...	...	...
G000.37+00.03	CS (2-1)	4	94.02	32.68 ± 0.23	20.20 ± 0.39	37.67 ± 0.87	1.750
	CS (2-1)	4	94.02	40.01 ± 0.12	5.70 ± 0.35	7.37 ± 0.62	1.210
	$C^{33}S$ (2-1)	4	54.64	...	...	...	...
	$C^{34}S$ (2-1)	4	47.64	29.80 ± 0.75	11.44 ± 2.40	2.17 ± 0.36	0.178
	$C^{34}S$ (2-1)	4	47.64	39.98 ± 0.30	6.50 ± 0.62	2.14 ± 0.29	0.309
	$C^{36}S$ (2-1)	4	50.95	...	...	...	...
	^{13}CS (2-1)	4	48.83	28.36 ± 0.72	9.74 ± 2.15	1.27 ± 0.21	0.123
	^{13}CS (2-1)	4	48.83	40.38 ± 0.24	5.33 ± 0.62	1.58 ± 0.16	0.279
	$^{13}C^{33}S$ (2-1)	4	45.90	...	...	...	...
	$^{13}C^{34}S$ (2-1)	4	52.56	...	...	...	...
	$C^{33}S$ (3-2)	4	95.46	...	...	...	...
	$C^{34}S$ (3-2)	4	83.99	39.48 ± 0.26	8.20 ± 1.00	3.56 ± 0.29	0.407
	$C^{36}S$ (3-2)	4	85.99	...	...	...	...
	^{13}CS (3-2)	4	77.88	39.42 ± 0.53	9.38 ± 1.88	2.30 ± 0.30	0.231
G0.25	CS (2-1)	58	43.20	8.80 ± 0.55	33.38 ± 0.69	54.74 ± 1.98	1.540

Table A.3. continued.

Source	transitions	Time (mins)	rms (mK)	V_{LSR} (km s^{-1})	FWHM (km s^{-1})	$\int T_{MB} dv$ (K km s^{-1})	T_{MB} (K)
	CS (2-1)	58	43.20	28.63 ± 0.84	21.50 ± 1.07	25.08 ± 2.26	1.100
	CS (2-1)	58	43.20	41.39 ± 0.12	13.64 ± 0.25	31.41 ± 1.90	2.160
	CS (2-1)	58	43.20	73.04 ± 0.16	13.77 ± 0.41	8.44 ± 0.20	0.576
	$C^{33}S$ (2-1)	58	14.83	22.39 ± 1.62	42.35 ± 2.82	1.47 ± 0.10	0.033
	$C^{34}S$ (2-1)	58	16.39	5.33 ± 0.61	23.07 ± 1.31	4.69 ± 0.28	0.191
	$C^{34}S$ (2-1)	58	16.39	27.74 ± 1.36	18.61 ± 0.69	2.76 ± 0.06	0.139
	$C^{34}S$ (2-1)	58	16.39	39.70 ± 0.19	11.01 ± 0.43	2.99 ± 0.19	0.255
	$C^{34}S$ (2-1)	58	16.39	70.84 ± 0.70	7.68 ± 1.87	0.35 ± 0.06	0.042
	$C^{36}S$ (2-1)	58	14.79	...	...	...	...
	^{13}CS (2-1)	58	15.59	12.74 ± 0.92	32.71 ± 1.92	4.05 ± 0.22	0.116
	^{13}CS (2-1)	58	15.59	38.57 ± 0.30	14.20 ± 0.77	2.56 ± 0.19	0.169
	$^{13}C^{33}S$ (2-1)	58	13.54	...	...	...	...
	$^{13}C^{34}S$ (2-1)	58	21.89	...	...	...	...
	$C^{33}S$ (3-2)	58	32.44	...	...	...	...
	$C^{34}S$ (3-2)	58	27.20	11.30 ± 0.96	33.43 ± 2.15	3.40 ± 0.18	0.096
	$C^{34}S$ (3-2)	58	27.20	39.63 ± 0.24	10.40 ± 0.68	1.94 ± 0.13	0.175
	$C^{36}S$ (3-2)	29	41.12	...	...	...	...
	^{13}CS (3-2)	58	25.47	9.84 ± 1.46	36.51 ± 4.07	2.45 ± 0.22	0.063
	^{13}CS (3-2)	58	25.47	39.13 ± 0.42	11.57 ± 1.08	1.38 ± 0.15	0.112
CloudD	CS (2-1)	46	22.39	-92.21 ± 0.60	14.08 ± 0.60	2.60 ± 0.28	0.173
	CS (2-1)	46	22.39	-43.85 ± 0.60	48.19 ± 0.60	5.91 ± 0.28	0.115
	CS (2-1)	46	22.39	-3.36 ± 0.60	28.68 ± 0.60	16.70 ± 0.28	0.547
	CS (2-1)	46	22.39	21.57 ± 0.60	24.87 ± 0.60	35.98 ± 0.28	1.360
	CS (2-1)	46	22.39	42.97 ± 0.60	14.96 ± 0.60	19.35 ± 0.28	1.220
	$C^{33}S$ (2-1)	46	17.30	...	...	...	...
	$C^{34}S$ (2-1)	46	14.98	23.32 ± 0.55	50.74 ± 1.22	6.14 ± 0.13	0.114
	$C^{36}S$ (2-1)	46	14.89	...	...	...	...
	^{13}CS (2-1)	46	15.01	24.98 ± 0.80	46.20 ± 1.76	3.69 ± 0.12	0.075
	$^{13}C^{33}S$ (2-1)	46	14.45	...	...	...	...
	$^{13}C^{34}S$ (2-1)	46	14.45	...	...	...	...
	$C^{33}S$ (3-2)	46	28.79	...	...	...	...
	$C^{34}S$ (3-2)	46	17.46	23.99 ± 1.81	57.06 ± 4.41	2.85 ± 0.18	0.047
	$C^{36}S$ (3-2)	23	37.14	...	...	...	...
	^{13}CS (3-2)	46	26.26	...	...	...	...
G000.31−00.20	CS (2-1)	4	108.00	18.42 ± 0.01	3.17 ± 0.03	25.77 ± 0.24	7.640
	CS (2-1)	4	108.00	30.80 ± 0.12	10.02 ± 0.25	-15.68 ± 0.38	-1.470
	$C^{33}S$ (2-1)	4	49.90	19.25 ± 0.28	3.58 ± 0.53	0.69 ± 0.10	0.182
	$C^{34}S$ (2-1)	4	61.48	18.43 ± 0.04	2.53 ± 0.12	3.21 ± 0.12	1.190
	$C^{36}S$ (2-1)	4	46.44	...	...	...	...
	^{13}CS (2-1)	4	59.74	18.47 ± 0.10	2.20 ± 0.29	1.16 ± 0.12	0.493
	$^{13}C^{33}S$ (2-1)	4	48.90	...	...	...	...
	$^{13}C^{34}S$ (2-1)	4	46.35	...	...	...	...
	$C^{33}S$ (3-2)	4	120.22	...	...	...	...
	$C^{34}S$ (3-2)	4	78.47	18.18 ± 0.04	2.76 ± 0.12	3.67 ± 0.13	1.250
	$C^{36}S$ (3-2)	4	87.17	...	...	...	...
	^{13}CS (3-2)	4	79.58	18.25 ± 0.13	2.57 ± 0.32	1.28 ± 0.13	0.467
SgrB2	CS (2-1)	93	443.00	50.37 ± 0.10	10.17 ± 0.28	105.30 ± 4.16	9.720
	CS (2-1)	93	443.00	66.97 ± 4.76	23.11 ± 3.31	-54.59 ± 19.10	-2.220
	CS (2-1)	93	443.00	84.07 ± 1.03	19.32 ± 1.19	133.60 ± 22.10	6.490
	$C^{33}S$ (2-1)	93	26.21	57.86 ± 0.54	21.14 ± 1.00	9.63 ± 0.41	0.428
	$C^{33}S$ (2-1)	93	26.21	66.45 ± 0.54	15.23 ± 1.07	-5.05 ± 4.13	-0.311
	$C^{33}S$ (2-1)	93	26.21	82.78 ± 1.41	15.37 ± 2.26	1.84 ± 0.39	0.112
	$C^{34}S$ (2-1)	93	12.43	53.18 ± 0.61	10.50 ± 0.61	21.51 ± 0.17	1.920
	$C^{34}S$ (2-1)	93	12.43	66.54 ± 0.61	11.80 ± 0.61	-12.52 ± 0.17	-0.997
	$C^{34}S$ (2-1)	93	12.43	83.38 ± 0.61	14.95 ± 0.61	11.40 ± 0.17	0.716
	$C^{36}S$ (2-1)	93	21.87	...	...	...	...
	^{13}CS (2-1)	93	52.97	53.80 ± 0.63	11.23 ± 0.63	17.48 ± 0.13	1.460

Table A.3. continued.

Source	transitions	Time (mins)	rms (mK)	V_{LSR} (km s^{-1})	FWHM (km s^{-1})	$\int T_{MB} dv$ (K km s^{-1})	T_{MB} (K)
	^{13}CS (2-1)	93	52.97	67.23 ± 0.63	12.04 ± 0.63	-8.45 ± 0.13	-0.660
	^{13}CS (2-1)	93	52.97	83.26 ± 0.63	16.20 ± 0.63	9.19 ± 0.13	0.533
	^{13}C^{33}S (2-1)	93	27.09	...	...	...	...
	^{13}C^{34}S (2-1)	93	9.56	55.60 ± 0.40	16.77 ± 0.81	1.89 ± 0.10	0.106
	^{13}C^{34}S (2-1)	93	9.56	65.48 ± 0.75	11.56 ± 1.77	-0.53 ± 0.03	-0.043
	^{13}C^{34}S (2-1)	93	9.56	81.93 ± 0.81	10.43 ± 1.85	0.36 ± 0.06	0.033
	C^{33}S (3-2)	93	62.06	56.94 ± 0.13	21.22 ± 0.32	22.30 ± 0.28	0.987
	C^{33}S (3-2)	93	62.06	91.58 ± 0.15	18.05 ± 0.36	15.53 ± 0.26	0.808
	C^{34}S (3-2)	93	62.94	54.74 ± 0.01	13.85 ± 0.09	44.61 ± 0.25	3.030
	C^{34}S (3-2)	93	62.94	71.72 ± 0.01	1.87 ± 0.42	0.41 ± 0.10	0.204
	C^{34}S (3-2)	93	62.94	81.92 ± 0.19	18.52 ± 0.48	14.33 ± 0.31	0.727
	C^{36}S (3-2)	46	51.81	...	...	...	...
	^{13}CS (3-2)	93	35.38	55.75 ± 0.42	15.36 ± 0.42	36.71 ± 0.23	2.240
	^{13}CS (3-2)	93	35.38	72.06 ± 0.42	7.44 ± 0.42	1.65 ± 0.23	0.209
	^{13}CS (3-2)	93	35.38	83.82 ± 0.42	15.17 ± 0.42	8.15 ± 0.23	0.505
G1.28+0.07	CS (2-1)	58	18.56	97.16 ± 0.60	29.78 ± 0.60	37.37 ± 0.33	1.180
	CS (2-1)	58	18.56	178.80 ± 0.60	41.59 ± 0.60	40.43 ± 0.33	0.913
	C^{33}S (2-1)	58	17.80	...	...	...	...
	C^{34}S (2-1)	58	16.52	98.64 ± 0.61	22.10 ± 0.61	1.45 ± 0.02	0.061
	C^{34}S (2-1)	58	16.52	177.50 ± 0.61	35.68 ± 0.61	1.90 ± 0.02	0.050
	C^{36}S (2-1)	58	16.52	...	...	...	...
	^{13}CS (2-1)	58	13.95	98.23 ± 0.68	16.25 ± 1.99	0.79 ± 0.07	0.046
	^{13}CS (2-1)	58	13.95	180.60 ± 2.12	49.79 ± 4.07	1.36 ± 0.11	0.026
	^{13}C^{33}S (2-1)	58	14.02	...	...	...	...
	^{13}C^{34}S (2-1)	58	15.73	...	...	...	...
	C^{33}S (3-2)	58	39.97	...	...	...	...
	C^{34}S (3-2)	58	37.99	...	...	...	...
	C^{36}S (3-2)	29	47.62	...	...	...	...
	^{13}CS (3-2)	58	31.94	...	...	...	...
SgrD	CS (2-1)	108	12.83	-65.23 ± 1.35	15.22 ± 3.11	2.84 ± 0.51	0.175
	CS (2-1)	108	12.83	-15.17 ± 0.06	3.56 ± 0.15	6.82 ± 0.24	1.79
	CS (2-1)	108	12.83	1.04 ± 0.58	11.79 ± 1.31	4.56 ± 0.44	0.364
	CS (2-1)	108	12.83	40.67 ± 0.57	22.41 ± 1.16	25.25 ± 1.35	1.058
	CS (2-1)	108	12.83	64.59 ± 0.99	18.75 ± 1.84	10.95 ± 1.31	0.549
	C^{33}S (2-1)	108	8.43	-14.83 ± 0.08	2.73 ± 0.20	0.304 ± 0.02	0.104
	C^{34}S (2-1)	108	8.91	-63.83 ± 1.45	13.41 ± 3.37	0.262 ± 0.05	0.0184
	C^{34}S (2-1)	108	8.91	-15.20 ± 0.01	3.17 ± 0.04	2.13 ± 0.02	0.631
	C^{34}S (2-1)	108	8.91	0.66 ± 0.59	10.12 ± 1.37	0.345 ± 0.03	0.0320
	C^{34}S (2-1)	108	8.91	40.31 ± 0.27	16.93 ± 0.67	2.05 ± 0.06	0.114
	C^{34}S (2-1)	108	8.91	63.37 ± 0.86	16.64 ± 1.68	0.651 ± 0.06	0.0367
	C^{36}S (2-1)	108	8.40	...	...	...	...
	^{13}CS (2-1)	108	7.56	-65.60 ± 1.34	7.63 ± 3.35	0.109 ± 0.03	0.0135
	^{13}CS (2-1)	108	7.56	-15.08 ± 0.03	3.05 ± 0.07	0.990 ± 0.02	0.305
	^{13}CS (2-1)	108	7.56	1.51 ± 0.73	7.80 ± 1.64	0.174 ± 0.03	0.0210
	^{13}CS (2-1)	108	7.56	40.11 ± 0.41	17.89 ± 1.06	1.32 ± 0.06	0.0693
	^{13}CS (2-1)	108	7.56	63.04 ± 1.00	15.33 ± 1.85	0.445 ± 0.05	0.0272
	^{13}C^{33}S (2-1)	108	9.11	...	...	...	...
	^{13}C^{34}S (2-1)	108	9.96	...	...	...	...
	C^{33}S (3-2)	108	15.00	-15.01 ± 0.12	4.00 ± 0.33	0.45 ± 0.03	0.106
	C^{34}S (3-2)	108	13.99	-15.02 ± 0.02	3.18 ± 0.05	1.60 ± 0.02	0.473
	C^{34}S (3-2)	108	13.99	40.38 ± 0.31	15.86 ± 0.79	1.39 ± 0.05	0.0825
	C^{36}S (3-2)	108	15.56	...	...	...	...
	^{13}CS (3-2)	108	13.79	-14.85 ± 0.04	2.99 ± 0.09	0.86 ± 0.02	0.268
	^{13}CS (3-2)	108	13.79	40.49 ± 0.49	14.33 ± 1.15	0.75 ± 0.05	0.0489
G001.00−00.23	CS (2-1)	4	73.96	0.40 ± 2.27	38.67 ± 2.48	14.42 ± 1.87	0.350
	CS (2-1)	4	73.96	17.41 ± 0.45	22.28 ± 1.32	-13.20 ± 1.87	-0.557
	CS (2-1)	4	73.96	77.27 ± 0.21	9.89 ± 0.51	-8.15 ± 0.38	-0.774

Table A.3. continued.

Source	transitions	Time (mins)	rms (mK)	V_{LSR} (km s^{-1})	FWHM (km s^{-1})	$\int T_{MB} dv$ (K km s^{-1})	T_{MB} (K)
	CS (2-1)	4	73.96	93.18 ± 0.37	12.74 ± 1.08	-7.03 ± 0.54	-0.518
	CS (2-1)	4	73.96	113.80 ± 0.25	16.81 ± 0.62	14.54 ± 0.46	0.813
	$C^{33}S$ (2-1)	4	51.09	···	···	···	···
	$C^{34}S$ (2-1)	4	53.56	0.97 ± 0.19	4.43 ± 0.45	1.49 ± 0.13	0.316
	$C^{36}S$ (2-1)	4	51.64	···	···	···	···
	^{13}CS (2-1)	4	52.09	0.95 ± 0.24	2.84 ± 0.54	0.61 ± 0.10	0.203
	$^{13}C^{33}S$ (2-1)	4	50.75	···	···	···	···
	$^{13}C^{34}S$ (2-1)	4	94.47	···	···	···	···
	$C^{33}S$ (3-2)	4	95.90	···	···	···	···
	$C^{34}S$ (3-2)	4	82.21	0.37 ± 0.26	5.09 ± 0.58	1.70 ± 0.17	0.314
	$C^{36}S$ (3-2)	4	86.98	···	···	···	···
	^{13}CS (3-2)	4	80.27	-0.59 ± 0.56	7.06 ± 1.14	1.39 ± 0.20	0.185
G001.14−00.12	CS (2-1)	4	98.38	-17.09 ± 0.11	5.95 ± 0.33	7.69 ± 0.27	1.210
	CS (2-1)	4	98.38	4.72 ± 0.56	15.03 ± 1.12	6.05 ± 0.42	0.378
	CS (2-1)	4	98.38	61.09 ± 0.36	25.66 ± 0.83	22.67 ± 0.64	0.830
	CS (2-1)	4	98.38	87.29 ± 0.20	10.68 ± 0.32	-11.24 ± 0.41	-0.989
	CS (2-1)	4	98.38	125.10 ± 0.24	17.84 ± 0.80	17.89 ± 0.56	0.942
	$C^{33}S$ (2-1)	4	48.32	···	···	···	···
	$C^{34}S$ (2-1)	4	54.81	-16.19 ± 0.75	5.71 ± 2.36	1.14 ± 0.26	0.187
	$C^{34}S$ (2-1)	4	54.81	89.43 ± 0.94	8.08 ± 1.60	-0.78 ± 0.17	-0.090
	$C^{36}S$ (2-1)	4	50.58	···	···	···	···
	^{13}CS (2-1)	4	53.99	···	···	···	···
	$^{13}C^{33}S$ (2-1)	4	47.75	···	···	···	···
	$^{13}C^{34}S$ (2-1)	4	62.24	···	···	···	···
	$C^{33}S$ (3-2)	4	95.72	···	···	···	···
	$C^{34}S$ (3-2)	4	85.49	-16.92 ± 0.36	3.83 ± 1.35	0.84 ± 0.20	0.205
	$C^{36}S$ (3-2)	4	85.25	···	···	···	···
	^{13}CS (3-2)	4	83.81	···	···	···	···
Clump2	CS (2-1)	127	12.94	13.96 ± 0.60	20.17 ± 0.60	18.94 ± 0.27	0.882
	CS (2-1)	127	12.94	41.56 ± 0.60	25.93 ± 0.60	7.04 ± 0.27	0.255
	CS (2-1)	127	12.94	80.79 ± 0.60	13.84 ± 0.60	23.55 ± 0.27	1.600
	CS (2-1)	127	12.94	108.50 ± 0.60	40.96 ± 0.60	14.36 ± 0.27	0.329
	CS (2-1)	127	12.94	142.10 ± 0.60	21.09 ± 0.60	15.84 ± 0.27	0.706
	$C^{33}S$ (2-1)	127	12.54	···	···	···	···
	$C^{34}S$ (2-1)	127	12.30	14.19 ± 0.61	14.60 ± 0.61	1.29 ± 0.02	0.083
	$C^{34}S$ (2-1)	127	12.30	35.84 ± 0.61	32.77 ± 0.61	0.75 ± 0.02	0.022
	$C^{34}S$ (2-1)	127	12.30	80.82 ± 0.61	8.90 ± 0.61	1.60 ± 0.02	0.169
	$C^{34}S$ (2-1)	127	12.30	99.32 ± 0.61	46.76 ± 0.61	1.36 ± 0.02	0.027
	$C^{34}S$ (2-1)	127	12.30	141.00 ± 0.61	27.45 ± 0.61	1.49 ± 0.02	0.051
	$C^{36}S$ (2-1)	127	11.72	···	···	···	···
	^{13}CS (2-1)	127	11.85	16.16 ± 0.72	22.17 ± 1.75	1.11 ± 0.07	0.047
	^{13}CS (2-1)	127	11.85	80.67 ± 0.19	9.81 ± 0.49	1.19 ± 0.05	0.114
	^{13}CS (2-1)	127	11.85	134.70 ± 1.68	49.26 ± 3.72	1.59 ± 0.10	0.030
	$^{13}C^{33}S$ (2-1)	127	10.47	···	···	···	···
	$^{13}C^{34}S$ (2-1)	127	60.28	···	···	···	···
	$C^{33}S$ (3-2)	127	24.90	···	···	···	···
	$C^{34}S$ (3-2)	127	24.96	13.76 ± 1.79	28.59 ± 4.82	1.05 ± 0.14	0.034
	$C^{34}S$ (3-2)	127	24.96	82.23 ± 0.57	13.47 ± 1.52	1.12 ± 0.09	0.078
	$C^{34}S$ (3-2)	127	24.96	140.60 ± 0.70	13.84 ± 3.28	0.90 ± 0.13	0.061
	$C^{36}S$ (3-2)	64	29.71	···	···	···	···
	^{13}CS (3-2)	127	14.37	15.01 ± 1.01	14.75 ± 2.03	0.55 ± 0.08	0.035
	^{13}CS (3-2)	127	14.37	81.58 ± 0.56	10.62 ± 1.37	0.62 ± 0.07	0.055
	^{13}CS (3-2)	127	14.37	140.20 ± 1.43	25.43 ± 4.14	0.96 ± 0.12	0.036
G002.70+00.04	CS (2-1)	4	60.90	96.39 ± 0.04	3.73 ± 0.12	5.65 ± 0.15	1.420
	$C^{33}S$ (2-1)	4	49.17	···	···	···	···
	$C^{34}S$ (2-1)	4	49.27	···	···	···	···
	$C^{36}S$ (2-1)	4	49.62	···	···	···	···

Table A.3. continued.

Source	transitions	Time (mins)	rms (mK)	V_{LSR} (km s^{-1})	FWHM (km s^{-1})	$\int T_{MB}dv$ (K km s^{-1})	T_{MB} (K)
	^{13}CS (2-1)	4	50.80	···	···	···	···
	^{13}C^{33}S (2-1)	4	45.76	···	···	···	···
	^{13}C^{34}S (2-1)	4	52.39	···	···	···	···
	C^{33}S (3-2)	4	93.52	···	···	···	···
	C^{34}S (3-2)	4	83.21	···	···	···	···
	C^{36}S (3-2)	4	84.17	···	···	···	···
	^{13}CS (3-2)	4	76.77	96.04 ± 0.42	3.10 ± 0.62	0.48 ± 0.12	0.144
PointD1	CS (2-1)	93	78.28	118.00 ± 0.08	19.85 ± 0.21	50.12 ± 0.42	2.370
	C^{33}S (2-1)	93	13.82	116.00 ± 1.50	19.95 ± 3.49	0.50 ± 0.07	0.023
	C^{34}S (2-1)	93	14.24	117.60 ± 0.14	15.50 ± 0.34	3.51 ± 0.07	0.212
	C^{36}S (2-1)	93	12.28	···	···	···	···
	^{13}CS (2-1)	93	13.61	118.50 ± 0.31	16.77 ± 0.71	1.82 ± 0.07	0.102
	^{13}C^{33}S (2-1)	93	11.91	···	···	···	···
	^{13}C^{34}S (2-1)	93	11.36	···	···	···	···
	C^{33}S (3-2)	93	25.71	···	···	···	···
	C^{34}S (3-2)	93	23.76	117.40 ± 0.29	14.71 ± 0.71	2.28 ± 0.09	0.145
	C^{36}S (3-2)	46	31.64	···	···	···	···
	^{13}CS (3-2)	93	22.34	117.00 ± 0.67	15.03 ± 1.88	1.05 ± 0.10	0.066
G006.79−00.25	CS (2-1)	62	51.45	20.76 ± 0.01	4.91 ± 0.03	23.10 ± 0.13	4.420
	C^{33}S (2-1)	62	11.92	11.45 ± 0.10	2.72 ± 0.28	0.30 ± 0.02	0.102
	C^{33}S (2-1)	62	11.92	21.50 ± 0.03	2.73 ± 0.07	1.07 ± 0.02	0.368
	C^{33}S (2-1)	62	11.92	29.11 ± 0.13	2.22 ± 0.32	0.18 ± 0.02	0.077
	C^{34}S (2-1)	62	16.95	20.88 ± 0.01	3.02 ± 0.02	5.88 ± 0.04	1.830
	C^{36}S (2-1)	62	12.71	···	···	···	···
	^{13}CS (2-1)	62	12.74	20.97 ± 0.01	2.70 ± 0.03	2.79 ± 0.03	0.971
	^{13}C^{33}S (2-1)	62	12.59	···	···	···	···
	^{13}C^{34}S (2-1)	62	16.08	20.95 ± 0.13	1.56 ± 0.35	0.15 ± 0.03	0.088
	C^{33}S (3-2)	62	27.66	20.62 ± 0.04	3.32 ± 0.10	2.04 ± 0.05	0.576
	C^{34}S (3-2)	62	22.53	20.71 ± 0.01	2.96 ± 0.02	7.51 ± 0.04	2.380
	C^{36}S (3-2)	62	24.29	···	···	···	···
	^{13}CS (3-2)	62	22.80	20.85 ± 0.01	2.69 ± 0.03	3.68 ± 0.04	1.280
G007.47+00.05	CS (2-1)	23	21.46	-14.38 ± 0.01	3.83 ± 0.03	7.44 ± 0.05	1.830
	C^{33}S (2-1)	23	16.66	-13.66 ± 0.34	3.12 ± 0.60	0.17 ± 0.03	0.052
	C^{34}S (2-1)	23	14.99	-14.58 ± 0.06	3.40 ± 0.13	0.92 ± 0.03	0.253
	C^{36}S (2-1)	23	15.34	···	···	···	···
	^{13}CS (2-1)	23	18.74	-14.11 ± 0.20	3.22 ± 0.43	0.32 ± 0.04	0.094
	^{13}C^{33}S (2-1)	23	17.39	···	···	···	···
	^{13}C^{34}S (2-1)	23	21.87	···	···	···	···
	C^{33}S (3-2)	23	35.97	···	···	···	···
	C^{34}S (3-2)	23	24.43	-14.62 ± 0.05	3.07 ± 0.13	1.11 ± 0.04	0.341
	C^{36}S (3-2)	23	32.49	···	···	···	···
	^{13}CS (3-2)	23	26.61	-14.50 ± 0.16	3.00 ± 0.32	0.41 ± 0.04	0.129
G008.34−01.00	CS (2-1)	4	59.28	···	···	···	···
	C^{33}S (2-1)	4	50.69	···	···	···	···
	C^{34}S (2-1)	4	48.34	···	···	···	···
	C^{36}S (2-1)	4	53.00	···	···	···	···
	^{13}CS (2-1)	4	40.19	···	···	···	···
	^{13}C^{33}S (2-1)	4	44.59	···	···	···	···
	^{13}C^{34}S (2-1)	4	51.81	···	···	···	···
	C^{33}S (3-2)	4	76.07	···	···	···	···
	C^{34}S (3-2)	4	74.48	···	···	···	···
	C^{36}S (3-2)	4	74.05	···	···	···	···
	^{13}CS (3-2)	4	79.88	···	···	···	···
G009.21−00.20	CS (2-1)	4	57.97	42.17 ± 0.07	5.50 ± 0.15	6.49 ± 0.16	1.110
	C^{33}S (2-1)	4	50.40	···	···	···	···
	C^{34}S (2-1)	4	47.72	42.25 ± 0.10	1.92 ± 0.28	0.71 ± 0.08	0.346
	C^{36}S (2-1)	4	45.51	···	···	···	···

Table A.3. continued.

Source	transitions	Time (mins)	rms (mK)	V_{LSR} (km s^{-1})	FWHM (km s^{-1})	$\int T_{MB} dv$ (K km s^{-1})	T_{MB} (K)
	^{13}CS (2-1)	4	46.43	42.33 ± 0.32	2.27 ± 0.78	0.31 ± 0.09	0.129
	^{13}C^{33}S (2-1)	4	41.00	···	···	···	···
	^{13}C^{34}S (2-1)	4	53.07	···	···	···	···
	C^{33}S (3-2)	4	76.70	···	···	···	···
	C^{34}S (3-2)	4	72.03	42.33 ± 0.25	2.84 ± 0.50	0.66 ± 0.11	0.218
	C^{36}S (3-2)	4	77.35	···	···	···	···
	^{13}CS (3-2)	4	74.12	···	···	···	···
G010.32−00.15	CS (2-1)	62	119.00	12.25 ± 0.02	3.20 ± 0.06	20.52 ± 0.28	6.030
	C^{33}S (2-1)	62	12.53	2.83 ± 0.14	2.23 ± 0.36	0.17 ± 0.02	0.070
	C^{33}S (2-1)	62	12.53	12.66 ± 0.05	2.66 ± 0.14	0.64 ± 0.03	0.225
	C^{33}S (2-1)	62	12.53	20.19 ± 0.31	3.49 ± 0.76	0.15 ± 0.03	0.041
	C^{34}S (2-1)	62	19.10	12.00 ± 0.01	2.75 ± 0.04	3.99 ± 0.04	1.360
	C^{36}S (2-1)	62	11.36	···	···	···	···
	^{13}CS (2-1)	62	14.44	12.12 ± 0.02	2.58 ± 0.05	1.77 ± 0.03	0.644
	^{13}C^{33}S (2-1)	62	10.15	···	···	···	···
	^{13}C^{34}S (2-1)	62	11.22	12.22 ± 0.14	1.64 ± 0.32	0.10 ± 0.02	0.056
	C^{33}S (3-2)	62	32.10	11.66 ± 0.09	3.74 ± 0.26	1.18 ± 0.06	0.296
	C^{34}S (3-2)	62	29.67	11.71 ± 0.02	3.00 ± 0.04	4.80 ± 0.05	1.500
	C^{36}S (3-2)	62	20.27	···	···	···	···
	^{13}CS (3-2)	62	21.45	11.88 ± 0.02	2.89 ± 0.06	2.25 ± 0.04	0.730
G010.62−00.33	CS (2-1)	4	54.98	-3.71 ± 0.01	3.47 ± 0.02	19.36 ± 0.12	5.240
	C^{33}S (2-1)	4	45.27	-2.95 ± 0.28	2.70 ± 0.67	0.40 ± 0.09	0.138
	C^{34}S (2-1)	4	46.03	-3.68 ± 0.05	2.73 ± 0.11	2.55 ± 0.09	0.877
	C^{36}S (2-1)	4	49.35	···	···	···	···
	^{13}CS (2-1)	4	52.74	-3.61 ± 0.14	2.61 ± 0.31	0.90 ± 0.10	0.324
	^{13}C^{33}S (2-1)	4	41.14	···	···	···	···
	^{13}C^{34}S (2-1)	4	49.05	···	···	···	···
	C^{33}S (3-2)	4	84.32	···	···	···	···
	C^{34}S (3-2)	4	78.05	-3.53 ± 0.10	3.07 ± 0.27	1.89 ± 0.14	0.577
	C^{36}S (3-2)	4	66.66	···	···	···	···
	^{13}CS (3-2)	4	72.48	-3.56 ± 0.16	2.24 ± 0.36	0.73 ± 0.10	0.307
G011.10−00.11	CS (2-1)	4	56.06	18.09 ± 0.10	3.43 ± 0.20	-2.18 ± 0.12	-0.598
	CS (2-1)	4	56.06	28.47 ± 0.04	3.23 ± 0.11	5.51 ± 0.15	1.600
	CS (2-1)	4	56.06	33.14 ± 0.11	3.27 ± 0.29	1.97 ± 0.15	0.565
	C^{33}S (2-1)	4	44.00	29.84 ± 0.20	1.45 ± 0.49	0.22 ± 0.06	0.143
	C^{34}S (2-1)	4	43.05	29.66 ± 0.11	2.95 ± 0.29	1.18 ± 0.09	0.375
	C^{36}S (2-1)	4	43.36	···	···	···	···
	^{13}CS (2-1)	4	49.01	···	···	···	···
	^{13}C^{33}S (2-1)	4	42.83	···	···	···	···
	^{13}C^{34}S (2-1)	4	43.64	···	···	···	···
	C^{33}S (3-2)	4	84.14	···	···	···	···
	C^{34}S (3-2)	4	71.93	29.91 ± 0.22	4.02 ± 0.64	1.22 ± 0.15	0.285
	C^{36}S (3-2)	4	76.48	···	···	···	···
	^{13}CS (3-2)	4	67.25	30.03 ± 0.21	2.41 ± 0.47	0.58 ± 0.10	0.225
W33	CS (2-1)	46	12.04	28.18 ± 0.44	6.77 ± 0.91	-0.32 ± 0.05	-0.045
	CS (2-1)	46	12.04	35.30 ± 0.04	1.41 ± 0.10	0.29 ± 0.02	0.190
	CS (2-1)	46	12.04	44.40 ± 0.47	16.25 ± 1.17	1.27 ± 0.07	0.073
	CS (2-1)	46	12.04	62.66 ± 0.02	1.41 ± 0.05	0.54 ± 0.02	0.359
	C^{33}S (2-1)	46	10.90	···	···	···	···
	C^{34}S (2-1)	46	10.75	···	···	···	···
	C^{36}S (2-1)	46	8.90	···	···	···	···
	^{13}CS (2-1)	46	10.34	···	···	···	···
	^{13}C^{33}S (2-1)	46	9.84	···	···	···	···
	^{13}C^{34}S (2-1)	46	9.71	···	···	···	···
	C^{33}S (3-2)	46	14.26	···	···	···	···
	C^{34}S (3-2)	46	15.49	···	···	···	···
	C^{36}S (3-2)	23	18.81	···	···	···	···

Table A.3. continued.

Source	transitions	Time (mins)	rms (mK)	V_{LSR} (km s^{-1})	FWHM (km s^{-1})	$\int T_{MB}dv$ (K km s^{-1})	T_{MB} (K)
	^{13}CS (3-2)	46	13.89	...	...	...	...
G013.71−00.08	CS (2-1)	4	84.73	47.17 ± 0.02	2.89 ± 0.06	10.24 ± 0.17	3.330
	C^{33}S (2-1)	4	48.08	...	...	...	...
	C^{34}S (2-1)	4	39.24	46.81 ± 0.07	2.13 ± 0.18	0.98 ± 0.07	0.431
	C^{36}S (2-1)	4	41.52	...	...	...	...
	^{13}CS (2-1)	4	40.65	47.16 ± 0.33	2.33 ± 0.64	0.27 ± 0.07	0.108
	^{13}C^{33}S (2-1)	4	47.51	...	...	...	...
	^{13}C^{34}S (2-1)	4	46.32	...	...	...	...
	C^{33}S (3-2)	4	68.80	...	...	...	...
	C^{34}S (3-2)	4	66.71	46.58 ± 0.09	2.41 ± 0.22	1.33 ± 0.10	0.520
	C^{36}S (3-2)	4	67.00	...	...	...	...
	^{13}CS (3-2)	4	66.46	46.66 ± 0.24	2.51 ± 0.51	0.54 ± 0.10	0.202
G015.66−00.49	CS (2-1)	4	114.00	-5.30 ± 0.06	6.45 ± 0.17	18.40 ± 0.36	2.680
	C^{33}S (2-1)	4	43.16	...	...	...	...
	C^{34}S (2-1)	4	43.73	-5.54 ± 0.18	4.47 ± 0.70	1.33 ± 0.14	0.279
	C^{36}S (2-1)	4	39.24	...	...	...	...
	^{13}CS (2-1)	4	43.10	-5.61 ± 0.39	6.18 ± 1.73	1.06 ± 0.18	0.161
	^{13}C^{33}S (2-1)	4	46.90	...	...	...	...
	^{13}C^{34}S (2-1)	4	40.13	...	...	...	...
	C^{33}S (3-2)	4	67.14	...	...	...	...
	C^{34}S (3-2)	4	64.99	-5.71 ± 0.23	6.39 ± 0.56	2.20 ± 0.16	0.324
	C^{36}S (3-2)	4	61.21	...	...	...	...
	^{13}CS (3-2)	4	62.06	-5.48 ± 0.28	5.21 ± 0.62	1.27 ± 0.14	0.229
G016.86−02.15	CS (2-1)	62	111.00	16.82 ± 0.02	4.12 ± 0.08	22.99 ± 0.31	5.250
	C^{33}S (2-1)	62	11.41	8.44 ± 0.24	4.25 ± 0.61	0.24 ± 0.03	0.054
	C^{33}S (2-1)	62	11.41	18.46 ± 0.05	3.32 ± 0.13	0.80 ± 0.02	0.226
	C^{33}S (2-1)	62	11.41	26.01 ± 0.15	2.17 ± 0.37	0.14 ± 0.02	0.062
	C^{34}S (2-1)	62	16.37	17.60 ± 0.01	3.36 ± 0.04	4.09 ± 0.04	1.150
	C^{36}S (2-1)	62	10.99	...	...	...	...
	^{13}CS (2-1)	62	12.96	17.91 ± 0.02	3.44 ± 0.06	2.01 ± 0.03	0.548
	^{13}C^{33}S (2-1)	62	11.41	...	...	...	...
	^{13}C^{34}S (2-1)	62	12.38	17.78 ± 0.39	4.24 ± 0.81	0.16 ± 0.03	0.036
	C^{33}S (3-2)	62	24.73	17.52 ± 0.08	4.33 ± 0.25	1.22 ± 0.05	0.265
	C^{34}S (3-2)	62	21.90	17.43 ± 0.01	3.20 ± 0.04	4.17 ± 0.04	1.230
	C^{36}S (3-2)	62	16.80	...	...	...	...
	^{13}CS (3-2)	62	16.85	17.70 ± 0.02	3.24 ± 0.06	2.05 ± 0.03	0.595
G017.02−02.40	CS (2-1)	120	29.65	19.47 ± 0.01	4.66 ± 0.02	20.73 ± 0.08	4.180
	C^{33}S (2-1)	120	7.70	11.04 ± 0.24	2.55 ± 0.55	0.07 ± 0.01	0.026
	C^{33}S (2-1)	120	7.70	20.65 ± 0.08	3.74 ± 0.23	0.41 ± 0.02	0.102
	C^{33}S (2-1)	120	7.70	28.05 ± 0.78	3.08 ± 2.28	0.07 ± 0.03	0.020
	C^{34}S (2-1)	120	11.64	19.91 ± 0.01	3.12 ± 0.04	2.47 ± 0.03	0.745
	C^{36}S (2-1)	120	7.03	...	...	...	...
	^{13}CS (2-1)	120	7.85	20.13 ± 0.02	3.10 ± 0.07	1.06 ± 0.02	0.320
	^{13}C^{33}S (2-1)	120	7.00	...	...	...	...
	^{13}C^{34}S (2-1)	120	7.87	...	...	...	...
	C^{33}S (3-2)	120	18.24	19.89 ± 0.11	4.03 ± 0.31	0.64 ± 0.04	0.150
	C^{34}S (3-2)	120	11.93	19.98 ± 0.01	3.15 ± 0.03	2.63 ± 0.02	0.783
	C^{36}S (3-2)	120	9.51	...	...	...	...
	^{13}CS (3-2)	120	11.15	20.17 ± 0.03	3.16 ± 0.07	1.18 ± 0.02	0.350
G017.55−00.12	CS (2-1)	4	46.70	...	...	...	...
	C^{33}S (2-1)	4	42.33	...	...	...	...
	C^{34}S (2-1)	4	40.74	...	...	...	...
	C^{36}S (2-1)	4	40.09	...	...	...	...
	^{13}CS (2-1)	4	42.85	...	...	...	...
	^{13}C^{33}S (2-1)	4	41.73	...	...	...	...
	^{13}C^{34}S (2-1)	4	44.34	...	...	...	...
	C^{33}S (3-2)	4	66.09	...	...	...	...

Table A.3. continued.

Source	transitions	Time (mins)	rms (mK)	V_{LSR} (km s^{-1})	FWHM (km s^{-1})	$\int T_{MB}dv$ (K km s^{-1})	T_{MB} (K)
	$C^{34}S$ (3-2)	4	60.64	···	···	···	···
	$C^{36}S$ (3-2)	4	65.05	···	···	···	···
	^{13}CS (3-2)	4	65.90	···	···	···	···
G017.63+00.15	CS (2-1)	4	47.31	22.44 ± 0.01	2.77 ± 0.02	17.59 ± 0.09	5.950
	$C^{33}S$ (2-1)	4	43.97	22.96 ± 0.29	2.74 ± 0.87	0.39 ± 0.09	0.134
	$C^{34}S$ (2-1)	4	41.97	22.41 ± 0.05	2.66 ± 0.12	2.11 ± 0.08	0.745
	$C^{36}S$ (2-1)	4	43.18	···	···	···	···
	^{13}CS (2-1)	4	37.86	22.56 ± 0.09	2.02 ± 0.18	0.75 ± 0.06	0.347
	$^{13}C^{33}S$ (2-1)	4	42.31	···	···	···	···
	$^{13}C^{34}S$ (2-1)	4	47.71	···	···	···	···
	$C^{33}S$ (3-2)	4	70.48	22.50 ± 0.23	2.14 ± 0.45	0.45 ± 0.09	0.195
	$C^{34}S$ (3-2)	4	59.66	22.67 ± 0.05	2.49 ± 0.11	2.40 ± 0.09	0.907
	$C^{36}S$ (3-2)	4	63.86	···	···	···	···
	^{13}CS (3-2)	4	71.03	22.86 ± 0.13	2.45 ± 0.31	1.00 ± 0.11	0.384
G018.34+01.76	CS (2-1)	66	40.92	33.43 ± 0.00	2.75 ± 0.01	25.00 ± 0.08	8.550
	$C^{33}S$ (2-1)	66	9.87	23.95 ± 0.31	2.73 ± 0.54	0.09 ± 0.02	0.030
	$C^{33}S$ (2-1)	66	9.87	34.29 ± 0.05	2.30 ± 0.13	0.38 ± 0.02	0.154
	$C^{33}S$ (2-1)	66	9.87	41.57 ± 0.16	1.37 ± 0.58	0.05 ± 0.02	0.037
	$C^{34}S$ (2-1)	66	10.49	33.53 ± 0.01	2.35 ± 0.02	2.49 ± 0.02	0.998
	$C^{36}S$ (2-1)	66	10.82	···	···	···	···
	^{13}CS (2-1)	66	10.66	33.70 ± 0.02	2.21 ± 0.05	0.95 ± 0.02	0.403
	$^{13}C^{33}S$ (2-1)	66	9.99	···	···	···	···
	$^{13}C^{34}S$ (2-1)	66	11.00	···	···	···	···
	$C^{33}S$ (3-2)	66	16.13	33.69 ± 0.05	3.00 ± 0.12	0.86 ± 0.03	0.270
	$C^{34}S$ (3-2)	66	17.82	33.65 ± 0.01	2.29 ± 0.02	3.95 ± 0.03	1.620
	$C^{36}S$ (3-2)	66	16.84	···	···	···	···
	^{13}CS (3-2)	66	14.35	33.88 ± 0.01	2.20 ± 0.03	1.65 ± 0.02	0.707
G019.00−00.02	CS (2-1)	4	96.79	59.85 ± 0.06	7.67 ± 0.17	19.40 ± 0.34	2.380
	$C^{33}S$ (2-1)	4	41.20	60.21 ± 0.27	1.75 ± 0.64	0.21 ± 0.07	0.116
	$C^{34}S$ (2-1)	4	43.04	59.71 ± 0.19	5.95 ± 0.61	1.93 ± 0.14	0.305
	$C^{36}S$ (2-1)	4	39.76	···	···	···	···
	^{13}CS (2-1)	4	38.32	59.37 ± 0.44	7.27 ± 1.26	0.99 ± 0.13	0.128
	$^{13}C^{33}S$ (2-1)	4	42.54	···	···	···	···
	$^{13}C^{34}S$ (2-1)	4	45.97	···	···	···	···
	$C^{33}S$ (3-2)	4	63.37	···	···	···	···
	$C^{34}S$ (3-2)	4	63.78	60.38 ± 0.24	6.53 ± 0.79	2.11 ± 0.18	0.304
	$C^{36}S$ (3-2)	4	62.93	···	···	···	···
	^{13}CS (3-2)	4	61.92	59.43 ± 0.41	5.16 ± 1.24	0.85 ± 0.15	0.154
G019.36−00.03	CS (2-1)	62	24.37	19.87 ± 0.60	8.86 ± 0.60	4.25 ± 0.53	0.451
	CS (2-1)	62	24.37	25.43 ± 0.60	1.29 ± 0.60	5.47 ± 0.53	3.980
	CS (2-1)	62	24.37	28.00 ± 0.60	7.00 ± 0.60	16.46 ± 0.53	2.210
	$C^{33}S$ (2-1)	62	11.03	16.96 ± 0.23	3.37 ± 0.69	0.19 ± 0.03	0.054
	$C^{33}S$ (2-1)	62	11.03	27.16 ± 0.05	3.02 ± 0.14	0.65 ± 0.02	0.203
	$C^{33}S$ (2-1)	62	11.03	34.40 ± 0.16	1.64 ± 0.48	0.09 ± 0.02	0.053
	$C^{34}S$ (2-1)	62	20.28	26.40 ± 0.02	3.14 ± 0.04	4.26 ± 0.04	1.270
	$C^{36}S$ (2-1)	62	10.65	···	···	···	···
	^{13}CS (2-1)	62	13.10	26.52 ± 0.02	2.91 ± 0.06	1.75 ± 0.03	0.566
	$^{13}C^{33}S$ (2-1)	62	11.59	···	···	···	···
	$^{13}C^{34}S$ (2-1)	62	13.93	26.74 ± 0.30	1.95 ± 0.73	0.08 ± 0.02	0.037
	$C^{33}S$ (3-2)	62	19.29	26.44 ± 0.09	5.09 ± 0.26	1.21 ± 0.05	0.223
	$C^{34}S$ (3-2)	62	28.04	26.54 ± 0.02	3.83 ± 0.05	5.14 ± 0.06	1.260
	$C^{36}S$ (3-2)	62	18.82	···	···	···	···
	^{13}CS (3-2)	62	17.84	26.74 ± 0.03	3.45 ± 0.07	2.18 ± 0.04	0.594
G019.49+00.11	CS (2-1)	4	42.47	119.10 ± 0.13	8.24 ± 0.38	4.64 ± 0.16	0.529
	$C^{33}S$ (2-1)	4	41.47	···	···	···	···
	$C^{34}S$ (2-1)	4	39.39	···	···	···	···
	$C^{36}S$ (2-1)	4	34.87	···	···	···	···

Table A.3. continued.

Source	transitions	Time (mins)	rms (mK)	V_{LSR} (km s^{-1})	FWHM (km s^{-1})	$\int T_{MB}dv$ (K km s^{-1})	T_{MB} (K)
	^{13}CS (2-1)	4	44.56	···	···	···	···
	^{13}C^{33}S (2-1)	4	41.03	···	···	···	···
	^{13}C^{34}S (2-1)	4	39.31	···	···	···	···
	C^{33}S (3-2)	4	60.23	···	···	···	···
	C^{34}S (3-2)	4	57.35	120.10 ± 0.24	1.40 ± 0.55	0.25 ± 0.07	0.169
	C^{36}S (3-2)	4	63.55	···	···	···	···
	^{13}CS (3-2)	4	60.99	···	···	···	···
G022.35+00.06	CS (2-1)	4	58.07	84.31 ± 0.02	3.54 ± 0.06	9.81 ± 0.13	2.610
	C^{33}S (2-1)	4	39.62	···	···	···	···
	C^{34}S (2-1)	4	33.96	84.17 ± 0.06	2.60 ± 0.16	1.35 ± 0.07	0.486
	C^{36}S (2-1)	4	38.06	···	···	···	···
	^{13}CS (2-1)	4	38.49	84.27 ± 0.12	1.77 ± 0.33	0.45 ± 0.06	0.238
	^{13}C^{33}S (2-1)	4	39.68	···	···	···	···
	^{13}C^{34}S (2-1)	4	45.33	···	···	···	···
	C^{33}S (3-2)	4	61.45	···	···	···	···
	C^{34}S (3-2)	4	56.41	84.14 ± 0.06	2.28 ± 0.15	1.63 ± 0.09	0.673
	C^{36}S (3-2)	4	56.42	···	···	···	···
	^{13}CS (3-2)	4	57.29	84.24 ± 0.17	2.54 ± 0.44	0.66 ± 0.09	0.245
G023.20−00.37	CS (2-1)	4	74.80	73.04 ± 0.11	6.35 ± 0.31	8.03 ± 0.35	1.190
	CS (2-1)	4	74.80	82.37 ± 0.09	8.00 ± 0.31	13.30 ± 0.39	1.560
	C^{33}S (2-1)	4	42.86	···	···	···	···
	C^{34}S (2-1)	4	40.77	77.61 ± 0.14	8.59 ± 0.44	4.15 ± 0.16	0.454
	C^{36}S (2-1)	4	38.70	···	···	···	···
	^{13}CS (2-1)	4	41.25	78.10 ± 0.32	9.54 ± 1.06	2.34 ± 0.18	0.230
	^{13}C^{33}S (2-1)	4	39.93	···	···	···	···
	^{13}C^{34}S (2-1)	4	42.11	···	···	···	···
	C^{33}S (3-2)	4	69.33	77.38 ± 0.54	10.81 ± 1.57	2.16 ± 0.24	0.188
	C^{34}S (3-2)	4	61.35	77.40 ± 0.09	8.74 ± 0.27	8.01 ± 0.19	0.861
	C^{36}S (3-2)	4	58.93	···	···	···	···
	^{13}CS (3-2)	4	62.54	77.76 ± 0.15	6.55 ± 0.42	3.47 ± 0.17	0.497
G023.25−00.24	CS (2-1)	4	70.86	61.24 ± 0.05	3.07 ± 0.16	4.11 ± 0.16	1.260
	C^{33}S (2-1)	4	39.39	···	···	···	···
	C^{34}S (2-1)	4	38.45	61.52 ± 0.35	3.35 ± 0.96	0.46 ± 0.09	0.128
	C^{36}S (2-1)	4	38.06	···	···	···	···
	^{13}CS (2-1)	4	41.49	···	···	···	···
	^{13}C^{33}S (2-1)	4	37.43	···	···	···	···
	^{13}C^{34}S (2-1)	4	40.53	···	···	···	···
	C^{33}S (3-2)	4	61.60	···	···	···	···
	C^{34}S (3-2)	4	57.34	60.81 ± 0.23	1.90 ± 0.58	0.32 ± 0.08	0.161
	C^{36}S (3-2)	4	57.72	···	···	···	···
	^{13}CS (3-2)	4	60.84	···	···	···	···
G023.38+00.18	CS (2-1)	4	67.67	75.42 ± 0.03	4.20 ± 0.09	10.57 ± 0.17	2.370
	C^{33}S (2-1)	4	40.75	···	···	···	···
	C^{34}S (2-1)	4	35.90	75.57 ± 0.10	2.78 ± 0.25	0.99 ± 0.07	0.335
	C^{36}S (2-1)	4	37.22	···	···	···	···
	^{13}CS (2-1)	4	42.37	75.50 ± 0.15	2.04 ± 0.42	0.47 ± 0.08	0.215
	^{13}C^{33}S (2-1)	4	36.19	···	···	···	···
	^{13}C^{34}S (2-1)	4	40.21	···	···	···	···
	C^{33}S (3-2)	4	69.64	···	···	···	···
	C^{34}S (3-2)	4	63.06	75.55 ± 0.13	2.97 ± 0.40	1.18 ± 0.12	0.374
	C^{36}S (3-2)	4	63.25	···	···	···	···
	^{13}CS (3-2)	4	63.28	75.77 ± 0.29	3.36 ± 0.85	0.65 ± 0.12	0.182
G023.43−00.18	CS (2-1)	33	78.51	93.52 ± 0.16	7.29 ± 0.48	5.29 ± 0.31	0.681
	CS (2-1)	33	78.51	103.40 ± 0.03	6.90 ± 0.10	28.84 ± 0.33	3.920
	C^{33}S (2-1)	33	13.91	92.35 ± 0.35	4.61 ± 0.86	0.25 ± 0.06	0.050
	C^{33}S (2-1)	33	13.91	102.70 ± 0.10	3.81 ± 0.34	0.62 ± 0.07	0.154
	C^{33}S (2-1)	33	13.91	105.20 ± 1.21	14.80 ± 1.87	0.71 ± 0.13	0.045

Table A.3. continued.

Source	transitions	Time (mins)	rms (mK)	V_{LSR} (km s^{-1})	FWHM (km s^{-1})	$\int T_{MB} dv$ (K km s^{-1})	T_{MB} (K)
	$C^{34}S$ (2-1)	33	25.07	102.10 ± 0.03	5.67 ± 0.09	5.92 ± 0.07	0.981
	$C^{36}S$ (2-1)	33	14.55	...	...	...	...
	^{13}CS (2-1)	33	17.81	102.10 ± 0.05	5.49 ± 0.13	2.88 ± 0.05	0.493
	$^{13}C^{33}S$ (2-1)	33	15.04	...	...	...	...
	$^{13}C^{34}S$ (2-1)	33	15.99	101.40 ± 0.80	5.65 ± 1.71	0.16 ± 0.04	0.026
	$C^{33}S$ (3-2)	33	23.86	102.30 ± 0.11	5.06 ± 0.31	1.17 ± 0.06	0.218
	$C^{34}S$ (3-2)	33	26.96	102.40 ± 0.02	4.71 ± 0.07	5.44 ± 0.06	1.090
	$C^{36}S$ (3-2)	33	20.88	...	...	...	...
	^{13}CS (3-2)	33	23.09	102.50 ± 0.04	4.35 ± 0.11	2.63 ± 0.05	0.569
G024.63−00.32	CS (2-1)	4	59.56	42.63 ± 0.03	3.92 ± 0.08	8.54 ± 0.14	2.050
	$C^{33}S$ (2-1)	4	41.28	...	...	...	...
	$C^{34}S$ (2-1)	4	33.66	42.69 ± 0.07	2.77 ± 0.21	1.23 ± 0.07	0.418
	$C^{36}S$ (2-1)	4	40.93	...	...	...	...
	^{13}CS (2-1)	4	36.21	43.14 ± 0.19	3.63 ± 0.47	0.77 ± 0.08	0.198
	$^{13}C^{33}S$ (2-1)	4	39.80	...	...	...	...
	$^{13}C^{34}S$ (2-1)	4	44.46	...	...	...	...
	$C^{33}S$ (3-2)	4	64.76	...	...	...	...
	$C^{34}S$ (3-2)	4	54.46	43.15 ± 0.11	2.95 ± 0.27	1.18 ± 0.09	0.375
	$C^{36}S$ (3-2)	4	62.90	...	...	...	...
	^{13}CS (3-2)	4	55.78	42.87 ± 0.27	2.71 ± 0.64	0.44 ± 0.09	0.154
G024.78+00.08	CS (2-1)	62	17.25	108.40 ± 0.60	11.19 ± 0.60	10.09 ± 0.72	0.847
	CS (2-1)	62	17.25	112.70 ± 0.60	26.10 ± 0.60	20.32 ± 0.72	0.731
	CS (2-1)	62	17.25	112.10 ± 0.60	5.06 ± 0.60	25.65 ± 0.72	4.760
	$C^{33}S$ (2-1)	62	10.56	101.60 ± 0.60	5.45 ± 0.60	1.00 ± 0.07	0.173
	$C^{33}S$ (2-1)	62	10.56	111.30 ± 0.60	4.29 ± 0.60	2.98 ± 0.07	0.653
	$C^{33}S$ (2-1)	62	10.56	118.30 ± 0.60	4.84 ± 0.60	0.64 ± 0.07	0.124
	$C^{33}S$ (2-1)	62	10.56	129.70 ± 0.60	6.86 ± 0.60	0.23 ± 0.07	0.031
	$C^{34}S$ (2-1)	62	30.92	110.70 ± 0.02	5.18 ± 0.04	13.89 ± 0.09	2.520
	$C^{36}S$ (2-1)	62	10.31	103.40 ± 0.38	5.27 ± 0.89	0.21 ± 0.03	0.038
	$C^{36}S$ (2-1)	62	10.31	111.70 ± 0.49	4.37 ± 0.93	0.12 ± 0.03	0.026
	^{13}CS (2-1)	62	19.25	110.80 ± 0.02	4.69 ± 0.04	7.62 ± 0.05	1.530
	$^{13}C^{33}S$ (2-1)	62	11.08	...	...	...	...
	$^{13}C^{34}S$ (2-1)	62	11.15	110.70 ± 0.11	4.34 ± 0.29	0.57 ± 0.03	0.123
	$C^{33}S$ (3-2)	62	72.18	110.80 ± 0.06	6.36 ± 0.17	8.80 ± 0.18	1.300
	$C^{34}S$ (3-2)	62	55.71	110.90 ± 0.02	5.93 ± 0.04	24.33 ± 0.14	3.860
	$C^{36}S$ (3-2)	62	20.86	110.70 ± 0.35	2.86 ± 0.90	0.14 ± 0.04	0.046
	^{13}CS (3-2)	62	30.35	111.00 ± 0.01	5.19 ± 0.04	13.52 ± 0.07	2.450
G024.85+00.08	CS (2-1)	4	43.90	109.10 ± 0.01	2.80 ± 0.03	8.91 ± 0.09	2.990
	$C^{33}S$ (2-1)	4	36.99	109.20 ± 0.14	1.27 ± 0.40	0.21 ± 0.05	0.155
	$C^{34}S$ (2-1)	4	36.24	109.00 ± 0.04	2.37 ± 0.09	1.98 ± 0.07	0.785
	$C^{36}S$ (2-1)	4	39.59	...	...	...	...
	^{13}CS (2-1)	4	36.82	109.20 ± 0.08	2.29 ± 0.16	0.98 ± 0.06	0.400
	$^{13}C^{33}S$ (2-1)	4	36.19	...	...	...	...
	$^{13}C^{34}S$ (2-1)	4	40.08	...	...	...	...
	$C^{33}S$ (3-2)	4	71.26	108.80 ± 0.19	3.20 ± 0.50	1.01 ± 0.13	0.296
	$C^{34}S$ (3-2)	4	59.69	108.80 ± 0.03	2.36 ± 0.08	3.06 ± 0.09	1.220
	$C^{36}S$ (3-2)	4	61.92	...	...	...	...
	^{13}CS (3-2)	4	58.70	108.90 ± 0.05	1.86 ± 0.12	1.40 ± 0.08	0.707
G028.14−00.00	CS (2-1)	4	48.98	98.92 ± 0.04	5.69 ± 0.12	9.38 ± 0.15	1.550
	$C^{33}S$ (2-1)	4	42.18	...	...	...	...
	$C^{34}S$ (2-1)	4	36.69	98.72 ± 0.08	2.83 ± 0.22	1.30 ± 0.08	0.432
	$C^{36}S$ (2-1)	4	37.98	...	...	...	...
	^{13}CS (2-1)	4	38.64	98.19 ± 0.27	3.23 ± 0.74	0.49 ± 0.09	0.141
	$^{13}C^{33}S$ (2-1)	4	36.32	...	...	...	...
	$^{13}C^{34}S$ (2-1)	4	45.77	...	...	...	...
	$C^{33}S$ (3-2)	4	65.87	...	...	...	...
	$C^{34}S$ (3-2)	4	56.89	98.97 ± 0.11	3.39 ± 0.29	1.58 ± 0.11	0.438

Table A.3. continued.

Source	transitions	Time (mins)	rms (mK)	V_{LSR} (km s^{-1})	FWHM (km s^{-1})	$\int T_{MB}dv$ (K km s^{-1})	T_{MB} (K)
	$C^{36}S$ (3-2)	4	59.84	···	···	···	···
	^{13}CS (3-2)	4	57.20	98.86 ± 0.26	3.16 ± 0.60	0.59 ± 0.10	0.176
G028.30−00.38	CS (2-1)	4	51.10	85.61 ± 0.01	3.21 ± 0.03	13.08 ± 0.11	3.830
	$C^{33}S$ (2-1)	4	40.85	86.89 ± 0.36	2.93 ± 0.78	0.33 ± 0.08	0.107
	$C^{34}S$ (2-1)	4	35.60	85.55 ± 0.05	3.21 ± 0.13	2.25 ± 0.08	0.659
	$C^{36}S$ (2-1)	4	40.40	···	···	···	···
	^{13}CS (2-1)	4	37.37	85.59 ± 0.09	2.75 ± 0.22	1.09 ± 0.07	0.374
	$^{13}C^{33}S$ (2-1)	4	36.18	···	···	···	···
	$^{13}C^{34}S$ (2-1)	4	43.43	···	···	···	···
	$C^{33}S$ (3-2)	4	63.40	85.31 ± 0.20	2.68 ± 0.44	0.66 ± 0.10	0.231
	$C^{34}S$ (3-2)	4	54.21	85.65 ± 0.04	2.72 ± 0.11	2.67 ± 0.09	0.922
	$C^{36}S$ (3-2)	4	63.59	···	···	···	···
	^{13}CS (3-2)	4	60.08	85.82 ± 0.10	2.69 ± 0.22	1.33 ± 0.10	0.466
G028.39+00.08	CS (2-1)	62	57.56	76.29 ± 0.03	4.11 ± 0.10	10.02 ± 0.18	2.290
	CS (2-1)	62	57.56	80.88 ± 0.08	2.00 ± 0.19	1.31 ± 0.20	0.619
	CS (2-1)	62	57.56	84.66 ± 0.29	5.54 ± 0.95	2.03 ± 0.28	0.343
	$C^{33}S$ (2-1)	62	9.16	69.07 ± 0.19	3.19 ± 0.49	0.16 ± 0.02	0.048
	$C^{33}S$ (2-1)	62	9.16	79.08 ± 0.05	3.04 ± 0.13	0.62 ± 0.02	0.192
	$C^{33}S$ (2-1)	62	9.16	86.27 ± 0.26	3.94 ± 0.97	0.15 ± 0.03	0.037
	$C^{34}S$ (2-1)	62	19.13	78.01 ± 0.04	4.61 ± 0.09	3.10 ± 0.05	0.633
	$C^{36}S$ (2-1)	62	8.84	···	···	···	···
	^{13}CS (2-1)	62	9.60	78.42 ± 0.02	3.77 ± 0.07	1.68 ± 0.02	0.417
	$^{13}C^{33}S$ (2-1)	62	9.01	···	···	···	···
	$^{13}C^{34}S$ (2-1)	62	9.58	78.95 ± 0.27	2.77 ± 0.81	0.11 ± 0.02	0.036
	$C^{33}S$ (3-2)	62	16.96	78.24 ± 0.06	4.39 ± 0.16	1.28 ± 0.04	0.274
	$C^{34}S$ (3-2)	62	16.02	78.10 ± 0.02	4.66 ± 0.04	4.92 ± 0.03	0.992
	$C^{36}S$ (3-2)	62	12.70	···	···	···	···
	^{13}CS (3-2)	62	13.15	78.44 ± 0.02	3.87 ± 0.05	2.42 ± 0.03	0.587
G028.83−00.25	CS (2-1)	120	35.29	87.69 ± 0.01	6.04 ± 0.02	19.75 ± 0.08	3.070
	$C^{33}S$ (2-1)	120	6.37	77.69 ± 0.13	2.50 ± 0.52	0.12 ± 0.02	0.046
	$C^{33}S$ (2-1)	120	6.37	87.82 ± 0.03	2.27 ± 0.08	0.47 ± 0.02	0.194
	$C^{33}S$ (2-1)	120	6.37	90.20 ± 0.68	15.48 ± 2.85	0.41 ± 0.04	0.025
	$C^{34}S$ (2-1)	120	10.61	87.19 ± 0.01	3.37 ± 0.03	3.80 ± 0.02	1.060
	$C^{36}S$ (2-1)	120	6.31	···	···	···	···
	^{13}CS (2-1)	120	6.31	87.27 ± 0.01	3.10 ± 0.03	1.73 ± 0.01	0.524
	$^{13}C^{33}S$ (2-1)	120	6.60	···	···	···	···
	$^{13}C^{34}S$ (2-1)	120	6.74	87.20 ± 0.24	3.40 ± 0.67	0.11 ± 0.02	0.029
	$C^{33}S$ (3-2)	120	12.12	87.16 ± 0.05	3.94 ± 0.12	0.97 ± 0.02	0.232
	$C^{34}S$ (3-2)	120	10.52	87.30 ± 0.01	3.36 ± 0.02	4.51 ± 0.02	1.260
	$C^{36}S$ (3-2)	120	9.10	···	···	···	···
	^{13}CS (3-2)	120	9.97	87.37 ± 0.01	3.07 ± 0.03	2.03 ± 0.02	0.621
G029.98+00.10	CS (2-1)	4	39.31	···	···	···	···
	$C^{33}S$ (2-1)	4	39.03	···	···	···	···
	$C^{34}S$ (2-1)	4	35.49	···	···	···	···
	$C^{36}S$ (2-1)	4	37.52	···	···	···	···
	^{13}CS (2-1)	4	39.35	···	···	···	···
	$^{13}C^{33}S$ (2-1)	4	36.35	···	···	···	···
	$^{13}C^{34}S$ (2-1)	4	43.62	···	···	···	···
	$C^{33}S$ (3-2)	4	58.98	···	···	···	···
	$C^{34}S$ (3-2)	4	55.21	···	···	···	···
	$C^{36}S$ (3-2)	4	55.21	···	···	···	···
	^{13}CS (3-2)	4	55.12	···	···	···	···
G030.19−00.16	CS (2-1)	4	55.60	103.30 ± 0.01	2.90 ± 0.04	10.37 ± 0.11	3.360
	$C^{33}S$ (2-1)	4	42.78	···	···	···	···
	$C^{34}S$ (2-1)	4	35.40	103.10 ± 0.05	2.43 ± 0.12	1.61 ± 0.07	0.625
	$C^{36}S$ (2-1)	4	40.39	···	···	···	···
	^{13}CS (2-1)	4	40.97	103.30 ± 0.11	1.78 ± 0.25	0.55 ± 0.07	0.288

Table A.3. continued.

Source	transitions	Time (mins)	rms (mK)	V_{LSR} (km s^{-1})	FWHM (km s^{-1})	$\int T_{MB} dv$ (K km s^{-1})	T_{MB} (K)
	$^{13}C^{33}S$ (2-1)	4	37.71	...	...	...	...
	$^{13}C^{34}S$ (2-1)	4	43.67	...	...	...	...
	$C^{33}S$ (3-2)	4	62.45	...	...	...	...
	$C^{34}S$ (3-2)	4	52.26	103.00 ± 0.04	2.61 ± 0.11	2.36 ± 0.08	0.847
	$C^{36}S$ (3-2)	4	62.76	...	...	...	...
	^{13}CS (3-2)	4	56.61	103.10 ± 0.10	2.27 ± 0.25	0.93 ± 0.08	0.383
G030.22−00.18	CS (2-1)	4	81.03	103.80 ± 0.02	2.80 ± 0.05	10.95 ± 0.16	3.670
	$C^{33}S$ (2-1)	4	38.52	...	...	...	...
	$C^{34}S$ (2-1)	4	35.34	103.90 ± 0.06	2.31 ± 0.14	1.29 ± 0.06	0.522
	$C^{36}S$ (2-1)	4	37.31	...	...	...	...
	^{13}CS (2-1)	4	41.60	103.70 ± 0.18	1.84 ± 0.67	0.37 ± 0.09	0.191
	$^{13}C^{33}S$ (2-1)	4	37.93	...	...	...	...
	$^{13}C^{34}S$ (2-1)	4	40.96	...	...	...	...
	$C^{33}S$ (3-2)	4	60.15	...	...	...	...
	$C^{34}S$ (3-2)	4	53.67	103.70 ± 0.08	2.70 ± 0.19	1.42 ± 0.08	0.493
	$C^{36}S$ (3-2)	4	57.83	...	...	...	...
	^{13}CS (3-2)	4	56.30	103.50 ± 0.32	5.14 ± 0.97	1.00 ± 0.14	0.183
G030.41−00.23	CS (2-1)	4	92.81	104.90 ± 0.02	4.34 ± 0.06	21.60 ± 0.23	4.670
	$C^{33}S$ (2-1)	4	43.12	...	...	...	...
	$C^{34}S$ (2-1)	4	43.43	105.10 ± 0.07	3.12 ± 0.20	2.06 ± 0.10	0.620
	$C^{36}S$ (2-1)	4	39.19	...	...	...	...
	^{13}CS (2-1)	4	41.30	105.20 ± 0.17	3.93 ± 0.46	1.09 ± 0.10	0.260
	$^{13}C^{33}S$ (2-1)	4	34.26	...	...	...	...
	$^{13}C^{34}S$ (2-1)	4	40.40	...	...	...	...
	$C^{33}S$ (3-2)	4	60.68	...	...	...	...
	$C^{34}S$ (3-2)	4	59.31	104.90 ± 0.09	4.42 ± 0.27	2.99 ± 0.14	0.636
	$C^{36}S$ (3-2)	4	60.09	...	...	...	...
	^{13}CS (3-2)	4	58.26	104.50 ± 0.35	6.20 ± 1.05	1.56 ± 0.17	0.237
G030.70−00.06	CS (2-1)	81	53.19	88.33 ± 0.02	4.51 ± 0.05	18.03 ± 0.14	3.760
	CS (2-1)	81	53.19	96.41 ± 0.06	4.81 ± 0.14	5.99 ± 0.15	1.170
	$C^{33}S$ (2-1)	81	8.61	81.27 ± 0.11	6.01 ± 0.30	0.59 ± 0.03	0.091
	$C^{33}S$ (2-1)	81	8.61	90.77 ± 0.04	4.85 ± 0.10	1.81 ± 0.03	0.350
	$C^{33}S$ (2-1)	81	8.61	97.89 ± 0.20	5.68 ± 0.62	0.41 ± 0.04	0.068
	$C^{33}S$ (2-1)	81	8.61	109.80 ± 0.53	7.12 ± 1.45	0.20 ± 0.03	0.026
	$C^{34}S$ (2-1)	81	23.69	89.94 ± 0.02	5.36 ± 0.05	8.44 ± 0.07	1.480
	$C^{36}S$ (2-1)	81	9.08	...	...	...	...
	^{13}CS (2-1)	81	9.37	90.31 ± 0.01	5.22 ± 0.03	4.96 ± 0.03	0.892
	$^{13}C^{33}S$ (2-1)	81	7.80	...	...	...	...
	$^{13}C^{34}S$ (2-1)	81	8.64	90.46 ± 0.19	5.05 ± 0.45	0.31 ± 0.02	0.058
	$C^{33}S$ (3-2)	81	80.58	89.79 ± 0.12	6.29 ± 0.32	4.89 ± 0.20	0.731
	$C^{34}S$ (3-2)	81	17.70	89.81 ± 0.01	5.44 ± 0.02	13.87 ± 0.04	2.390
	$C^{36}S$ (3-2)	81	19.44	...	...	...	...
	^{13}CS (3-2)	81	21.75	90.07 ± 0.02	5.12 ± 0.04	7.81 ± 0.05	1.430
G030.74−00.04	CS (2-1)	62	42.95	91.98 ± 0.02	4.89 ± 0.04	16.33 ± 0.11	3.140
	$C^{33}S$ (2-1)	62	9.82	82.20 ± 0.23	3.35 ± 0.58	0.16 ± 0.02	0.046
	$C^{33}S$ (2-1)	62	9.82	92.47 ± 0.05	3.55 ± 0.13	0.85 ± 0.03	0.224
	$C^{33}S$ (2-1)	62	9.82	99.92 ± 0.51	6.79 ± 1.87	0.21 ± 0.04	0.030
	$C^{34}S$ (2-1)	62	13.40	91.83 ± 0.01	3.70 ± 0.03	4.40 ± 0.03	1.120
	$C^{36}S$ (2-1)	62	9.45	...	...	...	...
	^{13}CS (2-1)	62	10.54	91.90 ± 0.02	3.41 ± 0.05	2.02 ± 0.02	0.558
	$^{13}C^{33}S$ (2-1)	62	9.80	...	...	...	...
	$^{13}C^{34}S$ (2-1)	62	11.13	92.23 ± 0.33	3.84 ± 1.27	0.16 ± 0.03	0.038
	$C^{33}S$ (3-2)	62	17.69	91.75 ± 0.04	4.24 ± 0.12	1.73 ± 0.04	0.383
	$C^{34}S$ (3-2)	62	16.92	91.76 ± 0.01	3.40 ± 0.02	6.02 ± 0.03	1.660
	$C^{36}S$ (3-2)	62	14.56	...	...	...	...
	^{13}CS (3-2)	62	14.58	91.89 ± 0.01	3.25 ± 0.03	2.85 ± 0.03	0.822
G030.78+00.20	CS (2-1)	4	119.00	79.19 ± 0.05	2.70 ± 0.07	5.61 ± 0.20	1.950

Table A.3. continued.

Source	transitions	Time (mins)	rms (mK)	V_{LSR} (km s^{-1})	FWHM (km s^{-1})	$\int T_{MB}dv$ (K km s^{-1})	T_{MB} (K)
	CS (2-1)	4	119.00	84.17 ± 0.08	4.59 ± 0.28	8.50 ± 0.37	1.740
	$C^{33}S$ (2-1)	4	41.97	83.09 ± 0.40	4.34 ± 0.95	0.57 ± 0.10	0.123
	$C^{34}S$ (2-1)	4	32.48	81.94 ± 0.07	4.99 ± 0.18	3.02 ± 0.09	0.569
	$C^{36}S$ (2-1)	4	35.44	···	···	···	···
	^{13}CS (2-1)	4	41.75	82.03 ± 0.17	4.12 ± 0.47	1.22 ± 0.11	0.278
	$^{13}C^{33}S$ (2-1)	4	41.03	···	···	···	···
	$^{13}C^{34}S$ (2-1)	4	40.58	···	···	···	···
	$C^{33}S$ (3-2)	4	60.91	81.88 ± 0.24	4.17 ± 0.66	1.00 ± 0.12	0.226
	$C^{34}S$ (3-2)	4	50.97	81.99 ± 0.05	4.44 ± 0.14	4.20 ± 0.10	0.888
	$C^{36}S$ (3-2)	4	50.92	···	···	···	···
	^{13}CS (3-2)	4	56.51	82.30 ± 0.13	4.38 ± 0.33	1.94 ± 0.12	0.416
G030.81−00.05	CS (2-1)	62	112.00	95.45 ± 0.03	3.03 ± 0.07	14.33 ± 0.37	4.440
	CS (2-1)	62	112.00	101.70 ± 0.06	6.80 ± 0.23	20.80 ± 0.51	2.870
	$C^{33}S$ (2-1)	62	8.15	89.83 ± 0.60	5.32 ± 0.60	0.54 ± 0.04	0.095
	$C^{33}S$ (2-1)	62	8.15	99.89 ± 0.60	6.15 ± 0.60	2.00 ± 0.04	0.305
	$C^{33}S$ (2-1)	62	8.15	108.00 ± 0.60	6.25 ± 0.60	0.31 ± 0.04	0.047
	$C^{33}S$ (2-1)	62	8.15	119.90 ± 0.60	11.35 ± 0.60	0.28 ± 0.04	0.024
	$C^{34}S$ (2-1)	62	43.05	98.90 ± 0.05	7.00 ± 0.11	9.54 ± 0.13	1.280
	$C^{36}S$ (2-1)	62	10.01	91.05 ± 0.27	2.57 ± 0.79	0.09 ± 0.03	0.034
	$C^{36}S$ (2-1)	62	10.01	98.68 ± 1.34	9.79 ± 2.46	0.20 ± 0.05	0.019
	^{13}CS (2-1)	62	11.95	99.05 ± 0.02	6.29 ± 0.05	5.22 ± 0.04	0.780
	$^{13}C^{33}S$ (2-1)	62	9.11	···	···	···	···
	$^{13}C^{34}S$ (2-1)	62	10.70	99.09 ± 0.28	5.84 ± 0.65	0.33 ± 0.03	0.053
	$C^{33}S$ (3-2)	62	115.00	99.80 ± 0.18	7.34 ± 0.47	5.86 ± 0.31	0.750
	$C^{34}S$ (3-2)	62	31.06	99.40 ± 0.02	6.96 ± 0.04	16.89 ± 0.08	2.280
	$C^{36}S$ (3-2)	62	19.14	···	···	···	···
	^{13}CS (3-2)	62	26.29	99.65 ± 0.02	6.27 ± 0.06	9.09 ± 0.07	1.360
G030.97−00.14	CS (2-1)	4	49.89	77.96 ± 0.03	4.11 ± 0.08	8.59 ± 0.13	1.960
	$C^{33}S$ (2-1)	4	39.43	···	···	···	···
	$C^{34}S$ (2-1)	4	38.10	77.62 ± 0.20	4.68 ± 0.94	1.12 ± 0.14	0.225
	$C^{36}S$ (2-1)	4	35.93	···	···	···	···
	^{13}CS (2-1)	4	41.18	77.15 ± 0.56	5.89 ± 1.72	0.67 ± 0.14	0.107
	$^{13}C^{33}S$ (2-1)	4	37.52	···	···	···	···
	$^{13}C^{34}S$ (2-1)	4	43.90	···	···	···	···
	$C^{33}S$ (3-2)	4	59.63	···	···	···	···
	$C^{34}S$ (3-2)	4	53.10	77.64 ± 0.19	4.01 ± 0.50	1.11 ± 0.11	0.260
	$C^{36}S$ (3-2)	4	55.43	···	···	···	···
	^{13}CS (3-2)	4	48.99	77.00 ± 0.35	3.64 ± 0.87	0.49 ± 0.09	0.125
G031.24−00.11	CS (2-1)	8	118.00	21.08 ± 0.04	4.18 ± 0.10	14.66 ± 0.29	3.300
	$C^{33}S$ (2-1)	8	24.79	21.16 ± 0.44	4.30 ± 1.23	0.31 ± 0.07	0.067
	$C^{34}S$ (2-1)	8	31.02	21.08 ± 0.07	3.72 ± 0.18	1.72 ± 0.07	0.434
	$C^{36}S$ (2-1)	8	26.92	···	···	···	···
	^{13}CS (2-1)	8	25.80	21.34 ± 0.14	3.79 ± 0.35	0.79 ± 0.06	0.195
	$^{13}C^{33}S$ (2-1)	8	28.26	···	···	···	···
	$^{13}C^{34}S$ (2-1)	8	26.36	···	···	···	···
	$C^{33}S$ (3-2)	8	44.83	21.21 ± 0.24	4.15 ± 0.60	0.76 ± 0.09	0.171
	$C^{34}S$ (3-2)	8	40.05	21.30 ± 0.04	3.76 ± 0.11	3.28 ± 0.08	0.819
	$C^{36}S$ (3-2)	8	38.58	···	···	···	···
	^{13}CS (3-2)	8	38.55	21.59 ± 0.09	3.42 ± 0.20	1.33 ± 0.07	0.366
G032.74−00.07	CS (2-1)	62	19.93	36.64 ± 0.01	8.95 ± 0.03	23.56 ± 0.07	2.470
	$C^{33}S$ (2-1)	62	9.34	31.26 ± 0.60	14.70 ± 0.60	0.46 ± 0.02	0.030
	$C^{33}S$ (2-1)	62	9.34	38.17 ± 0.60	4.54 ± 0.60	0.58 ± 0.02	0.119
	$C^{33}S$ (2-1)	62	9.34	45.24 ± 0.60	4.71 ± 0.60	0.12 ± 0.02	0.024
	$C^{34}S$ (2-1)	62	10.30	37.21 ± 0.03	6.69 ± 0.07	3.99 ± 0.03	0.560
	$C^{36}S$ (2-1)	62	9.25	···	···	···	···
	^{13}CS (2-1)	62	10.10	37.55 ± 0.04	5.69 ± 0.11	1.97 ± 0.03	0.325
	$^{13}C^{33}S$ (2-1)	62	9.22	···	···	···	···

Table A.3. continued.

Source	transitions	Time (mins)	rms (mK)	V_{LSR} (km s^{-1})	FWHM (km s^{-1})	$\int T_{MB} dv$ (K km s^{-1})	T_{MB} (K)
	$^{13}C^{34}S$ (2-1)	62	9.98	38.92 ± 0.37	2.38 ± 0.90	0.06 ± 0.02	0.024
	$C^{33}S$ (3-2)	62	37.79	36.99 ± 0.19	8.07 ± 0.49	2.18 ± 0.11	0.254
	$C^{34}S$ (3-2)	62	12.14	37.09 ± 0.02	7.32 ± 0.04	6.87 ± 0.03	0.881
	$C^{36}S$ (3-2)	62	12.12	...	...	...	...
	^{13}CS (3-2)	62	11.32	37.27 ± 0.03	6.60 ± 0.07	3.58 ± 0.03	0.510
G032.79+00.19	CS (2-1)	33	18.17	14.44 ± 0.00	7.96 ± 0.01	53.90 ± 0.06	6.360
	$C^{33}S$ (2-1)	33	15.06	2.25 ± 0.21	1.36 ± 0.59	0.07 ± 0.03	0.048
	$C^{33}S$ (2-1)	33	15.06	15.00 ± 0.12	4.78 ± 0.30	0.78 ± 0.08	0.153
	$C^{33}S$ (2-1)	33	15.06	13.66 ± 0.56	17.80 ± 1.33	1.34 ± 0.08	0.071
	$C^{34}S$ (2-1)	33	15.26	14.15 ± 0.02	6.79 ± 0.05	8.22 ± 0.05	1.140
	$C^{36}S$ (2-1)	33	12.97	...	...	...	...
	^{13}CS (2-1)	33	12.51	14.27 ± 0.03	6.79 ± 0.09	3.74 ± 0.04	0.517
	$^{13}C^{33}S$ (2-1)	33	14.00	...	...	...	...
	$^{13}C^{34}S$ (2-1)	33	14.77	...	...	...	...
	$C^{33}S$ (3-2)	33	21.06	13.99 ± 0.06	8.17 ± 0.16	3.60 ± 0.06	0.414
	$C^{34}S$ (3-2)	33	19.16	14.18 ± 0.01	7.47 ± 0.03	12.80 ± 0.05	1.610
	$C^{36}S$ (3-2)	33	20.42	...	...	...	...
	^{13}CS (3-2)	33	17.27	14.27 ± 0.03	7.25 ± 0.06	6.12 ± 0.05	0.793
G033.39+00.00	CS (2-1)	4	134.00	103.50 ± 0.09	6.63 ± 0.28	14.47 ± 0.45	2.050
	$C^{33}S$ (2-1)	4	39.01	...	...	...	...
	$C^{34}S$ (2-1)	4	41.08	103.60 ± 0.14	3.87 ± 0.45	1.33 ± 0.11	0.322
	$C^{36}S$ (2-1)	4	37.91	...	...	...	...
	^{13}CS (2-1)	4	41.02	103.30 ± 0.65	6.13 ± 1.41	0.61 ± 0.12	0.094
	$^{13}C^{33}S$ (2-1)	4	40.07	...	...	...	...
	$^{13}C^{34}S$ (2-1)	4	44.02	...	...	...	...
	$C^{33}S$ (3-2)	4	58.63	...	...	...	...
	$C^{34}S$ (3-2)	4	55.75	103.60 ± 0.15	3.94 ± 0.55	1.37 ± 0.13	0.326
	$C^{36}S$ (3-2)	4	50.82	...	...	...	...
	^{13}CS (3-2)	4	53.95	104.60 ± 0.44	6.04 ± 2.09	0.88 ± 0.18	0.136
G034.41+00.23	CS (2-1)	62	83.47	57.95 ± 0.00	6.74 ± 0.05	40.36 ± 0.26	5.630
	$C^{33}S$ (2-1)	62	8.51	48.64 ± 0.22	5.45 ± 0.62	0.30 ± 0.03	0.052
	$C^{33}S$ (2-1)	62	8.51	58.43 ± 0.06	4.56 ± 0.20	0.94 ± 0.03	0.194
	$C^{33}S$ (2-1)	62	8.51	65.63 ± 0.39	5.86 ± 0.85	0.26 ± 0.03	0.041
	$C^{33}S$ (2-1)	62	8.51	77.52 ± 0.55	5.25 ± 1.18	0.11 ± 0.02	0.019
	$C^{34}S$ (2-1)	62	24.44	57.73 ± 0.03	4.70 ± 0.07	5.45 ± 0.07	1.090
	$C^{36}S$ (2-1)	62	9.28	...	...	...	...
	^{13}CS (2-1)	62	11.51	57.92 ± 0.03	4.67 ± 0.08	2.50 ± 0.03	0.504
	$^{13}C^{33}S$ (2-1)	62	9.09	...	...	...	...
	$^{13}C^{34}S$ (2-1)	62	9.29	57.17 ± 0.58	5.44 ± 1.79	0.14 ± 0.03	0.024
	$C^{33}S$ (3-2)	62	67.11	57.91 ± 0.17	6.28 ± 0.46	2.98 ± 0.17	0.445
	$C^{34}S$ (3-2)	62	48.71	57.79 ± 0.03	5.45 ± 0.08	9.32 ± 0.12	1.610
	$C^{36}S$ (3-2)	62	14.65	...	...	...	...
	^{13}CS (3-2)	62	16.13	58.03 ± 0.02	5.01 ± 0.05	4.56 ± 0.04	0.855
G034.79−01.38	CS (2-1)	33	18.67	45.38 ± 0.03	9.36 ± 0.07	11.23 ± 0.08	1.130
	CS (2-1)	33	18.67	47.57 ± 0.01	1.29 ± 0.02	1.98 ± 0.03	1.440
	$C^{33}S$ (2-1)	33	13.77	35.91 ± 0.76	6.05 ± 2.45	0.19 ± 0.05	0.030
	$C^{33}S$ (2-1)	33	13.77	46.52 ± 0.07	2.40 ± 0.17	0.43 ± 0.03	0.166
	$C^{33}S$ (2-1)	33	13.77	54.55 ± 0.34	1.74 ± 0.60	0.06 ± 0.02	0.030
	$C^{34}S$ (2-1)	33	14.43	45.95 ± 0.01	2.61 ± 0.03	2.86 ± 0.03	1.030
	$C^{36}S$ (2-1)	33	12.16	...	...	...	...
	^{13}CS (2-1)	33	13.82	46.07 ± 0.02	2.28 ± 0.05	1.25 ± 0.03	0.516
	$^{13}C^{33}S$ (2-1)	33	12.62	...	...	...	...
	$^{13}C^{34}S$ (2-1)	33	14.72	...	...	...	...
	$C^{33}S$ (3-2)	33	18.39	45.82 ± 0.06	3.34 ± 0.17	0.83 ± 0.03	0.232
	$C^{34}S$ (3-2)	33	23.38	45.83 ± 0.01	2.59 ± 0.04	3.44 ± 0.04	1.250
	$C^{36}S$ (3-2)	33	17.37	...	...	...	...
	^{13}CS (3-2)	33	18.11	46.01 ± 0.02	2.45 ± 0.06	1.52 ± 0.03	0.584

Table A.3. continued.

Source	transitions	Time (mins)	rms (mK)	V_{LSR} (km s^{-1})	FWHM (km s^{-1})	$\int T_{MB}dv$ (K km s^{-1})	T_{MB} (K)
G035.79−00.17	CS (2-1)	4	81.00	58.93 ± 0.08	2.86 ± 0.19	3.21 ± 0.18	1.050
	CS (2-1)	4	81.00	63.71 ± 0.06	3.31 ± 0.21	4.91 ± 0.22	1.390
	$C^{33}S$ (2-1)	4	36.98	...	...	...	...
	$C^{34}S$ (2-1)	4	40.68	61.48 ± 0.17	4.83 ± 0.49	1.48 ± 0.11	0.288
	$C^{36}S$ (2-1)	4	34.15	...	...	...	...
	^{13}CS (2-1)	4	40.52	61.54 ± 0.40	4.77 ± 0.84	0.64 ± 0.10	0.126
	$^{13}C^{33}S$ (2-1)	4	38.10	...	...	...	...
	$^{13}C^{34}S$ (2-1)	4	40.16	...	...	...	...
	$C^{33}S$ (3-2)	4	58.94	61.40 ± 0.38	4.45 ± 0.80	0.68 ± 0.11	0.144
	$C^{34}S$ (3-2)	4	51.73	61.88 ± 0.13	5.96 ± 0.32	2.69 ± 0.12	0.423
	$C^{36}S$ (3-2)	4	55.79	...	...	...	...
	^{13}CS (3-2)	4	51.72	62.17 ± 0.23	5.49 ± 0.53	1.40 ± 0.12	0.240
G036.11+00.55	CS (2-1)	4	39.78	75.87 ± 0.03	3.49 ± 0.08	4.49 ± 0.09	1.210
	$C^{33}S$ (2-1)	4	39.00	76.41 ± 0.29	2.57 ± 0.50	0.32 ± 0.07	0.117
	$C^{34}S$ (2-1)	4	36.13	76.15 ± 0.07	1.98 ± 0.16	0.88 ± 0.06	0.415
	$C^{36}S$ (2-1)	4	34.77	...	...	...	...
	^{13}CS (2-1)	4	39.44	76.08 ± 0.13	1.53 ± 0.24	0.35 ± 0.05	0.214
	$^{13}C^{33}S$ (2-1)	4	35.94	...	...	...	...
	$^{13}C^{34}S$ (2-1)	4	42.69	...	...	...	...
	$C^{33}S$ (3-2)	4	59.66	75.97 ± 0.38	3.99 ± 1.28	0.61 ± 0.14	0.144
	$C^{34}S$ (3-2)	4	57.15	76.06 ± 0.05	1.80 ± 0.11	1.34 ± 0.07	0.695
	$C^{36}S$ (3-2)	4	58.67	...	...	...	...
	^{13}CS (3-2)	4	53.57	76.04 ± 0.12	2.13 ± 0.38	0.68 ± 0.09	0.299
G037.42+01.51	CS (2-1)	62	13.77	43.86 ± 0.00	3.63 ± 0.00	31.86 ± 0.02	8.230
	$C^{33}S$ (2-1)	62	8.25	34.69 ± 0.21	2.38 ± 0.56	0.10 ± 0.02	0.038
	$C^{33}S$ (2-1)	62	8.25	44.64 ± 0.05	3.18 ± 0.13	0.51 ± 0.02	0.151
	$C^{33}S$ (2-1)	62	8.25	51.42 ± 0.28	2.15 ± 0.53	0.05 ± 0.01	0.020
	$C^{34}S$ (2-1)	62	8.05	43.87 ± 0.01	3.12 ± 0.02	3.31 ± 0.02	0.996
	$C^{36}S$ (2-1)	62	7.33	...	...	...	...
	^{13}CS (2-1)	62	8.58	44.00 ± 0.02	3.06 ± 0.05	1.38 ± 0.02	0.423
	$^{13}C^{33}S$ (2-1)	62	9.27	...	...	...	...
	$^{13}C^{34}S$ (2-1)	62	9.82	...	...	...	...
	$C^{33}S$ (3-2)	62	70.24	43.76 ± 0.28	4.78 ± 0.90	1.25 ± 0.17	0.245
	$C^{34}S$ (3-2)	62	13.47	43.86 ± 0.01	3.22 ± 0.02	4.37 ± 0.02	1.270
	$C^{36}S$ (3-2)	62	11.21	...	...	...	...
	^{13}CS (3-2)	62	11.75	44.02 ± 0.02	3.13 ± 0.04	1.92 ± 0.02	0.576
G037.47−00.10	CS (2-1)	4	48.37	58.74 ± 0.02	3.19 ± 0.05	7.68 ± 0.10	2.260
	$C^{33}S$ (2-1)	4	40.88	...	...	...	...
	$C^{34}S$ (2-1)	4	33.15	59.16 ± 0.14	2.83 ± 0.30	0.65 ± 0.06	0.215
	$C^{36}S$ (2-1)	4	36.23	...	...	...	...
	^{13}CS (2-1)	4	39.40	...	...	...	...
	$^{13}C^{33}S$ (2-1)	4	36.27	...	...	...	...
	$^{13}C^{34}S$ (2-1)	4	37.99	...	...	...	...
	$C^{33}S$ (3-2)	4	58.68	...	...	...	...
	$C^{34}S$ (3-2)	4	46.99	59.23 ± 0.11	2.59 ± 0.27	0.85 ± 0.07	0.306
	$C^{36}S$ (3-2)	4	52.75	...	...	...	...
	^{13}CS (3-2)	4	55.45	59.54 ± 0.30	2.94 ± 0.81	0.47 ± 0.10	0.150
G038.03−00.30	CS (2-1)	4	42.85	62.23 ± 0.07	5.52 ± 0.21	4.66 ± 0.13	0.793
	$C^{33}S$ (2-1)	4	37.35	...	...	...	...
	$C^{34}S$ (2-1)	4	32.37	60.97 ± 0.33	3.08 ± 0.75	0.34 ± 0.07	0.105
	$C^{36}S$ (2-1)	4	37.08	...	...	...	...
	^{13}CS (2-1)	4	35.87	...	...	...	...
	$^{13}C^{33}S$ (2-1)	4	35.67	...	...	...	...
	$^{13}C^{34}S$ (2-1)	4	43.20	...	...	...	...
	$C^{33}S$ (3-2)	4	56.02	...	...	...	...
	$C^{34}S$ (3-2)	4	47.44	...	...	...	...
	$C^{36}S$ (3-2)	4	57.17	...	...	...	...

Table A.3. continued.

Source	transitions	Time (mins)	rms (mK)	V_{LSR} (km s^{-1})	FWHM (km s^{-1})	$\int T_{MB} dv$ (K km s^{-1})	T_{MB} (K)
	^{13}CS (3-2)	4	54.66	···	···	···	···
G038.11−00.22	CS (2-1)	4	52.60	83.49 ± 0.03	3.43 ± 0.08	6.19 ± 0.12	1.690
	C^{33}S (2-1)	4	38.13	···	···	···	···
	C^{34}S (2-1)	4	34.38	83.12 ± 0.07	2.65 ± 0.22	1.16 ± 0.07	0.413
	C^{36}S (2-1)	4	38.69	···	···	···	···
	^{13}CS (2-1)	4	38.43	83.06 ± 0.18	2.70 ± 0.42	0.57 ± 0.08	0.200
	^{13}C^{33}S (2-1)	4	36.02	···	···	···	···
	^{13}C^{34}S (2-1)	4	39.20	···	···	···	···
	C^{33}S (3-2)	4	58.41	···	···	···	···
	C^{34}S (3-2)	4	56.40	83.25 ± 0.08	2.98 ± 0.18	1.78 ± 0.09	0.562
	C^{36}S (3-2)	4	56.69	···	···	···	···
	^{13}CS (3-2)	4	50.94	83.23 ± 0.14	2.74 ± 0.45	0.81 ± 0.09	0.279
G040.28−00.21	CS (2-1)	4	41.77	73.59 ± 0.03	5.84 ± 0.12	12.95 ± 0.40	2.080
	CS (2-1)	4	41.77	71.61 ± 0.12	18.84 ± 0.27	25.07 ± 0.42	1.250
	C^{33}S (2-1)	4	38.40	73.98 ± 0.30	3.72 ± 1.00	0.52 ± 0.10	0.131
	C^{34}S (2-1)	4	39.30	73.65 ± 0.08	5.40 ± 0.23	3.53 ± 0.12	0.615
	C^{36}S (2-1)	4	38.94	···	···	···	···
	^{13}CS (2-1)	4	36.00	74.18 ± 0.17	5.35 ± 0.55	1.54 ± 0.11	0.271
	^{13}C^{33}S (2-1)	4	37.72	···	···	···	···
	^{13}C^{34}S (2-1)	4	41.87	···	···	···	···
	C^{33}S (3-2)	4	65.35	73.49 ± 0.29	6.43 ± 1.48	1.80 ± 0.24	0.262
	C^{34}S (3-2)	4	59.21	73.69 ± 0.06	5.52 ± 0.18	6.18 ± 0.15	1.050
	C^{36}S (3-2)	4	54.95	···	···	···	···
	^{13}CS (3-2)	4	54.59	73.93 ± 0.11	5.02 ± 0.32	2.71 ± 0.13	0.507
G040.42+00.70	CS (2-1)	4	46.66	12.48 ± 0.02	3.09 ± 0.05	7.85 ± 0.10	2.390
	C^{33}S (2-1)	4	44.64	···	···	···	···
	C^{34}S (2-1)	4	40.28	12.50 ± 0.08	3.00 ± 0.23	1.43 ± 0.09	0.447
	C^{36}S (2-1)	4	35.74	···	···	···	···
	^{13}CS (2-1)	4	38.24	12.62 ± 0.34	3.31 ± 1.79	0.41 ± 0.13	0.117
	^{13}C^{33}S (2-1)	4	33.29	···	···	···	···
	^{13}C^{34}S (2-1)	4	43.12	···	···	···	···
	C^{33}S (3-2)	4	56.25	11.80 ± 0.28	2.69 ± 0.84	0.42 ± 0.10	0.148
	C^{34}S (3-2)	4	54.23	12.65 ± 0.07	2.75 ± 0.18	1.78 ± 0.09	0.609
	C^{36}S (3-2)	4	56.43	···	···	···	···
	^{13}CS (3-2)	4	48.24	12.97 ± 0.09	2.20 ± 0.26	0.84 ± 0.08	0.357
G040.62−00.13	CS (2-1)	4	53.05	32.53 ± 0.02	5.18 ± 0.05	18.84 ± 0.14	3.420
	C^{33}S (2-1)	4	41.61	···	···	···	···
	C^{34}S (2-1)	4	31.55	32.84 ± 0.09	4.27 ± 0.23	1.75 ± 0.08	0.386
	C^{36}S (2-1)	4	40.16	···	···	···	···
	^{13}CS (2-1)	4	37.53	31.61 ± 0.32	4.90 ± 0.65	0.78 ± 0.10	0.150
	^{13}C^{33}S (2-1)	4	39.39	···	···	···	···
	^{13}C^{34}S (2-1)	4	43.60	···	···	···	···
	C^{33}S (3-2)	4	57.93	···	···	···	···
	C^{34}S (3-2)	4	49.42	32.86 ± 0.09	3.67 ± 0.20	1.89 ± 0.09	0.485
	C^{36}S (3-2)	4	49.09	···	···	···	···
	^{13}CS (3-2)	4	53.27	32.54 ± 0.21	3.33 ± 0.78	0.79 ± 0.12	0.222
G041.15−00.20	CS (2-1)	4	58.82	60.40 ± 0.05	2.58 ± 0.13	2.71 ± 0.11	0.984
	C^{33}S (2-1)	4	36.25	···	···	···	···
	C^{34}S (2-1)	4	37.47	···	···	···	···
	C^{36}S (2-1)	4	34.39	···	···	···	···
	^{13}CS (2-1)	4	41.15	···	···	···	···
	^{13}C^{33}S (2-1)	4	41.65	···	···	···	···
	^{13}C^{34}S (2-1)	4	41.70	···	···	···	···
	C^{33}S (3-2)	4	60.74	···	···	···	···
	C^{34}S (3-2)	4	51.68	···	···	···	···
	C^{36}S (3-2)	4	53.15	···	···	···	···
	^{13}CS (3-2)	4	53.36	···	···	···	···

Table A.3. continued.

Source	transitions	Time (mins)	rms (mK)	V_{LSR} (km s^{-1})	FWHM (km s^{-1})	$\int T_{MB}dv$ (K km s^{-1})	T_{MB} (K)
G041.22−00.19	CS (2-1)	4	67.16	59.31 ± 0.04	2.82 ± 0.11	4.21 ± 0.14	1.400
	$C^{33}S$ (2-1)	4	42.49	···	···	···	···
	$C^{34}S$ (2-1)	4	39.48	59.35 ± 0.15	1.41 ± 0.36	0.26 ± 0.06	0.173
	$C^{36}S$ (2-1)	4	37.50	···	···	···	···
	^{13}CS (2-1)	4	36.57	···	···	···	···
	$^{13}C^{33}S$ (2-1)	4	38.45	···	···	···	···
	$^{13}C^{34}S$ (2-1)	4	45.30	···	···	···	···
	$C^{33}S$ (3-2)	4	56.87	···	···	···	···
	$C^{34}S$ (3-2)	4	51.63	59.39 ± 0.16	1.71 ± 0.36	0.35 ± 0.06	0.192
	$C^{36}S$ (3-2)	4	58.30	···	···	···	···
	^{13}CS (3-2)	4	54.50	···	···	···	···
G042.03+00.19	CS (2-1)	4	36.41	17.87 ± 0.03	3.56 ± 0.06	5.02 ± 0.08	1.320
	$C^{33}S$ (2-1)	4	32.18	···	···	···	···
	$C^{34}S$ (2-1)	4	38.67	18.00 ± 0.20	3.15 ± 0.51	0.63 ± 0.08	0.188
	$C^{36}S$ (2-1)	4	40.89	···	···	···	···
	^{13}CS (2-1)	4	32.45	17.88 ± 0.36	2.79 ± 0.86	0.25 ± 0.07	0.083
	$^{13}C^{33}S$ (2-1)	4	36.14	···	···	···	···
	$^{13}C^{34}S$ (2-1)	4	41.05	···	···	···	···
	$C^{33}S$ (3-2)	4	50.58	···	···	···	···
	$C^{34}S$ (3-2)	4	53.71	17.40 ± 0.23	2.79 ± 0.86	0.53 ± 0.11	0.178
	$C^{36}S$ (3-2)	4	56.74	···	···	···	···
	^{13}CS (3-2)	4	50.34	···	···	···	···
G043.03−00.45	CS (2-1)	4	47.13	57.56 ± 0.02	5.41 ± 0.05	15.92 ± 0.13	2.770
	$C^{33}S$ (2-1)	4	35.91	···	···	···	···
	$C^{34}S$ (2-1)	4	32.61	57.54 ± 0.06	4.05 ± 0.14	2.47 ± 0.08	0.573
	$C^{36}S$ (2-1)	4	38.24	···	···	···	···
	^{13}CS (2-1)	4	39.05	57.81 ± 0.14	3.76 ± 0.30	1.20 ± 0.09	0.299
	$^{13}C^{33}S$ (2-1)	4	32.91	···	···	···	···
	$^{13}C^{34}S$ (2-1)	4	38.93	···	···	···	···
	$C^{33}S$ (3-2)	4	58.66	57.66 ± 0.26	4.54 ± 0.93	1.02 ± 0.14	0.210
	$C^{34}S$ (3-2)	4	52.27	57.54 ± 0.06	4.23 ± 0.14	3.69 ± 0.10	0.819
	$C^{36}S$ (3-2)	4	51.48	···	···	···	···
	^{13}CS (3-2)	4	52.61	57.73 ± 0.10	3.66 ± 0.22	1.69 ± 0.10	0.434
G045.45+00.06	CS (2-1)	4	43.86	58.15 ± 0.02	5.64 ± 0.04	19.94 ± 0.12	3.320
	$C^{33}S$ (2-1)	4	37.77	59.05 ± 0.45	6.08 ± 1.21	0.75 ± 0.12	0.115
	$C^{34}S$ (2-1)	4	32.60	58.08 ± 0.06	4.46 ± 0.15	3.05 ± 0.08	0.642
	$C^{36}S$ (2-1)	4	35.39	···	···	···	···
	^{13}CS (2-1)	4	36.33	58.05 ± 0.16	5.10 ± 0.35	1.55 ± 0.10	0.286
	$^{13}C^{33}S$ (2-1)	4	40.10	···	···	···	···
	$^{13}C^{34}S$ (2-1)	4	43.67	···	···	···	···
	$C^{33}S$ (3-2)	4	53.93	57.96 ± 0.19	5.28 ± 0.44	1.59 ± 0.12	0.282
	$C^{34}S$ (3-2)	4	50.30	58.09 ± 0.05	4.78 ± 0.12	5.09 ± 0.11	1.000
	$C^{36}S$ (3-2)	4	57.42	···	···	···	···
	^{13}CS (3-2)	4	56.66	58.13 ± 0.11	4.74 ± 0.27	2.51 ± 0.12	0.497
G045.49+00.12	CS (2-1)	4	42.11	60.46 ± 0.03	6.26 ± 0.08	12.49 ± 0.13	1.870
	$C^{33}S$ (2-1)	4	36.89	···	···	···	···
	$C^{34}S$ (2-1)	4	37.08	60.59 ± 0.15	4.66 ± 0.37	1.50 ± 0.10	0.302
	$C^{36}S$ (2-1)	4	32.99	···	···	···	···
	^{13}CS (2-1)	4	37.80	60.03 ± 0.16	1.99 ± 0.50	0.45 ± 0.08	0.215
	$^{13}C^{33}S$ (2-1)	4	37.27	···	···	···	···
	$^{13}C^{34}S$ (2-1)	4	42.51	···	···	···	···
	$C^{33}S$ (3-2)	4	60.07	···	···	···	···
	$C^{34}S$ (3-2)	4	55.31	61.26 ± 0.26	4.63 ± 0.45	1.05 ± 0.11	0.213
	$C^{36}S$ (3-2)	4	57.27	···	···	···	···
	^{13}CS (3-2)	4	53.00	···	···	···	···
G045.80−00.35	CS (2-1)	4	43.23	60.33 ± 0.03	4.54 ± 0.07	7.97 ± 0.11	1.650
	$C^{33}S$ (2-1)	4	36.69	···	···	···	···

Table A.3. continued.

Source	transitions	Time (mins)	rms (mK)	V_{LSR} (km s^{-1})	FWHM (km s^{-1})	$\int T_{MB} dv$ (K km s^{-1})	T_{MB} (K)
	$C^{34}S$ (2-1)	4	32.09	59.12 ± 0.08	3.47 ± 0.19	1.59 ± 0.07	0.431
	$C^{36}S$ (2-1)	4	37.56	···	···	···	···
	^{13}CS (2-1)	4	35.32	59.16 ± 0.17	2.71 ± 0.45	0.59 ± 0.07	0.204
	$^{13}C^{33}S$ (2-1)	4	40.79	···	···	···	···
	$^{13}C^{34}S$ (2-1)	4	40.31	···	···	···	···
	$C^{33}S$ (3-2)	4	55.54	58.87 ± 0.38	4.47 ± 1.88	0.78 ± 0.19	0.164
	$C^{34}S$ (3-2)	4	51.84	59.36 ± 0.08	4.23 ± 0.23	2.67 ± 0.11	0.593
	$C^{36}S$ (3-2)	4	59.38	···	···	···	···
	^{13}CS (3-2)	4	57.71	59.30 ± 0.14	3.38 ± 0.42	1.20 ± 0.11	0.332
G048.99−00.29	CS (2-1)	4	104.00	67.88 ± 0.02	5.49 ± 0.04	44.00 ± 0.29	7.530
	$C^{33}S$ (2-1)	4	38.82	68.65 ± 0.31	3.74 ± 0.67	0.52 ± 0.08	0.130
	$C^{34}S$ (2-1)	4	39.81	68.01 ± 0.05	3.94 ± 0.14	3.65 ± 0.10	0.869
	$C^{36}S$ (2-1)	4	36.76	···	···	···	···
	^{13}CS (2-1)	4	38.54	67.99 ± 0.12	4.21 ± 0.31	1.55 ± 0.10	0.347
	$^{13}C^{33}S$ (2-1)	4	36.42	···	···	···	···
	$^{13}C^{34}S$ (2-1)	4	38.38	···	···	···	···
	$C^{33}S$ (3-2)	4	58.03	67.98 ± 0.25	4.78 ± 0.83	1.15 ± 0.14	0.227
	$C^{34}S$ (3-2)	4	59.90	67.96 ± 0.05	4.57 ± 0.16	4.97 ± 0.13	1.020
	$C^{36}S$ (3-2)	4	53.59	···	···	···	···
	^{13}CS (3-2)	4	50.30	68.13 ± 0.11	4.46 ± 0.28	2.14 ± 0.11	0.452
G049.04−01.07	CS (2-1)	4	54.91	38.39 ± 0.03	3.20 ± 0.12	5.49 ± 0.14	1.610
	$C^{33}S$ (2-1)	4	36.97	···	···	···	···
	$C^{34}S$ (2-1)	4	33.57	39.09 ± 0.09	2.78 ± 0.24	0.96 ± 0.07	0.324
	$C^{36}S$ (2-1)	4	38.31	···	···	···	···
	^{13}CS (2-1)	4	41.68	···	···	···	···
	$^{13}C^{33}S$ (2-1)	4	34.58	···	···	···	···
	$^{13}C^{34}S$ (2-1)	4	47.93	···	···	···	···
	$C^{33}S$ (3-2)	4	53.91	···	···	···	···
	$C^{34}S$ (3-2)	4	54.03	39.01 ± 0.09	2.83 ± 0.27	1.28 ± 0.09	0.423
	$C^{36}S$ (3-2)	4	53.96	···	···	···	···
	^{13}CS (3-2)	4	45.31	39.00 ± 0.31	4.18 ± 1.21	0.60 ± 0.11	0.135
G049.26+00.31	CS (2-1)	4	43.66	3.21 ± 0.02	4.56 ± 0.06	9.79 ± 0.11	2.020
	$C^{33}S$ (2-1)	4	35.51	···	···	···	···
	$C^{34}S$ (2-1)	4	38.73	3.14 ± 0.16	2.98 ± 0.44	0.71 ± 0.08	0.225
	$C^{36}S$ (2-1)	4	34.06	···	···	···	···
	^{13}CS (2-1)	4	39.53	3.06 ± 0.41	4.13 ± 0.85	0.47 ± 0.09	0.107
	$^{13}C^{33}S$ (2-1)	4	28.59	···	···	···	···
	$^{13}C^{34}S$ (2-1)	4	42.27	···	···	···	···
	$C^{33}S$ (3-2)	4	47.92	···	···	···	···
	$C^{34}S$ (3-2)	4	51.38	3.41 ± 0.17	4.18 ± 0.54	1.18 ± 0.11	0.265
	$C^{36}S$ (3-2)	4	49.31	···	···	···	···
	^{13}CS (3-2)	4	52.92	3.48 ± 0.36	3.94 ± 1.15	0.57 ± 0.12	0.135
G049.34+00.41	CS (2-1)	4	40.54	66.35 ± 0.09	1.32 ± 0.21	0.37 ± 0.05	0.267
	$C^{33}S$ (2-1)	4	37.71	···	···	···	···
	$C^{34}S$ (2-1)	4	35.69	···	···	···	···
	$C^{36}S$ (2-1)	4	35.89	···	···	···	···
	^{13}CS (2-1)	4	33.48	···	···	···	···
	$^{13}C^{33}S$ (2-1)	4	36.70	···	···	···	···
	$^{13}C^{34}S$ (2-1)	4	37.28	···	···	···	···
	$C^{33}S$ (3-2)	4	53.77	···	···	···	···
	$C^{34}S$ (3-2)	4	56.61	···	···	···	···
	$C^{36}S$ (3-2)	4	55.54	···	···	···	···
	^{13}CS (3-2)	4	52.48	···	···	···	···
G049.41+00.32	CS (2-1)	4	40.49	-21.20 ± 0.03	3.59 ± 0.07	6.06 ± 0.09	1.580
	$C^{33}S$ (2-1)	4	36.82	···	···	···	···
	$C^{34}S$ (2-1)	4	31.87	-21.06 ± 0.17	3.36 ± 0.51	0.67 ± 0.08	0.188
	$C^{36}S$ (2-1)	4	40.77	···	···	···	···

Table A.3. continued.

Source	transitions	Time (mins)	rms (mK)	V_{LSR} (km s^{-1})	FWHM (km s^{-1})	$\int T_{MB}dv$ (K km s^{-1})	T_{MB} (K)
	^{13}CS (2-1)	4	40.29	-20.37 ± 0.41	3.32 ± 1.36	0.35 ± 0.10	0.099
	^{13}C^{33}S (2-1)	4	33.99	...	...	...	...
	^{13}C^{34}S (2-1)	4	38.39	...	...	...	...
	C^{33}S (3-2)	4	54.48	...	...	...	...
	C^{34}S (3-2)	4	54.56	-20.87 ± 0.15	3.16 ± 0.34	0.94 ± 0.09	0.278
	C^{36}S (3-2)	4	55.44	...	...	...	...
	^{13}CS (3-2)	4	55.94	-19.98 ± 0.46	4.32 ± 0.96	0.55 ± 0.11	0.120
G049.59−00.24	CS (2-1)	4	40.16	56.74 ± 0.01	3.23 ± 0.04	9.30 ± 0.09	2.700
	C^{33}S (2-1)	4	36.10	...	...	...	...
	C^{34}S (2-1)	4	32.18	57.06 ± 0.07	2.68 ± 0.16	1.24 ± 0.06	0.434
	C^{36}S (2-1)	4	40.34	...	...	...	...
	^{13}CS (2-1)	4	42.38	57.09 ± 0.36	2.50 ± 1.49	0.36 ± 0.12	0.136
	^{13}C^{33}S (2-1)	4	34.23	...	...	...	...
	^{13}C^{34}S (2-1)	4	42.70	...	...	...	...
	C^{33}S (3-2)	4	62.11	...	...	...	...
	C^{34}S (3-2)	4	48.11	56.99 ± 0.07	2.27 ± 0.16	1.14 ± 0.07	0.469
	C^{36}S (3-2)	4	48.49	...	...	...	...
	^{13}CS (3-2)	4	51.59	56.84 ± 0.23	2.46 ± 0.48	0.42 ± 0.08	0.162
W51-IRS2	CS (2-1)	278	33.55	49.96 ± 0.60	4.34 ± 0.60	14.26 ± 1.69	3.090
	CS (2-1)	278	33.55	60.95 ± 0.60	7.55 ± 0.60	90.86 ± 1.69	11.300
	C^{33}S (2-1)	278	4.92	40.67 ± 0.60	6.47 ± 0.60	0.10 ± 0.06	0.015
	C^{33}S (2-1)	278	4.92	50.54 ± 0.60	5.44 ± 0.60	0.78 ± 0.06	0.136
	C^{33}S (2-1)	278	4.92	61.59 ± 0.60	8.55 ± 0.60	2.83 ± 0.06	0.310
	C^{33}S (2-1)	278	4.92	75.98 ± 0.60	16.38 ± 0.60	0.55 ± 0.06	0.032
	C^{34}S (2-1)	278	16.51	49.95 ± 0.05	3.51 ± 0.12	1.28 ± 0.04	0.344
	C^{34}S (2-1)	278	16.51	61.09 ± 0.01	7.29 ± 0.04	12.29 ± 0.05	1.580
	C^{36}S (2-1)	278	5.77	53.54 ± 0.33	5.98 ± 0.70	0.20 ± 0.02	0.031
	C^{36}S (2-1)	278	5.77	63.94 ± 1.09	9.82 ± 3.52	0.12 ± 0.03	0.011
	C^{36}S (2-1)	278	5.77	78.27 ± 0.50	4.27 ± 1.00	0.06 ± 0.01	0.014
	^{13}CS (2-1)	278	5.21	50.02 ± 0.04	3.31 ± 0.09	0.47 ± 0.01	0.135
	^{13}CS (2-1)	278	5.21	61.24 ± 0.01	7.56 ± 0.03	5.54 ± 0.02	0.689
	^{13}C^{33}S (2-1)	278	9.30	61.96 ± 0.63	1.63 ± 1.13	0.02 ± 0.01	0.012
	^{13}C^{34}S (2-1)	278	4.32	50.35 ± 1.22	9.82 ± 2.10	0.13 ± 0.03	0.013
	^{13}C^{34}S (2-1)	278	4.32	60.59 ± 0.40	8.62 ± 0.76	0.33 ± 0.03	0.036
	C^{33}S (3-2)	278	10.87	60.68 ± 0.01	8.72 ± 0.05	6.11 ± 0.03	0.658
	C^{34}S (3-2)	278	10.44	50.18 ± 0.04	3.78 ± 0.11	0.89 ± 0.02	0.220
	C^{34}S (3-2)	278	10.44	60.91 ± 0.01	7.29 ± 0.01	17.26 ± 0.03	2.220
	C^{36}S (3-2)	139	13.02	31.10 ± 0.30	7.25 ± 0.65	0.40 ± 0.03	0.051
	C^{36}S (3-2)	139	13.02	51.81 ± 0.50	7.11 ± 1.30	0.23 ± 0.03	0.031
	C^{36}S (3-2)	139	13.02	61.67 ± 0.60	4.09 ± 1.10	0.09 ± 0.02	0.020
	C^{36}S (3-2)	139	13.02	104.90 ± 0.36	5.33 ± 0.78	0.22 ± 0.03	0.038
	^{13}CS (3-2)	278	13.12	49.45 ± 0.16	6.73 ± 0.58	0.73 ± 0.04	0.102
	^{13}CS (3-2)	278	13.12	60.99 ± 0.02	7.44 ± 0.04	8.15 ± 0.04	1.030
G054.10−00.08	CS (2-1)	4	73.63	38.39 ± 0.03	4.54 ± 0.07	15.75 ± 0.19	3.260
	C^{33}S (2-1)	4	39.94	...	...	...	...
	C^{34}S (2-1)	4	35.60	38.45 ± 0.06	3.25 ± 0.14	2.06 ± 0.08	0.595
	C^{36}S (2-1)	4	36.82	...	...	...	...
	^{13}CS (2-1)	4	36.62	38.72 ± 0.13	2.89 ± 0.32	0.82 ± 0.08	0.266
	^{13}C^{33}S (2-1)	4	36.46	...	...	...	...
	^{13}C^{34}S (2-1)	4	41.59	...	...	...	...
	C^{33}S (3-2)	4	56.20	37.95 ± 0.24	3.88 ± 0.85	0.85 ± 0.13	0.207
	C^{34}S (3-2)	4	48.49	38.15 ± 0.05	3.52 ± 0.14	3.01 ± 0.09	0.803
	C^{36}S (3-2)	4	53.06	...	...	...	...
	^{13}CS (3-2)	4	54.71	38.31 ± 0.15	3.55 ± 0.38	1.21 ± 0.10	0.322
G058.77+00.64	CS (2-1)	4	48.84	32.48 ± 0.01	3.51 ± 0.04	12.58 ± 0.11	3.360
	C^{33}S (2-1)	4	35.62	...	...	...	...
	C^{34}S (2-1)	4	33.78	32.36 ± 0.07	3.06 ± 0.15	1.62 ± 0.07	0.496

Table A.3. continued.

Source	transitions	Time (mins)	rms (mK)	V_{LSR} (km s^{-1})	FWHM (km s^{-1})	$\int T_{MB} dv$ (K km s^{-1})	T_{MB} (K)
	$C^{36}S$ (2-1)	4	37.87	···	···	···	···
	^{13}CS (2-1)	4	38.00	32.43 ± 0.21	3.49 ± 0.48	0.70 ± 0.08	0.188
	$^{13}C^{33}S$ (2-1)	4	34.38	···	···	···	···
	$^{13}C^{34}S$ (2-1)	4	41.79	···	···	···	···
	$C^{33}S$ (3-2)	4	59.01	32.10 ± 0.30	3.87 ± 0.71	0.73 ± 0.11	0.177
	$C^{34}S$ (3-2)	4	48.73	32.44 ± 0.05	2.81 ± 0.12	2.06 ± 0.08	0.688
	$C^{36}S$ (3-2)	4	51.79	···	···	···	···
	^{13}CS (3-2)	4	51.84	32.39 ± 0.13	2.62 ± 0.31	0.82 ± 0.08	0.295
G059.47−00.18	CS (2-1)	4	37.00	25.29 ± 0.01	1.59 ± 0.03	3.41 ± 0.06	2.010
	$C^{33}S$ (2-1)	4	35.76	···	···	···	···
	$C^{34}S$ (2-1)	4	34.42	25.23 ± 0.10	1.15 ± 0.20	0.26 ± 0.04	0.212
	$C^{36}S$ (2-1)	4	31.58	···	···	···	···
	^{13}CS (2-1)	4	38.99	···	···	···	···
	$^{13}C^{33}S$ (2-1)	4	33.87	···	···	···	···
	$^{13}C^{34}S$ (2-1)	4	38.47	···	···	···	···
	$C^{33}S$ (3-2)	4	53.11	···	···	···	···
	$C^{34}S$ (3-2)	4	50.72	25.43 ± 0.11	0.47 ± 0.26	0.12 ± 0.03	0.247
	$C^{36}S$ (3-2)	4	46.67	···	···	···	···
	^{13}CS (3-2)	4	57.68	···	···	···	···
G059.83+00.67	CS (2-1)	4	45.63	34.75 ± 0.01	3.97 ± 0.04	13.75 ± 0.11	3.260
	$C^{33}S$ (2-1)	4	34.82	···	···	···	···
	$C^{34}S$ (2-1)	4	35.09	34.70 ± 0.06	2.93 ± 0.15	1.70 ± 0.07	0.544
	$C^{36}S$ (2-1)	4	33.88	···	···	···	···
	^{13}CS (2-1)	4	41.83	35.02 ± 0.18	2.68 ± 0.40	0.60 ± 0.08	0.211
	$^{13}C^{33}S$ (2-1)	4	35.65	···	···	···	···
	$^{13}C^{34}S$ (2-1)	4	42.16	···	···	···	···
	$C^{33}S$ (3-2)	4	58.26	···	···	···	···
	$C^{34}S$ (3-2)	4	57.33	34.85 ± 0.05	3.10 ± 0.13	2.77 ± 0.10	0.840
	$C^{36}S$ (3-2)	4	53.01	···	···	···	···
	^{13}CS (3-2)	4	48.19	34.97 ± 0.11	3.13 ± 0.29	1.12 ± 0.09	0.337
G060.57−00.18	CS (2-1)	4	39.38	4.83 ± 0.02	2.11 ± 0.04	3.79 ± 0.07	1.690
	$C^{33}S$ (2-1)	4	36.12	···	···	···	···
	$C^{34}S$ (2-1)	4	35.72	4.84 ± 0.12	1.77 ± 0.28	0.42 ± 0.06	0.225
	$C^{36}S$ (2-1)	4	35.95	···	···	···	···
	^{13}CS (2-1)	4	38.86	4.86 ± 0.23	1.29 ± 0.55	0.17 ± 0.06	0.124
	$^{13}C^{33}S$ (2-1)	4	34.84	···	···	···	···
	$^{13}C^{34}S$ (2-1)	4	36.07	···	···	···	···
	$C^{33}S$ (3-2)	4	55.14	···	···	···	···
	$C^{34}S$ (3-2)	4	50.98	4.97 ± 0.10	1.74 ± 0.28	0.54 ± 0.07	0.289
	$C^{36}S$ (3-2)	4	51.05	···	···	···	···
	^{13}CS (3-2)	4	55.00	4.93 ± 0.15	1.66 ± 0.31	0.38 ± 0.07	0.215
G070.18+01.74	CS (2-1)	4	37.78	-22.03 ± 0.02	4.36 ± 0.04	10.93 ± 0.09	2.360
	$C^{33}S$ (2-1)	4	34.72	···	···	···	···
	$C^{34}S$ (2-1)	4	32.98	-21.80 ± 0.11	3.80 ± 0.28	1.24 ± 0.08	0.305
	$C^{36}S$ (2-1)	4	38.12	···	···	···	···
	^{13}CS (2-1)	4	45.63	···	···	···	···
	$^{13}C^{33}S$ (2-1)	4	37.88	···	···	···	···
	$^{13}C^{34}S$ (2-1)	4	41.77	···	···	···	···
	$C^{33}S$ (3-2)	4	52.59	···	···	···	···
	$C^{34}S$ (3-2)	4	55.08	-21.91 ± 0.16	3.33 ± 0.38	1.00 ± 0.10	0.281
	$C^{36}S$ (3-2)	4	54.44	···	···	···	···
	^{13}CS (3-2)	4	57.96	···	···	···	···
G071.31+00.82	CS (2-1)	4	39.11	9.00 ± 0.01	3.21 ± 0.02	13.03 ± 0.08	3.810
	$C^{33}S$ (2-1)	4	36.82	10.12 ± 0.26	2.25 ± 0.70	0.28 ± 0.07	0.119
	$C^{34}S$ (2-1)	4	31.73	9.00 ± 0.04	2.75 ± 0.10	2.01 ± 0.06	0.688
	$C^{36}S$ (2-1)	4	31.35	···	···	···	···
	^{13}CS (2-1)	4	40.75	9.20 ± 0.12	2.12 ± 0.24	0.63 ± 0.07	0.278

Table A.3. continued.

Source	transitions	Time (mins)	rms (mK)	V_{LSR} (km s^{-1})	FWHM (km s^{-1})	$\int T_{MB}dv$ (K km s^{-1})	T_{MB} (K)
	$^{13}C^{33}S$ (2-1)	4	34.73	...	...	...	...
	$^{13}C^{34}S$ (2-1)	4	46.78	...	...	...	...
	$C^{33}S$ (3-2)	4	61.51	8.78 ± 0.21	2.42 ± 0.57	0.51 ± 0.10	0.199
	$C^{34}S$ (3-2)	4	55.65	8.93 ± 0.05	2.92 ± 0.11	2.77 ± 0.09	0.892
	$C^{36}S$ (3-2)	4	48.35	...	...	...	...
	^{13}CS (3-2)	4	51.90	9.13 ± 0.10	2.57 ± 0.21	1.07 ± 0.08	0.390
G071.52−00.38	CS (2-1)	4	57.44	10.65 ± 0.02	3.10 ± 0.06	9.52 ± 0.13	2.890
	$C^{33}S$ (2-1)	4	36.97	...	...	...	...
	$C^{34}S$ (2-1)	4	36.00	10.65 ± 0.09	2.58 ± 0.23	0.93 ± 0.07	0.339
	$C^{36}S$ (2-1)	4	33.41	...	...	...	...
	^{13}CS (2-1)	4	39.51	10.60 ± 0.17	1.47 ± 0.43	0.23 ± 0.06	0.150
	$^{13}C^{33}S$ (2-1)	4	34.47	...	...	...	...
	$^{13}C^{34}S$ (2-1)	4	32.15	...	...	...	...
	$C^{33}S$ (3-2)	4	55.65	...	...	...	...
	$C^{34}S$ (3-2)	4	51.41	10.87 ± 0.09	3.09 ± 0.22	1.58 ± 0.09	0.480
	$C^{36}S$ (3-2)	4	48.24	...	...	...	...
	^{13}CS (3-2)	4	57.86	10.99 ± 0.46	4.35 ± 1.41	0.56 ± 0.13	0.122
G073.65+00.19	CS (2-1)	23	16.34	-73.48 ± 0.01	3.14 ± 0.02	5.83 ± 0.03	1.740
	$C^{33}S$ (2-1)	23	12.76	-73.10 ± 0.24	2.76 ± 0.74	0.14 ± 0.03	0.048
	$C^{34}S$ (2-1)	23	12.28	-73.62 ± 0.05	2.65 ± 0.11	0.66 ± 0.02	0.234
	$C^{36}S$ (2-1)	23	15.93	...	...	...	...
	^{13}CS (2-1)	23	16.35	-73.43 ± 0.19	2.80 ± 0.50	0.24 ± 0.03	0.079
	$^{13}C^{33}S$ (2-1)	23	13.65	...	...	...	...
	$^{13}C^{34}S$ (2-1)	23	16.96	...	...	...	...
	$C^{33}S$ (3-2)	23	20.44	-74.05 ± 0.20	2.88 ± 0.51	0.23 ± 0.03	0.075
	$C^{34}S$ (3-2)	23	18.28	-73.54 ± 0.04	2.92 ± 0.09	1.07 ± 0.03	0.345
	$C^{36}S$ (3-2)	23	20.39	...	...	...	...
	^{13}CS (3-2)	23	19.89	-73.61 ± 0.10	2.65 ± 0.25	0.39 ± 0.03	0.140
G074.56+00.84	CS (2-1)	4	55.56	-0.52 ± 0.06	5.81 ± 0.20	7.77 ± 0.18	1.260
	$C^{33}S$ (2-1)	4	35.91	...	...	...	...
	$C^{34}S$ (2-1)	4	33.40	-1.16 ± 0.12	2.44 ± 0.47	0.60 ± 0.08	0.232
	$C^{36}S$ (2-1)	4	27.94	...	...	...	...
	^{13}CS (2-1)	4	31.45	...	...	...	...
	$^{13}C^{33}S$ (2-1)	4	38.26	...	...	...	...
	$^{13}C^{34}S$ (2-1)	4	40.24	...	...	...	...
	$C^{33}S$ (3-2)	4	55.13	...	...	...	...
	$C^{34}S$ (3-2)	4	54.48	-1.29 ± 0.20	2.39 ± 0.58	0.56 ± 0.09	0.219
	$C^{36}S$ (3-2)	4	54.63	...	...	...	...
	^{13}CS (3-2)	4	53.31	...	...	...	...
G075.29+01.32	CS (2-1)	48	13.65	-56.60 ± 0.01	3.04 ± 0.01	7.51 ± 0.03	2.320
	$C^{33}S$ (2-1)	48	10.76	-56.22 ± 0.20	2.86 ± 0.44	0.15 ± 0.02	0.050
	$C^{34}S$ (2-1)	48	10.23	-56.64 ± 0.03	2.76 ± 0.07	0.94 ± 0.02	0.321
	$C^{36}S$ (2-1)	48	10.43	...	...	...	...
	^{13}CS (2-1)	48	10.89	-56.42 ± 0.10	3.05 ± 0.21	0.36 ± 0.02	0.110
	$^{13}C^{33}S$ (2-1)	48	10.16	...	...	...	...
	$^{13}C^{34}S$ (2-1)	48	11.60	...	...	...	...
	$C^{33}S$ (3-2)	48	17.57	-56.75 ± 0.12	2.83 ± 0.27	0.34 ± 0.03	0.112
	$C^{34}S$ (3-2)	48	15.74	-56.59 ± 0.02	2.71 ± 0.05	1.52 ± 0.02	0.528
	$C^{36}S$ (3-2)	48	16.78	...	...	...	...
	^{13}CS (3-2)	48	16.55	-56.39 ± 0.06	2.33 ± 0.14	0.49 ± 0.02	0.199
DR21	CS (2-1)	278	150.00	-2.75 ± 0.02	4.43 ± 0.07	34.28 ± 0.40	7.260
	$C^{33}S$ (2-1)	278	4.90	-11.88 ± 0.05	3.01 ± 0.14	0.26 ± 0.01	0.082
	$C^{33}S$ (2-1)	278	4.90	-1.78 ± 0.01	2.71 ± 0.03	0.92 ± 0.01	0.321
	$C^{33}S$ (2-1)	278	4.90	5.31 ± 0.09	3.24 ± 0.28	0.18 ± 0.01	0.053
	$C^{33}S$ (2-1)	278	4.90	17.03 ± 0.10	2.66 ± 0.26	0.13 ± 0.01	0.045
	$C^{34}S$ (2-1)	278	13.49	-2.50 ± 0.01	2.67 ± 0.02	5.14 ± 0.03	1.810
	$C^{36}S$ (2-1)	278	3.76	-9.46 ± 0.17	5.44 ± 0.39	0.16 ± 0.01	0.028

Table A.3. continued.

Source	transitions	Time (mins)	rms (mK)	V_{LSR} (km s^{-1})	FWHM (km s^{-1})	$\int T_{MB} dv$ (K km s^{-1})	T_{MB} (K)
	$C^{36}S$ (2-1)	278	3.76	0.23 ± 0.36	3.99 ± 0.71	0.05 ± 0.01	0.012
	^{13}CS (2-1)	278	6.38	-2.38 ± 0.01	2.59 ± 0.02	2.04 ± 0.01	0.742
	$^{13}C^{33}S$ (2-1)	278	11.06	-2.18 ± 1.18	2.82 ± 3.06	0.03 ± 0.02	0.009
	$^{13}C^{34}S$ (2-1)	278	4.12	-2.34 ± 0.10	2.20 ± 0.24	0.08 ± 0.01	0.033
	$C^{33}S$ (3-2)	278	6.93	-6.89 ± 0.55	6.01 ± 0.92	0.27 ± 0.05	0.042
	$C^{33}S$ (3-2)	278	6.93	-2.49 ± 0.02	3.15 ± 0.05	1.65 ± 0.05	0.493
	$C^{33}S$ (3-2)	278	6.93	2.22 ± 0.09	3.18 ± 0.24	0.22 ± 0.01	0.066
	$C^{34}S$ (3-2)	278	19.97	-2.45 ± 0.01	2.81 ± 0.02	6.99 ± 0.03	2.340
	$C^{36}S$ (3-2)	139	15.29	-2.07 ± 0.40	2.00 ± 0.69	0.05 ± 0.02	0.025
	^{13}CS (3-2)	278	8.42	-2.29 ± 0.01	2.65 ± 0.01	2.89 ± 0.01	1.030
G090.92+01.48	CS (2-1)	19	21.27	-72.05 ± 0.01	3.74 ± 0.02	14.13 ± 0.05	3.550
	$C^{33}S$ (2-1)	19	13.53	-71.06 ± 0.17	3.40 ± 0.37	0.29 ± 0.03	0.080
	$C^{34}S$ (2-1)	19	16.42	-71.92 ± 0.03	3.02 ± 0.08	1.54 ± 0.03	0.477
	$C^{36}S$ (2-1)	19	16.23	...	...	...	...
	^{13}CS (2-1)	19	16.99	-71.81 ± 0.08	2.62 ± 0.19	0.51 ± 0.03	0.184
	$^{13}C^{33}S$ (2-1)	19	16.76	...	...	...	...
	$^{13}C^{34}S$ (2-1)	19	17.24	...	...	...	...
	$C^{33}S$ (3-2)	19	20.38	-71.92 ± 0.14	3.79 ± 0.33	0.51 ± 0.04	0.127
	$C^{34}S$ (3-2)	19	20.70	-71.98 ± 0.03	3.37 ± 0.08	2.05 ± 0.04	0.572
	$C^{36}S$ (3-2)	19	19.68	...	...	...	...
	^{13}CS (3-2)	19	22.58	-71.71 ± 0.09	3.54 ± 0.25	0.78 ± 0.04	0.207
G097.53+03.18	CS (2-1)	77	9.78	-71.71 ± 0.00	4.99 ± 0.00	13.94 ± 0.01	2.630
	$C^{33}S$ (2-1)	77	9.36	-79.64 ± 0.38	5.51 ± 0.86	0.19 ± 0.02	0.032
	$C^{33}S$ (2-1)	77	9.36	-70.15 ± 0.11	5.22 ± 0.24	0.63 ± 0.03	0.114
	$C^{33}S$ (2-1)	77	9.36	-61.51 ± 0.46	3.65 ± 1.01	0.08 ± 0.02	0.021
	$C^{33}S$ (2-1)	77	9.36	-54.06 ± 0.50	4.00 ± 1.07	0.09 ± 0.02	0.021
	$C^{34}S$ (2-1)	77	8.76	-71.18 ± 0.03	5.20 ± 0.05	2.43 ± 0.02	0.440
	$C^{36}S$ (2-1)	77	9.94	...	...	...	...
	^{13}CS (2-1)	77	9.35	-70.70 ± 0.07	5.42 ± 0.16	0.94 ± 0.03	0.162
	$^{13}C^{33}S$ (2-1)	77	9.12	...	...	...	...
	$^{13}C^{34}S$ (2-1)	77	9.70	...	...	...	...
	$C^{33}S$ (3-2)	77	16.24	-71.10 ± 0.09	5.47 ± 0.21	1.09 ± 0.04	0.188
	$C^{34}S$ (3-2)	77	14.50	-71.47 ± 0.02	5.02 ± 0.05	3.57 ± 0.03	0.667
	$C^{36}S$ (3-2)	77	15.99	...	...	...	...
	^{13}CS (3-2)	77	14.09	-71.04 ± 0.06	5.04 ± 0.12	1.31 ± 0.03	0.244
G108.20+00.58	CS (2-1)	48	10.09	-50.34 ± 0.01	4.95 ± 0.02	6.61 ± 0.03	1.250
	$C^{33}S$ (2-1)	48	9.63	-49.83 ± 0.30	2.56 ± 0.81	0.07 ± 0.02	0.027
	$C^{34}S$ (2-1)	48	9.50	-50.70 ± 0.06	2.68 ± 0.17	0.44 ± 0.02	0.154
	$C^{36}S$ (2-1)	48	7.90	...	...	...	...
	^{13}CS (2-1)	48	10.49	-50.61 ± 0.31	3.48 ± 0.81	0.14 ± 0.03	0.038
	$^{13}C^{33}S$ (2-1)	48	8.41	...	...	...	...
	$^{13}C^{34}S$ (2-1)	48	7.92	...	...	...	...
	$C^{33}S$ (3-2)	48	13.59	...	...	...	...
	$C^{34}S$ (3-2)	48	13.72	-50.72 ± 0.08	2.72 ± 0.24	0.37 ± 0.02	0.127
	$C^{36}S$ (3-2)	48	14.22	...	...	...	...
	^{13}CS (3-2)	48	13.64	-50.84 ± 0.29	2.59 ± 0.75	0.11 ± 0.02	0.041
G108.42+00.89	CS (2-1)	4	29.26	...	...	...	...
	$C^{33}S$ (2-1)	4	30.30	...	...	...	...
	$C^{34}S$ (2-1)	4	31.05	...	...	...	...
	$C^{36}S$ (2-1)	4	33.83	...	...	...	...
	^{13}CS (2-1)	4	30.46	...	...	...	...
	$^{13}C^{33}S$ (2-1)	4	32.25	...	...	...	...
	$^{13}C^{34}S$ (2-1)	4	30.12	...	...	...	...
	$C^{33}S$ (3-2)	4	47.02	...	...	...	...
	$C^{34}S$ (3-2)	4	45.12	...	...	...	...
	$C^{36}S$ (3-2)	4	51.88	...	...	...	...
	^{13}CS (3-2)	4	53.07	...	...	...	...

Table A.3. continued.

Source	transitions	Time (mins)	rms (mK)	V_{LSR} (km s^{-1})	FWHM (km s^{-1})	$\int T_{MB} dv$ (K km s^{-1})	T_{MB} (K)
G109.87+02.11	CS (2-1)	58	59.35	-11.06 ± 0.01	4.68 ± 0.03	27.50 ± 0.15	5.530
	$C^{33}S$ (2-1)	58	9.76	-20.00 ± 0.28	2.75 ± 0.58	0.09 ± 0.02	0.032
	$C^{33}S$ (2-1)	58	9.76	-10.34 ± 0.08	3.19 ± 0.20	0.40 ± 0.02	0.117
	$C^{33}S$ (2-1)	58	9.76	-3.73 ± 0.38	4.61 ± 0.77	0.15 ± 0.02	0.031
	$C^{34}S$ (2-1)	58	11.66	-10.88 ± 0.01	3.33 ± 0.04	2.74 ± 0.03	0.773
	$C^{36}S$ (2-1)	58	8.22	...	...	...	...
	^{13}CS (2-1)	58	9.64	-10.81 ± 0.04	3.37 ± 0.08	0.98 ± 0.02	0.274
	$^{13}C^{33}S$ (2-1)	58	8.22	...	...	...	...
	$^{13}C^{34}S$ (2-1)	58	9.19	-10.44 ± 0.43	3.60 ± 1.06	0.09 ± 0.02	0.023
	$C^{33}S$ (3-2)	58	41.48	-10.71 ± 0.26	3.90 ± 0.67	0.59 ± 0.08	0.143
	$C^{34}S$ (3-2)	58	27.34	-10.79 ± 0.03	3.47 ± 0.08	2.88 ± 0.05	0.780
	$C^{36}S$ (3-2)	58	12.54	...	...	...	...
	^{13}CS (3-2)	58	15.85	-10.70 ± 0.05	3.37 ± 0.12	1.04 ± 0.03	0.291
NGC7538	CS (2-1)	371	280.00	-57.19 ± 0.03	4.38 ± 0.08	53.41 ± 0.72	11.400
	$C^{33}S$ (2-1)	371	4.29	-66.46 ± 0.08	3.79 ± 0.20	0.22 ± 0.01	0.055
	$C^{33}S$ (2-1)	371	4.29	-56.45 ± 0.02	3.71 ± 0.05	0.99 ± 0.01	0.252
	$C^{33}S$ (2-1)	371	4.29	-49.29 ± 0.09	4.09 ± 0.28	0.21 ± 0.01	0.049
	$C^{34}S$ (2-1)	371	17.41	-57.12 ± 0.01	3.68 ± 0.03	5.92 ± 0.04	1.510
	$C^{36}S$ (2-1)	371	4.40	...	...	...	...
	^{13}CS (2-1)	371	7.23	-57.01 ± 0.01	3.64 ± 0.03	2.24 ± 0.02	0.577
	$^{13}C^{33}S$ (2-1)	371	3.96	...	...	...	...
	$^{13}C^{34}S$ (2-1)	371	3.98	-57.05 ± 0.17	3.39 ± 0.39	0.08 ± 0.01	0.023
	$C^{33}S$ (3-2)	371	245.00	-57.41 ± 0.61	5.01 ± 1.68	2.15 ± 0.56	0.402
	$C^{34}S$ (3-2)	371	24.21	-57.26 ± 0.01	3.85 ± 0.03	8.17 ± 0.05	1.990
	$C^{36}S$ (3-2)	185	9.03	-57.54 ± 0.51	4.43 ± 1.34	0.08 ± 0.02	0.017
	^{13}CS (3-2)	371	9.44	-57.13 ± 0.01	3.82 ± 0.03	3.20 ± 0.02	0.786

Notes. Column (1): source name; Column (2): transition; Column (3): on+off source integration time; Column (4): rms noise obtained from Gaussian-fitting; Columns (5)–(8): LSR velocity, line width (FWHM), integrated line intensity and peak main beam brightness temperature, respectively.

A&A 670, A98 (2023)

Appendix B: Additional Figures

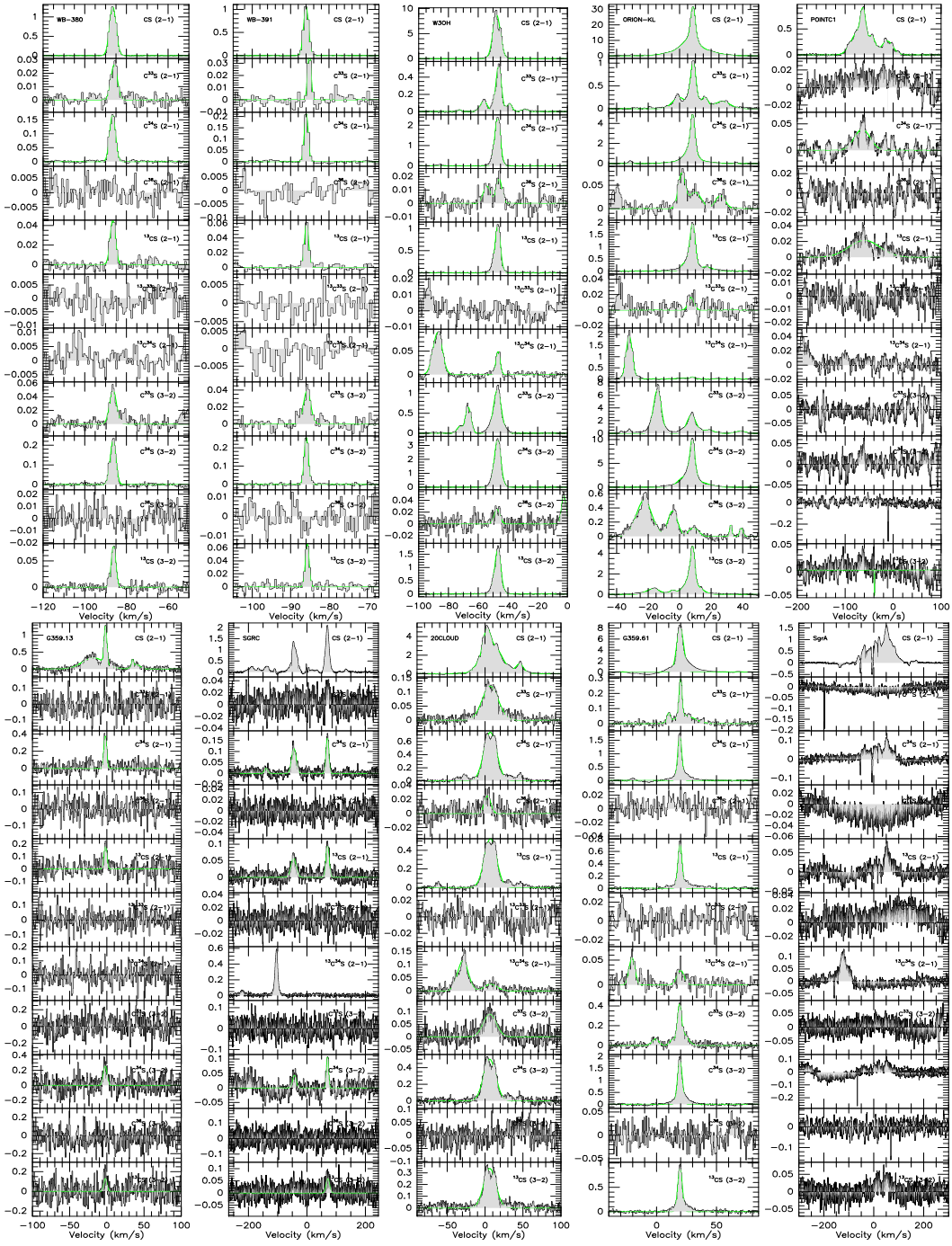

Fig. B.1. Line profiles of the $J = 2$-1 transitions of CS, $C^{33}S$, $C^{34}S$, $C^{36}S$, ^{13}CS, $^{13}C^{33}S$ and $^{13}C^{34}S$ as well as the $J = 3$-2 transitions of $C^{33}S$, $C^{34}S$, $C^{36}S$, and ^{13}CS toward 110 targets of our sample, after subtracting first-order polynomial baselines. The main beam temperature scales are presented on the left hand side of the profiles.

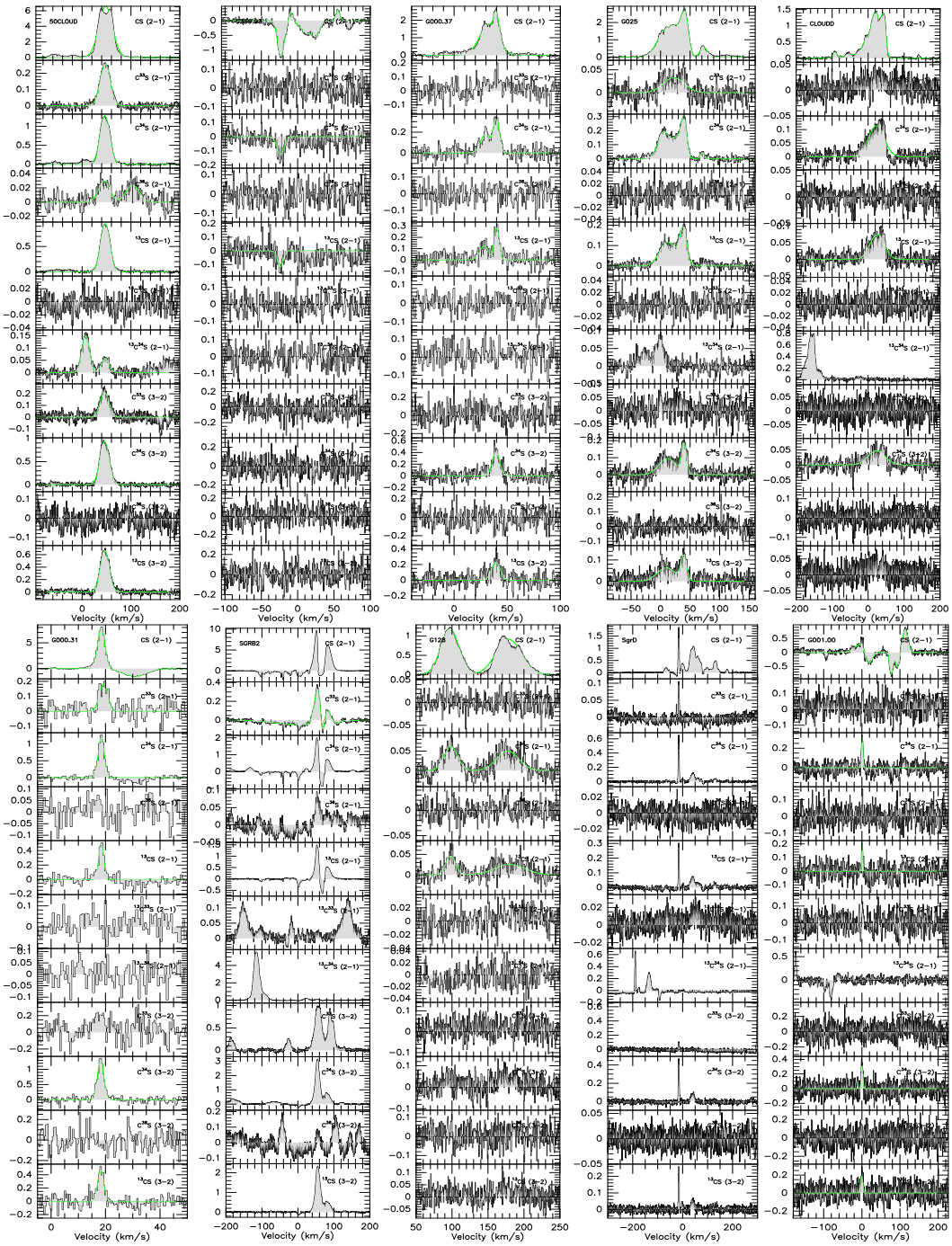
50CLOUD
CS (2–1)
G000.37
G025
CLOUDD
G000.31
SGRB2
G12B
SgrD
G001.00
Velocity (km/s)

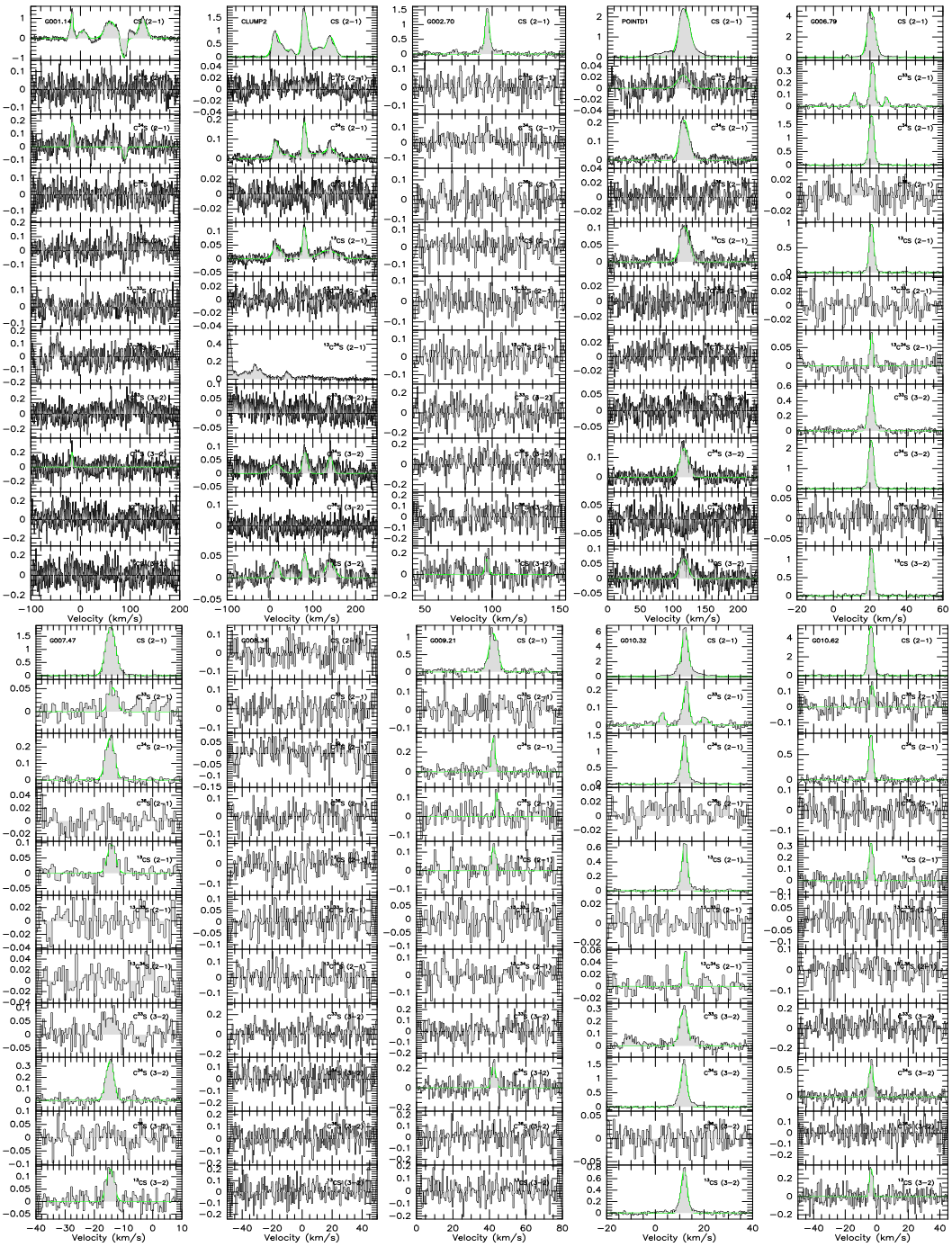
G001.14
CLUMP2
G002.70
POINTD1
G006.79
G007.47
G008.34
G009.21
G010.32
G010.62
Velocity (km/s)

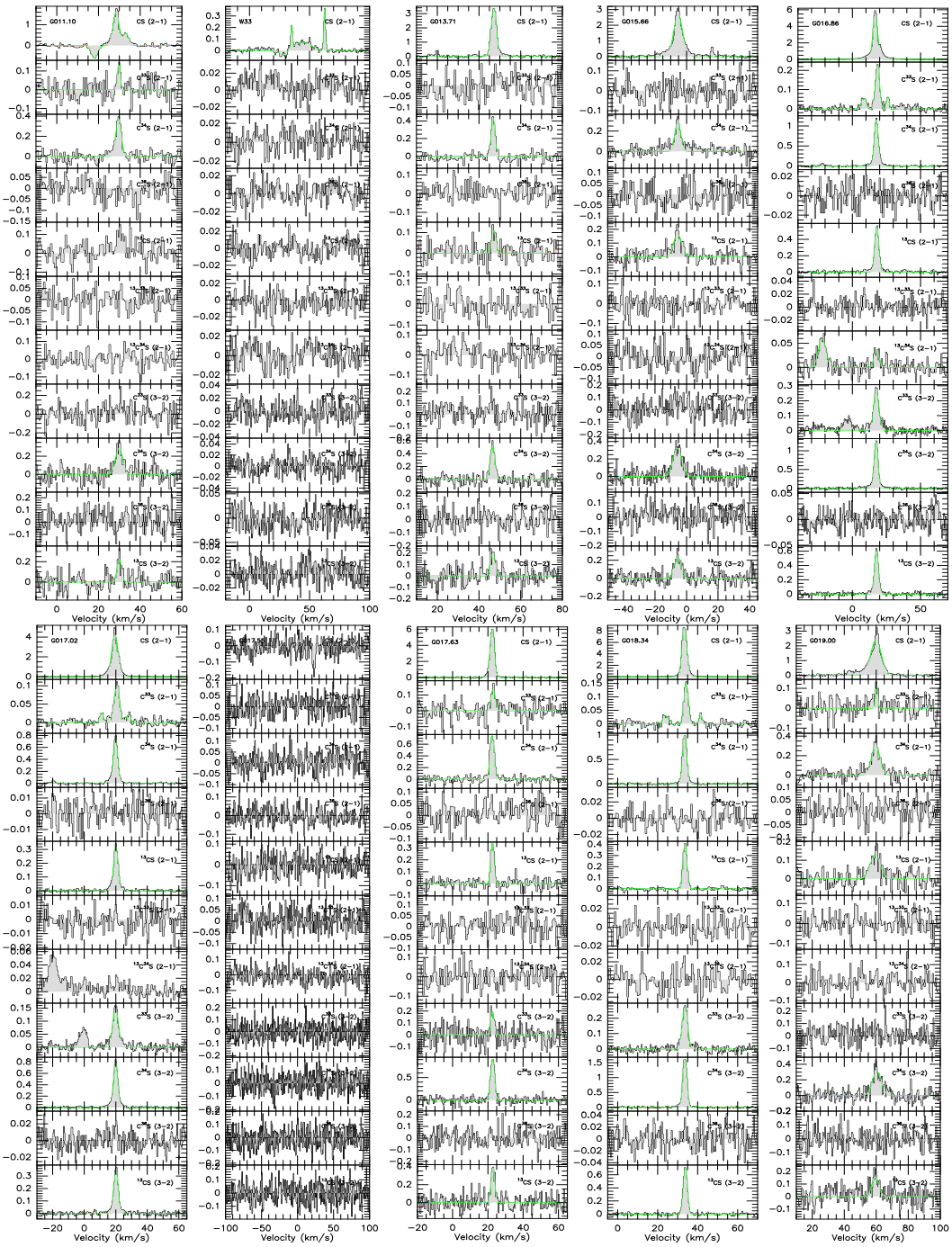
G011.10
W33
G013.71
G015.66
G016.86
G017.02
G017.63
G018.34
G019.00
CS (2–1)
Velocity (km/s)

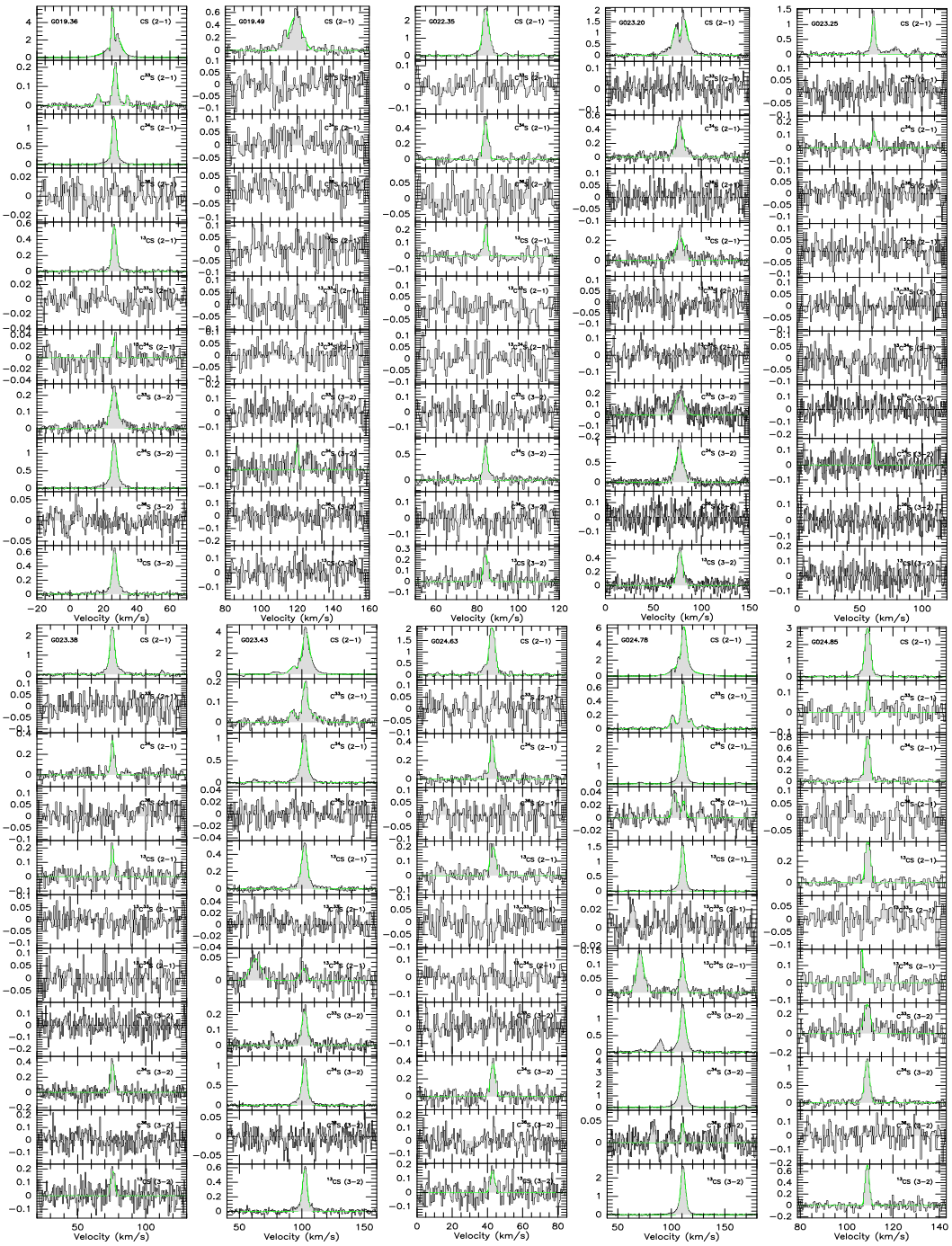
G019.36
G019.49
G022.35
G023.20
G023.25
G023.38
G023.43
G024.63
G024.78
G024.85
CS (2–1)
C34S (2–1)
13CS (2–1)
13C34S (2–1)
C34S (3–2)
13CS (3–2)
Velocity (km/s)

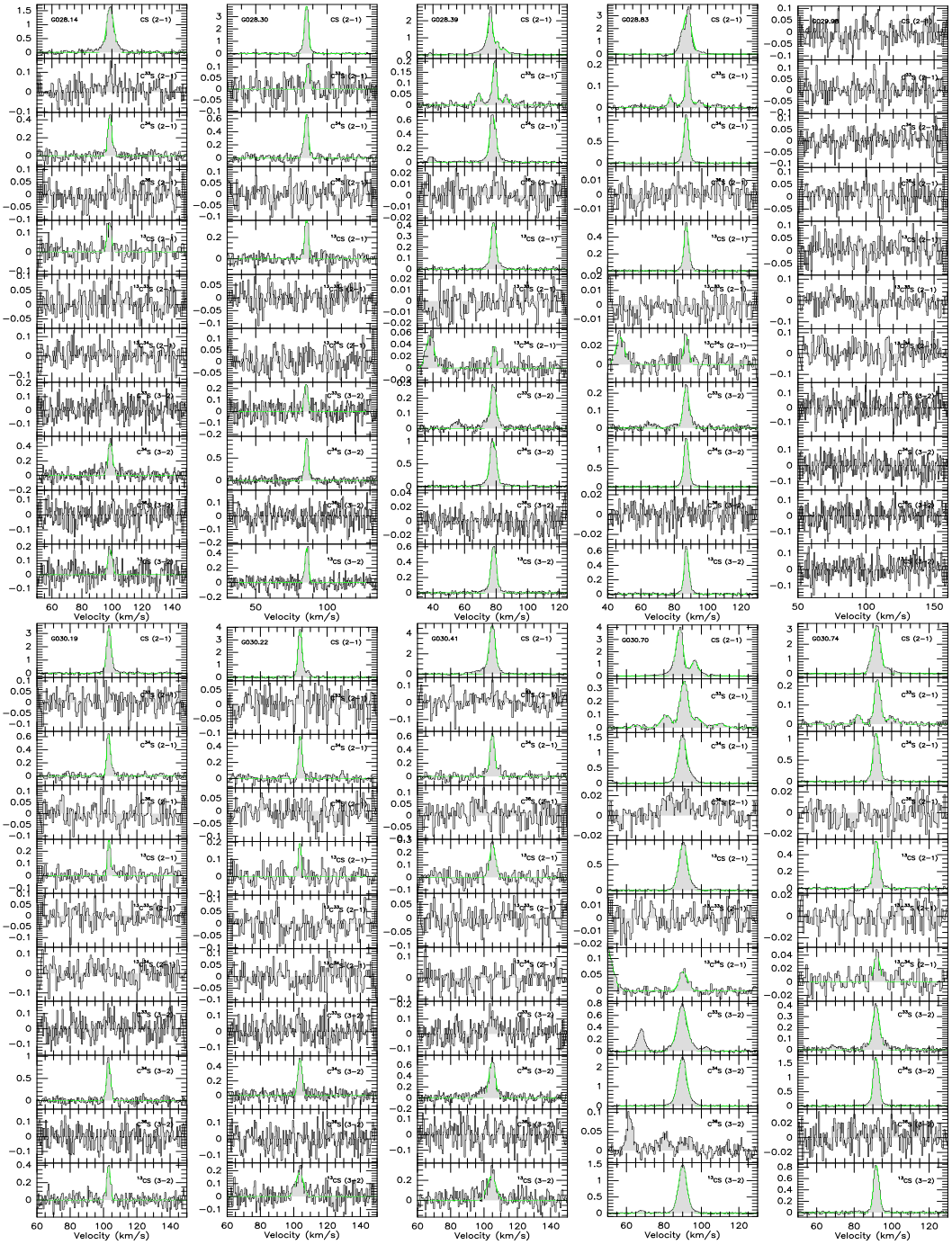
G028.14
G028.30
G028.39
G028.83
G029.96
G030.19
G030.22
G030.41
G030.70
G030.74
CS (2−1)
C34S (2−1)
13CS (2−1)
13C34S (2−1)
C33S (3−2)
C34S (3−2)
13CS (3−2)
Velocity (km/s)

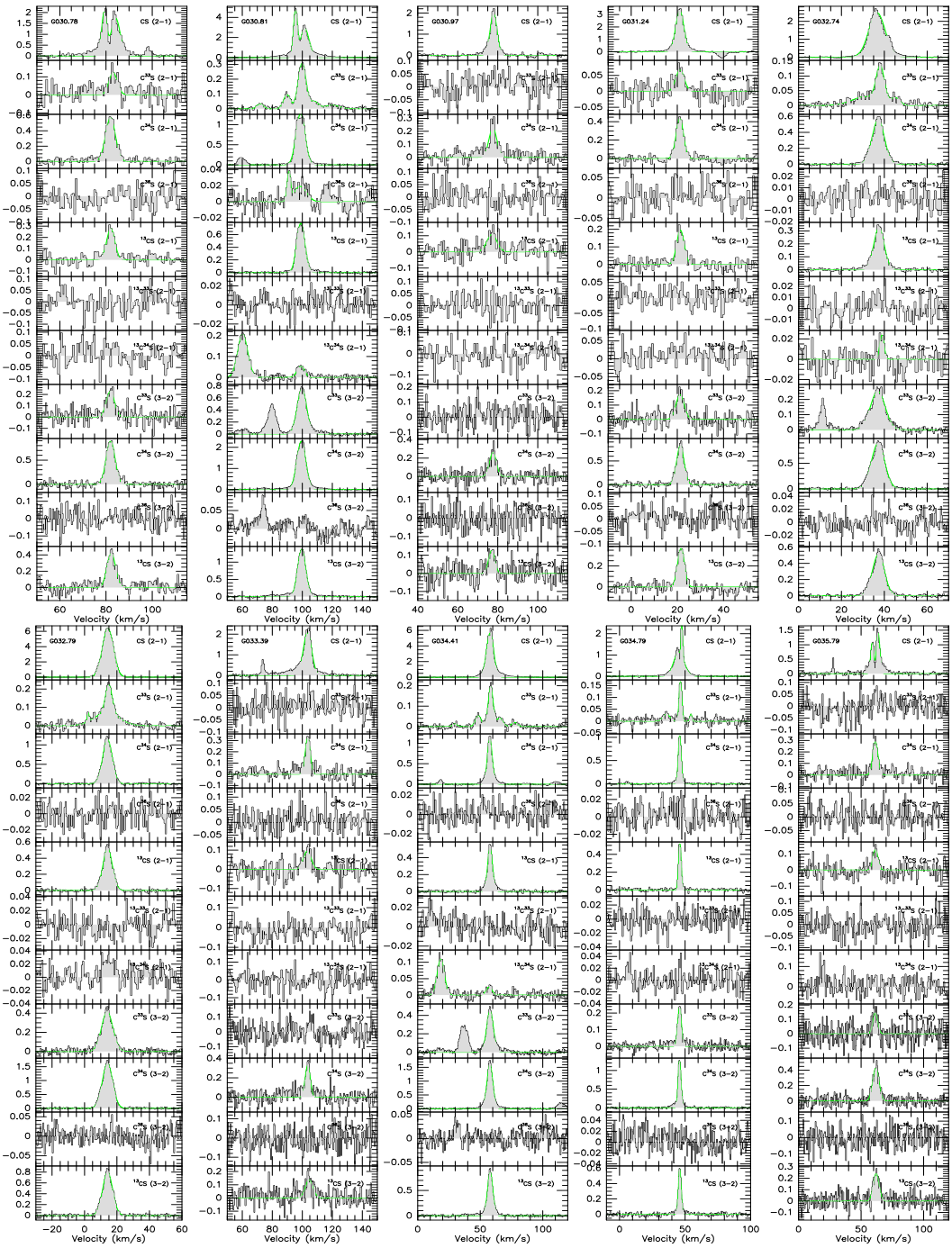
G030.78
G030.81
G030.97
G031.24
G032.74
G032.79
G033.39
G034.41
G034.79
G035.79
CS (2–1)
C34S (2–1)
C34S (2–1)
13CS (2–1)
13C34S (2–1)
13C34S (2–1)
C34S (3–2)
C34S (3–2)
C34S (3–2)
13CS (3–2)
Velocity (km/s)

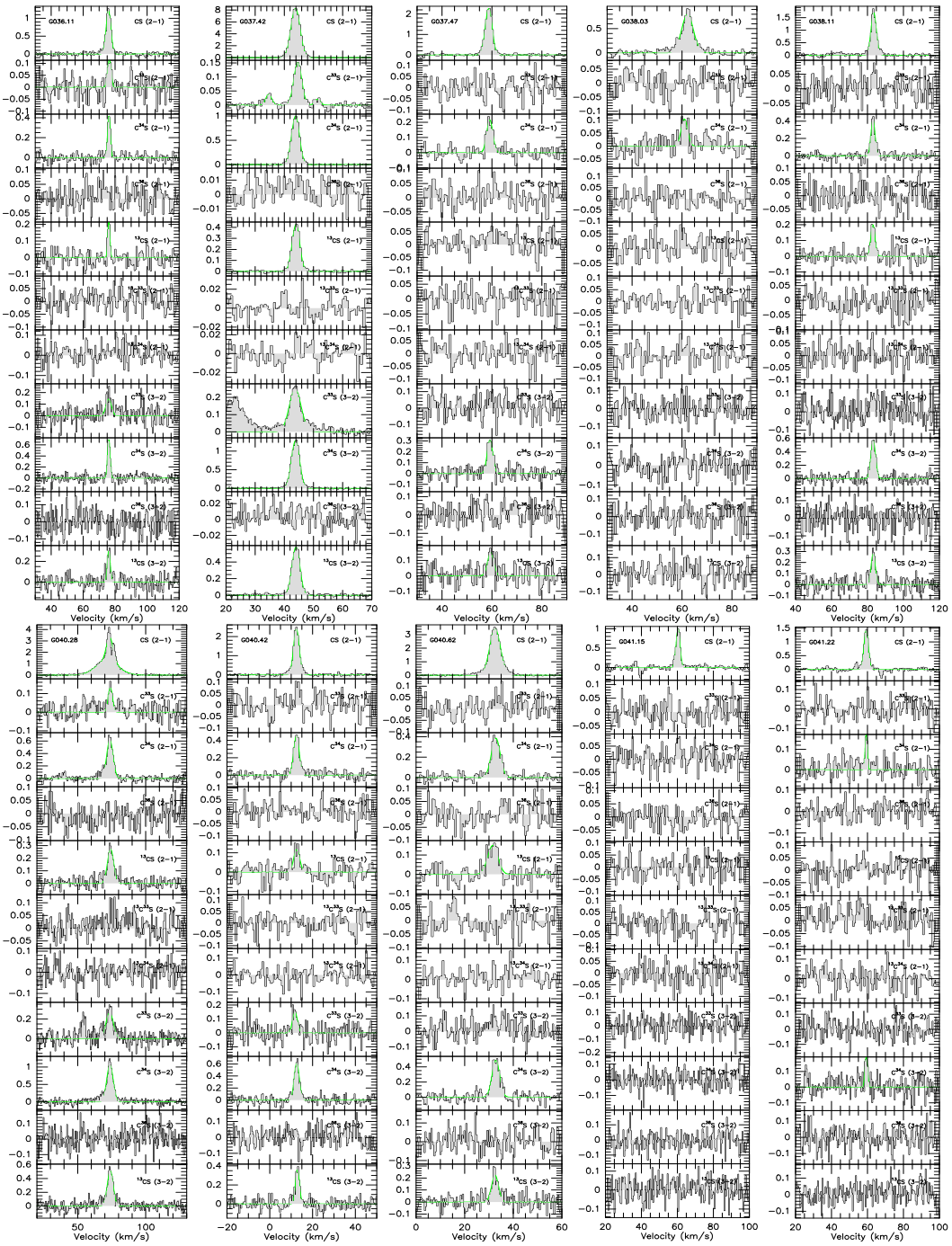
G036.11
G037.42
G037.47
G038.03
G038.11
G040.28
G040.42
G040.62
G041.15
G041.22
CS (2–1)
C34S (2–1)
13CS (2–1)
13C34S (2–1)
C34S (3–2)
13CS (3–2)
Velocity (km/s)

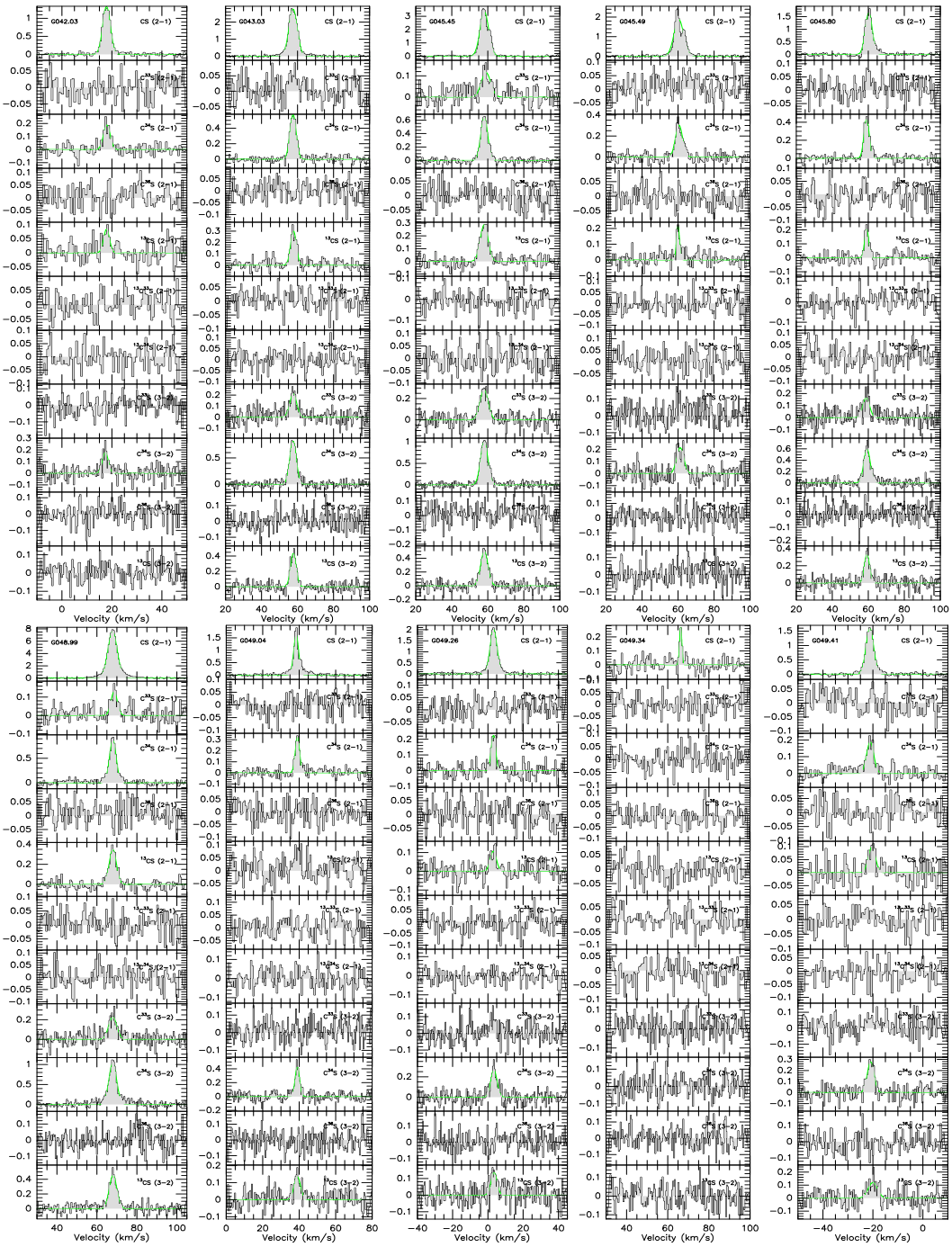
G042.03
G043.03
G045.45
G045.49
G045.80
G048.99
G049.04
G049.26
G049.34
G049.41
CS (2–1)
C34S (2–1)
13CS (2–1)
13C34S (2–1)
C34S (3–2)
13CS (3–2)
Velocity (km/s)

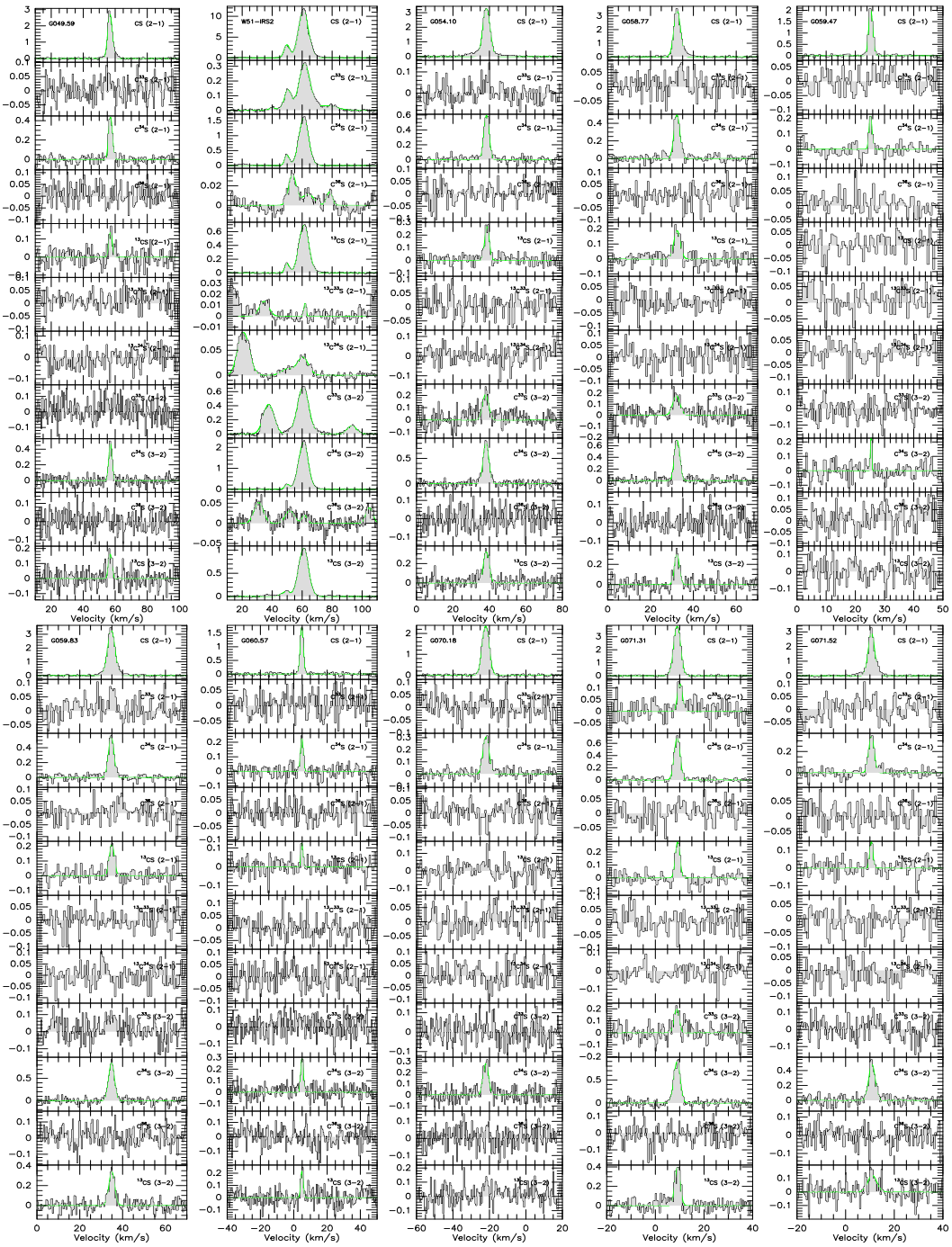
G049.59
W51−IRS2
G054.10
G058.77
G059.47
G059.83
G060.57
G070.18
G071.31
G071.52
CS (2−1)
C34S (2−1)
13CS (2−1)
13C34S (2−1)
C34S (3−2)
13CS (3−2)
Velocity (km/s)

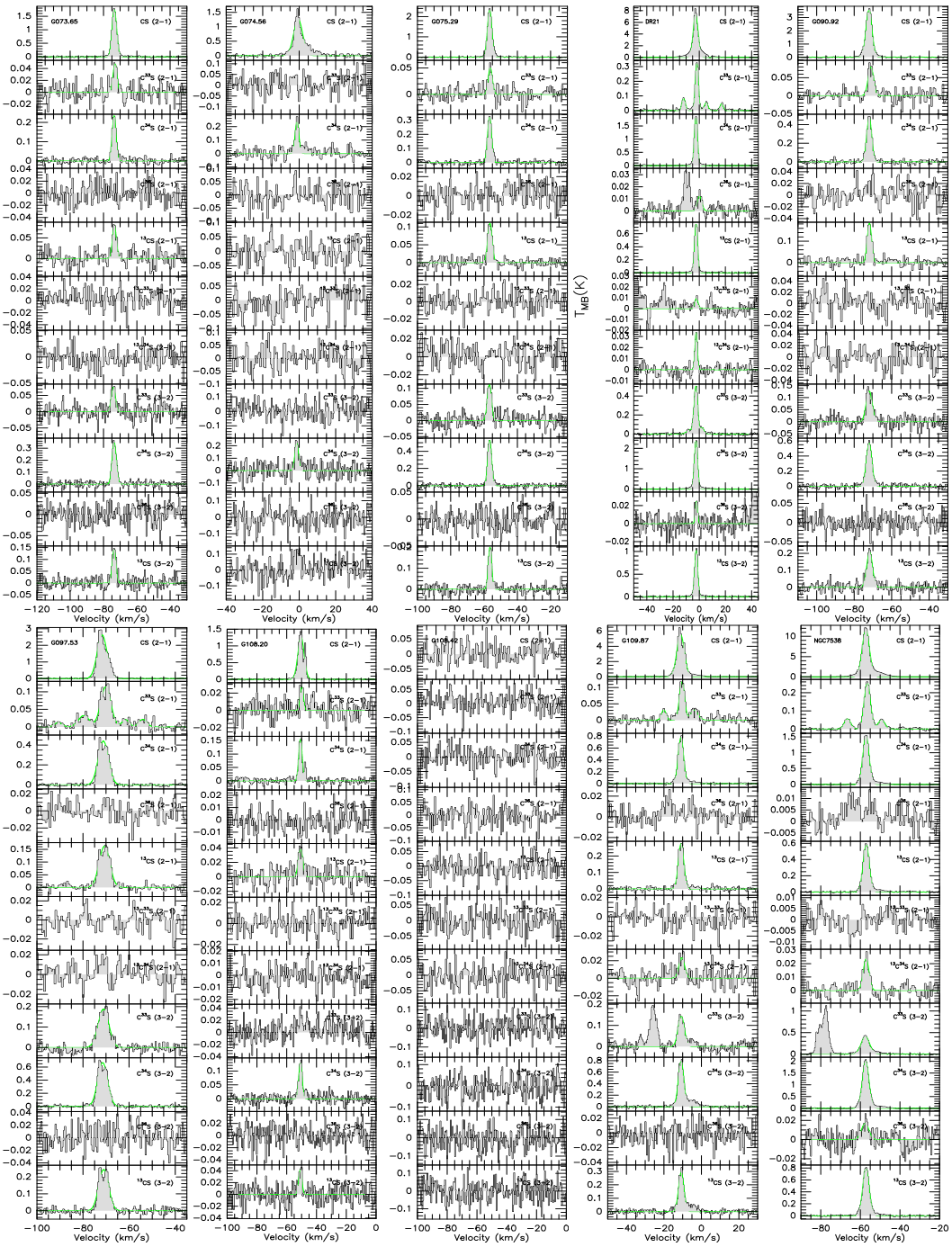
G073.65
G074.56
G075.29
DR21
G090.92
G097.53
G108.20
G108.47
G109.87
NGC7538
CS (2–1)
C34S (2–1)
13CS (2–1)
13C34S (2–1)
C34S (3–2)
13CS (3–2)
Velocity (km/s)
TMB (K)

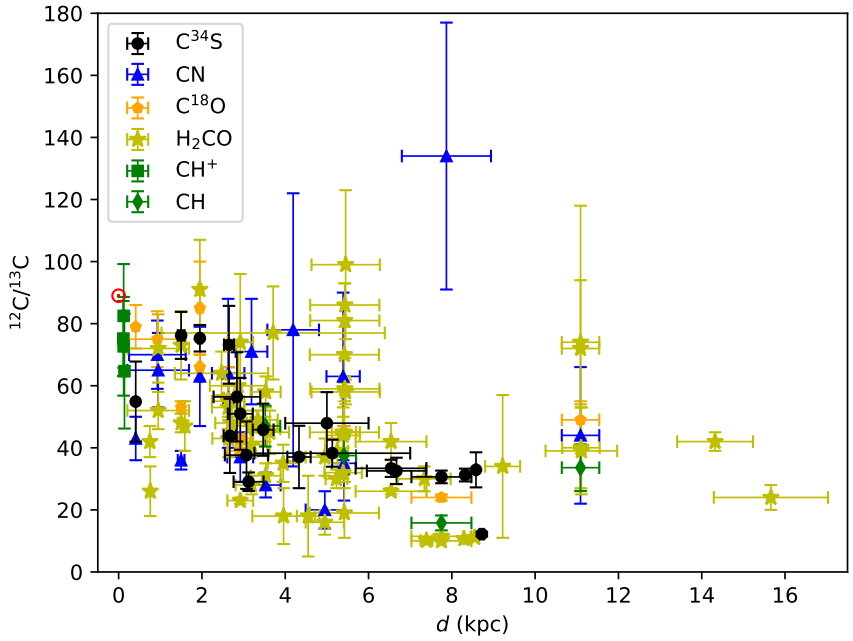

Fig. B.2. $^{12}C/^{13}C$ isotope ratios from $C^{34}S/^{13}C^{34}S$, $CN/^{13}CN$, $C^{18}O/^{13}C^{18}O$, $H_2CO/H_2^{13}CO$, $CH^+/^{13}CH^+$, and $CH/^{13}CH$ plotted as a function of the distance from the Sun. The red symbol ⊙ indicates the $^{12}C/^{13}C$ isotope ratio of the Sun. The $^{12}C/^{13}C$ ratios directly derived from $C^{34}S/^{13}C^{34}S$ in the $J = 2$-1 transition with minor opacity corrections in the current work are plotted as black filled circles. The blue triangles, orange pentagons, yellow stars, green squares, and green diamonds are values determined from CN (Savage et al. 2002; Milam et al. 2005), $C^{18}O$ (Langer & Penzias 1990; Wouterloot & Brand 1996; Keene et al. 1998), H_2CO (Henkel et al. 1980, 1982, 1983, 1985; Yan et al. 2019), CH^+ (Ritchey et al. 2011), and CH (Jacob et al. 2020), respectively, using state of the art distances.

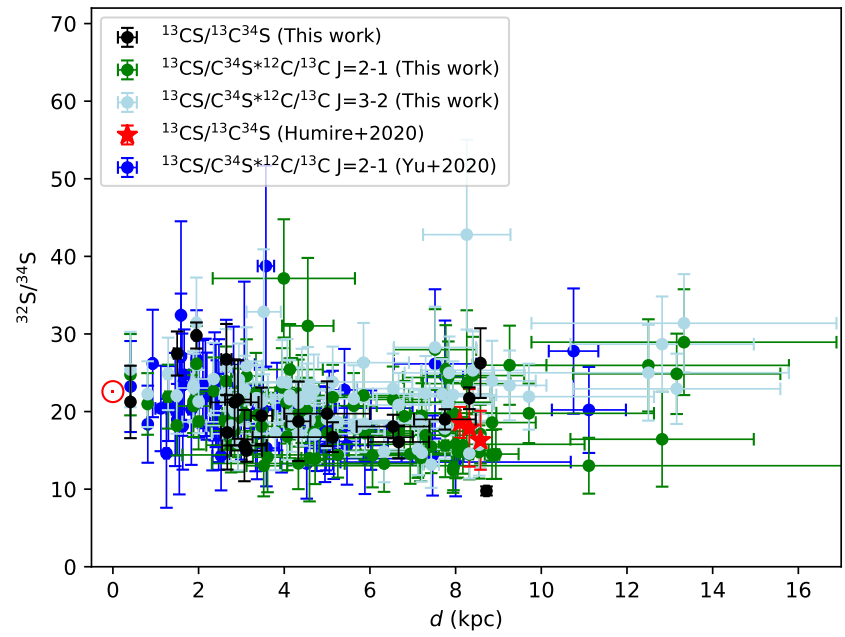

Fig. B.3. $^{32}S/^{34}S$ isotope ratios plotted as a function of the distance from the Sun. The symbol ⊙ indicates the $^{32}S/^{34}S$ isotope ratio in the Solar System. The $^{32}S/^{34}S$ ratios with corrections of opacity in the $J = 2$-1 transition derived from $^{13}CS/^{13}C^{34}S$ and obtained from the double isotope method are plotted as black and green dots, respectively. The $^{32}S/^{34}S$ ratios without corrections for optical depth in the $J = 3$-2 transition derived from the double isotope method are shown as light blue dots. The $^{32}S/^{34}S$ ratios in Yu et al. (2020) derived from the double isotope method in the $J = 2$-1 transitions are shown as blue dots. The $^{32}S/^{34}S$ values in the CMZ obtained from $^{13}CS/^{13}C^{34}S$ in Humire et al. (2020) are plotted as red stars.

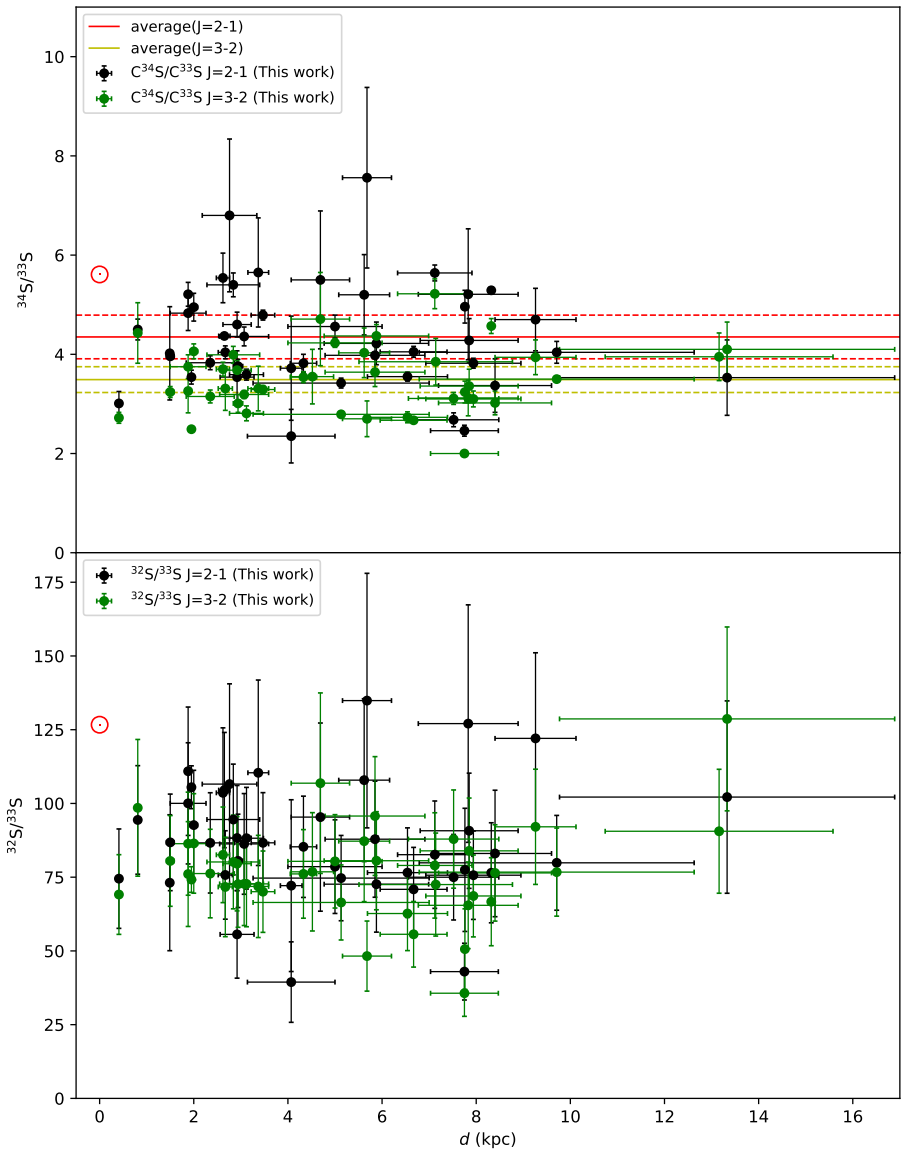

Fig. B.4. $^{34}S/^{33}S$ and $^{32}S/^{33}S$ isotope ratios plotted as functions of the distance from the Sun. Top: $^{34}S/^{33}S$ ratios derived from $C^{34}S/C^{33}S$ in the $J = 2$-1 and $J = 3$-2 transitions are plotted as black and green dots, respectively. The red solid and the two dashed lines show the average value and its standard deviation, 4.35 ± 0.44, for $^{34}S/^{33}S$ with corrections of optical depth toward our sample in the $J = 2$-1 transition. The yellow solid and the two dashed lines show the average value and its standard deviation, 3.49 ± 0.26, of $^{34}S/^{33}S$ toward our sample without opacity corrections for the $J = 3$-2 transition. The red symbol ⊙ indicates the $^{34}S/^{33}S$ isotope ratio in the Solar System. Bottom: Black and green dots show the $^{32}S/^{33}S$ ratios in the $J = 2$-1 and $J = 3$-2 transitions, respectively. The red symbol ⊙ indicates the $^{32}S/^{33}S$ value in the Solar System.

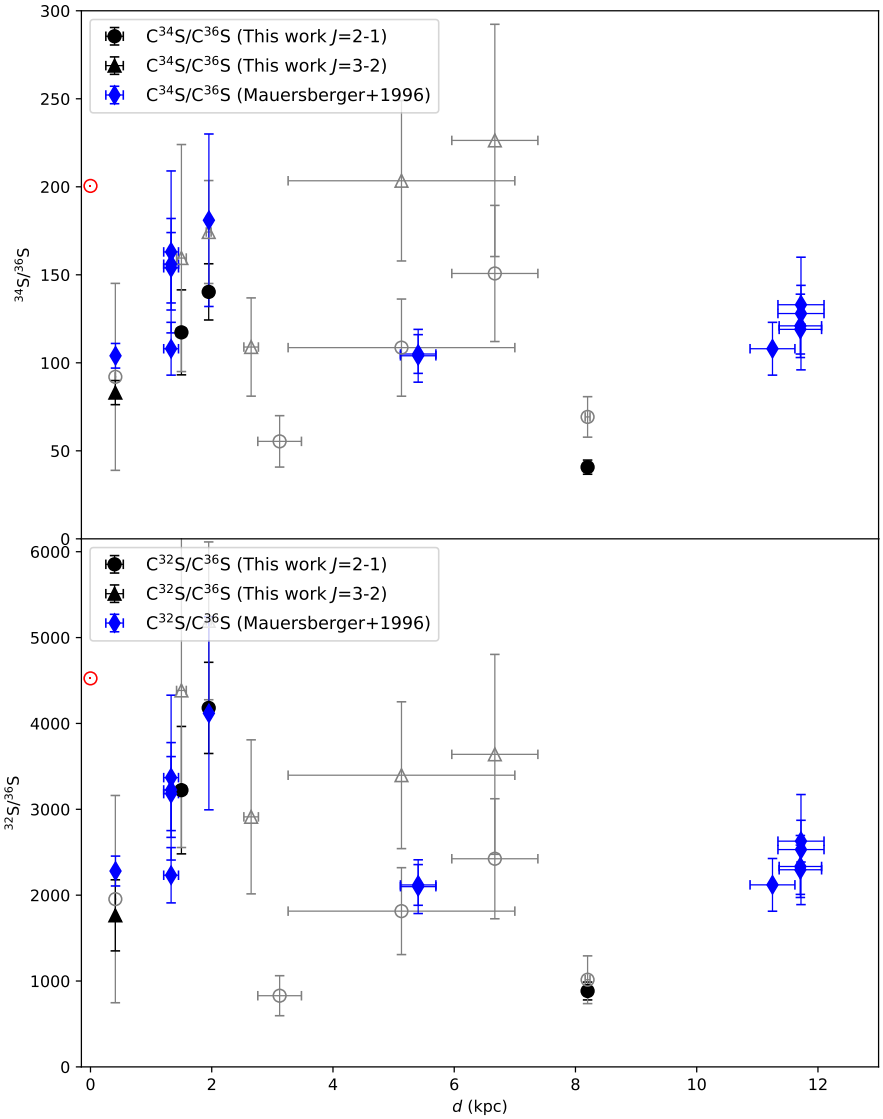

Fig. B.5. $^{34}S/^{36}S$ and $^{32}S/^{36}S$ isotope ratios plotted as functions of the distance from the Sun. **Top:** Filled black circles and filled black triangle present the $^{34}S/^{36}S$ ratios in the $J = 2$-1 and $J = 3$-2 transitions derived from $C^{34}S/C^{36}S$ in this work with detections of $C^{36}S$, respectively. The open gray circles and open gray triangles present the $^{34}S/^{36}S$ ratios in the $J = 2$-1 and $J = 3$-2 transitions derived from $C^{34}S/C^{36}S$ in this work with tentative detections of $C^{36}S$, respectively. The blue diamonds show the $^{34}S/^{36}S$ ratios in Mauersberger et al. (1996). The red symbol ⊙ indicates the $^{34}S/^{36}S$ isotope ratio in the Solar System. **Bottom:** $^{32}S/^{36}S$ ratios obtained from $^{34}S/^{36}S$ ratios combined with the $^{32}S/^{34}S$ ratios derived in this work. The filled black circles and filled black triangle present the values in the $J = 2$-1 and $J = 3$-2 transitions from this work with detections of $C^{36}S$, respectively. The open gray circles and open gray triangles present the ratios in the $J = 2$-1 and $J = 3$-2 transitions derived from this work with tentative detections of $C^{36}S$, respectively. The $^{32}S/^{36}S$ ratios, derived with $^{34}S/^{36}S$ values in Mauersberger et al. (1996) and the $^{32}S/^{34}S$ gradient in this work, are plotted as blue diamonds. The red symbol ⊙ indicates the $^{32}S/^{36}S$ isotope ratio in the Solar System.

Appendix B

Discovery of ammonia (9,6) masers in Cepheus A and G34.26+0.15

A&A 659, A5 (2022)
https://doi.org/10.1051/0004-6361/202142891
© Y. T. Yan et al. 2022

Astronomy & Astrophysics

Discovery of ammonia (9,6) masers in two high-mass star-forming regions

Y. T. Yan (闫耀庭)[1,⋆], C. Henkel[1,2,3], K. M. Menten[1], Y. Gong (龚龑)[1], J. Ott[4], T. L. Wilson[1], A. Wootten[4], A. Brunthaler[1], J. S. Zhang (张江水)[5], J. L. Chen (陈家梁)[5], and K. Yang (杨楷)[6,7]

[1] Max-Planck-Institut für Radioastronomie, Auf dem Hügel 69, 53121 Bonn, Germany
e-mail: yyan@mpifr-bonn.mpg.de
[2] Astronomy Department, Faculty of Science, King Abdulaziz University, PO Box 80203, Jeddah 21589, Saudi Arabia
[3] Xinjiang Astronomical Observatory, Chinese Academy of Sciences, 830011 Urumqi, PR China
[4] National Radio Astronomy Observatory, 520 Edgemont Road, Charlottesville, VA 22903-2475, USA
[5] Center for Astrophysics, Guangzhou University, 510006 Guangzhou, PR China
[6] School of Astronomy and Space Science, Nanjing University, 163 Xianlin Avenue, Nanjing 210023, PR China
[7] Key Laboratory of Modern Astronomy and Astrophysics (Nanjing University), Ministry of Education, Nanjing 210023, PR China

Received 13 December 2021 / Accepted 30 December 2021

ABSTRACT

Context. Molecular maser lines are signposts of high-mass star formation, probing the excitation and kinematics of very compact regions in the close environment of young stellar objects and providing useful targets for trigonometric parallax measurements.
Aims. Only a few NH_3 (9,6) masers are known so far, and their origin is still poorly understood. Here we aim to find new NH_3 (9,6) masers to provide a better observational basis for studying their role in high-mass star-forming regions.
Methods. We carried out NH_3 (9,6) observations toward Cepheus A and G34.26+0.15 with the Effelsberg 100-meter telescope (beam size 49″) and the *Karl G. Jansky* Very Large Array (JVLA; beam size about 1.″2).
Results. We discovered new NH_3 (9,6) masers in Cep A and G34.26+0.25, which increases the number of known high-mass star-forming regions hosting NH_3 (9,6) masers from five to seven. Long-term monitoring (20 months) at Effelsberg shows that the intensity of the (9,6) maser in G34.26+0.25 is decreasing, while the Cep A maser remains stable. Compared to the Effelsberg data and assuming linear variations between the epochs of observation, the JVLA data indicate no missing flux. This suggests that the NH_3 (9,6) emission arises from single compact emission regions that are not resolved by the interferometric measurements. As JVLA imaging shows, the NH_3 (9,6) emission in Cep A originates from a sub-arcsecond-sized region, slightly to the west ($0.''28 \pm 0.''10$) of the peak position of the 1.36 cm continuum object, HW2. In G34.26+0.25, three NH_3 (9,6) maser spots are observed: one is close to the head of the cometary ultracompact H II region C, and the other two are emitted from a compact region to the west of the hypercompact H II region A.
Conclusions. The newly found (9,6) masers appear to be related to outflows. The higher angular resolution of JVLA and very long baseline interferometry observations are needed to provide more accurate positions and constraints for pumping scenarios.

Key words. masers – ISM: clouds – ISM: individual objects: Cep A – ISM: individual objects: G34.26+0.15 – radio lines: ISM – HII regions

1. Introduction

Since its discovery more than five decades ago (Cheung et al. 1968), ammonia (NH_3) has been a most valuable molecule for investigating the physical properties of molecular clouds (e.g., Ho & Townes 1983). While thermally excited transitions in the centimeter-wavelength inversion transitions of ammonia are regarded as a reliable thermometer of molecular clouds (e.g., Walmsley & Ungerechts 1983; Danby et al. 1988), ammonia masers have attracted attention since the first detection of maser action in the $(J, K) = (3,3)$ metastable ($J = K$) line toward the massive star-forming region W33 (Wilson et al. 1982). Subsequent observations have led to the detection of new metastable ammonia masers, including $^{15}NH_3$ (3,3) (Mauersberger et al. 1986), NH_3 (1,1) (Gaume et al. 1996), NH_3 (2,2) (Mills et al. 2018), NH_3 (5,5) (Cesaroni et al. 1992), NH_3 (6,6) (Beuther et al. 2007), NH_3 (7,7), NH_3 (9,9), and NH_3 (12,12) (Henkel et al. 2013). These have led to the discovery of metastable maser lines in 22 different regions (Mauersberger et al. 1986, 1987; Wilson & Henkel 1988; Wilson et al. 1990; Pratap et al. 1991; Cesaroni et al. 1992; Wilson & Schilke 1993; Mangum & Wootten 1994; Kraemer & Jackson 1995; Zhang & Ho 1995; Zhang et al. 1999; Walsh et al. 2007; Hunter et al. 2008; Galván-Madrid et al. 2009; Brogan et al. 2011; Urquhart et al. 2011; Walsh et al. 2011; Wang et al. 2012; Henkel et al. 2013; Hoffman & Joyce 2014; McEwen et al. 2016; Mills et al. 2018; Hogge et al. 2019; Mei et al. 2020; Towner et al. 2021). Compared with the metastable ammonia masers, detected non-metastable ($J > K$) ammonia maser transitions are more numerous. The first highly excited non-metastable ammonia maser was detected by Madden et al. (1986) in the $(J, K) = (9,6)$ and (6,3) lines. Thereafter, many other NH_3 non-metastable inversion transition lines have been identified as masers, including the (5,3), (5,4), (6,1), (6,2), (6,4), (6,5), (7,3), (7,4), (7,5) (7,6), (8,3), (8,4), (8,5), (8,6), (9,3), (9,4), (9,5), (9,7), (9,8), (10,7), (10,8), (10,9), and (11,9) transitions (e.g., Mauersberger et al. 1987, 1988; Walsh et al. 2007; Henkel et al. 2013; Mei et al. 2020). Except for the NH_3

⋆ Member of the International Max Planck Research School (IMPRS) for Astronomy and Astrophysics at the universities of Bonn and Cologne.

Open Access article, published by EDP Sciences, under the terms of the Creative Commons Attribution License (https://creativecommons.org/licenses/by/4.0), which permits unrestricted use, distribution, and reproduction in any medium, provided the original work is properly cited.
Open Access funding provided by Max Planck Society.

(3,3) masers proposed to be associated with four supernova remnants (McEwen et al. 2016), almost all the other ammonia masers are detected in high-mass star-forming regions (HMSFRs). However, while many HMSFRs host water (H_2O), hydroxyl (OH), or methanol (CH_3OH) masers, ammonia masers are quite rare in these sources, and the role that the environment of a young high-mass star plays in their excitation remains unclear. Therefore, dedicated searches for ammonia masers in HMSFRs are indispensable in regard to their overall incidence and association with different environments, which can provide additional constraints on the pumping mechanism of ammonia masers.

So far, a total of 32 NH_3 inversion transitions ($\Delta K = 0$ and $\Delta J = 0$) have been identified as masers. Among these, and despite arising from energy levels as high as 1090 K above the ground state, the NH_3 (9,6) maser stands out as being the strongest and most variable one in W51-IRS2 (e.g., Henkel et al. 2013). Maser emission in this line has only been detected in five HMSFRs, W51, NGC 7538, W49, DR21 (OH) (Madden et al. 1986), and Sgr B2(N) (Mei et al. 2020). The NH_3 (3,3) masers are thought to be collisionally excited (e.g., Flower et al. 1990; Mangum & Wootten 1994); in contrast, the pumping mechanism of NH_3 (9,6) masers is less well constrained (Madden et al. 1986). Brown & Cragg (1991) have studied ortho-ammonia and found that it could possibly pump the (6,3) inversion line, but they did not extend their model to the (9,6) transition due to the fact that collision rates are only known for inversion levels up to $J = 6$ (e.g., Danby et al. 1988).

NH_3 (9,6) masers are found to be strongly variable, similar to H_2O masers (Madden et al. 1986; Pratap et al. 1991; Henkel et al. 2013). In W51-IRS2, Henkel et al. (2013) found that the (9,6) line showed significant variation in line shape within a time interval of only two days. Mapping of the (9,6) maser toward W51 with very long baseline interferometry (VLBI) suggests that the masers are closer to the H_2O masers than to the OH masers or to ultracompact (UC) H II regions (Pratap et al. 1991). While Henkel et al. (2013) and Goddi et al. (2015) showed that the SiO and NH_3 masers in W51-IRS2 are very close to each other, their positions, differing by 0.″065 (~0.015 pc), do not fully coincide.

In this paper we report the discovery of NH_3 (9,6) masers in two HMSFRs, Cepheus A and G34.26+0.15. This increases the number of (9,6) maser detections in our Galaxy from five to seven. In Sect. 2 observations with the Effelsberg 100-meter telescope and the *Karl G. Jansky* Very Large Array (JVLA) are described. Results are presented in Sect. 3. The morphology of Cep A and G34.26+0.15 as well as a comparison of the emission distributions of different tracers with the NH_3 (9,6) masers are presented in Sect. 4. Our main results are summarized in Sect. 5.

2. Observations and data reduction

2.1. Effelsberg observations and data reduction

The NH_3 (9,6) line was observed toward Cep A and G34.26+0.15 with the 100-meter Effelsberg telescope[1] in 2020 January and 2021 February, July, and August. The S14mm double beam secondary focus receiver was employed. The full width at half maximum (FWHM) beam size is 49″ at 18.5 GHz, the frequency of the target line. The observations were performed in position switching mode, and the off position was 10′ in azimuth away from the source. For observations made before 2021 August, we used a spectrometer that covered 2 GHz wide backends with a channel width of 38.1 kHz, corresponding to ~0.62 km s^{-1} at the line's rest frequency, 18.49939 GHz (Poynter & Kakar 1975). A high spectral resolution backend with 65 536 channels and a bandwidth of 300 MHz was employed in 2021 August, providing a channel width of 0.07 km s^{-1} at 18.5 GHz. Pointing was checked every 2 h using 3C 286 or NGC 7027. Focus calibrations were done at the beginning of the observations and during sunset and sunrise toward the abovementioned pointing sources. The system temperatures were 100–130 K on a main-beam brightness temperature, $T_{\rm MB}$, scale. This flux density was calibrated assuming a $T_{\rm MB}/S$ ratio of 1.95 K Jy^{-1}, derived from continuum cross scans of NGC 7027 (the flux density was adopted from Ott et al. 1994). Calibration uncertainties are estimated to be ~10%.

We used the GILDAS/CLASS[2] package (Pety 2005) to reduce the spectral line data. A first-order polynomial was subtracted from each spectrum for baseline removal.

2.2. JVLA observations and data reduction

Observations of the NH_3 (9,6) line toward Cep A and G34.26+0.15 were obtained on 2021 July 13 with the JVLA of the National Radio Astronomy Observatory[3] (NRAO) in the C configuration (project ID: 21A-157, PI: Yaoting Yan). We employed 27 antennas for the observations. The primary beam of the JVLA antennas is 150″ (FWHM) at 18.5 GHz. A mixture of mixed three-bit and eight-bit samplers were used to perform the observations. For the NH_3 (9,6) line observations, we used one subband with the eight-bit sampler covering a bandwidth of 16 MHz with full polarization, eight recirculations, and four baseline board pairs (BIBPs) to provide a velocity range of 260 km s^{-1} with a channel spacing of 0.13 km s^{-1}. Two additional subbands of bandwidth 16 MHz were used to cover the NH_3 (8,5) and (10,7) lines. The three-bit sampler with 32 subbands, each with a bandwidth of 128 MHz to cover a total range of 4 GHz between 20 and 24 GHz, was used to measure the continuum emission. 3C 286 with a flux density of 2.89 Jy at 18.5 GHz (Perley & Butler 2013) was used as a calibrator for pointing, flux density, bandpass, and polarization. J2230+6946 and J1851+0035 served as gain calibrators for Cep A and G34.26+0.15, respectively. The on-source times were $4^{\rm m}30^{\rm s}$ and $4^{\rm m}50^{\rm s}$ toward Cep A and G34.26+0.15, respectively.

Data from two antennas were lost due to technical issues. The data from the remaining 25 antennas were reduced through the Common Astronomy Software Applications package (CASA[4]; McMullin et al. 2007). We calibrated the data with the JVLA CASA calibration pipeline using CASA 6.1.2. The results were obtained after flagging data that contain artifacts. We inspected the phase, amplitude, and bandpass variations of the calibrated visibility data to search for additional artifacts before imaging. Then, the *uvcontsub* task in CASA was used to separate the calibrated visibilities into two parts, one with line-only data and the other with the continuum data. The *tclean* task with a cell size of 0.″2 and Briggs weighting with robust=0 was used to produce the images of spectral line and continuum emission. The synthesized beams for NH_3 (9,6) are 1.″47 × 0.″99 at PA = 58.°79 and 1.″33 × 1.″06 at PA = 5.°36 toward Cep A and G34.26+0.15, respectively. For the 1.36 cm (20–24 GHz) continuum emission, the synthesized beams are 1.″08 × 0.″67 at

[1] Based on observations with the 100-meter telescope of the MPIfR (Max-Planck-Institut für Radioastronomie) at Effelsberg.

[2] https://www.iram.fr/IRAMFR/GILDAS/

[3] The National Radio Astronomy Observatory is a facility of the National Science Foundation operated under cooperative agreement by Associated Universities, Inc.

[4] https://casa.nrao.edu/

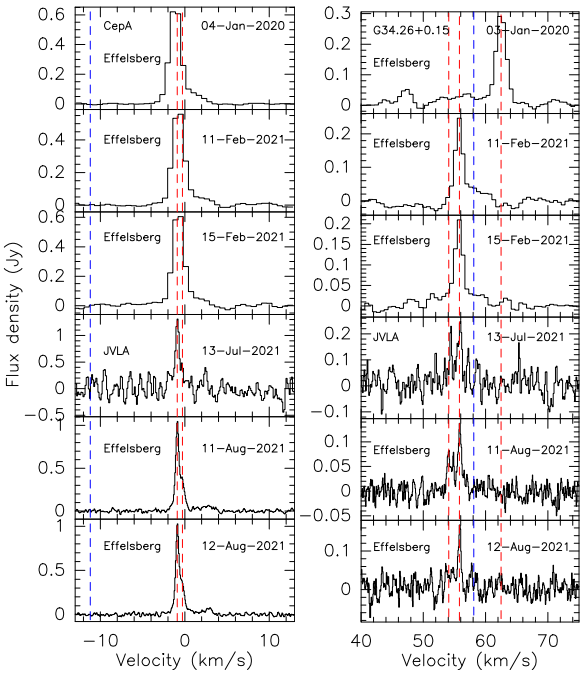

Fig. 1. Spectra from NH_3 (9,6) transition lines. *Left*: *top to bottom*: time sequence of NH_3 (9,6) profiles observed toward Cep A with the Effelsberg 100-meter telescope (after subtracting a first-order polynomial baseline). A JVLA spectrum is interspersed. The systemic velocity from CO and HCO^+ lines is indicated by a dashed blue line. The two dashed red lines at LSR velocities, V_{LSR}, of −0.90 km s^{-1} and −0.28 km s^{-1} indicate the central velocities of the two major components. *Right*: NH_3 (9,6) spectra from G34.26+0.15. The systemic velocity from $C^{17}O$ is indicated by a dashed blue line. The three dashed red lines at V_{LSR} = 54.1 km s^{-1}, 55.8 km s^{-1}, and 62.5 km s^{-1} show the central velocities of the main ammonia emission components.

PA = 60.°64 and 0.″95 × 0.″71 at PA = 5.°91 toward Cep A and G34.26+0.15. The typical absolute astrometric accuracy of the JVLA is ∼10% of the synthesized beam[5]. The flux density scale calibration accuracy is estimated to be within 15%.

3. Results

The spectra from different epochs are shown in Figs. 1 and 2. Toward Cep A, the NH_3 (9,6) line profile from the JVLA is extracted from an Effelsberg-beam-sized region (FWHM, 49″). In the case of G34.26+0.15, the NH_3 spectrum is below the noise level if a similarly large beam size is used. Therefore, we derived the JVLA NH_3 (9,6) spectrum from a smaller region, with radius 3.″5, that contains all the detected NH_3 (9,6) emission. In Table A.1, the observed NH_3 (9,6) line parameters obtained by Gaussian fits are listed. NH_3 (8,5) and (10,7) emission is not detected by our JVLA observations. The 3σ upper limits for the NH_3 (8,5) and (10,7) lines toward Cep A are 23.2 mJy beam^{-1} and 27.2 mJy beam^{-1}, respectively. In G34.26+0.15, the corresponding 3σ upper limits for the NH_3 (8,5) and (10,7) lines are 22.1 mJy beam^{-1} and 30.4 mJy beam^{-1}. For both sources, sensitivity levels refer to emission from a single channel of width

[5] https://science.nrao.edu/facilities/vla/docs/manuals/oss/performance-/positional-accuracy

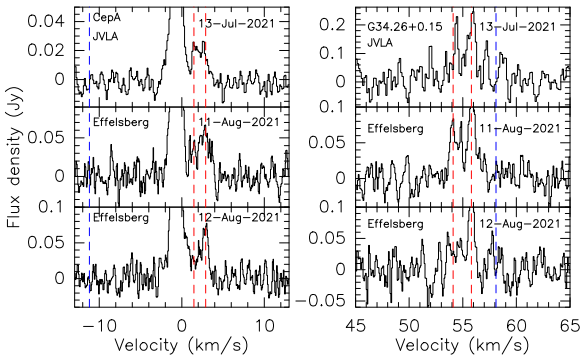

Fig. 2. NH_3 (9,6) line profiles emphasizing, in contrast to the spectra in Fig. 1, weaker features. Cep A spectra are presented on the *left*, G34.26+0.15 spectra on the *right*. The two dashed red lines in the *left panels* indicate V_{LSR} = 1.48 and 2.89 km s^{-1}. In the *right panels*, the two dashed red lines refer to 54.1 and 55.8 km s^{-1}.

0.13 km s^{-1}. Taking the larger measured line widths of the (9,6) maser features (see Table A.1), these limits could be further lowered by factors of two to four.

3.1. Centimeter-continuum emission

The 1.36 cm continuum, derived from our JVLA observations, toward Cep A is presented in Fig. 3. Six published compact sources, HW2, HW3a, HW3b, HW3c, HW3d, and HW9, are detected in our observations. Figure 4 shows the 1.36 cm continuum in G34.26+0.15. Three main continuum objects, A, B, and C, are detected. By using the *imfit* task in CASA, we measured the continuum flux at 1.36 cm toward individual compact source components in Cep A and G34.26+0.15. Details are given in Table A.2.

3.2. NH_3 (9,6) emission in Cep A

In 2020 January, NH_3 (9,6) emission with a peak flux density of 0.67 ± 0.07 Jy was first detected with the Effelsberg 100-meter telescope in Cep A. Emission with similar strength was also detected in 2021 February and August with the same telescope. Higher velocity resolution data, which were obtained in 2021 August, again with the Effelsberg 100-meter telescope, show that the (9,6) emission contains two main velocity components. Overall, the flux densities of the NH_3 (9,6) emission line measured with the Effelsberg 100-meter telescope are, within the calibration uncertainties, unchanged. This is valid for the time interval between 2020 January and August 2021, when we smoothed the obtained spectra to the same velocity resolution. We also see another two weaker components. Figure 2 emphasizes these weak components with an expanded flux density scale.

Higher angular resolution data from the JVLA pinpoint the position of the NH_3 (9,6) emission with an offset of (−0.″28, 0.″02) relative to the 1.36 cm continuum peak of Cep A HW2 (Fig. 3). The deconvolved NH_3 (9,6) component size is (0.″29 ± 0.″15) × (0.″19 ± 0.″14) at PA = 174°, derived with the *imfit* task in CASA, and can thus be considered, accounting for the uncertainties, as unresolved.

In view of the constancy of the flux densities obtained at Effelsberg and the similar JVLA flux density, measured in 2021 July, there is no missing interferometric flux density in the JVLA data.

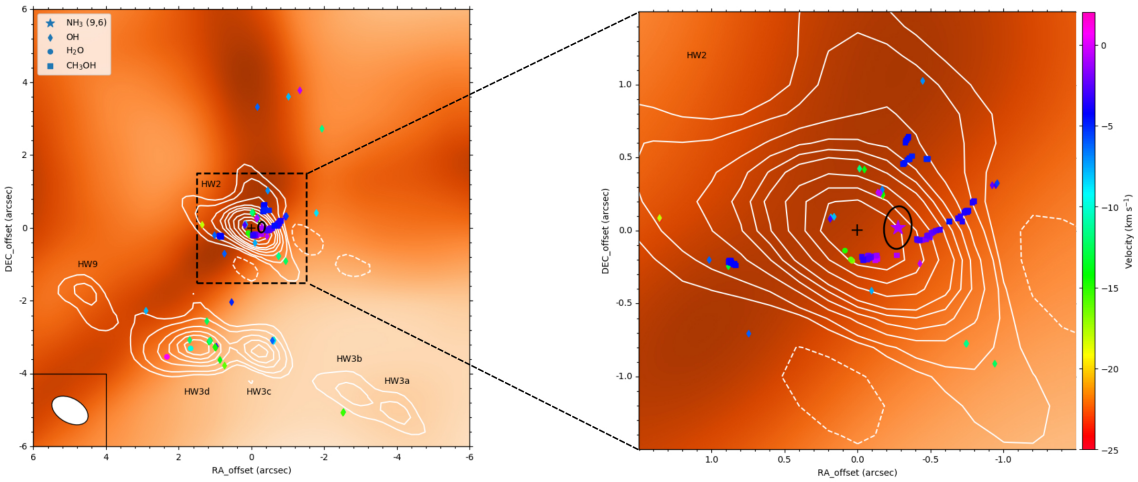

Fig. 3. Cepheus A. White contours mark the 1.36 cm JVLA continuum map of Cep A; levels are −5, 5, 10, 20, 30, 40, 50, 70, 90, and 110 × 0.125 mJy beam^{-1}. The background image is the *Spitzer* 4.5 μm emission, taken from the Galactic Legacy Infrared Mid-Plane Survey Extraordinaire (GLIMPSE; Benjamin et al. 2003; Churchwell et al. 2009). The reference position is $\alpha_{J2000} = 22^h56^m17^s.972$, and $\delta_{J2000} = 62°01'49''.587$, the peak position of the continuum map, is marked with a black cross. Slightly to the west of the cross is the black ellipse denoting the position of the NH_3 (9,6) emission with a purple star at its center. OH (Bartkiewicz et al. 2005), H_2O (Sobolev et al. 2018), and CH_3OH (Sanna et al. 2017) masers are presented as diamonds, circles, and squares, respectively. The color bar on the right-hand side indicates the LSR velocity range of the maser spots.

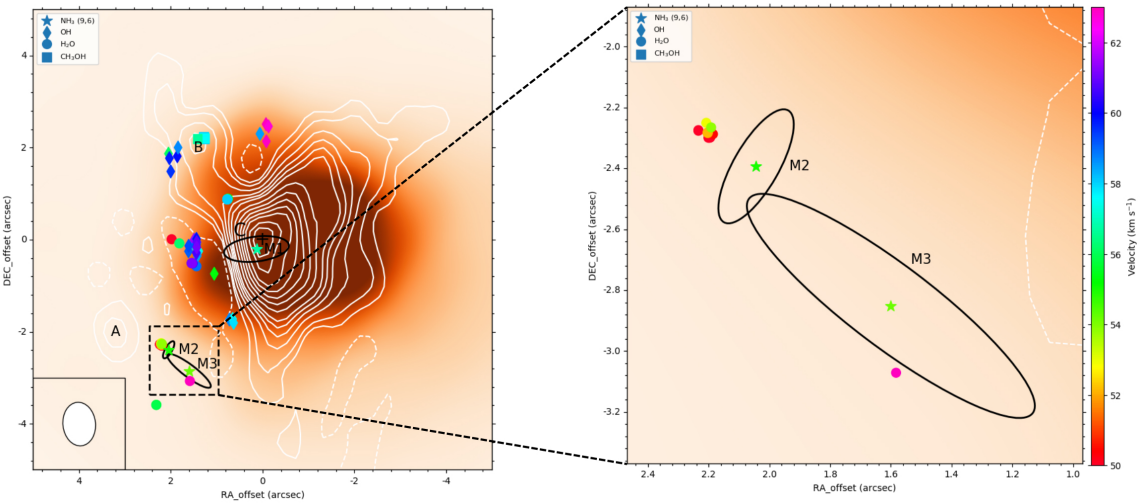

Fig. 4. 1.36 cm JVLA continuum map of G34.26+0.15 presented as white contours with levels of −5, 5, 10, 20, 30, 40, 50, 70, 90, 110, 130, 150, 180, and 200 × 5.0 mJy beam^{-1}. The background image is the *Spitzer* 4.5 μm emission, taken from GLIMPSE. The reference position is $\alpha_{J2000} = 18^h53^m18^s.560$, and $\delta_{J2000} = 01°14'58''.201$, the peak position, is marked by a black cross. The black ellipses show the positions of NH_3 (9,6) emissions with stars at their center (i.e., M1, M2, and M3). OH (Zheng et al. 2000), H_2O (Imai et al. 2011), and CH_3OH (Bartkiewicz et al. 2016) masers are presented as diamonds, circles, and squares, respectively. The color bar indicates the velocity range (V_{LSR}) of maser spots.

3.3. NH_3 (9,6) emission in G34.26+0.15

The NH_3 (9,6) emission was first detected toward G34.26+0.15 in 2020 January with the Effelsberg 100-meter telescope. Higher velocity resolution data from 2021 August show the NH_3 (9,6) emission to be composed of two different components. The spectra of weak components on a smaller flux density scale are presented in Fig. 2.

Three different locations showing NH_3 (9,6) emission are found toward G34.26+0.15 (Fig. 4). The deconvolved NH_3 (9,6) component sizes are (1''.42 ± 0''.43) × (0''.54 ± 0''.62) at PA = 97° (M1), (0''.42 ± 0''.27) × (0''.15 ± 0''.27) at PA = 150° (M2), and (1''.17 ± 0''.34) × (0''.27 ± 0''.46) at PA = 53° (M3) and are thus comparable to or smaller than the beam size.

Overall, the NH_3 (9,6) line from G34.26+0.15 weakened during the time interval from 2020 January to 2021 August by about

70%. A comparison between the JVLA spectrum and the Effelsberg data, assuming a linear decrease in the integrated intensity as a function of time between different epochs of the 100-meter observations, suggests there is no missing flux in the JVLA data. This is similar to the situation in Cep A.

4. Discussion

4.1. Morphology of Cep A and G34.26+0.15

Cep A, at a trigonometric parallax distance of 0.70 ± 0.04 kpc (Moscadelli et al. 2009; Dzib et al. 2011), is the second closest HMSFR (after Orion) and by far the closest NH_3 (9,6) maser known. About 16 compact (∼1″) radio sources (e.g., Hughes & Wouterloot 1984; Hughes 1991; Garay et al. 1996) have been identified in Cep A. Hughes & Wouterloot (1984) discovered these targets at radio wavelengths, which are UC and hypercompact (HC) H II regions and/or stellar wind sources, subsequently named as HW sources. The HW2 object is one of the best known examples of a protostellar jet or disk system driving a powerful outflow (e.g., Rodriguez et al. 1980; Güsten et al. 1984; Torrelles et al. 1986; Curiel et al. 2006; Carrasco-González et al. 2021). The observed NH_3 (9,6) emission is slightly offset (−0.″28, 0.″02) from the center of HW2 (see Fig. 3).

G34.26+0.15 is an HMSFR located at a distance of 3.3 kpc (Kuchar & Bania 1994). It hosts four radio continuum components named A, B, C, and D. Component C is a prototypical cometary UC H II region containing a compact head and a diffuse tail that extends from east to west (e.g., Reid & Ho 1985; Garay et al. 1986; Sewilo et al. 2004; Sewiło et al. 2011). Components A and B are HC H II regions, located to the east of component C. An extended ring-like H II region, called component D, is located southeast of components A-C. One of the three observed NH_3 (9,6) emission line sources, M1, is close to the head of component C, whereas M2 and M3 originate from another compact region in the west of the HC H II component A (see Fig. 4).

4.2. NH_3 (9,6) emission possibly caused by maser action

As shown in Fig. 1, the NH_3 (9,6) profiles in Cep A and G34.26+0.15 are narrow ($\Delta V_{1/2} \leq 2.0$ km s^{-1}), much narrower than the expected line widths ($\gtrsim$4 km s^{-1}) of thermal lines observed at a similar angular resolution (e.g., Torrelles et al. 1985, 1986, 1993, 1999; Henkel et al. 1987; Comito et al. 2007; Mookerjea et al. 2007; Wyrowski et al. 2012; Beuther et al. 2018). Velocity shifts with respect to the systemic velocities of the two sources are both observed, that is, $V \sim 10$ km s^{-1} in Cep A and $V \sim 4$ km s^{-1} in G34.26+0.15 (see details in Sect. 4.3). Furthermore, time variability is observed in the case of G34.26+0.15, which is also a characteristic feature of maser emission.

Additional evidence of their maser nature is the high brightness temperatures of the (9,6) emission spots toward Cep A and G34.26+0.15. The spectral parameters are listed in Table A.3. Because at least a significant part of the NH_3 (9,6) emission is not resolved by our JVLA observations, the derived brightness temperatures are only lower limits. Nevertheless, the lower limits on the brightness temperature are >800 K in Cep A (see Table A.3), which is much higher than the expected thermal gas temperature of ∼250 K (e.g., Patel et al. 2005; Comito et al. 2007; Beuther et al. 2018). This strongly suggests that the NH_3 (9,6) emission in Cep A is due to maser action. Because G34.26+0.15 is located at about five times the distance to Cep A, beam dilution effects reduce the lower main beam brightness temperature limit to 400 K in G34.26+0.15 (M2) (see Table A.3). We also note that the luminosity of the NH_3 (9,6) emission in G34.26+0.15 is higher than or comparable to that in Cep A, depending on the epoch of our observations.

Finally, the non-detections of the (8,5) and (10,7) lines also indicate that the (9,6) line is special. This allows us to derive lower 3σ limits of the (9,6)/(8,5) and (9,6)/(10,7) line intensity ratios. The (9,6) line arises from ortho-NH_3 ($K = 3n$), whereas the NH_3 (8,5) and (10,7) lines are para-NH_3 ($K \neq 3n$) lines. The minimum ortho-to-para ratios are in the range 12–42 and 1–8 toward Cep A and G34.26+0.15, respectively. The statistical weights for the ortho states are twice as large as those for the para states (e.g., Umemoto et al. 1999; Goddi et al. 2011; Henkel et al. 2013). In Cep A, the line intensity ratios are far higher than this factor of two. Thus, at least in Cep A the higher main beam brightness peak temperature of the (9,6) emission is caused by maser action, perhaps involving exponential amplification, and the case of G34.26+0.15 is likely similar.

4.3. Comparison of NH_3 (9,6) masers with previously published (quasi-)thermal NH_3 emission

The metastable (1,1), (2,2), (3,3), and (4,4) ammonia lines show thermal emission toward Cep A over a velocity range of -13 km s$^{-1} \leq V_{\rm LSR} \leq -4$ km s^{-1} (Brown et al. 1981; Güsten et al. 1984; Torrelles et al. 1985, 1986, 1993, 1999). An average NH_3 column density of $\sim 5 \times 10^{15}$ cm^{-2} was estimated for a region of 3″ around HW2 (Torrelles et al. 1999). This high NH_3 abundance could provide a suitable environment for maser species. Large line widths ($\Delta V_{1/2} \simeq 7.0$ km s^{-1}) with $V_{\rm LSR} \sim -10$ km s^{-1} in both (1,1) and (2,2) lines were found toward HW2 (Torrelles et al. 1993). The velocity is similar to the cloud's systemic local standard of rest (LSR) velocity of -11.2 km s^{-1}, which is based on CO (Narayanan & Walker 1996) and HCO^+ observations (Gómez et al. 1999). Our (9,6) maser is redshifted (-0.9 km s$^{-1} \leq V_{\rm LSR} \leq 2.9$ km s^{-1}) and shares positions with the outflowing gas seen in CO and HCO^+ with similarly redshifted velocities. Therefore, we argue that the (9,6) masers are related to outflowing gas.

In G34.26+0.15, a large NH_3 column density, $10^{18.5\pm0.2}$ cm^{-2}, and a kinetic temperature of 225 ± 75 K were derived by Henkel et al. (1987) based on measurements of 15 NH_3 inversion transitions in the frequency range of 22.0–26.0 GHz. These did not include the (9,6) transition. While these lines were measured with a beam size of about 40″, a comparison of the peak intensities of the optically thick lines with the kinetic temperature reveals the size of the hot, ammonia-emitting core to be only ∼2.5″. All those measured NH_3 lines were quasi-thermal and had LSR velocities of ∼58.5 km s^{-1}, close to the systemic velocity of ∼ 58.1 km s^{-1} obtained from $C^{17}O$ observations (Wyrowski et al. 2012). Their line widths ($\Delta V_{1/2} \geq 3.6$ km s^{-1}) are larger than what we find (0.35 km s$^{-1} \leq \Delta V_{1/2} \leq 0.94$ km s^{-1}) for each (9,6) maser component (see details in Table A.3). In all, we may have observed four different (9,6) velocity features. Three are blueshifted at $V_{\rm LSR} \sim 53.8$ km s^{-1}, 55.8 km s^{-1}, and 56.8 km s^{-1}, and a fourth, tentatively detected, at 62.5 km s^{-1}. This tentative redshifted feature was only potentially detected with Effelsberg in 2020 January. The velocity is similar to that of the JVLA measurements on the NH_3 (1,1) absorption line against continuum source C (∼7″ resolution; Keto et al. 1987) and the NH_3 (3,3) emission surrounding continuum source B as well as the head of C (1.″4 × 1.″2 resolution; Heaton et al. 1989). However,

we did not find this redshifted component in our JVLA observations. Therefore, its position within G34.26+0.15 cannot be determined. The blueshifted (9,6) masers with a velocity range of 53.8–56.8 km s^{-1} (M1, M2, and M3) show velocities compatible with those of the NH_3 (3,3) emission at the proper positions (Heaton et al. 1989), which might be a suitable environment for maser species.

4.4. Comparison of NH_3 (9,6) masers with other maser lines

To characterize the environment of NH_3 (9,6) masers, we can compare their positions with respect to those of other maser species (i.e., OH, H_2O, and CH_3OH). Toward Cep A HW2, many CH_3OH (e.g., Menten 1991; Sugiyama et al. 2008; Sanna et al. 2017) and H_2O maser spots (e.g., Torrelles et al. 1998, 2011; Sobolev et al. 2018) are detected and are associated with its disk. Sobolev et al. (2018) also found that most of the H_2O maser flux is associated with the compact H II region HW3d. OH maser features close to the H II regions are also seen in HW2 (e.g., Cohen & Brebner 1985; Bartkiewicz et al. 2005). These three kinds of masers in Cep A have a large velocity range of -25 km s^{-1} $\leq V_{\rm LSR}$ ≤ -2 km s^{-1} and are widespread around HW2 and HW3, while NH_3 (9,6) emission is only detected at -0.9 km s^{-1} $\leq V_{\rm LSR}$ ≤ 2.9 km s^{-1} toward a sub-arcsecond-sized region to the west of the peak continuum position of HW2 (see Fig. 3). This suggests that the NH_3 (9,6) maser in Cep A is unique and not related to maser spots seen in other molecular species.

In G34.26+0.15, OH (Zheng et al. 2000), H_2O (Imai et al. 2011), and CH_3OH (Bartkiewicz et al. 2016) masers have been detected east of source C (Fig. 4), and none of them coincides with the head of C. The NH_3 (9,6) maser M1 is also found slightly off the head of source C. This could suggest that M1 is powered by continuum source C or by an outflow. Near component B, there are some OH and CH_3OH masers but no H_2O or NH_3 masers. A group of H_2O masers, well-known tracers of outflows, with a large velocity distribution of 43 km s^{-1} $\leq V_{\rm LSR}$ ≤ 54 km s^{-1}, was found to the west of the centimeter-continuum source A and close to the peak of the millimeter-continuum emission (see details in our Fig. A.2 and also in Fig. 5 of Imai et al. 2011). The closeness of NH_3 (9,6) maser spots M2 and M3 to this group of water masers and their similar velocities again suggest an association of NH_3 (9,6) masers with outflow activity.

4.5. Constraints on pumping scenarios

Our observations have resulted in the detection of NH_3 (9,6) masers in Cep A and G34.26+0.15. The new detections could provide additional constraints on the maser line's pumping mechanism. As mentioned in Sect. 1, the pumping mechanism of the (9,6) maser is unclear (Madden et al. 1986; Brown & Cragg 1991). Previous studies have suggested that there are three main pumping scenarios to explain the observed NH_3 maser lines (Madden et al. 1986; Henkel et al. 2013): (1) infrared radiation from the dust continuum emission, (2) line overlap, and (3) collisional pumping.

For the first mechanism, infrared photons near 10 μm are needed for vibrational excitation. The high dust temperature (~300 K) of W51-IRS2 can provide substantial infrared photons near 10 μm, which is used for radiative pumping (Henkel et al. 2013). Both Cep A and G34.26+0.15 have similar kinetic temperatures of $\gtrsim$200 K (Henkel et al. 1987; Patel et al. 2005; Comito et al. 2007; Beuther et al. 2018). This suggests that high kinetic temperatures are needed to excite NH_3 (9,6) masers. However, it should be noted that the silicate dust absorption feature might dominate at 10 μm (see the spectral energy distribution of Cep A in De Buizer et al. 2017). Additionally, there is no bright infrared emission around the two (9,6) masers, M2 and M3, in G34.26+0.15 (see Fig. 4; see also Fig. 11 in De Buizer et al. 2003 for a 10.5 μm map). This indicates that the pumping mechanism via infrared photons near 10 μm may not be viable to explain the (9,6) masers in Cep A and G34.26+0.15. Furthermore, Wilson & Schilke (1993) argued that radiative pumping by dust emission tends to excite multiple adjacent ammonia maser transitions, which appears to contradict our failure to detect the adjacent (8,5) and (10,7) lines (with respect to quantum numbers and frequency) and to only measure the (9,6) transitions in Cep A and G34.26+0.15. Therefore, we suggest that infrared radiation from dust is not the main pumping source.

Madden et al. (1986) suggested that there might be some line overlaps between the rotational NH_3 transitions in the far-infrared band. However, this would be unlikely to affect only the (9,6) line. Nevertheless, far-infrared spectral observations will be needed to clarify this scenario.

Based on our observations, the (9,6) maser spots are close to, but not coincident with, the peaks of the radio continuum emission in Cep A and G34.26+0.25. Furthermore, the (9,6) masers show velocity offsets with respect to their systemic velocities. This indicates that the (9,6) masers are located at the base of outflows, similar to the H_2O masers. This is supported by VLBI observations that show that (9,6) masers tend to be closely associated with H_2O masers (Pratap et al. 1991). The observed time variability in G34.26+0.25 and W51-IRS2 can also be attributed to episodic molecular outflows. This indicates that collisional pumping could be the driver of the (9,6) maser. On the other hand, collisional pumping has been successfully used to explain the NH_3 (3,3) maser (Walmsley & Ungerechts 1983; Flower et al. 1990; Mangum & Wootten 1994). Collisions tend to pump from the $K = 0$ level to the $K = 3$ level with parity changes, that is, the upper level of the (3,3) metastable transition will be overpopulated. NH_3 (9,6) arises from the ortho species, so a similar mechanism might also occur in the case of the (9,6) transition. Further measurements of collisional rates of ammonia will allow us to test this scenario.

5. Summary

We report the discovery of NH_3 (9,6) masers in two HMSFRs, Cep A and G34.26+0.15. The narrow line width of the emission features ($\Delta V_{1/2} \leq 2.0$ km s^{-1}) and their high brightness temperatures (>400 K) indicate the maser nature of the lines. The intensity of the (9,6) maser in G34.26+0.25 is decreasing with time, while toward Cep A the maser is stable based on 20 months of monitoring at Effelsberg. Linearly interpolating the integrated intensities obtained at Effelsberg as a function of time, the JVLA measurements show that there is no missing flux density on scales on the order of 1.2 arcsec (4×10^{-3} and 2×10^{-2} pc) to the total single-dish flux. The JVLA-detected emission indicates that the NH_3 (9,6) maser in Cep A originates from a sub-arcsecond-sized region slightly ($0\farcs28 \pm 0\farcs10$) to the west of the peak position of the 1.36 cm continuum object, HW2. In G34.26+0.25, three NH_3 (9,6) maser spots are observed: one is close to the head of the cometary UC H II region C, and the other two are emitted from a compact region to the west of the HC H II region A. We suggest that the (9,6) masers may be connected to outflowing gas. Higher angular resolution JVLA

and VLBI observations are planned to provide more accurate positions and constraints on pumping scenarios.

Acknowledgements. We would like to thank the anonymous referee for the useful comments that improve the manuscript. Y.T.Y. is a member of the International Max Planck Research School (IMPRS) for Astronomy and Astrophysics at the Universities of Bonn and Cologne. Y.T.Y. would like to thank the China Scholarship Council (CSC) for its support. We would like to thank the staff at the Effelsberg for their help provided during the observations. We thank the staff of the JVLA, especially Tony Perreault and Edward Starr, for their assistance with the observations and data reduction. This research has made use of the NASA/IPAC Infrared Science Archive, which is funded by the National Aeronautics and Space Administration and operated by the California Institute of Technology.

References

Bartkiewicz, A., Szymczak, M., Cohen, R. J., & Richards, A. M. S. 2005, MNRAS, 361, 623
Bartkiewicz, A., Szymczak, M., & van Langevelde, H. J. 2016, A&A, 587, A104
Benjamin, R. A., Churchwell, E., Babler, B. L., et al. 2003, PASP, 115, 953
Beuther, H., Walsh, A. J., Thorwirth, S., et al. 2007, A&A, 466, 989
Beuther, H., Mottram, J. C., Ahmadi, A., et al. 2018, A&A, 617, A100
Brogan, C. L., Hunter, T. R., Cyganowski, C. J., et al. 2011, ApJ, 739, L16
Brown, R. D., & Cragg, D. M. 1991, ApJ, 378, 445
Brown, A. T., Little, L. T., MacDonald, G. H., Riley, P. W., & Matheson, D. N. 1981, MNRAS, 195, 607
Carrasco-González, C., Sanna, A., Rodríguez-Kamenetzky, A., et al. 2021, ApJ, 914, L1
Cesaroni, R., Walmsley, C. M., & Churchwell, E. 1992, A&A, 256, 618
Cheung, A. C., Rank, D. M., Townes, C. H., Thornton, D. D., & Welch, W. J. 1968, Phys. Rev. Lett., 21, 1701
Churchwell, E., Babler, B. L., Meade, M. R., et al. 2009, PASP, 121, 213
Cohen, R. J., & Brebner, G. C. 1985, MNRAS, 216, 51P
Comito, C., Schilke, P., Endesfelder, U., Jiménez-Serra, I., & Martín-Pintado, J. 2007, A&A, 469, 207
Curiel, S., Ho, P. T. P., Patel, N. A., et al. 2006, ApJ, 638, 878
Danby, G., Flower, D. R., Valiron, P., Schilke, P., & Walmsley, C. M. 1988, MNRAS, 235, 229
De Buizer, J. M., Radomski, J. T., Telesco, C. M., & Piña, R. K. 2003, ApJ, 598, 1127
De Buizer, J. M., Liu, M., Tan, J. C., et al. 2017, ApJ, 843, 33
Dzib, S., Loinard, L., Rodríguez, L. F., Mioduszewski, A. J., & Torres, R. M. 2011, ApJ, 733, 71
Flower, D. R., Offer, A., & Schilke, P. 1990, MNRAS, 244, 4
Galván-Madrid, R., Keto, E., Zhang, Q., et al. 2009, ApJ, 706, 1036
Garay, G., Rodriguez, L. F., & van Gorkom, J. H. 1986, ApJ, 309, 553
Garay, G., Ramirez, S., Rodriguez, L. F., Curiel, S., & Torrelles, J. M. 1996, ApJ, 459, 193
Gaume, R. A., Wilson, T. L., & Johnston, K. J. 1996, ApJ, 457, L47
Goddi, C., Greenhill, L. J., Humphreys, E. M. L., Chandler, C. J., & Matthews, L. D. 2011, ApJ, 739, L13
Goddi, C., Henkel, C., Zhang, Q., Zapata, L., & Wilson, T. L. 2015, A&A, 573, A109
Gómez, J. F., Sargent, A. I., Torrelles, J. M., et al. 1999, ApJ, 514, 287
Güsten, R., Chini, R., & Neckel, T. 1984, A&A, 138, 205
Heaton, B. D., Little, L. T., & Bishop, I. S. 1989, A&A, 213, 148
Henkel, C., Wilson, T. L., & Mauersberger, R. 1987, A&A, 182, 137
Henkel, C., Wilson, T. L., Asiri, H., & Mauersberger, R. 2013, A&A, 549, A90
Ho, P. T. P., & Townes, C. H. 1983, ARA&A, 21, 239
Hoffman, I. M., & Joyce, S. A. 2014, ApJ, 782, 83
Hogge, T. G., Jackson, J. M., Allingham, D., et al. 2019, ApJ, 887, 79
Hughes, V. A. 1991, ApJ, 383, 280
Hughes, V. A., & Wouterloot, J. G. A. 1984, ApJ, 276, 204
Hunter, T. R., Brogan, C. L., Indebetouw, R., & Cyganowski, C. J. 2008, ApJ, 680, 1271
Imai, H., Omi, R., Kurayama, T., et al. 2011, PASJ, 63, 1293
Keto, E. R., Ho, P. T. P., & Reid, M. J. 1987, ApJ, 323, L117
Kraemer, K. E., & Jackson, J. M. 1995, ApJ, 439, L9
Kuchar, T. A., & Bania, T. M. 1994, ApJ, 436, 117
Madden, S. C., Irvine, W. M., Matthews, H. E., Brown, R. D., & Godfrey, P. D. 1986, ApJ, 300, L79
Mangum, J. G., & Wootten, A. 1994, ApJ, 428, L33
Mauersberger, R., Wilson, T. L., & Henkel, C. 1986, A&A, 160, L13
Mauersberger, R., Henkel, C., & Wilson, T. L. 1987, A&A, 173, 352
Mauersberger, R., Wilson, T. L., & Henkel, C. 1988, A&A, 201, 123
McEwen, B. C., Pihlström, Y. M., & Sjouwerman, L. O. 2016, ApJ, 826, 189
McMullin, J. P., Waters, B., Schiebel, D., Young, W., & Golap, K. 2007, ASP Conf. Ser., 376, 127
Mei, Y., Chen, X., Shen, Z.-Q., & Li, B. 2020, ApJ, 898, 157
Menten, K. M. 1991, ApJ, 380, L75
Mills, E. A. C., Ginsburg, A., Clements, A. R., et al. 2018, ApJ, 869, L14
Mookerjea, B., Casper, E., Mundy, L. G., & Looney, L. W. 2007, ApJ, 659, 447
Moscadelli, L., Reid, M. J., Menten, K. M., et al. 2009, ApJ, 693, 406
Narayanan, G., & Walker, C. K. 1996, ApJ, 466, 844
Ott, M., Witzel, A., Quirrenbach, A., et al. 1994, A&A, 284, 331
Patel, N. A., Curiel, S., Sridharan, T. K., et al. 2005, Nature, 437, 109
Perley, R. A., & Butler, B. J. 2013, ApJS, 204, 19
Pety, J. 2005, in SF2A-2005: Semaine de l'Astrophysique Francaise, eds. F. Casoli, T. Contini, J. M. Hameury, & L. Pagani, 721
Poynter, R. L., & Kakar, R. K. 1975, ApJS, 29, 87
Pratap, P., Menten, K. M., Reid, M. J., Moran, J. M., & Walmsley, C. M. 1991, ApJ, 373, L13
Reid, M. J., & Ho, P. T. P. 1985, ApJ, 288, L17
Rodriguez, L. F., Ho, P. T. P., & Moran, J. M. 1980, ApJ, 240, L149
Sanna, A., Moscadelli, L., Surcis, G., et al. 2017, A&A, 603, A94
Sewilo, M., Churchwell, E., Kurtz, S., Goss, W. M., & Hofner, P. 2004, ApJ, 605, 285
Sewiło, M., Churchwell, E., Kurtz, S., Goss, W. M., & Hofner, P. 2011, ApJS, 194, 44
Sobolev, A. M., Moran, J. M., Gray, M. D., et al. 2018, ApJ, 856, 60
Sugiyama, K., Fujisawa, K., Doi, A., et al. 2008, PASJ, 60, 1001
Torrelles, J. M., Ho, P. T. P., Rodriguez, L. F., & Canto, J. 1985, ApJ, 288, 595
Torrelles, J. M., Ho, P. T. P., Rodriguez, L. F., & Canto, J. 1986, ApJ, 305, 721
Torrelles, J. M., Verdes-Montenegro, L., Ho, P. T. P., Rodriguez, L. F., & Canto, J. 1993, ApJ, 410, 202
Torrelles, J. M., Gómez, J. F., Garay, G., et al. 1998, ApJ, 509, 262
Torrelles, J. M., Gómez, J. F., Garay, G., et al. 1999, MNRAS, 307, 58
Torrelles, J. M., Patel, N. A., Curiel, S., et al. 2011, MNRAS, 410, 627
Towner, A. P. M., Brogan, C. L., Hunter, T. R., & Cyganowski, C. J. 2021, ApJ, 923, 263
Umemoto, T., Mikami, H., Yamamoto, S., & Hirano, N. 1999, ApJ, 525, L105
Urquhart, J. S., Morgan, L. K., Figura, C. C., et al. 2011, MNRAS, 418, 1689
Walmsley, C. M., & Ungerechts, H. 1983, A&A, 122, 164
Walsh, A. J., Longmore, S. N., Thorwirth, S., Urquhart, J. S., & Purcell, C. R. 2007, MNRAS, 382, L35
Walsh, A. J., Breen, S. L., Britton, T., et al. 2011, MNRAS, 416, 1764
Wang, K., Zhang, Q., Wu, Y., Li, H.-b., & Zhang, H. 2012, ApJ, 745, L30
Wilson, T. L., & Henkel, C. 1988, A&A, 206, L26
Wilson, T. L., & Schilke, P. 1993, Lecture Notes in Physics, Astrophysical Masers, eds. A. W. Clegg, & G. E. Nedoluha (Berlin: Springer), 412, 123
Wilson, T. L., Batrla, W., & Pauls, T. A. 1982, A&A, 110, L20
Wilson, T. L., Johnston, K. J., & Henkel, C. 1990, A&A, 229, L1
Wyrowski, F., Güsten, R., Menten, K. M., Wiesemeyer, H., & Klein, B. 2012, A&A, 542, L15
Zhang, Q., & Ho, P. T. P. 1995, ApJ, 450, L63
Zhang, Q., Hunter, T. R., Sridharan, T. K., & Cesaroni, R. 1999, ApJ, 527, L117
Zheng, X. W., Moran, J. M., & Reid, M. J. 2000, MNRAS, 317, 192

A&A 659, A5 (2022)

Appendix A: Additional material

Table A.1. Summary of NH_3 (9, 6) maser observations.

Source	Telescope	Beam size	Epoch	Channel spacing (km s^{-1})	S_ν (Jy)	rms (mJy)	$\int S_\nu dv$ (Jy km s^{-1})	V_{LSR} (km s^{-1})	$\Delta V_{1/2}$ (km s^{-1})
Cep A	Effelsberg	49″	2020, Jan. 04	0.62	0.67	3.41	1.19 ± 0.02	-1.11 ± 0.02	1.67 ± 0.04
	Effelsberg	49″	2021, Feb. 11	0.62	0.59	5.97	1.08 ± 0.02	-0.74 ± 0.02	1.70 ± 0.04
	Effelsberg	49″	2021, Feb. 15	0.62	0.65	10.98	1.11 ± 0.03	-0.75 ± 0.02	1.60 ± 0.05
	JVLA[a]	1.″47 × 0.″99	2021, Jul. 13	0.13	1.13	144	0.89 ± 0.09	-0.86 ± 0.03	0.74 ± 0.12
	Effelsberg	49″	2021, Aug. 11	0.07	0.98	13.36	0.49 ± 0.02	-0.90 ± 0.01	0.47 ± 0.01
					0.35		0.26 ± 0.02	-0.28 ± 0.02	0.69 ± 0.05
	Effelsberg	49″	2021, Aug. 12	0.07	0.98	13.35	0.50 ± 0.01	-0.89 ± 0.07	0.48 ± 0.07
					0.35		0.20 ± 0.01	-0.29 ± 0.07	0.54 ± 0.07
					0.06		0.07 ± 0.01	0.51 ± 0.07	1.09 ± 0.07
					0.02		0.02 ± 0.01	2.15 ± 0.07	0.80 ± 0.07
					0.07		0.06 ± 0.01	2.89 ± 0.07	0.92 ± 0.07
G34.26+0.15	Effelsberg	49″	2020, Jan. 03	0.62	0.30	1.26	0.65 ± 0.03	62.50 ± 0.05	2.05 ± 0.13
	Effelsberg	49″	2021, Feb. 11	0.62	0.24	2.42	0.40 ± 0.02	55.76 ± 0.04	1.60 ± 0.12
	Effelsberg	49″	2021, Feb. 15	0.62	0.20	4.86	0.38 ± 0.02	55.71 ± 0.05	1.80 ± 0.14
	JVLA[b]	1.″33 × 1.″06	2021, Jul. 13	0.13	0.23	37.1	0.09 ± 0.02	54.41 ± 0.03	0.38 ± 0.09
					0.22		0.22 ± 0.02	55.82 ± 0.05	0.95 ± 0.12
					0.15		0.06 ± 0.01	57.21 ± 0.04	0.35 ± 0.08
	Effelsberg	49″	2021, Aug. 11	0.07	0.08	13.92	0.06 ± 0.007	54.10 ± 0.05	0.68 ± 0.12
					0.07		0.02 ± 0.006	54.82 ± 0.03	0.31 ± 0.09
					0.12		0.10 ± 0.006	55.85 ± 0.02	0.75 ± 0.06
	Effelsberg	49″	2021, Aug. 12	0.07	0.16	27.40	0.09 ± 0.008	55.83 ± 0.02	0.56 ± 0.05

Notes. The spectral parameters are obtained from Gaussian fitting. [(a)] The JVLA spectrum toward Cep A is extracted from the Effelsberg-beam-sized region (FWHM 49″). [(b)] For G34.26+0.15, the JVLA beam samples the NH_3 (9,6) spectrum over a region of radius 3.″5, which contains all detected NH_3 (9,6) emissions.

Table A.2. 1.36 cm JVLA flux densities of individual continuum sources.

Source		R.A. (h m s)	Dec. (° ′ ″)	Size (arcsec)	P.A. (deg)	S_ν (mJy)
Cep A	HW2	22 56 17.972 ± 0.003	+62 01 49.587 ± 0.015	(0.45 ± 0.19) × (0.22 ± 0.10)	50.0	20.2 ± 1.4
	HW3a	22 56 17.420 ± 0.022	+62 01 44.576 ± 0.076	(2.35 ± 0.45) × (0.55 ± 0.14)	66.6	4.75 ± 0.74
	HW3b	22 56 17.578 ± 0.009	+62 01 45.041 ± 0.043	(1.43 ± 0.24) × (0.45 ± 0.10)	59.9	3.19 ± 0.36
	HW3c	22 56 17.956 ± 0.016	+62 01 46.224 ± 0.038	(1.44 ± 0.37) × (0.36 ± 0.19)	86.0	9.90 ± 1.7
	HW3d	22 56 18.195 ± 0.005	+62 01 46.325 ± 0.014	(1.26 ± 0.12) × (0.30 ± 0.19)	102.5	13.75 ± 0.92
	HW9	22 56 18.626 ± 0.014	+62 01 47.851 ± 0.137	(1.53 ± 0.51) × (0.29 ± 0.30)	28.0	3.26 ± 0.78
G34.26+0.15	A	18 53 18.774 ± 0.005	+01 14 56.208 ± 0.125	(0.66 ± 0.49) × (0.50 ± 0.33)	10.0	94 ± 33
	B	18 53 18.649 ± 0.005	+01 15 00.071 ± 0.180	(2.31 ± 0.49) × (0.85 ± 0.21)	17.4	597 ± 110
	C	18 53 18.560 ± 0.004	+01 14 58.201 ± 0.112	(2.03 ± 0.30) × (1.34 ± 0.20)	178.0	5070 ± 660

Table A.3. NH_3 (9,6) maser positions derived from the JVLA observations.

Source		R.A.	Dec.	S_ν	T_{MB}	V_{LSR}	$\Delta V_{1/2}$
		(h m s)	(° ′ ″)	(mJy beam^{-1})	(K)	(km s^{-1})	
Cep A	M	22 56 17.933 ± 0.002	+62 01 49.608 ± 0.011	985.2	2464.8	-0.88 ± 0.01	0.51 ± 0.02
				343.2	829.5	-0.24 ± 0.03	0.63 ± 0.05
G34.26+0.15	M1	18 53 18.569 ± 0.007	+01 14 57.997 ± 0.056	37.1	94.5	56.82 ± 0.06	0.68 ± 0.14
	M2	18 53 18.696 ± 0.002	+01 14 55.807 ± 0.034	48.4	122.4	53.77 ± 0.05	0.35 ± 0.08
				57.8	146.2	54.35 ± 0.07	0.83 ± 0.14
				180.8	457.6	55.83 ± 0.01	0.59 ± 0.03
	M3	18 53 18.667 ± 0.005	+01 14 55.348 ± 0.066	78.1	197.2	54.22 ± 0.04	0.94 ± 0.08
				73.7	186.3	55.78 ± 0.04	0.79 ± 0.08

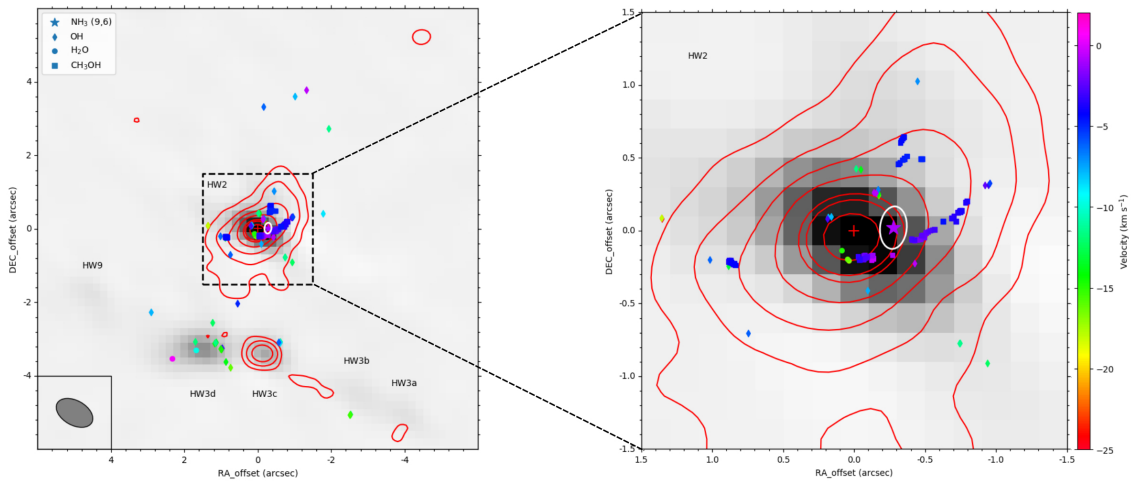

Fig. A.1. Cepheus A. The grey shaded areas mark the 1.36 cm JVLA continuum map of Cep A. The reference position is α_{J2000} = 22^{h}56^{m}17^s.972, and δ_{J2000} = 62°01′49″.587, the peak position of the continuum map, is marked by a red cross. Slightly to the west of the cross is the white ellipse denoting the position of the NH_3 (9,6) emission with a purple star at its center. The red contours show the NOrthern Extended Millimeter Array (NOEMA) 1.37 mm continuum, taken from Beuther et al. (2018). Contour levels are -5, 5, 10, 20, 40, 80, 100, 150, and 200 × 2.43 mJy beam^{-1}. OH (Bartkiewicz et al. 2005), H_2O (Sobolev et al. 2018), and CH_3OH (Sanna et al. 2017) masers are presented as diamonds, circles, and squares, respectively. The color bar on the right-hand side indicates the velocity range (V_{LSR}) of maser spots.

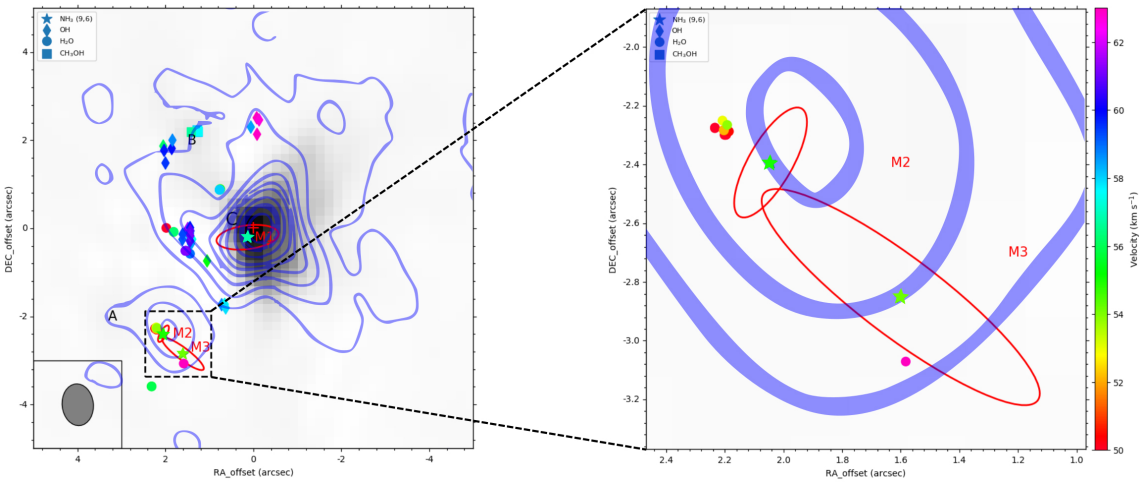

Fig. A.2. 1.36 cm JVLA continuum map of G34.26+0.15 presented as gray shaded areas. The reference position is α_{J2000} = 18^{h}53^{m}18^{s}.560, and δ_{J2000} = 01°14′58″.201, the peak position, is marked by a red cross. The red ellipses show the positions of NH_3 (9,6) emission with stars at their center (i.e., M1, M2, and M3). The blue contours show the Berkeley-Illinois-Maryland Association (BIMA) array 2.8 mm continuum, taken from Mookerjea et al. (2007). Contour levels are -3, 3, 10, 20, 30, 40, 50, 70, 90, 100, 120, and 140 × 20 mJy beam^{-1}. OH (Zheng et al. 2000), H_2O (Imai et al. 2011), and CH_3OH (Bartkiewicz et al. 2016) masers are presented as diamonds, circles, and squares, respectively. The color bar indicates the velocity range (V_{LSR}) of maser spots.

Appendix C

Discovery of non-metastable ammonia masers in Sagittarius B2

Appendix C. Discovery of non-metastable ammonia masers in Sagittarius B2

160

A&A 666, L15 (2022)
https://doi.org/10.1051/0004-6361/202245024
© Y. T. Yan et al. 2022

Astronomy & Astrophysics

LETTER TO THE EDITOR

Discovery of non-metastable ammonia masers in Sagittarius B2

Y. T. Yan (闫耀庭)[1]★, C. Henkel[1,2,3], K. M. Menten[1], Y. Gong (龚 龑)[1], H. Nguyen[1], J. Ott[4], A. Ginsburg[5], T. L. Wilson[1], A. Brunthaler[1], A. Belloche[1], J. S. Zhang (张江水)[6], N. Budaiev[5], and D. Jeff[5]

[1] Max-Planck-Institut für Radioastronomie, Auf dem Hügel 69, 53121 Bonn, Germany
e-mail: yyan@mpifr-bonn.mpg.de, astrotingyan@gmail.com
[2] Astronomy Department, Faculty of Science, King Abdulaziz University, PO Box 80203, Jeddah 21589, Saudi Arabia
[3] Xinjiang Astronomical Observatory, Chinese Academy of Sciences, 830011 Urumqi, PR China
[4] National Radio Astronomy Observatory, 520 Edgemont Road, Charlottesville, VA 22903-2475, USA
[5] Department of Astronomy, University of Florida, PO Box 112055, Florida, USA
[6] Center for Astrophysics, Guangzhou University, 510006 Guangzhou, PR China

Received 20 September 2022 / Accepted 23 September 2022

ABSTRACT

We report the discovery of widespread maser emission in non-metastable inversion transitions of NH_3 toward various parts of the Sagittarius B2 molecular cloud and star-forming region complex. We detect masers in the J, K = (6, 3), (7,4), (8,5), (9,6), and (10,7) transitions toward Sgr B2(M) and Sgr B2(N), an NH_3 (6,3) maser in Sgr B2(NS), and NH_3 (7,4), (9,6), and (10,7) masers in Sgr B2(S). With the high angular resolution data of the *Karl G. Jansky* Very Large Array (JVLA) in the A-configuration, we identify 18 maser spots. Nine maser spots arise from Sgr B2(N), one from Sgr B2(NS), five from Sgr B2(M), and three in Sgr B2(S). Compared to our Effelsberg single-dish data, the JVLA data indicate no missing flux. The detected maser spots are not resolved by our JVLA observations. Lower limits to the brightness temperature are >3000 K and reach up to several 10^5 K, manifesting the lines' maser nature. In view of the masers' velocity differences with respect to adjacent hot molecular cores and/or UCH II regions, it is argued that all the measured ammonia maser lines may be associated with shocks caused either by outflows or by the expansion of UCH II regions. Overall, Sgr B2 is unique in that it allows us to measure many NH_3 masers simultaneously, which may be essential in order to elucidate their thus far poorly understood origin and excitation.

Key words. masers – ISM: clouds – ISM: individual objects: Sgr B2 – HII regions – radio lines: ISM

1. Introduction

Since their discovery in the $(J, K) = (3,3)$ metastable ($J = K$) line toward the high-mass star-forming region (HMSFR) W33 (Wilson et al. 1982), sources emitting maser emission in the ammonia molecule (NH_3) have attracted much attention. To date, metastable ammonia maser lines have been detected in 22 HMSFRs (see Yan et al. 2022, and references therein), while non-metastable ($J > K$) ammonia masers have only been found in ten sources. The NH_3 (6,3), (7,4), (8,5), and (9,6) maser lines, which will be discussed below, arise from energy levels of 551 K, 713 K, 892 K, and 1089 K above the ground state, respectively. These four maser transitions have only been detected, respectively, in three (NGC 7538, W51, and Sgr B2(N)), in two (W51 and Sgr B2(N)), in two (W51 and Sgr B2(N)), and in seven (W51, NGC7538, W49, DR21 (OH), Sgr B2(N), Cep A and G34.26+0.15) HMSFRs (Madden et al. 1986; Henkel et al. 2013; Mei et al. 2020; Yan et al. 2022). The NH_3 (10,7) line, also observed by us, connects states as high as 1303 K above the ground state and has so far only been classified as a maser in W51 (Henkel et al. 2013). Among all the abovementioned regions of massive star formation, Sgr B2 hosts a particularly high number of active sites of star formation.

Sgr B2 is located at a projected distance of ~100 pc from Sgr A* (Reid et al. 2009), the compact radio source associated with the supermassive black hole in the Galactic center at a distance of $8.178 \pm 0.013_{\rm stat.} \pm 0.022_{\rm sys.}$ kpc (GRAVITY Collaboration 2019). This region is normally divided into three high-mass star-forming cores: Sgr B2(N), Sgr B2(M), and Sgr B2(S) (see our Fig. 1 for the locations of these). In total, Sgr B2 contains more than 50 H II regions, most of which are ultracompact H II regions (UCH II) with diameters smaller than 0.1 pc (Gaume et al. 1995; De Pree et al. 1998, 2014, 2015; Lazio & Cordes 2008; Ginsburg et al. 2018; Meng et al. 2019, 2022; Nguyen et al. 2021). In Sgr B2 (N) and (M), several deeply embedded high-mass young stellar objects are surrounded by dense, hot molecular cores with an exceedingly rich chemistry that gives rise to a plethora of lines from numerous complex organic molecules (e.g., Belloche et al. 2008, 2013, 2022). Detected molecular maser species are OH (Gaume & Claussen 1990; Caswell et al. 2013; Cotton & Yusef-Zadeh 2016), H_2O (Reid et al. 1988; McGrath et al. 2004; Walsh et al. 2014), SiO (Morita et al. 1992; Zapata et al. 2009), H_2CO (Mehringer et al. 1994; Hoffman et al. 2007; Lu et al. 2019), CH_3OH class I (Mehringer & Menten 1997; Cotton & Yusef-Zadeh 2016), and class II (Caswell 1996; Rickert et al. 2019; Lu et al. 2019), and

★ Member of the International Max Planck Research School (IMPRS) for Astronomy and Astrophysics at the universities of Bonn and Cologne.

Open Access article, published by EDP Sciences, under the terms of the Creative Commons Attribution License (https://creativecommons.org/licenses/by/4.0), which permits unrestricted use, distribution, and reproduction in any medium, provided the original work is properly cited.
This article is published in open access under the Subscribe-to-Open model. Open access funding provided by Max Planck Society.

A&A 666, L15 (2022)

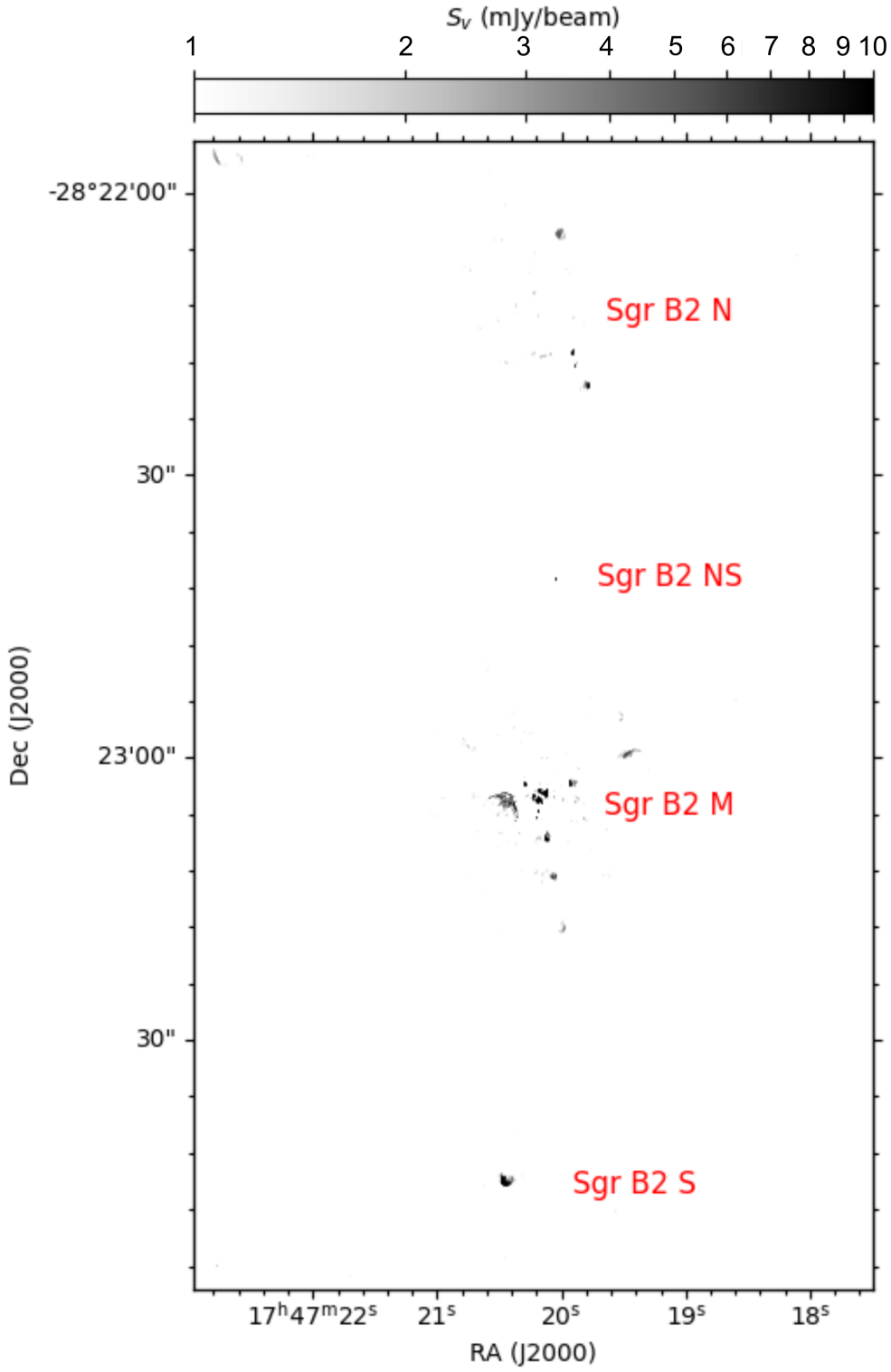

Fig. 1. JVLA 1.6-cm continuum map of Sgr B2, shown in gray. The synthesized beam is $0\overset{''}{.}22 \times 0\overset{''}{.}08$, PA $= -10\overset{\circ}{.}61$.

Table 1. Summary of the JVLA observations.

Transition (J, K)	ν (GHz)	$E_{\rm low}/k$ (K)	Baseband	Synthesized beam (arcsec)	Linear resolution (au)	PA (deg)	(K mJy^{-1})	rms (mJy beam^{-1})
(5,1)	19.838346	422	A0/C0	0.198×0.085	1624×697	−9.807	184	3.32
(6,3)	19.757538	551	A0/C0	0.203×0.087	1665×713	−9.806	177	4.30
(7,4)	19.218465	713	A0/C0	0.209×0.089	1714×730	−9.661	178	3.85
(8,5)	18.808507	892	B0/D0	0.214×0.091	1755×746	−9.527	177	3.54
(9,6)	18.499390	1089	B0/D0	0.215×0.097	1763×795	−7.385	171	3.79
(10,7)	18.285434	1303	B0/D0	0.220×0.094	1804×771	−9.874	177	2.95

Notes. Columns (1) and (2): observed lines and corresponding rest frequencies, taken from Henkel et al. (2013). Column (3): $E_{\rm low}/k$: energy above the ground state of the lower level of a given inversion doublet; k is the Boltzmann constant; $(E_{\rm up} - E_{\rm low})/k \sim 1.0$–$1.5$ K. Column (4): baseline board pairs' setup, see details in VLA resources page. Column (5): synthesized beam. Column (6): linear resolution at a distance of 8.2 kpc. Column (7): position angle of the synthesized beam. Column (8): conversion factor from mJy to Kelvin for each transition was calculated with $1.222 \times 10^3/(\nu^2 \theta_{\rm maj}\theta_{\rm min})$, where ν is the frequency in units of GHz; $\theta_{\rm maj}$ and $\theta_{\rm min}$ are the major and minor axis of the synthesized beam in units of arcseconds (https://science.nrao.edu/facilities/vla/proposing/TBconv). Column (9): rms noise in a channel image.

NH_3 (Martín-Pintado et al. 1999; Mills et al. 2018; Mei et al. 2020). In the case of NH_3, an ammonia maser in the metastable (3,3) transition was only detected in the southern part of Sgr B2(S) (Martín-Pintado et al. 1999). Another metastable ammonia maser, in the (2,2) line, was found toward SgrB2(M) (Mills et al. 2018). Recently, 18 ammonia non-metastable maser lines at frequencies of 13.0–24.0 GHz were detected toward Sgr B2(N) with the Shanghai 65-m Tianma radio telescope with characteristic beam sizes of $54 \times 18.5/\nu$(GHz) arcseconds (Mei et al. 2020).

In this Letter, we report the discovery of NH_3 (6,3), (7,4), (8,5), (9,6), and (10,7) masers in Sgr B2(M) and Sgr B2(N), an NH_3 (6,3) maser in Sgr B2(NS), as well as NH_3 (7,4), (9,6), and (10,7) masers in Sgr B2(S). All of these increase the number of (6,3), (7,4), (8,5), (9,6), and (10,7) maser detections in our Galaxy, respectively, from three to six, two to four, two to three, seven to nine, and one to four. Observations with the Effelsberg 100-m telescope and the *Karl G. Jansky* Very Large Array (JVLA) are presented in Sect. 2. Results are described in Sect. 3. A comparison of the positions of the different ammonia masers with those of other relevant tracers of the interstellar medium is presented in Sect. 4. Our main results are summarized in Sect. 5.

2. Observations and data reduction

2.1. Effelsberg observations and data reduction

The NH_3 (9,6) and (10,7) lines were observed toward Sgr B2 with the 100-m Effelsberg telescope[1] at 12 epochs in January 2020, February and August 2021, as well as in March, May, June, July, and August 2022. The observations were performed in position switching mode. The off position was 30′ in azimuth away from the source. An S14mm double beam secondary focus receiver was employed. The half power beam width (HPBW) is $49 \times 18.5/\nu$(GHz) arcseconds, that is 49″ at 18.5 GHz, the frequency of the NH_3 (9,6) line. Before August 2021, the spectrometer covered 2 GHz with a channel width of 38.1 kHz, corresponding to ∼0.62 km s^{-1} at 18.5 GHz. From August 2021, a high spectral resolution backend with 65 536 channels and a bandwidth of 300 MHz was employed, providing a channel width of 0.07 km s^{-1} at 18.5 GHz. Pointing was checked every hour using NGC 7027. Focus calibrations were done at the beginning of the observations, and during sunset and sunrise, toward NGC 7027. The calibrator was measured between elevations of 30 and 56 deg. The elevation on target was about 10 deg, requiring only minimal (≤2%) elevation-dependent flux density corrections. The system temperatures were 140–220 K in a main-beam brightness temperature, $T_{\rm MB}$, scale. The flux density was calibrated assuming a $T_{\rm MB}/S$ ratio of 1.95 K Jy^{-1}, derived from continuum cross scans of NGC 7027 (its flux density was adopted from Ott et al. 1994). Calibration uncertainties were estimated to be ∼10%.

We used the GILDAS/CLASS[2] package (Pety et al. 2005) to reduce the spectral line data. A first-order polynomial was subtracted from each spectrum for baseline removal.

2.2. JVLA observations and data reduction

Observations of six NH_3 lines, the (5,1), (6,3), (7,4), (8,5), (9,6), and (10,7) transitions (Table 1), toward Sgr B2 were made on 5 March 2022 with the JVLA of the National Radio Astronomy Observatory[3] (NRAO) in the A-configuration (project ID: 22A-106, PI: Yaoting Yan). Eight-bit samplers were used to perform the observations. For the NH_3 (9,6) and (10,7) line observations, we used two subbands with the eight-bit samplers covering a bandwidth of 16 MHz with full polarization, eight recirculations, and four baseline board pairs (BLBPs) to provide a velocity range of 260 km s^{-1} with a channel spacing of 0.13 km s^{-1}. Four additional subbands of bandwidth 16 MHz were used to cover the NH_3 (5,1), (6,3), (7,4), and (8,5) lines. The remaining ten subbands of the eight-bit sampler with a bandwidth of 128 MHz were used to measure the continuum emission between 18 and 20 GHz. The primary beam of the JVLA antennas is 150″ (FWHM) at 18.5 GHz, covering all prominent star-forming regions in Sgr B2 simultaneously. 3C 286 was used as a calibrator for pointing, flux density, bandpass, and polarization (Perley & Butler 2013). J1745−2900 served as our gain calibrator during the observations. The on-source time was 30 min toward Sgr B2.

A total of 27 antennas were employed for the observations. Data from two antennas were lost due to technical issues. The data from the remaining 25 antennas were reduced through the Common Astronomy Software Applications package (CASA[4];

[1] Based on observations with the 100-m telescope of the MPIfR (Max-Planck-Institut für Radioastronomie) at Effelsberg.

[2] https://www.iram.fr/IRAMFR/GILDAS/

[3] The National Radio Astronomy Observatory is a facility of the National Science Foundation, operated under a cooperative agreement by Associated Universities, Inc.

[4] https://casa.nrao.edu/

McMullin et al. 2007). We calibrated the data with the JVLA CASA calibration pipeline using CASA 6.2.1. The results were obtained after flagging and recalibrating data that contained artifacts. We inspected the phase, amplitude, and bandpass variations of the calibrated visibility data to search for additional artifacts before imaging. Then, the *uvcontsub* task in CASA was used to separate the calibrated visibilities into two parts: one with line-only data and the other with the line-free continuum data. The *tclean* task with a cell size of 0.″02 and Briggs weighting with robust = 0.5 was used to produce the images of spectral line and continuum emission. All of the images were corrected for primary beam response. The synthesized beams and the rms noises in a channel image for the observed lines are listed in Table 1. For the 1.6 cm (18–20 GHz) continuum emission, the synthesized beam is 0.″22 × 0.″08 at PA = −10.°61. The typical absolute astrometric accuracy of the JVLA is ∼10% of the synthesized beam[5]. The flux density scale calibration accuracy is estimated to be within 15%.

The maser spots were identified in two different ways and then cross-checked. First, we searched for masers using eyes in channel maps with a velocity spacing of 0.5 km s^{-1}. Second, we used an automated source extraction code (SEC; Murugeshan 2015; Nguyen 2015) running in CASA 5.4 to find the maser features. Emission with signal-to-noise ratios (S/Ns) larger than six identified in this way was considered to be a real detection. A detailed description of the SEC code can be found in Sect. 3.1 of Nguyen et al. (2022).

3. Results

In January 2020, with the Effelsberg 100-m telescope, we observed two strong NH_3 (9,6) maser features with velocities of ∼77 km s^{-1} and ∼84 km s^{-1}, and a weaker one at ∼72 km s^{-1}, toward the equatorial position α_{J2000} = 17^{h}47^{m}20.^{s}8, and δ_{J2000} = −28°23′32.″1, which is offset by (+3.″96,−26.″19) from Sgr B2(M). In addition, maser emission at ∼77 km s^{-1} was also found in the non-metastable para-NH_3 (10,7) transition. The NH_3 (9,6) and (10,7) maser spectra are shown in Fig. A.1. In February 2021, we extended our observations to 20 positions to cover, in a fully sampled way, an area of ∼5.0 square arc minutes surrounding Sgr B2(M) with a spacing of 25″, half the beam size. (9,6) maser emission was found to be quite widespread in Sgr B2, not only residing in Sgr B2(M), but also in Sgr B2(N) and Sgr B2(S), while (10,7) masers were detected in a more limited region comprising Sgr B2(M) and Sgr B2(N). The maps of NH_3 (9,6) and (10,7) spectra are presented in Figs. A.2 and A.3.

Effelsberg monitoring observations spanning 19 months show that the NH_3 (9,6) maser at V_{LSR} = 72.5 km s^{-1} toward Sgr B2(N) became weaker from February to August in 2021 and was not detectable from March 2022 on 3σ levels of 0.12 Jy with a 0.07 km s^{-1} channel width. A weaker (9,6) feature at V_{LSR} = 63.8 km s^{-1} was detected in March 2022. The (9,6) maser spectra from Sgr B2(N) are presented in Fig. A.4. NH_3 (9,6) line parameters obtained by Gaussian fits are listed in Table B.1. An NH_3 (10,7) maser was detected at a different velocity of 82.0 km s^{-1} toward Sgr B2(N). Its flux density was increasing from February to August 2021 but was decreasing from March to August 2022. In Table B.2, NH_3 (10,7) line parameters obtained from Gaussian fits are presented.

Toward Sgr B2(M), NH_3 (9,6) maser emission at V_{LSR} = 72.5 km s^{-1} became stronger between February 2021 and March 2022, then weakened until 2022 August. Higher spectral resolution data since March 2022 show the NH_3 (9,6) emission to be composed of three different components. The NH_3 (10,7) maser in Sgr B2(M) has a velocity offset with respect to the (9,6) maser, with a velocity of V_{LSR} = 70.0 km s^{-1}. The flux density in the Effelsberg beam remained constant within the uncertainties during the 19 months. Spectra are shown in Fig. A.5 and line parameters obtained by Gaussian fits are listed in Tables B.3 and B.4.

The 1.6 cm continuum, derived from our JVLA A-configuration measurements, is shown in Fig. 1. A total of 22 known compact H II regions (Gaume et al. 1995; De Pree et al. 1998, 2014, 2015) were detected by our observations. The locations and sizes of these sources, derived with the *imfit* task in CASA, are consistent with previous results from 7 mm continuum measurements (De Pree et al. 2015). Details are given in Table B.5.

The JVLA has a better angular resolution compared to the Effelsberg 100-m single dish and those data reveal 18 maser spots in the NH_3 (6,3), (7,4), (8,5), (9,6), and (10,7) transitions. We did not find any emission in the NH_3 (5,1) line from Sgr B2. The 3σ upper limit for the NH_3 (5,1) line is 9.96 mJy beam^{-1} (about 1800 K) for a channel width of 0.12 km s^{-1}. The JVLA NH_3 (9,6) and (10,7) line profiles toward Sgr B2(M), extracted from an Effelsberg-beam-size region (FWHM, 49″), are shown in Fig. A.5. From the similarity of the flux density obtained at Effelsberg and the JVLA, measured in March 2022, we conclude that there is no "missing spacing" flux density in the JVLA data, that is, emission on angular scales larger than defined by the shortest JVLA baseline. NH_3 (6,3) masers arise from four different locations, named 63A, 63B, 63C, and 63D. NH_3 (7,4), (8,5), (9,6), and (10,7) masers are detected toward three, two, four, and five spots, respectively. Positions and spectral parameters of these masers are listed in Table B.6. The detected isolated maser spots are distributed over a 16″ × 93″ area in Sgr B2, corresponding to 0.6 × 3.7 pc. Details related to the individual sources are given below.

Sgr B2(N). Among the 18 maser spots detected in Sgr B2, 50% are located in Sgr B2(N). These are seen in the NH_3 (6,3) transition toward 63A and 63B, in the (7,4) transition toward 74A, in the (8,5) line toward 85A, in the (9,6) transition toward 96A and 96B, as well as in the (10,7) line toward 107A, 107B, and 107C. Four of these sources, 85A, 96A, 96B, and 107C, are close to the UCH II region K2 (see Fig. 2). The two maser spots, 85A and 107C, share the same position and have similar velocity distributions. Three maser spots, 63A, 63B, and 74A, surround the compact continuum source K3. The two maser spots, 63A and 74A, share, within the uncertainties, the same position and have similar velocity distributions. One maser spot, 107A, originates from a region offset by (−0.″61 ± 0.″02, +0.″47 ± 0.″01) from the continuum source K7. The second maser spot in the (10,7) line, 107B, has the highest brightness temperature. The lower limit is no less than 6 × 10^5 K and originates from a region without any centimeter continuum source. Spectra from these nine maser spots are presented in Fig. 3.

Sgr B2(NS). Only one maser spot, 63C, in the NH_3 (6,3) transition was detected in this region. It is the strongest among all the detected (6,3) masers in Sgr B2 and is at a position with an offset of (−0.″09 ± 0.″02, +0.″01 ± 0.″01) from the H II2 region, Z10.24 (see Fig. A.6 and Table B.6). The spectrum is shown in Fig. A.7.

Sgr B2(M). We detected five maser spots in this area (see Fig. A.8). Three of them, 63D, 74B, and 96C, arise from sim-

[5] https://science.nrao.edu/facilities/vla/docs/manuals/oss/performance-/positional-accuracy

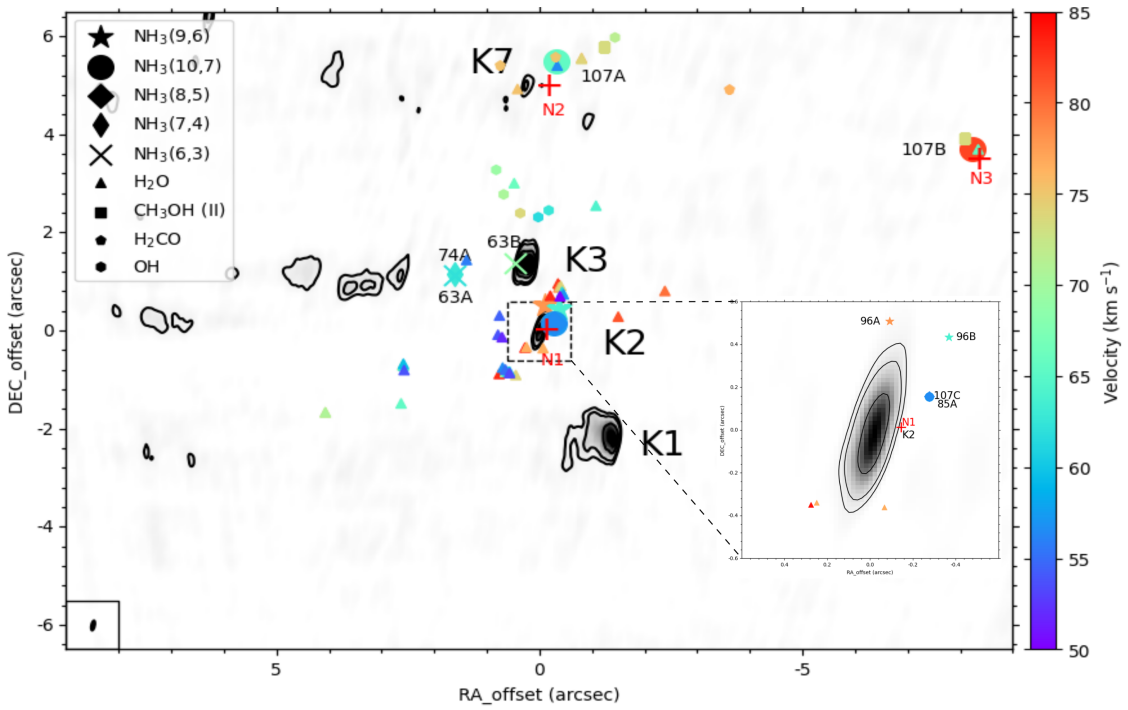

Fig. 2. JVLA 1.6 cm continuum map of Sgr B2(N), shown by the gray shaded areas and black contours with levels of 5, 10, 30, and 50×0.2 mJy beam^{-1}. The reference position is $\alpha_{J2000} = 17^h47^m19\overset{s}{.}883$, and $\delta_{J2000} = -28°22'18\overset{''}{.}412$, the peak position of the continuum source K2. The crosses, thin diamonds, diamonds, stars, and circles show the positions of NH_3 (6,3), (7,4), (8,5), (9,6), and (10,7) emissions. H_2O (McGrath et al. 2004), class II CH_3OH (Caswell 1996; Lu et al. 2019), H_2CO (Mehringer et al. 1994; Hoffman et al. 2007; Lu et al. 2019), and OH (Gaume & Claussen 1990) masers are presented as triangles, squares, pentagons, and hexagons, respectively. The color bar indicates the velocity range (V_{LSR}) of maser spots. Red crosses mark the positions of the hot cores Sgr B2(N1), N2, and N3, taken from the 3 mm imaging line survey "Exploring Molecular Complexity with ALMA" (EMoCA, Bonfand et al. 2017). The systemic velocities of the hot cores N1, N2, and N3 are $V_{LSR} = 64$ km s^{-1}, $V_{LSR} = 74$ km s^{-1} and $V_{LSR} = 74$ km s^{-1}, respectively (Bonfand et al. 2017).

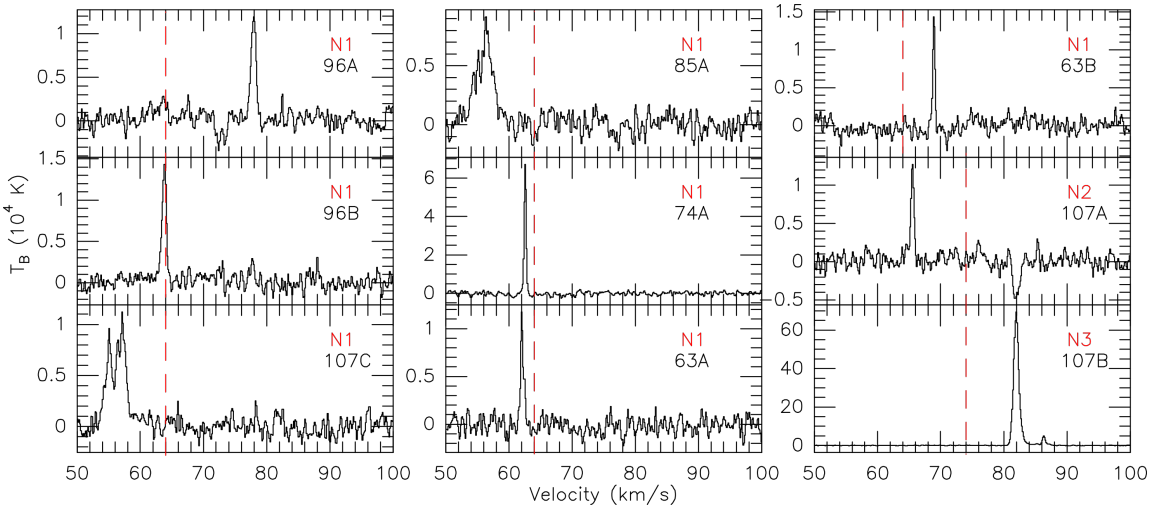

Fig. 3. JVLA A-configuration spectra of NH_3 transition lines toward Sgr B2(N). The dashed red lines indicate the systemic velocities of the associated hot cores. $V_{LSR} = 64$ km s^{-1} for N1, and $V_{LSR} = 74$ km s^{-1} for N2 and N3 (Bonfand et al. 2017). Main beam brightness temperature scales are presented on the left hand side of the profiles.

ilar positions close to the UCH II region F10.39. These three maser features are distributed in the same velocity range, from 70.0 km s^{-1} to 70.4 km s^{-1}, while the (6,3) maser, 63D, extends spectroscopically down to the lower velocity of 68.0 km s^{-1}. Spectra are presented in Fig. A.9. Another two maser spots, 85B and 107D, in the (8,5) and (10,7) transitions are located in regions close to the UCH II region F10.39.

Sgr B2(S). Three maser spots, 74C, 96D, and 107E, in the NH_3 (7,4), (9,6), and (10,7) transitions, are detected in this region. These are close to each other and are found slightly off the head of the cometary UCH II source (Fig. A.10). Spectra are shown in Fig. A.11.

4. Discussion

As shown in Figs. A.4 and A.5, and claimed in Sect. 3, our JVLA data of NH_3 (9,6) and (10,7) lines are not affected by missing flux. All of the detected maser spots are spatially unresolved, so the derived brightness temperatures are lower limits. Nevertheless, lower limits to the brightness temperature are >3000 K and reach 6×10^5 K (107B). A comparison with the NH_3 (6,3), (7,4), (8,5), and (9,6) observations toward Sgr B2(N), using the TMRT 65-m telescope in March 2020 (Mei et al. 2020), reveals that almost all maser spots in our JVLA data are new detections at different velocities, with the exception of 74A. This strongly suggests substantial variations of the NH_3 (6,3), (8,5), and (9,6) masers since March 2020.

Maser spots from other molecules, H_2O (McGrath et al. 2004), class II CH_3OH (Caswell 1996; Hu et al. 2016; Lu et al. 2019), H_2CO (Mehringer et al. 1994; Hoffman et al. 2007; Lu et al. 2019), and OH (Gaume & Claussen 1990), are presented in Figs. 2, A.6, A.8, and A.10. The class I CH_3OH masers at 44 GHz toward the Sgr B2(M) and N regions from Mehringer & Menten (1997) are outside the scales of Figs. 2, A.6, and A.8, and are therefore not shown. The SiO maser (Morita et al. 1992; Zapata et al. 2009) and the metastable NH_3 (2,2) masers in Sgr B2(M) (Mills et al. 2018) originate from a region around the radio object F3, which is more than two arcseconds north of source F10.39. These sources are, therefore, also not shown in Fig. A.8. The ammonia (3,3) masers are located in an area more than 15 arcsec south of Sgr B2(S) (Martín-Pintado et al. 1999) and outside the region shown in Fig. A.10. It is noteworthy that they are not spatially related to any (6,3) maser component, another transition within the same $K = 3$ ladder. Our detected non-metastable NH_3 masers and previously detected metastable NH_3 masers arise from different regions. This indicates that these types of ammonia masers are excited in different ways.

There are no apparent space and velocity correlations between our detected non-metastable NH_3 maser spots and other molecular masers. The locations of the hot cores Sgr B2(N1), N2 and N3 in Sgr B2(N), as well as Sgr B2(N5) in Sgr B2(NS), derived from the 3 mm imaging line survey "Exploring Molecular Complexity with ALMA" (EMoCA, Bonfand et al. 2017), are shown in Figs. 2 and A.6. A bipolar outflow in an east-west direction was found around the UCH II region K2, also known as Sgr B2(N1) (Higuchi et al. 2015; Bonfand et al. 2017). Bipolar outflows are also observed in a north-south direction and a northeast-southwest direction in the hot cores of Sgr B2 (N3) and N5, respectively (Bonfand et al. 2017). There is a class II CH_3OH maser spot and an H_2O maser spot close to the hot core Sgr B2(N3). Seven NH_3 maser spots, 63A, 63B, 74A, 85A, 96A, 96B, and 107C, are close to the hot core Sgr B2(N1). 107A and 107B originate from regions near the hot cores Sgr B2(N2) and N3, respectively. 63C arises from an area close to the hot core Sgr B2(N5). None of the NH_3 masers are spatially coincident with the hot cores in projection. The redshifts seen in 63B, 96A, and 107B, as well as blueshifts seen in 63A, 63C, 74A, 85A, 96B, 107A, and 107C with respect to the systemic velocities of the associated hot cores, may suggest that these maser spots are related to the outflows. The line profiles from these ten maser spots are shown in Figs. 3 and A.7. Bonfand et al. (2017) did not find any sign of an outflow around Sgr B2(N2), while our maser spot 107A, with a blueshifted velocity of $V_{\rm LSR} = 65.5$ km s^{-1} ($V_{\rm sys} = 74.0$ km s^{-1}), could indicate the presence of an outflow.

All detected NH_3 maser spots in Sgr B2(M) show redshifted velocities with respect to the systemic velocity of Sgr B2(M), $V_{\rm LSR} = 62$ km s^{-1} (Belloche et al. 2013). This supports the suggestion that NH_3 masers in Sgr B2(M) are also related to outflows.

Toward Sgr B2(S), the ammonia maser spots 74C, 96D, and 107E also have redshifted velocities with respect to the systemic velocity of Sgr B2(S), $V_{\rm LSR} = 60$ km s^{-1} (Meng et al. 2022), which may indicate that this emission takes part in outflows. Several hot cores were identified by Jeff et al. (in prep.) in Sgr B2(S) in ALMA data (project code: 2017.1.00114.S, PI: A. Ginsburg). No hot cores were found to be close to the ammonia masers. This indicates that the presence of hot, dense gas alone is not sufficient to excite these masers. The ammonia masers detected in Sgr B2(S) are close to the head of the cometary UCH II region, similar to the NH_3 (9,6) maser M1 in G34.26+0.15 (Yan et al. 2022). The maser spots in Sgr B2(S) show almost twice the angular distance compared to M1, with an offset of (+0.″36 ± 0.″13, −0.″07 ± 0.″11) in G34.26+0.15. In view of the different distances of G34.26+0.15 ($D \sim 3.3$ kpc, Yan et al. 2022) and Sgr B2 (8.2 kpc see Sect. 1), the linear distance is even five times larger in Sgr B2(S), that is 0.03 pc. The velocity difference between the masers and the cometary UCH II regions is ten times higher in Sgr B2(S) than in G34.26+0.15 ($\Delta V_{\rm SgrB2(S)} \geq 17.4$ km s^{-1} and $\Delta V_{\rm G34.26} \sim -1.3$ km s^{-1}). That indicates that the cometary UCH II region in Sgr B2(S) is more active than the one in G34.26+0.15.

Overall, the detected non-metastable ammonia masers in Sgr B2 are consistent with the discussion on pumping scenarios in Yan et al. (2022). Therefore, we speculate that the detected NH_3 masers in the non-metastable (6,3), (7,4), (8,5), (9,6), and (10,7) transitions in Sgr B2(N), Sgr B2(NS), Sgr B2(M), and Sgr B2(S) appear to be associated with shocks caused either by outflows or UCH II expansion.

5. Summary

We report the discovery of NH_3 non-metastable (6,3), (7,4), (8,5), (9,6), and (10,7) masers in Sgr B2(M) and Sgr B2(N), an NH_3 (6,3) maser in Sgr B2(NS), as well as NH_3 (7,4), (9,6), and (10,7) masers in Sgr B2(S). High angular resolution data from the JVLA A-configuration reveal 18 maser spots. Nine maser spots arise from Sgr B2(N), one from Sgr B2(NS), five from Sgr B2(M), and three originate in Sgr B2(S). All of these increase the number of (6,3), (7,4), (8,5), (9,6), and (10,7) maser detections in our Galaxy from three to six, two to four, two to three, seven to nine, and one to four. Compared to the Effelsberg 100-m telescope data, the JVLA data indicate no missing flux. The detected maser spots are not resolved by our JVLA observations. Lower limits to the brightness temperature are >3000 K and reach up to 6×10^5 K, manifesting their maser nature. Long-term Effelsberg monitoring (19 months) indicates that the inten-

sities of the (9,6) masers in Sgr B2(M), as well as the (9,6) and (10,7) masers in Sgr B2(N), show noticeable variations. However, the (10,7) maser in Sgr B2(M) is stable. While the NH_3 masers all arise near hot cores, there are many hot cores that do not exhibit NH_3 maser emission. All of these non-metastable ammonia maser lines show redshifted or blueshifted features that may be related to outflows or UCH II expansion.

Acknowledgements. The authors thank the anonymous referee for the useful comments that improve the manuscript. We thank Chris De Pree for providing the 7 mm continuum images of Sgr B2(M) and Sgr B2(N). Y.T.Y. is a member of the International Max Planck Research School (IMPRS) for Astronomy and Astrophysics at the Universities of Bonn and Cologne. Y.T.Y. thanks the China Scholarship Council (CSC) and the Max-Planck-Institut für Radioastronomie (MPIfR) for the financial support. Y.T.Y. also thanks his fiancee, Siqi Guo, for her support during this pandemic period. We would like to thank the staff at the Effelsberg telescope for their help provided during the observations. The National Radio Astronomy Observatory is a facility of the National Science Foundation operated under cooperative agreement by Associated Universities, Inc. We thank the staff of the JVLA, especially Tony Perreault and Drew Medlin, for their assistance with the observations and data reduction.

References

Belloche, A., Menten, K. M., Comito, C., et al. 2008, A&A, 482, 179
Belloche, A., Müller, H. S. P., Menten, K. M., Schilke, P., & Comito, C. 2013, A&A, 559, A47
Belloche, A., Garrod, R. T., Zingsheim, O., Müller, H. S. P., & Menten, K. M. 2022, A&A, 662, A110
Bonfand, M., Belloche, A., Menten, K. M., Garrod, R. T., & Müller, H. S. P. 2017, A&A, 604, A60
Caswell, J. L. 1996, MNRAS, 283, 606
Caswell, J. L., Green, J. A., & Phillips, C. J. 2013, MNRAS, 431, 1180
Cotton, W. D., & Yusef-Zadeh, F. 2016, ApJS, 227, 10
De Pree, C. G., Goss, W. M., & Gaume, R. A. 1998, ApJ, 500, 847
De Pree, C. G., Peters, T., Mac Low, M. M., et al. 2014, ApJ, 781, L36
De Pree, C. G., Peters, T., Mac Low, M. M., et al. 2015, ApJ, 815, 123
Gaume, R. A., & Claussen, M. J. 1990, ApJ, 351, 538
Gaume, R. A., Claussen, M. J., de Pree, C. G., Goss, W. M., & Mehringer, D. M. 1995, ApJ, 449, 663
Ginsburg, A., Bally, J., Barnes, A., et al. 2018, ApJ, 853, 171
GRAVITY Collaboration (Abuter, R., et al.) 2019, A&A, 625, L10
Henkel, C., Wilson, T. L., Asiri, H., & Mauersberger, R. 2013, A&A, 549, A90
Higuchi, A. E., Hasegawa, T., Saigo, K., Sanhueza, P., & Chibueze, J. O. 2015, ApJ, 815, 106
Hoffman, I. M., Goss, W. M., & Palmer, P. 2007, ApJ, 654, 971
Hu, B., Menten, K. M., Wu, Y., et al. 2016, ApJ, 833, 18
Lazio, T. J. W., & Cordes, J. M. 2008, ApJS, 174, 481
Lu, X., Mills, E. A. C., Ginsburg, A., et al. 2019, ApJS, 244, 35
Madden, S. C., Irvine, W. M., Matthews, H. E., Brown, R. D., & Godfrey, P. D. 1986, ApJ, 300, L79
Martín-Pintado, J., Gaume, R. A., Rodríguez-Fernández, N., de Vicente, P., & Wilson, T. L. 1999, ApJ, 519, 667
McGrath, E. J., Goss, W. M., & De Pree, C. G. 2004, ApJS, 155, 577
McMullin, J. P., Waters, B., Schiebel, D., Young, W., & Golap, K. 2007, in Astronomical Data Analysis Software and Systems XVI, eds. R. A. Shaw, F. Hill, & D. J. Bell, ASP Conf. Ser., 376, 127
Mehringer, D. M., & Menten, K. M. 1997, ApJ, 474, 346
Mehringer, D. M., Goss, W. M., & Palmer, P. 1994, ApJ, 434, 237
Mei, Y., Chen, X., Shen, Z.-Q., & Li, B. 2020, ApJ, 898, 157
Meng, F., Sánchez-Monge, Á., Schilke, P., et al. 2019, A&A, 630, A73
Meng, F., Sánchez-Monge, Á., Schilke, P., et al. 2022, A&A, 666, A31
Mills, E. A. C., Ginsburg, A., Clements, A. R., et al. 2018, ApJ, 869, L14
Morita, K.-I., Hasegawa, T., Ukita, N., Okumura, S. K., & Ishiguro, M. 1992, PASJ, 44, 373
Murugeshan, C. 2015, Master's Thesis, University of Bonn
Nguyen, H. 2015, Master's Thesis, University of Bonn
Nguyen, H., Rugel, M. R., Menten, K. M., et al. 2021, A&A, 651, A88
Nguyen, H., Rugel, M. R., Murugeshan, C., et al. 2022, A&A, 666, A59
Ott, M., Witzel, A., Quirrenbach, A., et al. 1994, A&A, 284, 331
Perley, R. A., & Butler, B. J. 2013, ApJS, 204, 19
Pety, J. 2005, SF2A-2005: Semaine de l'Astrophysique Francaise, eds. F. Casoli, T. Contini, J. M. Hameury, & L. Pagani, 721
Reid, M. J., Schneps, M. H., Moran, J. M., et al. 1988, ApJ, 330, 809
Reid, M. J., Menten, K. M., Zheng, X. W., Brunthaler, A., & Xu, Y. 2009, ApJ, 705, 1548
Rickert, M., Yusef-Zadeh, F., & Ott, J. 2019, MNRAS, 482, 5349
Walsh, A. J., Purcell, C. R., Longmore, S. N., et al. 2014, MNRAS, 442, 2240
Wilson, T. L., Batrla, W., & Pauls, T. A. 1982, A&A, 110, L20
Yan, Y. T., Henkel, C., Menten, K. M., et al. 2022, A&A, 659, A5
Zapata, L. A., Menten, K., Reid, M., & Beuther, H. 2009, ApJ, 691, 332

A&A 666, L15 (2022)

Appendix A: Figures

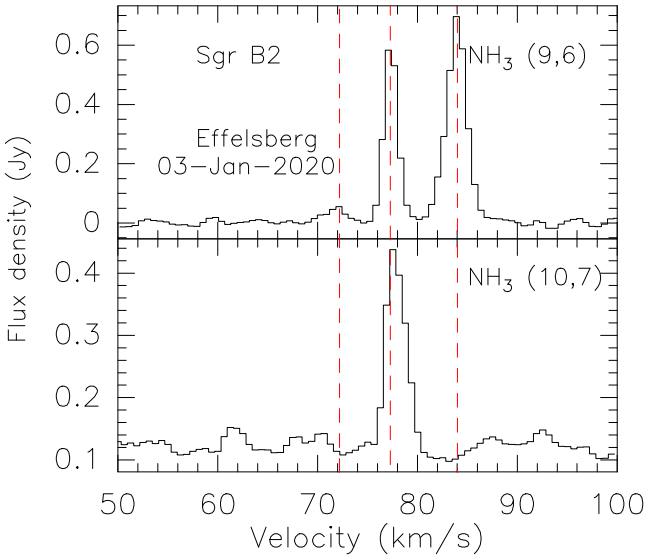

Fig. A.1. NH_3 (9,6) and (10,7) maser lines from the 100-m telescope at Effelsberg toward a region south of Sgr B2(M), at α_{J2000} = $17^h47^m20\overset{s}{.}8$, δ_{J2000} = −28°23′32″.1. The three red dashed lines indicate the three different velocity components at V_{LSR} = ∼72 km s^{-1}, ∼77 km s^{-1}, and ∼84 km s^{-1}.

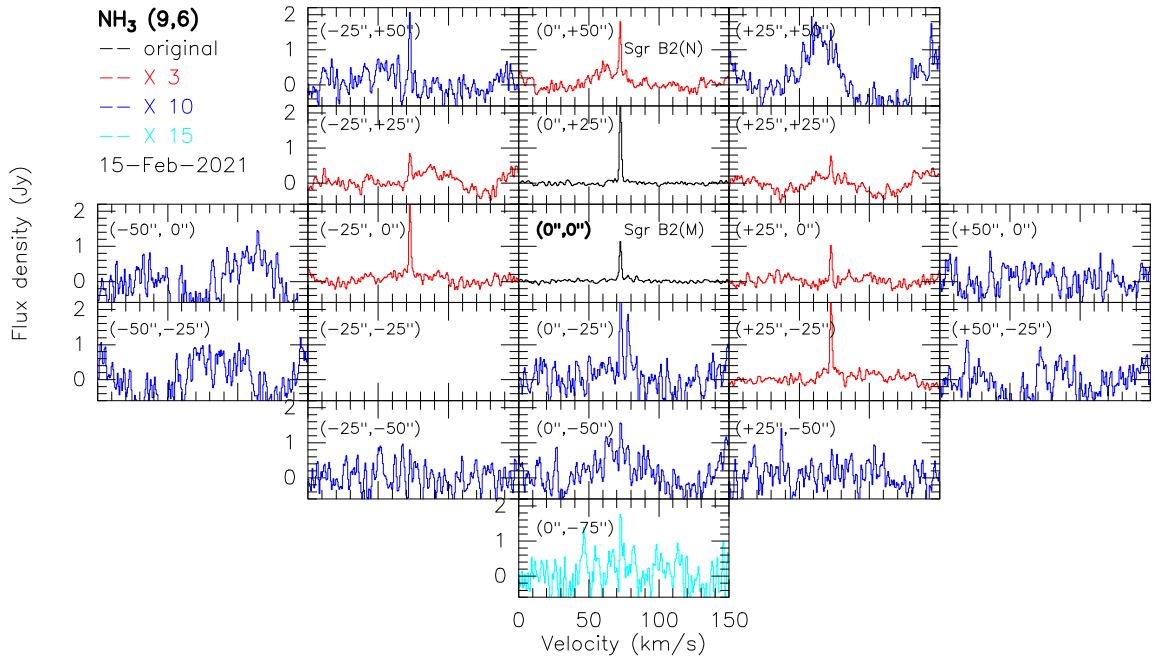

Fig. A.2. NH_3 (9,6) line profiles observed with the Effelsberg 100-m telescope over the region of Sgr B2. The black spectra show the original flux density scales. The red, blue, and cyan spectra are presented after multiplying the flux densities by factors of three, ten, and fifteen, respectively.

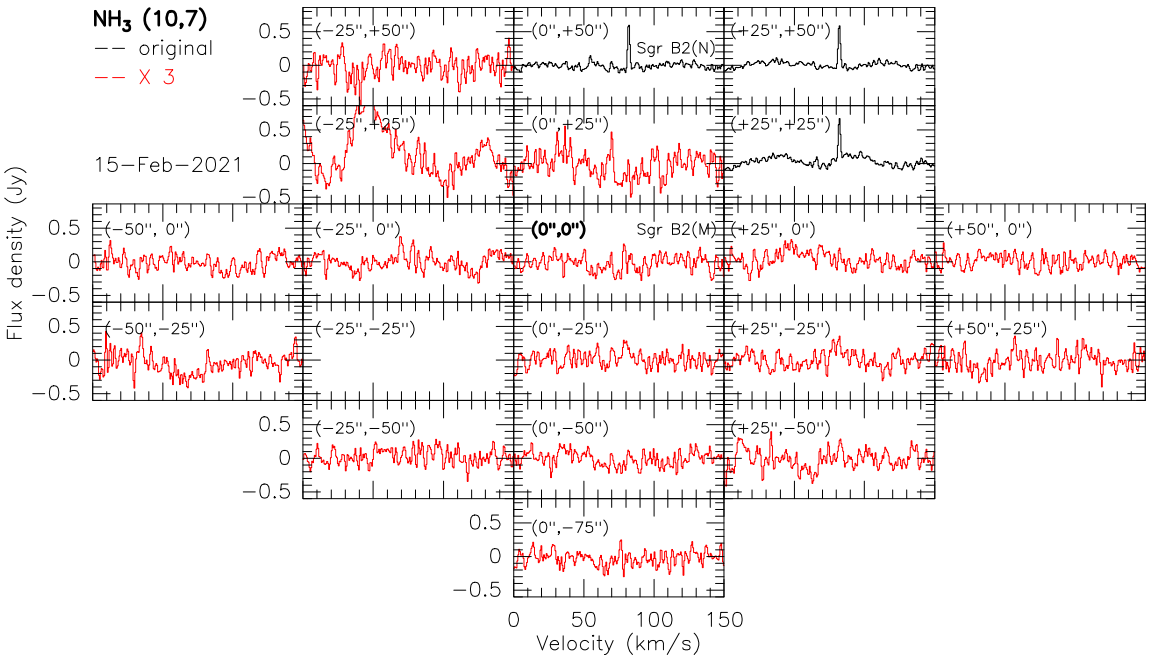

Fig. A.3. NH_3 (10,7) spectra observed with the Effelsberg 100-m telescope toward Sgr B2. The black spectra show the original flux density scales, while the red spectra are presented after multiplying the flux densities by a factor of three.

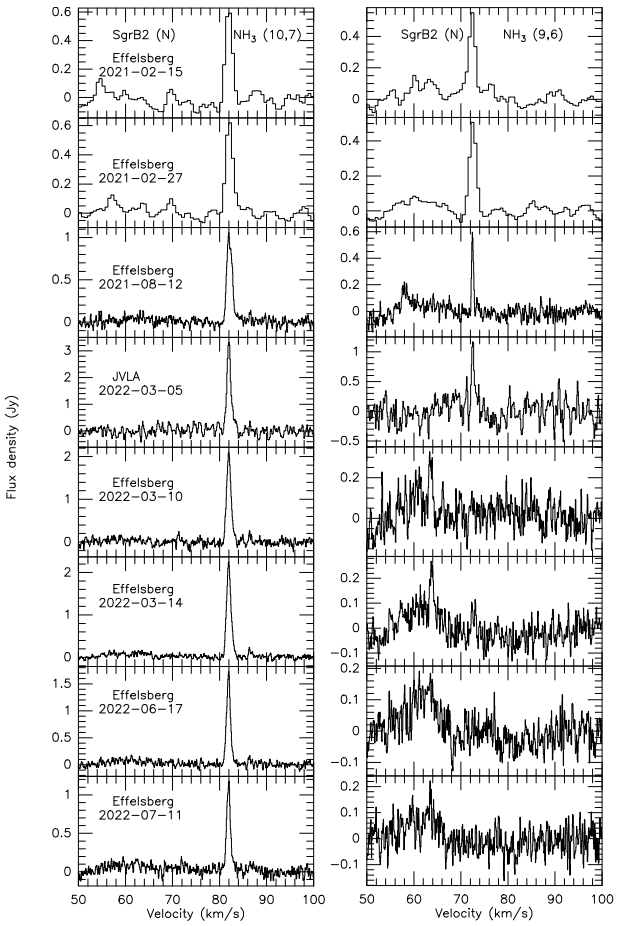

Fig. A.4. Effelsberg 100-meter telescope and JVLA A-configuration spectra from NH_3 (9,6) and (10,7) transition lines at eight epochs toward Sgr B2(N), after subtracting a first-order polynomial baseline. The JVLA spectra are extracted over a region of radius 35″ centered at Sgr B2(N).

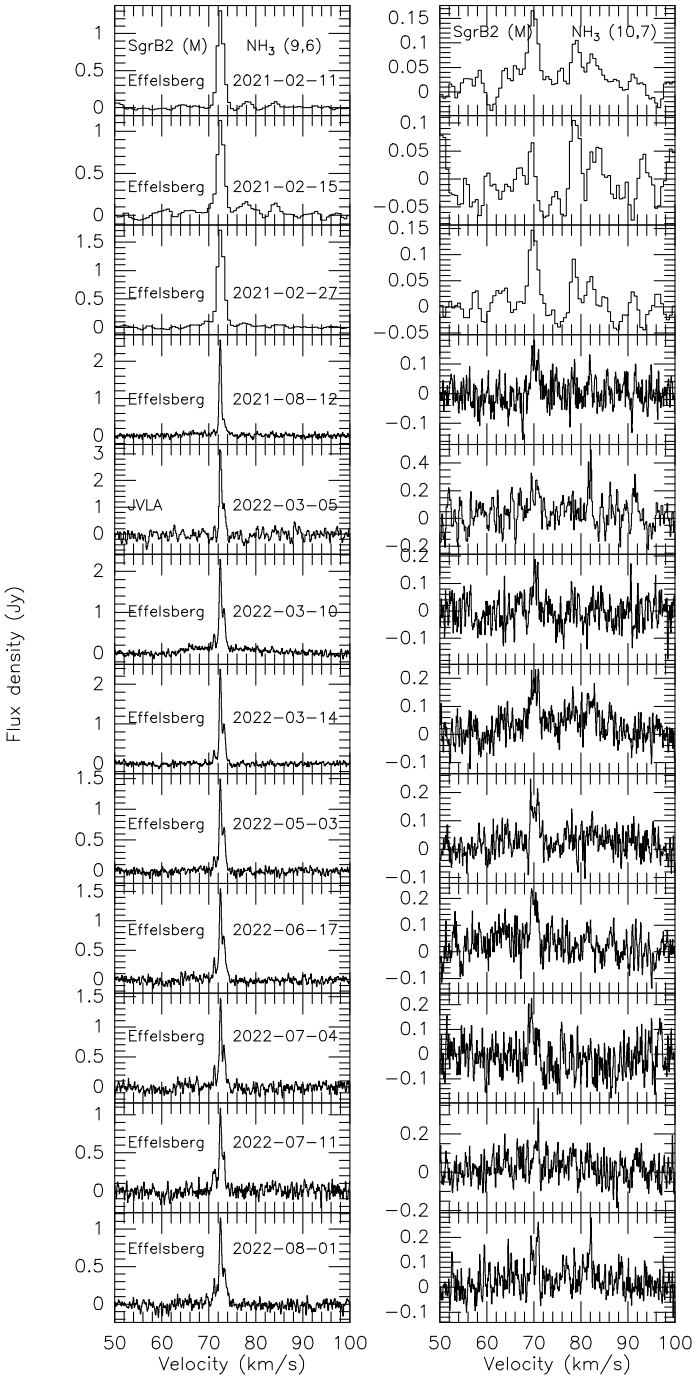

Fig. A.5. Effelsberg 100-meter telescope and JVLA A-configuration spectra from NH_3 (9,6) and (10,7) transition lines at 12 epochs toward Sgr B2(M), after subtracting a first-order polynomial baseline. The JVLA spectra are extracted from the Effelsberg beam (FWHM, 49″) sized region.

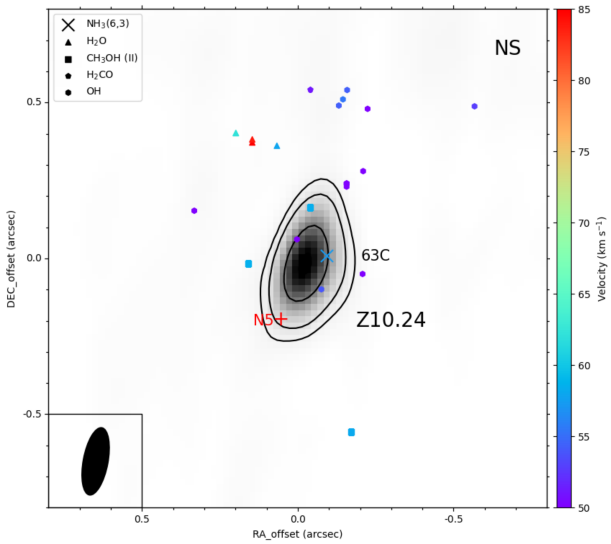

Fig. A.6. JVLA 1.6 cm continuum map of Sgr B2(NS) presented as gray shaded area and black contours with levels of 5, 10, 30, and 50×0.2 mJy beam^{-1}. The reference position is $\alpha_{J2000} = 17^h47^m20\overset{s}{.}043$, and $\delta_{J2000} = -28°22'41\overset{''}{.}143$, the peak position of continuum source Z10.24. The yellow cross shows the position of NH_3 (6,3) emission. H_2O (McGrath et al. 2004), class II CH_3OH (Caswell 1996; Hu et al. 2016; Lu et al. 2019), H_2CO (Hoffman et al. 2007), and OH (Gaume & Claussen 1990) masers are presented as triangles, squares, pentagons, and hexagons, respectively. The color bar indicates the velocity range (V_{LSR}) of the maser spots. The red cross marks the position of the hot core, Sgr B2(N5), taken from the 3 mm imaging line survey EMoCA (Bonfand et al. 2017). The systemic velocity of the hot core, N5, is $V_{LSR} = 60$ km s^{-1} (Bonfand et al. 2017).

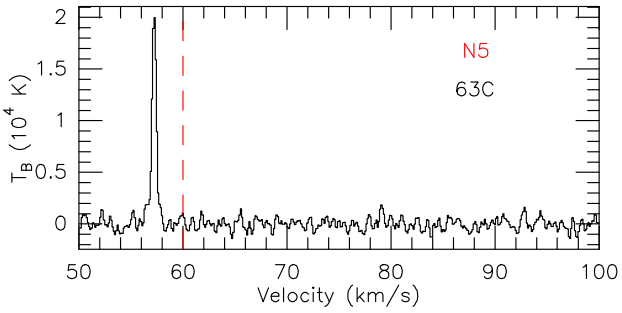

Fig. A.7. JVLA A-configuration spectrum of the NH_3 (6,3) transition line toward Sgr B2(NS). The systemic velocity of the associated hot core, $V_{LSR} = 60$ km s^{-1} in N5 (Bonfand et al. 2017), is indicated by the dashed red line.

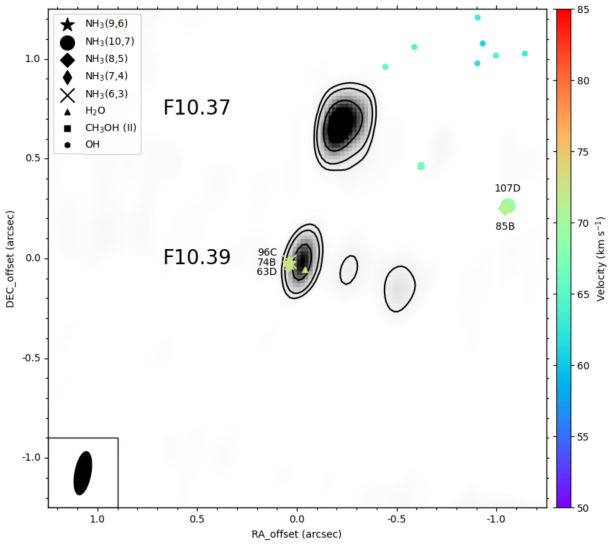

Fig. A.8. JVLA 1.6 cm continuum map of Sgr B2(M) presented as gray shaded areas and black contours with levels of 5, 10, 30, and 50×0.2 mJy beam^{-1}. The reference position is $\alpha_{J2000} = 17^h47^m20\overset{s}{.}197$, and $\delta_{J2000} = -28°23'06\overset{''}{.}484$, the peak position of continuum source F10.39. The cross, thin diamond, diamond, circle and star show the positions of NH_3 (6,3), (7,4), (8,5), (9,6), and (10,7) emissions. H_2O (McGrath et al. 2004), class II CH_3OH (Lu et al. 2019), and OH (Gaume & Claussen 1990) masers are presented as triangles, squares, and hexagons, respectively. The color bar indicates the velocity range (V_{LSR}) of the maser spots. The systemic velocity of Sgr B2(M) is $V_{LSR} = 62$ km s^{-1} (Belloche et al. 2013).

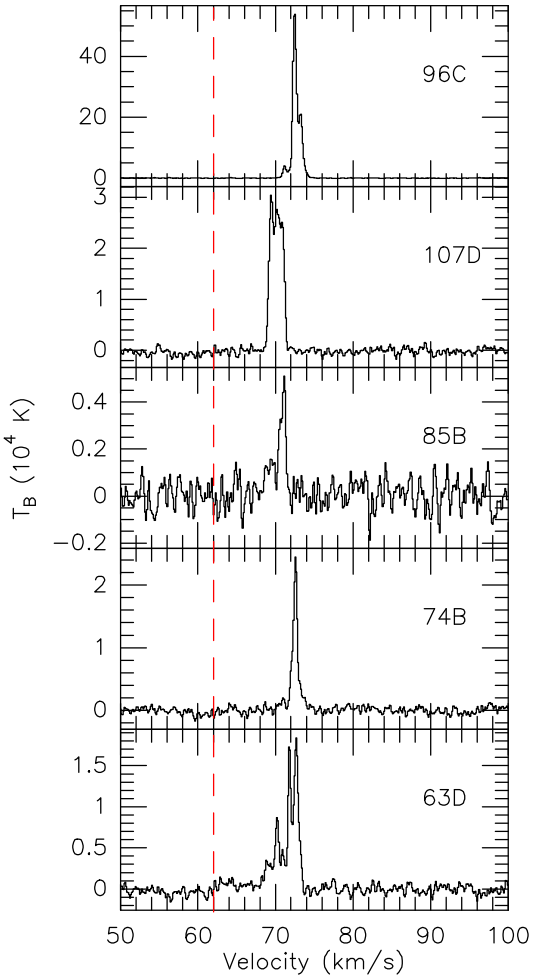

Fig. A.9. JVLA A-configuration spectra of NH_3 transition lines toward Sgr B2(M). The systemic velocity of Sgr B2(M), V_{LSR} = 62 km s^{-1} (Belloche et al. 2013), is indicated by the dashed red line.

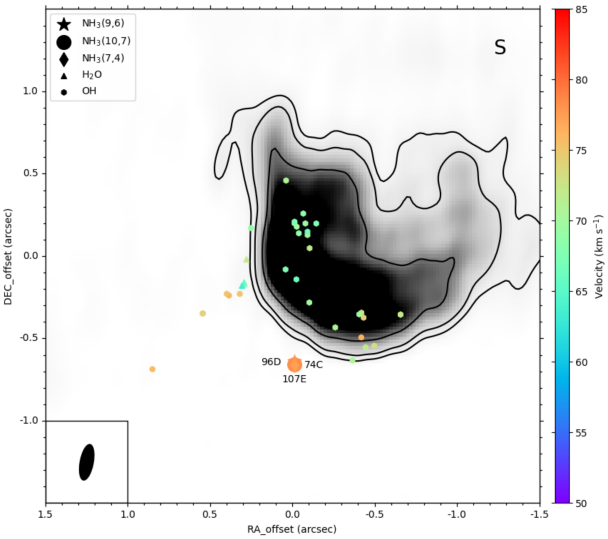

Fig. A.10. JVLA 1.6 cm continuum map of Sgr B2(S) presented as gray shaded areas and black contours with levels of 5, 10, 30, and 50 × 0.2 mJy beam^{-1}. The reference position is α_{J2000} = 17^{h}47^{m}20^s.472, and δ_{J2000} = −28°23′45″.120, the peak position of the continuum source. The thin diamond, star, and circle show the positions of NH_3 (7,4), (9,6), and (10,7) emissions. H_2O (McGrath et al. 2004) and OH (Gaume & Claussen 1990) masers are presented as triangles and hexagons, respectively. The color bar indicates the velocity range (V_{LSR}) of the maser spots. The systemic velocity of Sgr B2(S) is V_{LSR} = 60 km s^{-1} (Meng et al. 2022).

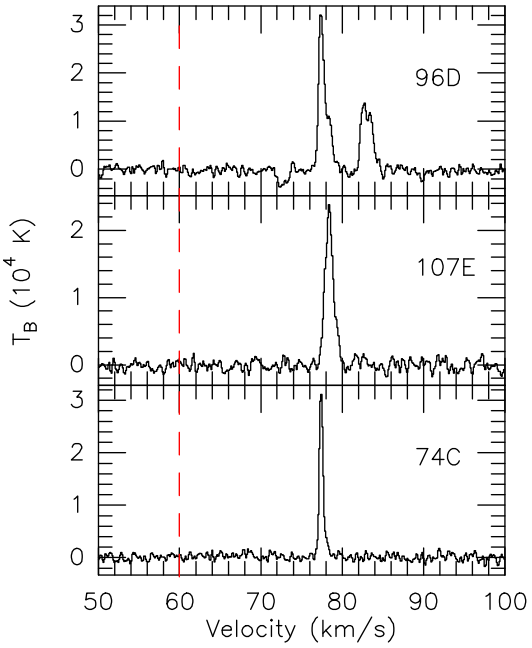

Fig. A.11. JVLA A-configuration spectra of NH_3 transition lines toward Sgr B2(S). The systemic velocity of Sgr B2(S), V_{LSR} = 60 km s^{-1} (Meng et al. 2022), is indicated by the dashed red line.

Appendix B: Tables

Table B.1. Summary of NH_3 (9,6) maser observations toward Sgr B2(N)

Source	Telescope	Beam size	Epoch	Channel spacing (km s^{-1})	S_ν (Jy)	rms (Jy)	$\int S_\nu dv$ (Jy km s^{-1})	V_{LSR} (km s^{-1})	$\Delta V_{1/2}$ (km s^{-1})
Sgr B2(N)	Effelsberg	49″	2021, Feb. 15	0.62	0.53	0.034	1.03 ± 0.09	72.34 ± 0.07	1.83 ± 0.21
	Effelsberg	49″	2021, Feb. 27	0.62	0.52	0.028	0.92 ± 0.06	72.54 ± 0.05	1.65 ± 0.12
	Effelsberg	49″	2021, Aug. 12	0.07	0.09	0.043	1.16 ± 0.09	63.02 ± 0.50	12.14 ± 0.88
					0.14		0.34 ± 0.06	58.09 ± 0.09	2.17 ± 0.39
					0.61		0.30 ± 0.01	72.48 ± 0.01	0.47 ± 0.02
	JVLA[a]	0.″215 × 0.″097	2022, Mar. 05	0.13	1.16	0.189	0.89 ± 0.09	72.55 ± 0.04	0.72 ± 0.10
	Effelsberg	49″	2022, Mar. 10	0.07	0.30	0.067	0.32 ± 0.03	63.52 ± 0.05	1.01 ± 0.12
	Effelsberg	49″	2022, Mar. 14	0.07	0.12	0.041	1.37 ± 0.06	60.99 ± 0.22	10.29 ± 0.47
					0.20		0.16 ± 0.02	63.81 ± 0.04	0.79 ± 0.09
					0.10		0.12 ± 0.02	72.66 ± 0.09	1.12 ± 0.15
	Effelsberg	49″	2022, Jun. 17	0.07	···	0.041	···	···	···
	Effelsberg	49″	2022, Jul. 11	0.07	···	0.047	···	···	···

Notes. The spectral parameters are obtained from Gaussian-fitting. [a]The JVLA spectrum is extracted from a region of radius 35″.

Table B.2. Summary of NH_3 (10,7) maser observations toward Sgr B2(N)

Source	Telescope	Beam size	Epoch	Channel spacing (km s^{-1})	S_ν (Jy)	rms (Jy)	$\int S_\nu dv$ (Jy km s^{-1})	V_{LSR} (km s^{-1})	$\Delta V_{1/2}$ (km s^{-1})
Sgr B2(N)	Effelsberg	49″	2021, Feb. 15	0.62	0.66	0.048	1.12 ± 0.07	81.99 ± 0.05	1.60 ± 0.11
	Effelsberg	49″	2021, Feb. 27	0.62	0.64	0.038	1.19 ± 0.06	82.10 ± 0.04	1.76 ± 0.10
	Effelsberg	49″	2021, Aug. 12	0.07	1.02	0.045	1.44 ± 0.02	82.10 ± 0.01	1.33 ± 0.02
	JVLA[a]	0.″220 × 0.″094	2022, Mar. 05	0.13	3.21	0.141	3.49 ± 0.09	81.99 ± 0.01	1.02 ± 0.03
	Effelsberg	49″	2022, Mar. 10	0.07	2.02	0.070	2.35 ± 0.03	81.97 ± 0.01	1.09 ± 0.02
	Effelsberg	49″	2022, Mar. 14	0.07	2.12	0.051	2.48 ± 0.02	81.96 ± 0.01	1.10 ± 0.01
	Effelsberg	49″	2022, Jun. 17	0.07	1.61	0.051	1.66 ± 0.02	81.90 ± 0.01	0.97 ± 0.02
	Effelsberg	49″	2022, Jul. 11	0.07	1.11	0.055	1.13 ± 0.03	81.91 ± 0.01	0.96 ± 0.03

Notes. The spectral parameters are obtained from Gaussian-fitting. [a]The JVLA spectrum is extracted from a region of radius 35″.

Table B.3. Summary of NH_3 (9,6) maser observations toward Sgr B2(M)

Source	Telescope	Beam size	Epoch	Channel spacing (km s^{-1})	S_ν (Jy)	rms (Jy)	$\int S_\nu dv$ (Jy km s^{-1})	$V_{\rm LSR}$ (km s^{-1})	$\Delta V_{1/2}$ (km s^{-1})
Sgr B2(M)	Effelsberg	49″	2021, Feb. 11	0.62	1.29	0.021	2.22 ± 0.03	72.49 ± 0.01	1.61 ± 0.03
					0.09		0.17 ± 0.03	78.23 ± 0.17	1.76 ± 0.32
					0.08		0.15 ± 0.04	84.05 ± 0.20	1.83 ± 0.51
	Effelsberg	49″	2021, Feb. 15	0.62	1.10	0.035	2.13 ± 0.06	72.52 ± 0.02	1.82 ± 0.06
					0.15		0.59 ± 0.08	77.83 ± 0.25	3.78 ± 0.59
					0.15		0.30 ± 0.06	84.18 ± 0.19	1.84 ± 0.40
	Effelsberg	49″	2021, Feb. 27	0.62	1.69	0.018	3.06 ± 0.05	72.53 ± 0.01	1.70 ± 0.03
	Effelsberg	49″	2021, Aug. 12	0.07	2.30	0.040	1.17 ± 0.03	72.47 ± 0.01	0.48 ± 0.01
					0.39		0.80 ± 0.04	72.92 ± 0.04	1.92 ± 0.11
	JVLA[a]	0.″215 × 0.″097	2022, Mar. 05	0.13	3.20	0.154	1.71 ± 0.15	72.45 ± 0.02	0.50 ± 0.03
					1.11		0.99 ± 0.16	73.19 ± 0.07	0.84 ± 0.13
	Effelsberg	49″	2022, Mar. 10	0.07	0.39	0.048	0.33 ± 0.02	71.22 ± 0.07	0.80 ± 0.07
					2.16		1.31 ± 0.02	72.45 ± 0.07	0.57 ± 0.07
					1.00		0.91 ± 0.02	73.27 ± 0.07	0.85 ± 0.07
	Effelsberg	49″	2022, Mar. 14	0.07	0.26	0.040	0.21 ± 0.02	71.26 ± 0.03	0.76 ± 0.07
					2.38		1.25 ± 0.02	72.46 ± 0.01	0.49 ± 0.01
					0.97		0.77 ± 0.02	73.26 ± 0.01	0.74 ± 0.03
	Effelsberg	49″	2022, May. 03	0.07	0.18	0.037	0.20 ± 0.02	71.36 ± 0.06	1.01 ± 0.12
					1.45		0.78 ± 0.03	72.47 ± 0.01	0.51 ± 0.02
					0.70		0.56 ± 0.03	73.25 ± 0.02	0.75 ± 0.04
	Effelsberg	49″	2022, Jun. 17	0.07	0.28	0.044	0.25 ± 0.01	71.27 ± 0.07	0.84 ± 0.07
					1.47		0.88 ± 0.01	72.48 ± 0.07	0.56 ± 0.07
					0.68		0.58 ± 0.01	73.27 ± 0.07	0.80 ± 0.07
	Effelsberg	49″	2022, Jul. 04	0.07	0.38	0.058	0.18 ± 0.01	71.22 ± 0.07	0.45 ± 0.07
					1.43		0.89 ± 0.01	72.52 ± 0.07	0.58 ± 0.07
					0.67		0.43 ± 0.01	73.32 ± 0.07	0.60 ± 0.07
	Effelsberg	49″	2022, Jul. 11	0.07	0.28	0.064	0.25 ± 0.02	71.21 ± 0.04	0.84 ± 0.08
					1.04		0.62 ± 0.03	72.51 ± 0.01	0.56 ± 0.04
					0.48		0.28 ± 0.03	73.23 ± 0.03	0.55 ± 0.07
	Effelsberg	49″	2022, Aug. 01	0.07	0.25	0.049	0.13 ± 0.03	71.14 ± 0.03	0.50 ± 0.13
					0.77		0.35 ± 0.02	72.50 ± 0.01	0.42 ± 0.02
					0.48		1.00 ± 0.05	72.93 ± 0.04	1.96 ± 0.10

Notes. The spectral parameters are obtained from Gaussian-fitting. [a]The JVLA spectrum toward Sgr B2(M) is extracted from the Effelsberg beam (FWHM, 49″) sized region.

Table B.4. Summary of NH_3 (10,7) maser observations toward Sgr B2(M)

Source	Telescope	Beam size	Epoch	Channel spacing (km s^{-1})	S_ν (Jy)	rms (Jy)	$\int S_\nu dv$ (Jy km s^{-1})	$V_{\rm LSR}$ (km s^{-1})	$\Delta V_{1/2}$ (km s^{-1})
Sgr B2(M)	Effelsberg	49″	2021, Feb. 11	0.62	0.15	0.020	0.38 ± 0.06	69.77 ± 0.19	2.46 ± 0.47
	Effelsberg	49″	2021, Feb. 15	0.62	···	0.032	···	···	···
	Effelsberg	49″	2021, Feb. 27	0.62	0.15	0.021	0.33 ± 0.05	69.86 ± 0.14	2.09 ± 0.32
	Effelsberg	49″	2021, Aug. 12	0.07	0.14	0.041	0.08 ± 0.02	69.59 ± 0.05	0.51 ± 0.17
					0.14		0.03 ± 0.02	70.07 ± 0.03	0.18 ± 0.09
					0.10		0.13 ± 0.04	70.80 ± 0.12	1.22 ± 0.59
	JVLA[a]	0.″220 × 0.″094	2022, Mar. 05	0.13	0.35	0.127	0.22 ± 0.06	69.55 ± 0.07	0.58 ± 0.22
					0.71		0.76 ± 0.06	81.90 ± 0.04	1.01 ± 0.09
	Effelsberg	49″	2022, Mar. 10	0.07	0.14	0.049	0.16 ± 0.03	70.10 ± 0.08	1.08 ± 0.25
					0.16		0.04 ± 0.01	70.80 ± 0.03	0.25 ± 0.06
	Effelsberg	49″	2022, Mar. 14	0.07	0.16	0.043	0.51 ± 0.04	70.13 ± 0.11	3.02 ± 0.37
	Effelsberg	49″	2022, May. 03	0.07	0.17	0.039	0.04 ± 0.02	69.26 ± 0.02	0.23 ± 0.09
					0.11		0.07 ± 0.03	69.62 ± 0.17	0.65 ± 0.18
					0.15		0.21 ± 0.05	70.72 ± 0.11	1.28 ± 0.33
	Effelsberg	49″	2022, Jun. 17	0.07	0.20	0.051	0.15 ± 0.05	69.53 ± 0.09	0.70 ± 0.22
					0.16		0.17 ± 0.05	70.48 ± 0.16	0.99 ± 0.25
	Effelsberg	49″	2022, Jul. 04	0.07	0.17	0.063	0.22 ± 0.04	69.39 ± 0.09	1.21 ± 0.30
	Effelsberg	49″	2022, Jul. 11	0.07	0.14	0.060	0.14 ± 0.03	70.30 ± 0.11	0.97 ± 0.22
					0.28		0.07 ± 0.02	70.92 ± 0.02	0.22 ± 0.06
	Effelsberg	49″	2022, Aug. 01	0.07	0.15	0.048	0.13 ± 0.01	69.54 ± 0.08	0.79 ± 0.08
					0.25		0.14 ± 0.01	70.81 ± 0.08	0.54 ± 0.08
					0.07		0.24 ± 0.01	81.52 ± 0.08	3.15 ± 0.08
					0.19		0.06 ± 0.01	82.10 ± 0.08	0.31 ± 0.08

Notes. The spectral parameters are obtained from Gaussian-fitting. [a]The JVLA spectrum toward Sgr B2(M) is extracted from the Effelsberg beam (FWHM, 49″) sized region.

Table B.5. 1.6 cm JVLA flux densities of individual continuum sources

Source		RA (h m s)	Dec (° ′ ″)	Deconvolved Size (arcsec)	PA (deg)	S_ν (mJy)
Sgr B2	B	17 47 19.927 ± 0.019	−28 23 02.832 ± 0.041	(0.796 ± 0.105) × (0.331 ± 0.046)	15.6	181 ± 22
	B10.06	17 47 19.864 ± 0.010	−28 23 01.247 ± 0.013	(~0.22) × (~0.12)		6 ± 1
	E	17 47 20.116 ± 0.013	−28 23 08.711 ± 0.021	(0.605 ± 0.056) × (0.389 ± 0.036)	10.5	184 ± 15
	F1	17 47 20.125 ± 0.053	−28 23 03.920 ± 0.062	(1.050 ± 0.170) × (0.680 ± 0.110)	144.0	1090 ± 170
	F2	17 47 20.167 ± 0.014	−28 23 03.588 ± 0.012	(0.316 ± 0.047) × (0.204 ± 0.060)	82.0	124 ± 15
	F3a	17 47 20.155 ± 0.012	−28 23 04.878 ± 0.016	(0.203 ± 0.061) × (0.129 ± 0.090)	64.0	34 ± 6
	F3cd	17 47 20.180 ± 0.014	−28 23 04.628 ± 0.015	(0.478 ± 0.054) × (0.445 ± 0.057)	118.0	518 ± 39
	F3e	17 47 20.219 ± 0.006	−28 23 04.582 ± 0.013	(0.206 ± 0.049) × (0.145 ± 0.030)	1.0	32 ± 4
	F4	17 47 20.218 ± 0.005	−28 23 04.205 ± 0.007	(0.243 ± 0.029) × (0.180 ± 0.032)	123.0	105 ± 7
	F10.27	17 47 20.081 ± 0.003	−28 23 05.220 ± 0.011	(~0.22) × (~0.08)		3 ± 0.6
	F10.37	17 47 20.182 ± 0.003	−28 23 05.797 ± 0.005	(0.151 ± 0.018) × (0.050 ± 0.044)	103.0	30 ± 2
	F10.39	17 47 20.197 ± 0.001	−28 23 06.484 ± 0.004	(~0.078) × (~0.055)		12 ± 1
	G	17 47 20.290 ± 0.014	−28 23 02.936 ± 0.015	(0.333 ± 0.055) × (0.179 ± 0.067)	55.0	93 ± 13
	I	17 47 20.385 ± 0.064	−28 23 05.167 ± 0.071	(3.88 ± 0.20) × (1.293 ± 0.10)	40.1	3740 ± 190
	I10.52	17 47 20.332 ± 0.006	−28 23 08.006 ± 0.013	(~0.140) × (~0.093)		8 ± 2
	K1	17 47 19.781 ± 0.009	−28 22 20.588 ± 0.022	(0.612 ± 0.056) × (0.285 ± 0.026)	8.9	123 ± 10
	K2	17 47 19.883 ± 0.002	−28 22 18.412 ± 0.007	(0.424 ± 0.018) × (0.088 ± 0.003)	164.1	32 ± 1
	K3	17 47 19.903 ± 0.013	−28 22 17.051 ± 0.014	(0.442 ± 0.054) × (0.429 ± 0.056)	129.0	181 ± 13
	K4	17 47 20.017 ± 0.015	−28 22 04.474 ± 0.020	(1.196 ± 0.049) × (0.848 ± 0.034)	159.8	289 ± 12
	K7	17 47 19.905 ± 0.008	−28 22 13.401 ± 0.027	(0.347 ± 0.081) × (0.104 ± 0.018)	166.2	7 ± 1
	Z10.24	17 47 20.043 ± 0.001	−28 22 41.143 ± 0.003	(0.175 ± 0.013) × (0.111 ± 0.007)	147.9	23 ± 1
	S	17 47 20.472 ± 0.041	−28 23 45.120 ± 0.034	(1.747 ± 0.113) × (0.840 ± 0.057)	54.0	1231 ± 79

Table B.6. NH_3 maser positions in Sgr B2, derived from the JVLA observations.

Transition		RA (h m s)	Dec (° ′ ″)	S_ν (Jy beam^{-1})	T_{MB} (10^4 K)	V_{LSR} (km s^{-1})	$\Delta V_{1/2}$
(6,3)	63A$^+$	17 47 20.005 ± 0.003	−28 22 17.285 ± 0.009	0.058	1.026	62.09 ± 0.02	0.60 ± 0.04
	63B$^+$	17 47 19.918 ± 0.002	−28 22 17.037 ± 0.008	0.085	1.503	68.94 ± 0.01	0.40 ± 0.02
	63C^x	17 47 20.036 ± 0.001	−28 22 41.135 ± 0.004	0.114	2.028	57.26 ± 0.01	0.49 ± 0.01
	63D*	17 47 20.200 ± 0.002	−28 23 06.500 ± 0.008	0.019	0.345	69.02 ± 0.12	1.14 ± 0.12
				0.048	0.850	70.22 ± 0.12	0.62 ± 0.12
				0.027	0.470	71.00 ± 0.12	0.48 ± 0.12
				0.098	1.720	71.80 ± 0.12	0.44 ± 0.12
				0.102	1.774	72.68 ± 0.12	0.75 ± 0.12
(7,4)	74A$^+$	17 47 20.005 ± 0.001	−28 22 17.255 ± 0.002	0.381	6.771	62.58 ± 0.002	0.37 ± 0.005
	74B*	17 47 20.200 ± 0.001	−28 23 06.512 ± 0.005	0.125	2.219	72.55 ± 0.006	0.72 ± 0.02
	74C**	17 47 20.471 ± 0.001	−28 23 45.783 ± 0.005	0.177	3.144	77.41 ± 0.004	0.54 ± 0.01
(8,5)	85A$^+$	17 47 19.862 ± 0.003	−28 22 18.254 ± 0.011	0.019	0.340	54.32 ± 0.06	0.88 ± 0.17
				0.019	0.350	55.14 ± 0.04	0.34 ± 0.07
				0.041	0.742	56.52 ± 0.04	2.12 ± 0.14
	85B*	17 47 20.118 ± 0.005	−28 23 06.230 ± 0.015	0.024	0.444	70.95 ± 0.04	0.95 ± 0.08
(9,6)	96A$^+$	17 47 19.876 ± 0.002	−28 22 17.903 ± 0.009	0.070	1.207	77.92 ± 0.02	0.94 ± 0.05
	96B$^+$	17 47 19.855 ± 0.003	−28 22 17.977 ± 0.010	0.083	1.416	63.78 ± 0.01	0.82 ± 0.03
	96C*	17 47 20.200 ± 0.001	−28 23 06.511 ± 0.005	0.217	3.712	71.24 ± 0.13	0.73 ± 0.13
				3.211	55.15	72.48 ± 0.13	0.56 ± 0.13
				1.208	20.59	73.24 ± 0.13	0.59 ± 0.13
	96D**	17 47 20.471 ± 0.002	−28 23 45.763 ± 0.008	0.172	3.214	77.38 ± 0.01	0.66 ± 0.03
				0.066	1.097	78.20 ± 0.09	1.27 ± 0.14
				0.079	1.378	82.60 ± 0.01	0.81 ± 0.03
				0.064	1.086	83.52 ± 0.01	0.90 ± 0.06
(10,7)	107A$^+$	17 47 19.859 ± 0.002	−28 22 12.925 ± 0.010	0.069	1.257	65.55 ± 0.02	0.57 ± 0.04
	107B$^+$	17 47 19.259 ± 0.001	−28 22 14.724 ± 0.003	3.710	67.17	81.98 ± 0.001	0.96 ± 0.002
				0.263	4.770	86.35 ± 0.01	0.60 ± 0.02
	107C$^+$	17 47 19.862 ± 0.003	−28 22 18.257 ± 0.011	0.041	0.751	55.08 ± 0.03	1.39 ± 0.10
				0.029	0.520	56.36 ± 0.03	0.46 ± 0.07
				0.053	0.961	57.24 ± 0.03	1.21 ± 0.09
	107D*	17 47 20.117 ± 0.002	−28 23 06.216 ± 0.006	0.165	2.967	69.48 ± 0.13	0.72 ± 0.13
				0.139	2.706	70.23 ± 0.13	0.61 ± 0.13
				0.137	2.446	70.89 ± 0.13	0.69 ± 0.13
	107E**	17 47 20.471 ± 0.002	−28 23 45.779 ± 0.007	0.123	2.224	78.42 ± 0.01	1.25 ± 0.02

Notes. $^+$These nine maser spots originate in Sgr B2(N). ^{x}63C arises in Sgr B2(NS). *These five maser sources belong to Sgr B2(M). **These three maser spots originate in Sgr B2(S). The flux density scale calibration accuracy is estimated to be within 15%.

Appendix D

Discovery of widespread non-metastable ammonia masers in the Milky Way

A&A, 686, A205 (2024)
https://doi.org/10.1051/0004-6361/202348931
© The Authors 2024

Astronomy & Astrophysics

Discovery of widespread non-metastable ammonia masers in the Milky Way

Y. T. Yan (闫耀庭)[1,⋆], C. Henkel[1,2], K. M. Menten[1], T. L. Wilson[1], A. Wootten[3], Y. Gong (龚龑)[1], F. Wyrowski[1], W. Yang (杨文锦)[4,1], A. Brunthaler[1], A. Kraus[1], and B. Winkel[1]

[1] Max-Planck-Institut für Radioastronomie, Auf dem Hügel 69, 53121 Bonn, Germany
e-mail: yyan@mpifr-bonn.mpg.de; astrotingyan@gmail.com
[2] Xinjiang Astronomical Observatory, Chinese Academy of Sciences, 830011 Urumqi, PR China
[3] National Radio Astronomy Observatory, 520 Edgemont Road, Charlottesville, VA 22903-2475, USA
[4] School of Astronomy & Space Science, Nanjing University, 163 Xianlin Avenue, Nanjing 210023, PR China

Received 13 December 2023 / Accepted 23 March 2024

ABSTRACT

We present the results of a search for ammonia maser emission in 119 Galactic high-mass star-forming regions (HMSFRs) known to host 22 GHz H_2O maser emission. Our survey has led to the discovery of non-metastable NH_3 inversion line masers toward 14 of these sources. This doubles the number of known non-metastable ammonia masers in our Galaxy, including nine new very high-excitation $(J, K) = (9,6)$ maser sources. These maser lines, including NH_3 (5,4), (6,4), (6,5), (7,6), (8,6), (9,6), (9,8), (10,8), and (11,9), arise from energy levels of 342 K, 513 K, 465 K, 606 K, 834 K, 1090 K, 942 K, 1226 K, and 1449 K above the ground state. Additionally, we tentatively report a new metastable NH_3 (3,3) maser in G048.49 and an NH_3 (7,7) maser in G029.95. Our observations reveal that all of the newly detected NH_3 maser lines exhibit either blueshifted or redshifted velocities with respect to the source systemic velocities. Among the non-metastable ammonia maser lines, larger velocity distributions, offset from the source systemic velocities, are found in the ortho-NH_3 ($K = 3n$) transitions than in the para-NH_3 ($K \neq 3n$) ones.

Key words. masers – ISM: clouds – HII regions

1. Introduction

The first maser was obtained from a source of ammonia (NH_3) molecules by Charles H. Townes and his group members in the laboratory (Gordon et al. 1954, 1955). Various maser species were discovered in the interstellar medium (ISM), such as hydroxyl (OH; Weaver et al. 1965), water (H_2O; Cheung et al. 1969), and methanol (CH_3OH; Barrett et al. 1971). Although thermal emission from NH_3 was discovered in 1968 by Cheung et al., the first NH_3 maser in the ISM was detected 14 yr later, in the $(J, K) = (3,3)$ metastable ($J = K$) line toward the massive star-forming region W33 (Wilson et al. 1982). The first highly excited non-metastable ($J > K$) ammonia masers were detected by Madden et al. (1986) in the $(J, K) = (9,6)$ and (6,3) lines. So far, a total of 34 NH_3 inversion transitions ($\Delta K = 0$ and $\Delta J = 0$) have been identified as masers in the ISM (see Yan et al. 2022b, and references therein). Even in its rare isotopolog $^{15}NH_3$, maser emission was detected in the (3,3) (Mauersberger et al. 1986), (4,3), and (4,4) transitions (Schilke et al. 1991) but only toward the high-mass star-forming region (HMSFR) NGC 7538. The ammonia transitions identified as masers in the ISM are summarized in Table A.1.

Ammonia masers are rare in the ISM compared to other maser species; that is, those of OH, H_2O, and CH_3OH. Over the last five decades after the first detection of astronomical masers, numerous successful maser surveys were carried out in different molecules and led to thousands of detections in the Milky Way. They targeted, for example, OH masers (e.g., te Lintel Hekkert et al. 1989; Lewis 1994; Hu et al. 1994; Sevenster et al. 1997; Caswell 1998; Wolak et al. 2012; Beuther et al. 2019), CH_3OH masers (e.g., Menten 1991; Caswell et al. 1993; Xu et al. 2009; Caswell 2009; Hu et al. 2016; Breen et al. 2016; Yang et al. 2017, 2019, 2020, 2023; Lu et al. 2019; Nguyen et al. 2022), and H_2O masers (e.g., Genzel & Downes 1979; Cesaroni et al. 1988; Menten et al. 1990; Wouterloot et al. 1993; Palagi et al. 1993; Wang et al. 2006; Urquhart et al. 2011; Breen & Ellingsen 2011; Motogi et al. 2011; Walsh et al. 2014; Xi et al. 2015; Titmarsh et al. 2016; Svoboda et al. 2016; Kim et al. 2018; Ladeyschikov et al. 2022a). All of these are collected and can be easily accessed from the online database, Maserdb[1] (Sobolev et al. 2019; Ladeyschikov et al. 2019, 2022b).

So far, ammonia maser lines have only been detected in 32 sources. Among them, metastable NH_3 masers are quite common and have been detected in 22 different regions. Non-metastable ($J > K$) ammonia masers have been found in 14 objects (Yan et al. 2022a,b). Only four sources host both metastable and non-metastable NH_3 masers. These are the HMSFRs DR 21 (Guilloteau et al. 1983; Madden et al. 1986; Mangum & Wootten 1994; Gaume et al. 1996), W51 (Madden et al. 1986; Mauersberger et al. 1987; Zhang & Ho 1995; Henkel et al. 2013), NGC 6334 (Kraemer & Jackson 1995; Beuther et al. 2007; Walsh et al. 2007), and Sgr B2(M) (Mills et al. 2018;

⋆ Member of the International Max Planck Research School (IMPRS) for Astronomy and Astrophysics at the universities of Bonn and Cologne.

[1] https://maserdb.net/

Open Access article, published by EDP Sciences, under the terms of the Creative Commons Attribution License (https://creativecommons.org/licenses/by/4.0), which permits unrestricted use, distribution, and reproduction in any medium, provided the original work is properly cited.
This article is published in open access under the Subscribe to Open model. Open access funding provided by Max Planck Society.

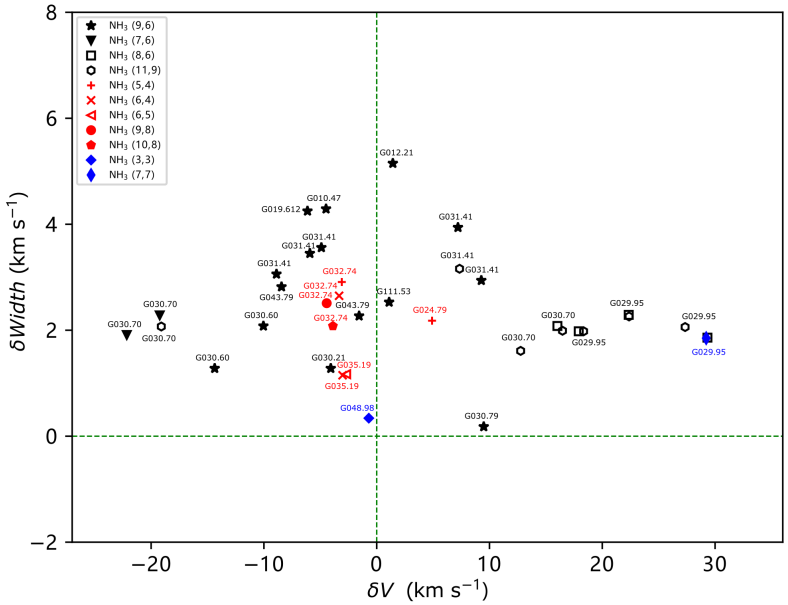

Fig. 1. Comparison of velocities and line widths of ammonia maser lines to the intrinsic line widths of ammonia $(J, K) = (1,1)$ thermal emission. The number of data points is substantially larger than the number of newly detected sources due to the occasional presence of more than one maser line in a given source and more than one velocity component in a specific maser line. $\delta V = V_{\rm LSR}$(maser) – $V_{\rm LSR}$(NH_3(1,1)) is the deviation from velocities of the NH_3 maser lines to those of NH_3 (1,1) thermal emission. $\delta Width = \Delta V_{1/2}$($NH_3$(1,1))-$\Delta V_{1/2}$(maser) refers to the difference between the line widths of ammonia maser lines and the intrinsic line widths of an individual NH_3 hyperfine structure component. The dashed green lines indicate positions with zero deviation. The metastable NH_3 transitions are marked in blue. Among the non-metastable NH_3 lines, ortho-NH_3 is presented in black and para-NH_3 is given in red.

Yan et al. 2022a). In Table A.2, we summarize the sources that are known to host ammonia masers. The metastable NH_3 (3,3) masers are thought to be collisionally pumped (e.g., Walmsley & Ungerechts 1983; Flower et al. 1990; Mangum & Wootten 1994; Zhang & Ho 1995; Zhang et al. 1999; McEwen et al. 2016). Pumping scenarios of other NH_3 transitions are still speculative. High-angular-resolution data show that the excitation of non-metastable NH_3 (9,6) masers in W51, Cepheus A, G34.26+0.15, and the Sgr B2 complex may be related to shocks by outflows or by the expansion of ultracompact (UC) H II regions (Pratap et al. 1991; Yan et al. 2022b,a). Furthermore, the NH_3 (9,6) maser stands out as being the strongest and most variable one in W51-IRS2. Its variability is comparable to the H_2O masers in the region (e.g., Henkel et al. 2013).

There exists no systematic survey to search for ammonia masers so far. Therefore, we selected 119 HMSFRs with high NH_3 column densities ($N_{\rm NH_3} \geq 10^{15.5}$ cm^{-2}) that are known to host water masers from previous K-band surveys. The sample is mainly based on the APEX Telescope Large Area Survey of the Galaxy (ATLASGAL, Schuller et al. 2009) catalogs (Wienen et al. 2012, 2018), and the Red MSX Source survey (RMS, Urquhart et al. 2011). Our sample is listed in Table A.3 together with the systemic local standard of rest (LSR) velocities and the source beam-averaged NH_3 column densities, which are based on ammonia (1,1), (2,2), and (3,3) thermal emission in previous studies with typical beam sizes of order 32″ at Green Bank and 38″ at Effelsberg. We performed a K-band line survey with the 100-m Effelsberg telescope of this source sample with the motivations: (1) to search for NH_3 maser lines, and (2) to search for the higher metastable ammonia transitions; in other words, the NH_3 (4,4) to (7,7) lines with excitation levels up to 500 K above the ground state to reveal so-far poorly studied warm gas components in the HMSFR sources. We also obtained H_2O and CH_3OH maser spectra simultaneously as well as quasi-thermal lines from other molecules. The data allow us to perform a new K-band spectral classification of massive star-forming clumps, uniquely complementing other surveys.

In this paper, we report the discovery of numerous non-metastable NH_3 and two probable metastable NH_3 maser sources in the Milky Way. Results for the high-excitation metastable ammonia thermal transitions, the non-metastable ammonia thermal lines, and the H_2O and CH_3OH maser spectra will be published in future papers.

2. Observations and data reduction

The K-band line survey was performed with the 100-meter Effelsberg telescope[2] in November 2022 and in February, April, May, and July 2023. The S14mm double-beam secondary focus receiver was employed to simultaneously cover the entire K-band frequency range; that is, 18.0–26.0 GHz. The receiver band was divided into four 2.5 GHz-wide subbands with the frequency ranges of 18.0–20.5 GHz, 19.9–22.4 GHz, 21.6–24.1 GHz, and 23.5–26.0 GHz. Each subband has 65536 channels, providing a channel width of 38.1 kHz, changing from ~0.62 km s^{-1} at 18.5 GHz to ~0.44 km s^{-1} at 26.0 GHz. The observations were performed in position-switching mode with the off position 10′ in azimuth away from the source. The half power beam width (HPBW) was 49 × 18.5/ν (GHz) arcseconds; that is, 49″ at 18.5 GHz, the frequency of the NH_3 (9,6) line. A high-spectral-resolution backend with 65 536 channels and a bandwidth of 300 MHz was employed to measure the new NH_3 (9,6) maser sources, providing a channel width of 0.07 km s^{-1} at 18.5 GHz. Pointing and focus calibrations were done at the beginning of the observations, during sunset and sunrise, as well as every 2 h toward NGC 7027. The calibrator was measured between elevations of 30 and 60 degrees. The pointing was checked using nearby quasars prior to on-source integrations. The elevations of

[2] Based on observations with the 100-m telescope of the MPIfR (Max-Planck-Institut für Radioastronomie) at Effelsberg.

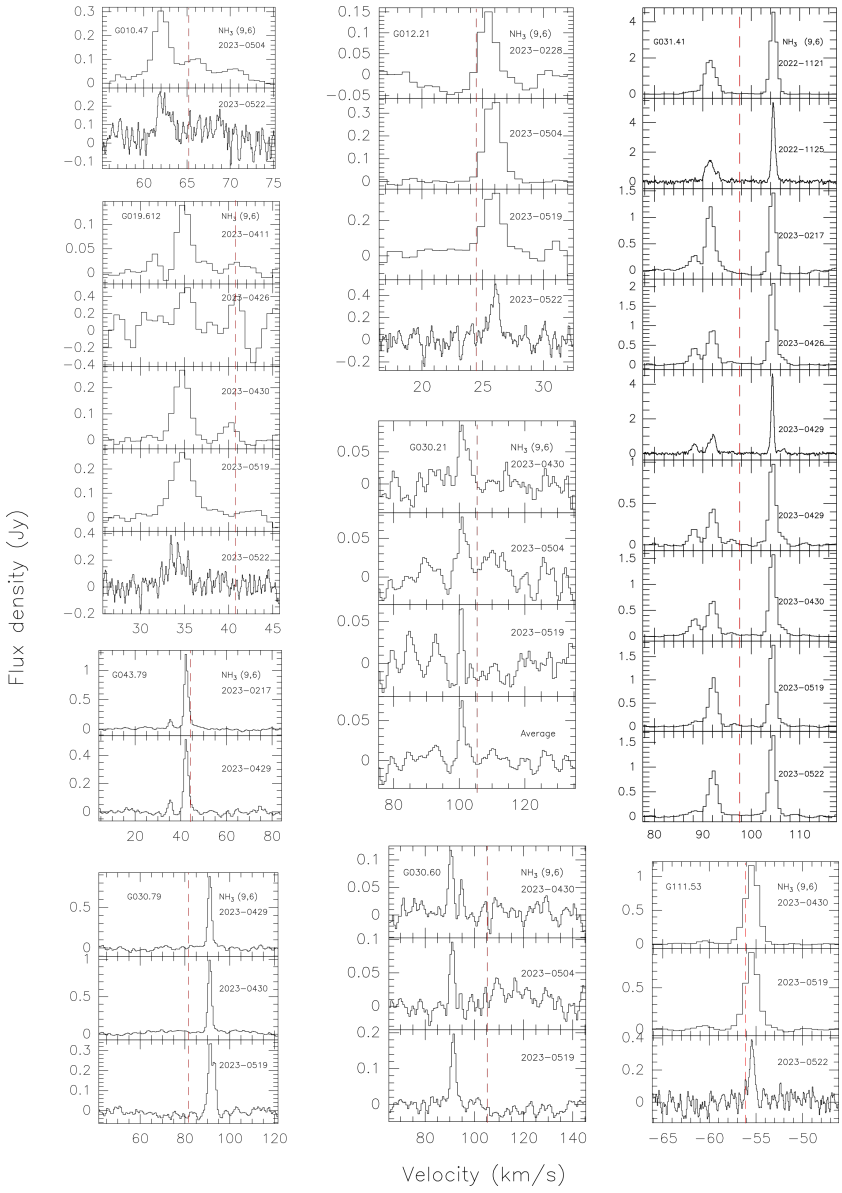

Fig. 2. NH_3 (9,6) spectra observed at different epochs toward nine sources. The dashed red lines indicate the systemic velocities of the sources.

our targets were in a range of 15–55 degrees. The system temperatures were 60–130 K on a main-beam brightness temperature, T_{MB}, scale.

We used the GILDAS/CLASS[3] package (Pety 2005) to reduce the spectral line data. The data were split into small frequency intervals with bandwidths of 300 MHz and were calibrated based on continuum cross scans of NGC 7027 (Winkel et al. 2012), whose flux density was adopted from Ott et al. (1994). The T_{MB}/S ratios are 1.95 K Jy^{-1}, 1.73 K Jy^{-1}, and 1.68 K Jy^{-1} at 18.5 GHz, 22.2 GHz, and 24.0 GHz, respectively. Calibration uncertainties were estimated to be ±10%. All of the NH_3 lines covered in our observations were measured simultaneously, which ensures a good relative calibration.

3. Results and discussion

We detected 15 new ammonia maser sources, resulting in a detection rate of ∼13%. These maser lines, including NH_3 (J, K) = (5,4), (6,4), (6,5), (7,7), (7,6), (8,6), (9,6), (9,8), (10,8), (11,9), and possibly the (3,3) line arise from energy levels of 342 K, 513 K, 465 K, 537 K, 606 K, 834 K, 1090 K, 942 K, 1226 K, 1449 K, and 122 K above the ground state. The maser line parameters obtained by Gaussian fits are listed in Table A.4. The masers are identified in three different ways: (1) narrow line widths compared to those of ammonia (J, K) = (1,1) thermal

[3] https://www.iram.fr/IRAMFR/GILDAS/

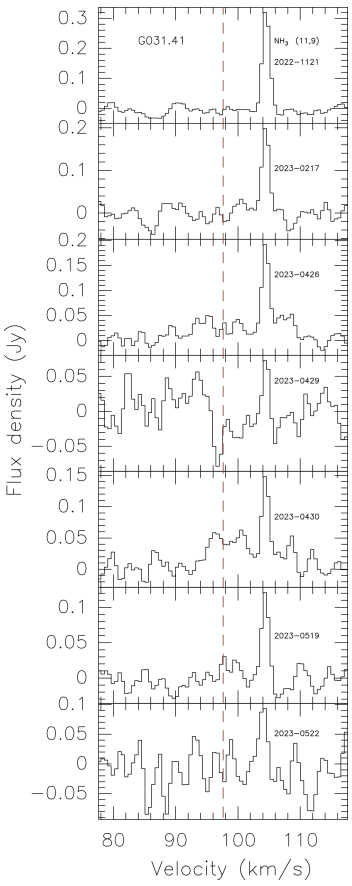

Fig. 3. NH_3 spectra toward G031.41. The dashed red lines indicate the systemic velocity.

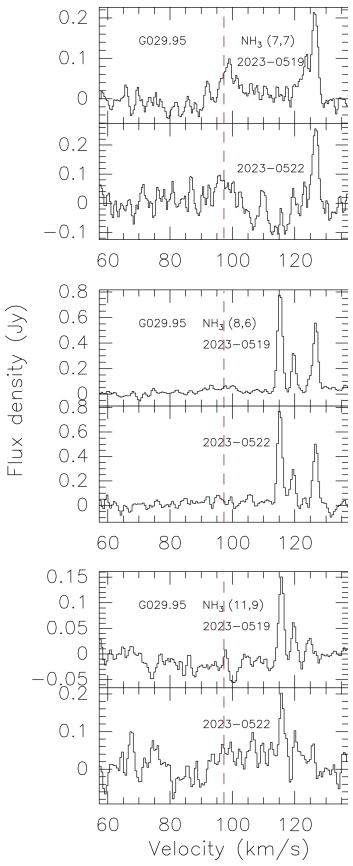

Fig. 4. NH_3 (7,7), (8,6), and (11,9) spectra toward G029.95. The dashed red lines indicate the systemic velocity.

emission, (2) blueshifted or redshifted velocities with respect to the sources' systemic LSR velocities, and (3) flux density variations. The first method can easily be verified by comparing the widths of putative maser lines with simultaneously observed quasi-thermal transitions.

Figure 1 shows the comparison of line widths of ammonia maser lines to the intrinsic line widths of hyperfine components of the (J, K) = (1,1) thermal emission as well as the difference between the systemic velocities of the sources and the maser velocities. We derived the intrinsic line width by using the hyperfine fitting in CLASS for the NH_3 (1,1) line. The line profiles of the NH_3 (1,1) thermal emission and maser transitions are presented in Fig. B.1. All of these maser lines have narrower features than the NH_3 (1,1) thermal emission. This further confirms their maser nature. Furthermore, their velocities are shifted with respect to the sources' systemic LSR velocities, by at least 0.7 km s^{-1}, and reaching up to 30 km s^{-1}. This is similar to recent discoveries of non-metastable NH_3 masers with $\delta V \sim 10$ km s^{-1} in Cep A, $\delta V \sim 4$ km s^{-1} in G34.26+0.15, and δV in a range of 0.3 km s^{-1} to 24 km s^{-1} toward the Sgr B2 complex (Yan et al. 2022b,a). Fourteen of the new ammonia maser sources contain non-metastable ammonia masers, which doubles the number of non-metastable ammonia maser detections in our Galaxy. Among the non-metastable ammonia maser lines, larger velocity distributions are found in the ortho-NH_3 ($K = 3n$) transitions than in the para-NH_3 ($K \neq 3n$) ones. The velocity range of para-NH_3 masers is limited within ±5 km s^{-1} with respect to the sources' systemic velocities, marked in red in Fig. 1. This is enlarged to about ±30 km s^{-1} for ortho-NH_3 masers.

Among the 14 non-metastable ammonia maser sources, NH_3 (9,6) masers are the most common and are detected in nine objects. The spectra of NH_3 (9,6) masers are shown in Fig. 2. The observations at different epochs indicate that the flux densities of these NH_3 (9,6) masers vary by at least 50% over timescales of several months. Even within two days, variations were observed in G031.41+0.30 (hereafter G031.41), similar to that detected by Henkel et al. (2013) toward W51-IRS2. The exception is G030.21-0.19 (hereafter G030.21): its NH_3 (9,6) flux density stays constant for 20 days. In order to increase the signal-to-noise ratios (S/Ns) of NH_3 (9,6) spectra toward G030.21, we averaged all three measurements at different epochs. The spectra and fitting results are presented in Fig. 2 and in Table A.4, respectively. Five targets, G010.47+0.03 (hereafter G010.47), G012.21-0.10 (hereafter G012.21), G019.61-0.23 (hereafter G019.612), G031.41, and G111.53+0.76 (hereafter G111.53), were also observed in the high-spectral-resolution mode (Fig. 2). These data show that the NH_3 (9,6) masers contain narrow components with line widths smaller than 1.0 km s^{-1}

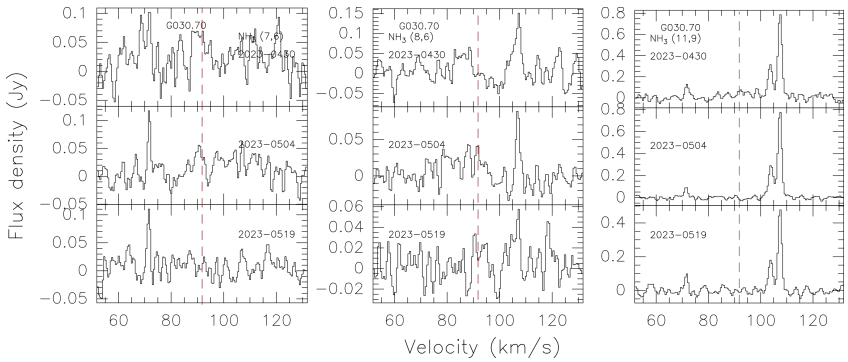

Fig. 5. NH_3 (7,6), (8,6), and (11,9) spectra toward G030.70. The dashed red lines indicate the systemic velocity.

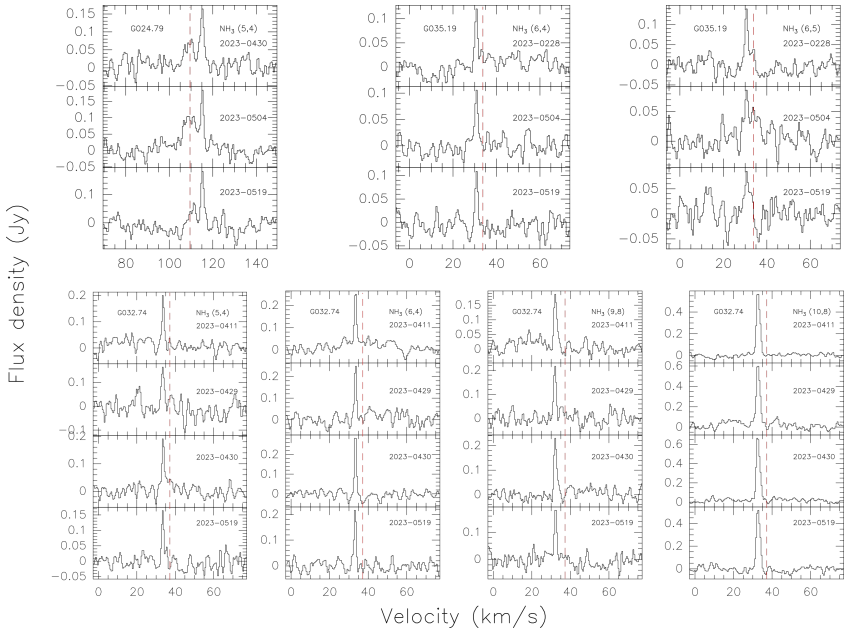

Fig. 6. NH_3 (5,4) spectra toward G024.79, NH_3 (6,4) and (6,5) spectra toward G035.19, and NH_3 (5,4), (6,4), (9,8), and (10,8) spectra toward G032.74. The dashed red lines indicate the systemic velocities of the sources.

and some even below the channel width of the wide band spectra (Sect. 2); that is, smaller than 0.6 km s^{-1}. In eight sources, G010.47, G012.21, G019.612, G030.21, G030.60+0.18 (hereafter G030.60), G030.79+0.20 (hereafter G030.79), G043.79-0.13 (hereafter G043.79), and G111.53, we detect only NH_3 (9,6) masers. Five of these eight targets show only blueshifted (9,6) features, and the other three only have redshifted features. G031.41, the ninth object, is unique in that it hosts both blueshifted and redshifted NH_3 (9,6) maser components.

The NH_3 (11,9) transition with an energy level of 1449 K above the ground state, the highest value in our maser sample, was also detected toward G031.41 (Fig. 3). Its velocity is consistent with a redshifted NH_3 (9,6) maser feature and its flux density decreased from November 2020 to May 2023 by 63%. In addition, NH_3 (11,9) masers were also detected in G029.95-0.02 (hereafter G029.95) and G030.70-0.07 (hereafter G030.70). In G029.95, NH_3 (8,6) and (7,7) masers were also detected (Fig. 4). The flux density of the NH_3 (7,7) maser increased by 55% in three days, while the NH_3 (8,6) and (11,9) maser lines show no obvious variability. Toward G030.70, we also detected NH_3 (7,6) and (8,6) masers. Their spectra are shown in Fig. 5. The NH_3 (7,6) maser stays constant for 20 days. During this time interval, NH_3 (8,6) and (11,9) masers initially showed the same trend; their flux densities are roughly the same from April 30 to May 4, 2023 but then decrease between May 4 and 19. Among the eleven sources mentioned above, G029.95 hosts both ortho- and para-NH_3 masers and the other ten sources only host ortho-NH_3 masers.

Three targets, G024.79+0.08 (hereafter G024.79), G032.74-0.08 (hereafter G032.74), and G035.19-0.74 (hereafter G035.19), only host para-NH_3 masers (Fig. 6). Toward G024.79, we only detected an NH_3 (5,4) maser. Toward G032.74, four transitions were identified as masers: the NH_3 (5,4), (6,4), (9,8), and (10,8) lines. Two NH_3 maser lines, (6,4) and (6,5), were detected in G035.19. Variations in the flux densities of the NH_3 (5,4) maser in G024.79, the NH_3 (10,8) maser in G032.74, and the NH_3 (6,5) maser in G035.19 were also observed. These variations amount to 24% or more, while the NH_3 (1,1) thermal emissions stay constant at the same time; thus, the maser variability appears to be significant.

The frequencies of the NH_3 (1,1), (2,2) and (3,3) transitions are within a range of only 200 MHz. The peak flux density

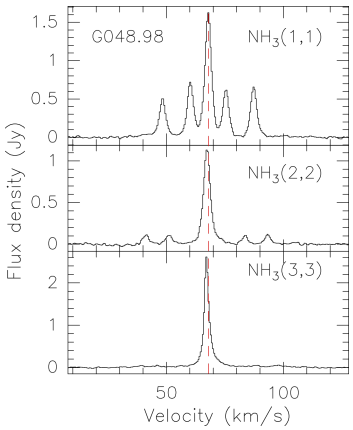

Fig. 7. NH_3 (1,1), (2,2), and (3,3) spectra toward G048.98. The dashed red lines indicate the systemic velocity.

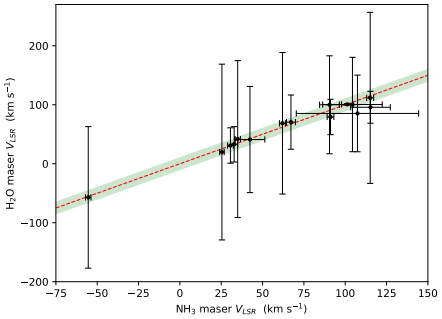

Fig. 8. Comparison of the velocity ranges of NH_3 and H_2O masers. Dots indicate the velocities of bright NH_3 and H_2O maser features. Error bars show the velocity ranges in detected NH_3 and H_2O masers. The dashed line marks locations where the velocity of NH_3 equals that of a water maser. The green region shows the ± 10 km s^{-1} zone.

ratios of NH_3 (3,3)/(1,1) and (3,3)/(2,2) toward G048.98-0.30 (hereafter G048.98) are ~0.83 and ~1.14, respectively, based on previous 100-m Green Bank Telescope (GBT) observations in 2010 (Urquhart et al. 2011), but these are ~1.57 and ~2.22 in our measurements. However, the ratios of NH_3 (1,1)/(2,2), which are ~1.38 and ~1.42, remain consistent, within the uncertainties due to noise in these two datasets. This indicates that the NH_3 (3,3) emission in G048.98 has become stronger and likely shows a maser nature. The spectra of NH_3 (1,1), (2,2), and (3,3) toward G048.98 are presented in Fig. 7.

In Fig. 8, we compare the velocity ranges of NH_3 and H_2O masers. The velocity range of NH_3 masers is always smaller than that of H_2O masers in each source. There are 12 objects, 80% of our maser sample, for which the velocities of their brightest NH_3 maser feature are similar to that of H_2O masers within ± 10 km s^{-1}. For the remaining three targets, G030.79, G029.95, and G030.70, the differences between velocities of their brightest NH_3 maser feature and brightest H_2O maser feature are large: 11 km s^{-1}, 19 km s^{-1}, and 22 km s^{-1}, respectively.

With the single-dish observations at Effelsberg, the sizes of ammonia masers, the spatial distributions of ammonia masers and thermal emissions cannot be accurately determined. This also excludes realistic determinations of kinetic temperatures, densities, column densities, and estimates of the ~10 μm infrared irradiation, potentially causing significant populations of vibrationally excited NH_3, right at the maser spots. So far, the NH_3 maser pumping processes under debate are collisional excitation, radiative excitation, and radiative excitation combined with infrared line overlap (e.g., Walmsley & Ungerechts 1983; Madden et al. 1986; Brown & Cragg 1991; Wilson & Schilke 1993; Henkel et al. 2013). Velocity offsets with respect to systemic velocities may suggest emission associated with outflows or disks (Yan et al. 2022a). Higher-angular-resolution observations are mandatory and proposed to provide precise physical positions and sizes of the newly detected ammonia masers. This will lead to a deeper comprehension of the NH_3 maser phenomenon and its connection to sites of massive star formation.

4. Summary

We report the discovery of at least 14 and likely 15 new ammonia maser sources in the Milky Way, based on our *K*-band line survey with the 100-meter Effelsberg telescope. Our total sample consists of 119 sources exhibiting 22 GHz H_2O maser emission, and thus yields a detection rate in excess of 10%. Fourteen of the newly detected masers are encountered in non-metastable inversion transitions and this doubles the number of non-metastable NH_3 masers in our Galaxy. Metastable ammonia masers are also detected in one or two sources: an NH_3 (7,7) maser in G029.95 and likely an NH_3 (3,3) maser in G048.98. Narrow line widths compared to those of ammonia $(J, K) = (1,1)$ thermal emission, as well as variations in flux density, indicate their maser nature. All of the NH_3 masers in our detections have blueshifted or redshifted velocities with respect to the source systemic LSR velocities.

Acknowledgements. The authors want to thank the anonymous referee for providing useful comments, which have improved the quality of the paper. Y.T.Y. is a member of the International Max Planck Research School (IMPRS) for Astronomy and Astrophysics at the Universities of Bonn and Cologne. Y.T.Y. thanks the China Scholarship Council (CSC) for the financial support. We would like to thank the staff at the Effelsberg telescope for their help provided during the observations.

References

Barrett, A. H., Schwartz, P. R., & Waters, J. W. 1971, ApJ, 168, L101
Beuther, H., Walsh, A. J., Thorwirth, S., et al. 2007, A&A, 466, 989
Beuther, H., Walsh, A., Wang, Y., et al. 2019, A&A, 628, A90
Breen, S. L., & Ellingsen, S. P. 2011, MNRAS, 416, 178
Breen, S. L., Ellingsen, S. P., Caswell, J. L., et al. 2016, MNRAS, 459, 4066
Brogan, C. L., Hunter, T. R., Cyganowski, C. J., et al. 2011, ApJ, 739, L16
Brown, R. D., & Cragg, D. M. 1991, ApJ, 378, 445
Caswell, J. L. 1998, MNRAS, 297, 215
Caswell, J. L. 2009, PASA, 26, 454
Caswell, J. L., Gardner, F. F., Norris, R. P., et al. 1993, MNRAS, 260, 425
Cesaroni, R., Palagi, F., Felli, M., et al. 1988, A&AS, 76, 445
Cesaroni, R., Walmsley, C. M., & Churchwell, E. 1992, A&A, 256, 618
Cheung, A. C., Rank, D. M., Townes, C. H., Thornton, D. D., & Welch, W. J. 1968, Phys. Rev. Lett., 21, 1701
Cheung, A. C., Rank, D. M., Townes, C. H., Thornton, D. D., & Welch, W. J. 1969, Nature, 221, 626
Endres, C. P., Schlemmer, S., Schilke, P., Stutzki, J., & Müller, H. S. P. 2016, J. Mol. Spectrosc., 327, 95
Flower, D. R., Offer, A., & Schilke, P. 1990, MNRAS, 244, 4P
Galván-Madrid, R., Keto, E., Zhang, Q., et al. 2009, ApJ, 706, 1036
Gaume, R. A., Wilson, T. L., & Johnston, K. J. 1996, ApJ, 457, L47
Genzel, R., & Downes, D. 1979, A&A, 72, 234
Gordon, J. P., Zeiger, H. J., & Townes, C. H. 1954, Phys. Rev., 95, 282
Gordon, J. P., Zeiger, H. J., & Townes, C. H. 1955, Phys. Rev., 99, 1264
Guilloteau, S., Wilson, T. L., Martin, R. N., Batria, W., & Pauls, T. A. 1983, A&A, 124, 322

Henkel, C., Wilson, T. L., Asiri, H., & Mauersberger, R. 2013, A&A, 549, A90
Hoffman, I. M. 2012, ApJ, 759, 76
Hoffman, I. M., & Joyce, S. A. 2014, ApJ, 782, 83
Hogge, T. G., Jackson, J. M., Allingham, D., et al. 2019, ApJ, 887, 79
Hu, J. Y., te Lintel Hekkert, P., Slijkhuis, F., et al. 1994, A&AS, 103, 301
Hu, B., Menten, K. M., Wu, Y., et al. 2016, ApJ, 833, 18
Hunter, T. R., Brogan, C. L., Indebetouw, R., & Cyganowski, C. J. 2008, ApJ, 680, 1271
Kim, C.-H., Kim, K.-T., & Park, Y.-S. 2018, ApJS, 236, 31
Kraemer, K. E., & Jackson, J. M. 1995, ApJ, 439, L9
Ladeyschikov, D. A., Bayandina, O. S., & Sobolev, A. M. 2019, AJ, 158, 233
Ladeyschikov, D. A., Gong, Y., Sobolev, A. M., et al. 2022a, ApJS, 261, 14
Ladeyschikov, D. A., Sobolev, A. M., Bayandina, O. S., & Shakhvorostova, N. N. 2022b, AJ, 163, 124
Lewis, B. M. 1994, ApJS, 93, 549
Lu, X., Mills, E. A. C., Ginsburg, A., et al. 2019, ApJS, 244, 35
Madden, S. C., Irvine, W. M., Matthews, H. E., Brown, R. D., & Godfrey, P. D. 1986, ApJ, 300, L79
Mangum, J. G., & Wootten, A. 1994, ApJ, 428, L33
Mauersberger, R., Wilson, T. L., & Henkel, C. 1986, A&A, 160, L13
Mauersberger, R., Henkel, C., & Wilson, T. L. 1987, A&A, 173, 352
Mauersberger, R., Wilson, T. L., & Henkel, C. 1988, A&A, 201, 123
McCarthy, T. P., Breen, S. L., Kaczmarek, J. F., et al. 2023, MNRAS, 522, 4728
McEwen, B. C., Pihlström, Y. M., & Sjouwerman, L. O. 2016, ApJ, 826, 189
Mei, Y., Chen, X., Shen, Z.-Q., & Li, B. 2020, ApJ, 898, 157
Menten, K. M. 1991, ApJ, 380, L75
Menten, K. M., Melnick, G. J., & Phillips, T. G. 1990, ApJ, 350, L41
Mills, E. A. C., Ginsburg, A., Clements, A. R., et al. 2018, ApJ, 869, L14
Motogi, K., Sorai, K., Honma, M., et al. 2011, MNRAS, 417, 238
Müller, H. S. P., Schlöder, F., Stutzki, J., & Winnewisser, G. 2005, J. Mol. Struct., 742, 215
Nguyen, H., Rugel, M. R., Murugeshan, C., et al. 2022, A&A, 666, A59
Ott, M., Witzel, A., Quirrenbach, A., et al. 1994, A&A, 284, 331
Palagi, F., Cesaroni, R., Comoretto, G., Felli, M., & Natale, V. 1993, A&AS, 101, 153
Pety, J. 2005, in SF2A-2005: Semaine de l'Astrophysique Francaise, eds. F. Casoli, T. Contini, J. M. Hameury, & L. Pagani, 721
Pickett, H. M., Poynter, R. L., Cohen, E. A., et al. 1998, J. Quant. Spec. Radiat. Transf., 60, 883
Pratap, P., Menten, K. M., Reid, M. J., Moran, J. M., & Walmsley, C. M. 1991, ApJ, 373, L13
Schilke, P., Walmsley, C. M., & Mauersberger, R. 1991, A&A, 247, 516
Schuller, F., Menten, K. M., Contreras, Y., et al. 2009, A&A, 504, 415
Sevenster, M. N., Chapman, J. M., Habing, H. J., Killeen, N. E. B., & Lindqvist, M. 1997, A&AS, 122, 79
Sobolev, A. M., Ladeyschikov, D. A., & Nakashima, J.-i. 2019, Res. Astron. Astrophys., 19, 034
Svoboda, B. E., Shirley, Y. L., Battersby, C., et al. 2016, ApJ, 822, 59
te Lintel Hekkert, P., Versteege-Hensel, H. A., Habing, H. J., & Wiertz, M. 1989, A&AS, 78, 399
Titmarsh, A. M., Ellingsen, S. P., Breen, S. L., Caswell, J. L., & Voronkov, M. A. 2016, MNRAS, 459, 157
Towner, A. P. M., Brogan, C. L., Hunter, T. R., & Cyganowski, C. J. 2021, ApJ, 923, 263
Urquhart, J. S., Morgan, L. K., Figura, C. C., et al. 2011, MNRAS, 418, 1689
Walmsley, C. M., & Ungerechts, H. 1983, A&A, 122, 164
Walsh, A. J., Longmore, S. N., Thorwirth, S., Urquhart, J. S., & Purcell, C. R. 2007, MNRAS, 382, L35
Walsh, A. J., Breen, S. L., Britton, T., et al. 2011, MNRAS, 416, 1764
Walsh, A. J., Purcell, C. R., Longmore, S. N., et al. 2014, MNRAS, 442, 2240
Wang, Y., Zhang, Q., Rathborne, J. M., Jackson, J., & Wu, Y. 2006, ApJ, 651, L125
Wang, K., Zhang, Q., Wu, Y., Li, H.-b., & Zhang, H. 2012, ApJ, 745, L30
Weaver, H., Williams, D. R. W., Dieter, N. H., & Lum, W. T. 1965, Nature, 208, 29
Wienen, M., Wyrowski, F., Schuller, F., et al. 2012, A&A, 544, A146
Wienen, M., Wyrowski, F., Menten, K. M., et al. 2018, A&A, 609, A125
Wilson, T. L., & Schilke, P. 1993, Ammonia Masers in the Interstellar Medium, 412, eds. A. W. Clegg, & G. E. Nedoluha, 123
Wilson, T. L., Batrla, W., & Pauls, T. A. 1982, A&A, 110, L20
Winkel, B., Kraus, A., & Bach, U. 2012, A&A, 540, A140
Wolak, P., Szymczak, M., & Gérard, E. 2012, A&A, 537, A5
Wouterloot, J. G. A., Brand, J., & Fiegle, K. 1993, A&AS, 98, 589
Xi, H., Zhou, J., Esimbek, J., et al. 2015, MNRAS, 453, 4203
Xu, Y., Voronkov, M. A., Pandian, J. D., et al. 2009, A&A, 507, 1117
Yan, Y. T., Henkel, C., Menten, K. M., et al. 2022a, A&A, 666, L15
Yan, Y. T., Henkel, C., Menten, K. M., et al. 2022b, A&A, 659, A5
Yang, K., Chen, X., Shen, Z.-Q., et al. 2017, ApJ, 846, 160
Yang, K., Chen, X., Shen, Z.-Q., et al. 2019, ApJS, 241, 18
Yang, W., Xu, Y., Choi, Y. K., et al. 2020, ApJS, 248, 18
Yang, W., Gong, Y., Menten, K. M., et al. 2023, A&A, 675, A112
Zhang, Q., & Ho, P. T. P. 1995, ApJ, 450, L63
Zhang, Q., Hunter, T. R., Sridharan, T. K., & Cesaroni, R. 1999, ApJ, 527, L117

Appendix A: Tables

Table A.1. Catalog of ammonia transitions that have been identified as masers in the ISM.

Number	Transition	ν	$E_{\rm low}/k$	$E_{\rm up}/k$	Discovery source & Reference
	(J, K)	(MHz)	(K)	(K)	
1	(1,1)	23694.49550	22.12769	23.26484	DR21, a
2	(2,2)	23722.63330	63.30956	64.44806	Sgr B2(M), b
3	(3,3)	23870.12920	122.39346	123.53904	W33, c
4	(5,5)	24532.98870	294.19337	295.37076	G9.26+0.19, d
5	(5,4)	22653.02200	342.22451	343.31167	W51-IRS2, e
6	(5,3)	21285.27500	379.43682	380.45835	W51-IRS2, f
7	(6,6)	25056.02500	406.85658	408.05908	NGC6334, g
8	(6,5)	22732.42900	465.55043	466.64141	W3(OH), h
9	(6,4)	20994.61700	513.33957	514.34714	Sgr B2(N), i
10	(6,3)	19757.53800	550.36513	551.31333	NGC7538, j
11	(6,2)	18884.69500	576.73689	577.64321	W51-IRS2, f
12	(6,1)	18391.56200	592.52954	593.41219	Sgr B2(N), i
13	(7,7)	25715.18200	537.31664	538.55077	W51-IRS2, f
14	(7,6)	22924.94000	606.67824	607.77846	W51-IRS2, f
15	(7,5)	20804.83000	665.02736	666.02583	W51-IRS2, e
16	(7,4)	19218.46500	712.53838	713.46072	W51-IRS2, f
17	(7,3)	18017.33700	749.35187	750.21656	Sgr B2(N), i
18	(8,6)	20719.22100	834.46640	835.46076	NGC6334, k
19	(8,5)	18808.50700	892.42835	893.33101	W51-IRS2, f
20	(8,4)	17378.11000	939.62715	940.46116	Sgr B2(N), i
21	(8,3)	16455.09900	976.19662	976.98634	Sgr B2(N), i
22	(9,9)	27477.94300	851.45423	852.77295	W51-IRS2, f
23	(9,8)	23657.47100	942.18255	943.31792	W51-IRS2, e
24	(9,7)	20735.45200	1021.61682	1022.61196	W51-IRS2, f
25	(9,6)	18499.39000	1089.99977	1090.88760	W51, NGC7538, W49, DR21(OH), j
26	(9,5)	16798.13400	1147.53483	1148.34101	Sgr B2(N), i
27	(9,4)	15523.90000	1194.38934	1195.13437	Sgr B2(N), i
28	(9,3)	14376.81700	1230.70171	1231.39168	Sgr B2(N), i
29	(10,9)	24205.28700	1136.46581	1137.62748	W51-IRS2, f
30	(10,8)	20852.52700	1226.43274	1227.43349	W51-IRS2, e
31	(10,7)	18285.43400	1305.21064	1306.08820	W51-IRS2, f
32	(10,6)	16319.32400	1373.03592	1373.81912	NGC7538, l
33	(11,9)	21070.73900	1448.86263	1449.87386	NGC6334, k
34	(12,12)	31424.94300	1454.90272	1456.41088	W51-IRS2, f
35	$^{15}NH_3$ (3,3)	22789.42170	124.64182	125.73554	NGC7538, m
36	$^{15}NH_3$ (4,3)	21637.89450	238.70035	239.73880	NGC7538, n
37	$^{15}NH_3$ (4,4)	23046.01580	202.51921	203.62523	NGC7538, n

Notes. The parameters of ammonia lines are taken from the Jet Propulsion Laboratory (JPL) molecular line catalog (Pickett et al. 1998, https://spec.jpl.nasa.gov/) and the Cologne Database for Molecular Spectroscopy (CDMS, Müller et al. 2005; Endres et al. 2016). For the last column, see a Gaume et al. (1996), b Mills et al. (2018), c Wilson et al. (1982), d Cesaroni et al. (1992), e Mauersberger et al. (1987), f Henkel et al. (2013), g Beuther et al. (2007), h Mauersberger et al. (1988), i Mei et al. (2020), j Madden et al. (1986), k Walsh et al. (2007), l Hoffman (2012), m Mauersberger et al. (1986), n Schilke et al. (1991).

Table A.2. Catalog of sources hosting ammonia masers.

Number	source	metastable	non-metastable	source type	Discovery Reference
		$(J = K)$	$(J > K)$		
1	W33	Y	N	SFR	a
2	DR 21	Y	Y	SFR	b, c, d, e
3	NGC7538	N	Y	SFR	c, f, g
4	W51	Y	Y	SFR	c, h, i, j
5	W49	N	Y	SFR	c
6	W3(OH)	N	Y	SFR	k

Table A.2. Continued.

Number	source	metastable ($J = K$)	non-metastable ($J > K$)	source type	Discovery Reference
7	G9.26+0.19	Y	N	SFR	l
8	NGC6334	Y	Y	SFR	m, n, o
9	IRAS20126+4104	Y	N	SFR	p
10	G05.89-0.39	Y	N	SFR	q
11	G19.61-0.23	N	Y	SFR	r
12	G23.33-0.30	Y	N	SNR	r, s
13	G030.7206-00.0826	Y	N	SFR	t
14	G20.08-0.14N	Y	N	SFR	u
15	G35.03+0.35	Y	N	SFR	v
16	G28.34+0.06	Y	N	SFR	w
17	W44	Y	N	SNR	x
18	G5.7-0.0	Y	N	SNR	x
19	W51C	Y	N	SNR	x
20	IC443	Y	N	SNR	x
21	Sgr B2(M)	Y	Y	SFR	y, z
22	Sgr B2(N)	N	Y	SFR	z, z1
23	G10.34-0.14	Y	N	SFR	z2
24	G14.33-0.64	Y	N	SFR	z2
25	G18.89-0.47	Y	N	SFR	z2
26	G19.36-0.03	Y	N	SFR	z2
27	G28.83-0.25	Y	N	SFR	z2
28	CepA	N	Y	SFR	z3
29	G34.26+0.15	N	Y	SFR	z3
30	Sgr B2(NS)	N	Y	SFR	z
31	Sgr B2(S)	N	Y	SFR	z
32	G358.931-0.030	N	Y	SFR	z4
33	G010.47+0.03	N	Y	SFR	this work
34	G012.21-0.10	N	Y	SFR	this work
35	G019.61-0.23	N	Y	SFR	this work
36	G024.79+0.08	N	Y	SFR	this work
37	G029.95-0.02	Y	Y	SFR	this work
38	G030.21-0.19	N	Y	SFR	this work
39	G030.60+0.18	N	Y	SFR	this work
40	G030.70-0.07	N	Y	SFR	this work
41	G030.79+0.20	N	Y	SFR	this work
42	G031.41+0.30	N	Y	SFR	this work
43	G032.74-0.08	N	Y	SFR	this work
44	G035.19-0.74	N	Y	SFR	this work
45	G043.79-0.13	N	Y	SFR	this work
46	G048.98-0.30	Y	N	SFR	this work
47	G111.53+0.76	N	Y	SFR	this work
count		24	28		

Notes. SFR: star-forming region, SNR: supernova remnant. Y indicates a detection and N marks a non-detection. a Wilson et al. (1982), b Guilloteau et al. (1983), c Madden et al. (1986), d Mangum & Wootten (1994), e Gaume et al. (1996), f Hoffman (2012), g Hoffman & Joyce (2014), h Zhang & Ho (1995), i Mauersberger et al. (1987), j Henkel et al. (2013), k Mauersberger et al. (1988), l Cesaroni et al. (1992), m Kraemer & Jackson (1995), n Beuther et al. (2007), o Walsh et al. (2007), p Zhang et al. (1999), q Hunter et al. (2008), r Walsh et al. (2011), s Hogge et al. (2019), t Urquhart et al. (2011), u Galván-Madrid et al. (2009), v Brogan et al. (2011), w Wang et al. (2012), x McEwen et al. (2016), y Mills et al. (2018), z Yan et al. (2022a), z1 Mei et al. (2020), z2 Towner et al. (2021), z3, Yan et al. (2022b), z4 McCarthy et al. (2023)

Table A.3. Our sample of 119 observed sources.

Source	R.A. (h m s)	Dec. ($^\circ$ $'$ $''$)	V_{LSR} (km s^{-1})	Log(N_{NH_3}) (cm^{-2})
G010.47+0.03	18 08 38.1	−19 51 50	65.20	16.01
G010.63-0.34	18 10 18.6	−19 54 17	-4.57	15.56
G010.68-0.03	18 09 15.8	−19 42 27	51.04	15.55
G010.99-0.08	18 10 06.5	−19 27 46	29.67	15.67
G011.90-0.14	18 12 10.8	−18 41 36	38.41	15.79

Table A.3. continued.

Source	R.A.	Dec.	$V_{\rm LSR}$	Log($N_{\rm NH_3}$)
	(h m s)	(° ′ ″)	(km s^{-1})	(cm^{-2})
G011.94-0.61	18 14 00.9	−18 53 24	36.72	15.63
G012.20-0.03	18 12 23.6	−18 22 52	50.86	15.70
G012.21-0.10	18 12 39.2	−18 24 22	24.46	15.61
G012.68-0.18	18 13 54.2	−18 01 46	55.37	15.84
G012.89+0.49	18 11 51.1	−17 31 27	34.30	15.62
G012.91-0.26	18 14 39.1	−17 51 58	38.05	15.55
G013.18+0.06	18 14 00.9	−17 28 41	49.06	15.67
G013.66-0.60	18 17 24.3	−17 22 12	46.75	15.67
G013.87+0.28	18 14 35.5	−16 45 41	48.52	15.53
G014.10+0.09	18 15 46.2	−16 39 09	9.15	15.54
G014.20-0.19	18 16 58.8	−16 42 05	39.91	15.53
G014.49-0.14	18 17 22.0	−16 25 00	39.57	15.81
G014.60+0.02	18 16 59.7	−16 14 51	26.62	15.60
G014.61+0.01	18 17 02.1	−16 14 36	25.14	15.62
G014.99-0.67	18 20 19.4	−16 13 31	19.43	16.00
G016.87-2.15	18 29 24.3	−15 15 42	18.58	16.00
G018.17-0.30	18 25 07.5	−13 14 33	49.14	15.55
G018.46-0.00	18 24 35.8	−12 51 08	53.72	15.69
G018.66+0.04	18 24 50.4	−12 39 21	81.05	15.70
G018.89-0.47	18 27 07.6	−12 41 40	66.28	15.66
G019.07-0.29	18 26 48.1	−12 26 28	65.48	15.70
G019.47+0.17	18 25 54.5	−11 52 35	21.03	15.88
G019.61-0.14	18 27 17.4	−11 53 56	58.65	15.81
G019.61-0.23	18 27 38.1	−11 56 39	40.76	15.80
G019.61-0.26	18 27 43.8	−11 57 06	42.91	15.52
G019.88-0.53	18 29 14.3	−11 50 30	43.48	15.60
G019.92-0.26	18 28 19.2	−11 40 36	64.70	15.72
G020.36-0.01	18 28 15.8	−11 10 26	52.15	15.53
G020.74-0.09	18 29 16.9	−10 52 27	58.21	15.60
G020.98+0.10	18 29 02.7	−10 34 28	18.34	15.52
G022.35+0.06	18 31 44.2	−09 22 17	84.18	15.60
G023.01-0.41	18 34 39.7	−09 00 42	77.97	15.66
G023.20+0.00	18 33 32.8	−08 39 10	76.17	15.55
G023.21-0.38	18 34 54.9	−08 49 17	77.87	15.68
G023.26+0.07	18 33 24.7	−08 33 50	77.93	15.60
G023.48+0.10	18 33 43.0	−08 21 30	85.41	15.67
G024.18+0.12	18 34 57.2	−07 43 27	113.53	15.80
G024.41+0.10	18 35 26.2	−07 31 44	113.62	15.54
G024.44-0.23	18 36 40.7	−07 39 27	58.11	15.63
G024.49-0.04	18 36 05.6	−07 31 31	109.74	15.58
G024.67-0.15	18 36 50.0	−07 24 49	112.97	15.62
G024.79+0.08	18 36 12.4	−07 12 10	109.49	15.69
G024.80+0.10	18 36 10.7	−07 11 18	109.93	15.70
G024.92+0.08	18 36 27.1	−07 05 10	43.76	15.54
G025.46-0.21	18 38 30.1	−06 44 29	118.95	15.60
G025.72+0.05	18 38 02.8	−06 23 46	99.19	15.70
G027.37-0.17	18 41 51.2	−05 01 43	91.05	15.51
G027.56+0.08	18 41 19.8	−04 44 21	84.21	15.65
G028.20-0.05	18 42 58.1	−04 13 58	96.08	15.53
G028.61+0.02	18 43 28.9	−03 50 17	102.02	15.70
G028.65+0.03	18 43 31.1	−03 47 54	103.59	15.57
G028.81+0.17	18 43 18.8	−03 35 26	105.80	15.56
G028.82+0.36	18 42 37.2	−03 29 42	86.40	15.51
G028.84+0.49	18 42 12.3	−03 24 54	86.43	15.53
G029.40-0.09	18 45 18.9	−03 11 19	105.58	15.53
G029.59-0.61	18 47 31.7	−03 15 14	76.51	15.70
G029.81+2.22	18 37 50.5	−01 45 39	45.42	15.60
G029.91-0.05	18 46 05.5	−02 42 27	99.71	15.56
G029.93-0.06	18 46 10.7	−02 41 52	99.20	15.54
G029.95-0.02	18 46 04.2	−02 39 21	97.24	15.60

Table A.3. continued.

Source	R.A.	Dec.	V_{LSR}	Log(N_{NH_3})
	(h m s)	(° ′ ″)	(km s^{-1})	(cm^{-2})
G030.01-0.27	18 47 03.8	−02 43 39	103.38	15.71
G030.21-0.19	18 47 08.3	−02 30 34	105.43	15.57
G030.30+0.05	18 46 26.0	−02 19 11	108.07	15.60
G030.42-0.23	18 47 40.3	−02 20 29	105.61	15.57
G030.59-0.04	18 47 18.9	−02 06 16	41.60	15.70
G030.60+0.18	18 46 33.3	−01 59 35	105.21	15.86
G030.68-0.07	18 47 35.6	−02 02 08	91.58	15.64
G030.70-0.07	18 47 36.1	−02 00 59	91.76	15.91
G030.73-0.07	18 47 40.3	−01 59 30	91.71	15.67
G030.74-0.06	18 47 38.9	−01 58 32	96.12	15.55
G030.77-0.22	18 48 16.1	−02 01 11	104.90	15.54
G030.79+0.20	18 46 47.6	−01 49 02	81.51	15.59
G030.83-0.06	18 47 48.9	−01 54 01	97.02	15.61
G031.28+0.06	18 48 12.1	−01 26 31	109.04	15.60
G031.41+0.30	18 47 34.6	−01 13 01	97.60	15.89
G032.04+0.06	18 49 36.6	−00 45 44	95.29	15.80
G032.15+0.13	18 49 31.8	−00 38 07	93.95	15.70
G032.45+0.39	18 49 11.6	−00 14 57	49.17	15.65
G032.74-0.08	18 51 21.8	−00 12 08	37.17	15.72
G032.82-0.33	18 52 24.6	−00 14 58	79.30	15.70
G033.21-0.01	18 51 58.2	+00 14 31	99.96	15.58
G033.91+0.11	18 52 50.5	+00 55 29	107.46	15.60
G034.40+0.23	18 53 18.6	+01 24 49	57.42	15.80
G034.82+0.35	18 53 37.9	+01 50 31	56.90	15.60
G035.19-0.74	18 58 13.1	+01 40 39	33.71	15.60
G035.23-0.36	18 56 54.1	+01 52 45	52.90	15.59
G035.47+0.14	18 55 34.4	+02 19 09	76.91	15.60
G035.58-0.03	18 56 22.6	+02 20 30	52.37	15.60
G035.75+0.15	18 56 02.1	+02 34 39	83.52	15.64
G036.41+0.02	18 57 41.9	+03 06 06	57.77	15.80
G037.55+0.20	18 59 09.9	+04 12 15	85.06	15.70
G037.74-0.11	19 00 36.9	+04 13 23	46.45	15.54
G037.76-0.22	19 01 02.2	+04 12 06	64.39	15.59
G037.82+0.41	18 58 53.9	+04 32 18	17.97	15.58
G037.87-0.60	19 02 36.1	+04 06 59	50.71	15.60
G038.69-0.45	19 03 35.5	+04 55 11	50.86	15.54
G040.43+0.70	19 02 39.6	+06 59 11	12.71	15.64
G040.60-0.72	19 08 03.3	+06 29 12	65.70	15.70
G043.18-0.52	19 12 08.8	+08 52 05	58.03	15.60
G043.31-0.21	19 11 16.9	+09 07 30	59.55	15.70
G043.79-0.13	19 11 54.1	+09 35 50	44.11	15.60
G043.89-0.78	19 14 26.1	+09 22 35	54.01	15.60
G045.46+0.04	19 14 25.6	+11 09 27	62.13	15.70
G045.80-0.36	19 16 31.1	+11 16 12	58.42	15.67
G045.94-0.40	19 16 56.0	+11 21 54	61.74	15.65
G048.98-0.30	19 22 26.2	+14 06 38	67.66	15.60
G049.27-0.34	19 23 07.0	+14 20 15	68.44	15.54
G049.45-0.35	19 23 33.1	+14 29 43	67.49	16.00
G051.68+0.72	19 23 58.6	+16 57 44	4.80	15.63
G053.18+0.21	19 28 51.9	+18 02 37	1.59	15.61
G069.54-0.97	20 10 08.9	+31 31 34	11.18	15.70
G078.98+0.35	20 31 10.7	+40 03 14	5.98	15.60
G108.76-0.99	22 58 47.5	+58 45 01	-51.46	15.60
G111.53+0.76	23 13 43.9	+61 26 58	-56.13	15.70

Notes. Column (1): source name; Columns (2) and (3): Equatorial coordinates (J2000); Column (4): LSR velocity; Column (5): NH_3 column densities.

Table A.4. New ammonia masers.

Source	transition	ν	Epoch	Channel spacing	S_ν	rms	$\int S_\nu dv$	$V_{\rm LSR}$	$\Delta V_{1/2}$	(1,1)*
	(J, K)	(MHz)		(km s^{-1})	(Jy)	(Jy)	(Jy km s^{-1})		(km s^{-1})	
G010.47	(9,6)	18499.390	2023, May 04	0.62	0.25	0.015	0.47 ± 0.03	62.05 ± 0.05	1.79 ± 0.11	6.08 ± 0.48
			2023, May 22	0.07	0.17	0.061	0.08 ± 0.03	61.81 ± 0.04	0.43 ± 0.10	
					0.12		0.02 ± 0.01	62.39 ± 0.04	0.15 ± 0.07	
					0.13		0.28 ± 0.06	62.58 ± 0.19	2.00 ± 0.39	
G012.21	(9,6)	18499.390	2023, Feb. 28	0.62	0.17	0.013	0.25 ± 0.02	25.42 ± 0.07	1.40 ± 0.16	6.55 ± 0.48
			2023, May 04	0.62	0.37	0.008	0.66 ± 0.01	25.86 ± 0.02	1.67 ± 0.04	
			2023, May 19	0.62	0.37	0.061	0.98 ± 0.15	25.83 ± 0.15	2.50 ± 0.55	
			2023, May 22	0.07	0.44	0.077	0.39 ± 0.03	26.02 ± 0.03	0.82 ± 0.08	
G019.612	(9,6)	18499.390	2023, Apr. 11	0.62	0.14	0.011	0.25 ± 0.02	34.96 ± 0.06	1.68 ± 0.15	5.93 ± 0.48
			2023, Apr. 26	0.62	···	0.185	···	···	···	
			2023, Apr. 30	0.62	0.27	0.019	0.59 ± 0.04	34.71 ± 0.07	2.07 ± 0.16	
			2023, May 19	0.62	0.27	0.037	1.60 ± 0.10	34.81 ± 0.15	3.68 ± 0.50	
			2023, May 22	0.07	0.18	0.055	0.05 ± 0.01	32.41 ± 0.03	0.27 ± 0.06	
					0.31		0.17 ± 0.03	33.50 ± 0.03	0.53 ± 0.15	
					0.28		0.16 ± 0.04	34.33 ± 0.04	0.52 ± 0.18	
					0.16		0.12 ± 0.03	35.28 ± 0.10	0.69 ± 0.21	
G024.79	(5,4)	22653.022	2023, Apr. 30	0.50	0.14	0.019	0.32 ± 0.03	115.10 ± 0.10	2.10 ± 0.25	3.37 ± 0.48
			2023, May 04	0.50	0.15	0.018	0.19 ± 0.04	115.21 ± 0.07	1.19 ± 0.19	
			2023, May 19	0.50	0.18	0.022	0.33 ± 0.03	115.28 ± 0.08	1.70 ± 0.21	
G029.95	(7,7)	25715.182	2023, May 19	0.44	0.18	0.017	0.36 ± 0.05	126.56 ± 0.07	1.87 ± 0.18	3.72 ± 0.48
			2023, May 22	0.44	0.28	0.030	0.71 ± 0.07	126.59 ± 0.11	2.36 ± 0.28	
	(8,6)	20719.221	2023, May 19	0.55	0.78	0.017	1.45 ± 0.03	115.26 ± 0.02	1.74 ± 0.03	
					0.30		0.45 ± 0.02	119.69 ± 0.04	1.43 ± 0.09	
					0.50		1.00 ± 0.03	126.67 ± 0.03	1.86 ± 0.07	
			2023, May 22	0.55	0.79	0.024	1.49 ± 0.05	115.22 ± 0.03	1.78 ± 0.07	
					0.28		0.55 ± 0.05	119.38 ± 0.09	1.85 ± 0.21	
					0.49		0.95 ± 0.05	126.66 ± 0.05	1.82 ± 0.11	
	(11,9)	21070.739	2023, May 19	0.54	0.16	0.017	0.29 ± 0.03	115.69 ± 0.08	1.74 ± 0.16	
					0.07		0.10 ± 0.02	119.72 ± 0.16	1.46 ± 0.36	
					0.03		0.06 ± 0.02	124.69 ± 0.34	1.66 ± 0.63	
			2023, May 22	0.54	0.18	0.035	0.48 ± 0.08	115.87 ± 0.18	2.51 ± 0.57	
G030.21	(9,6)	18499.390	2023, Apr. 30	0.62	0.08	0.015	0.32 ± 0.03	101.25 ± 0.18	3.51 ± 0.46	3.13 ± 0.05
			2023, May 04	0.62	0.07	0.014	0.25 ± 0.04	101.15 ± 0.26	3.54 ± 0.60	
			2023, May 19	0.62	0.07	0.016	0.09 ± 0.02	100.72 ± 0.15	1.18 ± 0.28	
			average	0.62	0.07	0.007	0.14 ± 0.01	100.77 ± 0.09	1.85 ± 0.24	
G030.60	(9,6)	18499.390	2023, Apr. 30	0.62	0.11	0.008	0.25 ± 0.02	90.50 ± 0.08	2.07 ± 0.18	3.35 ± 0.48
					0.06		0.08 ± 0.02	94.82 ± 0.13	1.27 ± 0.26	
			2023, May 04	0.62	0.09	0.008	0.19 ± 0.02	90.97 ± 0.10	1.89 ± 0.19	
			2023, May 19	0.62	0.20	0.010	0.53 ± 0.03	91.46 ± 0.06	2.50 ± 0.17	
G030.70	(7,6)	22924.940	2023, Apr. 30	0.50	0.09	0.023	0.18 ± 0.04	68.77 ± 0.21	1.86 ± 0.59	3.77 ± 0.01
					0.10		0.16 ± 0.04	71.69 ± 0.18	1.49 ± 0.38	
			2023, May 04	0.50	0.12	0.018	0.14 ± 0.02	71.72 ± 0.08	1.12 ± 0.17	
			2023, May 19	0.50	0.12	0.019	0.17 ± 0.02	71.47 ± 0.10	1.35 ± 0.21	
	(8,6)	20719.221	2023, Apr. 30	0.55	0.12	0.022	0.38 ± 0.05	106.91 ± 0.20	2.87 ± 0.49	
			2023, May 04	0.50	0.10	0.012	0.17 ± 0.03	106.95 ± 0.13	1.69 ± 0.30	
			2023, May 19	0.50	0.05	0.015	0.06 ± 0.02	107.02 ± 0.25	1.32 ± 0.55	
	(11,9)	21070.739	2023, Apr. 30	0.54	0.12	0.026	0.23 ± 0.05	71.83 ± 0.18	1.70 ± 0.41	
					0.31		0.72 ± 0.05	103.69 ± 0.08	2.16 ± 0.17	
					0.80		1.51 ± 0.05	107.40 ± 0.03	1.78 ± 0.06	
			2023, May 04	0.54	0.10	0.012	0.17 ± 0.02	71.44 ± 0.09	1.65 ± 0.25	
					0.29		0.75 ± 0.03	104.02 ± 0.04	2.42 ± 0.11	
					0.81		1.44 ± 0.02	107.36 ± 0.01	1.68 ± 0.03	
			2023, May 19	0.54	0.11	0.022	0.15 ± 0.02	71.56 ± 0.11	1.30 ± 0.24	
					0.18		0.40 ± 0.03	103.84 ± 0.07	2.02 ± 0.18	
					0.50		0.86 ± 0.03	107.37 ± 0.03	1.61 ± 0.06	
G030.79	(9,6)	18499.390	2023, Apr. 29	0.62	0.89	0.019	1.94 ± 0.04	91.10 ± 0.02	2.04 ± 0.05	2.22 ± 0.48
			2023, Apr. 30	0.62	0.98	0.017	2.03 ± 0.04	91.10 ± 0.02	1.95 ± 0.04	
			2023, May 19	0.62	0.33	0.012	1.16 ± 0.03	91.83 ± 0.05	3.32 ± 0.10	
G031.41	(9,6)	18499.390	2022, Nov. 21	0.62	1.86	0.006	5.32 ± 0.05	91.51 ± 0.01	2.69 ± 0.03	4.57 ± 0.48
					4.51		7.56 ± 0.04	104.60 ± 0.01	1.57 ± 0.01	
			2022, Nov. 25	0.07	0.62	0.006	0.41 ± 0.07	90.53 ± 0.07	0.61 ± 0.07	
					1.47		2.15 ± 0.07	91.56 ± 0.07	1.37 ± 0.07	
					0.56		0.53 ± 0.07	93.07 ± 0.07	0.88 ± 0.07	
					5.21		4.68 ± 0.07	104.58 ± 0.07	0.84 ± 0.07	
			2023, Feb. 17	0.62	0.28	0.019	0.64 ± 0.08	88.09 ± 0.14	2.12 ± 0.35	

Table A.4. continued.

Source	transition	ν	Epoch	Channel spacing	S_ν	rms	$\int S_\nu dv$	$V_{\rm LSR}$	$\Delta V_{1/2}$	$\Delta V_{1/2}$ (1,1)*
	(J, K)	(MHz)		(km s^{-1})	(Jy)	(Jy)	(Jy km s^{-1})		(km s^{-1})	
					1.20		2.52 ± 0.06	91.56 ± 0.03	1.98 ± 0.08	
					1.54		2.37 ± 0.06	104.43 ± 0.02	1.45 ± 0.04	
			2023, Apr. 26	0.62	0.44	0.008	1.01 ± 0.07	88.24 ± 0.06	2.15 ± 0.19	
					0.92		2.09 ± 0.06	91.92 ± 0.03	2.13 ± 0.08	
					2.18		3.54 ± 0.05	104.39 ± 0.01	1.52 ± 0.02	
			2023, Apr. 29	0.62	0.21	0.019	0.44 ± 0.04	88.14 ± 0.09	2.03 ± 0.23	
					0.45		0.95 ± 0.04	92.02 ± 0.03	2.00 ± 0.10	
					1.03		1.75 ± 0.03	104.40 ± 0.01	1.60 ± 0.04	
			2023, Apr. 29	0.07	0.48	0.043	0.59 ± 0.05	88.29 ± 0.07	1.16 ± 0.07	
					0.39		0.34 ± 0.05	91.13 ± 0.07	0.80 ± 0.07	
					0.97		1.23 ± 0.05	92.17 ± 0.07	1.19 ± 0.07	
					4.53		3.05 ± 0.02	104.39 ± 0.07	0.63 ± 0.07	
					0.24		0.35 ± 0.03	106.43 ± 0.07	1.38 ± 0.07	
			2023, Apr. 30	0.62	0.33	0.010	0.84 ± 0.06	88.25 ± 0.08	2.37 ± 0.24	
					0.69		1.59 ± 0.06	91.98 ± 0.04	2.14 ± 0.10	
					1.62		2.78 ± 0.05	104.41 ± 0.01	1.62 ± 0.03	
			2023, May 19	0.62	0.11	0.009	0.30 ± 0.20	88.91 ± 0.62	2.59 ± 0.62	
					1.03		2.07 ± 0.20	91.14 ± 0.62	1.88 ± 0.62	
					1.80		2.88 ± 0.20	104.40 ± 0.62	1.50 ± 0.62	
			2023, May 22	0.62	0.11	0.019	0.38 ± 0.19	88.10 ± 0.62	3.22 ± 0.62	
					0.86		2.14 ± 0.19	92.11 ± 0.62	2.32 ± 0.62	
					1.71		2.88 ± 0.19	104.40 ± 0.62	1.58 ± 0.62	
	(11,9)	21070.739	2022, Nov. 21	0.54	0.35	0.012	0.52 ± 0.02	104.52 ± 0.02	1.41 ± 0.06	
			2023, Feb. 17	0.54	0.21	0.019	0.31 ± 0.02	104.44 ± 0.05	1.41 ± 0.13	
			2023, Apr. 26	0.54	0.18	0.012	0.36 ± 0.05	104.49 ± 0.10	1.84 ± 0.34	
			2023, Apr. 29	0.54	···	0.021	···	···	···	
			2023, Apr. 30	0.54	0.14	0.015	0.23 ± 0.02	104.46 ± 0.07	1.51 ± 0.20	
			2023, May 19	0.54	0.12	0.012	0.15 ± 0.02	104.37 ± 0.07	1.20 ± 0.14	
			2023, May 22	0.54	0.13	0.038	0.39 ± 0.11	103.91 ± 0.32	2.94 ± 1.27	
G032.74	(5,4)	22653.022	2023, Apr. 11	0.50	0.18	0.017	0.25 ± 0.02	33.61 ± 0.05	1.30 ± 0.14	4.21 ± 0.48
			2023, Apr. 29	0.50	0.18	0.025	0.37 ± 0.05	33.43 ± 0.13	1.98 ± 0.29	
			2023, Apr. 30	0.50	0.18	0.018	0.34 ± 0.03	33.69 ± 0.08	1.80 ± 0.27	
			2023, May 19	0.50	0.17	0.020	0.25 ± 0.03	33.45 ± 0.07	1.39 ± 0.19	
	(6,4)	20994.617	2023, Apr. 11	0.54	0.26	0.014	0.43 ± 0.03	33.37 ± 0.06	1.56 ± 0.16	
			2023, Apr. 29	0.54	0.27	0.021	0.38 ± 0.04	33.39 ± 0.07	1.34 ± 0.18	
			2023, Apr. 30	0.54	0.33	0.012	0.41 ± 0.02	33.36 ± 0.03	1.17 ± 0.07	
			2023, May 19	0.54	0.22	0.019	0.30 ± 0.02	33.19 ± 0.05	1.28 ± 0.12	
	(9,8)	23657.471	2023, Apr. 11	0.48	0.18	0.020	0.32 ± 0.03	32.27 ± 0.07	1.70 ± 0.15	
			2023, Apr. 29	0.48	0.22	0.023	0.33 ± 0.03	32.01 ± 0.06	1.41 ± 0.14	
			2023, Apr. 30	0.48	0.23	0.016	0.39 ± 0.03	32.26 ± 0.06	1.58 ± 0.13	
			2023, May 19	0.48	0.20	0.019	0.32 ± 0.03	32.33 ± 0.06	1.46 ± 0.15	
	(10,8)	20852.527	2023, Apr. 11	0.55	0.58	0.015	1.32 ± 0.02	32.82 ± 0.02	2.13 ± 0.04	
			2023, Apr. 29	0.55	0.60	0.033	1.41 ± 0.06	32.79 ± 0.04	2.22 ± 0.11	
			2023, Apr. 30	0.55	0.66	0.019	1.47 ± 0.03	32.77 ± 0.02	2.11 ± 0.05	
			2023, May 19	0.55	0.53	0.023	1.21 ± 0.04	32.82 ± 0.04	2.16 ± 0.08	
G035.19	(6,4)	20994.617	2023, Feb. 28	0.54	0.12	0.013	0.22 ± 0.03	30.75 ± 0.10	1.73 ± 0.31	2.88 ± 0.48
			2023, May 04	0.54	0.10	0.011	0.22 ± 0.03	30.78 ± 0.11	2.07 ± 0.35	
			2023, May 19	0.54	0.12	0.017	0.17 ± 0.02	30.85 ± 0.08	1.39 ± 0.19	
	(6,5)	22732.429	2023, Feb. 28	0.50	0.13	0.017	0.24 ± 0.03	30.57 ± 0.08	1.71 ± 0.25	
			2023, May 04	0.50	0.07	0.013	0.17 ± 0.07	30.32 ± 0.21	2.41 ± 0.53	
			2023, May 19	0.50	0.06	0.019	0.21 ± 0.04	31.01 ± 0.30	3.04 ± 0.59	
G043.79	(9,6)	18499.390	2023, Feb. 17	0.62	0.15	0.014	0.39 ± 0.05	35.49 ± 0.14	2.39 ± 0.43	4.47 ± 0.12
					1.21		2.64 ± 0.04	42.37 ± 0.02	2.04 ± 0.04	
			2023, Apr. 29	0.62	0.09	0.013	0.16 ± 0.02	35.36 ± 0.11	1.65 ± 0.23	
					0.51		1.19 ± 0.02	42.33 ± 0.02	2.20 ± 0.05	
G111.53	(9,6)	18499.390	2023, Apr. 30	0.62	1.16	0.011	2.03 ± 0.02	-55.43 ± 0.01	1.65 ± 0.02	4.18 ± 0.48
			2023, May 19	0.62	0.91	0.012	1.62 ± 0.02	-55.45 ± 0.01	1.67 ± 0.03	
			2023, May 22	0.07	0.36	0.040	0.24 ± 0.01	-55.43 ± 0.02	0.63 ± 0.05	
G048.98	(3,3)	23870.100	2022, Nov. 21	0.48	2.40	0.015	6.93 ± 0.08	67.17 ± 0.01	2.71 ± 0.04	
	(2,2)				1.08	0.015	4.33 ± 0.04	67.35 ± 0.01	3.75 ± 0.04	
	(1,1)				1.53	0.009	5.89 ± 0.14	67.87 ± 0.48	3.61 ± 0.48	3.05 ± 0.4

Notes. * The intrinsic line widths of ammonia (J, K) = (1,1) thermal emission.

Appendix B: Figures

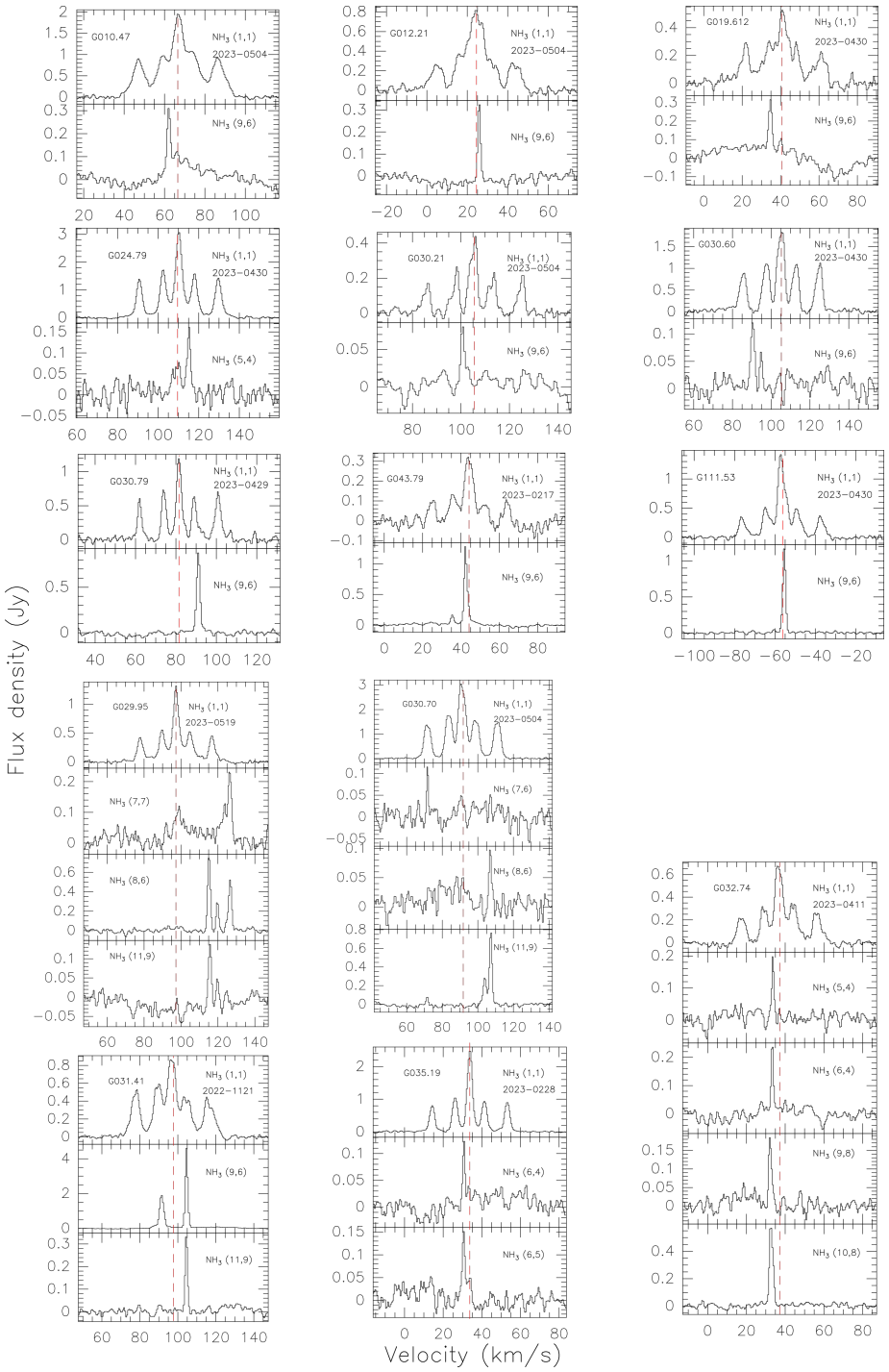

Fig. B.1. Line profiles of NH_3 (1,1) thermal emission and maser transitions in 14 sources. The dashed red lines indicate the systemic velocities of the sources.

Bibliography

Adande, G. R. & Ziurys, L. M. 2012, ApJ, 744, 194 (Cited on page 48.)

Anders, E. & Grevesse, N. 1989, Geochimica et Cosmochimica Acta, 53, 197 (Cited on pages 6 and 48.)

Bartkiewicz, A., Szymczak, M., & van Langevelde, H. J. 2016, A&A, 587, A104 (Cited on page 53.)

Benjamin, R. A., Churchwell, E., Babler, B. L., et al. 2003, PASP, 115, 953 (Cited on page 53.)

Beuther, H., Walsh, A. J., Thorwirth, S., et al. 2007, A&A, 466, 989 (Cited on pages 11, 13 and 16.)

Bonfand, M., Belloche, A., Menten, K. M., Garrod, R. T., & Müller, H. S. P. 2017, A&A, 604, A60 (Cited on page 61.)

Brogan, C. L., Hunter, T. R., Cyganowski, C. J., et al. 2011, ApJ, 739, L16 (Cited on pages 12 and 16.)

Brown, R. D. & Cragg, D. M. 1991, ApJ, 378, 445 (Cited on pages 12 and 51.)

Burbidge, E. M., Burbidge, G. R., Fowler, W. A., & Hoyle, F. 1957, Reviews of Modern Physics, 29, 547 (Cited on page 3.)

Cameron, A. G. W. 1957, PASP, 69, 201 (Cited on page 3.)

Caswell, J. L. 1996, MNRAS, 283, 606 (Cited on page 61.)

Cesaroni, R., Walmsley, C. M., & Churchwell, E. 1992, A&A, 256, 618 (Cited on pages 11, 13 and 16.)

Chen, J. L., Zhang, J. S., Henkel, C., et al. 2021, ApJS, 257, 39 (Cited on page 48.)

Cheung, A. C., Rank, D. M., Townes, C. H., Thornton, D. D., & Welch, W. J. 1968, Phys. Rev. Lett., 21, 1701 (Cited on pages 8 and 11.)

Chiappini, C., Matteucci, F., & Romano, D. 2001, ApJ, 554, 1044 (Cited on page 5.)

Chin, Y. N., Henkel, C., Whiteoak, J. B., Langer, N., & Churchwell, E. B. 1996, A&A, 305, 960 (Cited on pages 6, 7 and 78.)

Churchwell, E., Babler, B. L., Meade, M. R., et al. 2009, PASP, 121, 213 (Cited on page 53.)

Clayton, D. 2007, Handbook of Isotopes in the Cosmos (Cited on page 6.)

Clayton, D. D. 2007, Science, 318, 1876 (Cited on page 4.)

Colzi, L., Fontani, F., Caselli, P., et al. 2018, A&A, 609, A129 (Cited on page 48.)

Colzi, L., Romano, D., Fontani, F., et al. 2022a, A&A, 667, A151 (Cited on page 49.)

Colzi, L., Romano, D., Fontani, F., et al. 2022b, arXiv e-prints, arXiv:2209.10620 (Cited on page 79.)

Condon, J. J. & Ransom, S. M. 2016, Essential Radio Astronomy (Cited on pages 17, 20, 21, 23, 30, 31, 32 and 33.)

Danby, G., Flower, D. R., Valiron, P., Schilke, P., & Walmsley, C. M. 1988, MNRAS, 235, 229 (Cited on pages 8, 11, 12 and 51.)

De Pree, C. G., Goss, W. M., & Gaume, R. A. 1998, ApJ, 500, 847 (Cited on page 56.)

De Pree, C. G., Peters, T., Mac Low, M. M., et al. 2014, ApJ, 781, L36 (Cited on page 56.)

De Pree, C. G., Peters, T., Mac Low, M. M., et al. 2015, ApJ, 815, 123 (Cited on page 56.)

Di Vruno, F., Winkel, B., Bassa, C. G., et al. 2023, A&A, 676, A75 (Cited on page 20.)

Draine, B. T. 2011, Physics of the Interstellar and Intergalactic Medium (Cited on page 2.)

Einstein, A. 1917, Physikalische Zeitschrift, 18, 121 (Cited on page 8.)

Endres, C. P., Schlemmer, S., Schilke, P., Stutzki, J., & Müller, H. S. P. 2016, Journal of Molecular Spectroscopy, 327, 95 (Cited on pages 13 and 42.)

Flower, D. R., Offer, A., & Schilke, P. 1990, MNRAS, 244, 4P (Cited on page 12.)

Fontani, F., Caselli, P., Palau, A., Bizzocchi, L., & Ceccarelli, C. 2015, ApJ, 808, L46 (Cited on page 48.)

Fridman, P. A. & Baan, W. A. 2001, A&A, 378, 327 (Cited on page 20.)

Gaia Collaboration, Vallenari, A., Brown, A. G. A., et al. 2022, arXiv e-prints, arXiv:2208.00211 (Cited on page 18.)

Galván-Madrid, R., Keto, E., Zhang, Q., et al. 2009, ApJ, 706, 1036 (Cited on pages 12 and 16.)

Gardner, F. F. & Whiteoak, J. B. 1981, MNRAS, 194, 37P (Cited on page 48.)

Gaume, R. A. & Claussen, M. J. 1990, ApJ, 351, 538 (Cited on page 61.)

Gaume, R. A., Claussen, M. J., de Pree, C. G., Goss, W. M., & Mehringer, D. M. 1995, ApJ, 449, 663 (Cited on page 56.)

Gaume, R. A., Wilson, T. L., & Johnston, K. J. 1996, ApJ, 457, L47 (Cited on pages 11, 13 and 16.)

Girichidis, P., Offner, S. S. R., Kritsuk, A. G., et al. 2020, Space Sci. Rev., 216, 68 (Cited on page 2.)

Goddi, C., Henkel, C., Zhang, Q., Zapata, L., & Wilson, T. L. 2015, A&A, 573, A109 (Cited on page 15.)

Gong, Y., Henkel, C., Thorwirth, S., et al. 2015, A&A, 581, A48 (Cited on page 64.)

Gordon, J. P., Zeiger, H. J., & Townes, C. H. 1954, Physical Review, 95, 282 (Cited on page 10.)

GRAVITY Collaboration, Abuter, R., Amorim, A., et al. 2019, A&A, 625, L10 (Cited on page 55.)

Guilloteau, S., Wilson, T. L., Martin, R. N., Batria, W., & Pauls, T. A. 1983, A&A, 124, 322 (Cited on page 16.)

Haffner, L. M., Dettmar, R. J., Beckman, J. E., et al. 2009, Reviews of Modern Physics, 81, 969 (Cited on page 2.)

Halfen, D. T., Woolf, N. J., & Ziurys, L. M. 2017, ApJ, 845, 158 (Cited on page 5.)

Haslam, C. G. T., Klein, U., Salter, C. J., et al. 1981, A&A, 100, 209 (Cited on page 18.)

Haslam, C. G. T., Salter, C. J., Stoffel, H., & Wilson, W. E. 1982, A&AS, 47, 1 (Cited on page 18.)

Henkel, C., Guesten, R., & Gardner, F. F. 1985, A&A, 143, 148 (Cited on pages 5, 48 and 77.)

Henkel, C., Walmsley, C. M., & Wilson, T. L. 1980, A&A, 82, 41 (Cited on pages 5, 48 and 77.)

Henkel, C., Wilson, T. L., Asiri, H., & Mauersberger, R. 2013, A&A, 549, A90 (Cited on pages 11, 12, 13, 15, 16, 51 and 57.)

Henkel, C., Wilson, T. L., & Bieging, J. 1982, A&A, 109, 344 (Cited on pages 5, 48 and 77.)

Henkel, C., Wilson, T. L., Langer, N., Chin, Y. N., & Mauersberger, R. 1994, in The Structure and Content of Molecular Clouds, ed. T. L. Wilson & K. J. Johnston, Vol. 439, 72–88 (Cited on pages 1 and 5.)

Henkel, C., Wilson, T. L., Walmsley, C. M., & Pauls, T. 1983, A&A, 127, 388 (Cited on pages 5, 48 and 77.)

Ho, P. T. P. & Townes, C. H. 1983, ARA&A, 21, 239 (Cited on pages 7 and 11.)

Hoffman, I. M. 2012, ApJ, 759, 76 (Cited on pages 12, 13 and 16.)

Hoffman, I. M., Goss, W. M., & Palmer, P. 2007, ApJ, 654, 971 (Cited on page 61.)

Hoffman, I. M. & Joyce, S. A. 2014, ApJ, 782, 83 (Cited on pages 12 and 16.)

Hogge, T. G., Jackson, J. M., Allingham, D., et al. 2019, ApJ, 887, 79 (Cited on pages 12 and 16.)

Hoyle, F. 1946, MNRAS, 106, 384 (Cited on page 3.)

Hoyle, F. 1954, ApJS, 1, 121 (Cited on page 3.)

Humire, P. K., Thiel, V., Henkel, C., et al. 2020, A&A, 642, A222 (Cited on pages 6 and 78.)

Hunter, T. R., Brogan, C. L., Indebetouw, R., & Cyganowski, C. J. 2008, ApJ, 680, 1271 (Cited on pages 12 and 16.)

Imai, H., Omi, R., Kurayama, T., et al. 2011, PASJ, 63, 1293 (Cited on page 53.)

Jacob, A. M., Menten, K. M., Wiesemeyer, H., et al. 2020, A&A, 640, A125 (Cited on page 6.)

Jansky, K. 1932, Proceedings of the Institute of Radio Engineers, 20, 1920 (Cited on page 17.)

Jansky, K. G. 1933a, Popular Astronomy, 41, 548 (Cited on page 17.)

Jansky, K. G. 1933b, Nature, 132, 66 (Cited on page 17.)

Keene, J., Schilke, P., Kooi, J., et al. 1998, ApJ, 494, L107 (Cited on pages 48 and 77.)

Kobayashi, C., Karakas, A. I., & Lugaro, M. 2020, ApJ, 900, 179 (Cited on pages 5, 45, 47, 48, 49 and 79.)

Kobayashi, C., Karakas, A. I., & Umeda, H. 2011, MNRAS, 414, 3231 (Cited on pages 45, 47 and 48.)

Kobayashi, C., Tsujimoto, T., & Nomoto, K. 2000, ApJ, 539, 26 (Cited on page 48.)

Kraemer, K. E. & Jackson, J. M. 1995, ApJ, 439, L9 (Cited on pages 12 and 16.)

Kroupa, P. 2001, MNRAS, 322, 231 (Cited on page 48.)

Kroupa, P. 2008, in Astronomical Society of the Pacific Conference Series, Vol. 390, Pathways Through an Eclectic Universe, ed. J. H. Knapen, T. J. Mahoney, & A. Vazdekis, 3 (Cited on page 48.)

Kukolich, S. G. 1967, Physical Review, 156, 83 (Cited on page 7.)

Langer, N. 1989, A&A, 210, 93 (Cited on page 6.)

Langer, W. D. & Penzias, A. A. 1990, ApJ, 357, 477 (Cited on pages 5, 48 and 77.)

Langer, W. D. & Penzias, A. A. 1993, ApJ, 408, 539 (Cited on page 48.)

Laughton, D., Freund, S. M., & Oka, T. 1976, Journal of Molecular Spectroscopy, 62, 263 (Cited on page 7.)

Liebe, H. J. 1981, Radio Science, 16, 1183 (Cited on page 20.)

Linke, R. A. & Goldsmith, P. F. 1980, ApJ, 235, 437 (Cited on page 43.)

Lu, X., Mills, E. A. C., Ginsburg, A., et al. 2019, ApJS, 244, 35 (Cited on page 61.)

Madden, S. C., Irvine, W. M., Matthews, H. E., Brown, R. D., & Godfrey, P. D. 1986, ApJ, 300, L79 (Cited on pages 12, 13, 16 and 51.)

Mangum, J. G. & Wootten, A. 1994, ApJ, 428, L33 (Cited on pages 12 and 16.)

Mauersberger, R., Henkel, C., Langer, N., & Chin, Y. N. 1996, A&A, 313, L1 (Cited on pages 6, 46 and 78.)

Mauersberger, R., Henkel, C., & Wilson, T. L. 1987, A&A, 173, 352 (Cited on pages 11, 12, 13 and 16.)

Mauersberger, R., Ott, U., Henkel, C., Cernicharo, J., & Gallino, R. 2004, A&A, 426, 219 (Cited on page 6.)

Mauersberger, R., Wilson, T. L., & Henkel, C. 1986, A&A, 160, L13 (Cited on pages 11 and 13.)

Mauersberger, R., Wilson, T. L., & Henkel, C. 1988, A&A, 201, 123 (Cited on pages 12, 13 and 16.)

McCarthy, T. P., Breen, S. L., Kaczmarek, J. F., et al. 2023, MNRAS, 522, 4728 (Cited on page 16.)

McEwen, B. C., Pihlström, Y. M., & Sjouwerman, L. O. 2016, ApJ, 826, 189 (Cited on pages 12, 15 and 16.)

McGrath, E. J., Goss, W. M., & De Pree, C. G. 2004, ApJS, 155, 577 (Cited on page 61.)

McMullin, J. P., Waters, B., Schiebel, D., Young, W., & Golap, K. 2007, in Astronomical Society of the Pacific Conference Series, Vol. 376, Astronomical Data Analysis Software and Systems XVI, ed. R. A. Shaw, F. Hill, & D. J. Bell, 127 (Cited on page 56.)

Mehringer, D. M., Goss, W. M., & Palmer, P. 1994, ApJ, 434, 237 (Cited on page 61.)

Mei, Y., Chen, X., Shen, Z.-Q., & Li, B. 2020, ApJ, 898, 157 (Cited on pages 12, 13, 16 and 51.)

Menten, K. M. 1991, ApJ, 380, L75 (Cited on page 11.)

Menten, K. M., Reid, M. J., Forbrich, J., & Brunthaler, A. 2007, A&A, 474, 515 (Cited on page 11.)

Meyer, B. S. 1994, ARA&A, 32, 153 (Cited on pages 1 and 5.)

Milam, S. N., Savage, C., Brewster, M. A., Ziurys, L. M., & Wyckoff, S. 2005, ApJ, 634, 1126 (Cited on pages 5, 48 and 77.)

Mills, E. A. C., Ginsburg, A., Clements, A. R., et al. 2018, ApJ, 869, L14 (Cited on pages 11, 12, 13 and 16.)

Morris, M., Zuckerman, B., Palmer, P., & Turner, B. E. 1973, ApJ, 186, 501 (Cited on page 7.)

Müller, H. S. P., Schlöder, F., Stutzki, J., & Winnewisser, G. 2005, Journal of Molecular Structure, 742, 215 (Cited on pages 13 and 42.)

Oka, T., Shimizu, F. O., Shimizu, T., & Watson, J. K. G. 1971, ApJ, 165, L15 (Cited on page 7.)

Ott, M., Witzel, A., Quirrenbach, A., et al. 1994, A&A, 284, 331 (Cited on page 37.)

Perley, R. A. & Butler, B. J. 2013, ApJS, 204, 19 (Cited on pages 38, 39 and 69.)

Perley, R. A. & Butler, B. J. 2017, ApJS, 230, 7 (Cited on page 69.)

Pety, J. 2005, in SF2A-2005: Semaine de l'Astrophysique Francaise, ed. F. Casoli, T. Contini, J. M. Hameury, & L. Pagani, 721 (Cited on page 56.)

Pickett, H. M., Poynter, R. L., Cohen, E. A., et al. 1998, J. Quant. Spec. Rad. Trans., 60, 883 (Cited on page 13.)

Pilkington, K., Few, C. G., Gibson, B. K., et al. 2012, A&A, 540, A56 (Cited on page 5.)

Pratap, P., Menten, K. M., Reid, M. J., Moran, J. M., & Walmsley, C. M. 1991, ApJ, 373, L13 (Cited on pages 11, 13 and 15.)

Reid, M. J., Menten, K. M., Brunthaler, A., et al. 2019, ApJ, 885, 131 (Cited on pages 11, 42 and 77.)

Reid, M. J., Menten, K. M., Brunthaler, A., et al. 2014, ApJ, 783, 130 (Cited on pages 11, 42 and 77.)

Reid, M. J., Menten, K. M., Zheng, X. W., et al. 2009a, ApJ, 700, 137 (Cited on pages 42 and 77.)

Reid, M. J., Menten, K. M., Zheng, X. W., Brunthaler, A., & Xu, Y. 2009b, ApJ, 705, 1548 (Cited on pages 11 and 55.)

Ritchey, A. M., Federman, S. R., & Lambert, D. L. 2015, ApJ, 804, L3 (Cited on page 48.)

Rohlfs, K. & Wilson, T. L. 2004, Tools of radio astronomy (Cited on pages 17 and 21.)

Romano, D., Magrini, L., Randich, S., et al. 2021, A&A, 653, A72 (Cited on pages 49 and 79.)

Rosenkranz, P. W. 1998, Radio Science, 33, 919 (Cited on page 20.)

Savage, C., Apponi, A. J., Ziurys, L. M., & Wyckoff, S. 2002, ApJ, 578, 211 (Cited on pages 5, 48 and 77.)

Schilke, P., Walmsley, C. M., & Mauersberger, R. 1991, A&A, 247, 516 (Cited on pages 11 and 13.)

Schuller, F., Menten, K. M., Contreras, Y., et al. 2009, A&A, 504, 415 (Cited on page 64.)

Snell, R. L. 2015, in Encyclopedia of Astrobiology, ed. M. Gargaud, W. M. Irvine, R. Amils, I. Cleaves, Henderson James (Jim), D. L. Pinti, J. C. Quintanilla, D. Rouan, T. Spohn, S. Tirard, & M. Viso, 1244–1251 (Cited on page 2.)

Thielemann, F. K. & Arnett, W. D. 1985, ApJ, 295, 604 (Cited on page 6.)

Thompson, A. R., Moran, J. M., & Swenson, George W., J. 2017, Interferometry and Synthesis in Radio Astronomy, 3rd Edition (Cited on pages 17, 20 and 21.)

Timmes, F. X., Woosley, S. E., & Weaver, T. A. 1995, ApJS, 98, 617 (Cited on pages 1 and 4.)

Tolman, R. C. 1924, Phys. Rev., 23, 693 (Cited on page 8.)

Towner, A. P. M., Brogan, C. L., Hunter, T. R., & Cyganowski, C. J. 2021, ApJ, 923, 263 (Cited on pages 12 and 16.)

Townes, C. H. & Schawlow, A. L. 1955, Microwave Spectroscopy (Cited on page 7.)

Townes, C. H. & Schawlow, A. L. 1975, Microwave spectroscopy. (Cited on page 7.)

Urquhart, J. S., Morgan, L. K., Figura, C. C., et al. 2011, MNRAS, 418, 1689 (Cited on pages 12, 16, 64 and 66.)

Vlemmings, W. H. T., Diamond, P. J., & van Langevelde, H. J. 2002, A&A, 394, 589 (Cited on page 71.)

Walmsley, C. M. & Ungerechts, H. 1983, A&A, 122, 164 (Cited on pages 8 and 11.)

Walsh, A. J., Breen, S. L., Britton, T., et al. 2011, MNRAS, 416, 1764 (Cited on pages 12 and 16.)

Walsh, A. J., Longmore, S. N., Thorwirth, S., Urquhart, J. S., & Purcell, C. R. 2007, MNRAS, 382, L35 (Cited on pages 12, 13 and 16.)

Wang, K., Zhang, Q., Wu, Y., Li, H.-b., & Zhang, H. 2012, ApJ, 745, L30 (Cited on pages 12 and 16.)

Whiteoak, J. B. & Gardner, F. F. 1979, MNRAS, 188, 445 (Cited on page 5.)

Wielebinski, R. 2009, A&A, 500, 245 (Cited on page 18.)

Wienen, M., Wyrowski, F., Menten, K. M., et al. 2018, A&A, 609, A125 (Cited on page 64.)

Wienen, M., Wyrowski, F., Schuller, F., et al. 2012, A&A, 544, A146 (Cited on page 64.)

Wilson, T. L., Batrla, W., & Pauls, T. A. 1982, A&A, 110, L20 (Cited on pages 1, 11, 13 and 16.)

Wilson, T. L., Bieging, J., Downes, D., & Gardner, F. F. 1976, A&A, 51, 303 (Cited on page 5.)

Wilson, T. L. & Henkel, C. 1988, A&A, 206, L26 (Cited on page 11.)

Wilson, T. L., Johnston, K. J., & Henkel, C. 1990, A&A, 229, L1 (Cited on page 11.)

Wilson, T. L., Rohlfs, K., & Hüttemeister, S. 2013, Tools of Radio Astronomy (Cited on pages 17, 20, 21 and 22.)

Wilson, T. L. & Rood, R. 1994, ARA&A, 32, 191 (Cited on pages 1, 4, 5 and 48.)

Wilson, T. L. & Schilke, P. 1993, in Astrophysical Masers, ed. A. W. Clegg & G. E. Nedoluha, Vol. 412, 123–126 (Cited on page 11.)

Winkel, B., Kraus, A., & Bach, U. 2012, A&A, 540, A140 (Cited on page 37.)

Woosley, S. E. & Weaver, T. A. 1995, ApJS, 101, 181 (Cited on page 6.)

Wouterloot, J. G. A. & Brand, J. 1996, A&AS, 119, 439 (Cited on pages 5, 48 and 77.)

Yan, Y. T., Henkel, C., Kobayashi, C., et al. 2023, A&A, 670, A98 (Cited on pages 44, 45, 47, 48, 205 and 207.)

Yan, Y. T., Henkel, C., Menten, K. M., et al. 2022a, A&A, 666, L15 (Cited on pages 16, 55, 57, 59, 60, 61, 66, 205 and 206.)

Yan, Y. T., Henkel, C., Menten, K. M., et al. 2022b, A&A, 659, A5 (Cited on pages 16, 52, 53, 66 and 205.)

Yan, Y. T., Henkel, C., Menten, K. M., et al. 2024, A&A, 686, A205 (Cited on pages 16 and 68.)

Yan, Y. T., Zhang, J. S., Henkel, C., et al. 2019, ApJ, 877, 154 (Cited on pages 6, 48 and 77.)

Yu, H. Z., Zhang, J. S., Henkel, C., et al. 2020, ApJ, 899, 145 (Cited on pages 6, 7 and 78.)

Zhang, J. S., Liu, W., Yan, Y. T., et al. 2020, ApJS, 249, 6 (Cited on page 48.)

Zhang, Q. & Ho, P. T. P. 1995, ApJ, 450, L63 (Cited on pages 12 and 16.)

Zhang, Q., Hunter, T. R., Sridharan, T. K., & Cesaroni, R. 1999, ApJ, 527, L117 (Cited on pages 12 and 16.)

Zheng, X. W., Moran, J. M., & Reid, M. J. 2000, MNRAS, 317, 192 (Cited on page 53.)

Nomenclature

Frequently Used Acronyms

AGB	Asymptotic giant branch
APEX	Atacama Pathfinder Experiment
ATLASGAL	APEX Telescope Large Area Survey of the Galaxy
BeSSeL	Bar and Spiral Structure Legacy
CNO	Carbon-nitrogen-oxygen
CMZ	Central molecular zone
CNM	Cold neutral medium
FWHM	Full width at half maximum
GCE	Galactic chemical evolution
HPBW	Half power beam width
HMSFRs	High-mass star-forming regions
HIM	Hot ionized medium
ISM	Interstellar medium
IMF	Initial mass function
JVLA	Karl G. Jansky Very Large Array
LSR	Local standard of rest
LTE	Local Thermodynamic Equilibrium
Maser	Microwave Amplification by Stimulated Emission of Radiation
PA	Position angle
PWV	Precipitable water vapor
RMS	Red MSX Source survey
S/N	Signal-to-noise ratio
UC	Ultra-compact
UV	Ultraviolet
WIM	Warm ionized medium
WNM	Warm neutral medium

Physical Constants

Speed of light in vacuum	$c = 2.99792458 \times 10^{8}\,\mathrm{m\,s^{-1}}$
Planck constant	$h = 6.62607015 \times 10^{-34}\,\mathrm{J\,Hz^{-1}}$=$6.62607015 \times 10^{-27}\,\mathrm{erg\,s}$
Boltzmann constant	$k_\mathrm{B} = 1.380649 \times 10^{-23}\,\mathrm{J\,K^{-1}}$= $1.380649 \times 10^{-16}\,\mathrm{erg\,K^{-1}}$
Electron mass	$m_\mathrm{e} = 9.1093837015 \times 10^{-31}\,\mathrm{kg}$
Proton mass	$m_\mathrm{p} = 1.67262192369 \times 10^{-27}\,\mathrm{kg}$
Proton-electron mass ratio	$m_\mathrm{p}/m_\mathrm{e}$=1836.152673

Astronomical Constants

Astronomical unit (1 AU)	$= 1.495978707 \times 10^{11}\,\mathrm{m}$
Parcec (1 pc)	$= 2.06 \times 10^{5}\,AU = 3.086 \times 10^{18}\,\mathrm{cm}$
Solar mass ($1\,\mathrm{M_\odot}$)	$= 1.989 \times 10^{27}\,\mathrm{gr}$
Solar luminosity ($1\,\mathrm{L_\odot}$)	$= 3.9 \times 10^{33}\,\mathrm{erg\,s^{-1}}$
Jansky (1 Jy)	$= 10^{-23}\,\mathrm{erg\,s^{-1}\,cm^{-2}\,Hz^{-1}}$

List of Figures

List of Tables

Acknowledgements

"Heaven has made us talents, we're not made in vain. A thousand gold coins spent, more will turn up again. (天生我材必有用，千金散尽还复来。)" As said by Li Bai (李白), a poet during the Tang dynasty around 1300 years ago, I also believe in myself that I should be useful in some way to human beings. Now I am very close to finishing my Ph.D. thesis, which has provided some little information to help us better understand the universe. Getting to this point would not have been possible without the help of many people. I would like to sincerely thank them.

First of all, I want to thank Prof. Dr. Karl M. Menten, who invited me to join the International Max-Planck Research School (IMPRS) and offered me the position as a doctoral student in his research department at the Max-Planck-Institute for Radio Astronomy (MPIfR) in Bonn as well as at the University of Bonn. Thank you very much for your understanding and for providing me with a six-month scholarship and also language lessons during the difficulties of this thesis. I also want to thank you for your useful suggestions and comments on my observational proposals and published papers.

I want to thank Prof. Dr. Pavel Kroupa agreed to be my second advisor as well as a member of my thesis committee. I would also like to thank Prof. Dr. Klaus Desch and Prof. Dr. Florian Bernard are willing to be my thesis committee members.

A special thanks to my day-to-day supervisor, Dr. Christian Henkel. You are always enthusiastic and amiable. I enjoyed the conversations with you and eager mores. I can always learn something after talking with you. I am grateful for your guidance on my research, not only for my Ph.D. works at the MPIfR but also for my Master's studies at Guangzhou University. I also want to thank you for your invitation to me to come to Bonn for this Ph.D. thesis. Thanks to your foresight, we found the new ammonia masers in the Milky Way. I also want to thank you for your help on my application for the scholarship from the China Scholarship Council (CSC). Furthermore, I kindly thank you for your contacts with other excellent scientists in the world and for expanding my networks in astronomical research.

I want to thank the China Scholarship Council (CSC) for the financial support for the first three years. Many thanks to Dr. Christian Henkel and Prof. Dr. Karl M. Menten from the MPIfR, Prof. Dr. Jiangshui Zhang and Prof. Dr. Junhui Fan from Guangzhou University, and Prof. Dr. Junzhi Wang from the Guangxi University, for their support on my application of the CSC scholarship. I also want to thank Prof. Dr. Jun-ichi Nakashima from Sun Yat-sen University, for his help on my application for the Ph.D. project at the MPIfR.

It has been exactly ten years since I first had a connection with radio astronomy. I would like to thank my former supervisor, Prof. Dr. Jiangshui Zhang from Guangzhou University. You gave me a lot of chances to perform scientific observations with the Shanghai Tianma radio 65-m telescope (TMRT), the ARO 12-m telescope, the SMT 10-m telescope, and the Arecibo 305-m telescope, even when I was an undergraduate

student. Thank you for your guidance during my Master's studies and for establishing my connection with Dr. Christian Henkel. I also want to thank you for encouraging me to apply for the Ph.D. project at the MPIfR.

Time flies. I enjoyed a lot for the duration of this important part of my life at the MPIfR. As a foreigner, I was quickly suitable to live here. All these cannot come out without help from Eva Schmelmer, Barbara Menten, and Tuyet-Le Tran. I want to thank you for your help with my applications for my resident permit and for searching for apartments. The colleagues at the MPIfR are always friendly. I would like to thank Dr. Yan Gong, Dr. Nina Brinkmann, Dr. Hans Nguyen, Dr. Arshia Maria Jacob, Dr. Maitraiyee Tiwari, Dr. Rohit Dokara, Liang-Hao Lin, Dr. Yali Shao, Dr. Wenjin Yang, Dr. Aiyuan Yang, Dr. Gang Wu, Dr. Si-Yue Yu, Dr. Su Yao, Dr. Chang-Hui (Rosie) Chen, Dr. Xiao-Tian Xu and Dr. Huanchen Hu. It was a pleasure to meet you. Special thanks to my officemates, Nina and Hans, for your kindness and for making the office laugh. Thanks to my friend and cycling partner, Rongchuan Zhao, it was a great time between September 2022 and February 2023, we cycled more than 10 times from Koeln to Bonn with a total distance of 40 kilometers. I got not only fresh air but also fresh minds.

Collaboration with many excellent scientists in the world makes me grow up and have a lot of fun in astronomy and astrophysics. I kindly thank Dr. Thomas L. Wilson and Prof. Dr. Alwyn Wootten. You are always patient and provide useful suggestions and comments on my papers and observational proposals. I also want to thank you for your support, whenever I asked for you, you were always willing to write recommendation letters for me.

To get this so far is impossible without the support of my parents, Yan Maichao (闫麦朝) and Yang Xiangjuan (杨香娟). I love both of you very much! I want to thank you for raising me and supporting my studies. Especially, you did not push me anything in my studies and always trusted and supported my choices. I will never forget the moment that I saw the surface of the Moon for the first time with my naked eyes through my first optical telescope with a diameter of 70 mm. Thank you for letting me own a telescope when I was a high school student.

Ultimately, I want to thank a very very very very very very very special person, my fiancée, Siqi Guo (郭思祺). As foreigners, we met in Germany, supported, and fell in love with each other. I am grateful and enjoy living with you every day. The biggest motivation to finish this Ph.D. thesis was your encouragement and support. I can't imagine how I have overcome all of the difficulties without you, especially during the pandemic period. You and our lovely girl (cat), Naicha (奶茶), can always make me happy and feel no stress. I want to tell you I love you so much and will absolutely love you forever. Let's move on to the next stage of our lives and keep going for a better livelihood.